Durham E-Theses

Induced seismicity and environmental change at the geysers geothermal area in California.

Gunasekera, Rashmin C.

How to cite:

Gunasekera, Rashmin C. (2001) *Induced seismicity and environmental change at the geysers geothermal area in California.*, Durham theses, Durham University. Available at Durham E-Theses Online: http://etheses.dur.ac.uk/3817/

Use policy

The full-text may be used and/or reproduced, and given to third parties in any format or medium, without prior permission or charge, for personal research or study, educational, or not-for-profit purposes provided that:

- a full bibliographic reference is made to the original source
- a link is made to the metadata record in Durham E-Theses
- the full-text is not changed in any way

The full-text must not be sold in any format or medium without the formal permission of the copyright holders.

Please consult the full Durham E-Theses policy for further details.

Academic Support Office, Durham University, University Office, Old Elvet, Durham DH1 3HP
e-mail: e-theses.admin@dur.ac.uk Tel: +44 0191 334 6107
http://etheses.dur.ac.uk

Induced Seismicity and Environmental Change at The Geysers Geothermal Area in California.

Rashmin C. Gunasekera

The copyright of this thesis rests with the author. No quotation from it should be published in any form, including Electronic and the Internet, without the author's prior written consent. All information derived from this thesis must be acknowledged appropriately.

A thesis submitted in partial fulfilment of the requirements for the degree of Doctor of Philosophy

Department of Geological Sciences

University of Durham

November 2001

19 APR 2002

Abstract

Intensive exploitation of the reservoir at The Geysers geothermal area, California, induces myriads of small-magnitude earthquakes that are monitored by a dense, permanent seismometer network that covers most of the reservoir. However, majority of the seismic stations, which belong to the UNOCAL network are poorly calibrated. Station polarities, and sensor orientations for the 8 three-component stations of this network were determined by using accurate focal mechanism solutions from a temporary network and using a simple method of observing the waveform from known earthquake locations.

Using data from the UNOCAL network, tomographic inversions were performed for the three-dimensional *Vp* and *Vp/Vs*-ratio structure of the reservoir for February 1993, October 1996 and August 1998, adding to the inversions for April 1991 and December 1994 that had already been performed by other investigators. The extensive low-*Vp/Vs* anomaly known to characterise the reservoir grew progressively in strength from a maximum of 9% to a maximum of 12.4% at sea level during the seven-year study period.

The anomaly growth is attributed to the depletion of pore liquid water in the reservoir and its replacement with steam. This causes *Vp* to decrease by increasing compressibility, and *Vs* to increase because of the reduction in pore pressure and the drying of argillaceous minerals, e.g., illite, which increases the shear modulus. All these effects serendipitously combine to lower the *Vp/Vs* ratio, resulting in an exceptionally strong overall effect that provides a convenient tool for monitoring reservoir depletion in the seismogenic zone. Variations in the separate *Vp* and *Vs* fields indicate that water depletion was the most important process in the central part of the exploited reservoir, and that pressure reduction and mineral drying were the dominant effects more northwesterly and southeasterly.

Relative relocation of microearthquakes was also performed using the same network. Four regions were studied. Although most multiplets relocated into tighter clusters and the reduction in the RMS of the relative relocations was good, further work is needed to substantiate these initial findings.

Declaration

I declare that this thesis, which I submit for the degree of Doctor of Philosophy at the University of Durham, UK is my own work and is not substantially the same as any which has previously been submitted for a degree at this or any other university.

Rashmin Chaminda Gunasekera
University of Durham
November 2001

Copyright © 2001 by Rashmin Chaminda Gunasekera
The copyright of this thesis rests with the author. No quotation from it should be published without his prior written consent and information derived from it should be acknowledged.

Dedicated to

Lisa Lau Ee Jia

Acknowledgments

I would like to thank:

My supervisors Gill Foulger and Bruce Julian for providing invaluable advice, guidance and support during my research.

Jean-Luc Got at Universite of Savoie, for all the advice, help and enabling me to carry out research work on relative relocations.

Doug Neuhauser at NCEDC for providing raw seismograms used in the study and for trouble shooting.

Mitch Stark at Calpine Corporation for providing information and answering all my queries.

Stanford University Geothermal program and Geothermal Resources Council for providing useful information.

Mike Rymer at the USGS for encouragement and information regarding The Geysers-Clear Lake area.

Phil Dawson at the USGS for advice and useful comments and making my stay at the USGS and in the US a pleasure.

Charlotte Rowe at New Mexico Tech. for useful discussions, advice and comments on relative relocation of multiplets.

Greg Boitnott at New England Research Inc. for providing information and for his interest in my work.

Lisa Lau for patience, understanding, tolerating me and invaluable help, without which this thesis would not be a reality.

My parents and brother for all their support, encouragement, their belief in me and facilitating this research.

Alwyn Ross, Angus Miller, David Barton, Matt Prichard and Konstantinos Konstantinou for explanations, advice, help and making my research work so much easier.

Pedro Rocha for keeping me on track, useful discussions and encouragement.

Donald and Bhadra Gaminithilake for all their interest, help and support in my work.

Abigail Brailey, Jens Lamping, Abdurrazaq Ushah and James Day for being great office mates and showing interest in my research.

Alan, Gernot, Larus, Tim, Gareth, Corinne and Asta for the US and French experience.

Staff at the Department of Geological Sciences and Information Technology Service at University of Durham, Earthquake Hazards Team at US Geological Survey and Laboratoire de Geophysique Interne et Tectonophysique at Universite de Savoie for all their help and making this research possible.

Collingwood College and the Graduate Society at University of Durham, Teikyo University of Japan in Durham, Universite de Savoie and Bruce Julian for providing accommodation.

(Picture of Poseidon: *source unknown*)

"In Nature's infinite book of secrecy
A little I can read"
(Shakespeare W., *Antony and Cleopatra,* II.1.10-11)

LIST OF CONTENTS

CHAPTER 1

INTRODUCTION

1.1 Overview..... 1

1.2 Tectonic evolution..... 1

1.2.1 Tectonics of Northern California..... 1

1.2.2 Seismicity in Northern California..... 4

1.2.3 Tectonics of The Geysers..... 7

1.3 Geology..... 9

1.3.1 Regional Geology..... 9

1.3.2 Geology at The Geysers 12

1.3.3 Formation and evolution..... 14

1.4 Geophysical studies at The Geysers..... 16

1.5 Commercial development of The Geysers..... 22

1.5.1 History of commercial activity at The Geysers..... 22

1.5.2 Commercial exploitation of The Geysers..... 26

1.5.3 Reinjection of water to the reservoir..... 29

1.6 Seismicity at The Geysers..... 33

1.6.1 History of seismic monitoring at The Geysers..... 33

1.6.2 Seismicity within the reservoir..... 34

1.6.3 Processes that induce earthquakes at The Geysers..... 40

1.6.4 Seismic networks at The Geysers..... 41

1.6.5 Tomography studies at The Geysers..... 44

1.7 Summary..... 47

CHAPTER 2

STATION ORIENTATION AND POLARITY DETERMINATION

2.1 Background to the study..... 49

2.1.1 Introduction..... 49
2.1.2 Background to the UNOCAL and IRIS networks..... 51
2.1.2.1 The UNOCAL network..... 51
2.1.2.2. The IRIS network..... 52
2.1.3 Polarity determination 53
2.1.3.1 Use of moment tensor solutions..... 53
2.1.3.2 Quality of moment tensor solutions..... 53
2.1.4 Station orientation..... 54
2.2 Theory..... 55
2.3 Method..... 56
2.3.1 Method of finding station polarity..... 56
2.3.2 Method of finding sensor orientation..... 58
2.4 Results..... 59
2.4.1 Polarity determination..... 59
2.4.2 Sensor orientation..... 68
2.5 Summary..... 75

CHAPTER 3

TOMOGRAPHY THEORY AND RESULTS

3.1 Background..... 76
3.2 Local Earthquake Tomography (LET) theory..... 76
3.2.1 Introduction to LET..... 76
3.2.2 LET Theory 78
3.2.2.1 Introduction..... 78
3.2.2.2 The velocity structure representation..... 80
3.2.2.3 Calculation of the travel-times and ray-paths..... 81
3.2.2.4 Hypocentre-velocity coupling and the method of inversion. 82
3.2.2.5 The effect of inclusion of *S*-waves..... 84
3.2.2.6 Assessment of the quality of the solution..... 84
3.3 Method..... 85

3.3.1 The network and data used for the study..... 85
3.3.2 *autopick*..... 86
3.3.3 *epick*..... 87
3.3.4 The initial 1-D and 3-D velocity models for The Geysers..... 87
3.3.5 *SIMULPS12*..... 90
3.3.5.1 Program parameters..... 90
3.3.5.2 The inversion procedure..... 93
3.3.5.3 Selection of damping parameters..... 94
3.3.5.4 Terminating the inversion..... 95
3.3.6 Model resolution..... 95
3.3.6.1 Derivative-weight sum..... 96
3.3.6.2 Spread function..... 97
3.4 Results..... 98
3.4.1 Recording of earthquakes at stations and distribution 98
3.4.1.1 Recording of events..... 98
3.4.1.2 Event distribution..... 98
3.4.1.3 Relocated events..... 106
3.4.2 Damping trade-off curves..... 106
3.4.3 Results..... 110
3.4.3.1 *Vp*, *Vs* and *Vp/Vs* anomalies in April 1991..... 110
3.4.3.2 Temporal variations in *Vp* and *Vs* between 1991 and 1998 115
3.4.3.3 Spatial variations in *Vp/Vs* between 1991 and 1998..... 115
3.4.4 Resolution of quality of results..... 116
3.4.5 Results of other inversion strategies..... 117
3.5 Summary..... 117

CHAPTER 4

RELATIVE RELOCATION OF MICROEARTHQUAKES

4.1 Background..... 120

4.2 Method..... 121

4.2.1 Multiplet selection and the coherency matrix..... 121

4.2.2 Theoretical relative relocation and time-delay calculation..... 124

4.3 Data and processing..... 126

4.3.1 The seismic data used..... 126

4.3.1.1 Seismic event selection 126

4.3.1.2 Multiplet event selection..... 128

4.3.2 The coherency matrix..... 131

4.3.3 Time-delay computation and relative relocation..... 131

4.4 Results..... 133

4.4.1 Introduction..... 133

4.4.2 Region sr001..... 135

4.4.3 Region sr002..... 148

4.4.4 Region sr003..... 159

4.4.5 Region sr004..... 170

4.4.6 Multiplet event distribution with time..... 182

4.5 Summary..... 186

CHAPTER 5

DISCUSSION AND CONCLUSIONS

5.1 Background..... 188

5.1.1 Commercial Development of The Geysers..... 188

5.1.2 Seismicity and well activity..... 190

5.1.3 Political implications for The Geysers area..... 190

5.2 Station polarity determination and calibration..... 191

5.3 4-D Local Earthquake Tomography..... 193

5.3.1 Local earthquake tomography at The Geysers..... 193
5.3.2 Development in integrated *Vp*, *Vs* and *Vp/Vs* anomalies..... 194
5.3.3 Causes of the *Vp/Vs* anomalies..... 196
5.3.4 The 1994 results..... 198
5.3.5 Variation in results of *Vp*, *Vs* over *Vp/Vs*..... 201
5.3.6 Interpretation of the growing *Vp/Vs* anomaly at The Geysers..... 203
5.3.7 Comparison with LET at Mammoth Mountain..... 205
5.4 Relative relocation of multiplets 206
5.4.1 Errors in relative relocations..... 206
5.4.2 Different velocity models 208
5.4.3 Attenuation or tremor microcosms..... 210
5.4.4 Station effects..... 212
5.4.5 Interpretation of relative relocation results..... 212
5.4.6 Relation between commercial activity and multiplets..... 213
5.4.7 Comparison with other methods of relative relocation..... 216
5.5 Future work..... 217
5.6 Conclusions..... 218

BIBLIOGRAPHY..... 220

Appendix 1 Station coordinates of seismic networks..... 231
Appendix 2 Script for program *Staor.sh*..... 233
Appendix 3 Example of seismic picks and *epick* program..... 236
Appendix 4 SIMULPS212 program..... 237
Appendix 5 Location of events used in tomographic inversion..... 239
Appendix 6 Final *Vp* and *Vp/Vs* models from 1991 to 1998..... 262
Appendix 7 Output of program *rms* for main multiplets..... 272
Appendix 8 waveform for selected stations for main multiplets..... 274

LIST OF FIGURES

CHAPTER 1
INTRODUCTION

Figure 1.01: The interaction of plate tectonics in northern California..... 3
Figure 1.02: Schematic diagram of plate interaction in northern California..... 4
Figure 1.03: Tectonic environment of coastal northern California..... 4
Figure 1.04: Seismicity near the Mendocino Triple Junction..... 6
Figure 1.05: Regional seismicity in California..... 7
Figure 1.06: Cross-section of regional seismicity in California..... 7
Figure 1.07: Reservoir boundary of The Geysers geothermal area..... 9
Figure 1.08: Extrusion of magma under The Geysers..... 11
Figure 1.09: Geological units at The Geysers..... 12
Figure 1.10: Vertical structural model of The Geysers..... 14
Figure 1.11: Conceptual model for The Geysers reservoir..... 14
Figure 1.12: Map of the subsurface batholith..... 16
Figure 1.13: Digital Elevation Model (DEM) of The Geysers area..... 18
Figure 1.14: Regional gravity and magnetic maps of The Geysers area..... 19
Figure 1.15: Model for The Geysers from gravity and magnetic data..... 21
Figure 1.16: Pressure contoured map of The Geysers area..... 21
Figure 1.17: View of The Geysers resort complex..... 22
Figure 1.18: Process of geothermal electricity production..... 24
Figure 1.19: Schematic diagram steam extraction..... 24
Figure 1.20: PG&E power plant units 5 and 6 at The Geysers..... 25
Figure 1.21: Development and proprietors at The Geysers..... 25
Figure 1.22: Power plants at The Geysers..... 26
Figure 1.23: Commercial development at The Geysers with time..... 28
Figure 1.24: Extraction of steam and daily flowing wellhead pressure..... 30
Figure 1.25: Injection rates at The Geysers with time..... 31
Figure 1.26: Monthly average injection rates at SEGEP..... 31
Figure 1.27: Ratio of injection to extraction of steam..... 33
Figure 1.28: An injection well at The Geysers geothermal area..... 33
Figure 1.29: Relationship between seismicity and volume injected..... 34
Figure 1.30: Biannual seismicity at The Geysers with time..... 39
Figure 1.31: Relationship between steam flow rate and seismicity..... 40
Figure 1.32: Seismometer networks at The Geysers..... 43

CHAPTER 2
STATION ORIENTATION AND POLARITY DETERMINATION

Figure 2.01: Map of UNOCAL, IRIS and CALNET stations..... 51
Figure 2.02: Difficulty of empirically deducing nodal planes..... 52
Figure 2.03: Diagram of amplitude ratios of horizontal components..... 56
Figure 2.04: The affect on azimuth by different polarities..... 57
Figure 2.05: Affect of good focal sphere coverage..... 59
Figure 2.06: Map of events used in polarity determination..... 61
Figure 2.07: Polarity determination plots..... 62
Figure 2.08: Percentage of consistent polarity results..... 66
Figure 2.09: Map of determined polarities for U-N-T stations..... 70
Figure 2.10: Calculated orientations of sensors..... 71
Figure 2.11: Location of events used in sensor orientation..... 74
Figure 2.12: Orientation of UNOCAL 3-component stations..... 75

CHAPTER 3
TOMOGRAPHY THEORY AND RESULTS

Figure 3.01: Map of tomographic grid and stations..... 78
Figure 3.02: Diagram of velocity structure representation..... 82
Figure 3.03: Sketches of minimum travel time ray paths..... 83
Figure 3.04 An example of P and S wave picks..... 89
Figure 3.05: The starting one-dimensional model of The Geysers..... 90
Figure 3.06: *Vp* and *Vp/Vs* model of Ross (1996)..... 92
Figure 3.07: Nodal configurations in a "graded" inversion..... 95
Figure 3.08: Number of P- and S-waves used in inversions..... 100
Figure 3.09: Map and cross-sections of final locations..... 102
Figure 3.10: Map and cross-sections of differences in locations..... 108
Figure 3.11: Damping trade-off curves..... 111
Figure 3.12: *Vp* model for 1991 and changes in *Vp* with time..... 114
Figure 3.13: *Vs* model for 1991 and changes in *Vs* with time..... 115
Figure 3.14: *Vp/Vs* model for 1991 and changes in *Vp/Vs* with time..... 116
Figure 3.15: Effect of different number of events on tomographic results..... 119

CHAPTER 4
RELATIVE RELOCATION OF MICROEARTHQUAKES

Figure 4.01: Example of a doublet and cross-phase analysis..... 126
Figure 4.02: Schematic diagram of a doublet..... 127
Figure 4.03: Map of UNOCAL station locations..... 130
Figure 4.04: Epicentre for all events for 1993 picked by Barton (1999)..... 132
Figure 4.05: Location of events for study and selected regions..... 133
Figure 4.06: An example of the procedure of choosing coherency threshold value..... 135
Figure 4.07: An example of a coherency matrix..... 136
Figure 4.08: Sketch of reading cosine plots..... 138
Figure 4.09: Number of events for sr001 and estimated error..... 141
Figure 4.10: Coherency matrix for sr001 with 95% coherency..... 142
Figure 4.11: Original locations of multiplet sr001_01_95 on map..... 142
Figure 4.12: Relative relocation of multiplet sr001_01_95..... 143
Figure 4.13: Plot of time delay against azimuth for each station for sr001_01_95..... 145
Figure 4.14: Time-delay estimates and frequency of stations used in sr001_01_95..... 147
Figure 4.15: Coherency matrix for area sr001 with 92% coherency..... 148
Figure 4.16: Original locations of multiplet sr001_01-92 on map..... 148
Figure 4.17: Relative relocation of multiplet sr001_01_92..... 149
Figure 4.18: Plot of time delay against azimuth for each station for sr001_01_92..... 150
Figure 4.19: Time-delay estimates and frequency of stations used in sr001_01_92..... 152
Figure 4.20: Relative relocation of multiplet sr001_01_95_T2..... 154
Figure 4.21: Plot of time delay against azimuth for each station for sr001_01_95_T2..... 155
Figure 4.22: Time-delay estimates and frequency of stations used in sr001_01_95_T2..... 156
Figure 4.23: Relative relocation of multiplet sr001_01_95_T1..... 157
Figure 4.24: Plot of time delay against azimuth for each station for sr001_01_95_T1..... 158
Figure 4.25: Time-delay estimates and frequency of stations used in sr001_01_95_T1..... 159
Figure 4.26: Correlation of waveform and time-delay estimates for stations in sr001_01_95..... 160
Figure 4.27: Number of events for sr002 and estimated error..... 161
Figure 4.28: Coherency matrix for sr002 with 96% coherency..... 162
Figure 4.29: Original locations of multiplet sr002_01_96 on map..... 162
Figure 4.30: Relative relocation of multiplet sr002_01_96..... 163
Figure 4.31: Plot of time delay against azimuth for each station for sr002_01_96..... 164
Figure 4.32: Time-delay estimates and frequency of stations used in sr002_01_96..... 166
Figure 4.33: Relative relocation of multiplet sr002_01_96_T2..... 168
Figure 4.34: Plot of time delay against azimuth for each station for sr002_01_96_T2..... 169

Figure 4.35: Time-delay estimates and frequency of stations used in sr002_01_96_T2..... 170
Figure 4.36: Correlation of waveform and time-delay estimates for stations in sr002_01_96..... 171
Figure 4.37: Number of events for sr003 and estimated error..... 172
Figure 4.38: Coherency matrix for sr003 with 95% coherency..... 173
Figure 4.39: Original locations of multiplet sr003_01_95 on map..... 173
Figure 4.40: Relative relocation of multiplet sr003_01_95..... 174
Figure 4.41: Plot of time delay against azimuth for each station for sr003_01_95..... 175
Figure 4.42: Time-delay estimates and frequency of stations used in sr002_01_96..... 177
Figure 4.43: Correlation of waveform and time-delay estimates for stations in sr003_01_95..... 178
Figure 4.44: Number of events for sr004 and estimated error..... 180
Figure 4.45: Coherency matrix for sr004 with 95% coherency..... 181
Figure 4.46: Original locations of multiplet sr004_01_95 on map..... 181
Figure 4.47: Relative relocation of multiplet sr003_01_95..... 182
Figure 4.48: Plot of time delay against azimuth for each station for sr003_01_95..... 183
Figure 4.49: Time-delay estimates and frequency of stations used in sr002_01_96..... 185
Figure 4.50: Correlation of waveform and time-delay estimates for stations in sr003_01_95..... 186
Figure 4.51: Relative relocation of multiplet sr004_01_95_Tt..... 187
Figure 4.52: Plot of time delay against azimuth for each station for sr004_01_95..... 188
Figure 4.53: Time-delay estimates and frequency of stations used in sr004_01_95_Tt..... 189
Figure 4.54: Frequency of events of each year used in each multiplet..... 190
Figure 4.55: Map and cross sections of multiplets with 3-D velocity model..... 191

CHAPTER 5
DISCUSSION AND CONCLUSIONS

Figure 5.01: Number of events and total seismic moment per month..... 195
Figure 5.02: Changes in gravity between 1977 and 2000..... 200
Figure 5.03: Plots of integrated anomalies for *Vp*, *Vs*, and *Vp/Vs*..... 201
Figure 5.04: Relationship between *Vp/Vs*, *Vp* and *Vs*..... 203
Figure 5.05: The affect of pore-fluid pressure on *Vp/Vs* ratio..... 206
Figure 5.06: Summary diagram of causes of *Vp/Vs* anomaly..... 207
Figure 5.07: Location difference map for events used in 1994 inversion..... 209
Figure 5.08: Differences in waveforms with regard to different stations..... 216
Figure 5.09: Plot of seismic clusters with regard to selected multiplets..... 220

LIST OF TABLES

CHAPTER 1
INTRODUCTION

Table 1.1: Major development phases at The Geysers..... 27
Table 1.2: Power plants at The Geysers..... 29
Table 1.3: Major contributions to The Geysers from seismology..... 36
Table 1.4: Possible processes for seismicity at The Geysers..... 41
Table 1.5: Seismic networks at The Geysers..... 44
Table 1.6: Major tomographic studies performed at The Geysers..... 46

CHAPTER 2

POLARITY DETERMINATION AND SENSOR ORIENTATION

Table 2.1: UNOCAL station locations and number of seismometer components..... 53
Table 2.2: Earthquakes selected for polarity determination..... 58
Table 2.3: Results of polarity investigation..... 67
Table 2.4: Polarity results for UNOCAL stations..... 68
Table 2.5: Orientations of three-component stations..... 69

CHAPTER 3
TOMOGRAPHY THEORY AND RESULTS

Table 3.1:Data concerning the tomographic inversions..... 96
Table 3.2: Areas of increased amplitude in Vp/Vs anomaly with time..... 118

CHAPTER 4
RELATIVE RELOCATION OF MICROEARTHQUAKES

Table 4.1: Step-wise procedure for relative relocation of microearthquakes..... 131
Table 4.2: An example of the output of the *rms* program..... 139

CHAPTER 5
DISCUSSION AND CONCLUSIONS

Table 5.1 Regression lines for Vp/Vs over Vp and Vp/Vs over Vs plots..... 202
Table 5.2: Effect on Vp/Vs ratio during liquid to vapour transition..... 206
Table 5.3: Differences in sampled 1994 tomography inversion picks..... 208
Table 5.4: Correlation between waveform, cosine and TOA..... 213
Table 5.5: Median for horizontal and vertical relocations vectors..... 214
Table 5.6 Final RMS travel-time residuals for earthquakes located with the 3-D model..... 215
Table 5.7: Seismic clusters of Barton (1999) the correlation to multiplets..... 219

CHAPTER 1:

INTRODUCTION

1.1 Overview

The Geysers geothermal area is the largest exploited vapour-dominated reservoir in the world. The Geysers name itself is a misnomer, as there are no geysers but only fumeroles and mudpots. The Geysers currently produces 6% of northern California's electricity supply. Although, it has been exploited for more than a century, a large expansion began in the 1960s. Earthquake seismicity has increased in the reservoir, hand in hand with increased steam production stimulating seismic monitoring and research. The research work described in this thesis was based on utilizing the seismicity at the reservoir.

The tectonic setting and geology of northern California gives an insight into the evolution of the geothermal reservoir. To monitor the high rate of seismicity several seismic networks have been in operation since early the 1970s. There is a direct correlation between commercial activity and rate of seismicity at The Geysers.

The largest permanent seismic network at The Geysers, the UNOCAL network, has 22 stations of which 8 are three-component stations. However, polarities of these stations and orientations of the horizontal sensors of the three component stations are ill-determined. The network needs to be accurately calibrated to make better use of the retrieved information for studies such as moment tensor determinations. To achieve this aim, accurate focal mechanism solutions from a temporary network was made use of to determine station polarities. Orientations of

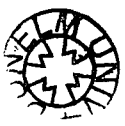

the eight three-component stations of the network were also determined by making use of known event locations.

Commercial development at The Geysers has caused extensive depletion of the geothermal reservoir. Accelerated pressure decline since 1987 and pressure fluctuations since 1995 has made monitoring the reservoir of paramount importance but difficult with conventional tools such as well logs. Three-dimensional seismic tomography provides images of *Vp*, *Vs* and *Vp/Vs* structural changes of the reservoir. Repeat local earthquake tomography on a two-year time interval show progressive depletion of the reservoir. It also indicates which areas could be further exploited and different mechanisms, which affect changes in *Vp*, *Vs* and *Vp/Vs* structures. These results can be qualitatively interpreted by increases in pore compressibility, decreases in pore pressure and drying of argillaceous minerals.

Relative relocation of microearthquakes help to delineate and identify fault structures, geometries and orientartions which are used to delineate fluid flow paths and identify time history of activity. Four seismic clusters at The Geysers were studied for such effects.

1.2 Tectonic evolution

1.2.1 Tectonics of Northern California

The tectonics of northern California are dominated by the San Andreas fault system and the Mendocino Triple Junction (MTJ). This triple junction, between the Gorda, North American and Pacific plates, is of the trench-transform-transform type (Figure 1.01). The MTJ formed at about 30 Ma when the oceanic Gorda plate

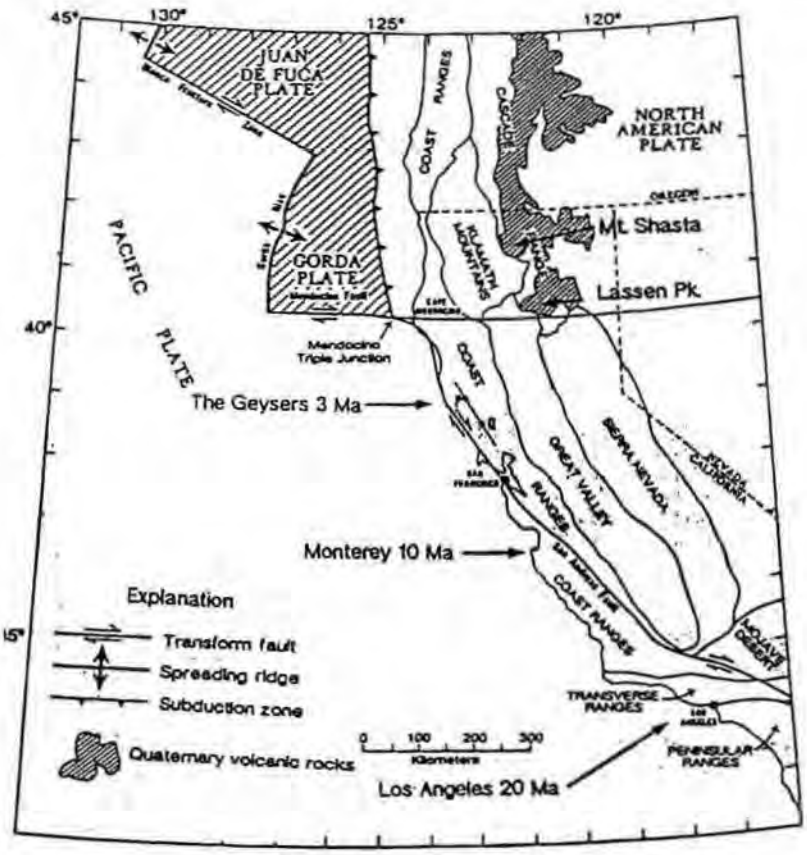

Figure 1.1: Plate tectonics of northern California at the Mendocino triple junction involving the Pacific, Gorda and North American plates. Relative plate motions are shown with estimates of the position of the triple junction as it migrates northwards (*from* Jachens and Grimson, 1983).

started subducting under the continental North American plate (Furlong, 1993). Since then, the MTJ has migrated northwards from southern California along the North American plate boundary reaching The Geysers-Clear Lake area at ~ 3.3 Ma (McLaughlin, 1981; Furlong, 1993). The MTJ is migrating at a rate of 5 cm/yr and is currently located at Cape Mendocino.

The San Andreas fault system commenced at ~ 30 Ma when the MTJ migrated northwards forming a right-lateral transform boundary between the Pacific and the North American plate. When the MTJ passes by, subduction of the Gorda plate ceases and the resultant void is termed the "slabless window" (Figure 1.02). The geodynamic processes associated with the formation of this window caused a broad lateral shear zone to form in the wake of the propagating transform front.

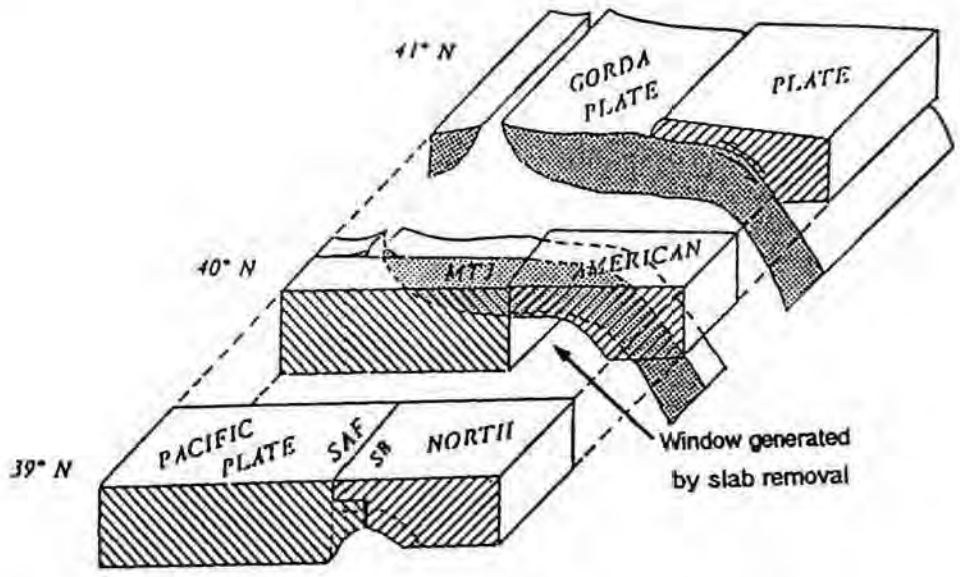

Figure 1.2: Schematic diagram illustrating plate interaction in the vicinity of the Mendocino Triple Junction (MTJ). North of the MTJ (41°N), the Gorda plate subducts under the North American plate. South of the MTJ (40°N), subduction is terminated and the subducting slab is removed to form a "slabless window". SAF: San Andreas Fault; SB: Sebastopol Block (*from* Furlong et al., 1989).

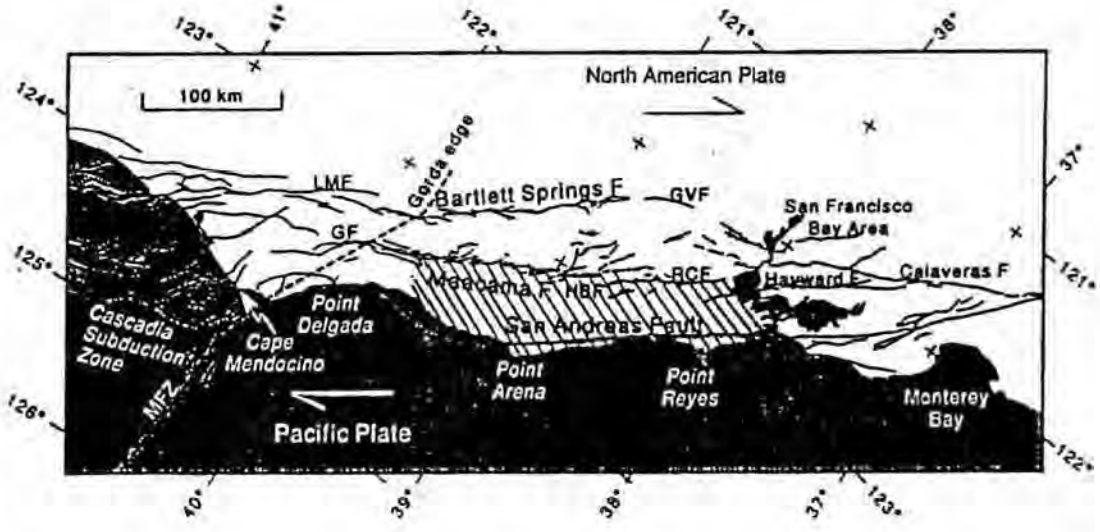

Figure 1.3: The tectonic environment of coastal northern California showing the main Holocene and Quaternary faults. Relative plate motion between the North American plate and the Pacific plate are shown by the arrows. The Sebastopol block is enclosed by the hatched pattern and surface projection of the south-east edge of the Gorda plate is represented by the dashed line. CF: Calaveras Fault; GF: Garberville Fault; GVF: Green Valley Fault; HBF: Healdsburg Fault; HF: Hayward Fault, LMF: Lake Mountain Fault; MFZ: Mendocino Fracture Zone; RCF: Rogers Creek Fault (*from* Castillo and Ellsworth, 1993).

Along the San Andreas fault zone, stress changes from being subduction-related to shear-dominated. The fault zone is more than 1000 km in length and up to 100 km in width. However, the relative plate motion is accommodated mostly by the main branch of the fault zone (Hill *et al.*, 1990). Although the San Andreas fault accommodates the majority of the deformation south of the San Francisco bay area, from latitude 39° N to 36.5° N, motion is distributed over several faults. The principal components of the fault zone in northern California include the Maacama, Bartlett Springs, Roger Creek, Green Valley and Healdsburg faults (Figure 1.03).

1.2.2 Seismicity in Northern California

Seismicity in northern California is dominated by subduction-related and transform-related earthquakes. North of the MTJ, the Gorda plate subducts under the continental North American plate. Hypocentral depths increase from the coast landwards in an east-southeast direction defining a 20°-30° dipping Wadati-Benioff zone (Walter, 1986; Costillo and Ellsworth, 1993; Hill *et al.*, 1990) (Figure 1.04). Some events in the North American plate at the MTJ are also caused by compression due to the subduction environment.

South of the MTJ great (M>8) events have occurred approximately once a century as most of the plate motion is accommodated along the San Andreas fault zone. In the time duration between these large-magnitude events, smaller-magnitude events occur along lesser faults within the San Andreas fault system. These faults are sub-parallel to the San Andreas fault system and are easily identified from lineations in earthquake epicentres (Figure 1.05). These sub-parallel faults are 2-3 km wide and include faults such as Maacama and Bartlett Springs (Costillo and Ellsworth, 1993; Hill *et al.*, 1990). The events are influenced by the transform shear zone with focal mechanism solutions indicating right lateral slip movement with faults dipping at 50°-75°. In the vertical plane, from northwest to southeast seismicity is more diffuse and becomes shallower (from 12 km in the southeast to approximately 8 km in the northwest) (Figure 1.06a). However, from southwest to

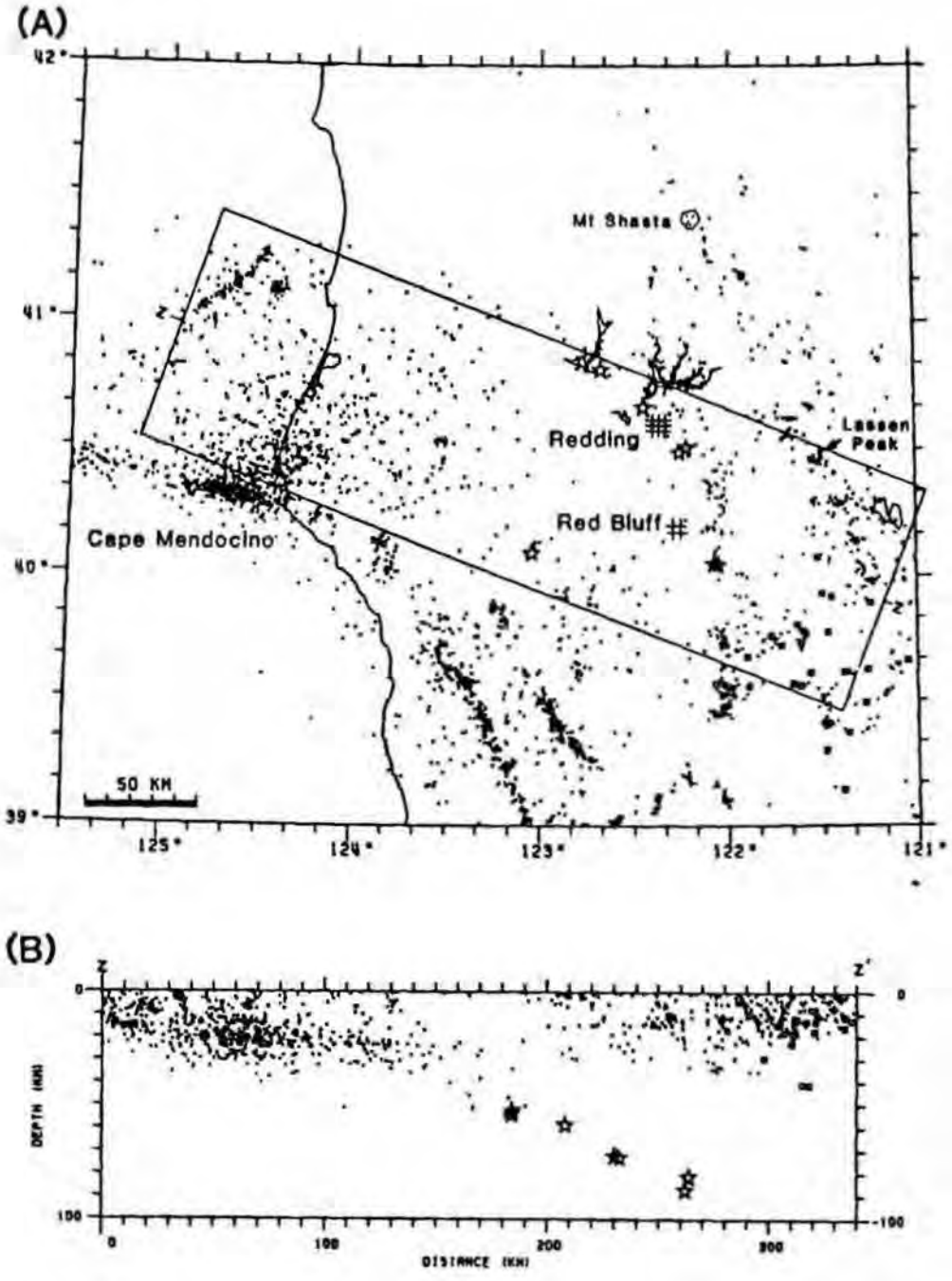

Figure 1.4: (A) Seismicity in the vicinity of the MTJ. The linear zones of high seismicity are the Mendocino fault zone between Gorda and Pacific plates and the San Andreas fault zone between the North American and Pacific plates. (B) Cross-section of seismicity shown in the box plan view (A) with the hypocentral pattern showing subduction of the Gorda plate under the North American plate (*from* Walter, 1986).

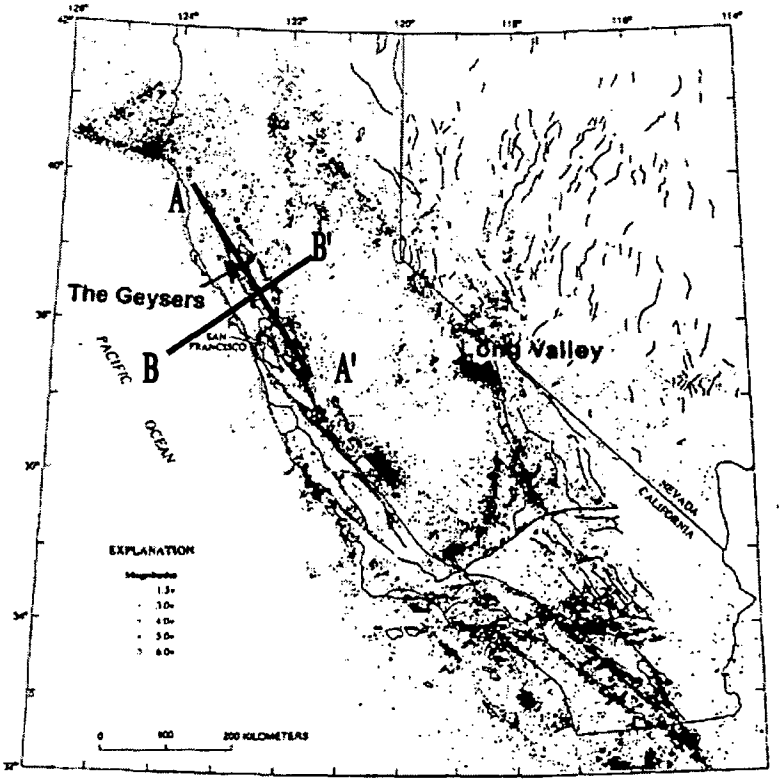

Figure 1.5: Regional seismicity in California with epicentres of earthquakes of M ≥ 1.5 from 1980 to 1986 and mapped Holocene faults (*from* Hill et al., 1990).

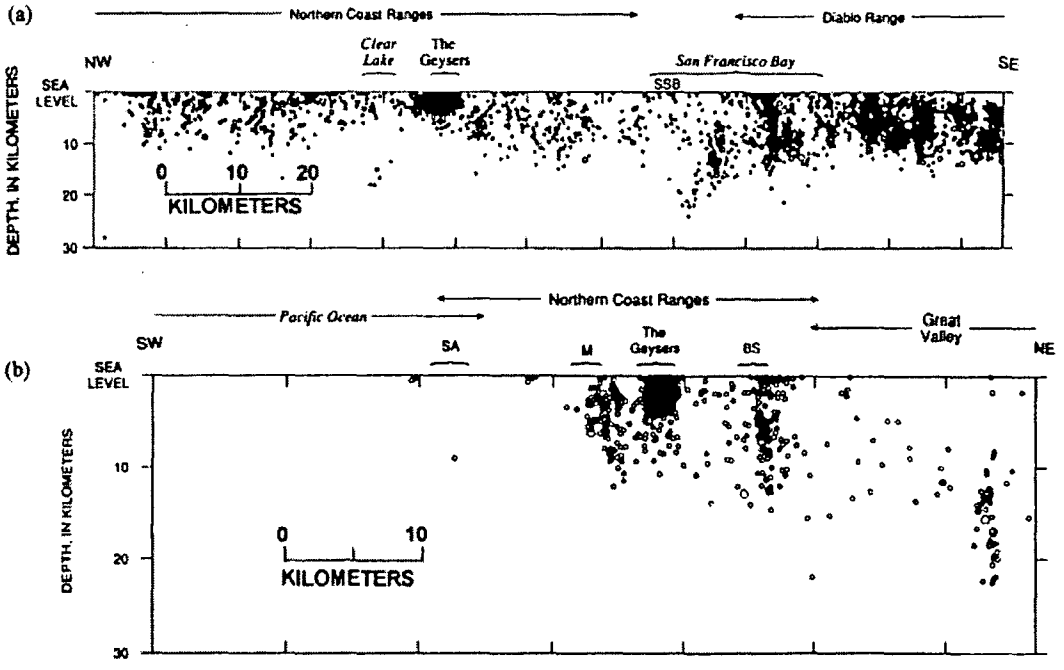

Figure 1.6: (a) Cross-section of regional seismicity from north-west to south-east showing earthquakes with magnitude M ≥ 1.5 from 1980 to 1986 in the vicinity of The Geysers. (b) Same as (a) except from south-west to north-east. M: Maacama; BS: Bartlett Springs, SA: San Andreas (*from* Hill et al., 1990).

northeast, there is relatively little seismicity in the San Andreas fault compared with Maacama and Bartlett Springs faults. Seismic events also deepen to the east and a very high rate of seismic activity is observed at The Geysers (Figure 1.06b).

1.2.3 Tectonics of The Geysers

The Geysers and Clear-Lake regions underwent complex processes of deformation during the Cretaceous to early Tertiary reflecting the transition from subduction to shear tectonics. While Franciscan-assemblage rocks were formed in a subduction zone setting, the Great Valley Sequence units were formed in a fore-arc basin setting. During the Cretaceous to early Tertiary, both units underwent significant deformation and strike-slip movement, before being uplifted to their present positions during the later Tertiary. The thickness of the crust at The Geysers is estimated at about 24 km (Oppenheimer and Eaton, 1984).

The tectonic history of The Geysers is recorded in the Franciscan rocks. Compressional deformation in the subduction regime formed thrust pockets. In general, steeply dipping thrust pockets formed the reservoir caprock with old high-angle faults being bound together by younger high-angle faults. These in turn were truncated by the shear motion of the San Andreas fault system (Thompson, 1992). The orientation of the major faults at The Geysers, the Maacama, Mercuryville and Collayomi faults, reflects the regional trend which is northwest–southeast. The displacement history of this zone is complicated, with high-angle northeast dipping surfaces reflecting episodes of reverse slip, thrusting, normal, and more dominant right-lateral strike-slip faulting (Hearn *et al.*, 1981; McLaughlin, 1981). There are numerous high-angle faults between the major fault zones at The Geysers. They vary from northeast, north-northwest to northwest-oriented normal faults and northwest trending strike-slip faults. (Hearn *et al.*, 1976) (Figure 1.07).

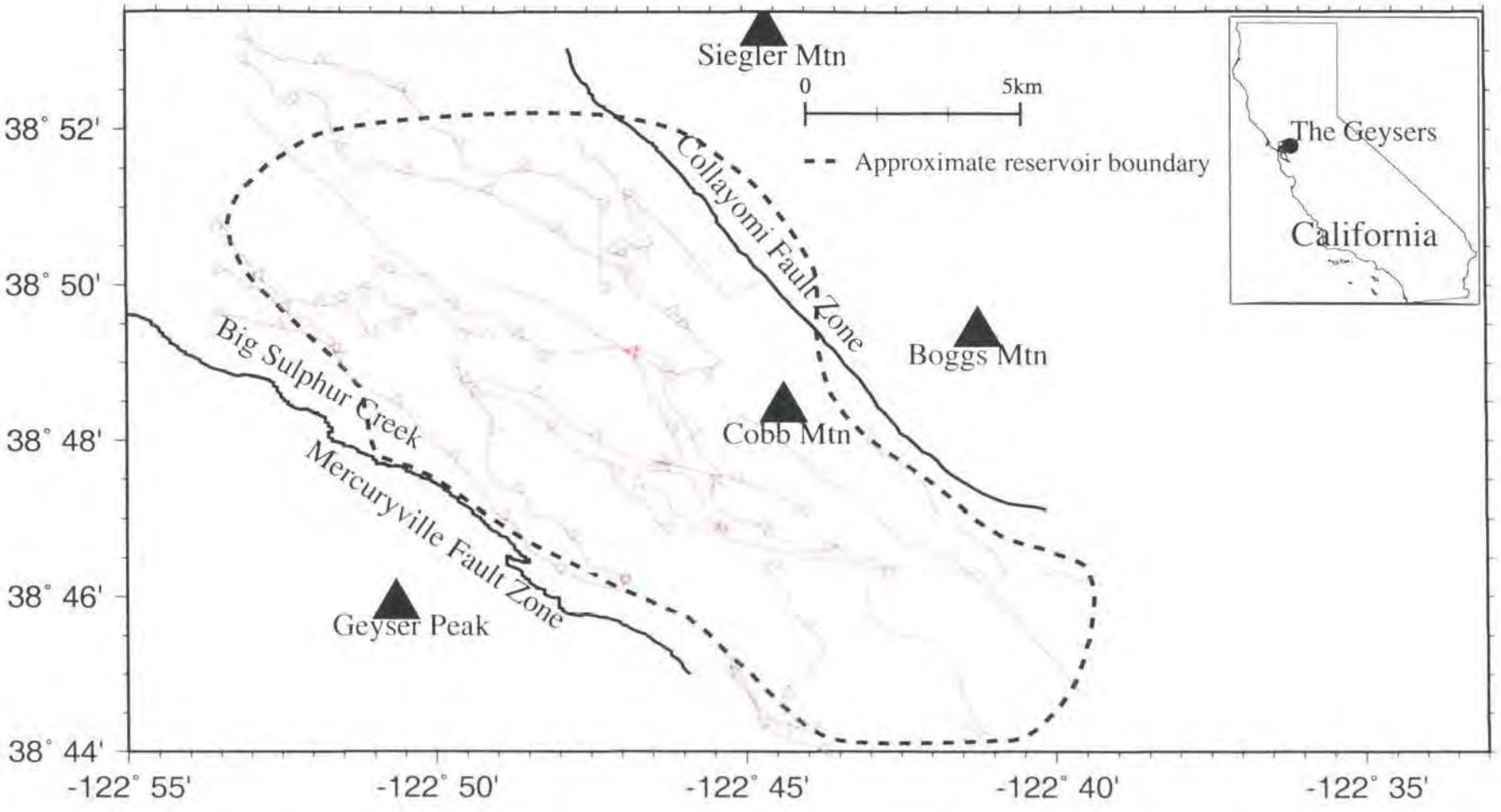

Figure 1.7: Map of The Geysers showing the approximate reservoir boundary (dashed line) and major fault zones (solid lines). Inset shows location of The Geysers in California.

1.3 Geology

1.3.1 Regional Geology

The Geysers region comprises two Jurassic-Cretaceous units assigned to the Franciscan and Great Valley Sequences which are partially overlain by Quaternary rocks (Figure 1.08). The Franciscan assemblage is heterogeneous and is broadly divided into three thrust-fault-bounded structural units. These units young upwards and comprise the eastern, central and coastal belts. They are intensely deformed, mildly metamorphosed sandstone, chert and mafic igneous rocks. While the sandstone may have island-arc or continental origin, the mafic igneous rocks and chert show evidence of an oceanic origin. The Franciscan assemblage is thought to have been deposited in a trench environment on an easterly dipping subduction zone (McLaughlin, 1981).

The Great Valley Sequence consisting of moderately deformed conglomerate mudstone and sandstone, and was deposited in a series of submarine fans within an arc-trench gap or in an fore-arc basin environment. These rocks range in age from late Jurassic to late Creteceous. Rocks of the Great Valley Sequence are overlain by Jurassic Coast Range ophiolites, which are thought to represent ancient oceanic crust.

Volcanic activity at The Geysers area commenced at about 2 Ma and continued up to 10,000 years ago. The volcanic field covers an area of approximately 400 km^2 and was extruded onto the Franciscan assemblage and the Great Valley Sequence during the Quaternary (Figure 1.09). These rocks are the eruptive products of mantle heating, crystal fractionation, and assimilation of rocks from the lower crust. K/Ar age data from The Great Valley Sequence and the Franciscan assemblage show that volcanic rocks young towards the north implying that the formation of the volcanic field might have been the result of the northward migration of the MTJ (McLaughlin, 1981; Hearn *et al.*, 1981; Furlong *et al.*, 1989).

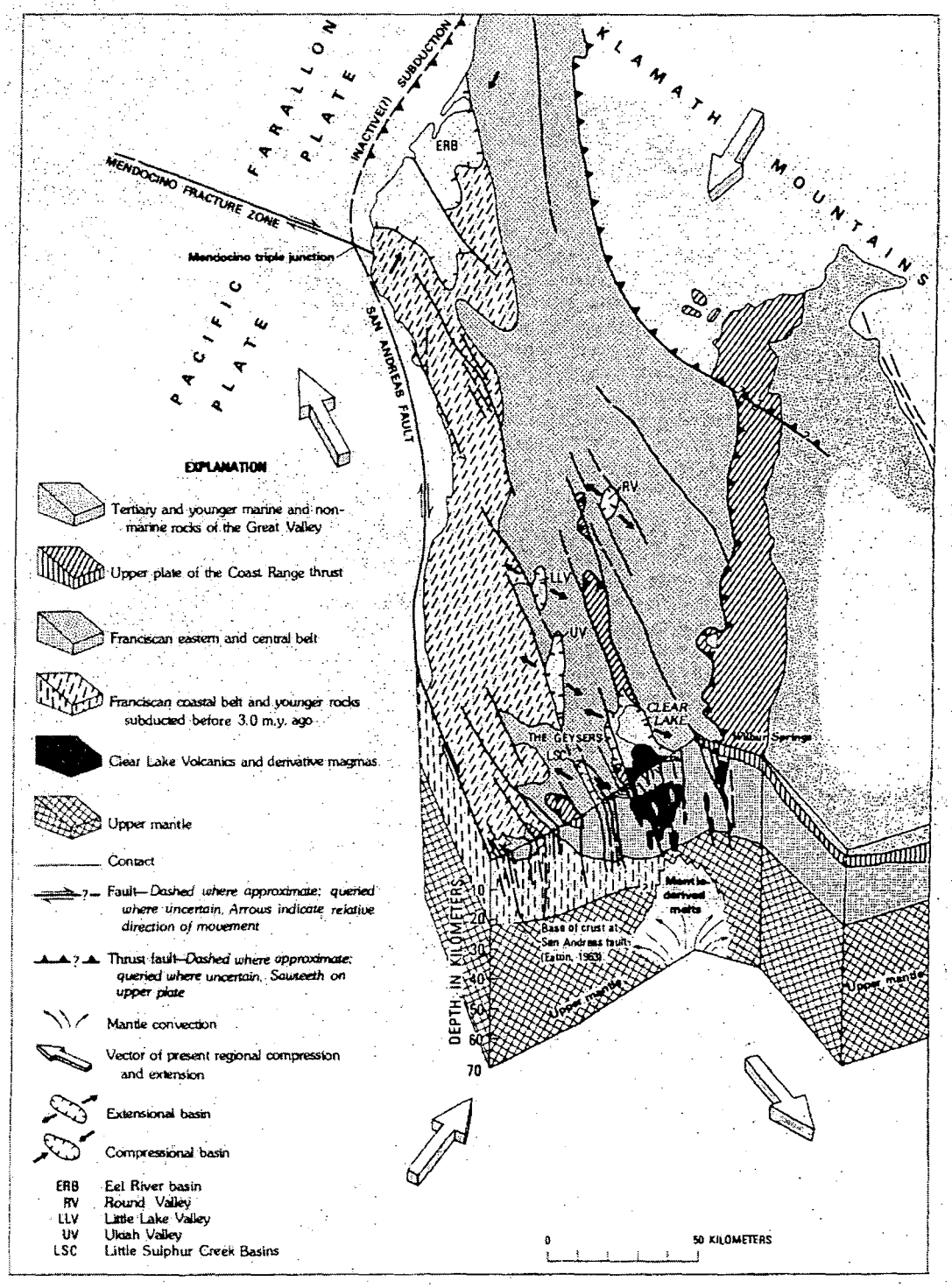

Figure 1.8: Extrusion of magma under The Geysers area with major crustal features (*from* McLaughlin, 1981).

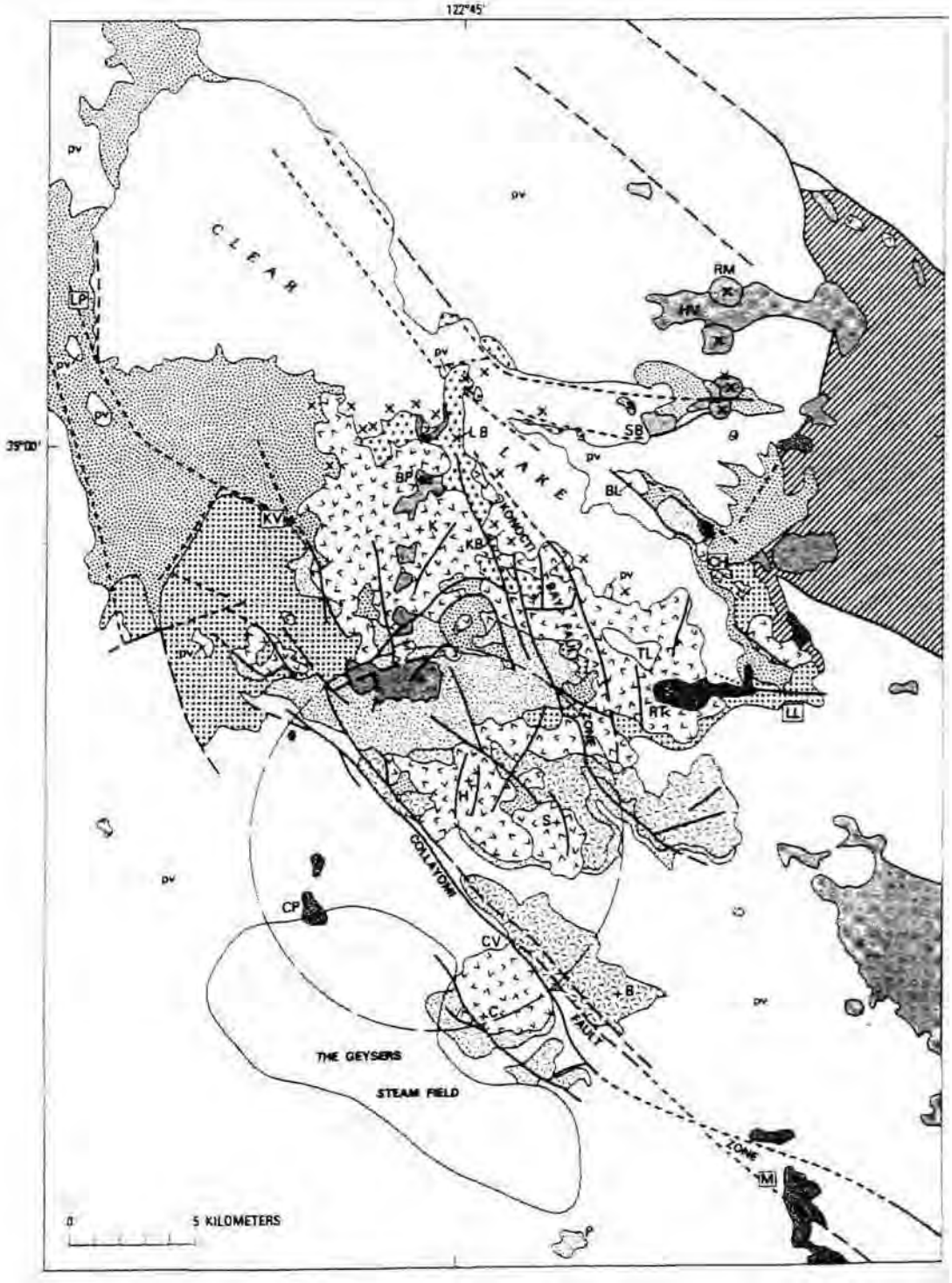

Figure 1.9: Map of geological units at the Clear-Lake volcanic field. C: Cobb mountain; H: Mt. Hannah; HV: High Valley; K: Mt. Konocti; S: Seigler mountain; BP: Buckingham Peak; KB: Konocti Bay; CP: Caldwell Pines; CV: Cobb Valley; SB: Sulphur Bank; BL: Borax Lakes; LB: Little Borax Lakes; TL: Thurston Lake; CH: Clear-Lake Highlands; KV: Kelseyville; LL: Lower Lake; LP: Lakeport; M: Middleton; P: Pine mountain; RM: Round Mountain; RT: Roundtop mountain; + mountain summit (*from* Hearn et al., 1981).

A felsite batholith is intruded into the Franciscan assemblage beneath The Geysers that is composed of ophiolite, rhyolite porphyry, granite and granodiorite. There are close similarities in geochemistry between the felsite and the outcrops of Cobb Mountain, suggesting that the two are equivalent (Hulen and Nielson, 1993). However, the age of the felsite is 1.3 Ma as opposed to 1.7 Ma for the Clear Lake volcanics. The great age of these units suggests that the felsite is too old to be the geothermal heat source at The Geysers (Dalrymple *et al.*, 1999).

1.3.2 Geology at The Geysers

The three main geologic units at The Geysers are the caprock, the metagreywacke and the felsite. The steam reservoir is confined to the northeastern limb of Maacama antiform that plunges to the southwest (McLaughlin, 1981). The caprock in the southeast mainly comprises Franciscan greenstone, serpentinised peridotitie and chert and is about 1100 m thick. However, the caprock increases in thickness towards the northwest to about 3300 m. In the northwest, the caprock mainly comprises the greywacke, of identical composition to that found in the steam reservoir beneath. The reservoir caprock is relatively impermeable.

Most of the reservoir comprises Franciscan-assemblage greywacke sandstone. The fracture network of the greywacke was increased in repeated episodes of felsite intrusion (Truesdale *et al.*, 1993) (Figure 1.10). The fracture pattern in the steam-bearing fractures in the metagreywacke is generally random but it includes many low-angle fractures which permit laterally extensive zones of high steam extraction (Thompson and Gunderson, 1992). Porosity in the reservoir is unusually high and mainly related to the fractures. Porosity in the greywacke is about 2.3% as opposed to 1.6% in the non-reservoir greywacke (Gunderson, 1992). The thickness of the reservoir varies from 600-1000 m in the northwest to approximately 1500-5000 m in the central and southeast Geysers (Figure 1.11). However, the top of the steam zone is deeper in the northwest varying between 760-1370 m below sea level (bsl) compared to the southeast Geysers where it varies between 610-760 m bsl.

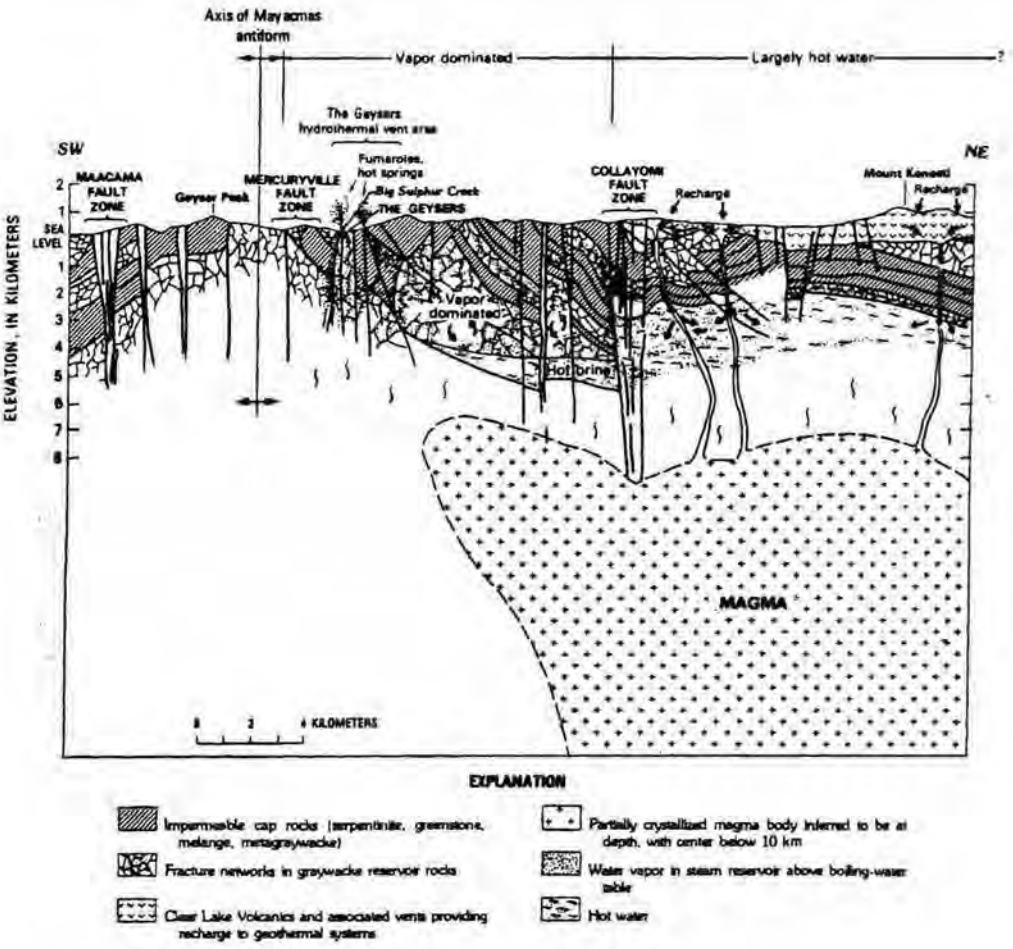

Figure 1.10: Vertical section showing a structural model for The Geysers (*from* McLaughlin, 1981).

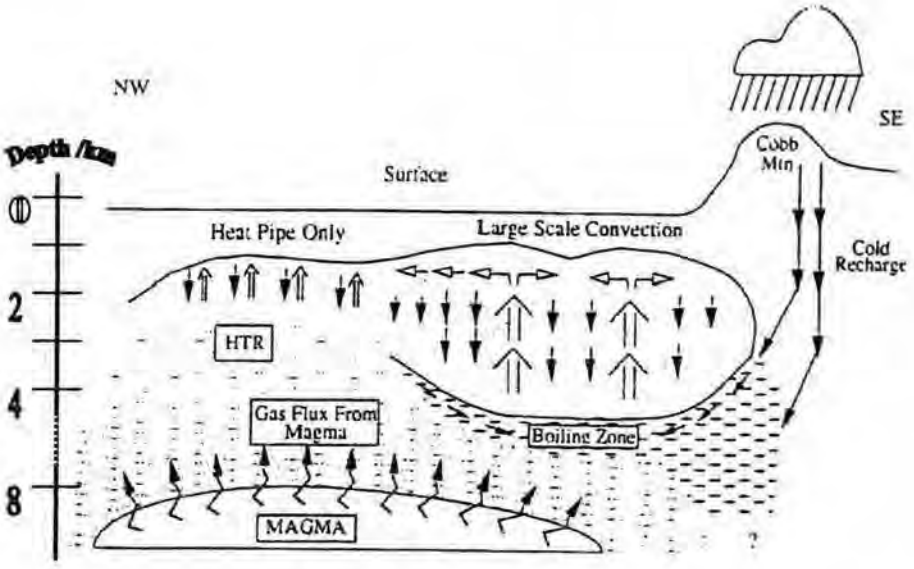

Figure 1.11: Schematic conceptual model for The Geysers with a vertical cross-section from north-west to south-east showing the probable processes of the geothermal system. HTR: High Temperature Reservoir, open arrows show the flow of steam and solid arrows show the flow of condensate water. Cobb Mtn. provides meteoric water recharge to the reservoir (*from* Truesdale et al., 1993).

The lower portion of the steam reservoir is in the upper part of the felsite with a mean porosity of 2%. In the felsite batholith, the fracture pattern is predominantly one of high-angle fractures and is related to recent strike-slip tectonic movements (Thompson and Gunderson, 1992). The felsite has the same shape as the steam reservoir (Figure 1.12). There have been at least three episodes of intrusion of silicic magma in forming the batholith, which is composed mainly of three major rock types ranging in composition from granite to granodiorite (Hulen and Nielson, 1993) (Figure 1.12).

The steam reservoir has two distinct parts on the basis of temperature. Most of the reservoir comprises the "normal reservoir" with temperatures up to 235° C. However, to the northwest there exists a High Temperature Reservoir (HTR) that underlies the normal reservoir with a temperature of about 342° C. They are vertically separated by a steep temperature gradient of 100° C over a 100-200 m depth interval (Truesdale *et al.*, 1993). The steam pressure in both reservoirs are the same which suggests they are connected horizontally at depth. The method of heat transfer differs between the normal reservoir and the HTR. An efficient convection system exists in the central and southeast Geysers (Figure 1.11). However, in the HTR heat transfer is thought to take place by a "heat pipe" mechanism by conduction through the igneous intrusion.

There is a considerable amount of commercial injection of liquid taking place at The Geysers making natural recharge essentially negligible. However, a probable source of natural recharge to the normal reservoir is meteoric water from Cobb mountain flowing via the reservoir greywacke, volcanic vents or outcrops in the southeast Geysers (Figure 1.11). Due to the location and depth of the HTR, natural recharge might be through magmatic and metamorphic processes.

1.3.3 Formation and evolution

The steam reservoir has hosted at least three distinct hydrothermal systems. The first system was an ancient regional metamorphic system, heated in response to

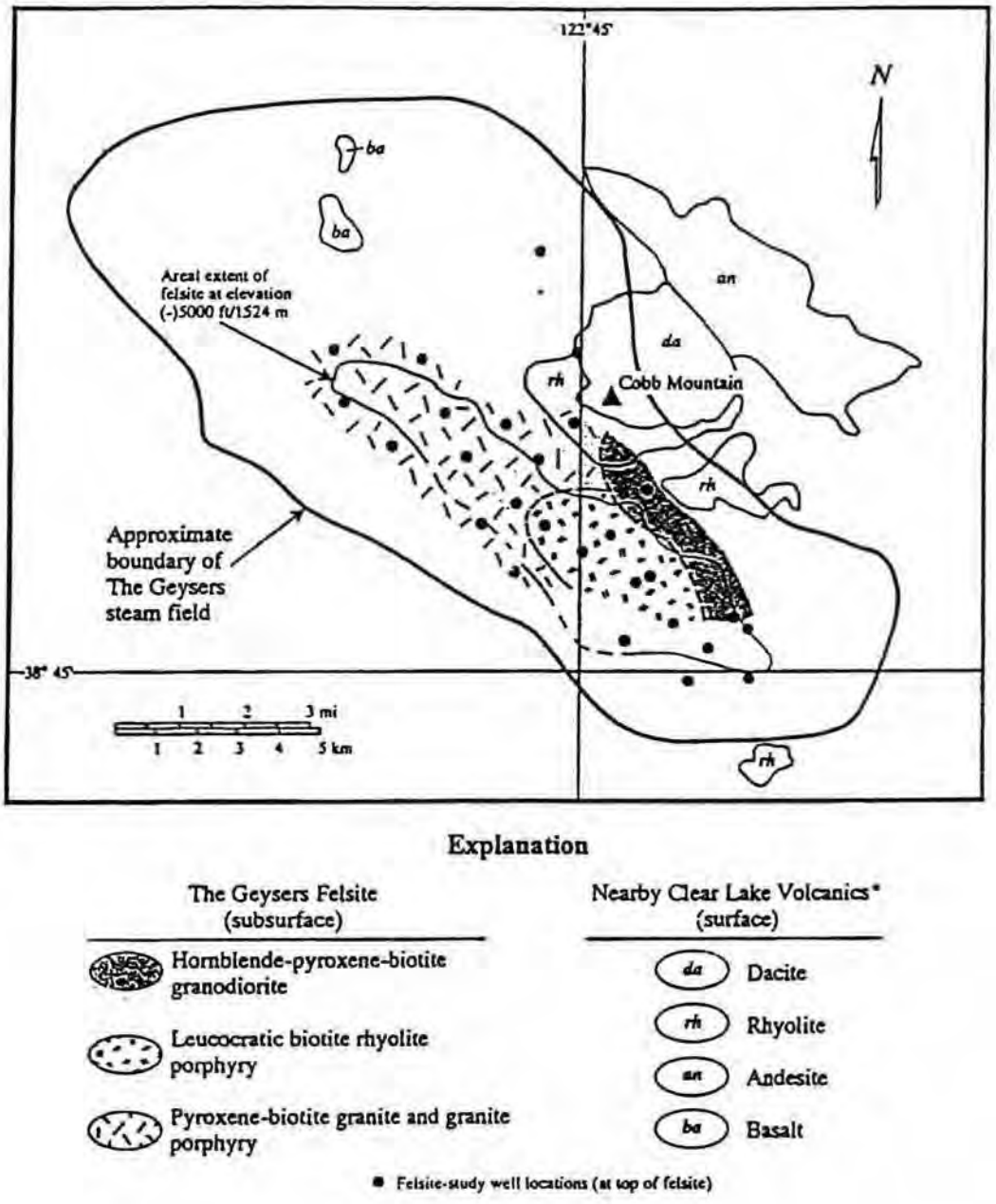

Figure 1.12: Map of the subsurface felsite batholith. The type and distribution of the igneous intrusive rocks of the felsite and the rocks of the Clear Lake volcanic field are shown. The steam field boundary shows the felsite is wholly within the production area (for 1992) (*from* Hulen and Nielson, 1993).

rapid burial in the presence of a normal geothermal gradient, and had a temperature of 175-200° C. The second hot water system had a probable magmatic source at temperatures of 175-350° C. The third and present day system, which evolved from the hot water system, is a vapour-dominated reservoir with temperatures of 235-342° C (Walters *et al.*, 1992). The transition from liquid- to vapour-dominated conditions occurred at The Geysers at around 0.25 Ma in response to dilation of the fracture volume at depth due to tectonic extension and/or magmatic intrusions beneath the reservoir, coupled with limited fluid flow and low near-surface permeability (Allis and Shook, 1999).

The fracture pattern produced by the emplacement of the felsite body was important in the evolution of the reservoir as it influenced the fluid-flow characteristics of the host rocks. In the central and southeast Geysers, the fractures reach the surface. The resultant venting and decompressing of the liquid-dominated reservoir led to boiling of the reservoir fluids, loss of original gaseous contents and flushing by meteoric water. However, in the northwest Geysers, the fractures are much deeper and did not reach the surface which led to the slow evolution of the HTR. Steam from the HTR shows a mixing of high-$^{3}He/^{4}He$, low radiogenic ^{40}Ar gas with a nearly pure Mid-Ocean Ridge (MOR) type magmatic gas. These noble gas isotopes also suggest a heat source from the cooling of magma (Kennedy and Truesdale, 1996; Truesdale *et al.*, 1992).

1.4 Geophysical studies at The Geysers

Since commercial exploitation of The Geysers reservoir began, seismicity has progressively increased. The earthquakes are of low magnitude and largely restricted to the reservoir making this ideal for 3-D tomography studies. As the heat source beneath is unknown and the causes of the earthquakes are not fully understood, seismic and other geophysical research techniques have been widely applied at The Geysers. Seismic methods can be classified into two groups: active and passive. Active methods include seismic reflection studies, which have been unsuccessful because most of the energy is scattered by the complex geologic

structure. The rough terrain of the area also hinders application of this method (Figure 1.13). However, two Vertical Seismic Profiling experiments have been carried out to investigate the extent of fracturing of the reservoir. Passive methods involve use of the microearthquakes (MEQ), for example to monitor injection of condensate (Stark, 1990).

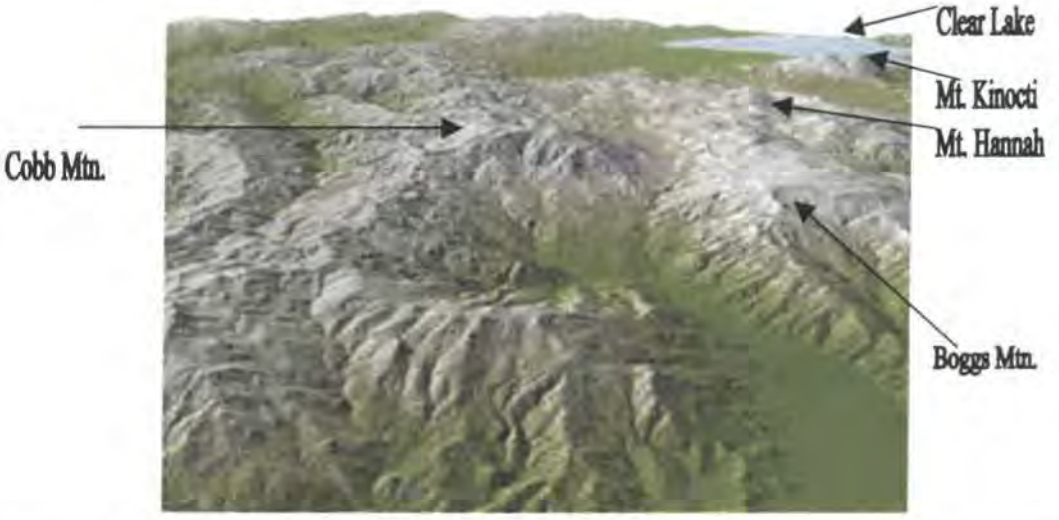

Figure 1.13: Digital Elevation Model (DEM) of The Geysers area. View is north-eastwards with 30 m grid sampling and lighting from the east (*Source*: Mike Rymer, US Geological Survey, Menlo Park, CA).

Although seismic surveys have been the predominant geophysical technique used to study The Geysers, there also have been contributions from gravity, magnetics and resistivity. Gravity surveys by the California Division of Mines and Geology (DMG) and the U. S. Geological Survey (USGS) in 1975 revealed -30 mGal gravity anomalies near Mt. Hannah to the northeast and in The Geysers area (Figure 1.14a) (Isherwood 1975). Resurveys of the same locations in 1999 suggested that the gravity anomaly at The Geysers has increased by between –100 μGal and –700 μGal (Allis *et al.*, 2001). The greatest gravity decrease was at the central Geysers. However, in the old production area, west of the central part of the reservoir, gravity decreased by 200 μGal although significant liquid injection takes place in the vicinity. The negative anomaly near Mt. Hannah has been interpreted to a partially molten magma chamber. The observed negative anomaly at The Geysers is most probably caused by a combination of factors such as high temperature, excess porosity, low density rocks, steam-filled pores and hydrothermal alteration (Delinger and Kovach, 1981). A model with

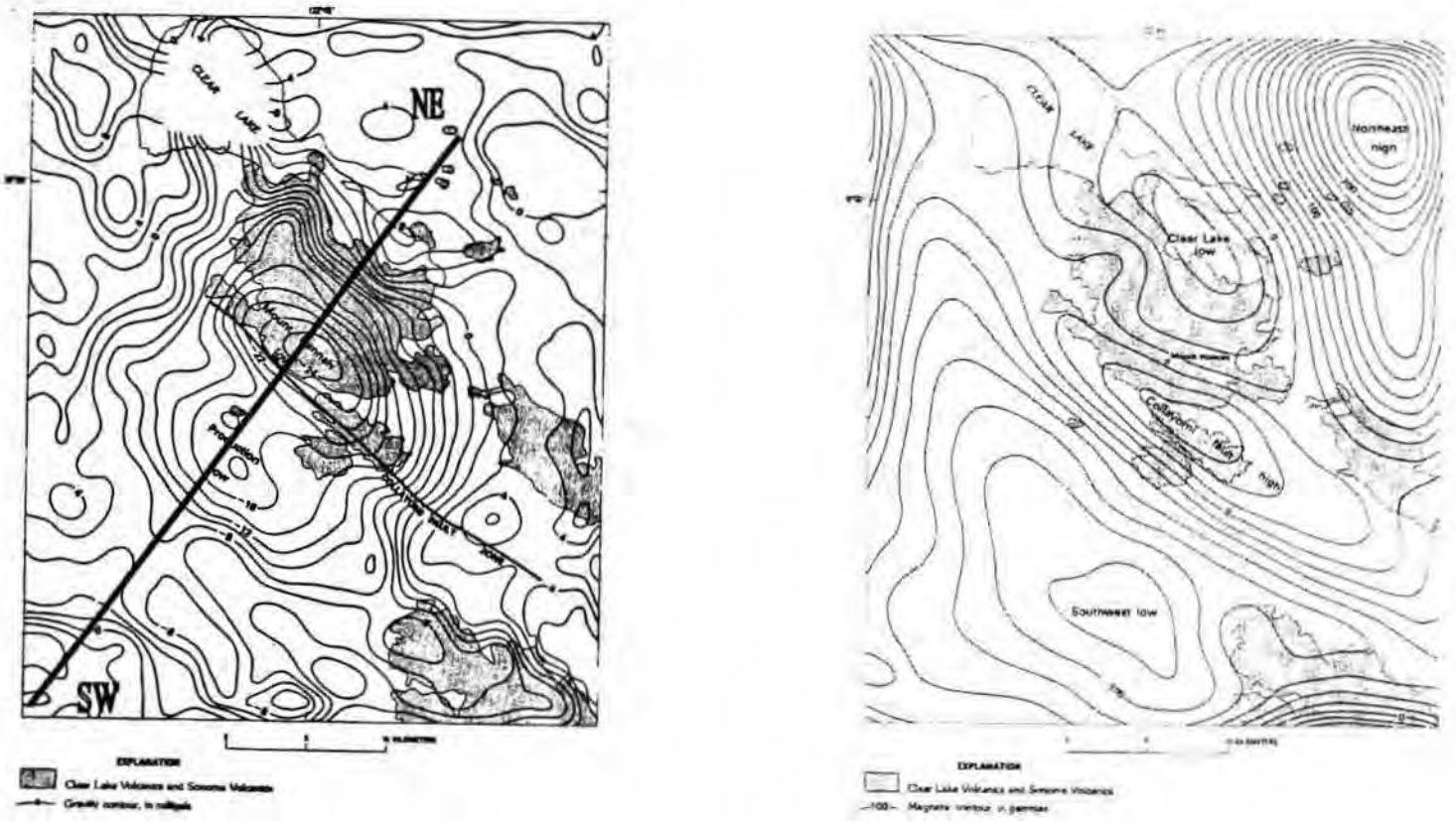

(a) (b)

Figure 1.14: (a) Residual gravity contours for The Geysers area based on a reduction density of 2.67 g/cm^3 with contour intervals of 2 mGal. (from Isherwood, 1975). (b) Magnetic contours over the same area as (a) continued upward to 3 km with a 20-gamma contour interval (*from* Isherwod, 1975). The south-west to north-east cross-section for the gravity and magnetic modelling shown in Figure 1.15 is indicated in (a).

partial melt centred at a depth of 15-20 km with complex shallow structure has also been proposed (Blakley and Stanley 1993) (Figure 1.15). However, assuming the changes in gravity are due to mass withdrawal from a reservoir thickness of 1 km, the changes imply the mass loss is equivalent to 2% of the porosity (Allis *et al.*, 2001).

Aeromagnetic surveys conducted do not show magnetic anomalies that coincide with the observed gravity anomalies. There are two negative magnetic anomalies of –120 nT, one lying approximately 10 km south of The Geysers and other of –60 nT lying 10 km northeast of Mt. Hannah (Figure 1.14b) (Isherwood 1976). In between, a +60 nT anomaly exists, and is centred on the Collayomi fault zone. These anomalies have been interpreted as indicating Coast Range ultramafic rocks (e.g. serpentinite) and Clear Lake volcanics (Figure 1.15).

Time-domain electromagnetic, magnetotelluric, direct-current and bipole-dipole measurements from geoelectrical surveys show that the resistivity of rocks at The Geysers has a wide range of 7-100 Ωm (Stanley and Blakely, 1995). While the high- resistivity bodies have been interpreted as unfractured greywacke, greenstone and mafic rocks, the low resistivity bodies have been interpreted as altered greywacke in the reservoir.

Geodetic measurements between 1973 and 1977 revealed horizontal compression and vertical subsidence at The Geysers reservoir, which is thought to be related to steam extraction. The most intensely exploited areas show maximum subsidence of 0.048 ± 0.006 m/yr and horizontal compression of 0.02 ± 0.006 m/yr. Three GPS surveys conducted between 1994 and 1996 using the GEOID 96 geoid revealed the maximum rate of subsidence between 1997 and 1996 to be 0.047 ± 0.002 m/yr and to be located 2 km north of the maximum subsidence site of 1977. The observed subsidence corresponds to a minimum volume strain of 5×10^{-4} consistent with a model of poroelastic contraction with a low quasi-static effective bulk modulus, as expected for a fracture-dominated reservoir (Mossop and Segall, 1997). This model is also supported by pressure lows that have developed at The Geysers (Figure 1.16).

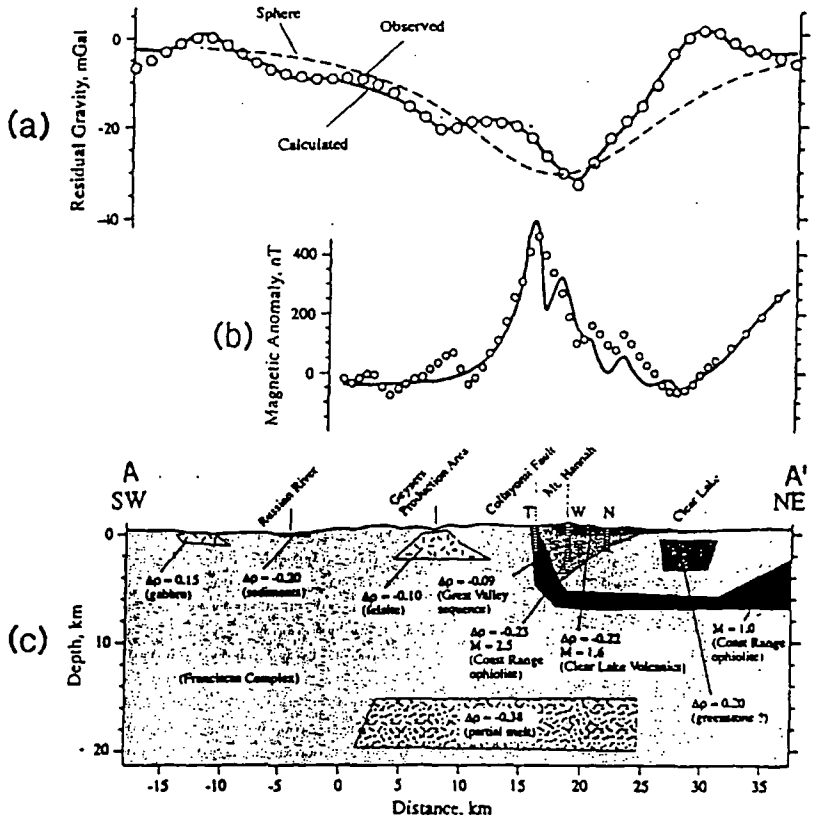

Figure 1.15: Gravity and magnetic field modelling for the cross-section shown in Fig. 1.14a. Top: Observed and calculated gravity fields along with a calculated gravity field for a spherical body centred at 13.5 km depth. Middle: Calculated and observed magnetic field for the same profile. Bottom: Crustal model derived from gravity and magnetic modelling (*from* Blakely and Stanley, 1993; Isherwood, 1975).

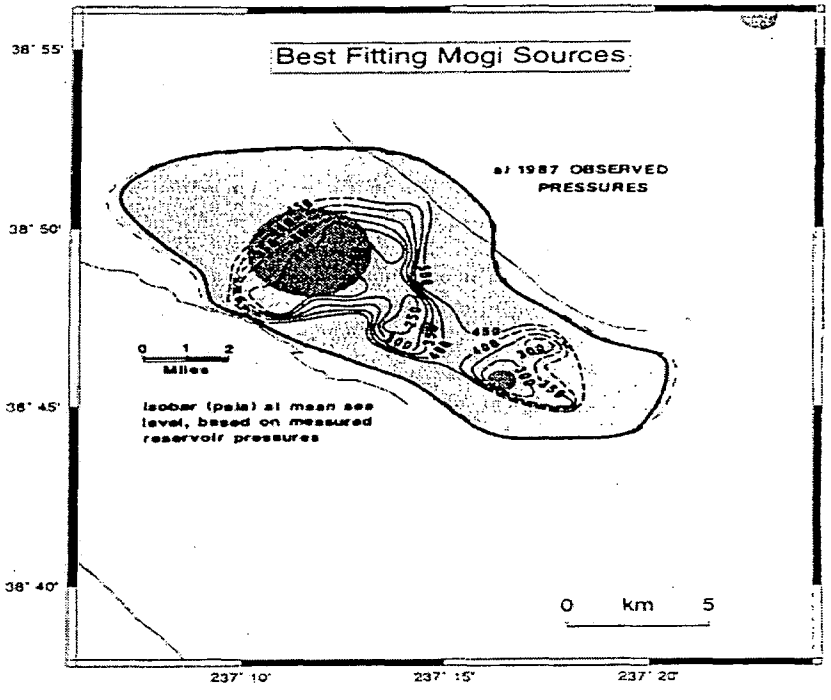

Figure 1.16: The best fitting Mogi source model overlain by 100 psi interval isobars with measured pressure lows for 1987 from Williamson (1992) (*from* Mossop and Segall, 1997).

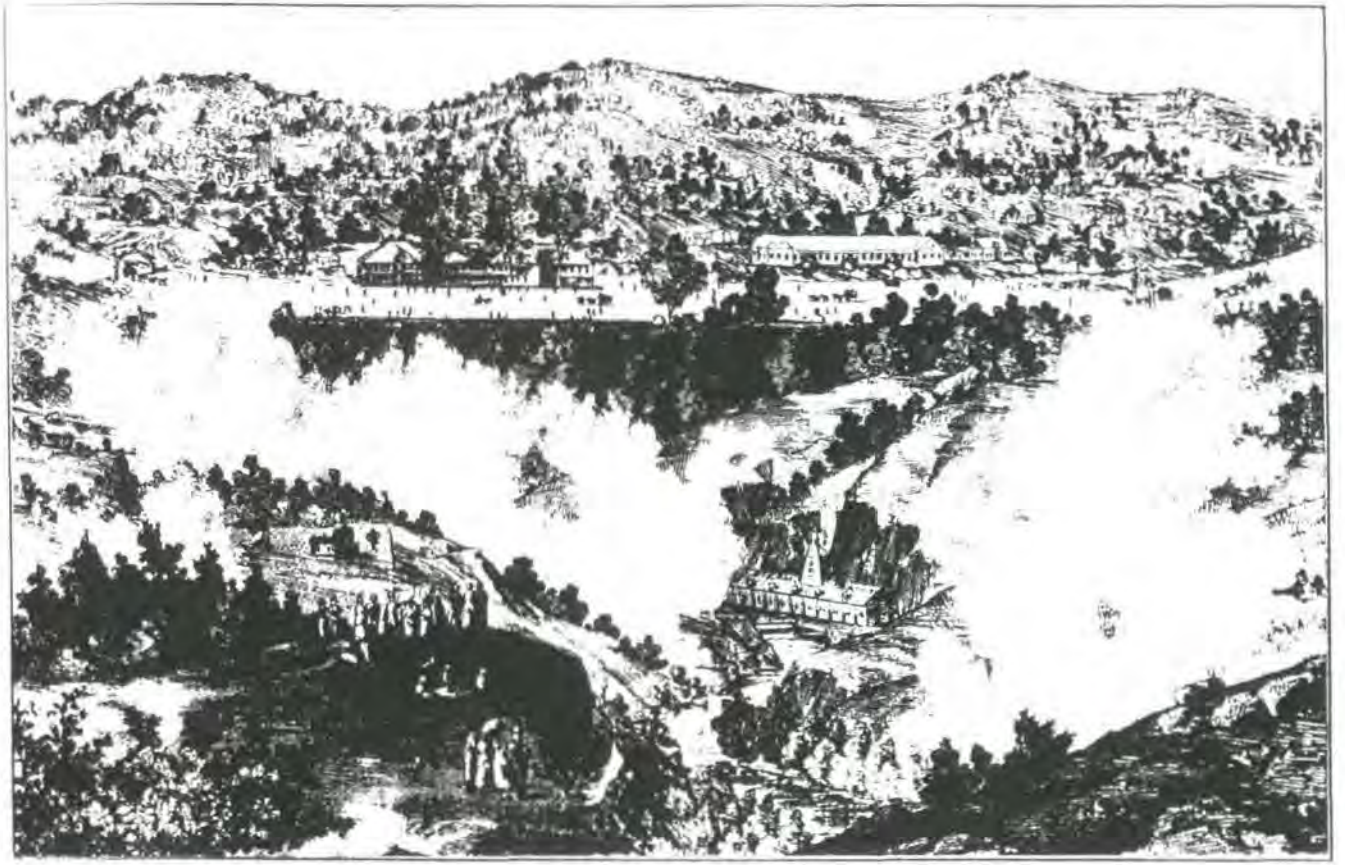

Figure 1.17: View from top of Geyser Canyon west of the geothermal area facing southwest in the direction of The Geysers Resort complex (W. Anderson, 1892). (*from* Hodgson, 1992).

1.5 Commercial development of The Geysers

1.5.1 History of commercial activity at The Geysers

Commercial activity at The Geysers has continued for over 140 years. In the 1860s, a resort hotel was established south of Big Sulphur Creek with a health spa using the mudpots, hot water springs and fumaroles at The Geysers (Figure 1.17). In 1922 electricity was first produced from steam at The Geysers by two small reciprocating steam-driven generators with a total capacity of 1 kW. The power was used for lighting the resort close by. However, this project was subsequently abandoned in 1940 after steam had corroded the pipes and generator. After the development of stainless steel alloys which withstand corrosion effects of steam, and wells were thought economical, communal contracts were drawn in 1955. The Magma Power Company obtained leases and initiated a drilling program in collaboration with the Thermal Power Company as the Magma-Thermal Power Company. By 1960 Pacific Gas and Electricity (PG&E) had purchased steam for its 12 MW unit 1 from the Magma-Thermal Power Company. In 1967, the Union Oil Company of California (UNOCAL) formed a joint venture with the Magma-Thermal Power Company forming the UMT partnership and UNOCAL became the operating partner. However, in 1981, the Magma Power Company was sold to Nortomas as the NEC Company. After 1981, UNOCAL-NEC-Thermal (UNT) supplied steam to Pacific Gas & Electricity (PG&E). In 1985, UNOCAL acquired the NEC Company.

Other companies that utilise geothermal energy from The Geysers are the Northern California Power Agency (NCPA), the California Department of Water Resources (DWR), the Central California Power Agency (CCPA), the Sacramento Municipal Utility District (SMUD) and Freeport McMoran. Other developer/suppliers who have built power plants include Santa Fe International and Geothermal Energy Patrons. The process of electricity generation at The Geysers is made simpler than is possible at most geothermal areas by the vapour-dominated nature of the reservoir. Extracted steam is dry and can be used directly to run the turbines (Figures 1.18 and 1.19). The power plants are distributed throughout The Geysers

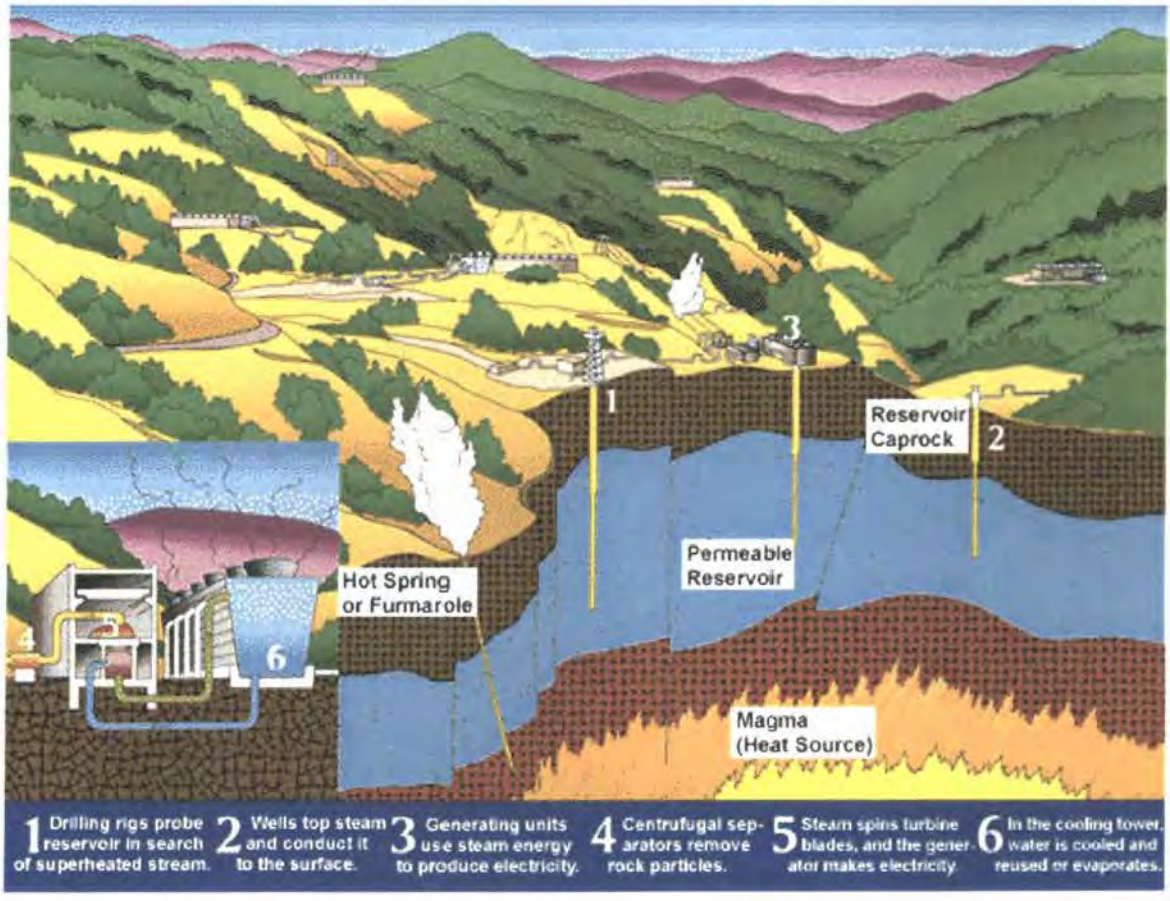

Figure 1.18: Schematic diagram illustrating the processes involved in producing electricity from geothermal energy. (*source*: http://www.calpine.com/energy_assets_4/calpine_4_4.html).

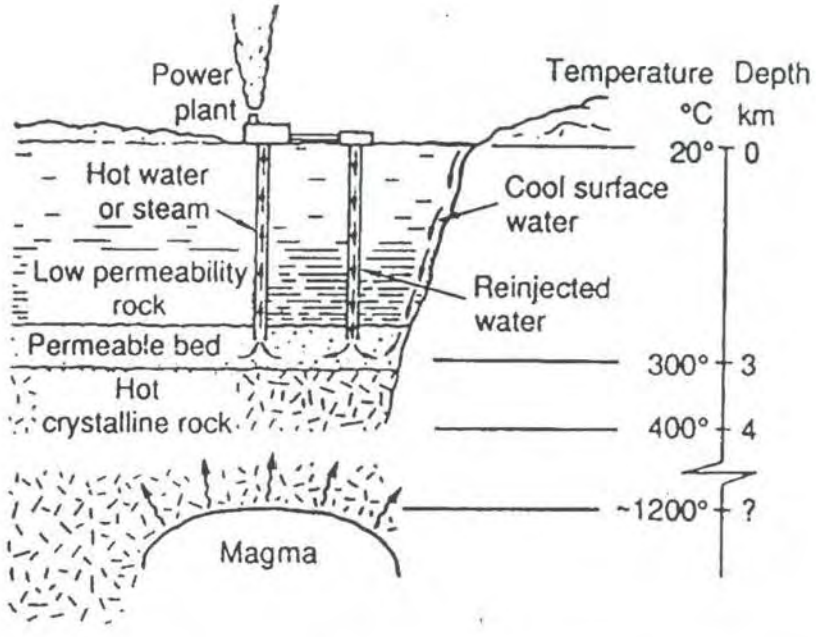

Figure 1.19: Schematic diagram showing a deep-seated magmatic source at depth heating the water, where it is extracted as steam to generate electricity at the power plant. Extracted steam is replaced by liquid injection.

with many companies claiming parts of the reservoir, although there is the largest concentration of sites in the central Geysers where UNOCAL controls most of the area (Figures 1.20, 1.21 and 1.22). However, with the acquisition of the PG&E

Figure 1.20: PG&E power plant units 5 and 6 at The Geysers, showing the cooling towers and pipelines to extraction wells (*source*: http://www.eren.doe.gov/geothermal/geysers5and6too.html)

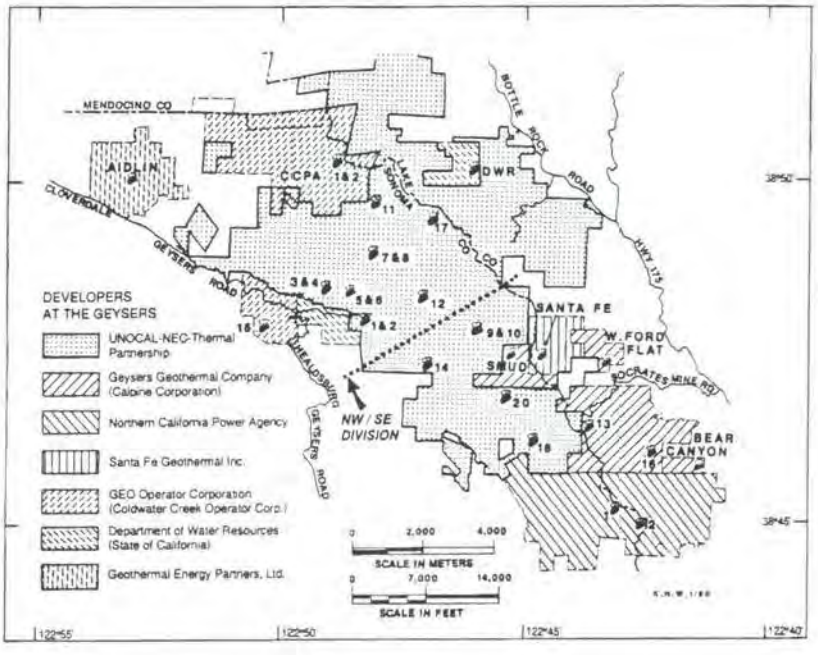

Figure 1.21: Map of The Geysers production area showing the areas exploited by each of the field developers. Numbers refer to power plant units of PG&E (*from* Barker *et al.*, 1992).

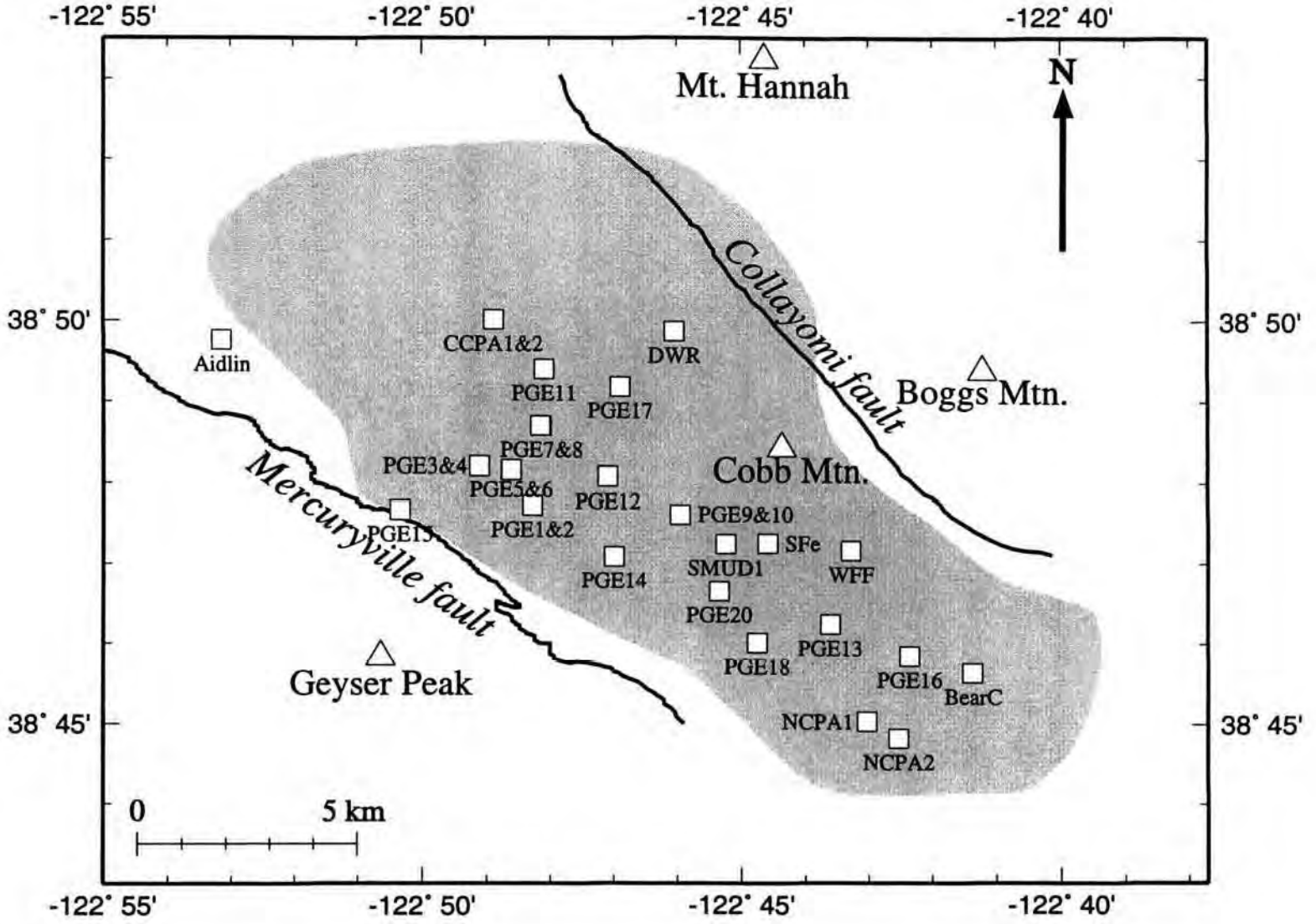

Figure 1.22: Map showing the location of power generating units at The Geysers geothermal area. At sites where two units are indicated, they are housed in the same building. Key: BearC: Bear Canyon; SFe: Santa Fe; WWF: West Ford Flat; PGE: PG&E; NCPA and CCPA: North and Central Calif. Power Agency*(from Ross, 1996).*

power plants that were auctioned in 1998 and with the purchase of all UNOCAL assets by Calpine Corporation in March 1999, the Calpine Corporation now enjoys a virtual monopoly of The Geysers geothermal area. 90% is now owned by the Calpine Corporation and 10% by NCPA.

1.5.2 Commercial exploitation of The Geysers

Production at The Geysers has occurred in three phases (Tables 1.1 and 1.2, Figure 1.23). During phase I the UMT leases had two units in use. When production began in 1960 steam deliverability was $1.0x10^4$ kg/hr. By 1964, a production rate of $7.25x10^5$ kg/hr had been accomplished and this rate remained constant until 1971. At this time, the reservoir had a maximum capacity of 3000 MW with an estimated life time of 30 years. The projections were purely based on estimates on the amount of heat available to generate steam and no research on reservoir mechanics was conducted at this time (Kerr, 1991).

Table 1.1: Major development phases at The Geysers.

Development Phase	Period	Installed generating capacity (MW)	Yearly increase in power generation (MW)	Steam withdrawal kg/hr
I	1960-1968	82	10	$0.1x10^6$ (1960) $0.73x10^6$ (1968)
II	1969-1981	943	67	$6.58x10^6$ (1981)
III	1981-1989	2043	150	$13.61x10^6$ (1987)

During the second phase, 12 additional units were installed with a capacity of 861 MW, which increased steam withdrawal to $6.8x10^6$ kg/hr. Production increased at a rate of 63 MW per year until 1981. The success of the UNOCAL/PG&E partnership as supplier and producer, coupled with rises in oil prices and additional incentive for research into alternative energy by the US federal government encouraged more commercial activity.

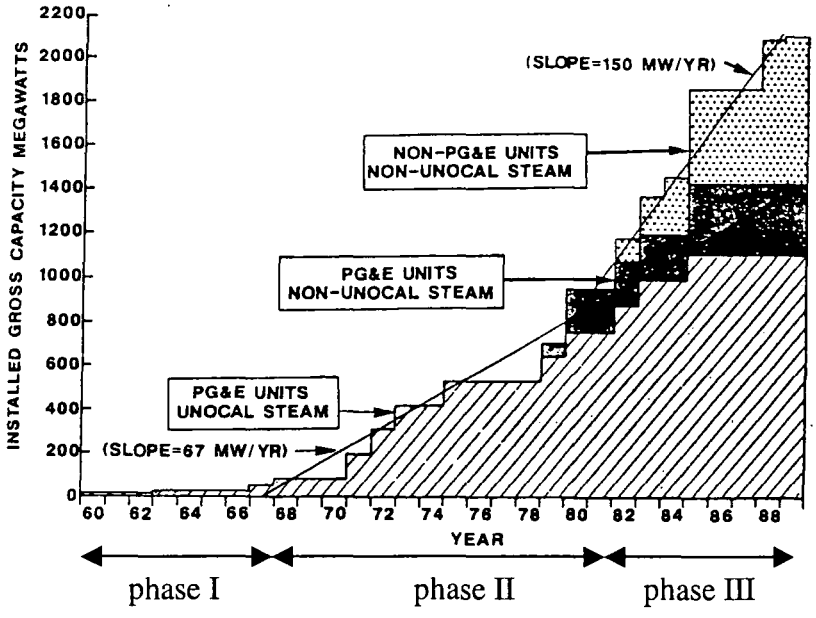

Figure 1.23: Commercial development and power generation at The Geysers with time. A large portion of power generation is with the PG&E and UNOCAL partnership. Three stages are shown by installed capacity, with development phases 1960 to 1968, 1969 to 1981 and 1981 to 1989 (*from* Barker *et al.*,1992).

During phase III an additional 14 units were installed and between 1981 and 1989 power generation increased by 150 MW/yr to peak at an unsustainable 1800 MW/yr in 1987, when steam was extracted at a rate of ~13.6 x 10^6 kg /hr (Barker *et al.*, 1992). As a result of such a high rate of steam withdrawal, reservoir pressure declined steadily at an average rate of 11% per year. Pressure has declined since 1987 by 2.1 MPa to reach 1.4 MPa by the late 1980s and an estimated 0.7 MPa at present. Without proper communication between rival companies and in the belief that the drops in pressure were localised, no immediate action was taken by the operators. New power plant generators were built as late as 1989. However, since 1989, no new power plants have been built on UNOCAL leases. During the 1990s pressure continued to decline and power generated is currently 2/3 of the 1989 installed capacity.

Since then, methods such as reducing turbine inlet pressure, infill drilling and water reinjection have been used to mitigate steam reservoir pressure decline. In 1995, due to a collapse in energy prices "economic curtailments" were imposed resulting in very low production levels (Barker and Pinogol, 1997). Thermal

Table 1.2: Table showing each of the power generation units currently operating at The Geysers (updated *from* Barker *et al.*, 1992). At present, all UNOCAL assets, all PG&E power plants, Bear Canyon Creek, West Ford flat and Aidlin power plants are owned by Calpine.

Phase	Unit	Start-up Date	Steam Supplier	Gross Capacity (MW)	Cumulative Capacity (MW)
I	PG&E-1	Sep-60	Retired 1991	12	12
I	PG&E-2	Mar-60	Retired 1992	14	26
I	PG&E-3	Apr-67	Retired 1992	28	54
I	PG&E-4	Nov-68	Retired 1992	28	82
II	PG&E-5&6	Dec-71	UNOCAL	110	192
II	PG&E-7&8	Nov-72	UNOCAL	110	302
II	PG&E-9&10	Nov-73	UNOCAL	110	412
II	PG&E-11	May-75	UNOCAL	110	522
II	PG&E-12	Mar-79	UNOCAL	110	632
II	PG&E-15	Jun-79	Retired 1989	60	692
II	PG&E-13	May-80	Calpine-SRGC	137	829
II	PG&E-14	Sep-80	UNOCAL	114	943
III	PG&E-17	Dec-82	UNOCAL	119	1062
III	NCPA-1	Jan-83	NCPA	110	1172
III	PG&E-18	Feb-83	UNOCAL	119	1291
III	SMUDGEO-1	Oct-83	GGC	72	1363
III	Santa Fe	Apr-84	SFI	80	1443
III	DWR –Bottle Rock	Mar-85	Retired 1990	55	1498
III	PG&E-16	Oct-85	Calpine-SRGC	119	1617
III	PG&E-20	Oct-85	UNOCAL	119	1736
III	NCPA-2	Nov-85	NCPA	110	1846
III	CCPA-1	May-88	GEO	65	1911
III	CCPA-2	Oct-88	GEO	65	1976
III	Bear Canyon Creek	Sep-88	GGC	20	1996
III	West Ford Flat	Dec-88	GGC	27	2023
III	Aidlin	Jun-89	GEP	20	2043

cycling damage to wells occurred during this period, wellhead pressure rose, and steam production declined further, especially during the winter months of 1995-1996 and 1996-1997 (A. Pinogol, *pers. comm.*) (Figure 1.24). However, water was injected throughout this period, which reduced depletion. It was thought conceivable that this might reduce back pressure on the production wells, fostering higher steam production and lower field wide pressure (Atkinson, 1998).

Contractual disagreements between steam suppliers and electricity producers have also contributed to plant closure (Atkinson, 1998). Since April 1998, vying for high electricity prices, PG&E responded to the new deregulated electricity market in California and increased cycling of its Sonoma County power plants. In

response UNOCAL increased cycling of its wells with grave consequences for reservoir pressure monitoring.

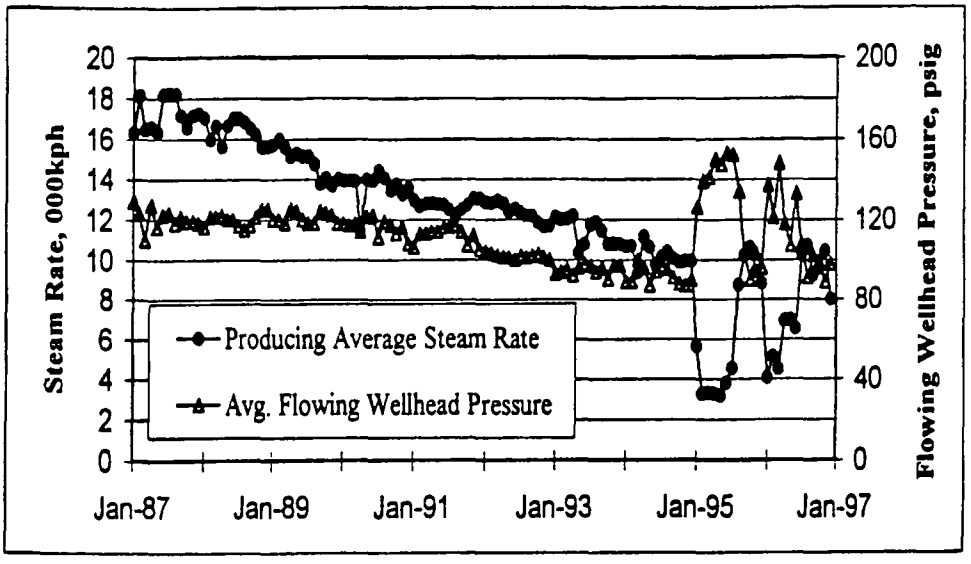

Figure 1.24: Relationship between extraction rate of steam to produce electricity and daily flowing wellhead pressure. There is a correlative trend in extraction and wellhead pressure from Jan. 1987 to Jan. 1995 when "economic curtailments" commenced. Fluctuations in wellhead pressure made estimates of field-wide reservoir pressure very difficult. (*from* Barker and Pinogol, 1997).

1.5.3 Reinjection of water to the reservoir

Water injection has been the primary method used to mitigate the growing decline in reservoir pressure. In theory, as most of the heat in the reservoir is stored in the rocks rather than in the water, replenishing water lost due to production would prolong the life span of the reservoir. However, before an injection well can be developed, factors such as fracture density, fracture distribution, rock permeability, temperature, steam pressure, rock type and liquid saturation need to be examined (Barton, 1999).

In the 1980s, a total of 700 kg/s of water was injected at a temperature of 25-35° C. A condensate reinjection program was conducted and 25% of the condensate and fresh water from Big Sulphur Creek was retrieved (Stark, 1992). In Sept 1997, the

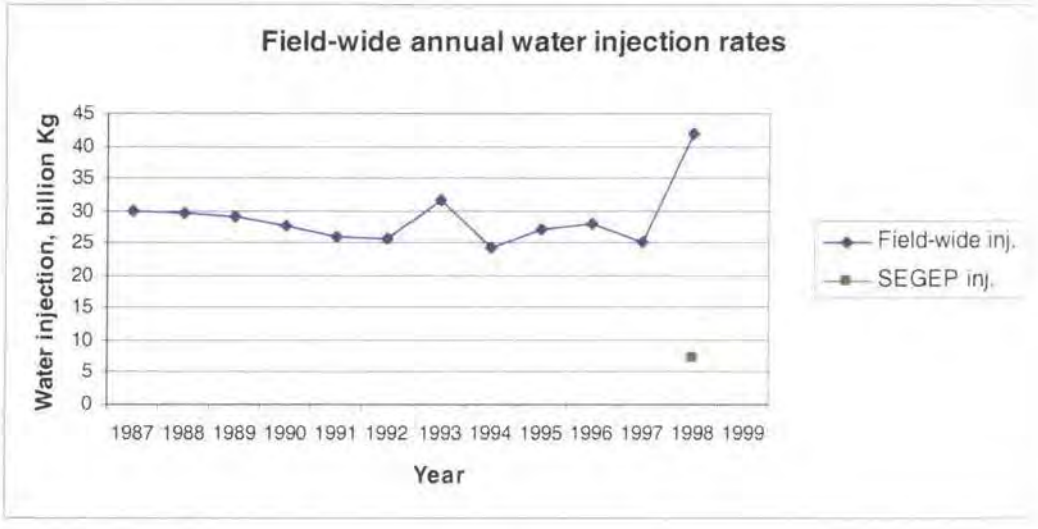

Figure 1.25: Geysers field-wide and SEGEP annual water injection by water year (July-June). SEGEP injection for 1998 was 7.2 x 10^{10} Kg (*from* Atkinson, 1998).

(a)

(b)

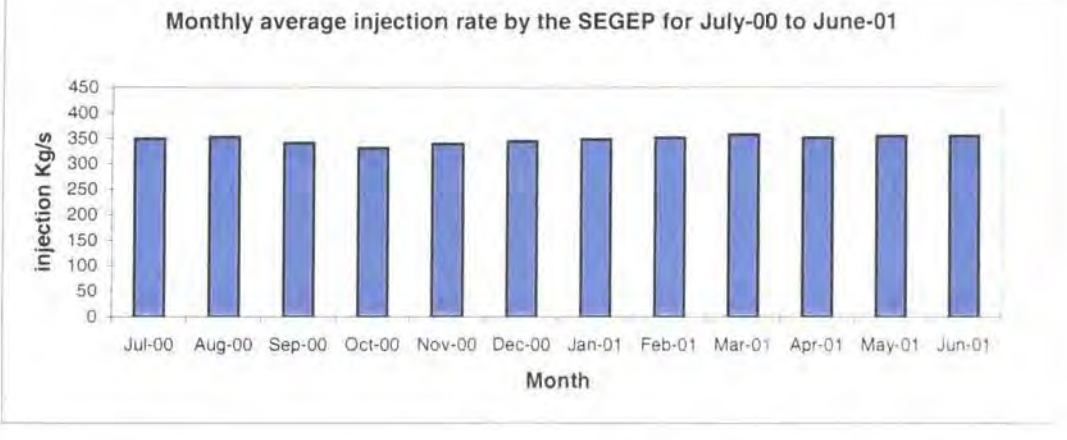

Figure 1.26: Monthly average injection rates at SEGEP. (a) When SEGEP commenced operations in Sep. 1997 to July 1998 and (b) Most recent data from July 2000 to June 2001 (*Source*: http://www.geysers-pipeline.org/operations.htm).

South East Geysers Effluent Pipeline (SEGEP) project was initiated with injection amounting to approximately 1 x 10^{10} kg/yr (Figures 1.25 and 1.26). It is hoped that 40-100% of reinjected liquid will be converted to steam and will result in an increase in power generation of 70 MW. High injection recovery is achieved in areas with low reservoir pressure, high temperature and high permeability. In 1991, Unit 13 had the highest recovery factor from liquid injection amounting to 73% of injected liquid corresponding to 10.1 MW generation of electricity per year. However in other areas such as Bear Canyon and the Sonoma steam fields, recovery was very poor to at ~ 3% of injected liquid (Goyal, 1999). However, the balance between liquid and vapour content in the reservoir is currently thought to be threatened by the rate of injection and at present there is more water injection than steam extracted for production (Figure 1.27). Large-scale recovery of the steam field is thought to be a long term possibility.

Another project in collaboration with the city of Santa Rosa and UNOCAL has commenced. A pipeline was built between Santa Rosa and The Geysers via which semi-purified "grey water" at temperatures of < 10° C is delivered to the reservoir at a rate of 1.25 x 10^{10} kg/yr (Atkinson, 1998). The rate of steam retrieved from liquid injection is mainly monitored by injection of trace fluids, which recently included environmentally friendly Hydrofluorocarbons (HFC) tracers. The full environmental impact of reinjection of liquid into the reservoir is as yet unknown. However, the Northern California Power Agency (NCPA) has reported a large drop in non-condensable gases such as H_2S in the extracted steam.

Injection involves simply pouring water into wells (Figure 1.28) as the reservoir pressure is lower than the hydrostatic pressure. There are several negative aspects to liquid injection, which include the plugging of fractures in the reservoir, silica-scale build-up in injection wells, and cooling of the reservoir rock. Also, in areas of high permeability, lateral conduits can carry injected liquid into production wells causing extensive damage (e.g. at an injection well near Unit 13 in October 1995) (Goyal, 1999). Extensive chilling of the rocks adjacent to the rock surface may not only damage the well base but also may convert the mode of deformation from ductile to brittle. Injection also induces seismicity at the base of wells (Figure 1.29).

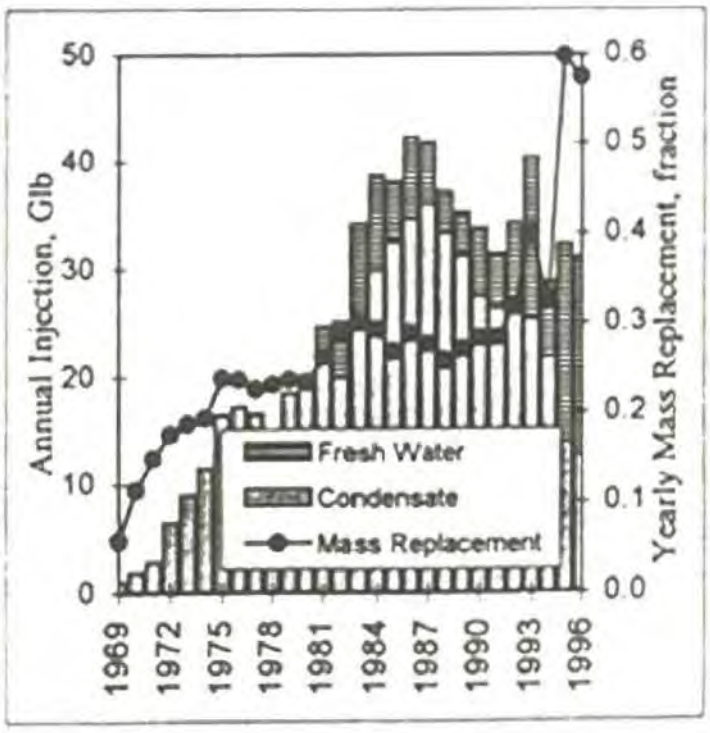

Figure 1.27: Field-wide injection of fresh water and condensate and ratio of injection to extraction of steam. Since the early 1980's more fresh water has been injected than condensate. Fresh water is the darker column and condensate is the lighter column. There are high mass replacement ratios registered for 1995 and 1996 as continued injection took place during periods of power plant shut-down (*from* Barker and Pinogol, 1997).

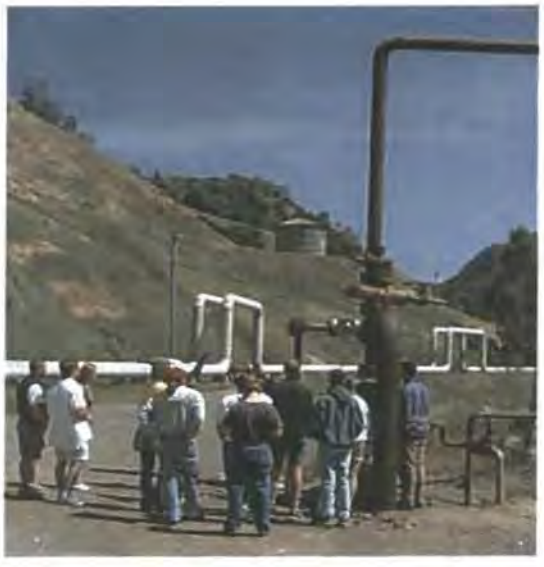

Figure 1.28: An injection well at The Geysers geothermal area. Most injection wells are located in the vicinity of the power plants. (*from* : http://corporate.stanford.edu/research/programs/geoth.html)

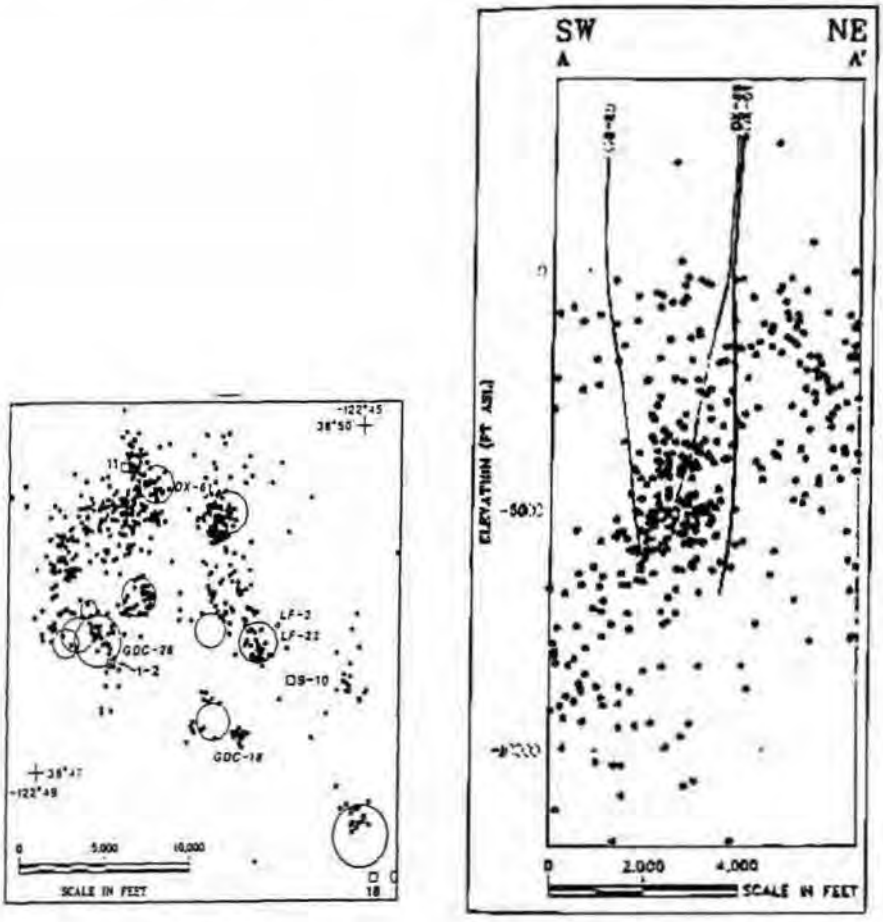

Figure 1.29: (a) Seismic events with $M_D \geq 0.7$ located by the UNOCAL network between 11/1989 and 08/1989. Open circles are injection wells with circle area proportional to volume injected over the study period. Unfilled labelled squares are power plants. (b) Cross-section of earthquakes clustered near injection well DX-61 from Sep. to Dec. 1986 (*from* Stark, 1992).

1.6 Seismicity at The Geysers

1.6.1 History of seismic monitoring at The Geysers

The first earthquake survey at The Geysers was conducted by Lange and Westphal (1969). Prior to 1975, sensor coverage at The Geysers was inadequate to detect many of the earthquakes. Since then, continuous monitoring of earthquakes has been undertaken by the U.S. Geological Survey using the California Network (CALNET) (section 1.6.4). The number of earthquakes recorded more than

doubled between 1962 and 1975-77 (Marks *et al.*, 1978). Although, the *b*-value of 1.1 calculated for this period is similar to the regional value, the rate of seismicity at The Geysers was 45 times higher than the surrounding area (Ludwin and Bufe, 1980). Subsequent to these early observations there has been an increase in intensity and expansion of the seismogenic volume at The Geysers.

A causal relationship between steam extraction and earthquakes was suggested as early as 1972 (Hamilton and Muffler, 1972). This relationship was supported by later research (e.g. Marks *et al.*, 1978; Majer and McEvilly, 1979; Ludwin and Bufe 1980; Allis, 1982). Most of the seismic activity is thought to be induced by geothermal exploitation including both the removal of steam and fluid injection (Eberhart-Phillips and Oppenheimer, 1984; Stark, 1990). Injecting cool condensate into the reservoir may have generated up to 50% of the earthquakes recorded at The Geysers (Stark, 1992). Liquid reinjection may also generate larger earthquakes than production-induced events (Ross, 1996). Other independent studies generated 3-D seismic velocity models using earthquakes at The Geysers (O'Connell, 1986; Zucca *et al.*, 1994; Ross, 1996 and Julian *et al.*, 1996) (see section 1.6.5). Some localised studies were also conducted to monitor seismicity and to develop highly accurate 3-D velocity models (Romero *et al.*, 1994, Kirkpatrick, 1995). Microearthquake clusters extending from the bottoms of the injection wells were also used to provide 3-D images of the path of injected water and to track its migration within the reservoir. This method may be used in place of the earlier method of using tritinium dye to track fluid migration. Non-double-couple source mechanisms have been identified that may help to identify the genesis process (Ross *et al.*, 1999). The major contributions to monitoring seismicity at The Geysers reservoir are listed in Table 1.3.

1.6.2 Seismicity within the reservoir

There has been a great increase in the number of earthquakes, and in their spatial distribution at The Geysers, as seen by events located by the CALNET catalogue from 1972 to 1995 with a threshold magnitude of $M_D \geq 1.2$ (Figure

Table 1.3: Major contributions to understanding seismicity at The Geysers geothermal area. MEQ: Microearthquakes.

Author	Contribution
Lange and Westphal (1969)	Recorded very shallow seismicity mainly induced in the reservoir.
Byerlee and Brace (1970)	Demonstrated lack of stick slip (earthquake-producing) faulting at high temperatures at The Geysers.
Ward (1972)	Suggested MEQ at The Geysers not caused by steam extraction because earthquakes occurred also in undeveloped areas in field. Accurate location of MEQs can be used to map active faults that channel hot water to surface.
Hamilton and Muffler (1972)	Suggested MEQs gave indication of temperature at depth and that the presence or absence of earthquakes could reflect hot or cold spots respectively.
Steeples and Iyer (1976)	Teleseismic body waves showed delayed arrivals correlating with gravity low.
Marks *et al.* (1978)	Observed the absence of earthquakes deeper than about 5 km in the region of the gravity low, consistent with hypothesis of elevated temperatures.
Majer and McEvilly (1979)	Showed low-velocity material absent in the upper 3 km of the crust.
Denlinger (1979)	Observed MEQs to be clustered in the reservoir where fluid depletion and high strain occurred.
Denlinger & Kovach (1981)	Used vibroseis survey and suggested fracture zones that could be mapped from the surface.
Bufe *et al.*, (1981)	Observed extensional motion along short faults more northerly orientated than the Maacama, Collayomi and Mercuryville fault zones.
Bufe and Shearer (1981)	Suggested injection of fluid primarily responsible for induced seismicity of The Geysers.
Iyer *et al.*, (1981)	Suggested teleseismic *P*-wave arrival time delays caused by magma chamber between Mt. Hannah and The Geysers that extends from 4 km to > 30 km depth.
Young and Ward (1981)	Two-layer model for upper crust. Region of high attenuation of seismic waves roughly corresponding to gravity low.
Oppenheimer and Herkenhoff (1981)	Used teleseismic arrival time data and gravity data to model a low velocity-density body beneath Mt. Hannah which could be the heat source. Suggested that steam extraction induces earthquakes.

Author	Contribution
Eberhart-Phillips and Oppenheimer (1984)	Carried out simultaneous inversions of *P*-wave arrival times for hypocentres and velocity structure. Presented a 1-D model showing velocity increase in Geysers and clustering of earthquakes near well heads.
Oppenheimer (1986)	Calculated focal mechanisms constrained to be double-couple. Solutions strike-slip at 3 km below sea level but mostly dip-slip at deeper than 3 km bsl.
O'Connell and Johnson (1988)	Used waveform inversion to determine moment tensors for MEQs. Found non-double-couple components but attributed them to error.
Segall (1989)	Studied poroelastic stress and pressure resulting from fluid extraction/injection in reservoir
Benz *et al.* (1992)	Suggested shallow asthenosphere for heating the crust and producing crustal magma bodies.
Romero *et al.* (1994)	Studied increased seismicity and diffuse attenuation structure of NW Geysers and showed injection paths and clustering of MEQs even closer to wells than previously determined.
Zucca *et al.*, (1994)	Conducted *Vp* and attenuation study using the UNOCAL network at The Geysers and commented on the low-*Vp* zone at the top of the reservoir.
Ross (1996); Julian *et al.* (1996)	Used local earthquake tomography and found *Vp/Vs* ratio is anomalously low (-9%) in steam reservoir.
Ross (1996); Ross *et al.* (1996)	Found 20% of earthquakes at The Geysers are non-double couple and suggested reinjection of water into reservoir.
Evans *et al.* (1995)	Observed shear-wave splitting and wave-speed anisotrophy with northeast and northwest polarisation directions caused by permeablilty anisotropy at The Geysers.
Foulger *et al.* (1997)	Conducted 4-D *Vp* and *Vp/Vs* local earthquake tomography for the whole Geysers and observed an increase in the low *Vp/Vs* anomaly of 4% which was attributed to depletion of fluids in the reservoir caused by steam extraction.
Boitnott and Kirkpatrick (1997)	Interpreted the low *Vp/Vs* anomaly observed at The Geysers as a result of fluid compressibility and hardening of the shear modulus upon drying of argillaceous material found in the reservoir rocks.
Ross (1996); Ross *et al.* (1999)	Highly accurate moment-tensors were determined which suggested source processes such as cavity creation and collapse result from steam withdrawal and fluid reinjection.

1.30). This time period also corresponds to the increase in commercial activity at The Geysers (Figure 1.31). In the 1970s, events were few (Figure 1.30a - c).

The seismogenic volume expanded from the late 1970s to the early 1980s to the northwest and southeast parts of the reservoir from the central part of the reservoir. The number of events located within the reservoir dramatically increased in the 1980s (Figure 1.30e-i). During Phase III of The Geysers exploitation period (1981-1989), the deeper, seismically active volume remained constant in volume despite an increase in the number of events. Diffuse seismicity also occurred in the northwest and southeast Geysers. However, the base of the seismogenic zone, which normally is at about 5 km below sea level, is less clearly defined in these areas. From the mid-1980s event distribution has been largely confined to two depth intervals 0-2.5 km bsl and 4 km bsl. The low seismicity area between 2.5 and 4 km bsl in the central Geysers is less active and is termed the "dead zone" (Ross, 1996). The lack of deeper events below 4 km bsl could be a result of elevated temperatures and partial melt in the felsite batholith (Oppenheimer and Herkenhoff, 1981; Bufe *et al.*, 1981) (Figure 1.30g-h).

Since pressure began to decline in the late 1980s, the intensity of activity in the central Geysers decreased. PG&E units 1, 2, 3, 4, and 15 at The Geysers were decommissioned between 1989 and 1992, and clear reduction in earthquake activity occurred (Figure 1.30i-l). However, since the mid-1990s events have become more clustered. The correlation between the locations of power plants and events is very strong. The diffuse events in the southeast Geysers could also occur in response to power plant shut-down in those areas due to reduced commercial activity. Power plants are not directly responsible for seismic activity, but most injection wells and extraction sites are in close proximity to power plants. It is conceivable that the very tight clusters are injection-induced events, which in some areas in the southeast Geysers account for 40% of the seismic events observed (Figure 1.29). Since SEGEP began the average number of seismic events recorded monthly by the Northern California Seismic Network (NCSN) at The Geysers has increased by 50 to 80 events. The correlation between the number of events and the rate of steam extraction is strong until 1987 after which the correlation breaks down due to decrease in steam extraction and increase in injection (Figure 1.31).

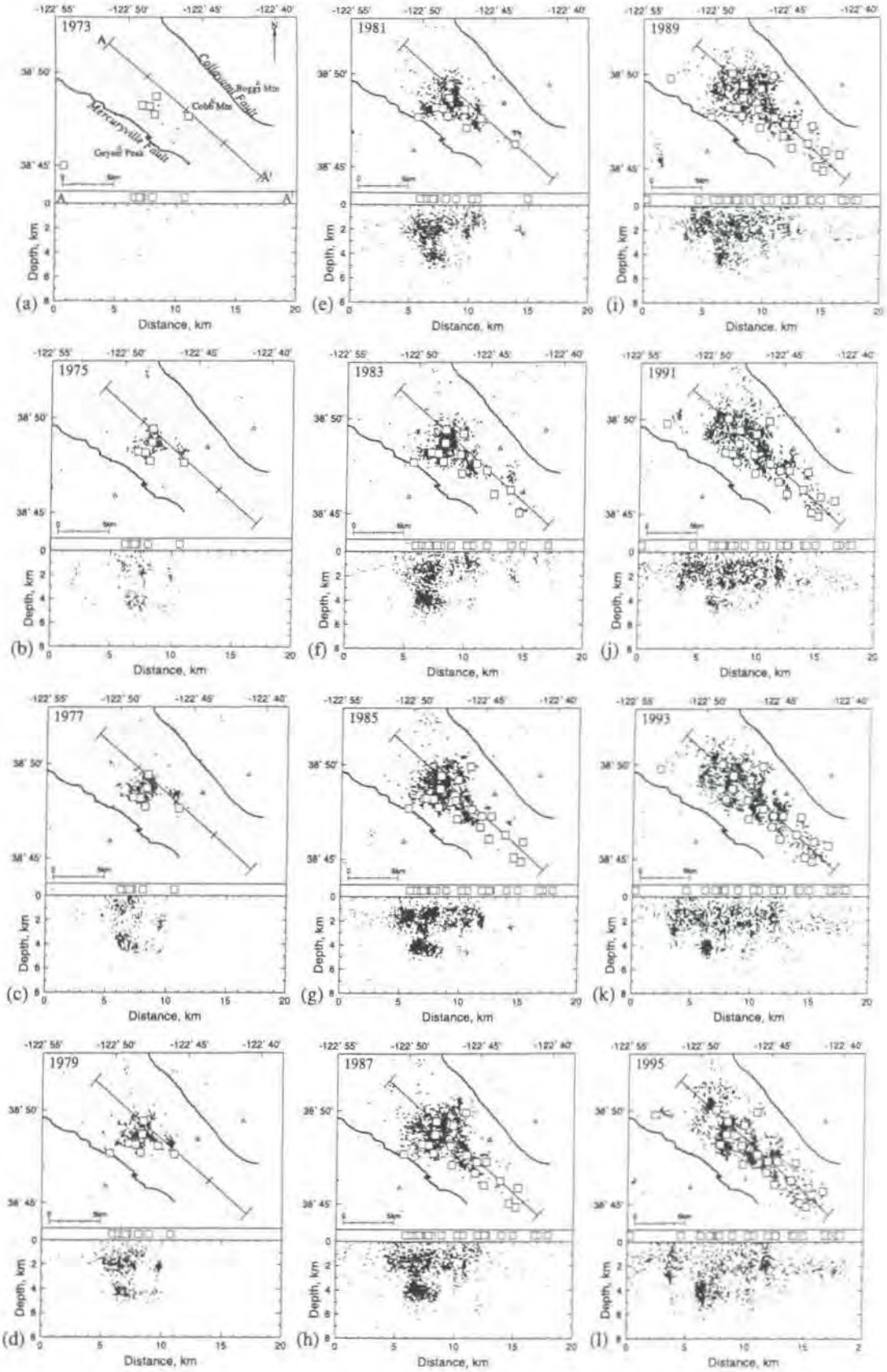

Figure 1.30: Biannual seismicity at The Geysers recorded by the NCSN network with epicentre and hypocentre for events $M_D > 1.2$ between 1973 and 1995. Superimposed are the power plants operat time (*from* Ross, 1996).

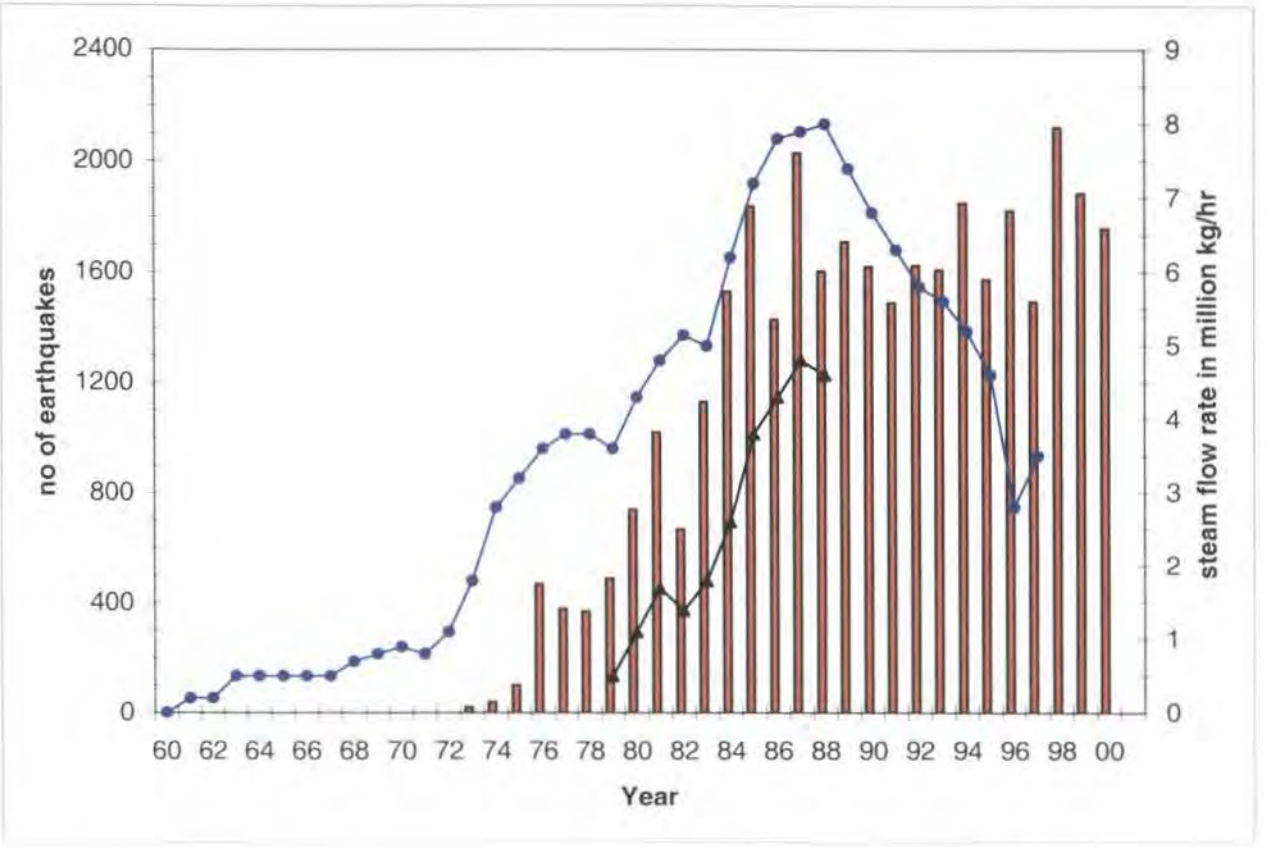

Figure 1.31: Flow rate of steam from UNOCAL-owned leases shown as blue dots from 1960 to 1997 and non-UNOCAL-owned leases are shown as black triangles (modified from Barker *et al.*, 1992; Barker and Pinogol, 1997). Non-UNOCAL flow rates were not available from 1988 onwards. Red columns are number of earthquakes for magnitude $M_D \geq 1.2$ recorded at The Geysers by NSCN 1973 to 2000 (*from* NCSN).

1.6.3 Processes that induce earthquakes at The Geysers

It is clear that The Geysers reservoir has been over-developed because pressure has declined since 1987. While the companies involved try to maximise and recover the resources using methods such as infill drilling, turbine inlet pressure changes, steam conservation and water injection, researchers are still trying to understand the processes that induce the earthquakes. Although there have been many suggestions involving temperature, pressure, volume and reservoir strength, which is the true seismogenic process is still being debated (Table 1.4).

Table 1.4: Some proposed mechanisms for inducing earthquakes at The Geysers geothermal area.

Author	Proposed Mechanism
Hubert and Rubey (1959)	Earthquakes associated with fluid injection result from change of hydrostatic pressure as it increases pore pressure and lowers effective normal stress.
Majer and McEvilly (1979)	An increase in shear stress due to fracture deflation causes earthquakes. Seismicity related to volumetric change associated with steam withdrawal. Estimated the annual volumetric change necessary to account for observed annual seismic moment rate and it correlated well with the geodetically measured subsidence of the reservoir.
Denlinger (1979)	Cooling is responsible for the induced seismicity by reducing the normal stress across fracture surfaces. However, reservoir temperatures have not changed significantly.
Lofgren (1981)	Supported the idea of Majer and McEvilly (1979) by using geodetic measurements to show that the horizontal and vertical contraction of the reservoir support the mechanism.
Allis (1982)	Suggested two mechanisms for induced earthquakes: a) pressure changes and hardening of fault gouge, and b) an increase in reservoir strength. Pre-production aseismic slip (creep) at The Geysers is converted to stick-slip creep by either a substantial decline in fluid pressure or by an increase in the coefficient of friction due to deposition of silica on the fracture surfaces.
Denlinger and Bufe (1982)	Reservoir pressure decline could convert creep to stick-slip movement.
Segall (1989)	Related poro-elastic theory to earthquakes genesis. As a result of fluid extraction and injection into the reservoir, poro-elastic stress increases pressure and decreases effective normal stress which allow fault movement and induces earthquakes.

Earthquakes are clustered around injection wells at shallow levels (Romero *et al.*, 1994) (Figure 1.29). It has been firmly established that both steam extraction and water injection induce earthquakes. Changes in hydraulic pressure and fluid injection have been suggested as they are known to trigger small earthquakes in reservoirs behind dams (e.g., Hubert & Rubey, 1959). Steam withdrawal causes volumetric change and probably induces seismicity at The Geysers (Majer & McEvilly, 1979). Geodetic measurements also supported volume change at The Geysers (Mossop and Segall, 1997). Following the work of Majer & McEvilly (1979), Allis (1982) suggested a mechanism linking induced earthquakes to increase in reservoir strength. Although, The Geysers area has presumably always deformed by aseismic creep, the onset of steam extraction may have converted this to stick-slip movement through an increase of coefficient of friction along the surfaces of the faults (Allis, 1982). Another mechanism that has been suggested is pore-pressure increase and cooling by injection (Stark, 1990).

1.6.4 Seismic networks at The Geysers

Several temporary networks have been deployed at The Geysers to detect seismicity (Figure 1.32 and Table 1.5) (Appendix 1). Initial surveys were carried out by Lange and Westphal (1969) and by Hamilton and Muffler (1972) (Table 1.5). These studies showed the need for continuous monitoring of The Geysers because of the anomalously high seismicity within the geothermal area. The first permanent seismic network, the Northern California Seismic Network (NCSN) was deployed at The Geysers in 1975 by the U.S. Geological Survey as part of the CALNET network, which monitors seismicity in the state of California.

NCSN has eight seismic stations located within a 25-km radius of The Geysers and more than 40 stations commonly record events located within the production area (Eberhart Phillips and Oppenheimer, 1984) (Figure 1.32). Analogue signals from stations are radioed to U.S. Geological Survey Western Regional Headquarters at Menlo Park where the signals are digitised at 100 samples per second. These seismic stations are mostly one-component vertical stations. The *P*-waves are

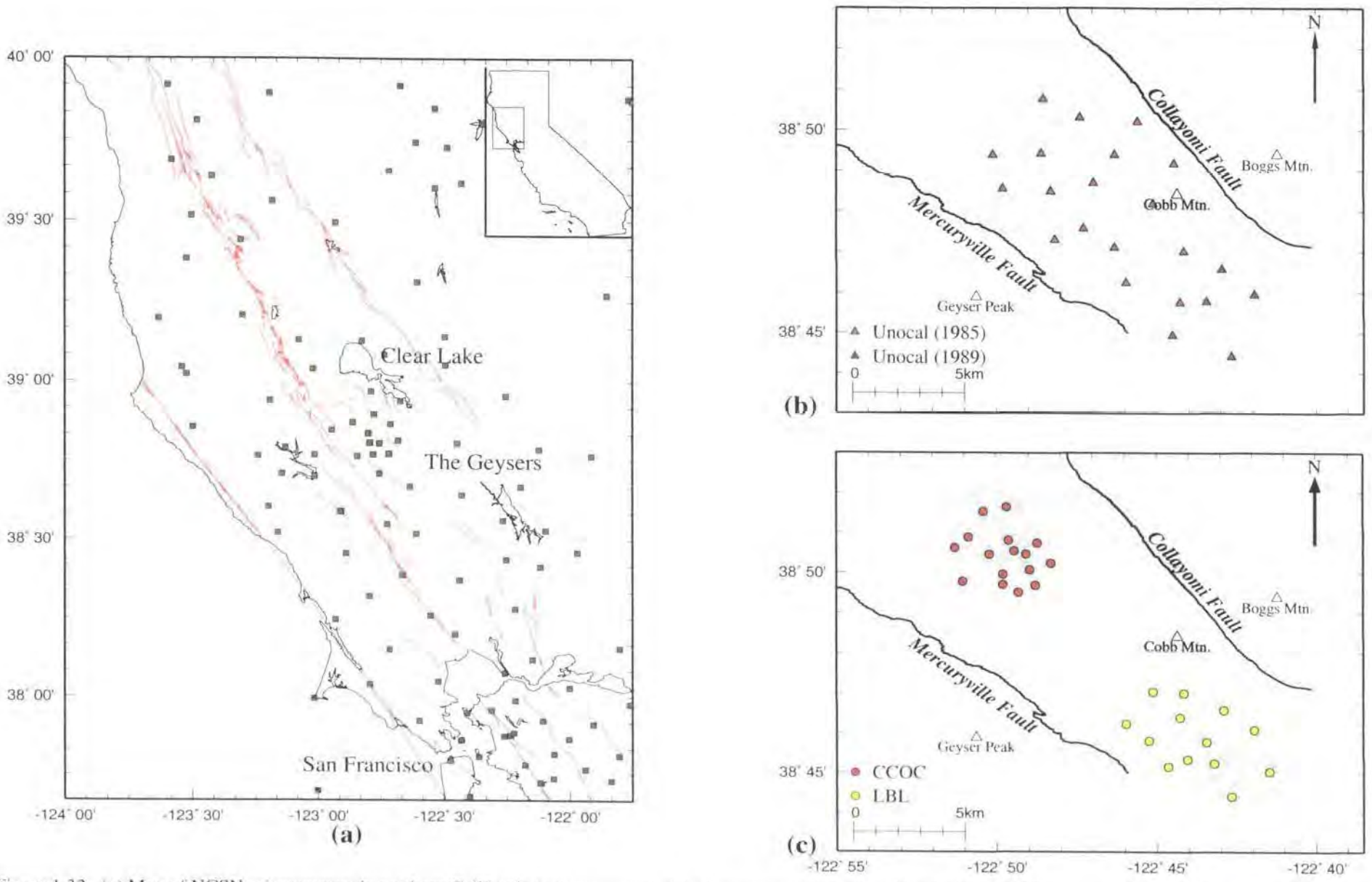

Figure 1.32. (a) Map of NCSN seismometers in northern California (green squares). The Geysers area is enclosed by the box. Red lines are faults. (b) Map of The Geysers production area showing the location of UNOCAL seismometers. Magenta triangles: stations deployed in 1985; green triangles: stations deployed in 1989; white triangles: mountains (c) Map of The Geysers showing the CCOC network (red circles) in the northwest and the LBL network (yellow) in the southeast. (from Ross, 1996).

automatically picked, events located, and catalogued at the Northern California Earthquake Data Centre (NCEDC) at U.C. Berkeley and available for public-domain use. The NCSN detection threshold has increased from M_D = 1.2 in 1975 to M_D = 0.5 in 1981 due to improvements to the network. The largest event recorded in The Geysers by this network occurred in 1992 in the northeast Geysers 3 km bsl with M_D = 4.3. On average, 10 events are detected every day by the network, although numerous, very small magnitude events occur in the production area that cannot be detected by NCSN.

Table 1.5: Seismic networks at The Geysers (*from* Barton, 1998).

Network/Reference	**Dates**	**No. of stations**	**Array diameter (km)**	**No. of events reported**
Lange & Westphal (1969)	10-19 Oct., 1968 (120 hrs.)	6	Not available	19
Hamilton & Muffler (1972)	16 Mar.–7 Apr, 1971	7 remote, 1 base station	Not available	53
NCSN	From 1975 in The Geysers	8 stations within The Geysers; 40 within detection threshold	15 in The Geysers	120 $M_D \geq 1.2$ events/month
O'Connell (1986)	26 days in 1982	Not available	6	Not available
UNOCAL network	From 1985	22 since 1989	15	40-50 events/day
GEO (NW Geysers)	1988-1994	16	4	5000
IRIS (Ross *et al.*, 1999)	Apr. 1991	15	15	3096
LBL (SE Geysers)	1992-1995	13	7	~75 events/month

Because of the need to understand and monitor seismicity at The Geysers, which could potentially impact both steam production and integrity of power plant installations, a field-wide permanent seismic network was established in The Geysers. It has been in place since 1985 and is known as the UNOCAL network after the company and operating partner, although currently operated by the Calpine Corporation. The network covers the whole geothermal reservoir. Seismicity is monitored continuously by 22 seismic stations. Of these 8 are three-component stations and the others have vertical-only sensors (Figure 1.32).

Seismic recordings are digitized at 100 sps. The network geometry changed little between 1991 and 1998 (section 2.1.3).

Two smaller networks of higher density but smaller spatial extent were in operation in the northwest Geysers, formerly by CCOC, and then by the Central California Power Agency (CCPA), and in the southeast Geysers by Lawrence Berkeley Laboratories (LBL). In 1988, in partnership with Geo East Mesa Ltd (GEO), LBL installed a 4-km-diameter network with 16 high-frequency boreholes sensors (Romero *et al.*, 1994). The temporary network in the southeast Geysers operated by LBL had 13 high-frequency 4.5 Hz sensors in a 7-km array (Kirkpatrick *et al.*, 1994). Both networks were operated intermittently, in 1988-1989 and 1993-1994 in the northwest and 1992-1995 and 1997-1999 in the southeast. In their respective areas, the networks detected 50 to 90% more events than detected by the permanent network.

In April 1991, in the collaboration with the IRIS consortium and University of Durham, UK, 15 digital, three-component sensors were deployed covering the whole geothermal area. All except one station used 2 Hz, 3-component sensors and the other shared a 4.5 Hz, 3-component sensor of the GEO network. Data were sampled at 100 sps and the GPS was used for timing and locations (Ross, 1996). During the month of April 1991, 3906 events were detected. From this dataset, 500 events were located and 296 events were used in tomographic modelling and moment tensor determination, a task that comprised the Ph.D. work of A. Ross (Ross, 1996; Julian *et al.*, 1996; Ross *et al.*, 1996; Ross *et al.*, 1999).

1.6.5 Tomography studies at The Geysers

A number of seismic wave-speed tomography studies of The Geysers have been performed (Table 1.6). Eberhart-Phillips (1986) conducted simultaneous inversion of local earthquake and refraction travel times for velocity, and hypocentral parameters were used to determine three-dimensional *P*-wave velocity structure for the Coast Ranges, which also includes The Geysers. The study associated low

velocities with the Clear Lake Volcanics while a high-velocity body was associated with the felsite in the southeast Geysers. However, as this was a regional model, interpretation of velocity-depth variations in the production area of The Geysers was limited.

Table 1.6: Major tomography studies performed at The Geysers (updated *from* Ross, 1996).

Reference	**Modelled parameter**		**No. of seismic stations**		**No. of events**	**No. of picks**		**Dimensions of modelled volume (km)**
	Vp	***Vp/Vs***	**3-co.**	**Vert.**		***P***	***S***	
Eberhart-Phillips (1986)	Yes	No	14	64	170	N/A	N/A	18x15x5
O'Connell (1986)	Yes	Yes	9	8	38	469	294	N/A
Zucca *et al.*, (1994)	Yes	No	N/A	N/A	N/A	N/A	N/A	8.5x5.5x5
Romero *et al.*, (1994)	Yes	Yes	16	0	480	9700	2700	5x5x4
Ross (1996); Julian *et al.*, (1996)	Yes	Yes	20	16	185	4032	944	20x20x7
Foulger *et al.*, (1997)	Yes	Yes	7	15	146	2522	656	20x20x7

Using 39 events, *P*- and *S*-velocity inversions were performed for *Vp*, *Vs*, and *Vp/Vs* structure by O'Connell (1986). Event location accuracy was increased by using high quality *S*-waves. Low *Vp/Vs* was observed in areas of maximum steam production. The results showed that the reservoir rock is more fluid saturated with increasing depth and *Vp/Vs* can delineate the top of the steam reservoir (O'Connell and Johnson, 1991).

Zucca *et al.*, (1994) used approximately 300 earthquakes spread throughout The Geysers reservoir and obtained high-resolution *P*- and attenuation tomography models. The study computed a three-dimensional *P*-wave structure with 0.8 km nodal spacing and a one-dimensional attenuation structure. Low *P*-wave velocities correlated with known mapped geological units. However, in areas of heavy

production where steam pressure was low, the correlation was most striking. The Quality factor *Q*, which is inversely proportional to attenuation, decreased with depth within the reservoir and was interpreted as indicating liquid saturation of 30 to 70% at depth with drier conditions near the top of the reservoir (Zucca *et al.*, 1994).

A three-dimensional differential attenuation structure beneath the northwest Geysers was mapped using 480 high-quality events. (Romero *et al.*, 1997). While high differential attenuation structure and low *P*-wave velocity structures correlated with the Fransican melange, low attenuation and high *P*-wave velocity structures correspond to the metagreywacke units (Romero *et al.*, 1997).

Using data collected from the IRIS, UNOCAL and NCSN networks, *Vp* and *Vp/Vs* LET of the whole field was conducted (Ross, 1996; Julian *et al.*, 1996). High-quality *Vp*, *Vs* and *Vp/Vs* images were obtained. The most significant finding was a strong (-9%) *Vp/Vs* anomaly that correlated with the production zone. Theoretical considerations, laboratory experiments and field studies suggested that this low *Vp/Vs* anomaly represents a zone where the pore fluid is predominately vapour and pressure is lowered. These changes probably result from the removal of reservoir fluids by exploitation.

Ross (1996) found that tomographic images of comparable quality could be obtained using only data from the 22-station permanent network operated then by the UNOCAL Corporation. This meant that four-dimensional LET could potentially be used to study changes in reservoir structure with time. A repeat, field-wide *Vp/Vs* LET study of The Geysers was therefore performed using comparable data sets recorded in April 1991 and December 1994 on the UNOCAL network (Foulger *et al.*, 1997). A significant increase in the strength of the low-*Vp/Vs* anomaly in the reservoir area during the three-year interim period was detected. This increase was attributed to the effects of progressive fluid depletion of the reservoir. Section 3 of this thesis extends that work by conducting additional LET inversions using earthquakes recorded on the same network.

1.7 Summary

The tectonics of northern California is dominated by plate interactions at the Mendocino triple junction and along the San Andreas shear zone. The Geysers area, situated in the San Andreas shear zone, had a complex tectonic history at around 3.3 Ma. Regional seismicity in the area is mainly associated with right-lateral movement in the San Andreas shear zone. The Geysers geothermal area consists of two Jurassic-Cretaceous units belonging to the Franciscan and Great Valley sequences and is partially overlain by Quaternary rocks. The geothermal reservoir has caprock on top underlain by a highly fractured metagreywacke reservoir rock. The reservoir has two principal components: the normal reservoir in the central and southeast part of The Geysers, and the high temperature reservoir in the northwestern part. The normal reservoir temperature is about 240° C and this has remained fairly constant throughout the exploitation period. The felsite-hosted alteration and vein mineralisation partially controlled by hydrothermal breccia increases permeability and fracture density within the steam reservoir. Although the origin of the heat source at The Geysers is not well understood, it is postulated to be a magmatic intrusion or a body of partial melt in the mid-crust. Various geophysical methods have been used to study The Geysers. During the exploitation period, at the central part of The Geysers, gravity has decreased by –100 to –700 μGal (Allis *et al.*, 2001). Magnetic anomalies have been interpreted as due to Coast Range ultramafic rocks and Clear-Lake volcanics (Isherwood, 1976).

The Geysers geothermal area has undergone heavy commercial exploitation since the mid 1960s. Liquid pore water in the reservoir flashes to steam in boreholes during extraction. Commercial activity at The Geysers peaked in 1987 and reservoir pressure then declined at a steady rate until 1995. Since then, reservoir pressure monitoring and forecasting has been made much more difficult by power-plant shut down, cycling of wells, and liquid injection.

Seismicity at The Geysers is as much as 45 times that of the surrounding areas (Ludwin and Bufe, 1982) and approximately 140 $M_D \geq 1.2$ earthquakes are recorded per month. Annual seismicity plots reveal strong correlation of seismic

events with commercial development attributed to extraction of steam and fluid injection. The seismogenic volume has expanded since the late 1970s. In the 1990s events became more tightly clustered. Injection-induced seismicity may be approximately 40% of total seismicity in the southeast Geysers. Several different mechanisms have been proposed to explain the earthquake activity including increase in shear stresses due to fracture deflation, reservoir pressure decline causing movement to change from creep to stick-slip, and a modified poro-elastic theory that predicts that increasing pore pressure and decreasing effective normal stress induces earthquakes.

Seismicity at The Geysers is monitored by the permanent CALNET and UNOCAL networks and several temporary networks. In April 1991, a field-wide, temporary network was installed and monitored seismicity for that month. In the northwest and southeast Geysers two separate networks have been operational intermittently. Making use of the high-quality data from these networks, several tomography studies have been presented. Zucca *et al.* (1994) presented a high resolution *P*-wave and attenuation model, while Julian *et al.* (1996) and Ross (1996) presented well-resolved *Vp* and *Vp/Vs* models for The Geysers. Section 3 of this thesis extends the study of 4-D *Vp* and *Vp/Vs* tomography of Foulger *et al.* (1997) at The Geysers area.

CHAPTER 2:

STATION ORIENTATION AND POLARITY DETERMINATION

2.1 Background to the study

2.1.1 Introduction

Of the many networks deployed at The Geysers, that operated by the UNOCAL corporation has the largest number of stations and widest network coverage with 22 stations (section 1.6.4) (Figure 2.1). However, the UNOCAL stations were uncalibrated at the start of this project. The orientations of the horizontal instruments and the polarities of the verticals were not known. Of the 22 seismic stations, eight are 3-component. In order to calibrate these stations, I used a simple method making use of known event locations and *P*-wave amplitudes recorded on the horizontal components. To determine polarities a separate data set with good focal mechanism solutions from an independent, temporary network were used. The aim of this study was to provide information for future determination of accurate focal mechanism solutions.

Conventional focal mechanism solutions assume double-couple (DC) source mechanisms. However, in volcanic and geothermal areas, due to volumetric strain and commercial activity, some events have source mechanisms with non-DC components. Many earthquakes at The Geysers, have non-DC components in the focal mechanism solutions (Ross, 1996; Ross *et al.*, 1996). For this reason, it is not possible to assume that nodal lines are orthogonal great circles on the focal sphere. Polarities are weak at constraining non-DC components (Figure 2.2) and additional information such as amplitudes must be used.

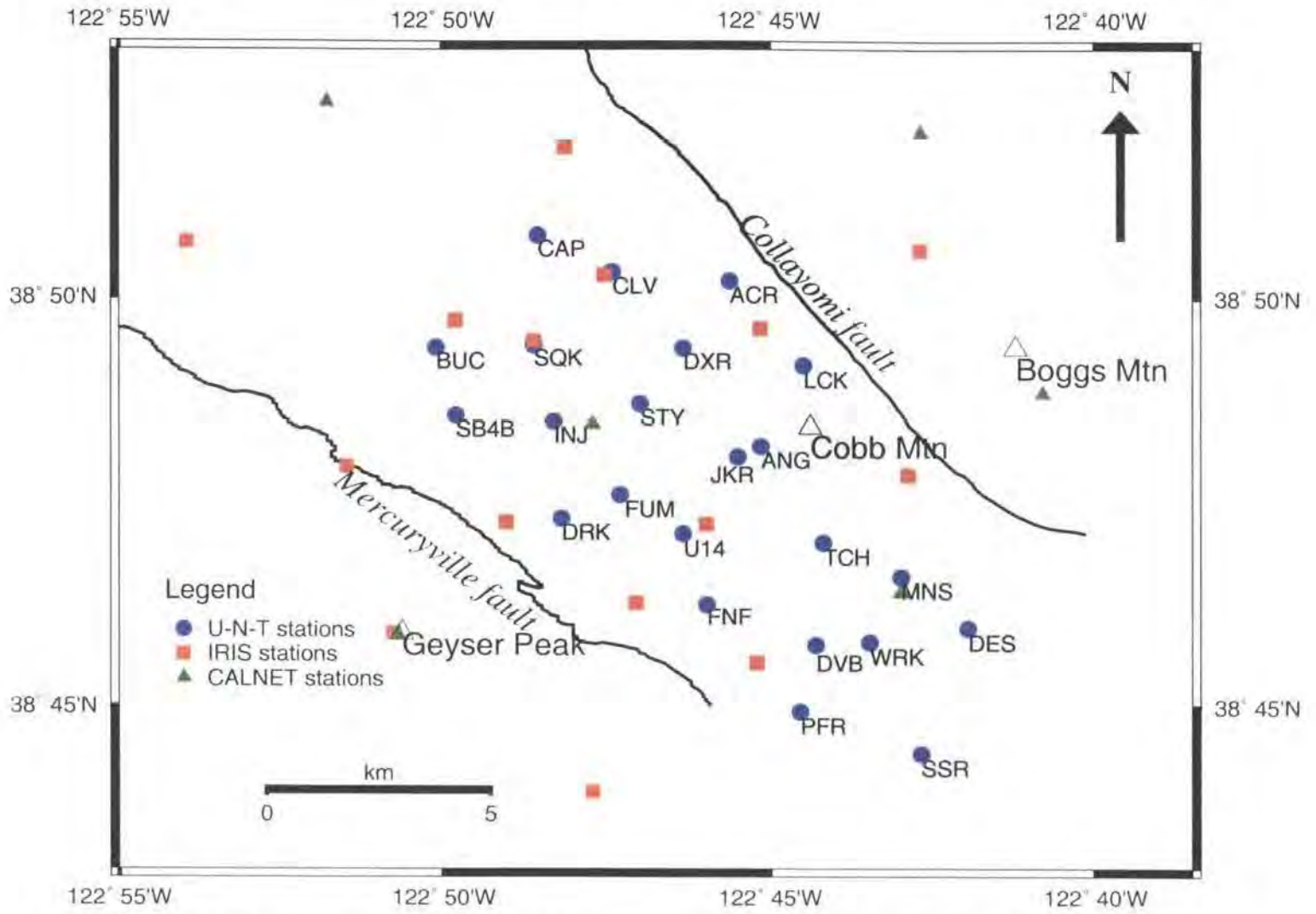

Figure 2.1: Map showing the locations of the UNOCAL stations as blue circles, IRIS stations as red sqaures and CALNET stations as green triangles. UNOCAL station names are labelled

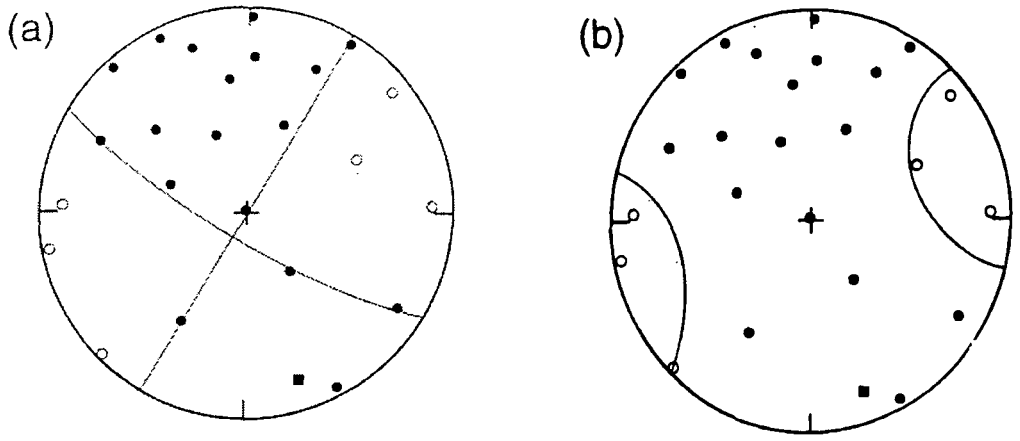

Figure 2.2: Illustration of the difficulty in deducing nodal surfaces using only polarities. The *P*-wave polarity data shown are for an earthquake at 07:41 UTC, September 15, 1991 at the Hengill geothermal field. Solid circles are compressions and open circles are dilations. (a) A DC mechanism that fits the data well. (b) A non-DC mechanism with a large isotropic component that also satisfies the data. (*from* Julian *et al.*, 1998).

2.1.2 Background to the UNOCAL and IRIS networks

2.1.2.1 The UNOCAL network

With the discovery of a very high level of seismicity at The Geysers in 1985, the UNOCAL partnership installed a dense seismometer network. In 1989 this network was expanded to 22 stations in an attempt to distribute stations evenly over the geothermal area (Figure 2.1) (Table 2.1). The average station spacing in the network is 1500 m with half of the seismometers in 39-m-deep boreholes, one in a 85-m-deep borehole and the remainder at the surface. The seismometers have a natural frequency of 4.5 Hz and signals are transmitted to a central recording station by FM telemetry, and digitised at 100 sps (Stark, 1990). The data are archived on site and also at the Northern California Earthquake Data Centre (NCEDC) at U.C. Berkeley.

The network has been upgraded three times. This study uses data from the latest network, the F network. The increased detection threshold was $M_D = 0.2$ (Stark and Davis, 1996). Events that were located with the 1-D velocity model as done by the UNOCAL personnel had a vertical hypocentre error of approximately 0.4 km and horizontally of approximately 0.2 km (Stark & Davis, 1996). The dynamic range of the UNOCAL stations is quite low, so larger events saturate the instruments and the signals are clipped and these have been discarded in this calibration study. The effect of the small dynamic range is especially severe for traces corrupted by a DC shift.

Table 2.1: UNOCAL station locations and number of seismometer components.

Station name	Latitude (°)	Longitude (°)	Height/m (asl)	Number of components
ACR	38.83661	-122.75848	768.90	1
ANG	38.80278	-122.75067	1291.41	1
BUC	38.82315	-122.83423	858.75	1
DES	38.76611	-122.69775	831.56	1
CAP	38.84608	-122.80771	962.09	1
CLV	38.83867	-122.78917	518.91	1
DRK	38.78858	-122.80242	716.00	1
DVB	38.76267	-122.73633	854.92	1
DXR	38.82283	-122.77167	989.86	3
FNF	38.77037	-122.76431	794.82	3
FUM	38.79323	-122.78673	616.63	3
INJ	38.80820	-122.80357	734.53	3
LCK	38.81967	-122.74002	1137.01	3
MNS	38.77640	-122.71530	676.25	1
PFR	38.74892	-122.74115	961.95	1
SB4B	38.80945	-122.82871	327.88	1
SQK	38.82344	-122.80892	637.39	3
SSR	38.74019	-122.70995	1047.58	1
STY	38.81181	-122.78204	1019.84	1
TCH	38.78389	-122.73502	936.37	1
U14	38.78542	-122.77084	636.30	3
WRK	38.76276	-122.72272	963.76	3

2.1.2.2 The IRIS network

This network was set up for the month of April 1991 using equipment supplied by the IRIS consortium in collaboration with the University of Durham UK and the

USGS. This network was used for high-quality wave-speed tomography within the steam reservoir, and to study focal mechanisms (Ross, 1996; Ross *et al.*, 1999). The network geometry was optimised to provide an even distribution of ray paths and dense coverage of the upper focal hemisphere for determining focal mechanism solutions. The stations used IRIS-PASSCAL data loggers.

2.1.3 Polarity determination

2.1.3.1 Use of moment tensor solutions

Deployed for the month of April 1991, the IRIS temporary network (section 1.6.4) had 15 three-component digital stations spread over The Geysers reservoir (Figure 2.1). The polarities and orientation of those stations were known permitting good moment tensor solutions to be determined for events recorded during this period. (Ross, 1996). As a reference network, the IRIS network was ideal, with a good network geometry and spatial design. By calculating the positions of the UNOCAL stations on the focal spheres of the earthquake studied using the IRIS network, their theoretical polarities could be compared with those observed and corrections calculated. A similar analysis was performed using data from the NCSN (CALNET) network operated by the USGS.

2.1.3.2 Quality of moment tensor solutions

The moment tensor solutions determined using the IRIS network were highly accurate, partly because of the high-quality digital three-component seismograms used and partly because of the linear programming method used (Ross, 1996; Ross *et al.*, 1996; Ross *et al.*, 1999). The theory, method and application of the linear programming is given by Julian and Foulger (1996). The locations of the events studied were determined using IRIS, UNOCAL and CALNET networks. However, polarities and amplitudes could only be obtained from the IRIS network since this was the only one calibrated (Ross, 1996). The moment tensor solutions made use of both *P*- and *S*- polarities and *P*:*S* amplitude ratios. All traces were filtered with a

low pass filter with a corner frequency of 5.0 Hz to reduce wave-propagation effects such as scattering and attenuation, which strongly influence the high-frequency component of the seismic signal. Picks were made to an accuracy of 0.01 s for *P*-waves and 0.02 s for *S*-waves. Seismograms were also rotated such that the best possible *S*-wave pick could be made on the transverse component. Measured amplitudes were also corrected for attenuation and free-surface effects (Miller, 1996; Ross *et al.*, 1996).

To address the effects of attenuation values of $Qp \cong 60$ and $Qs \cong 84$ were used. Possible errors due to unmodeled wave-propagation effects were estimated empirically and the optimum value was found by inverting for moment tensors using different estimates of the error (Ross et al., 1999). Errors due to noise were also estimated by measuring the amplitude of the noise prior to the *P*-wave (Ross, 1996). An earthquake with 11 *P*-wave and 10 *S*-wave polarities observations was used to determine the minimum number of events needed to determine a reasonably good moment tensor. The result showed that even with only 4 *P*-wave, 3 *S*-wave and 3 *P*:*S* amplitude ratio observations, the resultant solution was fairly good.

2.1.4 Station orientation

The orientations of the horizontal components of the three-component sensors need to be determined to calculate focal mechanism solutions using amplitudes, and to rotate seismograms in order to enhance *S*-wave amplitudes. The orientations were determined using earthquakes with known locations and using the relative amplitudes of the arrivals on the horizontal components. Sensor orientations for all 8 stations were deduced.

2.2 Theory

The ratio of *P*-wave amplitudes on the two horizontal orthogonal axes of a three-component seismometer is dependent on the direction of the approach of the wave and on the sensor orientation (Figure 2.3).

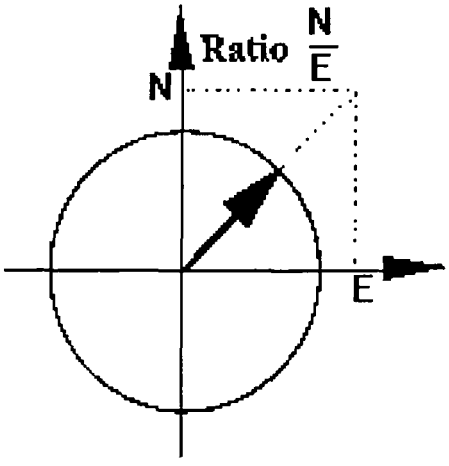

Figure 2.3: Amplitude ratio of N-S:E-W components represented by unit vector.

Since the arriving *P*-wave could be compressional or dilatational from a source at a particular point in space there is a 180° ambiguity in azimuthal direction (Figure 2.4). This ambiguity can be resolved using the polarity of the *P*-wave on the vertical component. An up motion indicates a compressional arrival and down motion a dilatational arrival. Hence, the azimuth to the event from the station with respect to the orientation of the station can be deduced. The locations of the stations and earthquakes are accurately known. Using simple spherical trigonometry the azimuth of the event from the station with respect to true north can be deduced. The azimuthal difference between the results from these two procedures yields the angle of deviation from true North of the north component of the sensor.

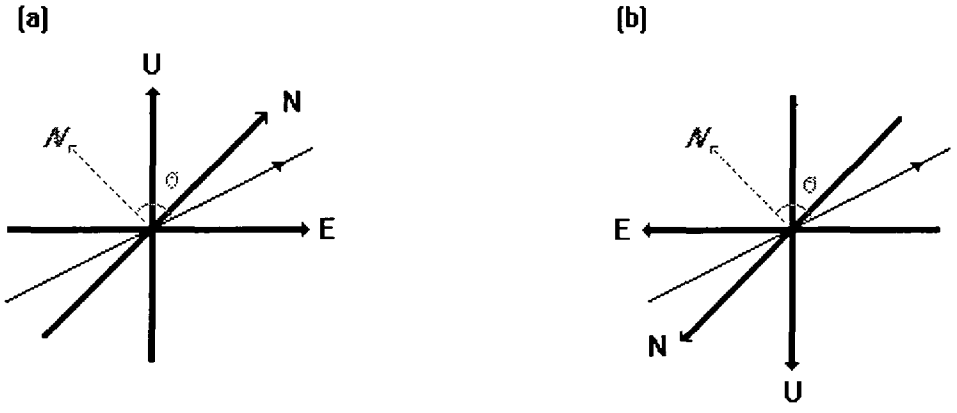

Figure 2.4: Orientation of a 3-component station illustrating that azimuthal direction is affected by the polarity of the station. (a) Normally polarised station (b) Reverse polarised station. Ray path (shaded), True North (Dash line), Sensors; Up-Down, North-South and East-West.

2.3 Method

2.3.1 Method of finding station polarity

Twelve good focal mechanism solutions determined using the IRIS network, with good spatial coverage on the focal sphere were selected from moment tensor solutions determined by A. Ross (Ross, 1996) (Table 2.2). The same events were well-recorded on the uncalibrated UNOCAL network.

P-waves from the UNOCAL stations were picked using the program *epick (*Julian *pers. comm).* The displayed trace using this program, shows a compressional arrival at an IRIS station as a down motion. For the UNOCAL data, a compressional arrival appears as an up motion if the station is normally polarised. A low-pass filter was used (corner frequency 5.0 Hz) to reduce effects of scattering. A three-dimensional crustal model was used to calculate the azimuths and take-off angles. This was the velocity model determined by Ross (1996) using tomography and used to calculate focal mechanisms using the IRIS data. The script *fsp.poldist* (A. Miller, *pers. comm.)* was used to plot *P*-wave polarities on the upper hemisphere in equal area projection. Open circles denote dilatations while filled

circles denote compressions. The polarities plotted on the lower hemisphere were plotted as squares at their antipodal points. Solid lines are the nodal lines calculated for focal mechanism solutions using the IRIS network by Ross (1996). UNOCAL stations polarity plots were superimposed on the corresponding IRIS focal mechanism solutions. It was noted whether the UNOCAL station polarities agreed or disagreed with the IRIS focal mechanism (Section 2.4.1). A cautious policy was adopted, and data points that were close to a nodal line were down-weighted. A station directly on the nodal line was denoted by a question mark (?), while a station directly beside the nodal line was denoted by a "v" and a question mark (v?). A mismatch was denoted by a cross and a question mark (x?) depending on the merit of the result. Each station was analysed without reference to others to minimise the human bias to find systematic results. To observe the degree of consistency, the results were weighted. A correct (i.e. consistent) result was given a value of 1.0, a result correct but close to a nodal line was given a value of 0.5. A result directly on the nodal line was given a value of 0.0, a result wrong (i.e. reversed) but close to the nodal line was given a value of –0.5 and a wrong result was assigned –1.0.

Table 2.2: Selected events used, showing the earthquake codes used by Ross (1996) and corresponding hypocentral and magnitude information.

Event list	Earthquake	Latitude	Longitude	Depth /km	M_w
(a)	104073739.1	38:47.17	-122:46.44	1.85	2.5
(b)	107133652.1	38:48.71	-122:48.20	2.02	0.6
(c)	108021016.2	38:47.83	-122:48.78	3.70	0.6
(d)	114015820.1	38:47.56	-122:45.17	2.14	0.4
(e)	114212724.1	38:49.72	-122:49.28	1.32	1.5
(f)	115155752.1	38:47.18	-122:46.38	2.10	0.5
(g)	115160329.1	38:49.17	-122:48.32	3.30	0.5
(h)	116052923.1	38:47.97	-122:48.32	3.88	0.6
(i)	117062926.1	38:49.13	-122:48.20	3.52	0.7
(j)	120013734.1	38:49.09	-122:48.70	3.14	0.5
(k)	120013734.2	38:49.08	-122:48.73	3.03	0.5
(l)	120021319.1	38:48.00	-122:48.42	2.18	0.8

A similar procedure was followed using NCSN data whose station polarities were thought to all be normally polarised (D.H. Oppenheimer *pers. comm.)*. The results strengthend the IRIS polarity datasets as they improved focal sphere coverage. However, NCSN stations are few. As a result, not all the selected events could be picked on the NCSN network.

The aim of this work is to investigate the polarities, not the focal mechanism solutions, and focal sphere coverage from UNOCAL stations alone was not necessarily good as illustrated by event 117062926.1 (Figure 2.5).

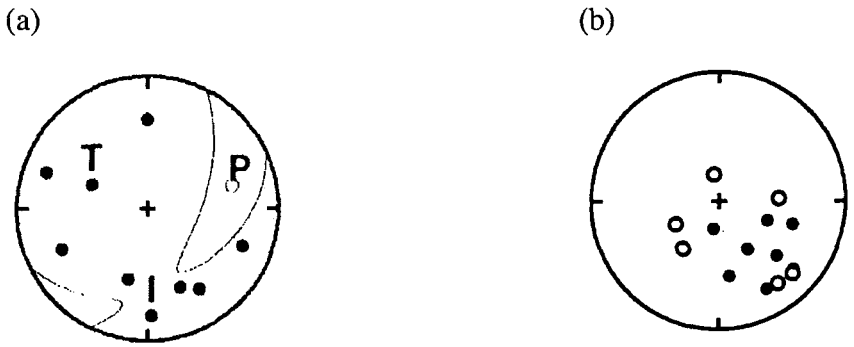

Figure 2.5: An example of (a) good focal sphere coverage by the IRIS network and (b) poor focal sphere coverage by UNOCAL stations.

2.3.2 Method of finding sensor orientation

Twenty events for each three-component station from two time periods, February 1993 and January 1994 were selected for the study of sensor orientation. Events were selected on the basis that good first motions on both the horizontal components of the seismograms could be identified. Program *epick* (B. R. Julian, *pers. comm.*) was used to select these events. A band pass filter (0.5-30 Hz) was used to suppress high-frequency noise resulting from wave scattering. When events with clear first motions arrivals on the horizontals were identified the respective amplitudes of the first motions were measured along with the first motion on the vertical (up or down). The amplitude ratios of the horizontals were then calculated.

P-waves at all stations were picked and a 3-dimensional velocity model was used to generate the best possible locations. The script *staor.sh* (Appendix 2), written by the author was used to calculate the azimuthal deviation from true north. The input parameters needed are the name of the event, the longitude and latitude of the event, the longitude and latitude of station, the amplitudes of the N-S and E-W components and the polarity registered on the vertical component. The script calculates the difference in angle between the azimuth of the incoming ray relative to the north component of the sensor and relative to true North.

2.4 Results

2.4.1 Polarity determination

To determine the correct polarity of the UNOCAL stations 12 events with good focal mechanism solutions were analysed. Most of these were located in the central part of The Geysers reservoir which gave good focal sphere coverage (Figure 2.6) (Table 2.2). All UNOCAL stations except station INJ were included in the study. This station had operational difficulties during April 1991 and the waveforms were poor. Most UNOCAL stations frequently recorded the events studied (Figure 2.7). Stations with 5 or fewer recordings were DES, FNF, MNS, U14 and WRK. Some UNOCAL stations were obviously reversed as they were the single station with one polarity in a tight cluster of stations showing the other. Some notable examples are station DES in event 104070339.1 (Figure 2.7a), station SSR in event 114212724.1 (Figure 2.7e) and station DVB in event 116052923.1 (Figure 2.7h).

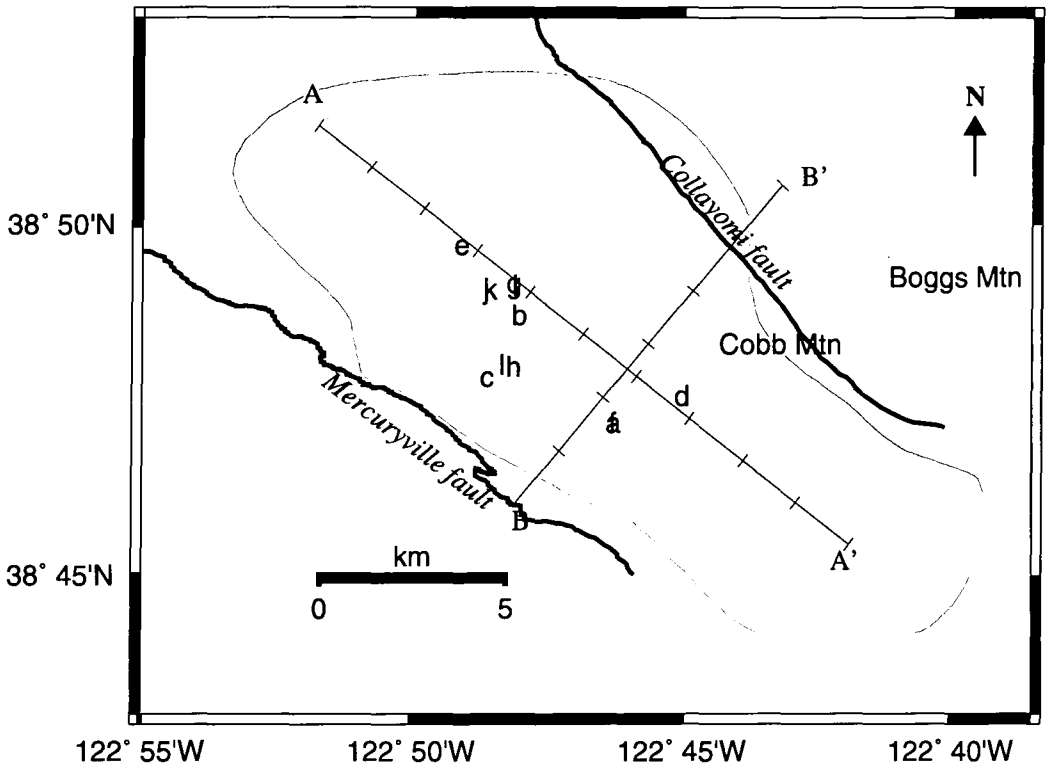

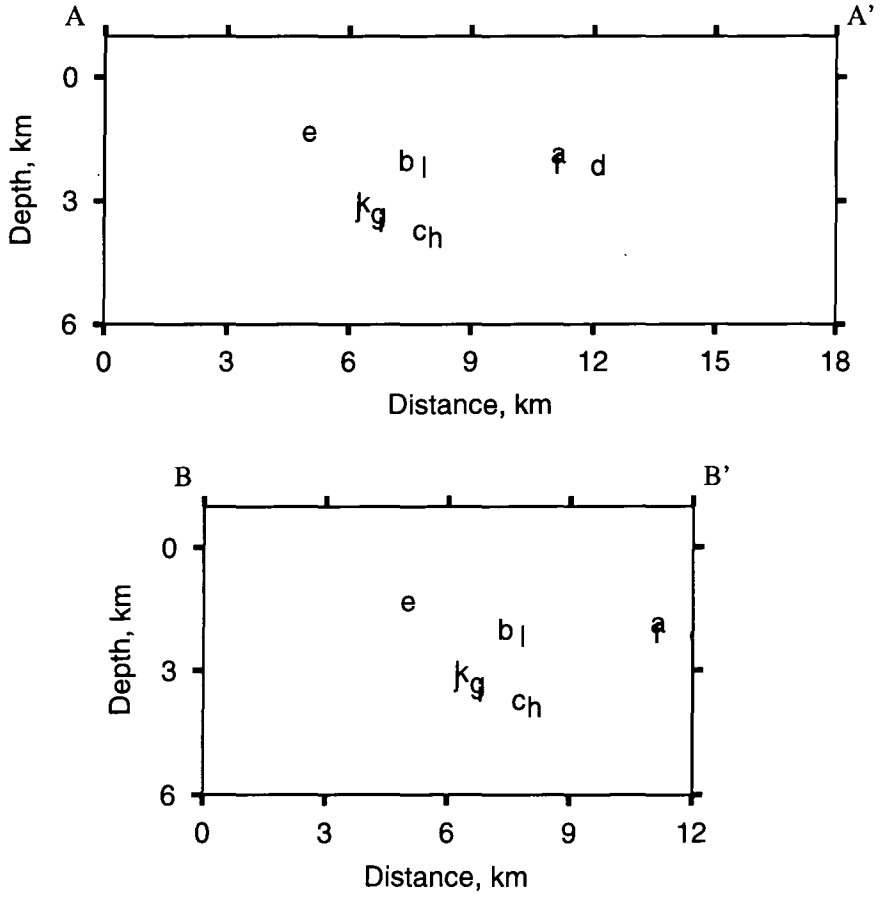

Figure 2.6: Maps showing the locations of events used for polarity determination.

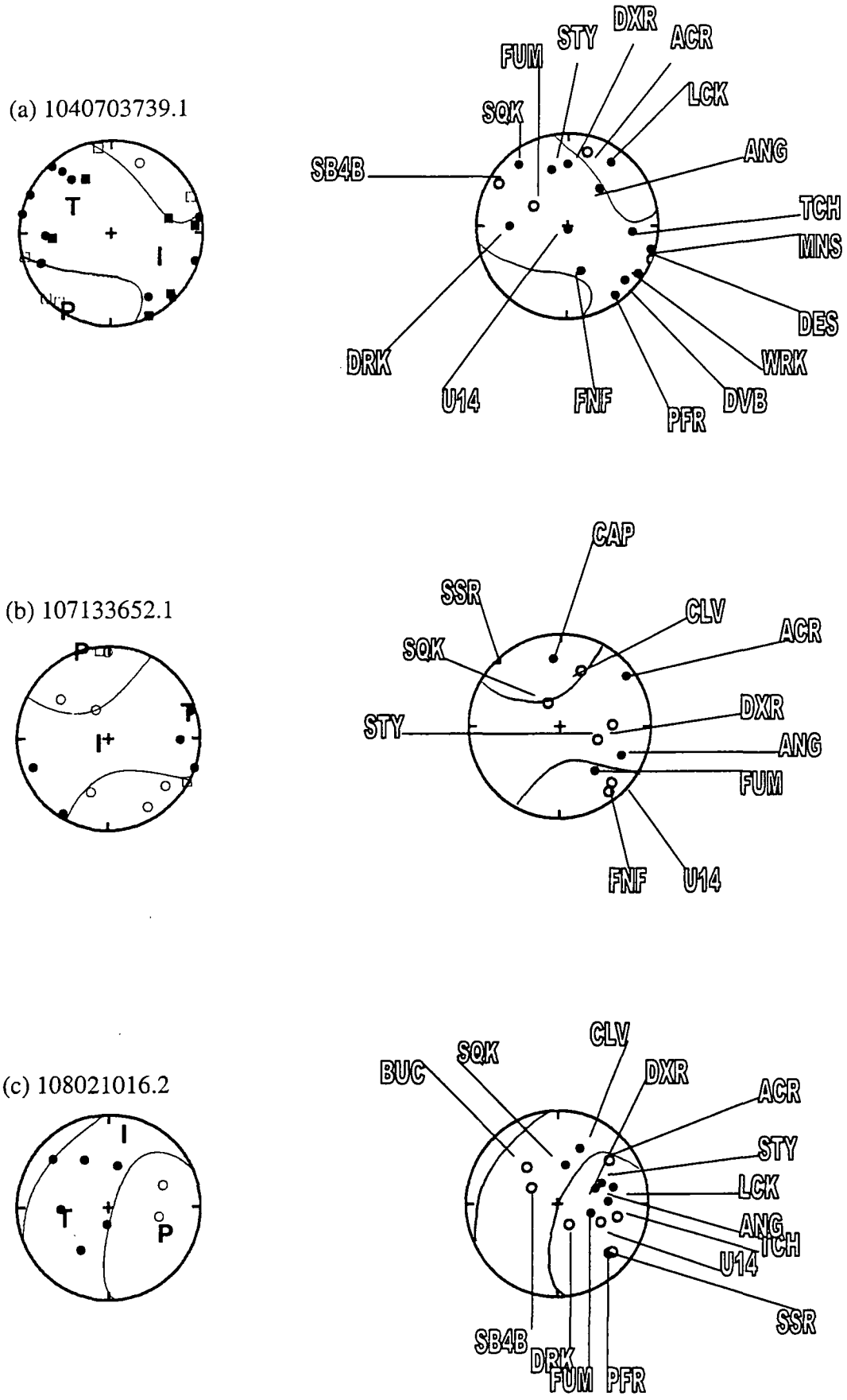

Figure 2.7: Polarity determinations for focal mechanism solutions *from* Ross (1996) (left hand side) for events a, b and c with UNOCAL stations (right hand side).

(d) 1140158520.1

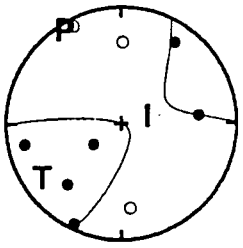

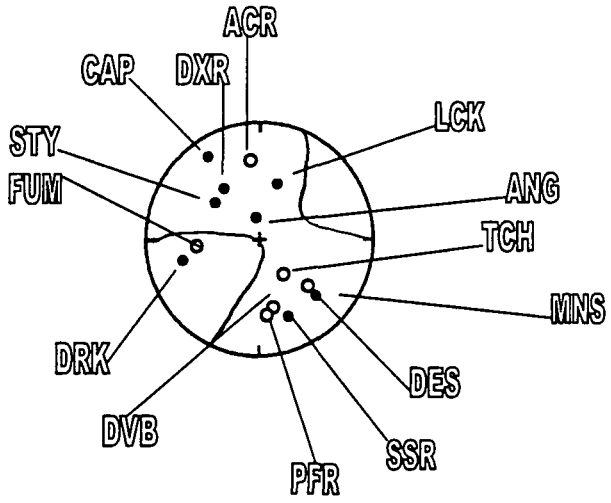

(e) 114212724.1

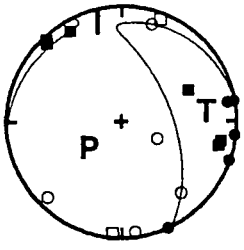

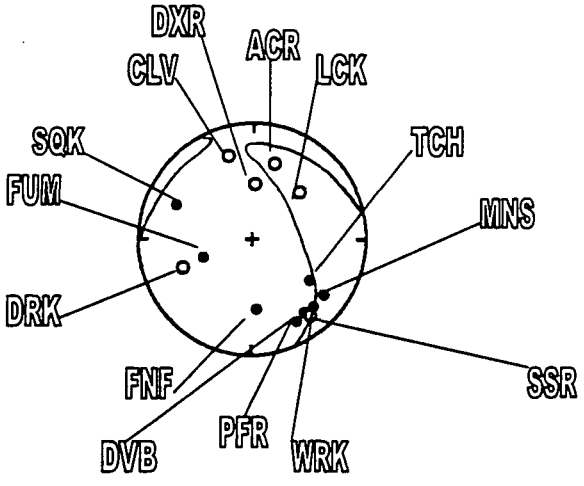

(f) 115155752.1

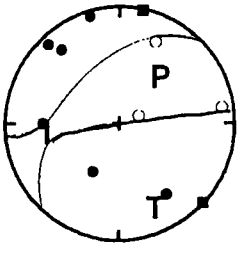

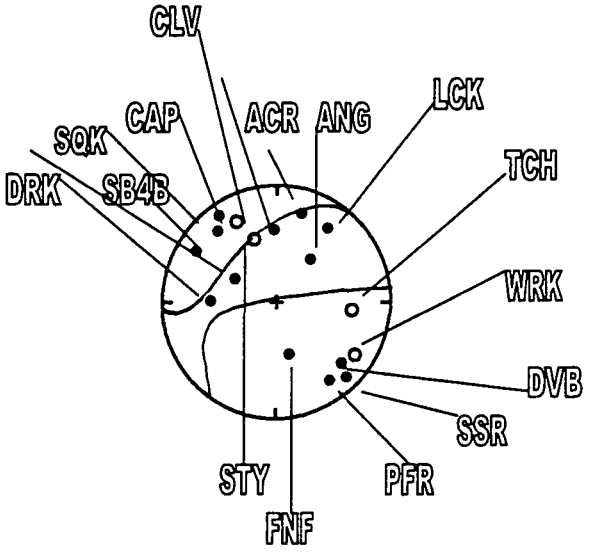

Figure 2.7 (cont.) events d to f.

(g) 115160329.1

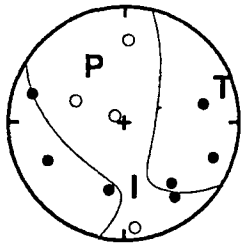

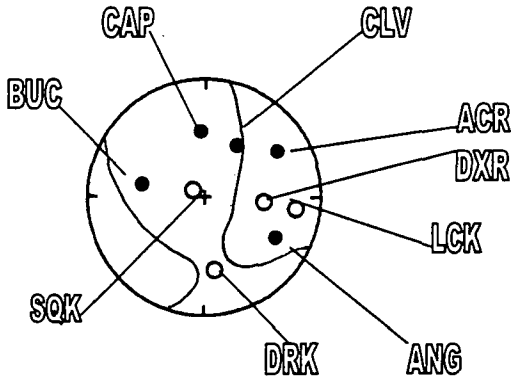

(h) 116052923.1

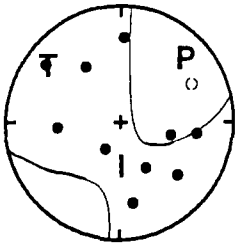

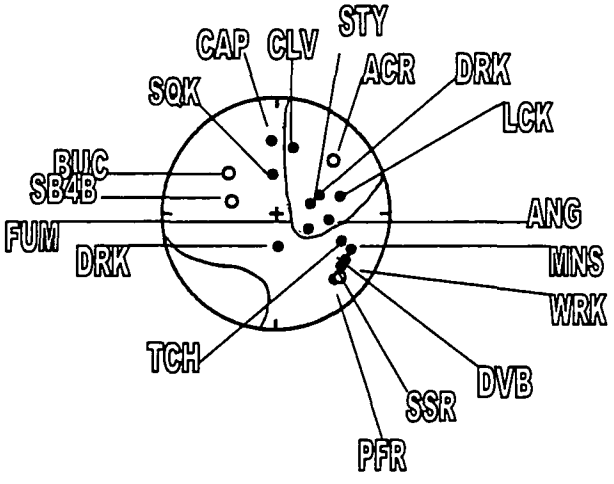

(i) 117062926.1

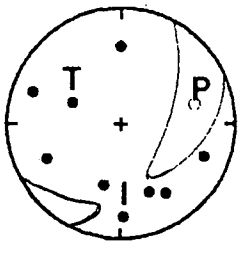

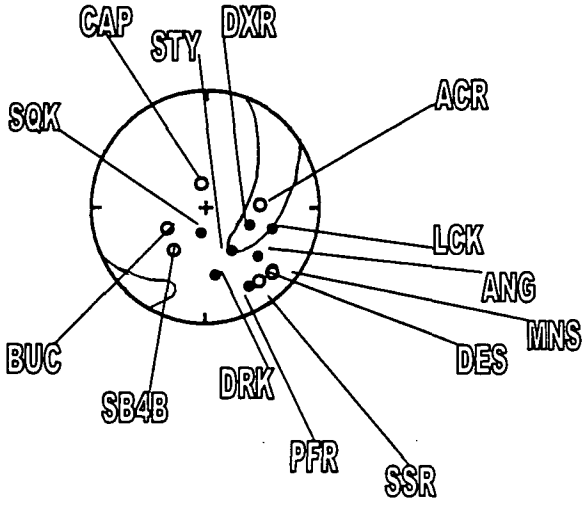

Figure 2.7 (cont.) events g to i.

(j) 120013734.1

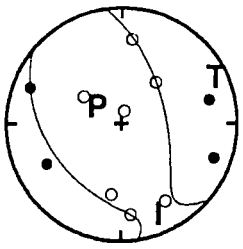

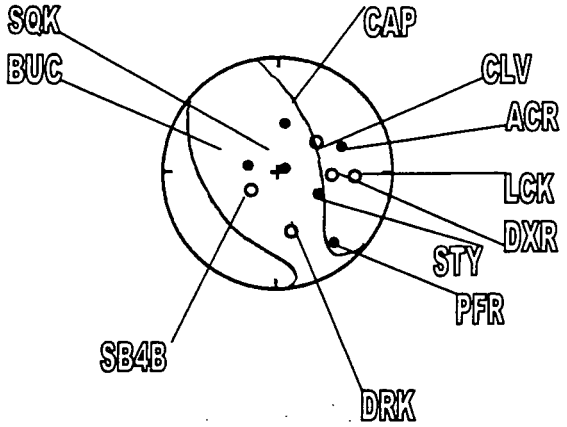

(k) 120013734.2

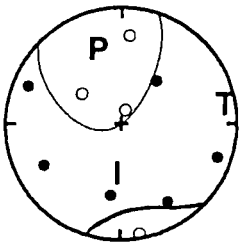

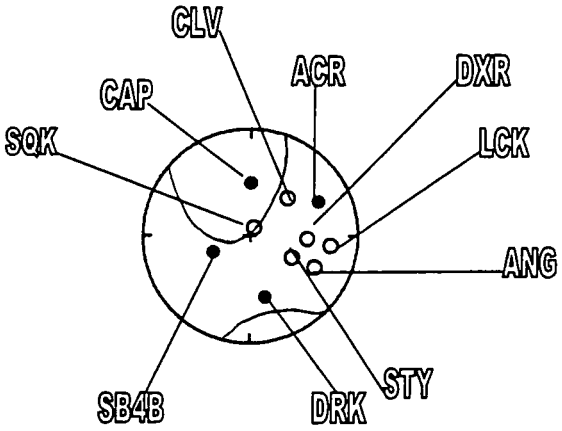

(l) 120021319.1

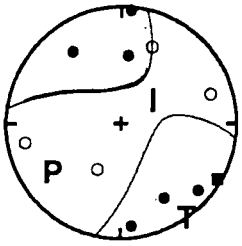

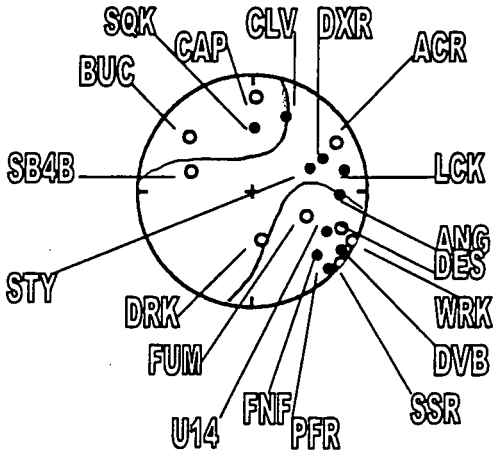

Figure 2.7 (cont.) events j to l.

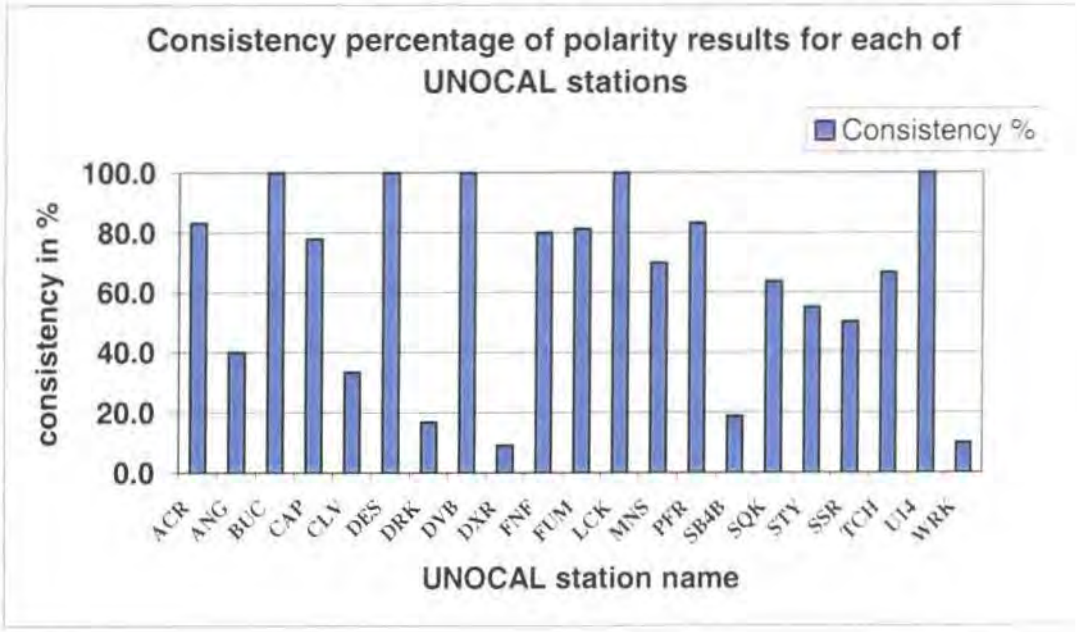

Figure 2.8: Percentage of consist results for polarity determination.

The results are shown in Table 2.3. All stations except station DXR and WRK showed fairly consistent results (Table 2.4). A consistency percentage was computed such that calculated consistency number is given as a percentage of the total number of observations (Table 2.4). Stations BUC, DES, DVB, LCK and U14 showed 100% consistent results, meaning that an accurate estimation of the nature of their relevant station polarity could be determined. However, stations DES and U14 were recorded only 4 times each in the 12 polarity plots analysed which reduces confidence in the results. The average consistency of results as a percentage over all stations was 63.7% (Figure 2.8). Inconsistent readings may have been due to topography and heterogeneity of the geology. Ten stations were found to be normally polarised, including seven 3-component stations. Eleven stations had their polarities reversed (Table 2.4).

The effort to determine the polarities of the UNOCAL stations was fairly successful, but attention should also be drawn to some problems. There were slight variations in location of the same earthquake with the IRIS and UNOCAL networks. This was minimsed by using a good three-dimensional crustal model obtained from tomography. Inaccuracies in the locations lead to inaccurate azimuths and take-off angles and mapping of the stations on the focal sphere.

Table 2.3: Results of polarity investigation. V: Consistent, ?: Doubtful, on or close to nodal line, X: Inconsistent. Highlighted results are anomalous results.

Station	104073739.1	107133652.1	108021016.2	114.015820.1	114212724.1	115.155752.1	115.160329.1	116.052923.1	117.062926.1	120.013734.1	120.013734.2	120021319.1
ACR	V	V	V?	V	V?	V?	V	V	V?	V	V	V
ANG	X?	V	X	X		X	X	?	V?		X	?
BUC			X				X	X	X	X		X
CAP		X		X		V	X	X	X	X	X	X
CLV		?	V		X	X	X?	X?		?	X?	X?
DES	X			X					X			X
DRK	V	V	V?	X	X	X	V	X	V?	V	V	?
DVB	V			V	V	V		V				V
DXR	X?	V		X	V	?	X	X	?	V?	X	V
FNF	?	V			V	V						V
FUM	X	X	X	X?	X	X		?				X
LCK	X		X	X	X	X	X	X	X	X	X	X
MNS	V			V	X?			V	V			
PFR	V		V	V	V	V		V	V	X?		V
SQK	V	?	V		V	V	V	X?	V	X	V?	V
STY	V	X	X	X		?		X	?	X?	X	X
SSR		X	V	X	X	V		X	X			X
SB4B	X		X			V		X	X	V	V?	?
TCH	V		V	V	X	V		V				
U14	V	V	V									V
WRK	V				V?	X		V				X

Table 2.4: Polarity results for 21 stations. Consistent = 1.0; Probably consistent = 0.5; Unknown = 0.0; Probably inconsistent = -0.5; Inconsistent = -1.0.

Station	Sensor type	Polarity	Consistency No.	No. of observations	Consistency %
ACR	Vertical	Normal	10	12	83.3
ANG	Vertical	Reversed	4	10	40.0
BUC	Vertical	Reversed	6	6	100.0
CAP	Vertical	Reversed	7	9	77.8
CLV	Vertical	Reversed	3	9	33.3
DES	Vertical	Reversed	4	4	100.0
DRK	Vertical	Normal	2	12	16.7
DVB	3-component	Normal	6	6	100.00
DXR	3-component	Reversed	1	11	9.1
FNF	3-component	Normal	4	5	80.0
FUM	Vertical	Reversed	6.5	8	81.2
LCK	Vertical	Reversed	11	11	100.0
MNS	Vertical	Normal	3.5	5	70.0
PFR	Vertical	Normal	7.5	9	83.3
SB4B	Vertical	Reversed	1.5	8	18.8
SQK	3-component	Normal	7	11	63.6
STY	Vertical	Reversed	5.5	10	55.0
SSR	Vertical	Reversed	4	8	50.0
TCH	Vertical	Normal	4	6	66.7
U14	3-component	Normal	4	4	100.0
WRK	3-component	Normal	0.5	5	10.0

The frequency responses of the IRIS, UNOCAL and CALNET stations differ. Radio telemetered analogue networks such as the UNOCAL networks have less dynamic range than the IRIS stations which were all recorded digitally at the station. Events for which good IRIS focal mechanism solutions were available often recorded a weak signal at UNOCAL stations, with high noise and poor signal:Noise, S/N ratio. Hence to obtain clear first-motion arrivals, large magnitude earthquakes were selected. Many earthquakes were shallow, resulting in small computed take-off angles, which led to points being close to the perimeter of the focal sphere which rendered these events less useful.

UNOCAL stations in the northern part of the reservoir appear to be reversely polarised and most of the stations in the south normally polarised (Figure 2.9). This suggests systematic errors when installing the stations at The Geysers.

2.4.2 Sensor orientation

As for the polarity study, most stations gave fairly consistent results (Figure 2.10). Station DXR was the most consistent (Figure 2.10) and the results for stations U14 and INJ were scattered. The numerical results are given in Table 2.5. Station DVB gave very consistent results, and showed that the "pseudo north-south" horizontal axis is 205.9° clockwise away from true north with σ of 12.9°. A histogram for station DVB shows six out of twenty observations were within a bin width of 5° falling between an azimuth of 200 and 205°, which suggests the results are reliable (Figure 2.10a) (Table 2.5). However, the events did not cover all azimuths around the station, which was peripheral to the network (Figure 2.11a).

Table 2.5: Orientations of 3-component stations and standard deviation errors.

Station name	Longitude	Latitude	No. of Observations	Mean orientation °	Range in orientation values °	σ °
DVB	-122:44:17	38:45:45	20	206	50	12.9
DXR	-122:46:19	38:49:23	20	309	82	18.4
FNF	-122:45:56	38:46:15	20	194	67	20.5
FUM	-122:47:16	38:47:35	20	359	53	15.5
INJ	-122:48:16	38:48:29	20	300	88	25.1
SQK	-122:48:35	38:49:25	20	78	76	23.8
U14	-122:46:19	38:47:07	20	81	95	26.4
WRK	-122:43:25	38:45:46	20	285	31	8.3

For Station DXR, the results showed that the mean angle of deviation from true north in a clockwise direction was 309.0° (Table 2.5). Three data points are considerably different from the others, increasing the range of the results to 82.0°. Station FNF had readings with a range of 66.5° and with a mean deviation from true north of 144.0°. The results are scattered, although this station was sampled by

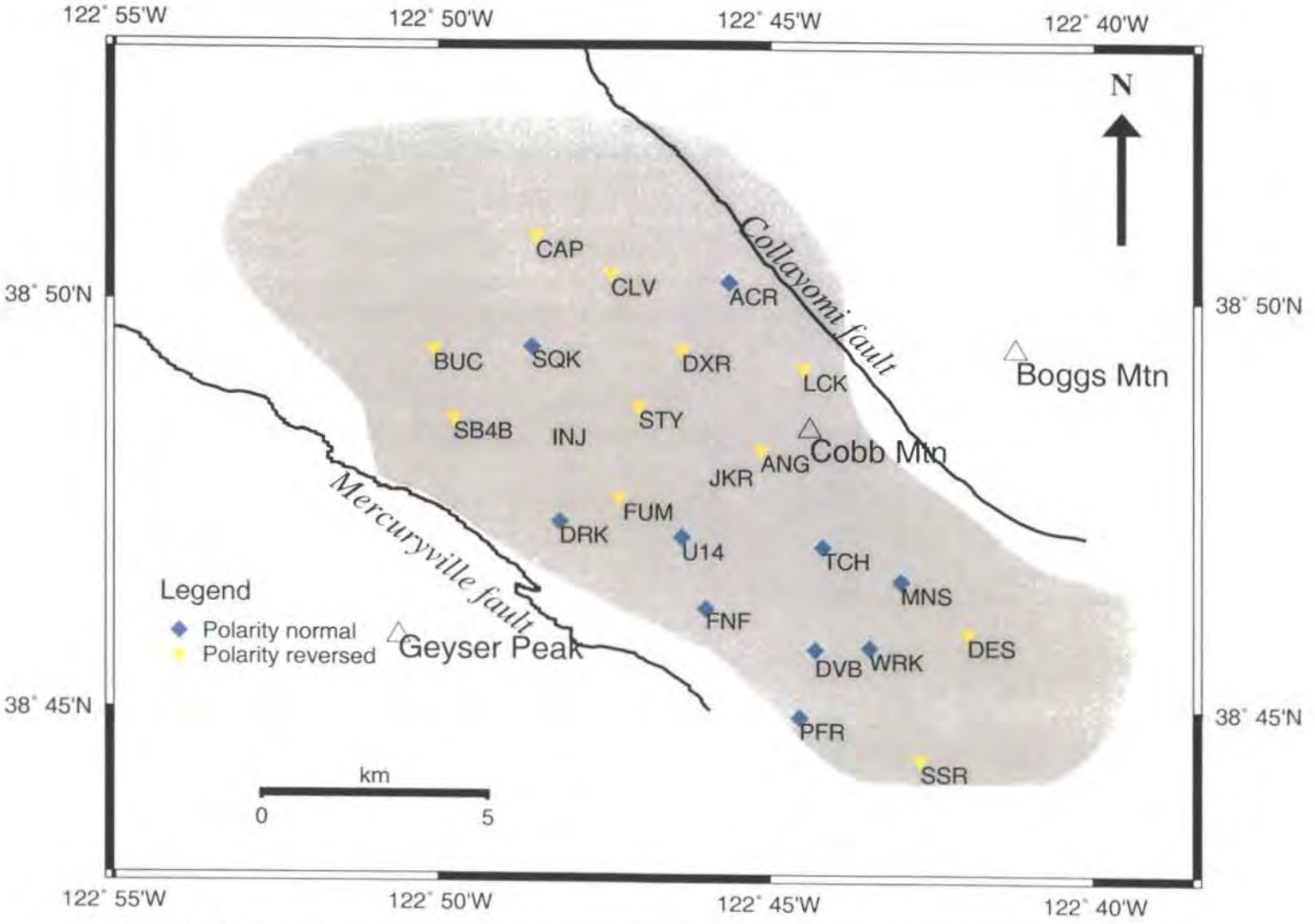

Figure 2.9: Map showing the polarities for the UNOCAL stations. Light blue diamonds are normally polarized while inverted triangles are reverse polarized.

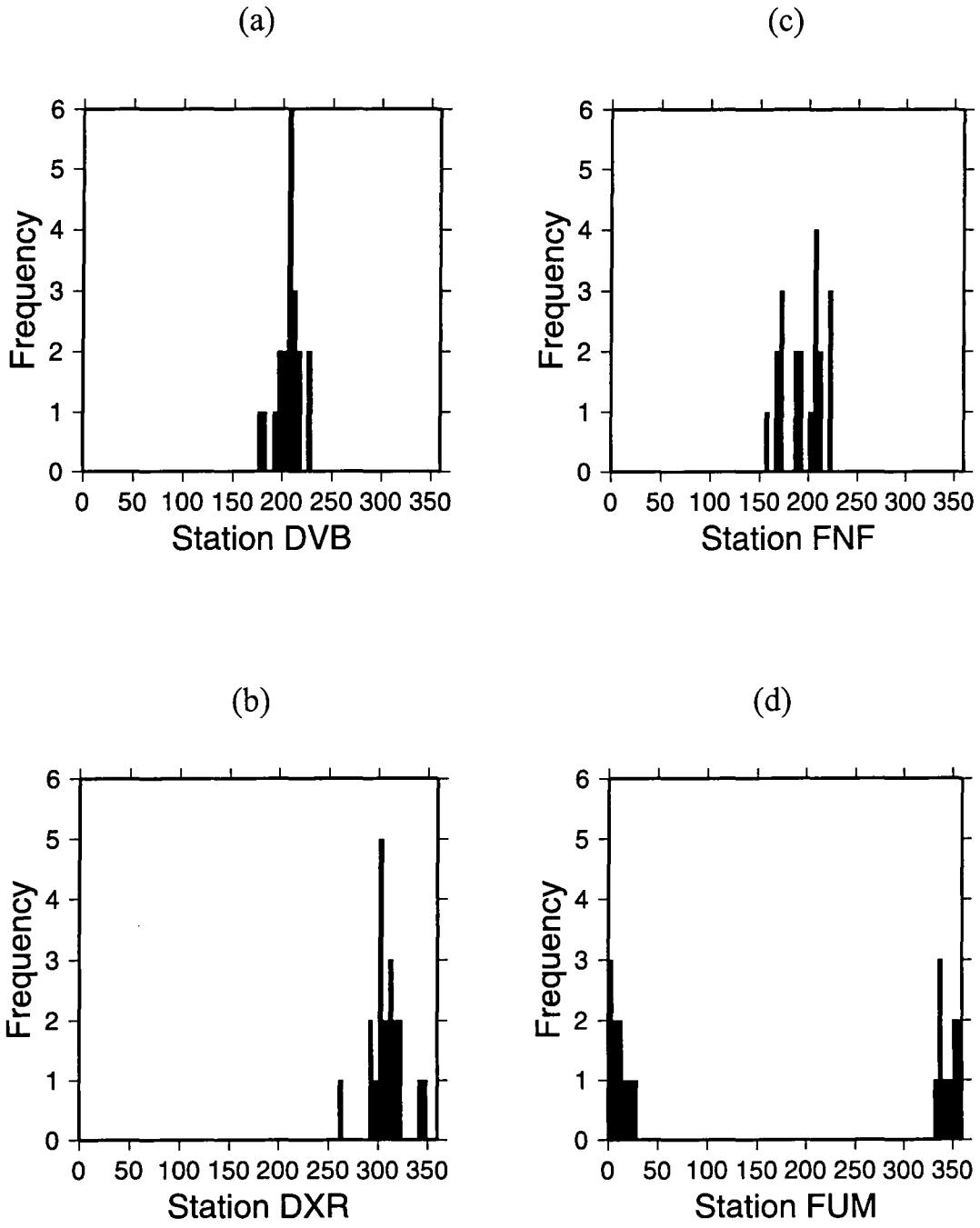

Figure 2.10(a-d): Calculated orientations of sensors east of true north.

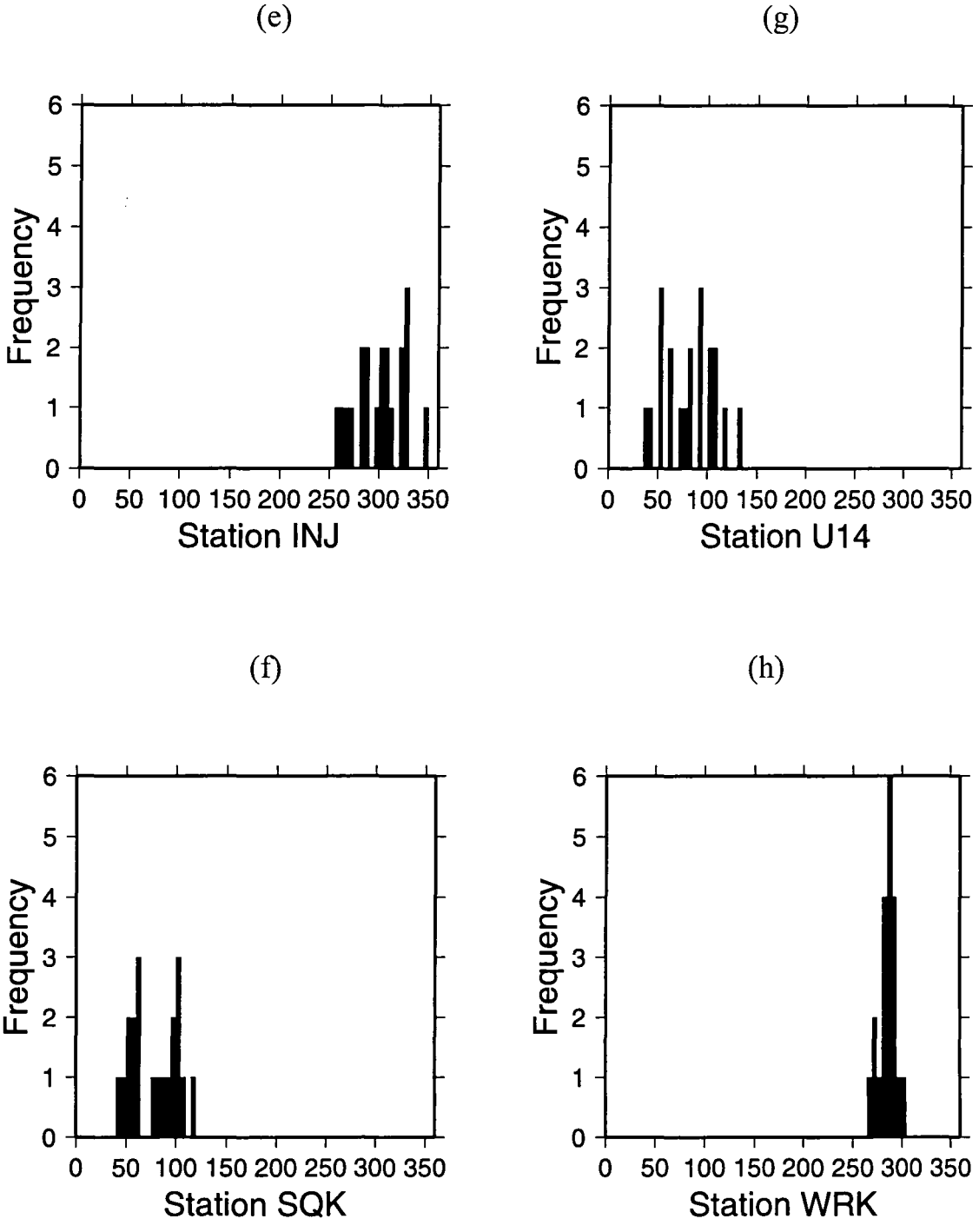

Figure 2.10(cont.) for stations e-h.

events with a broad azimuthal range (Figure 2.10c) (Figure 2.11c). The results for station FUM were good, with standard deviation of 15.5°. Although, the frequency of readings in the histogram for station FUM, with a bin width of 5° is low (Figure 2.10d) the events used in the study have a greater azimuthal coverage around the station (Figure 2.11d). The result is what would be expected of a properly orientated seismic station, orientated towards true north. Station FUM was upgraded to a 3-component station on 05/08/92. However, confirmation whether station FUM had been correctly orientated has not been possible due to data unavailability at the Calpine Corporation (Mitchell Stark, *pers. comm.*).

Stations INJ, SQK and U14 show more scattered results with a standard deviation error for station U14 of 26.4° (Table 2.5). The maximum number of occurrences within any of the 5° bin windows used for these stations was 3 (Figure 2.10e,f,g). Stations INJ and SQK had very good spatial coverage (Figure 2.11e,f,g). Station INJ, is close to the edge of the strong *Vp/Vs* anomaly that occupies the steam reservoir, which may cause distortion of the waveform and scattering that reduces the S/N ratio and distorts the incoming wavefront.

Station WRK was the most consistent station with a mean deviation from the "pseudo north-south" axis to true north of 285.2° (Figure 2.10h) (Table 2.5). The events used had limited azimuthal coverage, however, since the station is located at the periphery of the network (Figure 2.11h).

The mean orientations for the eight three-component stations are fairly random (Figure 2.12). The data for some stations are more consistent than for others. This could be attributed to errors in earthquake locations, ray path geometry, inhomogeneous structure at The Geysers and near-surface effects. Most events were shallow as rays with high take-off angles were required and events closer to the station than 1.5 km were not selected. An effort was made to select events as far as possible from station in question to achieve greater reliability as computations of the waveform, such as the calculating amplitude ratios of the two orthogonal components of the seismometer, are more accurate for events at greater distances.

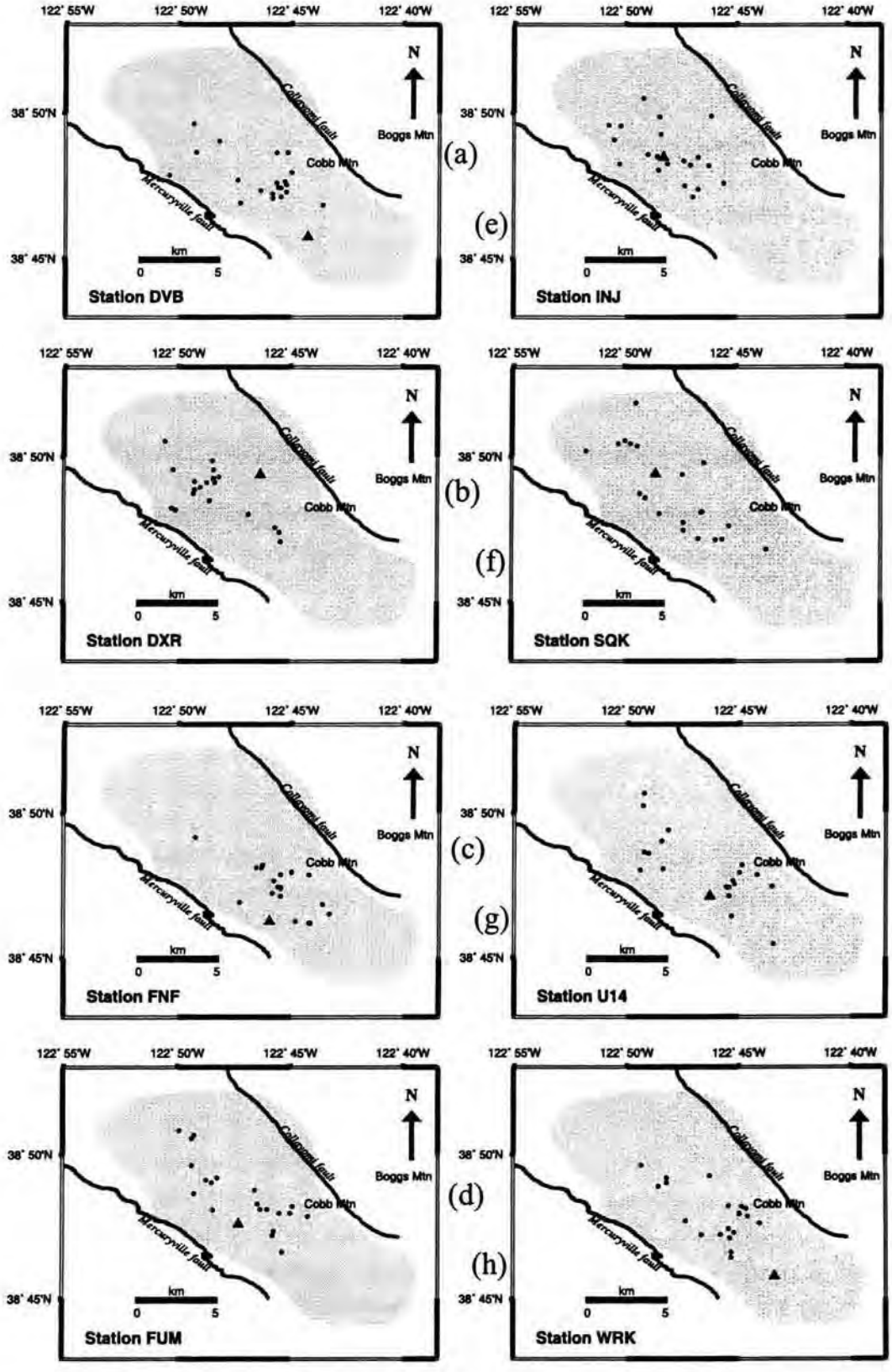

Figure 2.11: Events used in the orientation study (black dots) for individual stations (triangles). Cobb Mtn is shown as a white triangle.

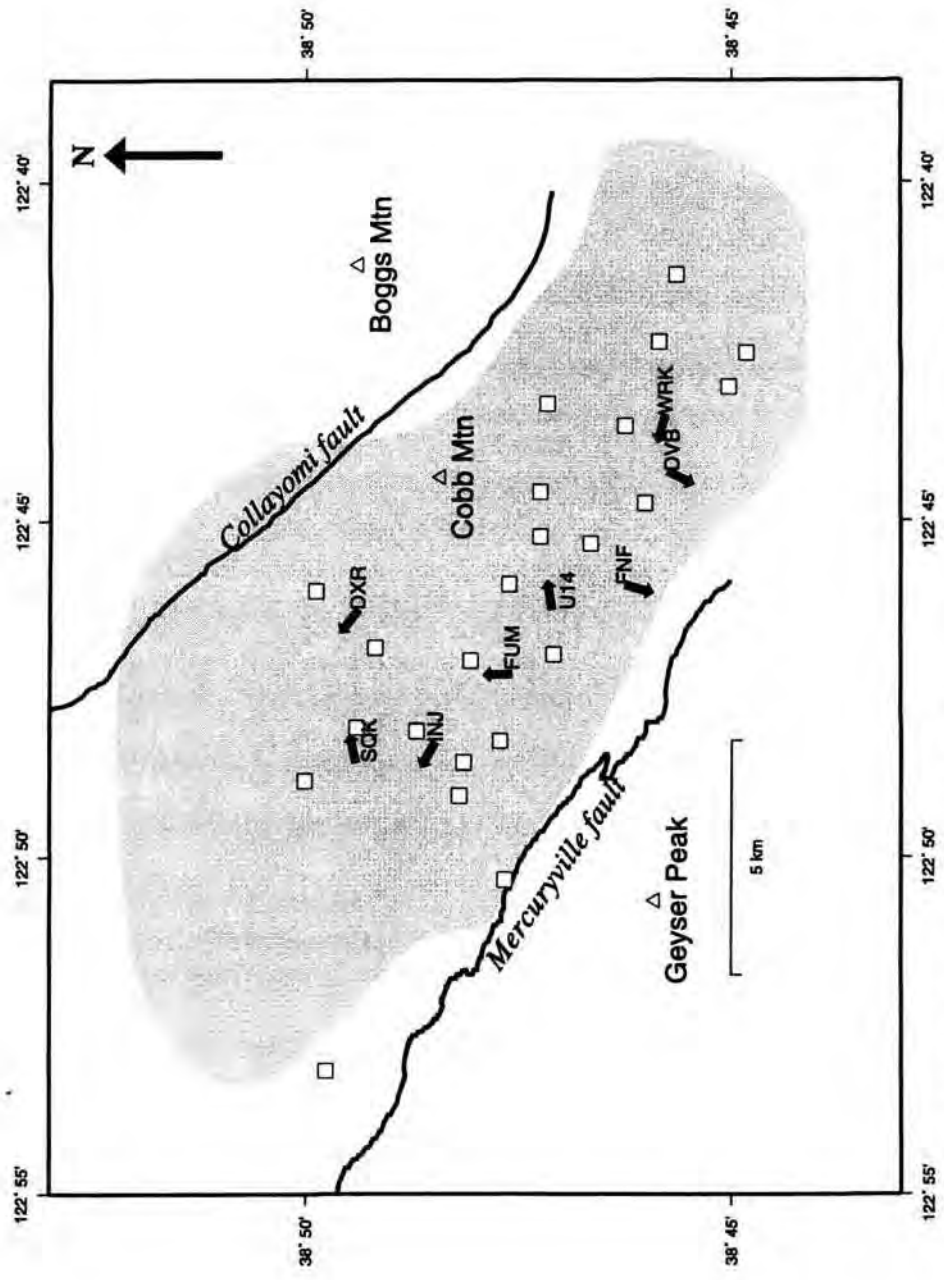

Figure 2.12: Mean orientations of the horizontal components of the three-component stations.

2.5 Summary

To make more use of the permanent UNOCAL field-wide seismic station network deployed at The Geysers, it needed to be calibrated. The polarities and orientations of stations at The Geysers were determined by studying events for which independent high-quality focal mechanisms and locations were available. To determine the polarities of the UNOCAL stations, focal mechanism solutions from the temporary IRIS network were used. The UNOCAL polarities were plotted on a focal sphere and compared with the results of Ross (1996). Only clearly associated events on the two networks were used. To determine sensor orientation, events with strong first motions on the vertical and strong first motion amplitudes in the horizontal sensors were utilized. This information was used to calculate the azimuthal deviation of the horizontal components from true north.

Of the 22 UNOCAL stations, 21 were calibrated successfully. The stations that are normally polarised are ACR, DVB, DRK, FNF, MNS, PFR, SQK, TCH, U14 and WRK. Stations that are reverse polarized are ANG, BUC, CAP, CLV, DES, DXR, FUM, LCK, STY, SSR and SB4B. The confidence limits for stations DRK, DXR, SB4B and WRK are below 20%. These results will enable focal mechanism solutions to be obtained for The Geysers earthquakes using the UNOCAL network, which has not been possible in the past.

CHAPTER 3:

TOMOGRAPHY THEORY AND RESULTS

3.1 Background

Seismic tomography images the Earth's structure in three dimensions and may give insight into tectonic processes at work in the study volume. This study makes use of local earthquake tomography to study the effects of depletion and interaction of seismic wave speeds at The Geysers geothermal area. Making use of the UNOCAL permanent seismic network and the same tomographic grid, three-dimensional images of the reservoir could be constructed during selected time periods to observe the evolution of the reservoir (Figure 3.1). *Vp*, *Vs* and *Vp/Vs* models are presented for the months of April 1991, February 1993, December 1994, October 1996 and August 1998, of which February 1993, October 1996 and August 1998 were calculated as part of this thesis work. *Vp*, *Vs* and *Vp/Vs* models for April 1991 was determined from a "graded" inversion using an initial 1-D velocity model for The Geysers and UNOCAL network only (Ross, 1996). The models for December 1994 were determined using a 1-step inversion and the UNOCAL network only (Grant, 1995; Foulger *et al.*, 1997)

3.2 Local Earthquake Tomography (LET) theory

3.2.1 Introduction to LET

In LET, the study volume is imaged using a large set of arrival-time observations from local earthquakes recorded on a seismic network. Various different methods are available to invert the data. There are parallels between seismic tomography

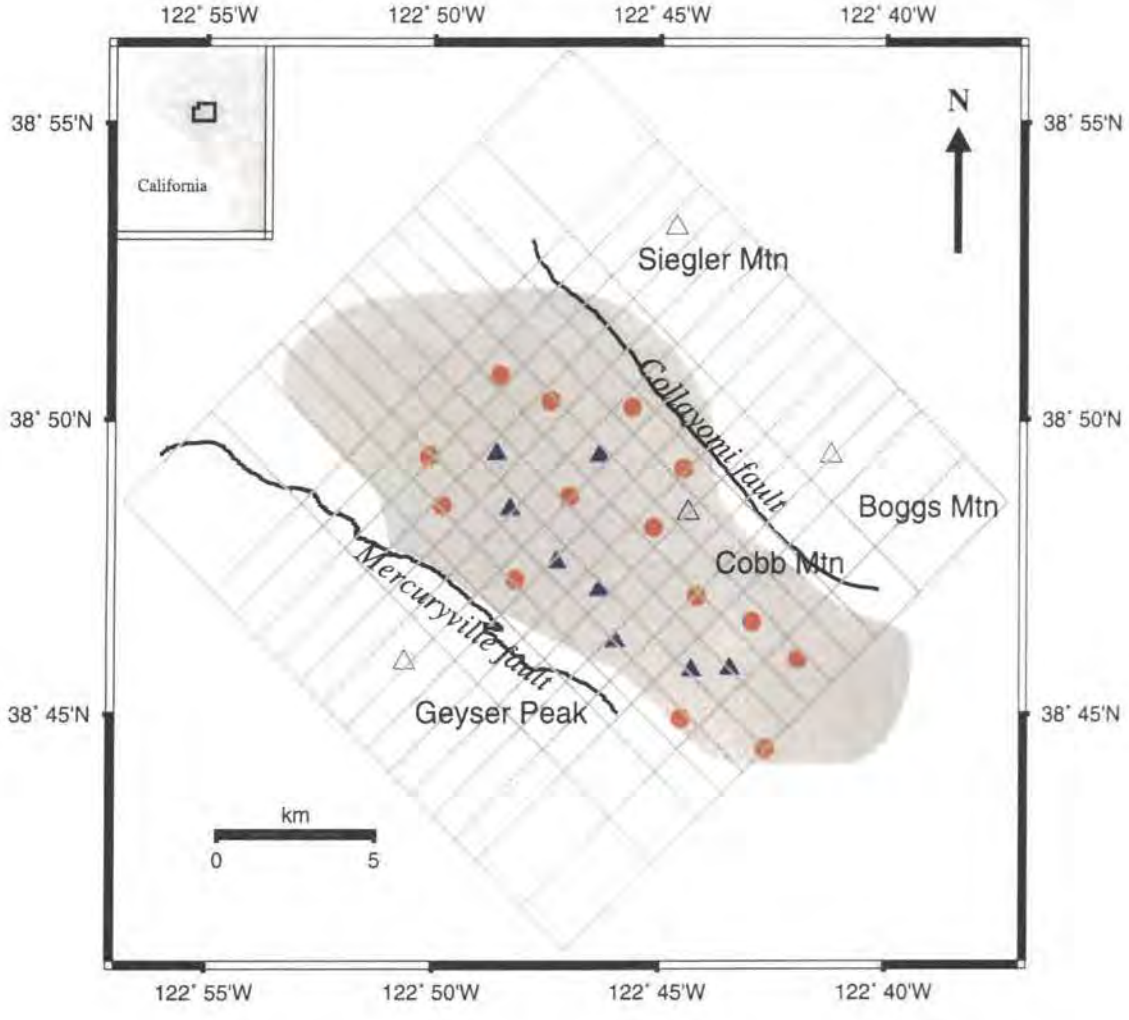

Figure 3.1: Map of UNOCAL stations with single component stations shown as red circles and three-component stations shown as blue triangles. The grid was used for all tomographic inversions and velocity nodes correspond to the intersection of the grid lines. The grid was rotated 45° from north and centred on 38:48.60° N, 122:47.05° W.

and body scanning used in the medical profession. Seismic tomography is more complicated than medical tomography since the locations of the sources are not known *a-priori*, but must be solved for in the inversion process. LET is a non-linear inverse problem that may be ill-behaved.

Seismic tomography may be applied to volumes varying by many orders of magnitude in size. Teleseismic studies have successfully imaged regional- and global-extent volumes e.g. the mantle and the core-mantle boundary region (e.g. Morelli, 1993). The method has been successful in identifying low-velocity zones beneath hotspots and zones interpreted as partial melt beneath active volcanic regions. Teleseismic tomography makes use of lower frequency waves than LET and is thus limited to larger-scale structures. For smaller-scale studies, of the order of kilometres, methods such as NeHT tomography and LET are used.

NeHT tomography was pioneered by the Nercessian-Hirn-Tarantola group and further developed by Achauer *et al.* (1980). This is a high resolution tomographic method that utilises explosions and blasts for sources. Knowing the origin time and locations of the sources makes the problem much easier, but the method is not suitable for *Vs* or *Vp/Vs* imaging as controlled sources generate S-waves poorly. Furthermore, since the sources are close to the surface depth penetration is poor. To counter this problem, a ray-theoretical method is used that involves impulsive relative arrival times such that the rays undershoot the target volume (Evans and Zucca, 1988). NeHT is very expensive because of the large numbers of explosions needed.

A more cost effective method of seismic tomography is LET, which uses natural earthquakes as sources. Where the source and station density is high, imaging on a scale as small as 0.5 km is possible (Zucca *et al.*, 1994). LET is widely applied to areas with heterogeneous geology such as volcanic and geothermal areas.

3.2.2 LET Theory

3.2.2.1 Introduction

Ray theory shows that for a body wave the travel time, T from an earthquake at location i to a seismic station j may be expressed as the path integral

$$T_{ij} = \int_{source}^{receiver} u \, ds \tag{3.1}$$

where u is the slowness (the inverse of velocity) and ds represents an element of the path. The only known parameters are the station locations and the arrival times. The travel time can be expressed as

$$T_{ij} = t_{ij} - \tau_i \tag{3.2}$$

where t_{ij} is the arrival time of the wave and τ_i is the event origin time. The unknown model parameters are the origin time, hypocentre coordinates (x_1, x_2, x_3), ray-path and field slowness.

A theoretical arrival time is introduced using *a priori* information: a trial hypocentre, origin time and velocity structure. The difference between the observed and the calculated arrival times is the residual

$$r_{ij} = t_{ij}^{obs} - t_{ij}^{cal} \tag{3.3}$$

For both *P*- and *S*-waves these residuals are related to a pertubation in the hypocentre location and velocity structure using the linear approximation:

$$r_{ij} = \sum_{k=1}^{3} \frac{\partial T_{ij}}{\partial x_k} \Delta x_k + \Delta \tau_i + \int_{source}^{receiver} \delta u \, ds \tag{3.4}$$

where Δx_k represents the hypocentre coordinates, $\partial T_{ij}/\partial x_k$ represents the hypocentre partial derivatives, and $\Delta \tau_i$ represents a perturbation in origin time. For discretised velocity structure equation 3.4 becomes

$$r_{ij} = \sum_{k=1}^{3} \frac{\partial T_{ij}}{\partial x_k} \Delta x_k + \Delta \tau_i + \sum_{l=1}^{L} \frac{\partial T_{ij}}{\partial m_l} \Delta m_l \qquad (3.5)$$

where m_l represents the L parameters of the velocity model. The velocity model partial derivatives, $\partial T_{ij} / \partial m_l$ are the line integrals along the raypath and reflect the relative influence of each of the model parameters on the raypath. The aim of LET is to minimise the residuals by pertubating the hypocentral parameters and the model structure. Certain aspects of the problem need to be addressed :

- The velocity structure representation
- Calculation of the travel-times and ray-paths
- Hypocentre-velocity coupling and the method of inversion
- The effect of inclusion of *S*-waves
- Assessment of the quality of the solution

3.2.2.2 The velocity structure representation

The objective is to obtain a velocity model that is most representative of the true velocity structure of the target region. For a good result, a high density of crossing rays throughout the target region is required.

Aki and Lee (1976) used constant velocity cubes to represent the model volume. This method does not allow for velocity gradients within the cubes and may thus yield only a crude model result. Hawley *et al.* (1981) divided the model into layers, where velocity is constant in the vertical direction, but gradients are allowed in the horizontal directions. Model parameterisation using a three dimensional grid to define velocity nodes and where velocity gradients are allowed in all directions, with linear b-spline interpolation between nodes, was introduced by Thurber

(1983) (Figure 3.2). This method was refined later to use cubic b-splines which have continous second-order derivatives.

A variant of this procedure involves using four nodes to define the vertices of tetrahedra, and allowing the velocity gradient to change in any direction (Lin and Roecker, 1990). The main advantage of this procedure is that it allows analytical ray tracing to be used, as ray paths are circular arc segments in a medium of constant velocity gradient.

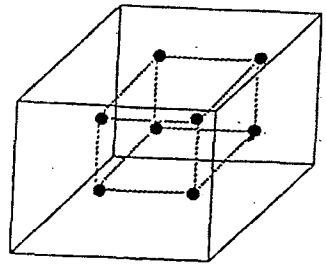

Figure 3.2 Schematic diagram of velocity structure representation where a velocity is assigned to each node, with linear interpolation between nodes (*from* Thurber, 1983).

3.2.2.3 Calculation of the travel-times and ray-paths

Ray-path and travel-time determination is controlled by the representation of the velocity structure. Changes in one affect the other. Determination of the travel times is needed to calculate the arrival times and the ray path is required to compute hypocentre and velocity-model partial derivatives.

The computation method for tracing rays may utilise shooting, bending, approximate- or finite-differences (Vidale, 1990). Ray tracing is essentially a two-point Boundary Value Problem (BVP) as the source and receiver locations are fixed. The shooting method involves varying the trajectory of the ray at the source until one is found that arrives at the receiver. The bending method involves perturbing a source-receiver ray to find the minimum travel-time path. Both methods suffer from the problem of possibly converging on a local minimum

rather than the global travel time minimum, or determining a global minimum travel time path that delivers a ray with negligible amplitude.

Approximate ray tracing (Thurber and Ellsworth, 1980) uses large sets of arcs between source and receiver with varying radii. The travel times are computed and the minimum travel-time path is selected (Figure 3.3). Searching arcs in a single plane may be inadequate in areas where there is strong lateral heterogeneity. In an improved version, Thurber (1983) dealt with lateral heterogeneity with a fast but simple technique whereby accurate ray paths in a family of dipping planes were searched for the minimum travel-time path. For raypaths of modest length (< 45 km) such as in The Geysers this assumption is a reasonable approximation. Arrivals from events with moderate epicentral distances, between 20 and 45 km (Eberhart-Phillips, 1986), are downweighted to account for the increasing proportionate error in estimated travel time with path length.

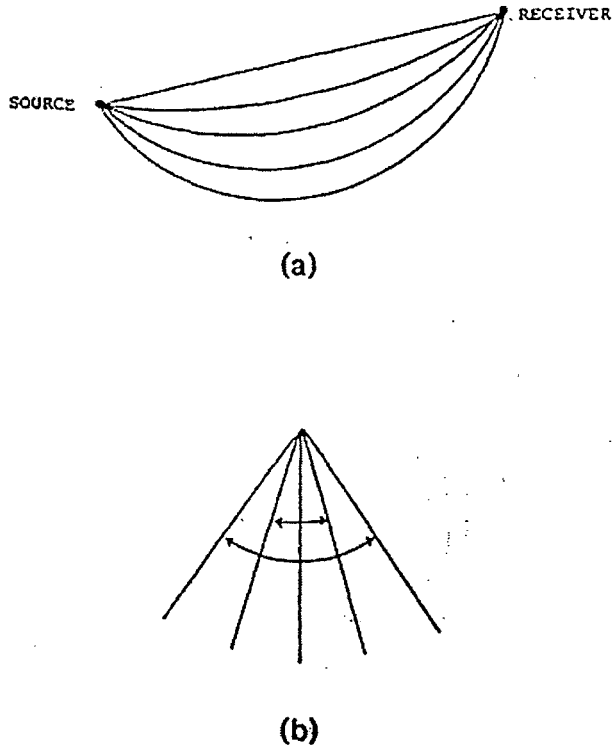

Figure 3.3 Sketches to illustrate the ray paths studied in the search for the minimum travel-time ray. (a) view of plane of one set of arcuate rays and (b) view of family of planes, in direction of wave propagation.

3.2.2.4 Hypocentre-velocity coupling and the method of inversion

If adjustment of the hypocentre is ignored in geologically complex areas, hypocentre mislocation will introduce bias into the velocity model results. However, addressing hypocentre-velocity model coupling increases the size of the matrix to be inverted. If hypocentre-velocity coupling is explicitly treated, then the simultaneous inversion equations can be expressed in matrix notation form

$$\begin{array}{cccccccc} r_i & = & H_i & \Delta h_i & + & M_i & \Delta m \\ (L \times 1) & = & (L \times 4) & (4 \times 1) & + & (L \times N) & (N \times 1) \end{array} \qquad (3.6)$$

where r_i and Δh_i are vectors containing the L residuals and four unknowns for the hypocentre parameter adjustments for the ith event. H_i represents the matrix of hypocentre partial derivatives, M_i velocity partial derivatives for the ith event and Δm is the vector of N velocity adjustments. The problem is viewed in a manner analogous to the parameter separation method of Pavlis and Booker (1980). A matrix Q_0 is constructed such that

$$Q_0^T H_i = 0 \qquad (3.7)$$

(Lawson and Hanson, 1974). When equation (3.6) is multiplied by Q_0 such that

$$Q_0 r_i = r_i' = Q_0 H_i \Delta h_i + Q_0 M_i \Delta m = M_i' \Delta m \qquad (3.8)$$

equation (3.6) is simplified to

$$r_i' = M_i' \Delta m \ . \qquad (3.9)$$

Parameter separation operates on matrices of hypocentre and velocity partial derivatives, separating the hypocentre and velocity problems and reducing the size of the matrix. This procedure is effective when the estimated hypocentres are "linearly within range" of the true positions (Thurber, 1993). Synthetic simulations reveal that the linear range is 2-3 km for hypocentres and ~ 10% velocity

perturbation. M′ and r′ are large if many events are used. To mitigate the inversion problem normal equations are used to reduce the matrix size (Spencer and Gubbins, 1980; Thurber, 1983). Equation 3.9 may be written as

$$(M'^{T} r') = (M'^{T} M') \Delta m \qquad (3.10)$$

As events are added on to the normal equations, the matrix $M'^{T} M'$, and the vector $M'^{T} r'$ are accumulated sequentially, to produce a vector of fixed size having a symmetric matrix. Equation 3.10 is solved using damped least squares which also suppress large model fluctuations (Aki and Lee, 1976). The events are then relocated using the updated velocity parameters. Iterative improvements are subsequently made to the velocity model and hypocentral locations.

3.2.2.5 The effect of inclusion of *S*-waves

The use of *S*-wave data improves constraints on earthquake source depths. *S*-waves can only be used if 3-component stations are available since *S*-waves are recorded poorly on vertical instruments. *S*-waves cannot be picked as accurately as *P*-waves because they arrive in the coda of the *P*-wave and are subject to shear wave splitting resulting from anisotropy. The systematic differences in data quality and ray path abundance make inversion for the *Vp/Vs* ratio a better strategy than separate and independent inversion for *Vs* (Eberhart-Phillips, 1990). To calculate perturbations in *Vp/Vs*, initially it is assumed that *Vp/Vs* is constant. For a constant *Vp/Vs*, the ray paths are identical for both *P*- and *S*-waves, and the *S-P* time difference dt_{ij} is expressed as

$$dt_{ij} = \int [\, (Vp/Vs) - 1 \,] / Vp \; ds \quad . \qquad (3.11)$$

Using a well-determined three-dimensional *Vp* velocity model and a constant *Vp/Vs* ratio, predicted *S-P* travel times dt_{ij}^{cal} are calculated and compared with the observed times dt_{ij}^{obs}, to produce *S-P* travel-time residuals. These residuals are inverted to obtain perturbation in the *Vp/Vs* nodes. Using the updated *Vp/Vs* velocity model and the *P*-wave velocity model, an *S*-wave model is generated and S-wave travel times are re-calculated.

3.2.2.6 Assessment of the quality of the solution

The interpretation of LET structural results should be governed by solution quality as assessed by variance reduction, model resolution and model covariance (Menke, 1989). The variance reduction indicates the improvement in fit between the observed and predicted data. Resolution, as measured by the variance-covariance matrix, is a measure of the ability of the experiment to retrieve structure as parameterised. Hence, the resolution at a particular grid point is a weighted average of the velocity throughout a localised volume. The "Derivative Weight Sum" (DWS) (Toomy and Foulger, 1989; Foulger and Toomy, 1989) is sometimes used to measure the ray-density near a given velocity node and is used to design the 3-D grid of discrete velocity nodes in LET modelling (section 3.3.6).

3.3 Method

3.3.1 The network and data used for the study

All data used in the tomography inversions came from the UNOCAL network. The original data released are in PCQL trace file format with files named :

dddhhmns.nyr,

where *dddhhmns.nyr* is the starting time of the file, where *ddd* represented the day of the year, *hh* is the hour and *mns* minute and seconds expressed in hexadecimal format. *nyr* represents the network in operation (w,g,f), and this changed as the network was upgraded (Section 1.6.4).

The PCQL data were converted into eXternal Data Representative (XDR) format using AH (ad hoc) format with the program *pcql2ah* (B.R. Julian, *pers. comm.*) An ASCII list file was created for each earthquake using the script *mkah2list* (B.R. Julian, *pers. comm.)* containing a list of the AH files corresponding to all the

seismograms for that event. The list files were used to display traces using the interactive picking program *epick* and to drive the program *autopick* (B.R. Julian, *pers. comm.*) which makes automatic picks.

A tomographic inversion for *Vp* and *Vp/Vs* was performed using data recorded at 22-month intervals from April 1991 to August 1998. For each time period, the selection criteria used to choose data were as follows:

- Good Signal:Noise (S/N) ratio.
- Impulsive *P* and *S* waves.
- Uniform distribution of events.
- Good azimuthal coverage of ray paths.
- Maximum azimuthal gap between adjacent stations < 180° for each earthquake.
- Minimum of 10 picks.
- Residual of RMS of 0.1 for *P*-waves and 0.15 for *S*-waves.

As the data sets were very large, and events with high S/N ratio abundant, only the events with largest numbers of picks were selected. The automatic picker, *autopick*, was employed to shortlist suitable events.

3.3.2 *autopick*

Program *autopick* picks *P*-waves on digital raw seismograms in AH format and assigns polarities and quality factors. *Autopick* uses the ratio of the amplitudes within two sliding triangular weighted windows. To make a *P*-wave pick, *autopick* traverses the seismic trace twice. First it identifies the broad window of the arrival time of the *P*-wave phase. The second traverse refines the pick in the selected portion using different sliding window parameters involving a low pass filter and a narrower triangle. The success of the analysis dictates the quality factor assigned to the pick. If the clarity of the signal falls below a user-defined threshold criterion, no pick is made.

3.3.3 *epick*

epick is a digital interactive picking program which enables the user to display, study, and modify seismic traces. Measurements include P, S and coda picks, amplitude, frequency, polarity and quality, 0 being the best 4 being the worst. *epick* displays three work windows, the squash, display and pick windows. All traces are displayed simultaneously in the squash window. Traces of interest can be selected and then shown in the display window. The pick window is shown below the display window and draws a selected portion of the trace where measurements can be made.

All traces were low-pass filtered with a corner frequency of 0.1 to 30.0 Hz to reduce noise. Only the horizontal components of the seismograms were used to pick *S*-waves. On the vertical components, converted *P* phases can easily be confused for *S*-waves. The effect of anisotropy and *S*-wave birefringence was dealt with where applicable by picking the earliest *S*-waves. *S*-wave picks with low quality factors were checked by band-pass filtering at 0.1 to 5.0 Hz, which is effective in clarifying which is the *S* phase. *P*-waves were picked to an accuracy of 0.01 seconds and *S*-waves to an accuracy of 0.02 s (Figure 3.4) (Appendix 3). Program *qloc* (B.R. Julian, *pers. comm.*) locates the earthquakes, performing an iterative least-squares damped inversion to minimise the RMS travel time residual of *P*- and *S*-waves. The initial hypocentre assumed is directly beneath the closest station at a depth of 3 km. A three-dimensional velocity model for The Geysers obtained from tomographic inversion of data from 1991 (Ross, 1996; Julian *et al.*, 1996) was used for locating the events. All events were hand picked.

3.3.4 The initial 1-D and 3-D velocity models for The Geysers

A tomographic study of The Geysers was performed by A. Ross, using data from 1991 (Ross, 1996; Julian *et al.*, 1996). A one-dimensional *P*-wave velocity model was derived using the program *VELEST* (Kissling *et al*, 1994; Ross, 1996) (Figure 3.5). This model was used as a starting model for tomographic inversion of the

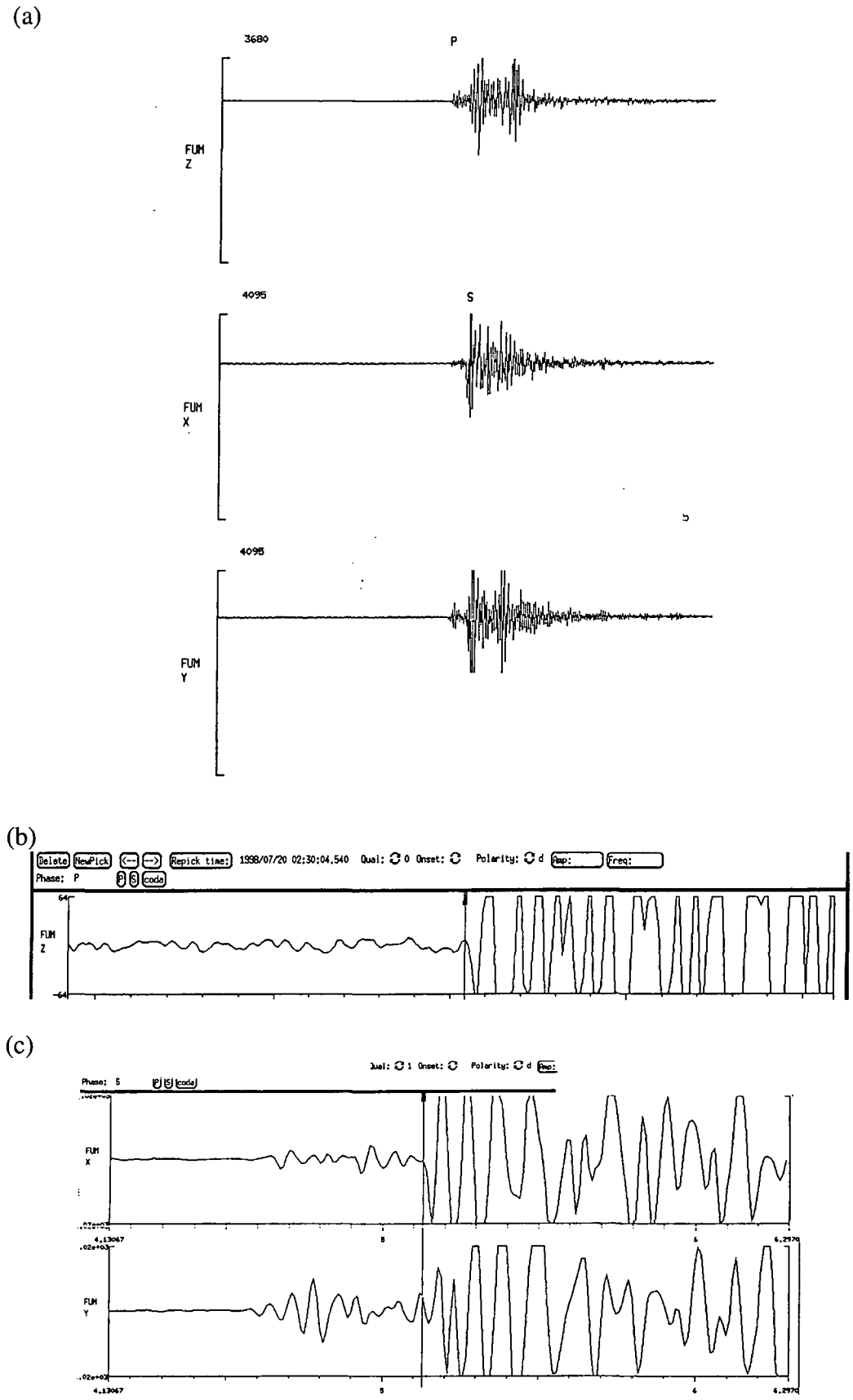

Figure 3.4: Example of a seismogram and *P*- and *S*-waves picked to 0.01 s and 0.02 s accuracy respectively. The event is 19980230023004.54 recorded at station FUM. (a) All three traces. (b) *P*-wave pick in detail, and (c) *S*-wave pick in detail.

1991 data. Recordings from the temporary IRIS network of 15 3-component stations, the permanent UNOCAL network, and the NCSN network were combined. The dataset contained 185 events with 4032 P-wave and 944 *S*-wave arrival times. A 20 x 20 km^2 area was modelled throughout a depth range of –1 to 6 km bsl. The grid was oriented parallel to the tectonic trend of the San Andreas shear zone. Orientating the grid parallel to the tectonic trend of the study area enhances model fidelity (Toomy and Foulger, 1989). The grid encompasses the whole seismic network. A graded simultaneous tomographic inversion was performed using the method of Thurber (1983) (Ross, 1996; Julian *et al.*, 1996). The three-dimensional model reduced the data variance by 70% and the final RMS residuals were 0.022 s for *P*-waves and 0.048 s for *S*-waves. Models for both *Vp* and *Vp/Vs* were generated. A starting *Vp/Vs* ratio of 1.74 was used. This was derived from values obtained using Wadati diagrams for events with five or more *S-P* travel time measurements.

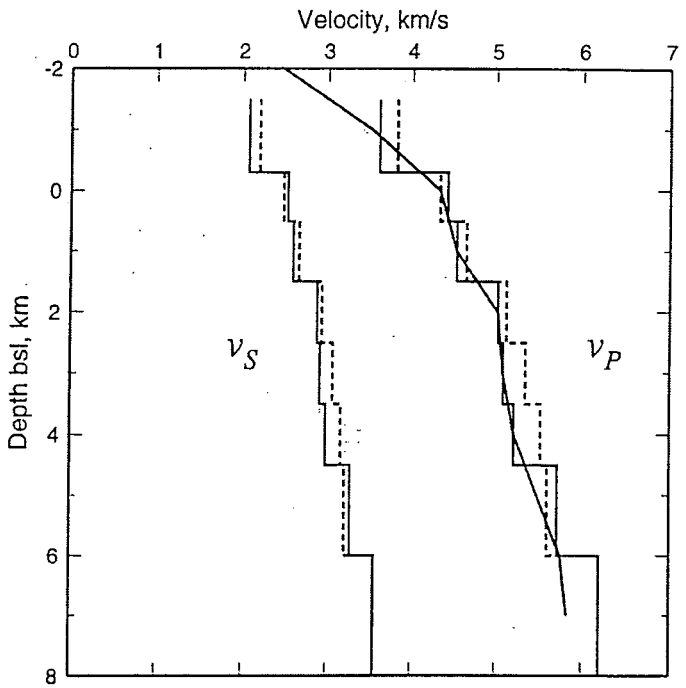

Figure 3.5: The final one-dimensional velocity model used (black lines) as a starting model for the tomographic inversion for three-dimensional structure at The Geysers (*from* Ross, 1996). The one-dimensional regional velocity model of Eberhart-Phillips and Oppenheimer (1986) is shown by the dashed line. The continuous solid black line is the initial one-dimensional *Vp* model used to calculate the final *Vp* one-dimensional model for The Geysers. The final one-dimensional *Vs* model for The Geysers was calculated assuming a *Vp/Vs* ratio of 1.74 while the regional *Vs* model was calculated using a *Vp/Vs* ratio of 1.80.

The *Vp* model exhibited an anomaly of ~ -10% in the west Geysers compared with the central Geysers. The low velocity modelled to the northeast of the Collayomi fault correlated with the Clear Lake Volcanics at shallow depth and the Coast Range Ophilotes at greater depth (Figure 3.6a). The *Vp/Vs* model was dominated by a low *Vp/Vs* anomaly surrounded by high *Vp/Vs*, at depths up to 2 km bsl. The low *Vp/Vs* anomaly correlated closely with the steam reservoir (Figure 3.6b).

3.3.5 *SIMULPS12*

3.3.5.1 Program parameters

The tomographic inversions reported in this thesis were done using the program *SIMULPS12*. (Thurber, 1983; Eberhart-Phillips, 1993; Evans *et al.*, 1994). *SIMULPS12* was developed from *SIMUL3* (Thurber, 1981; Thurber, 1983) which includes 'pseudo-bending' ray tracing (Um & Thurber, 1987) and the ability to invert also for *Vp/Vs*.

The program uses a control file where several user-defined parameters such as number of events, damping parameters are included. In addition, the following files are required (Appendix 4):

- Fort 2: Seismic station location information
- Fort 3: starting velocity model and nodal configuration
- Fort 4: earthquake locations and travel time data

The main output files are:

- Fort 16: changes in the model and earthquake locations at each iteration
- Fort 17: resolution matrix
- Fort 20: calculations of the residuals of the travel times for each iteration

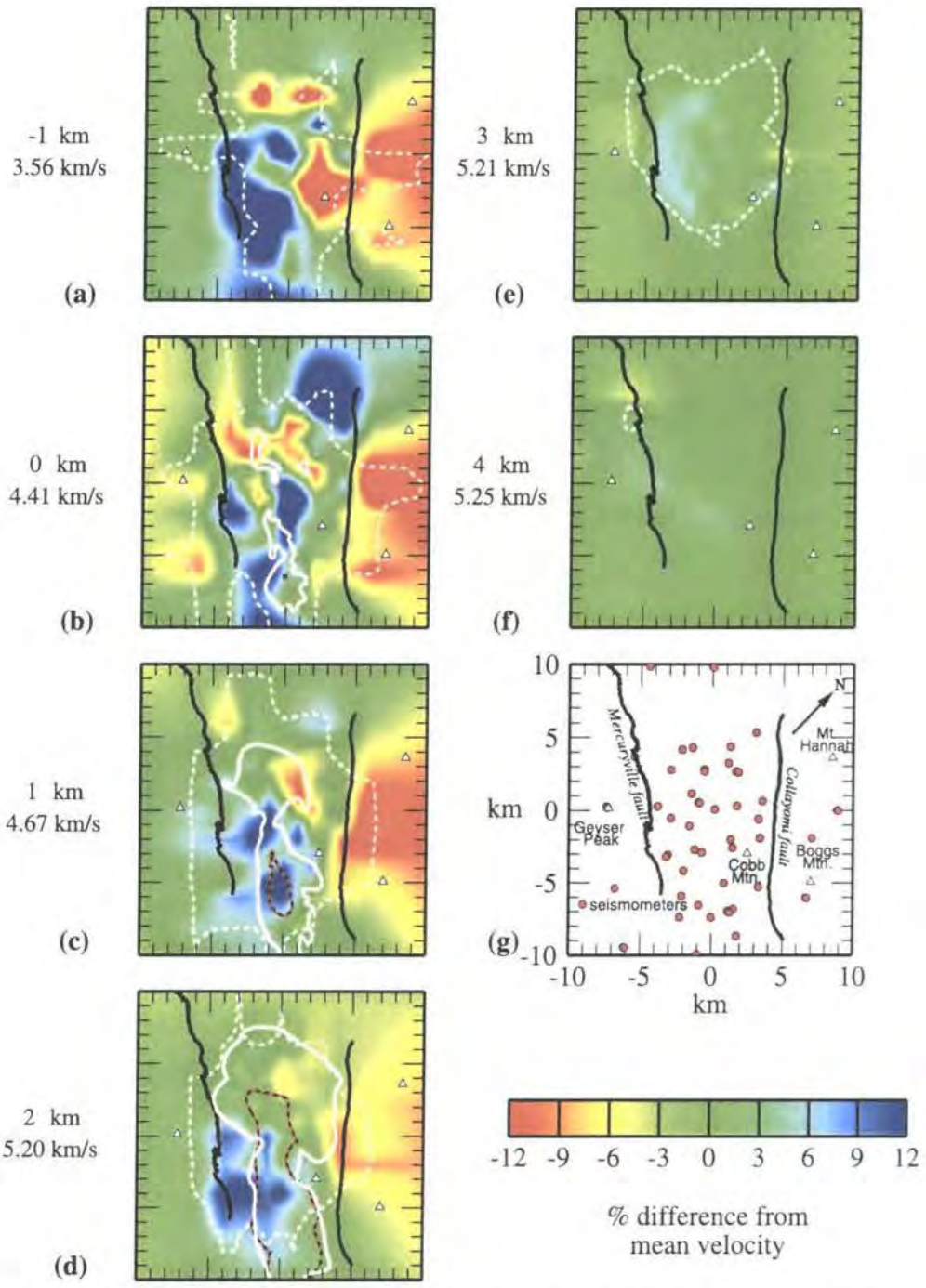

Figure 3.6a: Maps showing percentage variation in v_p from mean values for horizontal depth slices through the model (values to the left of map). The location map (g) details surface features within the modelled volume including the 1992 production area (shaded) and seismometers (red circles). Areas enclosed by white dashed lines (a-f) are well resolved (spread <4 km). Solid white lines: boundary of steam reservoir; black and red lines: boundary of the felsite batholith; white triangles: mountains; black lines: faults (from Ross, 1996).

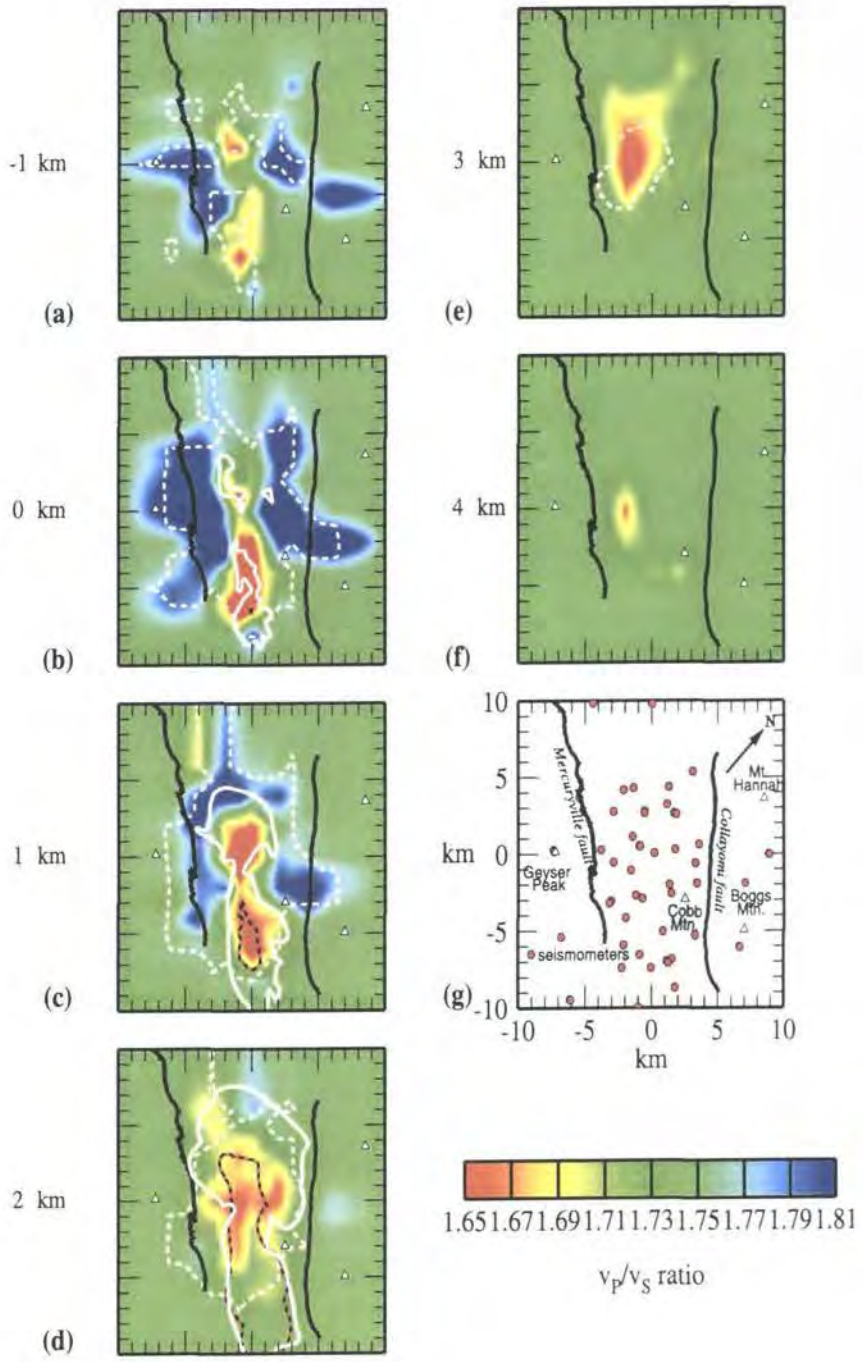

Figure 3.6b. Maps showing variation in v_P/v_S for horizontal depth slices through the model. v_P/v_S varies from 1.64 to 1.84 with and average of 1.74. The same convention as Figure 3.6a is used for map features (from Ross, 1996).

- Fort 23: the final velocity model
- Fort 24: final locations and travel times
- Fort 36: summary information for each iteration

3.3.5.2 The inversion procedure

A one-step direct-inversion approach involves starting with a one-dimensional velocity model and performing a single inversion using a fine grid. This method may not converge on the global minimum since the starting model may be far from the final model. A better approach is to use a graded inversion. Graded inversions are suitable for most datasets as they progressively introduce more structural detail as the nodal spacing is reduced from an initial large value. This means that the starting models used are always as close as possible to the final model. For the April 1991 data a graded inversion approach was used. The nodal spacing was progressively decreased from 10 km to 4 km, 2 km and finally to 1 km, involving 1232 nodes (Figure 3.7). Study of the spread function for selected nodes, (Foulger *et al.*, 1995) and node resolution, confirmed that the reservoir volume is best resolved at depths 0 to 2 km bsl for all the inversions. To continue the model smoothly outside the grid, nodes were spaced at large distances of ±10.0 km in depth and ±150.0 km laterally outside the grid.

For inversions in this thesis, a hybrid approach was used. The objective of this study was to model temporal structural changes in the three-dimensional model (i.e. four-dimensional tomography). A "graded" tomographic inversion using only the UNOCAL network was performed by A. Ross for April 1991 (Ross, 1996; Foulger *et al.*, 1997; A. Ross, *pers. comm.*). The model used for April 1991 in this study and the April 1991 model referred to henceforth is the April 1991 inversion using only UNOCAL stations (Ross, 1996; Foulger *et al.*, 1997).

The April 1991 model was used as the starting model for each inversion, along with the same grid. Tomographic inversions and relevant data are shown in Table 3.1. The number of *S*-picks used in the 1991 inversion is considerably smaller than in the other inversions. The RMS for *P*-picks was ~0.020 s for all inversions but

RMS for *S*-picks varied from 0.035 s to 0.052 s. A large reduction in variance was achieved for the 1991 inversion. As the final model from 1991 was used as the starting model for the other inversions, the variance reduction was much smaller since the structural change from year to year was relatively small. However, the variance reduction increases progressively with time, since the growth in strength of the anomaly resulted in the 1991 model being progressively further away from the final model with time.

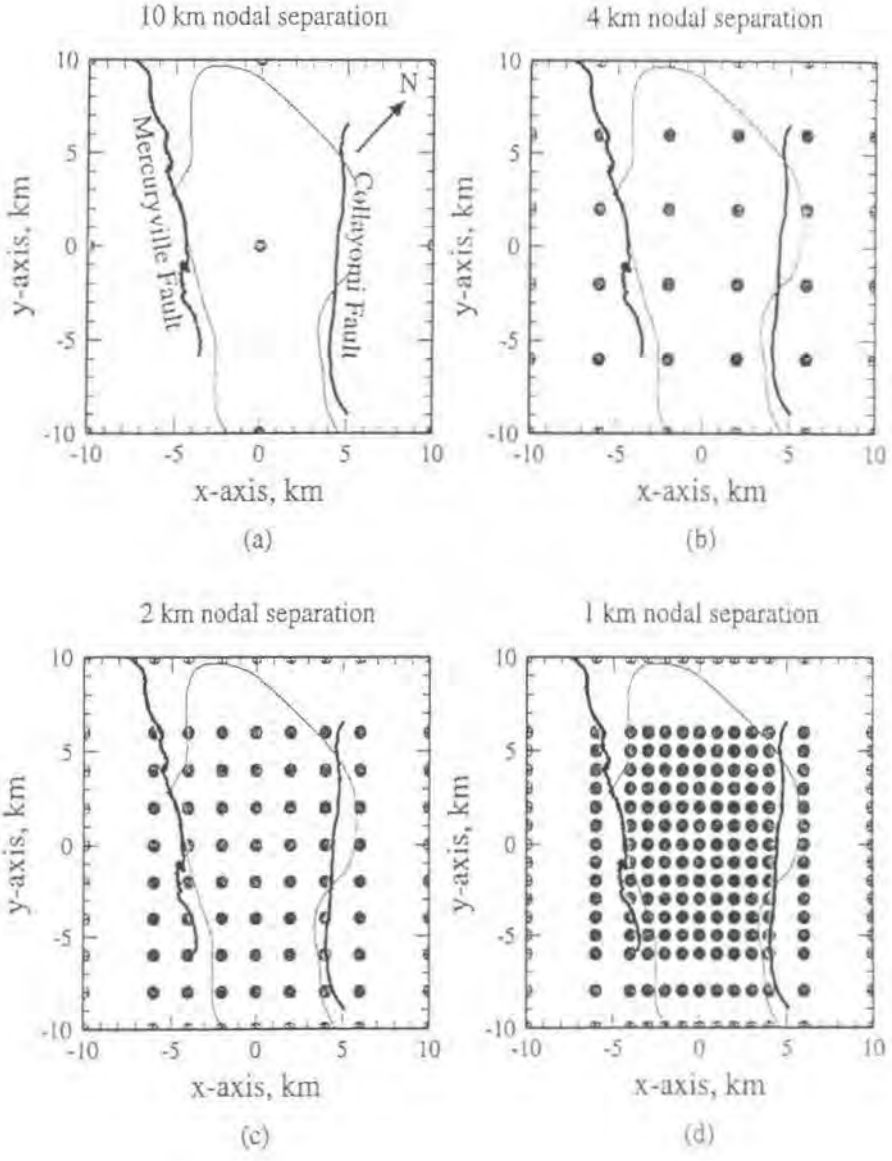

Figure 3.7: Nodal configurations used in the graded tomographic inversion for April 1991 by Ross (1996). For inversions for subsequent years, only nodal configuration (d) with 1.0 km spacing, was used.

Table 3.1:Data concerning the tomographic inversions.

	Foulger et al. (1997)	*This study*	*Foulger et al. (1997)*	*This study*	*This study*
	Apr. 1991	**Feb. 1993**	**Dec. 1994**	**Oct. 1996**	**Aug. 1998**
No. of events	163	241	146	295	302
No. of data	2494	4043	3178	3762	4853
No. of *P*-arrivals	2268	3444	2522	3193	4128
No. of *S*-arrivals	226	599	656	569	725
Vp dmp. (s^2/ km)	5.0	20.0	5.0	5.0	5.0
Vp/Vs dmp. (s)	2.0	20.0	2.0	5.0	2.0
final RMS resid. for *P*-arrivals (s)	0.021	0.022	0.020	0.016	0.015
final RMS resid. For *S*-arrivals (s)	0.036	0.043	0.052	0.035	0.035
Variance reduction (%)	75	9.3	13.9	15.5	26.3
chng. in max. *Vp/Vs* wrt 1991 (%) at sea level	N/A	0.6	1.3	1.3	3.4
Increase in *Vp/Vs* anomaly	0.16	0.17	0.18	0.18	0.22

3.3.5.3 Selection of damping parameters

Inversions using damped least squares are highly sensitive to the choice of damping parameter, ε^2, and the optimum value will vary with the amount and distribution of the data, and size and spacing of the model grid nodes (Eberhart-Phillips, 1986). If too small a value is used, the velocities determined will oscillate from one grid point to the other resulting in large lateral changes in velocity that are geologically implausible and reflect the fitting of noise in the data. If too high a value is selected, the quality of the result is compromised because real signals in the data are suppressed. The damping parameter balances the two factors that damped least square minimises:

$$\min (\Sigma r^2 + \varepsilon^2 |\Delta m|^2) . \qquad (3.12)$$

If all of the residuals r could be explained by changes to model parameters Δm, and then on succeeding iterations Σr^2 decreases at the same rate as $|\Delta m|^2$ until both approaches 0, there would be no need to adjust the damping parameter (Eberhart-Phillips, 1993). However, in practice, even after the inversion has converged on the final model, there will be some part of the residual component present. An iterative inversion would benefit from adjusting the damping value after each iteration.

To obtain a damping value that gives a large variance reduction without an unnecessarily complicated model, an empirical approach was used, whereby a series of one-iteration inversions for a range of damping values (0.1 to 999) were performed to ascertain the optimal damping value. The nodal configurations, travel times, and velocity model were identical for all inversions. Data variance is then plotted against model variance. Damping values on the high side were used to ensure conservative, significant results (Table 3.1).

3.3.5.4 Terminating the inversion

SIMULPS12 will terminate if:

- The F-test fails, indicating that variance reduction has become insignificant with further iterations
- The number of iterations specified in the control file has been completed
- The weighted RMS has fallen below a user-defined value
- The solution norm has fallen below a user-defined value.

3.3.6 Model resolution

Model resolution is limited by the non-uniformness of the station geometry, earthquake locations and the distribution of rays within the model volume. At the periphery of the model, the structure is generally less well sampled than in the middle. The spatial extent of velocity variations may be poorly constrained

because smearing along the dominant ray-path direction can occur if there are insufficient crossing rays. Resolution of *Vp* and *Vs* differs as a result of differences in the numbers of events used and differences in station locations.

The Derivative Weight Sum (DWS) is a measure of the ray density surrounding a given velocity node. It is weighted to the proximity of each ray passing the velocity node in question and is useful in determining the best possible three-dimensional grid. The DWS has been defined as:

$$DWS\ (n) = N \sum_i \sum_j \left(w_n \int_{P_{ij}} (x)\ ds \right) \qquad (3.13)$$

For the *n*th velocity model parameter at position x_n where P_{ij} corresponds to the ray path from event *i* to station *j*, and w_n is the weighting of the nth model parameter used interpolate the wave-speed at position x. N is a normalisation factor that accounts for the volume influenced by the *n*th model parameter (Toomey and Foulger, 1989; Ross, 1996). A threshold value of 50 is recommended to distinguish well-resolved nodes from poorly resolved nodes in a similar LET experiment to those done at The Geysers (Arnott and Foulger, 1994).

The spread function is a statistical measurement of how realiable each velocity node is. The spread function is defined as:

$$spread = \left[\left\| R_j \right\|^{-2} \sum_k D_{jk}^2\ R_{jk}^2 \right]^{-\frac{1}{2}} \qquad (3.14)$$

where $\left\| R_j \right\|^{-2}$ is the Euclidean (L2) norm of the *j*th row of the resolution matrix, D_{jk} is the distance between the *j*th and *k*th nodes and R_{jk} is the element (*j*,*k*) of the resolution matrix. The spread function indicates a value for each grid point which expresses the extent of local averaging involved in determing the velocity for that particular node. Small spreads (< 4 km) indicate well-resolved node velocities (Foulger *et al.*, 1995; Miller, 1996).

3.4 Results

3.4.1 Recording of earthquakes at stations and distribution

3.4.1.1 Recording of events

During the period 1991-1998 the network remained fairly constant in geometry and number of stations. In April 1991, Station FUM was a single-component vertical station (Figure 2.1). In August 1992 it was upgraded to a three-component station (Figure 2.1). Station ANG was decommissioned in 1994 and replaced by station JKR directly west of the location of station ANG (Figure 2.1). Figure 3.8 shows histograms of the numbers of picks at each station for each inversion.

The numbers of events used in the 1991 and 1994 inversions are about half those used in the other inversions. In 1994, there are many more *S*-waves picked than for the other inversions. Most stations had similar numbers of picks for all the inversions apart from station TCH in the southeast Geysers in 1998. For the data acquisition period used in 1998, station TCH was temporarily dysfunctional. Other stations in the southeast Geysers such as stations DES and SSR recorded few *P*-waves as most 1998 events were located and in the central part of The Geysers.

3.4.1.2 Event distribution

A good spatial distribution of events was achieved for all tomographic datasets (Figure 3.9) (Appendix 5). The events are located fairly evenly throughout central part of the reservoir where most of the steam extraction and liquid re-injection takes place. If more events are used, spatial clustering negates the benefit of the larger dataset, since ray paths are simply duplicated. Such clustering may not be apparent until after relocation through the three-dimensional model. In 1996, two weak clusters were identified southwest of Cobb Mtn. and a larger elongated cluster in the northeast trending north-northeast and south-southwest. This latter cluster is even more apparent in Aug. 1998 (compare Figure 3.9d,e). Few events were located in the northwest and southeast extremes of the reservoir as they fell

(a)

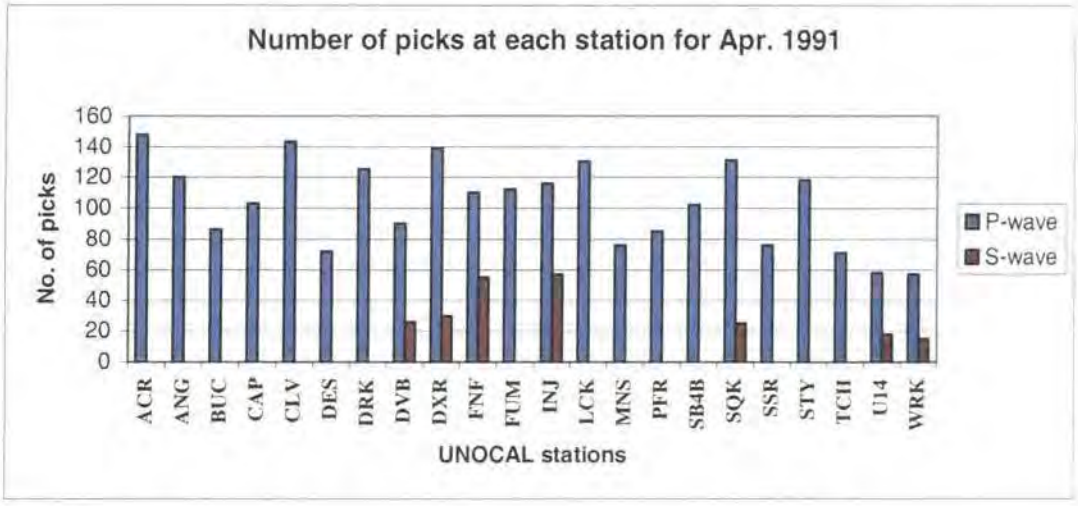

(b)

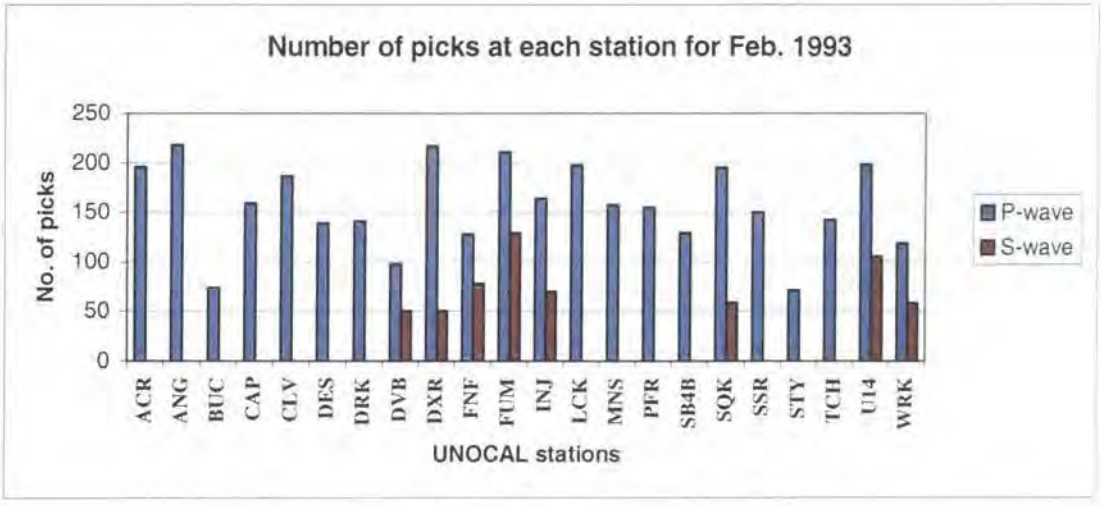

Figure 3.8: Histogram showing numbers of *P*- and *S*-wave picks used in each of the tomographic inversions. Only three-component stations were used to pick *S*-waves. (a) April 1991 (*from* Foulger *et al.*, 1997), Station FUM was then a single-component station and no *S*-waves were picked there. (b) Picks made for February 1993.

(c)

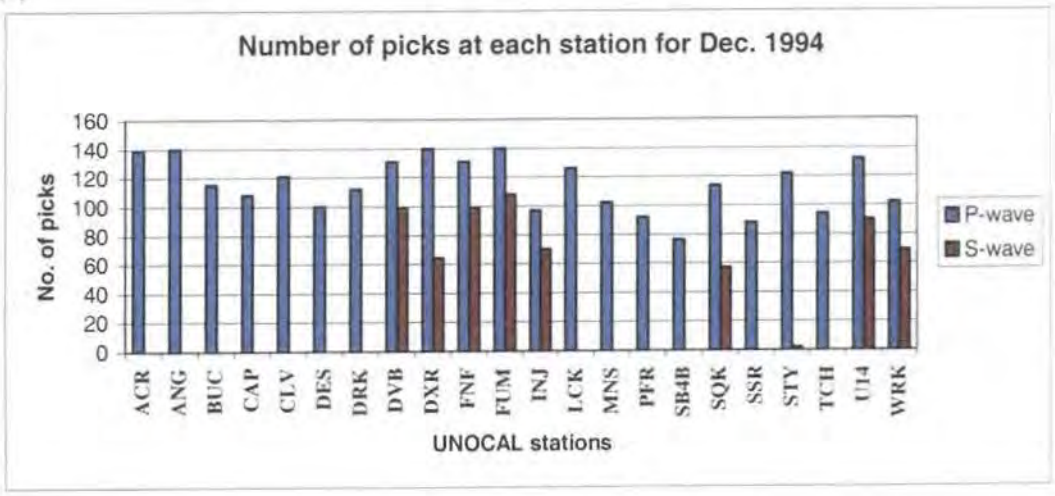

(d)

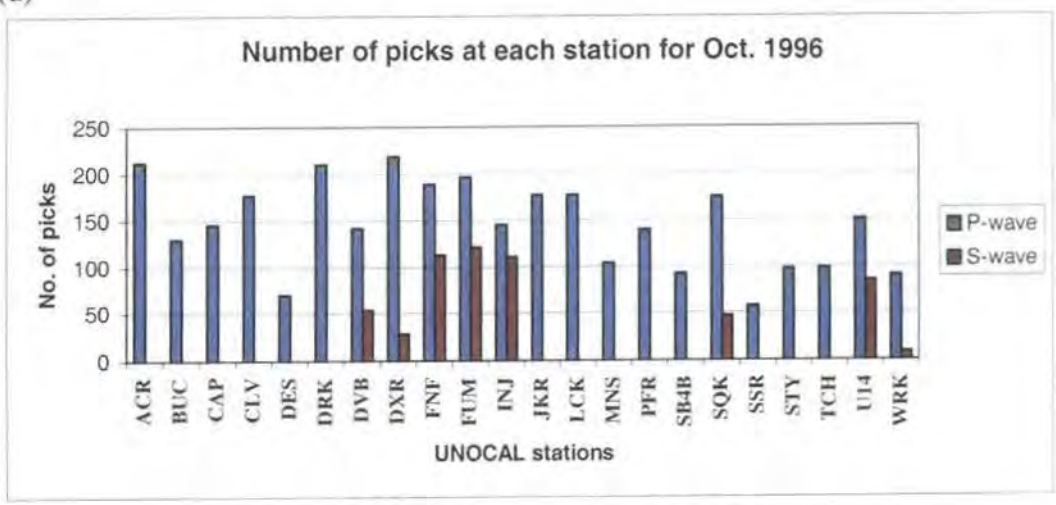

(e)

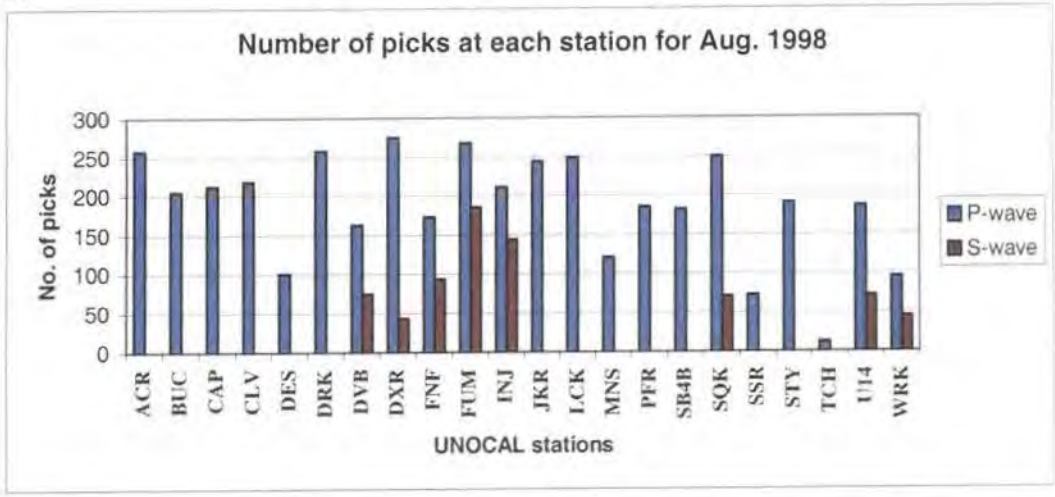

Figure 3.8 (cont.) Histograms for (c) December 1994 (*from* Foulger *et al.*, 1997), (d) October 1996 and (e) August 1998.

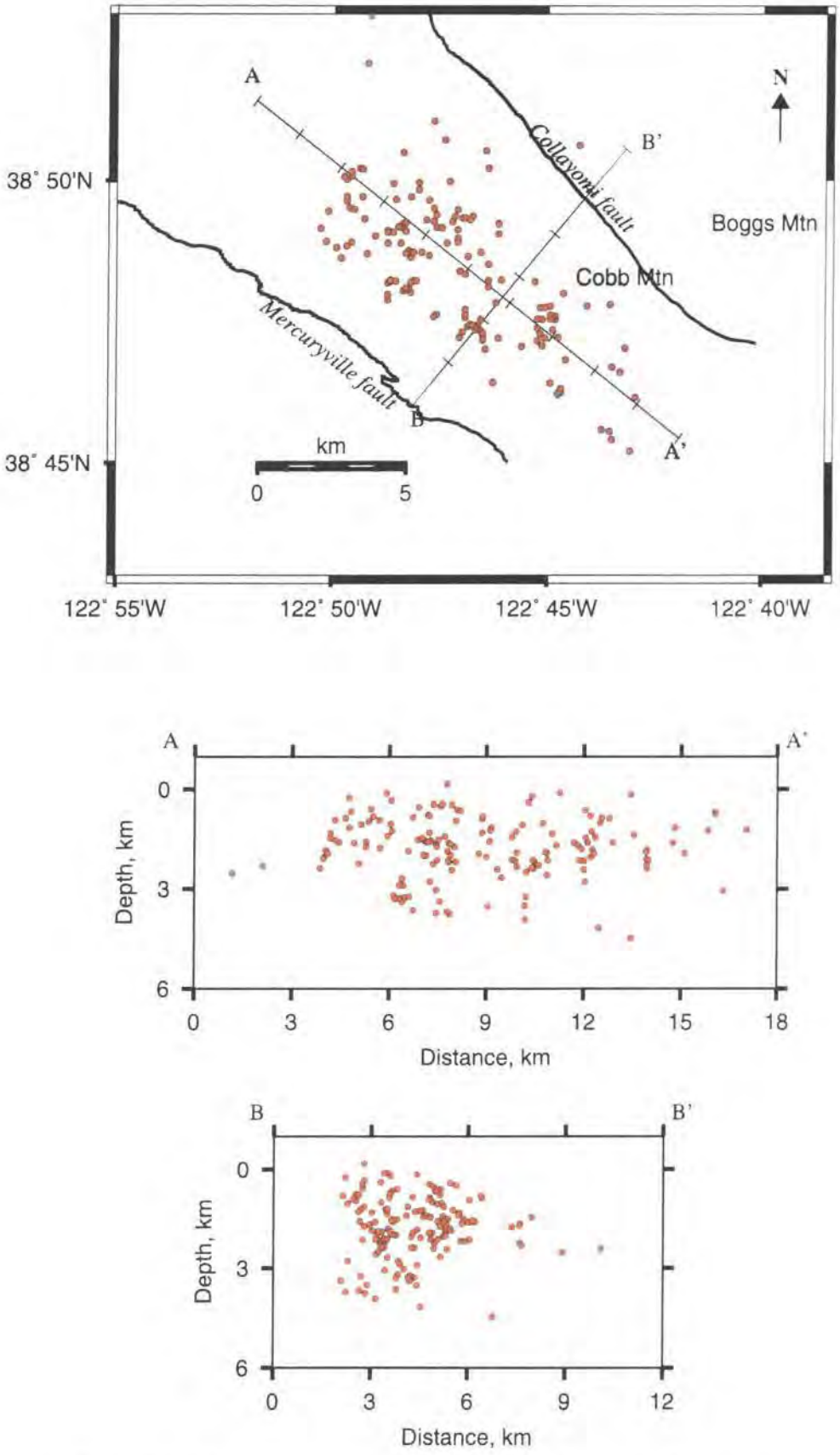

Figure 3.9a: Map and cross sections showing the final locations of events used in the tomographic inversion for 1991 (*from* Foulger *et al.*, 1997).

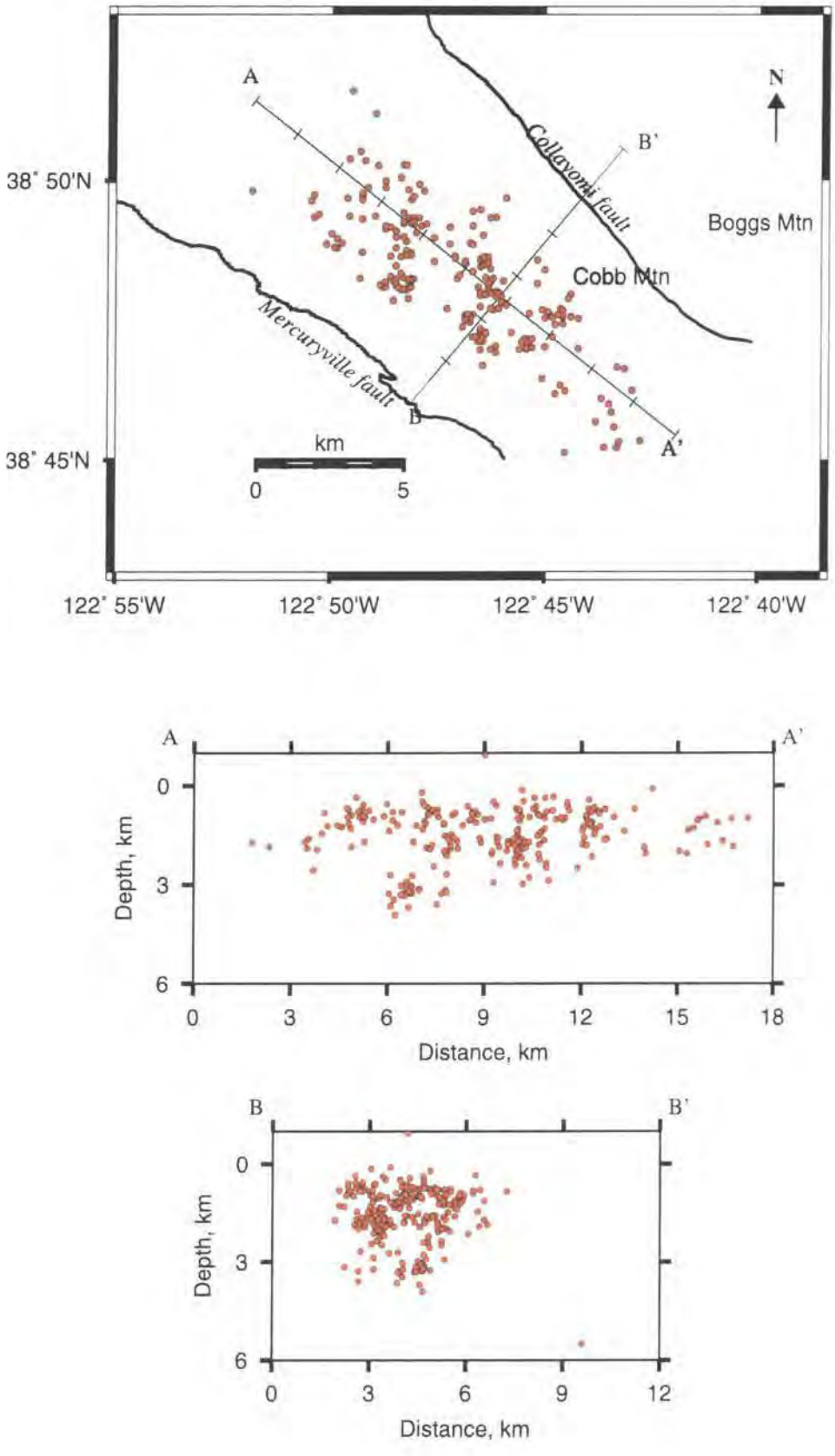

Figure 3.9b: Same as for figure 3.9a, except for the inversion for 1993.

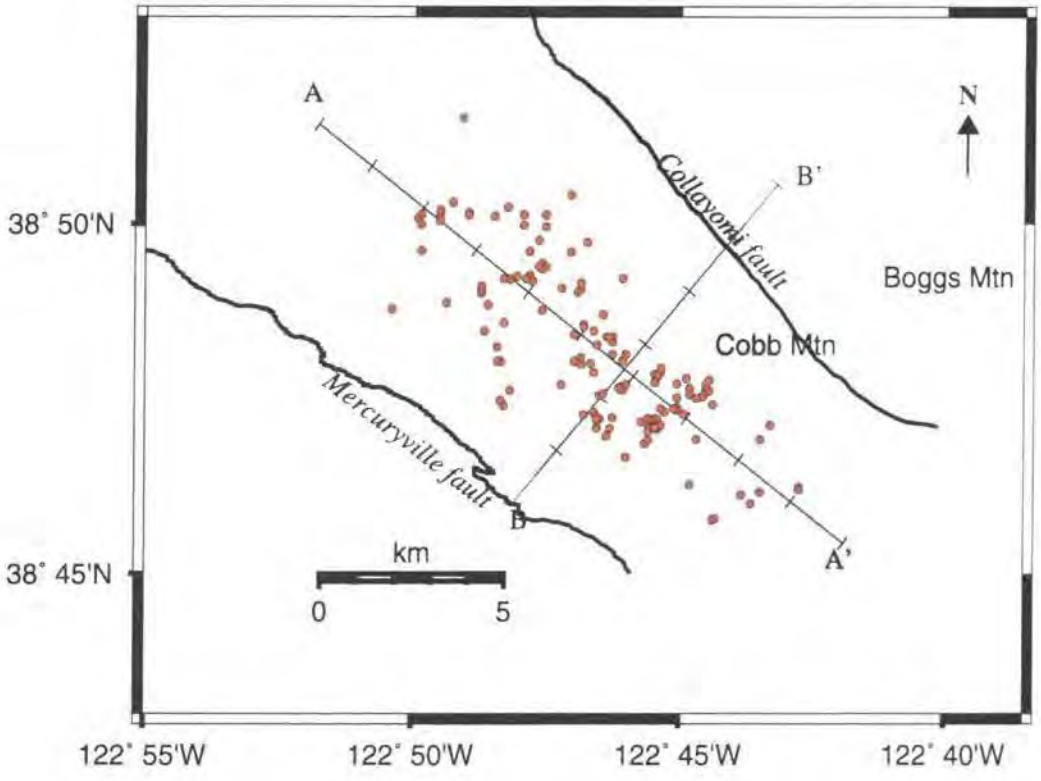

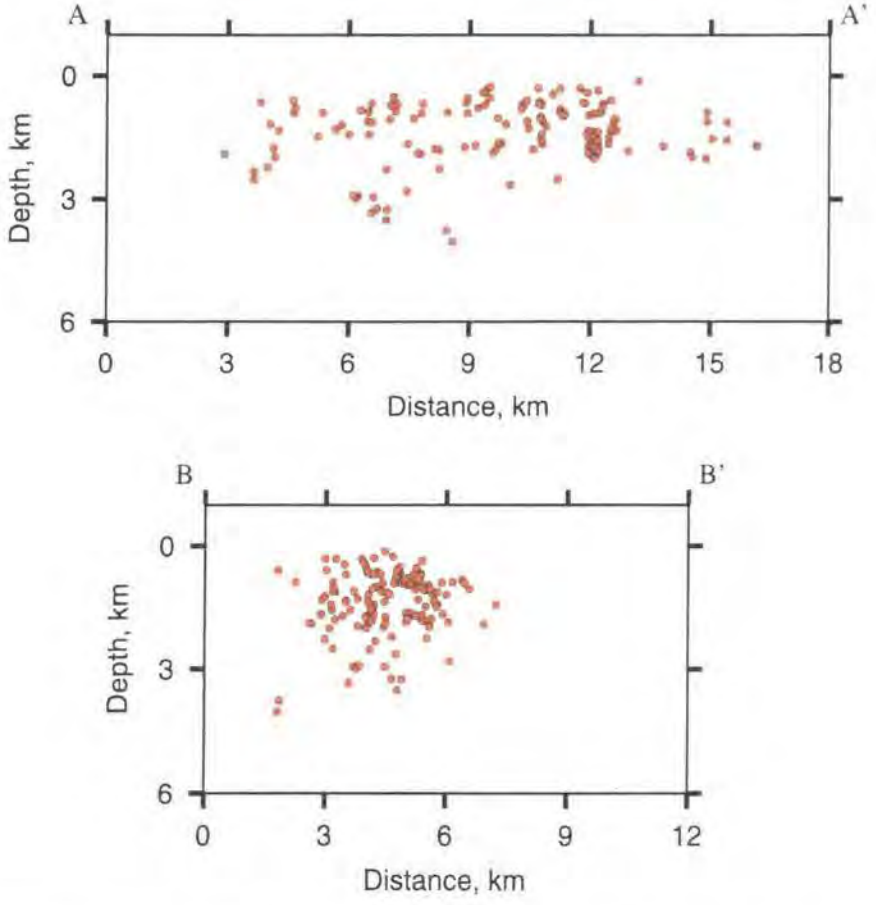

Figure 3.9c: Same as for figure 3.9a, except for the inversion for 1994 (*from* Foulger *et al.*, 1997).

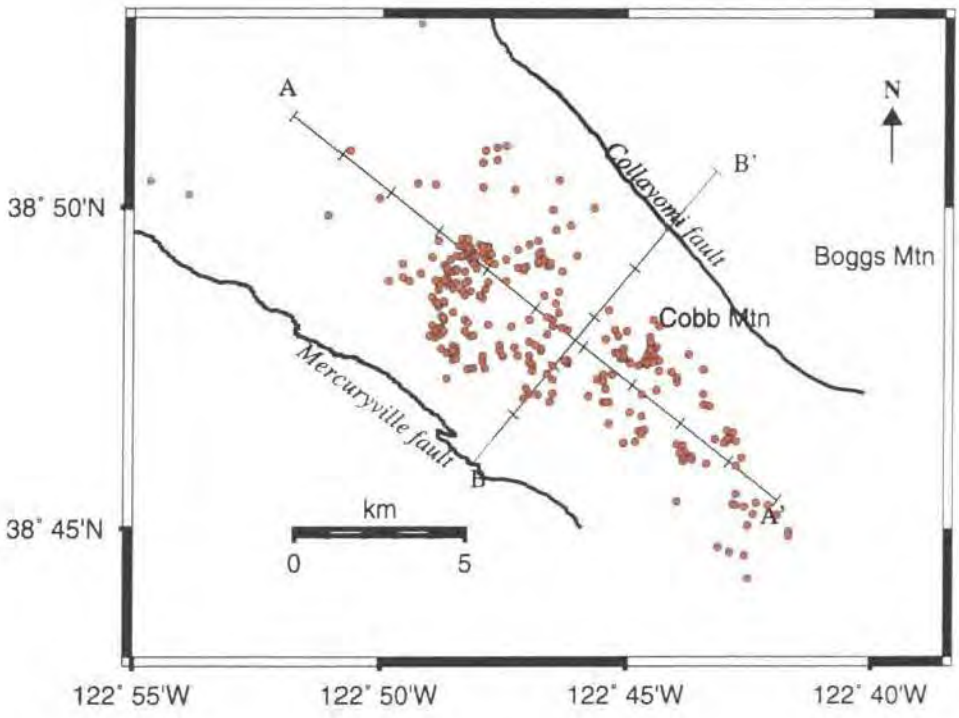

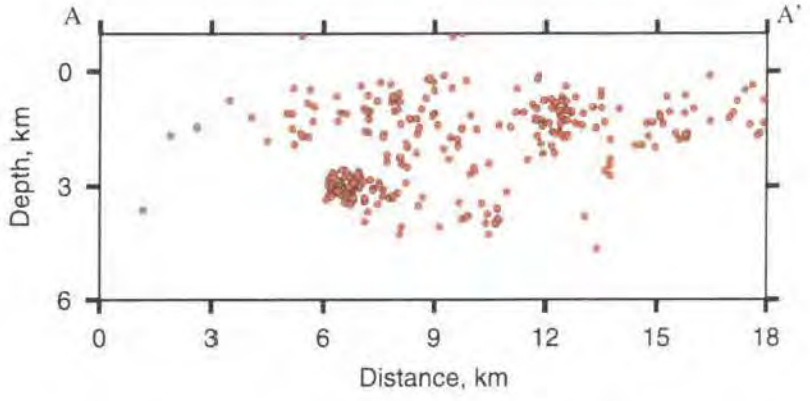

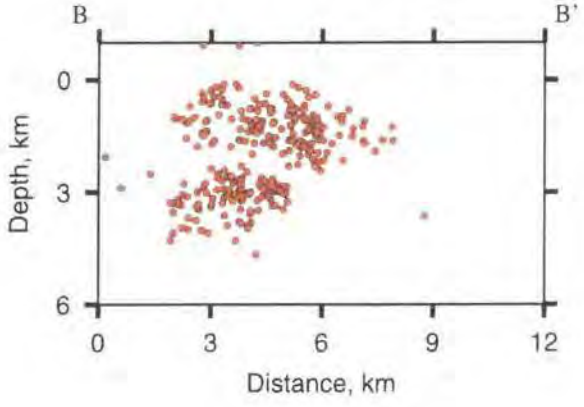

Figure 3.9d: Same as for figure 3.9a, except for the inversion for 1996.

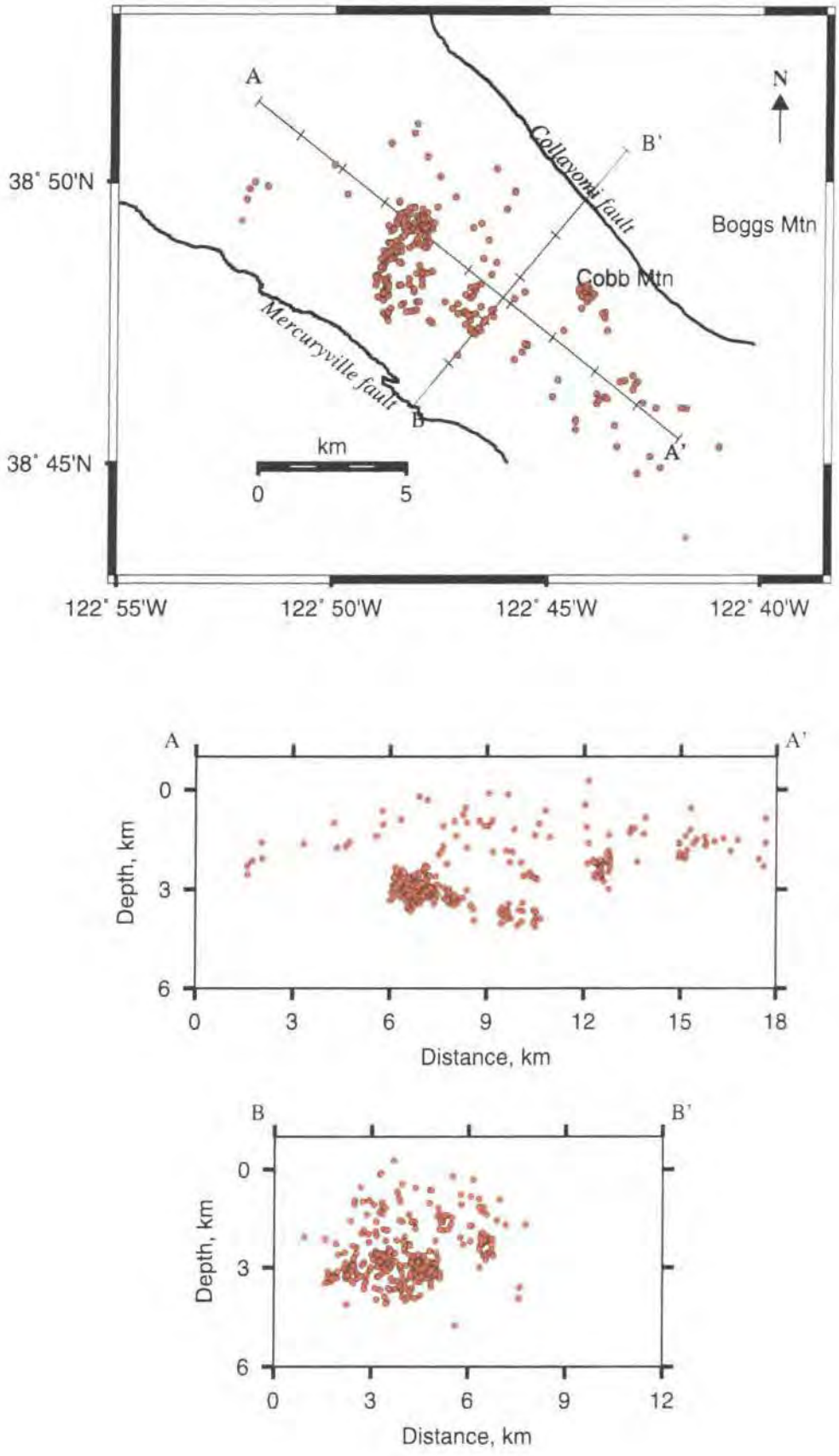

Figure 3.9e: Same as for figure 3.9a, except for the inversion for 1998.

below the threshold of selection due to source-receiver distance and few arrivals. Most events are shallower than ~ 4.0 km bsl which is the base of the seismogenic layer at The Geysers. Very few events are located above sea level. Seismicity is intense at depths of 0.0 km to 2.0 km bsl but the interval ~ 2.0-2.5 km bsl is much less active (e.g. Figure 3.9d). At depths of 2.5 to 4.0 km bsl a prominent cluster is observed, a feature, which has been reported in previous tomographic investigations at The Geysers (Ross, 1997; Romero *et al.*, 1994). Clustering has increased with time, suggesting increasingly localised steam removal, and perhaps an increase in injection-induced events as the amount of injection has increased (Section 1.5.2).

3.4.1.3 Relocated events

Locations of the events used in the inversions of February 1993, October, 1996 and August 1998 after relocation through the tomographic inversions are shown in Figure 3.10. Relocation vectors are in general minor as is to be expected since the original three-dimensional model from 1991 was very close to the final models for later years.

3.4.2 Damping trade-off curves

Trade-off curves comparing data variance (a measure of residual size) and solution variance (a measure of model perturbation size) with a suite of damping values help to select the optimum damping factor and reveal the optimum damping values below which decreased damping leads to rapidly increased solution variance with little or no decrease in data variance. Damping values strongly influence the amplitude of anomalies but the overall pattern is little affected for a suite of damping values. Relatively high damping parameters for 1993 of 20 s^2/km for *Vp* and 20 s for *Vp/Vs* were found to be necessary (Figure 3.11a,d). For the other inversions, the optimal damping parameters were 5 s^2/km and 2 s, except for 1996 where 5 s for the *Vp/Vs* damping value was used (Figure 3.11; Table 3.1).

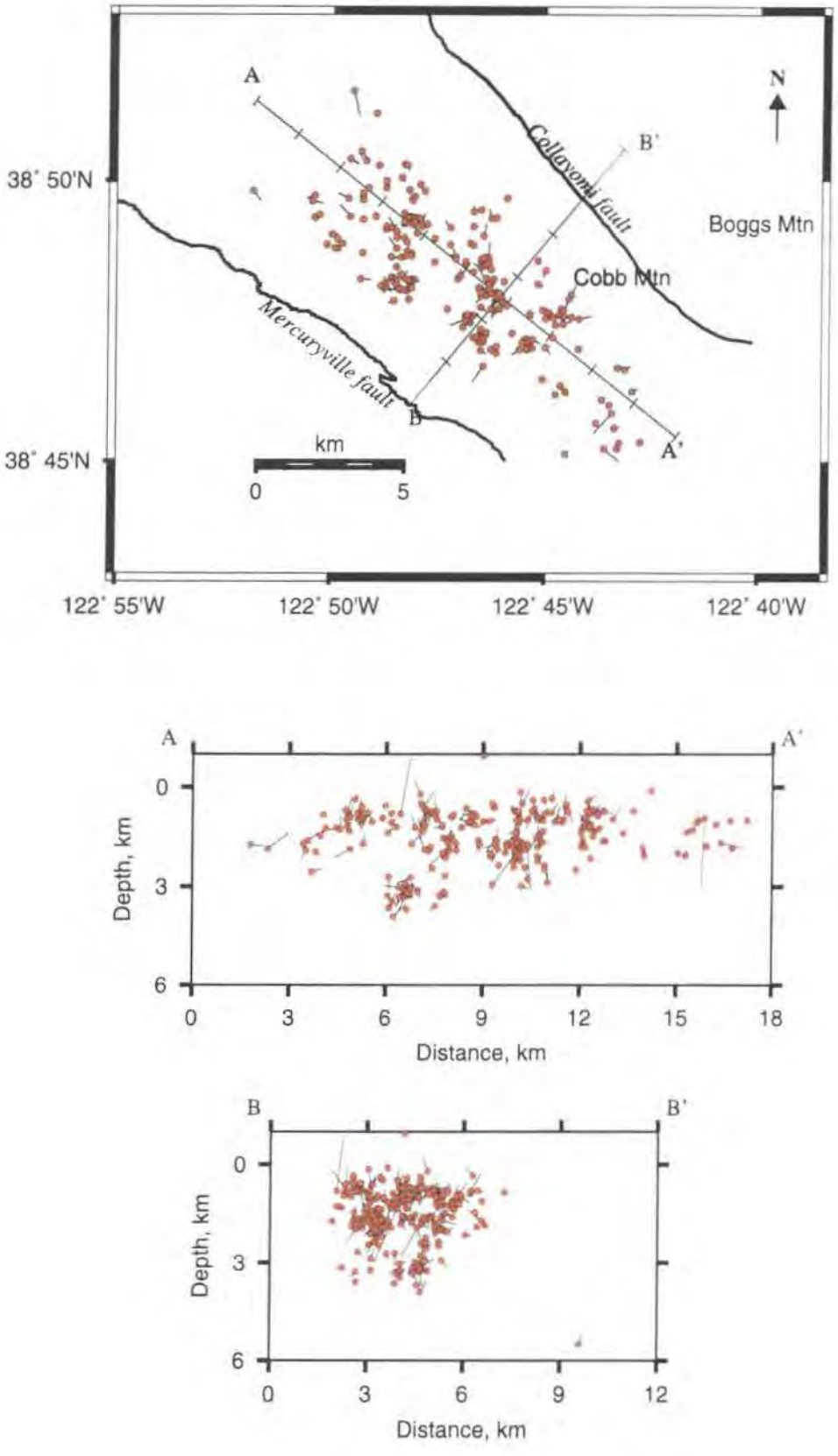

Figure 3.10a: Map and cross-sections showing the final locations of events used in the tomographic inversion for 1993 with vectors pointing to inital locations.

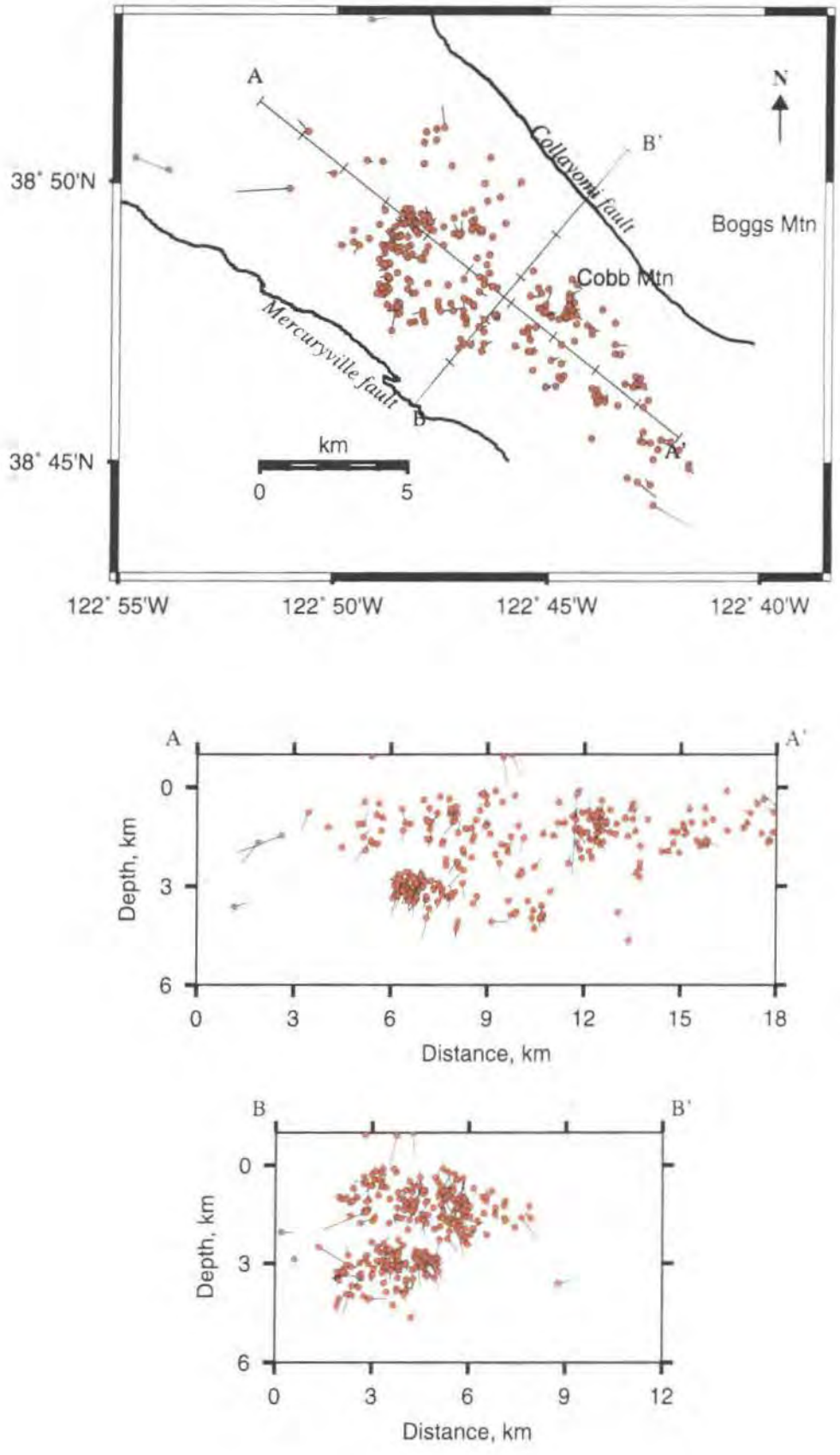

Figure 3.10b: Same as figure 3.10a, except for inversion for year 1996.

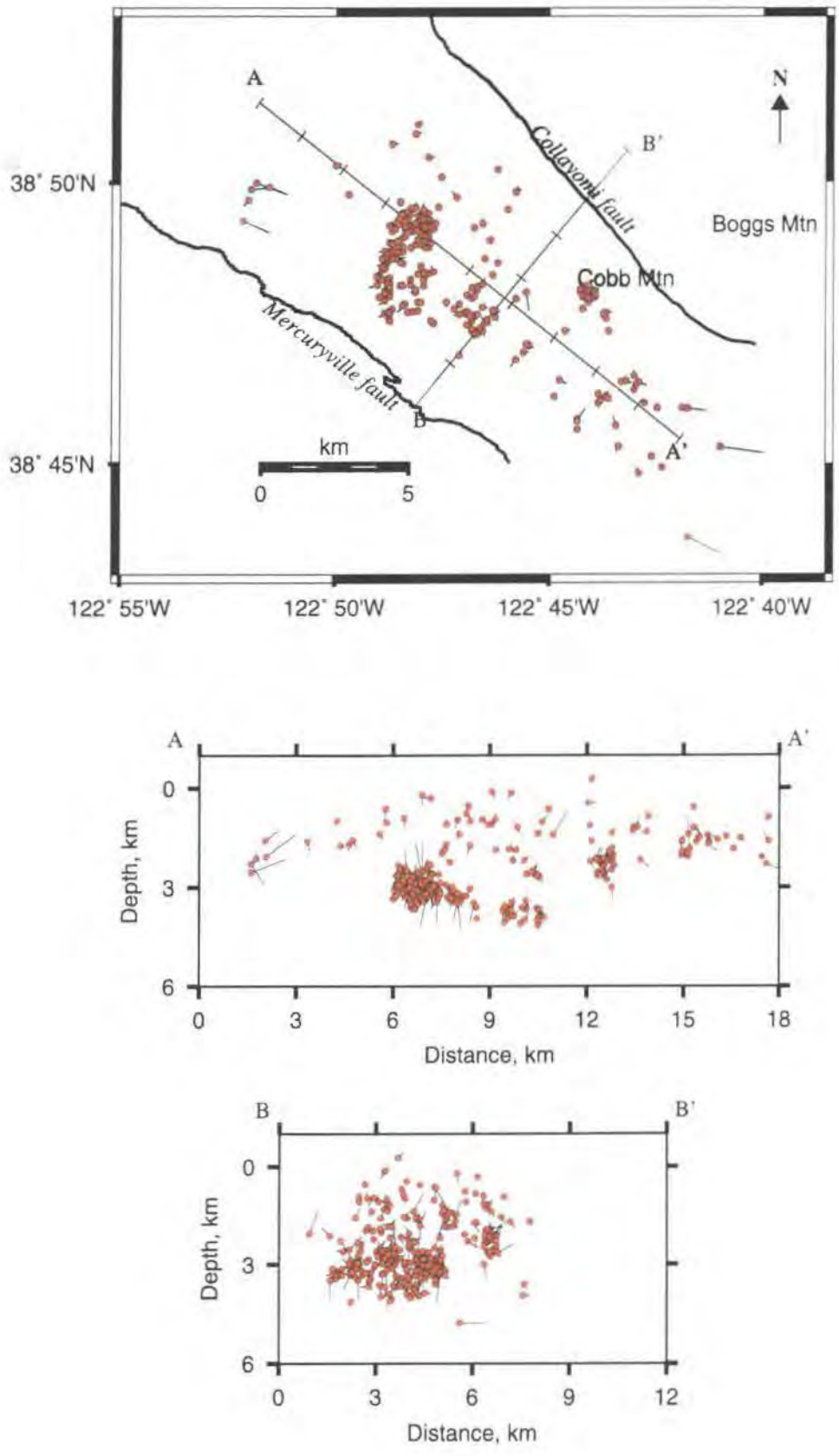

Figure 3.10c: Same as figure 3.10a, except for inversion for year 1998.

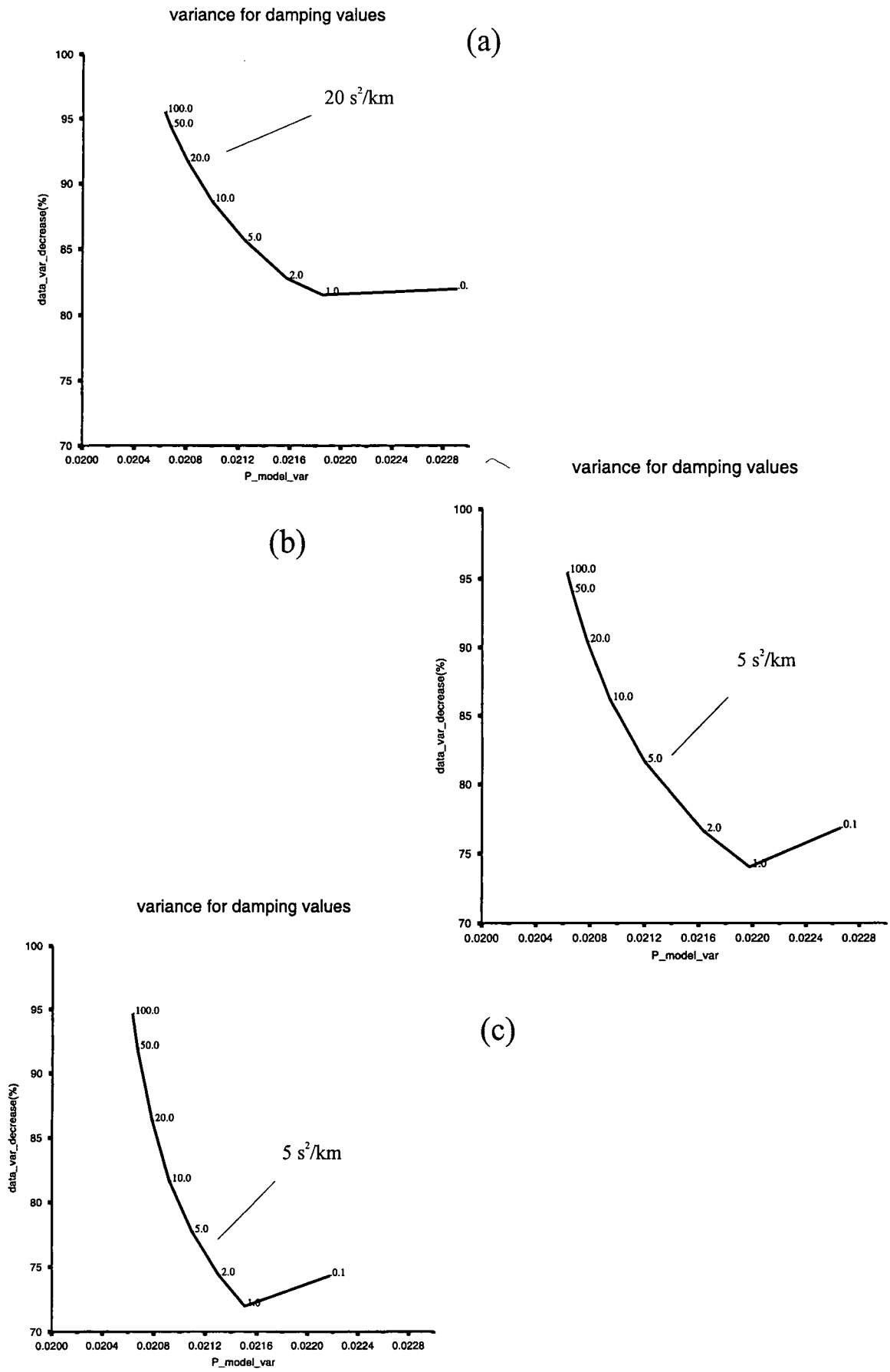

Figure 3.11a: Damping curves for *Vp* and *Vp/Vs* tomographic inversions. Selected values for *Vp* were (a) Feb. 1993 with 20 s^2/km, (b) Oct. 1996 with 5 s^2/km and (c) Aug. 1998 with 5 s^2/km.

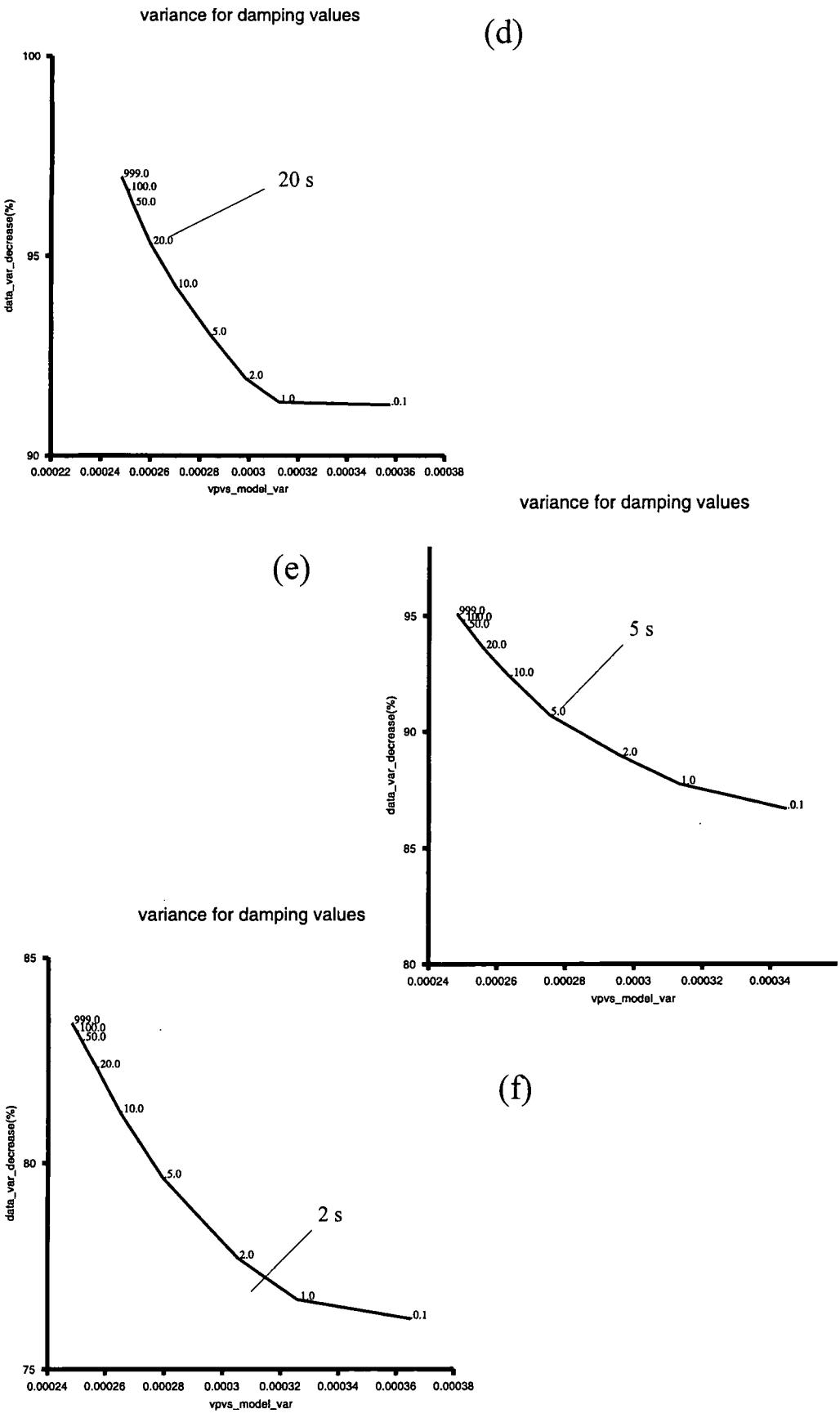

Figure 3.11: (cont.) Selected values for *Vp/Vs* were (a) Feb. 1993 with 20 s, (b) Oct. 1996 with 5 s and (c) Aug. 1998 with 2 s.

3.4.3 Results

3.4.3.1 *Vp*, *Vs* and *Vp/Vs* anomalies in April 1991

First order-spatial variations in the *Vp* and *Vs* structures at The Geysers determined from inversion of the April 1991 data are similar, and dominated by a substantial low-wave-speed volume in the northwest Geysers and higher wave speeds beneath the central and southeastern part of the reservoir (Figure 3.12 and 3.13, panels at left). These features reflect variations in lithology and pore fluid (Ross, 1996; Julian *et al.*, 1996). In the northwest Geysers at sea level and 1.0 km bsl low *Vp* and *Vs* anomalies characterise the caprock and normal reservoir that overlies a deeper HTR. In the central and southeast part, velocities are lowest in the Cobb Mtn. region, probably reflecting lithologies of the Clear Lake volcanics. Velocities are higher more southerly in the reservoir, in rocks of the Franciscan assemblage.

A strong, coherent low *Vp/Vs* anomaly correlates well with the steam reservoir (Figure 3.14, leftmost panels). It is wider to the northwest and southeast than in the middle, reflecting the general shape of the reservoir. The anomaly does not extend to the extreme northwest and southeast parts of the reservoir. The strength of the low anomaly was as great as 9% or more which can be explained as the effect of differences in pore space compressibility (Ross, 1996; Julian *et al.*, 1996), related to the presence of low-pressure water vapour in the reservoir (Barker *et al.*, 1992; Barker and Pinogol, 1997).

3.4.3.2 Temporal variations in *Vp*, *Vs* anomalies between April 1991 and August 1998

Progressive changes in the *Vp*, *Vs* and *Vp/Vs* fields occur with time (Figures 3.12, 3.13 and 3.14)(Appendix 6). In general, the pattern of anomaly growth with time is systematic. The December 1994 epoch is less consistent with the others. This may reflect analyst-dependent variations since this inversion was conducted independently from the April 1991, February 1993, October 1996 and August 1998 inversions (Foulger *et al.*, 1997) (section 5.3.5). In general, *Vp* and *Vs* decrease

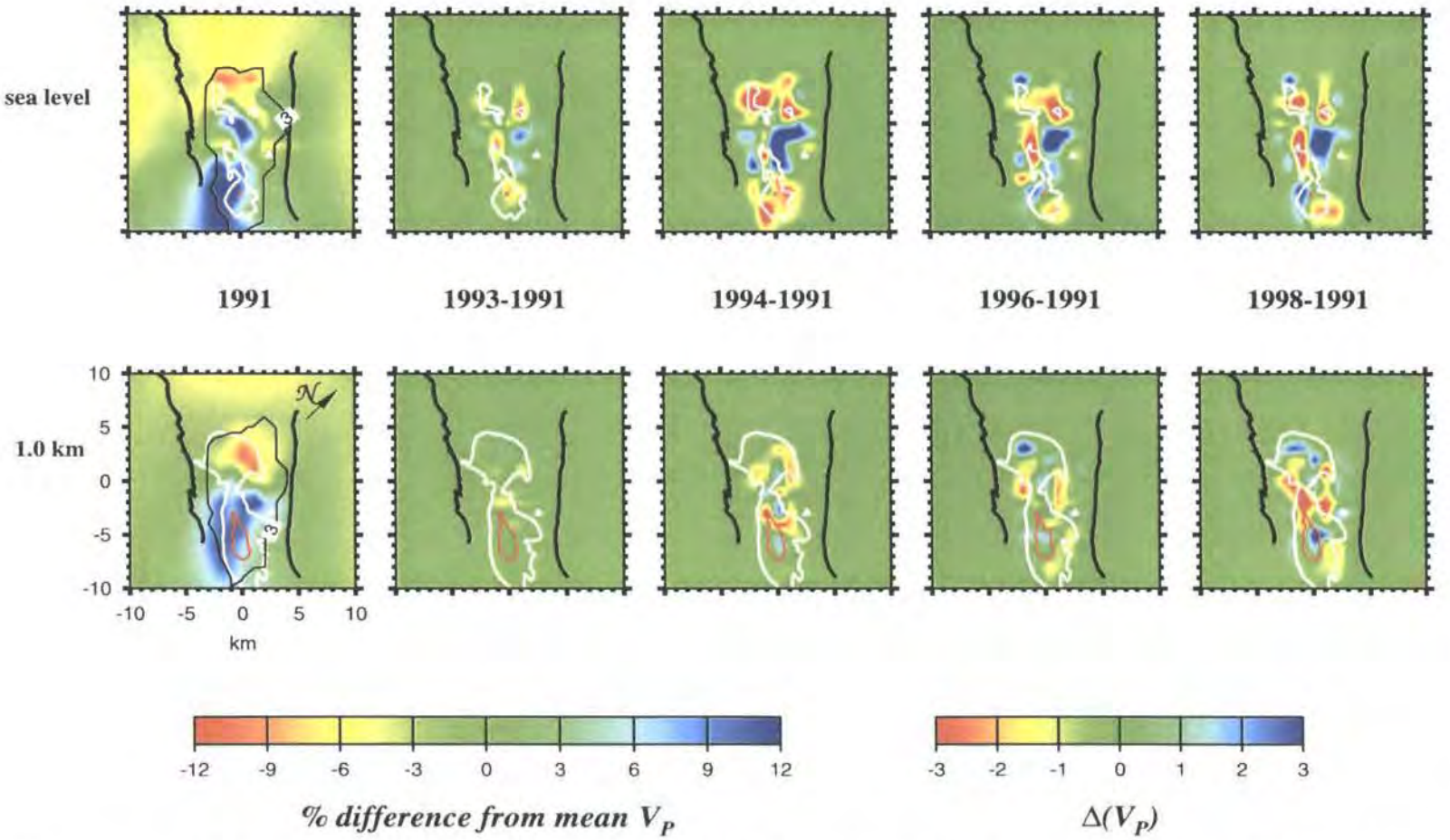

Figure 3.12: Anomalies in the V*p* field at sea level and 1 km bsl. Leftmost panel show the structure for 1991(*from* Foulger *et al.*, 1997). Other panels show changes from this for subsequent years. The white boundary is the steam reservoir and the red boundary the felsite batholith that occupies the deeper parts of the reservoir. The thin black line shows the well-resolved area for a spread of less than 3 km. The white triangle is Cobb Mtn. and the thick black lines are the Mercuryville and Collayomi faults.

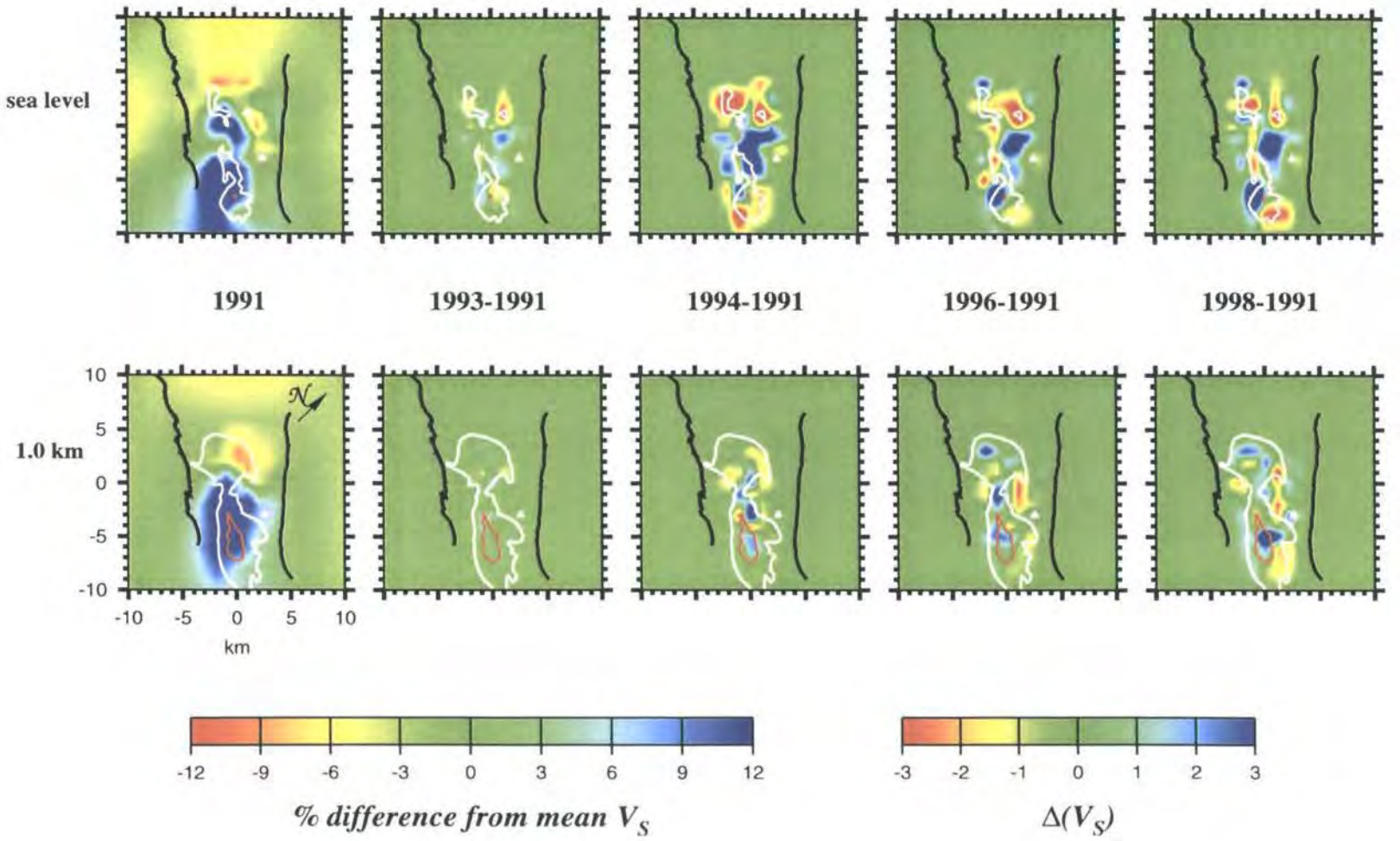

Figure 3.13: Same as for Figure 3.12, except for the *Vs* fields.

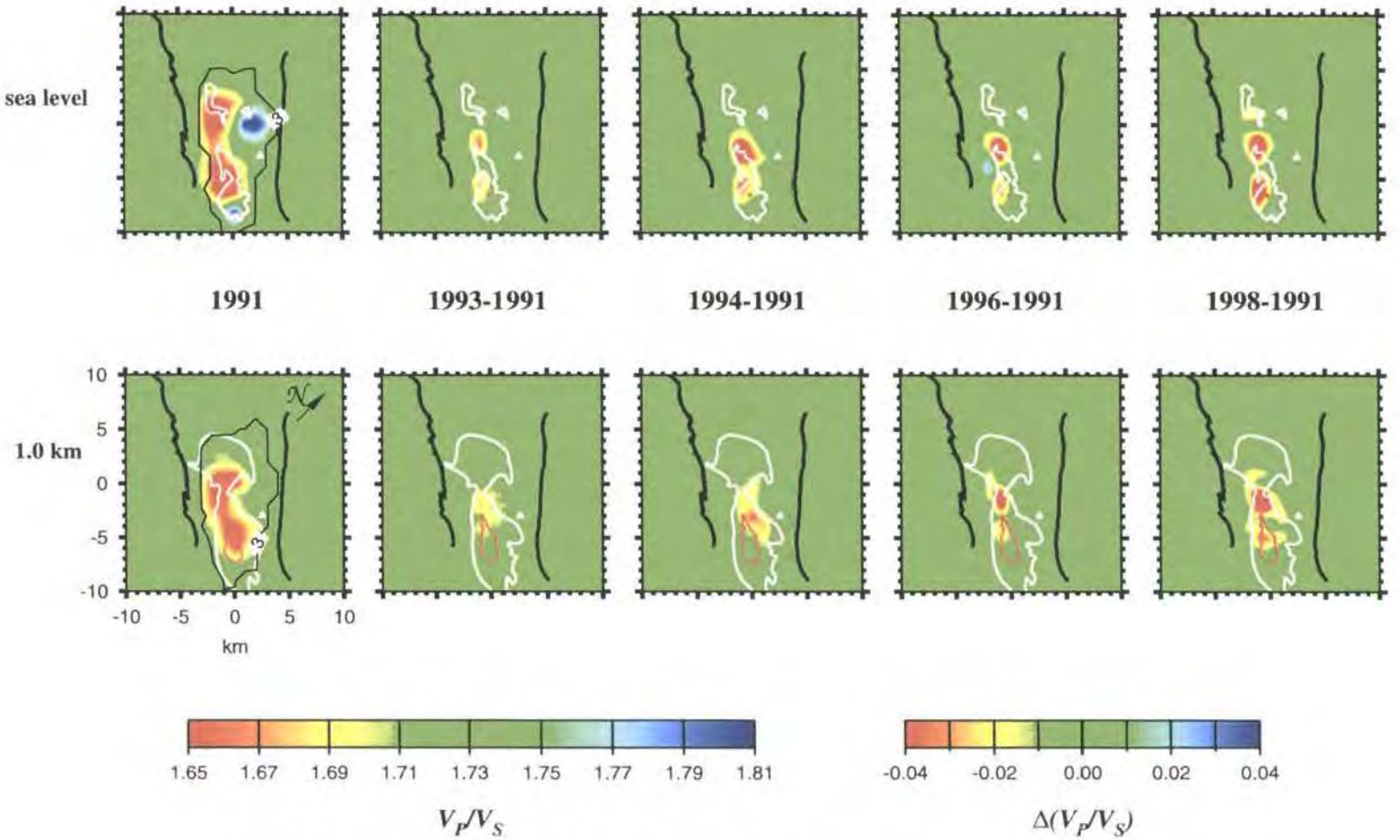

Figure 3.14: Same as for Figure 3.12, except for the *Vp/Vs* fields.

with time in the northwest and southeast Geysers, and along the southwestern boundary of the reservoir. *Vp* and *Vs* increase at sea level beneath the northeast boundary of the reservoir, but decrease at 1 km bsl beneath the same area. The patterns of change in *Vp* and *Vs* are broadly similar but vary in detail. Areas of coherent anomaly change trend northwest-southeast in general, parallel to the tectonic strike of the area. At sea level *Vp* varies by -8.3% to +19.2% from the mean in 1991, but by 1998 these variations have increased to -10.2% to +23.6%. Changes in *Vs* are greater than in *Vp*. At sea level *Vs* varies by -8.4% to 29.3% of the average for that depth in 1991 but by 1998 this has increased to -10.4 to 41.4%. At 1.0 km bsl changes in *Vp* and *Vs* with time are less than at sea level.

3.4.3.3 Temporal variations in *Vp/Vs* anomalies between April 1991 and August 1998

The strength of the *Vp/Vs* anomaly progressively increased between 1991 and 1998 (Figure 3.14). As is the case for the *Vp* and *Vs* fields, the December 1994 epoch is less consistent with this trend than the others. At sea level, by 1993, two distinct areas of *Vp/Vs* anomaly growth had developed with increases in anomaly strength of up to 0.6%. Both anomalies increased progressively in strength and size with time and by August 1998 a third negative *Vp/Vs* anomaly had developed further north. The increase in anomaly strength by 1998 was up to a maximum of 3.4%.

A similar pattern of anomaly growth occurred at 1 km bsl. In February 1993 a single area of anomaly growth is detected in the centre of the reservoir. This increased in strength by October 1996 and a second area of significant anomaly growth developed further to the south. By 1998, these two areas of growth had increased further in strength and were up to 4.6% stronger than in 1991. By 1998 a third area of anomaly growth may have begun to form in the northwest. At 2 km bsl a single area of anomaly growth was detected directly below the strongest, central area of anomaly growth at 1 km bsl. This anomaly increased in strength by up to 4.1% between April 1991 and August 1998. The increases in strength of the *Vp/Vs* anomaly in the separate areas of The Geysers are shown in Table 3.2.

Table 3.2: Areas of increase amplitude in *Vp/Vs* with time.

Anomaly area	Growth in strength of the *Vp/Vs* anomaly (1991 to 1998) in % (±0.25%)
North (sea level)	1.8
Middle (sea level)	1.1
South (sea level)	3.4
Middle (1.0 km bsl)	4.6
South (1.0 km bsl)	1.1

3.4.4 Resolution and quality of the results

The quality of the final results are illustrated by contouring the spread function (Menke, 1989; Toomey and Foulger, 1989; Foulger *et al.*, 1995) (section 3.3.6). A spread of less than 3 km characterises the best-resolved nodes (Figure 3.12 and 3.14). Resolution for all years is good throughout most of the reservoir except in the extreme southwest. This is probably be a result of the station geometry in that area. The Central Geysers has the densest ray path coverage and most rays pass through the production area. Within well-resolved areas anomalies are considered to be significant if the anomaly is defined by more than one node (Ross, 1996). Final RMS travel-time residuals all lie in the range ~ 0.015 – 0.022 s for *P*-waves and 0.035 to 0.052 for *S*-waves.

3.4.5 Results of other inversion strategies

A critical aspect of the results is reliability of the subtle changes observed. Each tomographic inversion used a different set of earthquakes, which had different spatial distributions, and different numbers of arrival times measured at the stations. The consistency of the results for a single year was tested by splitting the February 1993 dataset in two halves, each containing approximately 120 events, and inverting each separately (Figures 3.15 a,b). Damping parameters of 5 s^2/km for *Vp* and 5s for *Vp/Vs* were used. The plots show that provided suitable damping

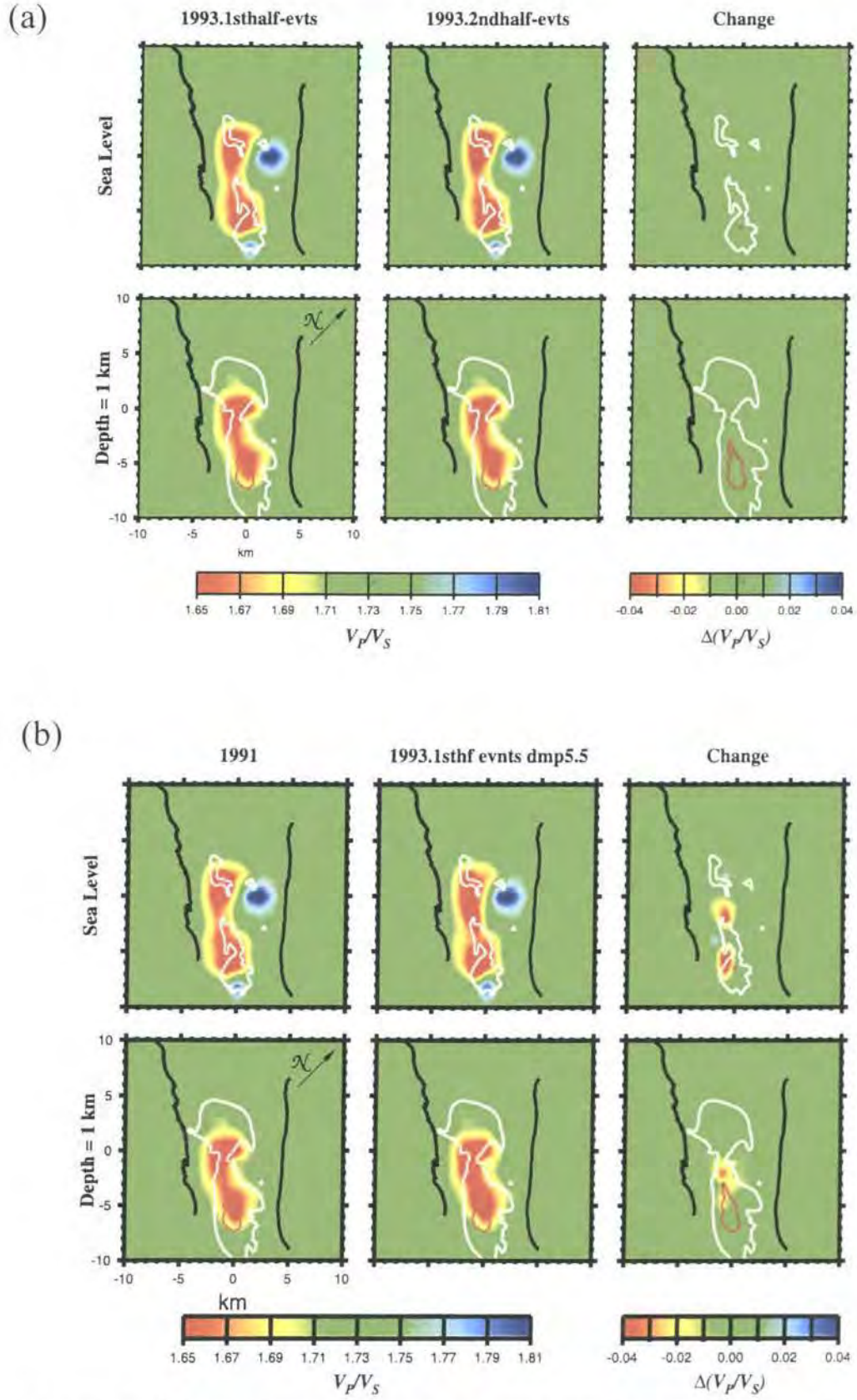

Figure 3.15: a) Difference between equal number of events inverted from the February 1993 dataset showing no change in anomaly. b) Shows the recovery of the *Vp/Vs* anomaly in comparison to 1991 *Vp/Vs* results by using half the number of events used in the 1993 inversion and optimum damping parameter of 5 s^2 /km for *Vp* and 5 s for *Vp/Vs*.

parameters are selected, the 1993-1991 *Vp/Vs* anomaly could be observed using different event distributions, but with the same station geometry, starting model and inversion technique. It also illustrate the robustness of the anomaly pattern for different damping parameters (of Figures 3.14 and 3.15 (b)). The observed anomaly patterns are independent of the number or location of events used in the inversion.

3.5 Other examples of use of *SIMULPS12*

The *SIMULPS12* inversion method could also be used in areas of great deformation and volcanic areas such as Central Apennines. A three-dimensional *P*- and *S*- wave velocity model of the first 9 km of the crust in the central Apennine was derived from local earthquakes using the *SIMULPS12* technique (Alessandrini et al., 2001). The data consisting of 984 earthquakes was recorded by three-component stations in regional and local networks. At least 8 phases were picked with a RMS residual less than 0.6 s. The results showed a large positive *P*- and *S*-velocity anomaly in the main seismogenic volume of the Central Apennines. A synthetic test demonstrated that this anomaly is not an artefact produced by the substantially higher density of earthquakes within the seismic velocity anomaly. This highlights the strength of *SIMULPS12* technique at deriving velocity structure (Alessandrini *et al.*, 2001).

A three-dimensional velocity model of the *Vp* and *Vp/Vs* structure of the Central Transverse Ranges and Los Angeles basin was conducted by Hauksson and Haase (1997). Data from 1973 to 1995 was used with sufficient data from the 1994 Northridge earthquake and its aftershock sequences. 5225 earthquakes and 53 explosions recorded by the Southern California Seismographic Network (SCSN) were used in the study. The modelled area was approximately 130 x 400 x 20 km in size. The program *SIMULPS12* used a gradational inversion approach reducing the nodal spacing from 40 to 20 to 10 km. The reduction in data variance was approximately 80% in the gradational inversion approach. Hauksson and Haase

(1997) interpreted high *Vp/Vs* ratios near the surface as a result of high pore fluid pressures in the basin sediments. The *Vp* model showed features at depth that indicated deformation of the hanging wall or basin closure. These examples highlight the versatility of the *SIMULPS12* inversion approach to resolve structure not only in small areas such as The Geysers but also in areas with high volcanism such as Central Apennines, Mammoth Mtn. (Section 5.3.7) and in much larger areas such as the Los Angeles basin.

3.6 Summary

Seismic tomography is good method for determining geological structure spanning many orders of magnitude in spatial extent. Teleseismic studies have been successful in imaging regional- and global-extent volumes. Local earthquake tomography has been successful in obtaining high-resolution images of specific target volumes. For localised areas NeHT offers a high resolution tomographic method that utilises explosions and blasts for sources. However, this method is costly, and as controlled sources generate poor *S*-waves, it is not suitable for imaging *Vs* or *Vp/Vs* structures.

This study utilised the local earthquake tomography inversion method of Thurber (1983). It is a continuation of a 4-D tomographic study performed for April 1991 and December 1994 (Foulger et al., 1997). The method simultaneously inverts for changes in the velocity model and arrival times from hypocentre locations. Tomographic inversions for February 1993, October 1996 and August 1998 were chosen such that set of *Vp*, *Vs* and *Vp/Vs* images could be obtained at 22-month intervals between April 1991 and August 1998. A grid 20 x 20 x 7 km in size rotated 45° anticlockwise was chosen to comply with previous tomographic inversions (Ross, 1996; Julian et al., 1996; Foulger et al., 1997). A direct inversion approach was chosen using the final 3-D model of 1991 (Foulger *et al.*, 1997) as a starting model. The *SIMULPS12* program was used to perform the tomographic inversions, where a control file incorporates several user-defined parameters such

as number of events, and damping parameters. The damping parameter controls the variation in model complexity and variance reduction. For February 1993 *Vp* damping of 20 s^2/km and *Vp/Vs* damping of 20 s was used. The 1993 *Vp* and *Vp/Vs* models were very similar to the 1991 models and high damping values were needed. For both 1996 and 1998 *Vp* inversions a damping factor of 5 s^2/km was used while a *Vp/Vs* damping factor of 5 s for 1996 and 2 s for 1998 was used. Final RMS *Vp* residuals varied from 0.015 s to 0.022 s and for *Vs* they varied from 0.035 s to 0.043 s.

Vp and *Vs* structures modelled are similar to those determined for April 1991, where first order-spatial variations in the *Vp* and *Vs* structures are dominated by a substantial low-wave-speed volume in the northwest Geysers and higher wave speeds beneath the central and southeastern part of the reservoir. The *Vp/Vs* structure showed a strong low anomaly, which correlated with the steam reservoir. Progressive, changes in the *Vp*, *Vs* and *Vp/Vs* fields occured with time. *Vp* and *Vs* increase at sea level beneath the northeastern boundary of the reservoir, but decrease at 1 km bsl beneath the same area. At sea level *Vp* varies by -8.3% to +19.2% from the mean in 1991, but by 1998 these variations have increased to -10.2% to +23.6%. Changes in *Vs* are greater than in *Vp*. At sea level *Vs* varies by -8.4% to 29.3% of the average for that depth in 1991 but by 1998 this has increased to -10.4 to 41.4%.

The strength of the *Vp/Vs* anomaly progressively increased between 1991 and 1998. In February 1993 a single area of anomaly growth is detected in the centre of the reservoir. This increased in strength by October 1996 and a second area of significant anomaly growth developed further to the south. By 1998, these two areas of growth had increased further in strength and were up to 4.8% stronger than in 1991. A spread of less than 3 km was considered to indicate well-resolved nodes (Toomey and Foulger, 1989; Foulger et al., 1995) for *Vp* and *Vp/Vs* indicating that the images were of high quality throughout most of the reservoir. The *SIMULPS12* inversion technique has been used a wide range of experiments and proven to be a good tool to model velocity structures.

CHAPTER 4:

RELATIVE RELOCATION OF MICROEARTHQUAKES

4.1 Background

Relating observed patterns of seismic events to geological and tectonic structure has been a key aim in seismology. Relative earthquake relocations can potentially reveal seismically active structural features to high precision. The results may enable identification of fault geometries, and the nature, orientation and time history of activity.

There are two main classes of relative relocation methods. The first uses arrival times only, and simultaneously locates earthquakes and adjusts station corrections such that a best fit is found for the arrival times for a large event set. This is known as Joint Hypocentre Determination (JHD) (Douglas, 1967; Block *et al.*, 1994). Station corrections absorb the effects of inaccuracy in the velocity model. In the "coupling" method, hypocentres are shifted towards the centre of mass of the events within certain bounds, which are set as the location error ellipsoids with dimensions equal to 4σ of the location uncertainty (Jones and Stuart, 1997). A "point pattern" method has also been developed, which uses the principle of identifying patterns in sparse hypocentre location datasets (Amorese *et al.*, 1999).

Cross-spectral methods (Poupinet *et al.* 1984: Ito, 1985) are the second class of relative relocation methods. This involves cross-correlating waveforms and thus requires digital event waveforms, but offers increased accuracy in the results. This approach is used in this thesis and involves identifying earthquakes with similar waveforms. The method used is that of Got *et al.* (1994). Events with similar waveforms are expected to have similar source mechanisms, source time functions

and close hypocentral locations. Such similar events may also occur along the same rupture plane. Minor differences in waveform may be attributed to minor variations in path effects. In the method used, a doublet is defined as a pair of events with similar waveforms and multiplet as three or more events with similar waveforms. Similarity of the waveform is measured by the modulus of the coherency spectrum, which is termed the coherency. A coherency matrix of doublets is used to select a multiplet, which is used to calculate the time delays required for relative relocation.

4.2 Theory

4.2.1 Multiplet selection and the coherency matrix

To select a suitable multiplet and perform time-delay calculations the cross correlation method of Jenkins and Watts (1968) was used. Jenkins and Watts (1968) discuss the building of a cross-correlation function to suit the time lag of two waveforms and they also discuss the use of the cross-spectrum phase.

The similarity between waveforms can be either studied in the time domain (e.g. Deichmann and Garcia-Fernandez, 1992) or in the frequency domain (e.g. Poupinet, *et al.* 1984) as is done in this study. Coherency is the smoothed cross spectrum normalized by the smoothed auto-spectrum of each seismogram window. The coherency computed is the average coherency over 1.28 s (128 samples) of the signal encompassing the *P*-wave first arrival. The smoothing function of the spectral densities is the Fourier transform of a Tukey window of order two (Got *et al.*, 1994). The coherency matrix contains the coherencies of all possible doublets, and reveals all possible multiplets.

The time delay of each doublet in a multiplet (the difference in arrival times of two earthquakes at a given station) is used to relocate relatively each event in the multiplet. The delay between the two signals is evaluated in the frequency domain

with the cross-correlation method. The two traces are aligned to 0.01s (the data sampling rate) to avoid any bias in the final time-delay estimate. For a given window *i*, the Fourier transform is :

$$s_1(f) = a_1 \, e^{i\Phi_1} \tag{4.1}$$

and

$$s_2(f) = a_2 \, e^{i\Phi_2} \tag{4.2}$$

where a_1 and a_2 represent amplitude and ϕ_1 and ϕ_2 phase. The phase shift is assumed constant. The resulting time series are simply shifted by τ such that

$$s_1 = k \; s_2 (t + \tau) \tag{4.3}$$

where $k = \frac{a_1}{a_2}$. The constant phase shift is represented by,

$$\theta (f) = 2 \pi \tau \, f \tag{4.4}$$

where *f* is the frequency. In the Fourier transform domain, equation (4.2) becomes

$$S_2(f) = 1/k \; e^{-2 i\pi\tau f} \; S_1(f) . \tag{4.5}$$

The slope of the phase of the cross spectrum provides an estimate of the time shift where (Figure 4.1)

$$\tau = \text{slope} / k. \tag{4.6}$$

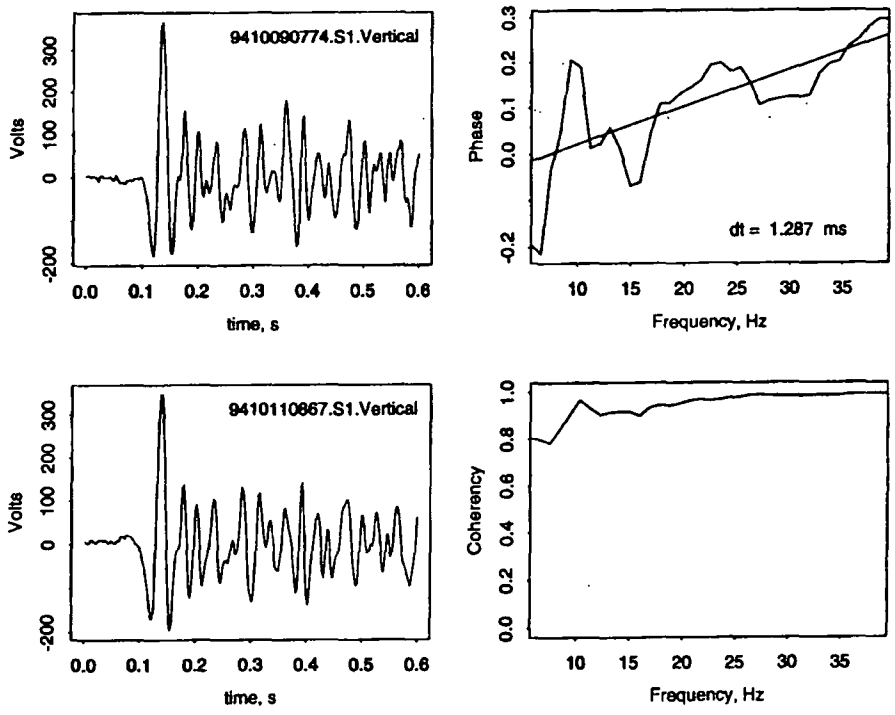

Figure 4.1: An example of a doublet and its cross-spectral analysis. For the signals in the left hand panels, the right hand panels show the cross phase and linear fit. The slope of the linear fit is the phase shift of one signal relative to the other (*from* Lees, 1998).

Weighted linear adjustments of the phase of the cross-spectrum reveal the time delays between two windows of the signal recorded at each station (Poupinet *et al.*, 1984). The weight used is the coherency threshold and it is inversely proportional to the variance of the cross-spectrum phase:

$$w_k^2 = \frac{c_k^2}{1-c_k^2} \qquad 90\% \le c_k < 100\%$$

$$w_k^2 = 0 \qquad c_k < 90\% \tag{4.7}$$

where c_k is the coherency and w_k the weight of the kth frequency sample. This enables the time precision to exceed the digitisation rate. To obtain the time delay, the linear fit of the cross-spectrum phase is used. This avoids the necessity of any interpolation of the cross-correlation function.

4.2.2 Theoretical relative relocation and time-delay calculation

To relocate events, the method of Fréchet (1985) was used. The spatial coordinates of an event relative to another event assume x-positive to the east, y-positive to the north and z-positive downwards. T is the time difference between the origin times, and *NSTA* is the number of stations recording the doublet.

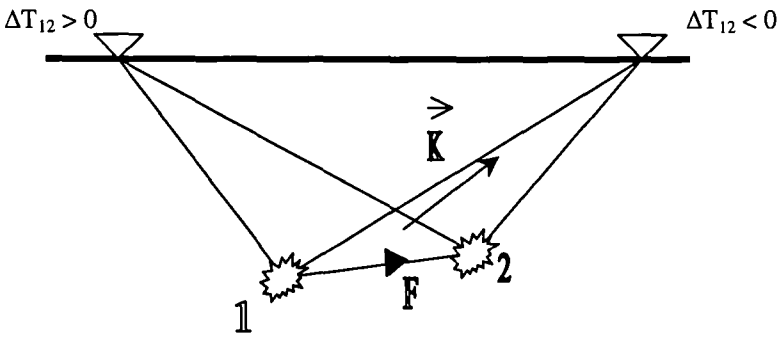

Figure 4.2: Schematic diagram of a doublet, events 1 and 2. $\mathbf{K}_k$ is the wave vector in the vicinity of the hypocentres, for station k. **F** is the inter-event vector. Travel paths are also shown.

For events that are extremely close to each other, the relocation problem can be considered linear and therefore a single slowness vector is used in the vicinity of the hypocentre for each station k. The time delay for a doublet recorded at the kth station at azimuth Az_k and take-off angle Ain_k from the hypocentre as shown in Figure 4.2 is:

$$\Delta T_k = (\sin Az_k \sin Ain_k\, x + \cos Az_k \sin Ain_k\, y + \cos Ain_k\, z) / v + T \qquad (4.8)$$

where v is the P-wave velocity in the immediate vicinity of the hypocentre. To expand this to all stations, a system of linear equations is used and expressed as:

$$\mathbf{Gm = d} \qquad (4.9)$$

where **G** is a *NSTA* x 4 matrix (to include all partial derivatives of ΔT_k), **m** is the unknown vector composed relative to **G** such that $\mathbf{m} = (x, y, z, T)^T$ and **d** is the data vector containing the time delays.

For a multiplet, the number of linear equations becomes:

$$\frac{Nev\ (Nev-1)\ NSTA}{2}$$

where *Nev* is the number of events with 4(*Nev* –1) unknowns. Also, **G** increases as Nev^3, increasing the number of computations rapidly and making computation of the multiplet time consuming. As the **G** matrix is well-conditioned, the least squares solution of this problem is solved using a normal equations approach to reduce the number of computations (Got *et al.*, 1994):

$$\mathbf{G}^T \mathbf{C_d}^{-1} \mathbf{G}\, \mathbf{m} = \mathbf{G}\, \mathbf{C_d}^{-1}\, \mathbf{d} \qquad (4.10)$$

to obtain

$$\mathbf{m} = (\mathbf{G}^T \mathbf{C_d}^{-1} \mathbf{G})^{-1}\, \mathbf{G}^T \mathbf{C_d}^{-1}\, \mathbf{d} \qquad (4.11)$$

where $\mathbf{C_d}$ is the data variance-covariance matrix. The elements in the matrix of $\mathbf{G}^T\mathbf{C_d}^{-1}\mathbf{G}$ are directly computed by deriving the misfit function relative to **m**. The solution **m** is obtained by performing a scaled Cholesky decomposition of $\mathbf{G}^T\mathbf{C_d}^{-1}\mathbf{G}$. The matrix $\mathbf{G}^T\mathbf{C_d}^{-1}\mathbf{d}$ is a positive definite matrix.

The calculations contain errors of two types: coherency-dependent errors and errors caused by different instrument delays. The coherency-dependent errors are taken into account by the weight used in the least squares estimation of the time delay. To address the problem of different instrument delays, a bi-square weighting proposed by Mosteller and Tukey (1979) and tested by Fréchet (1985) was used:

$$w_k = \left[1 - \left(\frac{R_k}{dR_{MED}}\right)^2\right]^2 \quad if \left(\frac{R_k}{dR_{MED}}\right)^2 < 1 \; else \; 0 \qquad (4.12)$$

where $R_k = \Delta T_k - \Delta \tau_k$ is the residual of each time delay, ΔT_k is the observed time delay and $\Delta \tau_k$ is the theoretical time delay computed for the kth station after relocation. R_{MED} is the median of the set of absolute values of R_k. This weighting scheme effectively rejects residuals that are greater than 4 to 6 times the median. The algorithm is linear, so only a few iterations are needed to re-discard blunders. Typically, 1 or 2 iterations are needed to get a solution with an RMS lower than 10^{-2} s. Although the initial solution is obtained for unit weights, at each subsequent iteration the weight is modified and more weight is given to more frequently sampled stations, which helps to reduce the RMS residual. This iterative process continues until a pre-defined maximum number of iterations has been completed or the residual RMS reaches a minimum. This method allows time-delay calculations for the whole set of event pairs in the multiplet.

4.3 Method

4.3.1 Event selection for multiplets

A step-wise summary of the procedure used in relative relocation of microearthquakes is given in Table 4.1. All 22 seismic stations of the UNOCAL network at The Geysers were used in this study (Figure 4.3). Only the vertical components were used, since experience has shown that little is gained by using all three components (J. L. Got, *pers. comm.*). Data used were from day 279 in 1989 to day 365 in 1994. Prior to day 279 in 1989, the network geometry was sparse and the data are poor and after day 365 in 1994 the network was upgraded.

Data in PCQL format were extracted from 8 mm exabyte tapes. First, the PCQL files were converted to AH (*ad hoc*) format and the program *autopick* (B. R. Julian,

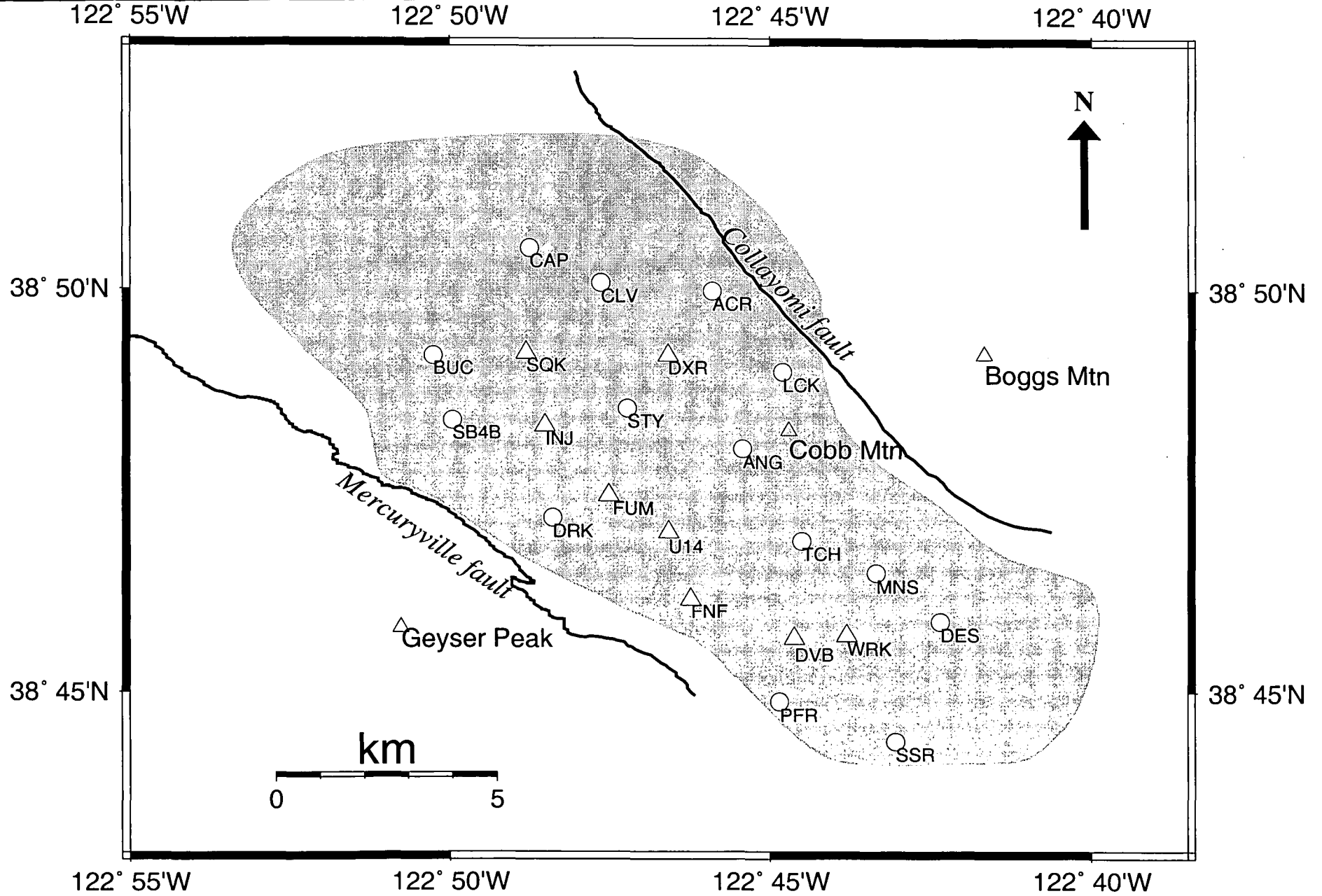

Figure 4.3: Map showing the locations and names of the UNOCAL stations at The Geysers geothermal area.

3-component stations are shown as white triangles and 1-component as white circles. Moutains are shown as open triangles.

pers. comm.) was used to measure *P*-wave arrivals and locate arrival times using the best 1-D velocity model available (Ross, 1996) for The Geysers (Steps 1 and 2, Table 4.1). The dataset was large, station coverage of the events was very good, and only events with more than 12 picks were selected. Using the program *log_geysers* (J. L. Got, *pers. comm.*) a header file which includes information such as event identification number, hypocentre information, travel times, take-off angles and azimuths for each station and binary data files that contain the digitised waveforms were created (Step 4, Table 4.1). Seismicity at The Geysers forms north-south trending volumes (Barton, 1999) (Figure 4.4). Four seismic regions were selected for study: sr001, sr002, sr003 and sr004 (Figures 4.4 and 4.5).

Table 4.1: Step-wise procedure for relative relocation of microearthquakes.

Step	Program	Comment
1	*autopick*	Auto pick all UNOCAL trace files from October 1989 to December 1994.
2	*eloc*	Locate all events picked by the autopicker.
3		Four regions with clustered seismicity were selected for study using the Barton catalogue of UNOCAL events for 1993 (Barton, 1998).
4	*log_geysers*	For events located in the selected regions the data were divided into a) a header (ASCII) file containing information about the origin time, location of event, each station name, distance to station, azimuth and take-off angle of event to station and the stations that recorded the event, and b) a data (binary) file containing the digitised waveforms.
5	*erragu* & *cohstat*	Select a suitable coherency threshold. a) Program *erragu* calculates how the estimated error in relocation varies with the number of events in a multiplet (e.g. Figure 4.6, left panel). b) Program *cohstat* plots the number of events in the multiplet against corresponding coherency threshold (e.g. Figure 4.6 right panel).
6	*csparse*	Compute the coherency matrix for events with coherency ≥ the chosen coherency threshold (e.g. Figure 4.7).
7	*speq*	Select multiplet from the coherency matrix.
8		Choose multiplet with largest number of events for the selected coherency threshold.
9	*mktablg*	Lists events in the multiplet, including station name, azimuth and take-off angle in preparation for time-delay calculations.
10	*dbhg*	Performs time-delay calculations for all doublets in the multiplet.
11	*relnew*	Performs iterative relative relocation of events.
12	*plotsin* & *rms*	Calculates and plots the cosine curves (e.g. Figure 4.14a) and frequency of non-weighted residuals before relocation and weighted residuals after relocation (e.g. Table 4.2)

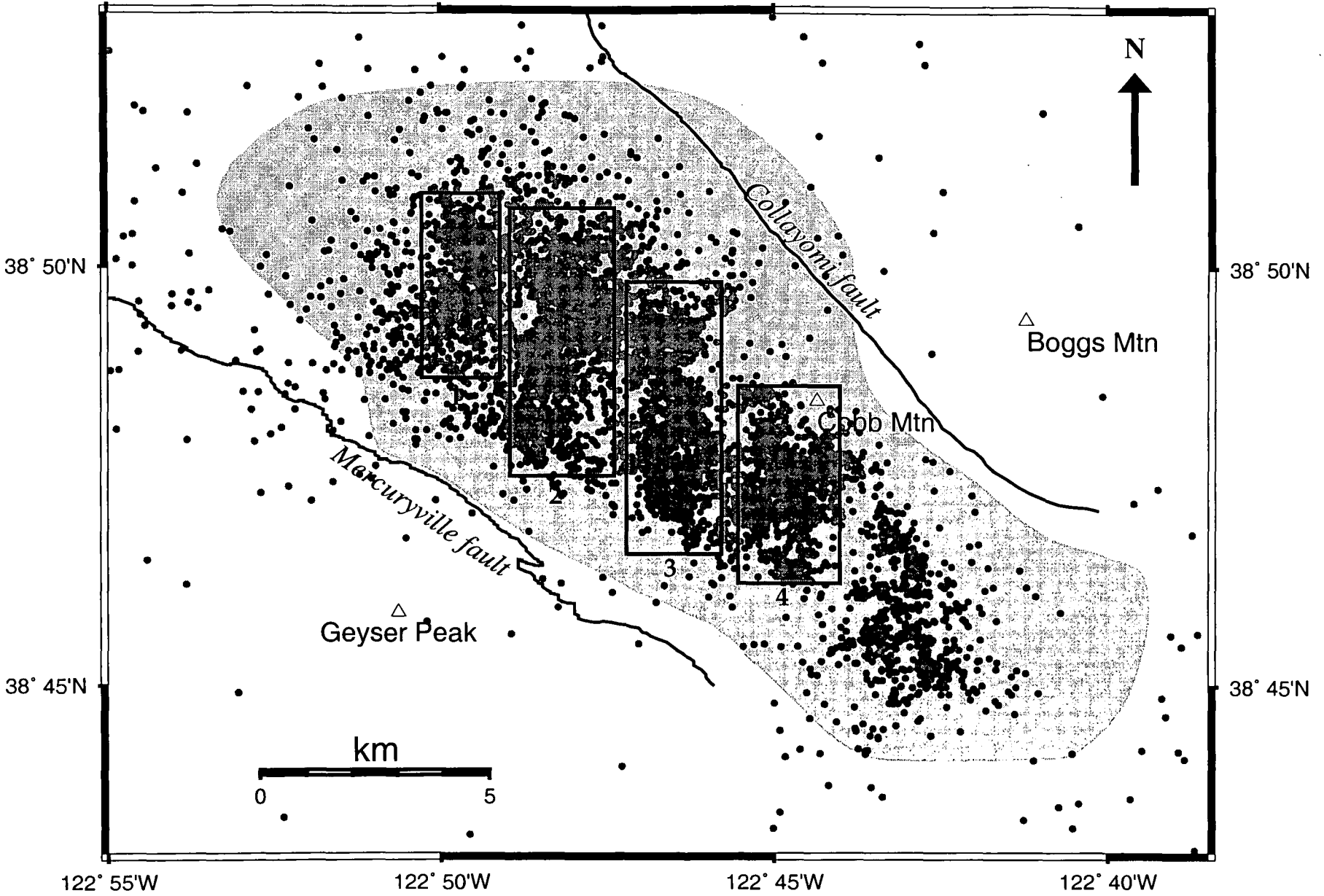

Figure 4.4: Map showing the epicentres of all events auto picked by D.J. Barton for the year 1993. Epicentres are black filled circles. Windows 1, 2, 3, and 4 enclose seismic regions used for relative relocation study.

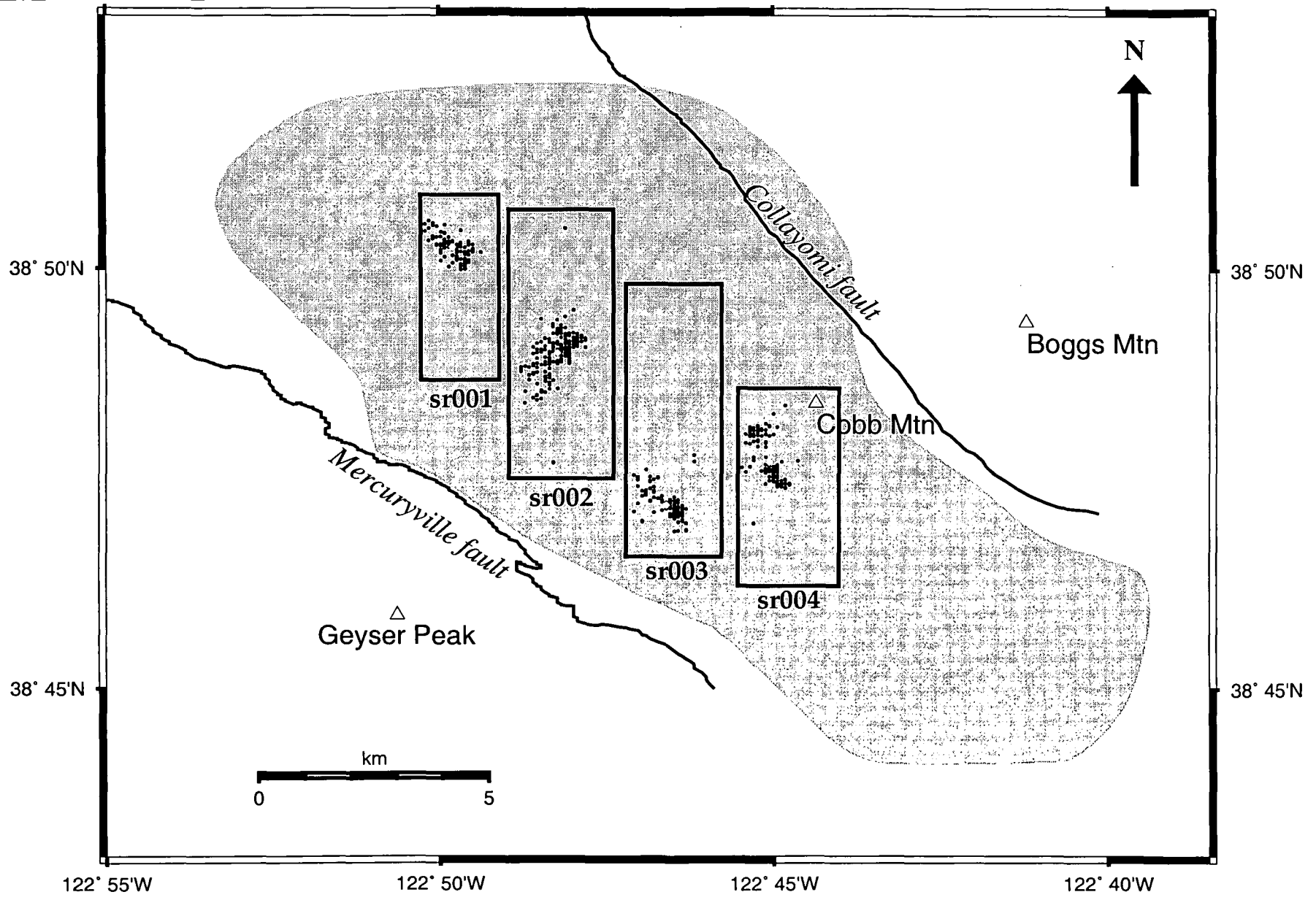

Figure 4.5: Map showing the epicentres of events of the selected multiplets within each region with coherency of 95 - 96%. Epicentres are black filled circles. Mean barycentre of each multiplet is shown by white diamond symbols.

To measure coherency, a window of length 1.28 s, centred on the *P*-wave arrival was chosen. For some traces the *S-P* travel time was less than 1.28 s causing the *S*-waves to arrive within this time window. These traces were eliminated. Sample traces were inspected for quality checking.

Multiplet selection is controlled by the number of events in the multiplet and the coherency threshold. There is a trade-off between the size of the multiplet and the coherency threshold used. A statistical function predicts the relative error in the relocated events using the equation:

$$\text{stat error} = \left[\frac{1-coh^2}{coh^2} \; / \; sqrt(n) \right] \qquad (4.13)$$

where *coh* is the coherency threshold and n is the number of events in the multiplet. The error in the relative relocations decreases with increase in coherency (J. L. Got, *pers. comm.*). The program *erragu* calculates how the estimated error in relocation varies with number of events in the multiplet (Figure 4.6a). The multiplet size was inferred for the lowest RMS residual error achievable given difficulties in computing excessively large multiplets. Due to the computational difficulties of processing large matrices, the number of events per multiplet was not allowed to exceed 200. Large, spatially dispersed multiplets also pose the additional problems of varying azimuths and take-off angles. The program *cohstat* plots number of events in the largest multiplet against coherency threshold values, which help to determine the optimum coherency threshold for the chosen number of events to be relocated (Step 5, Table 4.1) (Figure 4.6b).

From the coherency threshold diagrams for each region it was evident that between coherencies of 89 and 94%, the number of associated events decreased sharply (~476 events per 1% drop in coherency threshold, except for region sr001 where the decrease was 130 events per 1% drop in coherency threshold) (Figure 4.6b). Events with coherencies greater than 89% had very similar waveforms. The objective was to include as many events as possible in each multiplet, to use the highest coherency threshold possible and to achieve the smallest estimated

statistical error given the size of the multiplet. Most events with a coherency greater than 90% yielded post-location residuals as small as a few milliseconds.

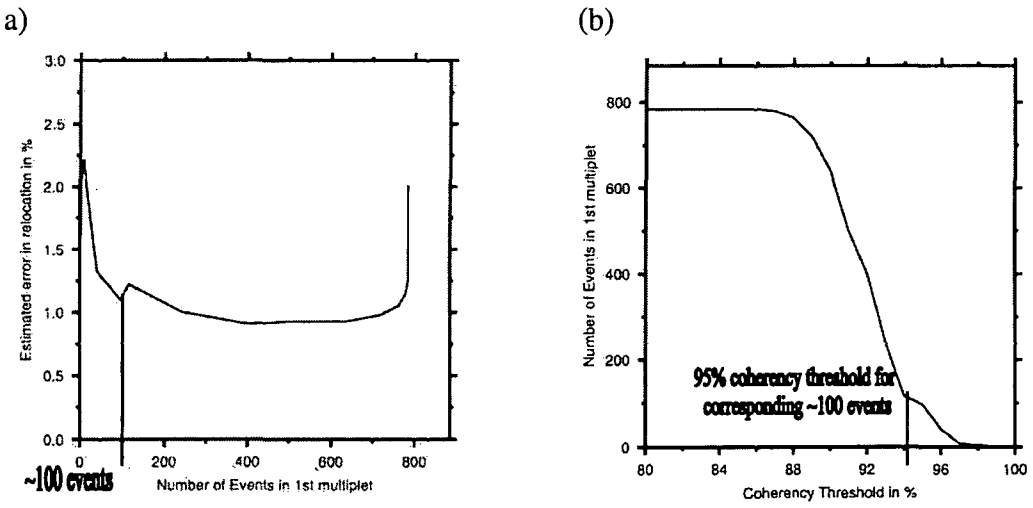

Figure 4.6: An example to illustrate procedure on choosing a coherency threshold value. (a) Choose the least estimated error in relative relocation (y-axis) and select the corresponding number of events that could be used in the multiplet (x-axis). However, due to computational difficulties with high number of events in a multiplet, events are restricted to less than 200. (b) For the chosen number of events in the multiplet (y-axis) find the corresponding coherency threshold (x-axis).

4.3.2 The coherency matrix

Doublets with coherencies of less than ~ 90% introduced error and caused rapid deterioration of the result quality. The program *csparse* (J. L. Got, *pers. comm.*) was used to compute the coherency matrix used to identify possible multiplets that could be relocated (Step 6, Table 4.1). Results of the computation of coherencies show that numerous pairs have high coherencies (e.g. > 95%). The coherency plot is computed for each pair of events in the selected seismic region that has a coherency greater than the chosen coherency threshold (Figure 4.7). Multiplet selection was made from the coherency matrix by using program *speq* (J. L. Got *pers. comm.*), an equivalence class algorithm that selects similar events and groups them into multiplets (Step 7, Table 4.1). For a given coherency threshold value a main multiplet and several smaller multiplets with ~20 events each were identified. Only the largest multiplet was relative relocated since the average separation of closest neighbours was smallest for the largest multiplets, yielding smaller final relocation errors (Step 8, Table 4.1). Multiplets were named according the seismic

region, the multiplet number and corresponding coherency threshold. For example sr001_01_95 corresponded to the largest and 1st multiplet in area sr001 and a coherency threshold of 95%.

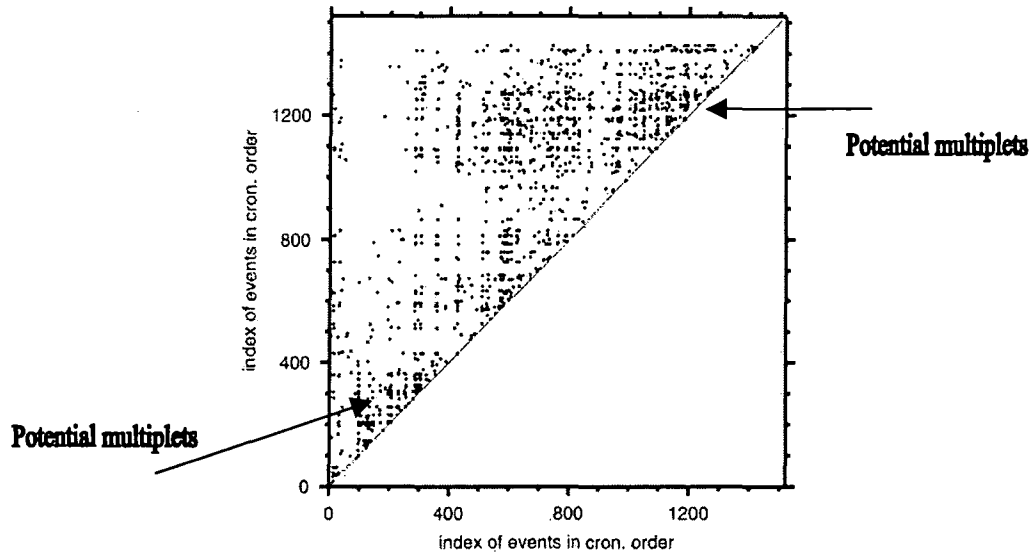

Figure 4.7: An example to illustrate a coherency matrix. Each coordinate is the index of each event in chronological list of events selected for relocation. Each dot indicates a coherence greater than the selected threshold for the corresponding pair of events. The events that appear to be clustered are potential multiplets. The highly coherent pairs of events more or less confined to the main diagonal are events that occur during limited crises in time and space.

4.3.3 Time-delay computation and relative relocation

Preparatory information for time-delay calculations was assembled by program *mktablg* (J. L. Got *pers. comm.*) (Step 9, Table 4.1). For each pair of events recorded at each station, time delays were computed along the seismogram using a moving window technique (Poupinet *et al.*, 1984; Frechet, 1985) utilizing the cross-spectral method of Jenkins and Watts (1968). Using a weighted linear fit of the cross-spectrum, phase time delays were computed for each window (Step 10, Table 4.1). The weight used is a function of the coherency and is inversely proportional to the phase error (Poupinet *et al.*, 1984; Frechet, 1985). A few blunders were found by identifying outliers in the travel times computed.

The relocations were performed relative to one arbitrary event using the normal equations method (Got *et al.*, 1994). Relative relocation is a least squares inversion

process and the iterations are designed to eliminate blunders and down-weight inconsistent data (Step 11, Table 4.1). For good results, the process will converge after only one or two iterations and the final RMS is expected to be less than ~7.5 ms. More than five iterations of the location process was indicative of inconsistent data and thus poor results. Relative relocation accuracies were of the order of 10 to 100 m.

4.3.4 Quality of relative relocation

The programs *plotsin* and *rms* (J. L. Got, *pers. comm.*) were used to verify the quality of the relocations (Step 12, Table 4.1). Travel time delays vary according to the event-pair and station geometry. After relocation, program *plotsin* makes a quality check of the relocated results by plotting the normalized time delay as a function of the azimuth between the direct ray to the station (wave vector) and the inter-event vector for each station for all doublets in the multiplet (Figure 4.8). The normalised time-delays are the time delay measurements normalised by d/V where d is the event separation distance and V is the hypocentral velocity.

Consider a doublet and a station recording the doublet (Figure 4.2). The time delay is the dot product of the wave vector, **K** and the inter-event vector, **F** divided by velocity V at the hypocentre. The expected pattern for the time delay as a function of the azimuth of **K** is then a cosine curve of unit amplitude. The time delay should be a maximum in the direction of the inter-event vector (Figure 4.8a) and zero along the normal to the direction of the inter-event vector (Figure 4.8c). The shape of the cosine curve is dependent on the shape of the multiplet and the geometry of the seismic stations recording the multiplet. Three-dimensional velocity variations can also degrade the cosine curve. Large scatter in the plot indicates inconsistencies in the delay time data, and this could indicate either dispersed events where inter-event distances are large (> 500 m) in comparison to event-station distances, or outliers in the measured time-delays.

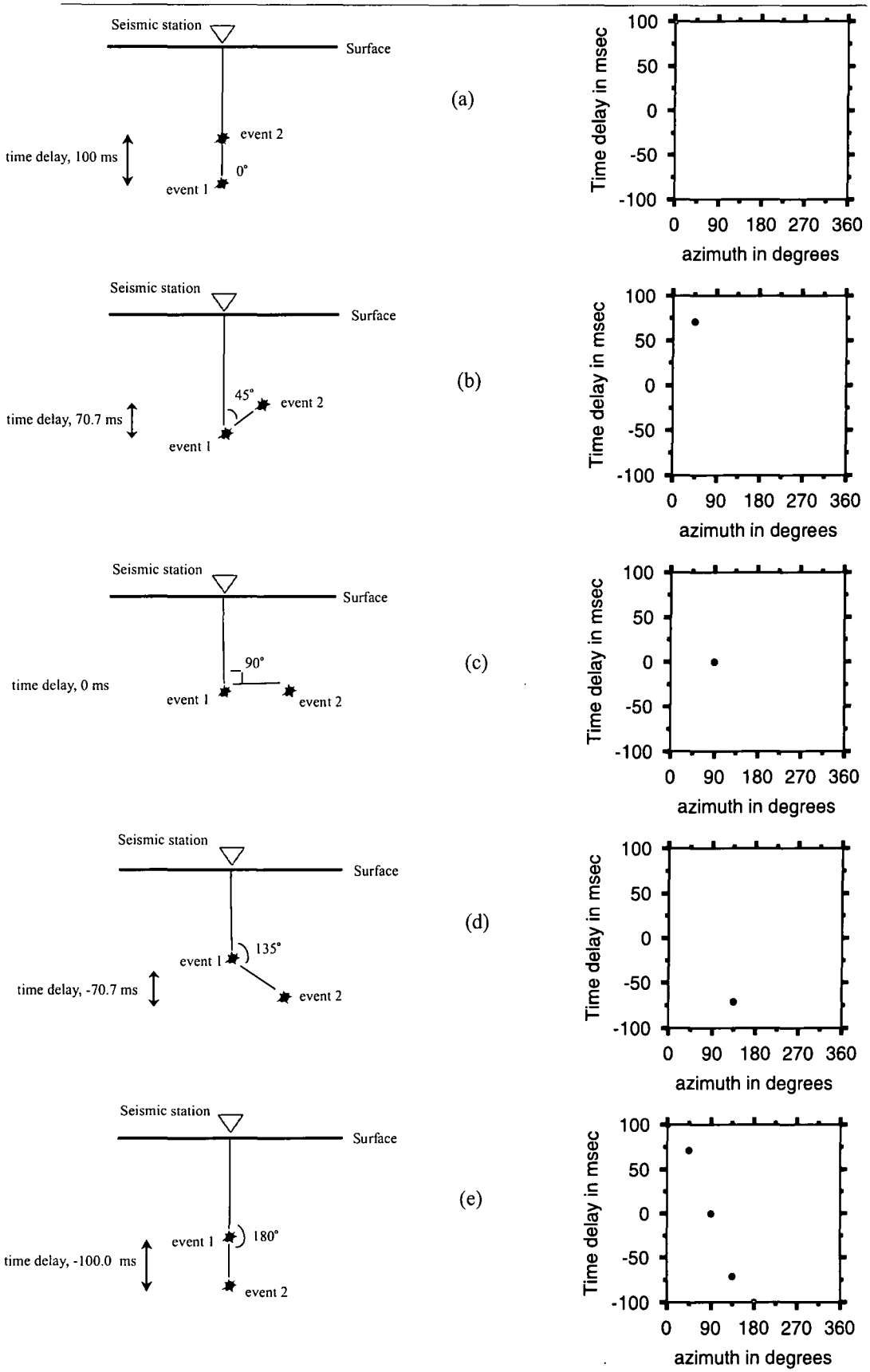

Figure 4.8: An example/explanation of cosine plot (right side) with respect to a sketch of a doublet in space (left side). The cosine plot shows the normalised time-delay between the pair of events against the azimuth between the direct ray to the station and the inter-event vector. Red dots are translated positions from corresponding space and blue dots illustrate the shape of the cosine curve for all positions illustrated in the figure. For (a) time-delay is maximum, (c) time-delay is minimum and (e) time-delay is maximum in opposite direction. For azimuth 181° to 360° time-delay s a reflection at the azimuth on 180°.

Program *rms* computes the number of times each station was used in the relocation process. Residuals are the difference between the observed and theoretical time-delay. The theoretical time-delays are computed from the relative locations of events. However, during the iterative relocation of events, weights are introduced and adjusted such that after each iteration, large residuals are down weighted (Table 4.2) (Appendix 7).

Table 4.2: An example of the output of the *rms* program for multiplet sr001_01_95. Stn: Station name, Common Az.: common azimuth from multiplet to station, Comm. TOA: take-off angle from the multiplet to the station, Freq. Non-weighted residuals: The number of time-delay residuals calculated for a particular station before relocation, Freq. Weighted residuals: The number of time-delay residuals included in the relative relocation after the iterative process.

Stn.	Common Az.	Comm. TOA	Freq. Non-weighted residuals (before reloc.)	Freq. Weighted residuals. (after reloc.)
ACR	91	114	694	353
ANG	119	108	105	925
BUC	195	154	331	1257
CAP	63	148	42	1296
CLV	88	133	231	1305
DES	125	89	24	1050
DRK	157	114	143	757
DVB	136	96	572	503
DXR	108	119	1401	413
FNF	143	102	108	802
FUM	143	114	214	510
INJ	146	127	708	573
LCK	104	107	395	491
MNS	124	90	949	328
PFR	142	94	138	801
SB4B	180	133	48	1176
SQK	131	143	107	796
SSR	136	84	6	952
STY	125	121	600	790
TCH	126	96	762	442
U14	139	107	102	726

4.4 Results

4.4.1 Region sr001

The relative relocation results are presented as follows. First, the optimum number of events included in the multiplet, the chosen coherency threshold value and its associated statistical error are presented. This is followed by a map of the absolute locations of the earthquakes in the study area and a coherency matrix plot. This reveals possible multiplets that are suitable for relocation. The difference between the absolute and relative relocations are then shown, followed by plots that enable assessment of the quality of the result.

The size of the data set that could be processed was limited by the power and speed of the computer used. There were 1420 events in region sr001. Two multiplets were studied with coherencies of 95% (97 events) and 92% (400 events). For the multiplet with 95% coherency threshold with 97 events, the estimated error in relocation was 1.2% and for the multiplet with a 92% coherency threshold with 400 events, the estimated error was 0.9% (Figure 4.9). The objective was to reduce the estimated error as much as possible while limiting the increase in the number of events included in the 1st multiplet. The coherency matrix for the 95% threshold shows very few multiplets of significant size, which would tend to appear as distinct groups of events closely related in time (Figure 4.10).

The events selected for relative relocation are at the periphery of the UNOCAL network with poor spatial coverage of stations (Figure 4.11). The relative relocation program iterated 3 times and the final RMS error in travel time was 5.9 ms. The relocated events form a linear zone trending northwest-southeast (Figure 4.12). The relocations are more diffuse than the original locations, a surprising result that casts doubt on the quality of the relocations. A possible reason for this is that the velocity used to relocate the events may not correspond to the velocity at this hypocentral depth. A one-dimensional wave speed model was used and *P*-wave velocity in the northwest Geysers is known to be 8.3% lower than in the central

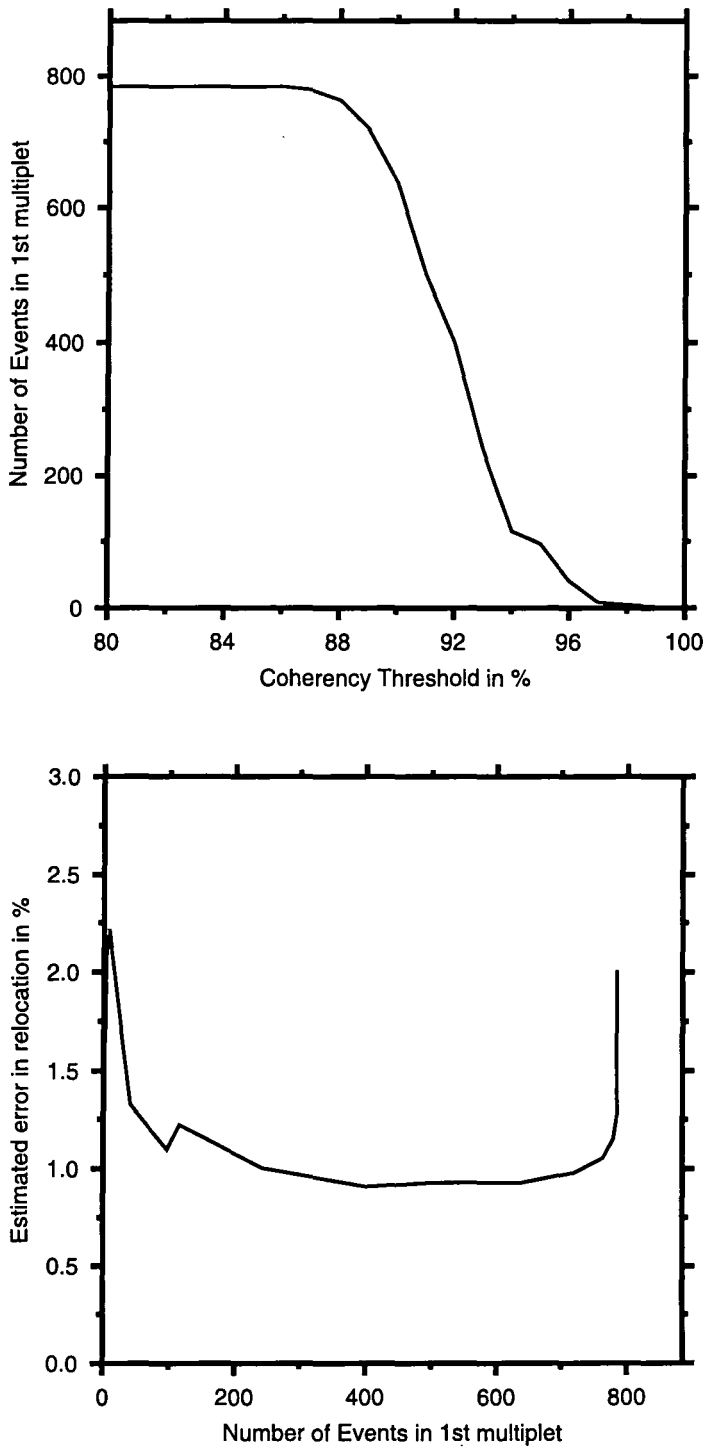

Figure 4.9: Top: Plot showing number of events in the 1st multiplet in region sr001 against coherency values. Bottom: Plot showing the estimated error in relative relocations against multiplet size.

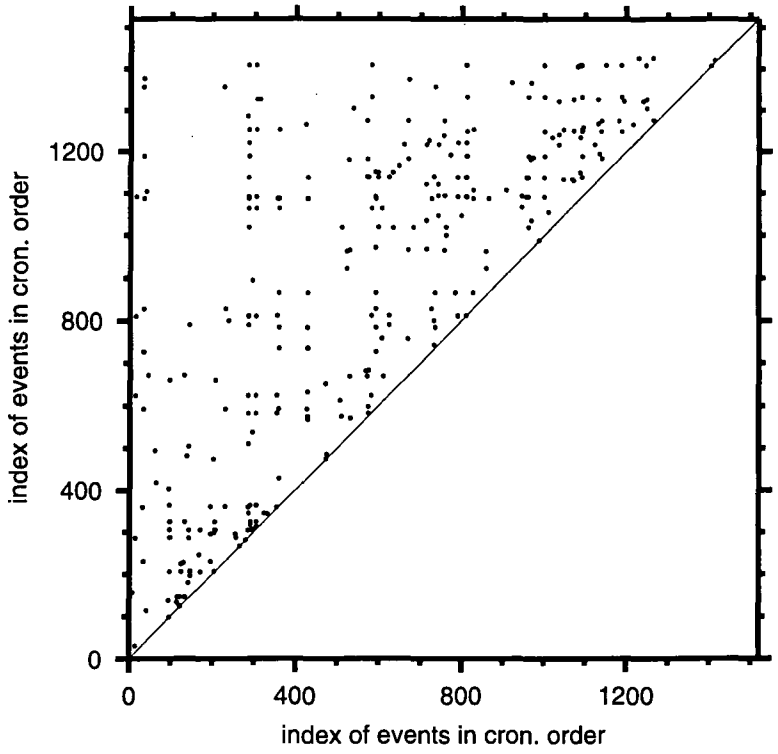

Figure 4.10: Top: Coherency matrix for area sr001 and events with 95% coherency.

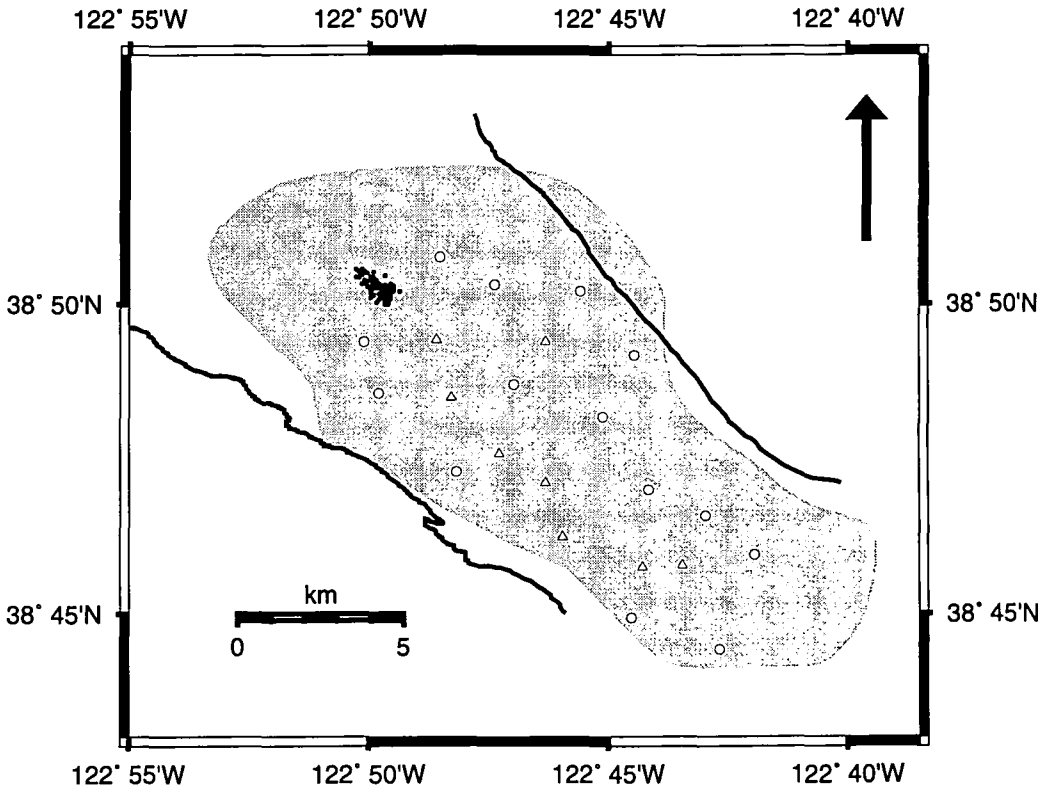

Figure 4.11: Bottom: Map of UNOCAL stations (refer Figure 4.3) and absolute (initial) locations of events in multiplet, sr001_01_95.

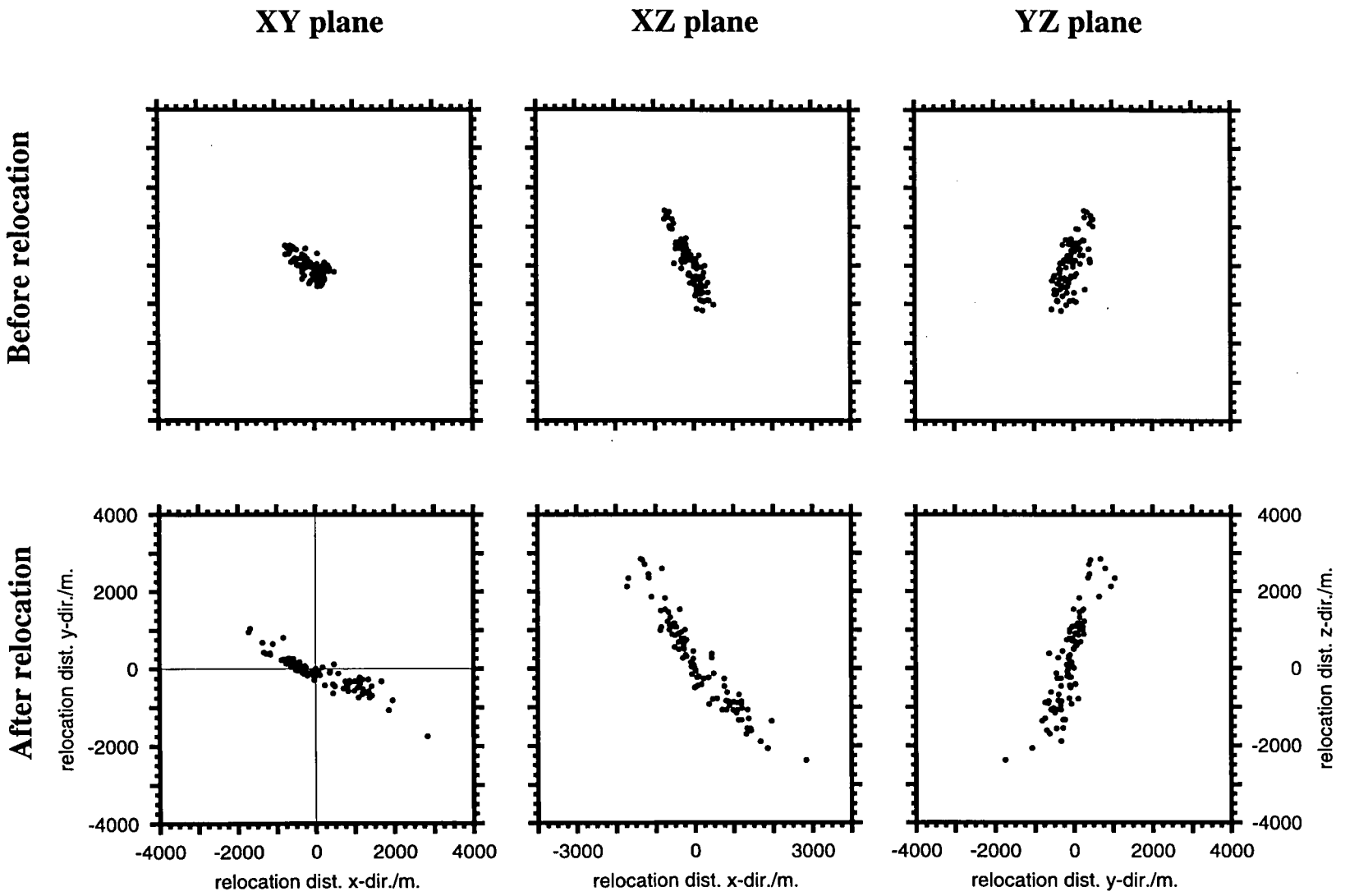

Figure 4.12: Map showing 97 relocated events for multiplet sr001_01_95 in the XY, XZ and YZ planes. Lines of section are shown in panel at lower left. X-dirrection is latitude, Y-direction is longitude and Z is depth (positive downwards). Top row shows original locations and bottom row shows relative relocations. Both rows are to the same scale.

and southeastern parts of The Geysers (section 3.4.3.1). The orientation of cluster sr001_01 was NW-SE, the dominant trend of faulting at The Geysers which is intuitively expected. This would, however, also be the expected direction of elongation if the locations are degraded by the poor station geometry. The hypocentral volume of the relocated events in multiplet sr001_01_95 is tube-shaped.

The quality of the 95% coherency results was investigated using a cosine plot. A smooth, compact cosine curve indicates high quality results. For a multiplet that is spatially elongated, points would be expected to cluster at 0 and 180° and this is indeed observed (Figures 4.13, 4.14). The distant stations MNS and TCH also showed high-quality cosine plots (Figure 4.13n, t). The distribution pattern for all the stations combined was as expected, with scattered time delays clustered at azimuths of 0 and 180° (Figure 4.14a). Station DXR was the most frequently sampled station for this multiplet with a good mean take-off angle of 119° (Figure 4.14b). However, the waveforms recorded at stations with good cosine plots tended to have poor S/N ratios.

The coherency matrix for the multiplet with a 92% coherency threshold, involves many more events and many more small sub-multiplets (Figure 4.15). The epicentral distribution of this multiplet was diffuse, with one major cluster of events and two sub-clusters (Figure 4.16). After three iterations an RMS of 6.2 ms was achieved, but again, the relative relocations showed a larger scatter than the original locations and several outliers are evident (Figure 4.17). The cosine plots were excellent at stations ANG, DVB, MNS, PFR, TCH and U14 (Figure 4.18). These stations recorded numerous data which dominated the relocation calculations (Figure 4.19).

The results were investigated further by relocating multiplet, sr001_01_95 using stations in the northern and southern half of the area independently. This exercise illustrated the effects of using close and distant stations only, and the importance of good network geometry. Stations with clear waveform signals and fairly good cosine plots were obtained for the multiplet sr001_01_95_T2, which involved only stations in the northern half of the network. The relative relocation program

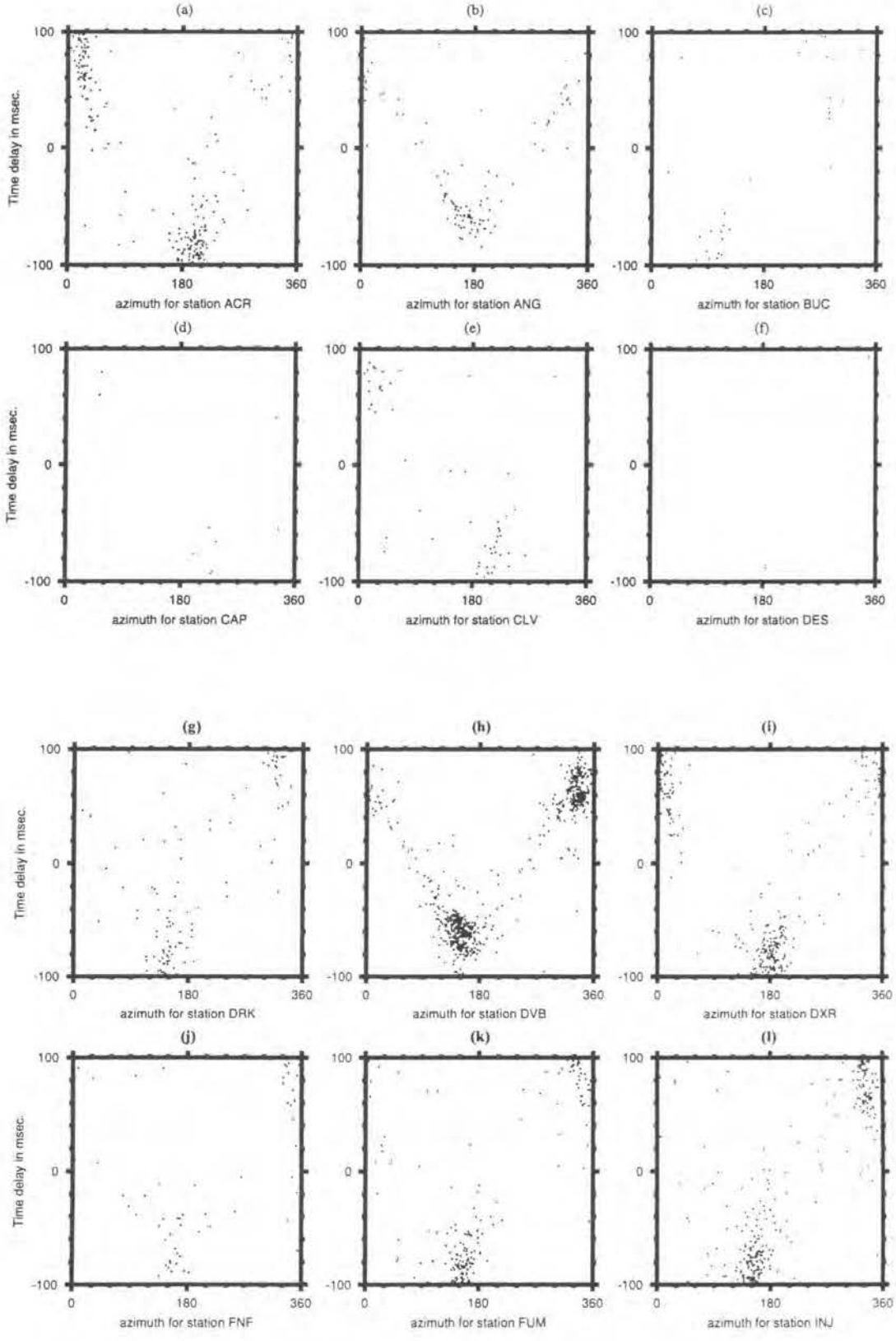

Figure 4.13: Plots of normalised time delays between earthquake pairs against angle between the azimuth to the station and the inter-event vector for multiplet sr001_01_95, for individual stations of the network.

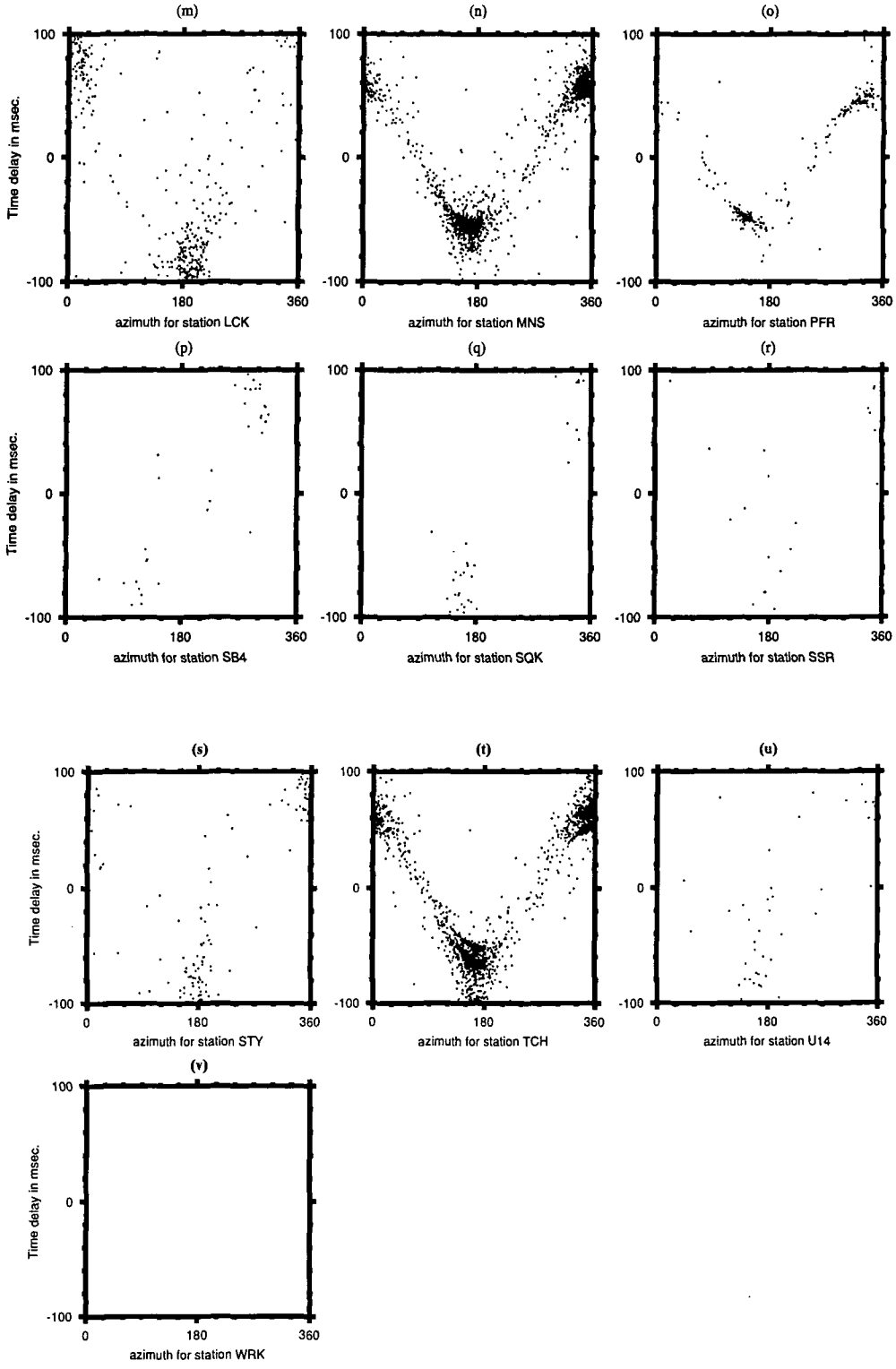

Figure 4.13 continued.

(a)

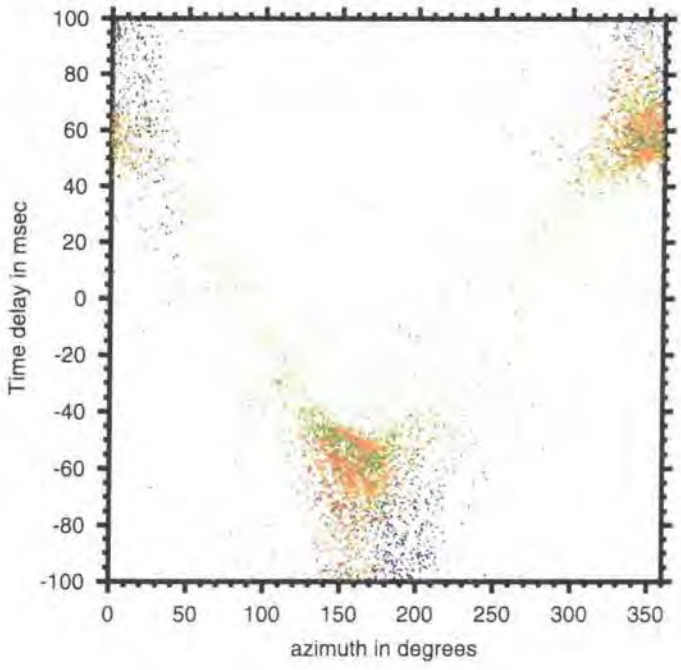

(b)

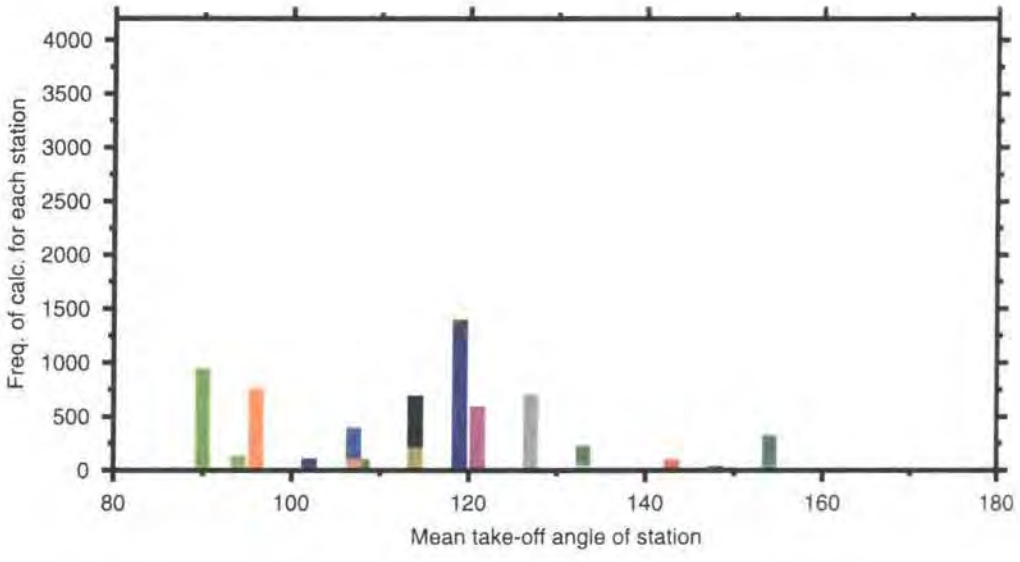

Stations with respect to colour coding for multiplet sr001_01_95 :

ACR	ANG	BUC	CAP	CLV	DES	[illegible]
DVB	DXR	FNF	[illegible]	[illegible]	LCK	[illegible]
[illegible]	[illegible]	SQK	[illegible]	STY	[illegible]	[illegible]
WRK						

Figure 4.14: (a) Composite curve for the whole multiplet (b) Frequency of stations used in time-delay estimates vs. mean take-off angle.

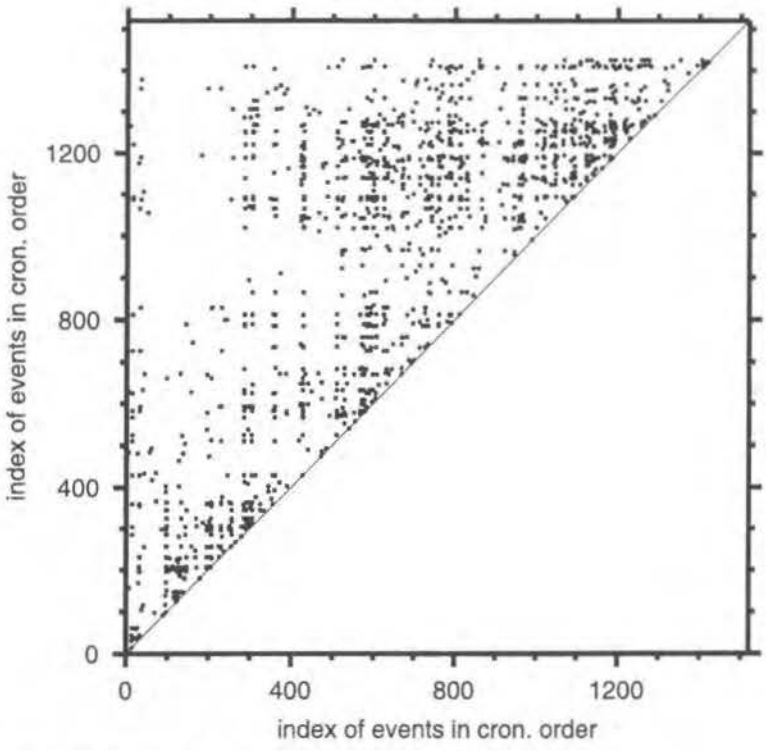

Figure 4.15: As for Figure 4.10 except for 92% coherency.

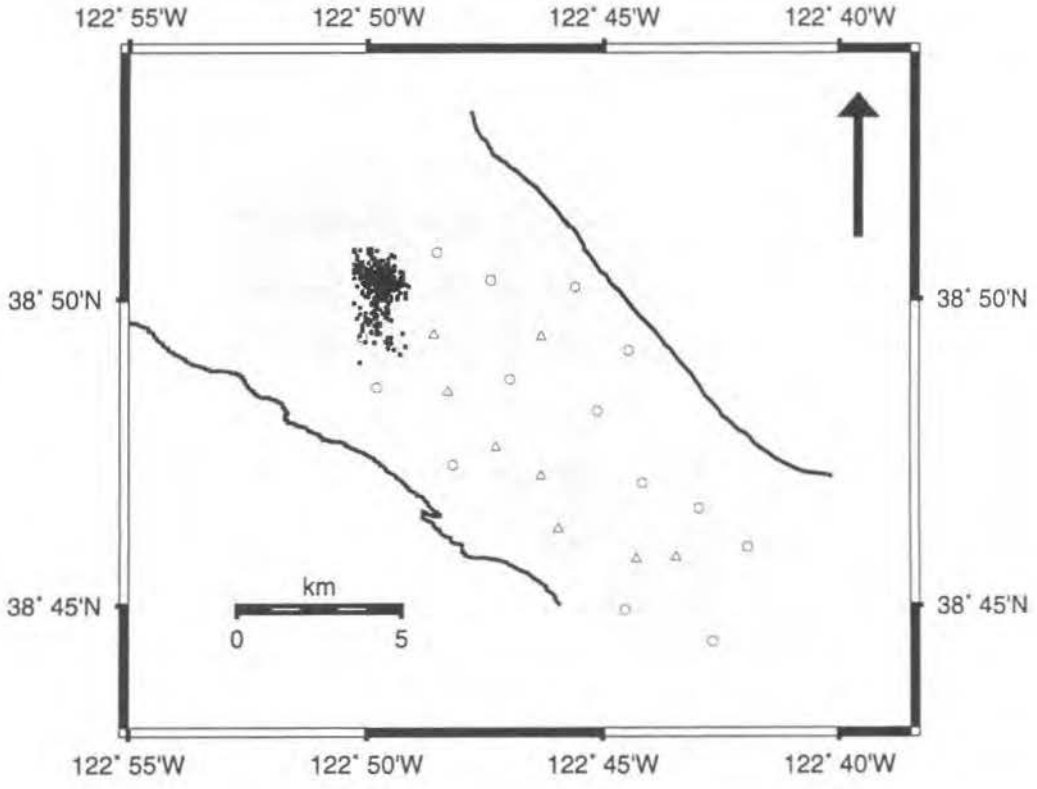

Figure 4.16: As for Figure 4.11 except for multiplet sr001_01_92.

Figure 4.17: As for figure 4.12 except for multiplet sr001_01_92, with 400 events.

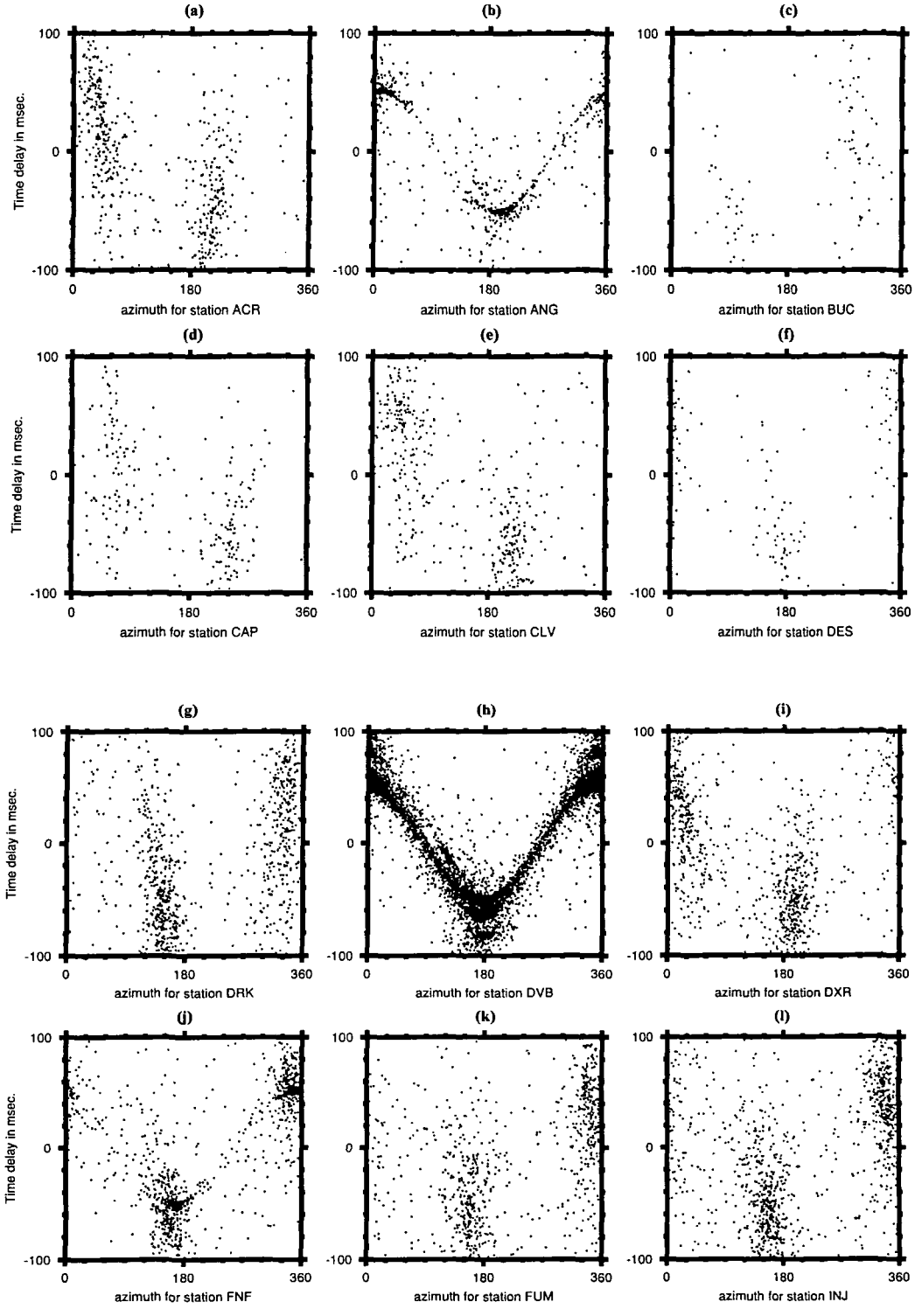

Figure 4.18: As for Figure 4.13 except for multiplet sr001_01_92.

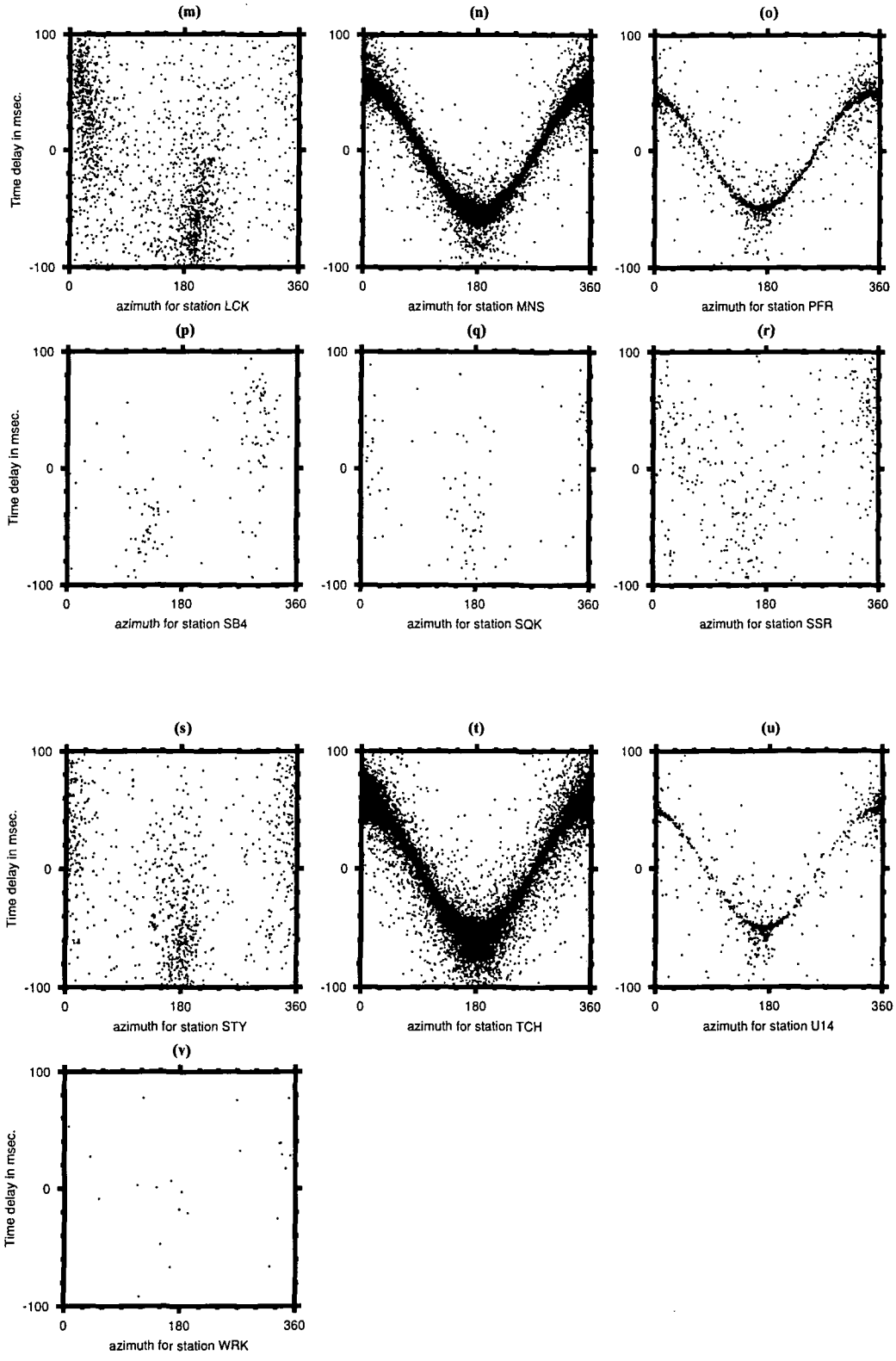

Figure 4.18 continued.

(a)

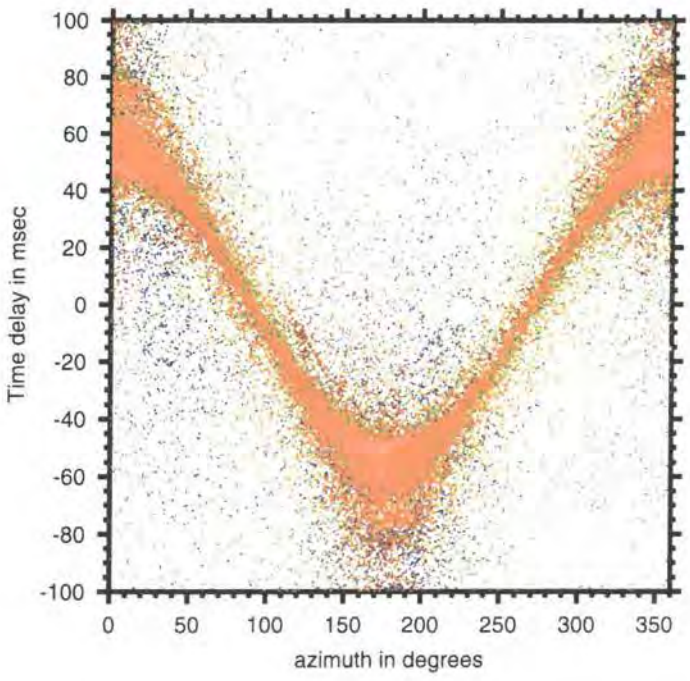

(b)

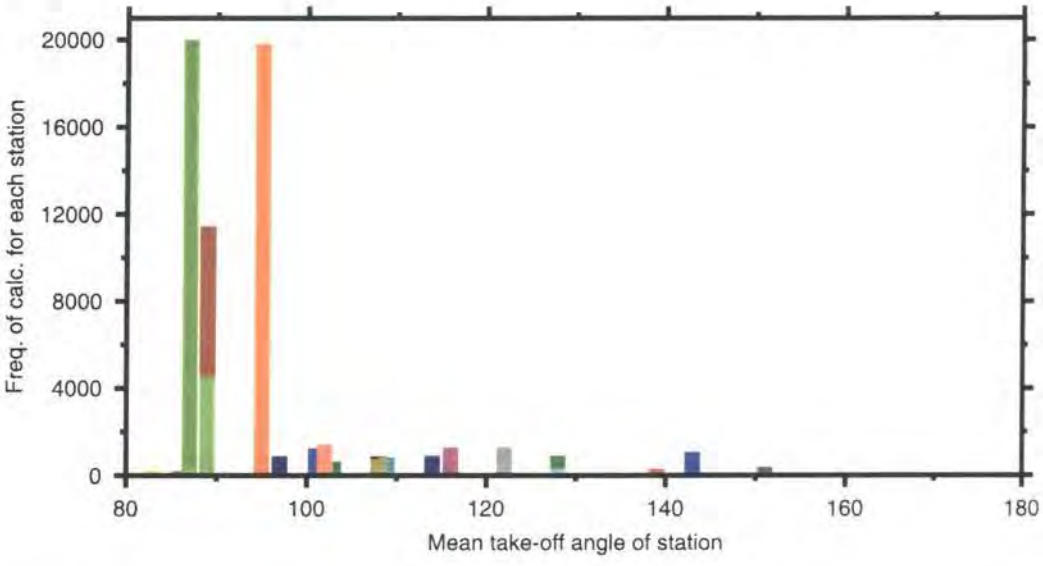

Stations with respect to colour coding for multiplet sr001_01_92 :

ACR	ANG	BUC	CAP	CLV	DES	DRK
DVB	DXR	FNF	[illegible]	[illegible]	LCK	MNS
PER	[illegible]	SQK	[illegible]	STY	TCH	[illegible]
WRK						

Figure 4.19: As for Figure 4.14 except for multiplet sr001_01_92.

completed after two iterations with an RMS of 5.6 ms. The results were similar but more clustered than for multiplet sr001_01_95 (Figures 4.20, 4.21 and 4.22). The multiplet using only the southern part of the network involved seven seismic stations and was called multiplet sr001_01_95_T1. It yielded very poor, highly scattered relative relocations (Figure 4.23). This result was anticipated, but it serves to illustrate the effect of extremely poor station geometry. Although, the cosine plots were very good for stations DVB and MNS (Figure 4.24 and Figure 4.25a) the waveforms from these stations had a very low S/N ratio and a clear seismic signal cannot be identified (Appendix 8). All the stations in the southern part of the network have very low take-off angles (Figure 4.25b). The relocation process gives less weight to stations with low take off angles (distant stations) and poor waveforms but this is of limited help if the majority of the stations are of this kind. It is clear from this analysis that waveforms with clear arrivals and good time-delay calculations from stations close to the multiplet (e.g. sr001_01_95_T2) yield better relative relocations than stations further away (Figure 4.26).

4.4.2 Region sr002

For region sr002 the number of events predicted to minimise the statistical errors in the multiplet is 1800 (Figure 4.27). However, in view of the computational limitations 192 events were selected which gave an estimated error of 0.61% and corresponded to a coherency threshold of 96% (Figure 4.27). The whole region contained 5104 events, which enabled a good dataset to be selected with high coherency in the waveforms. The coherency matrix (Figure 4.28) shows that highly coherent events are widely separated in time. The relative relocation program completed two iterations and achieved an RMS of 7.4 ms. The final locations fell into tighter clusters than the original locations and formed a northeast-southwest orientated epicentral area (Figure 4.30). The cluster is about 2 km in diameter. The cosine plots yield good results for stations such as DES, DVB, MNS, PFR, SSR, and TCH (Figure 4.31f, h, n, o, r, t and Figure 4.32a). However, only station PFR (Figure 4.31o) yielded both good waveforms and a good cosine plot. Station PFR did not yield many arrivals (only 700) compared with approximately 4000 for station STY (Figure 4.32b). Although station WRK yielded many data (Figure

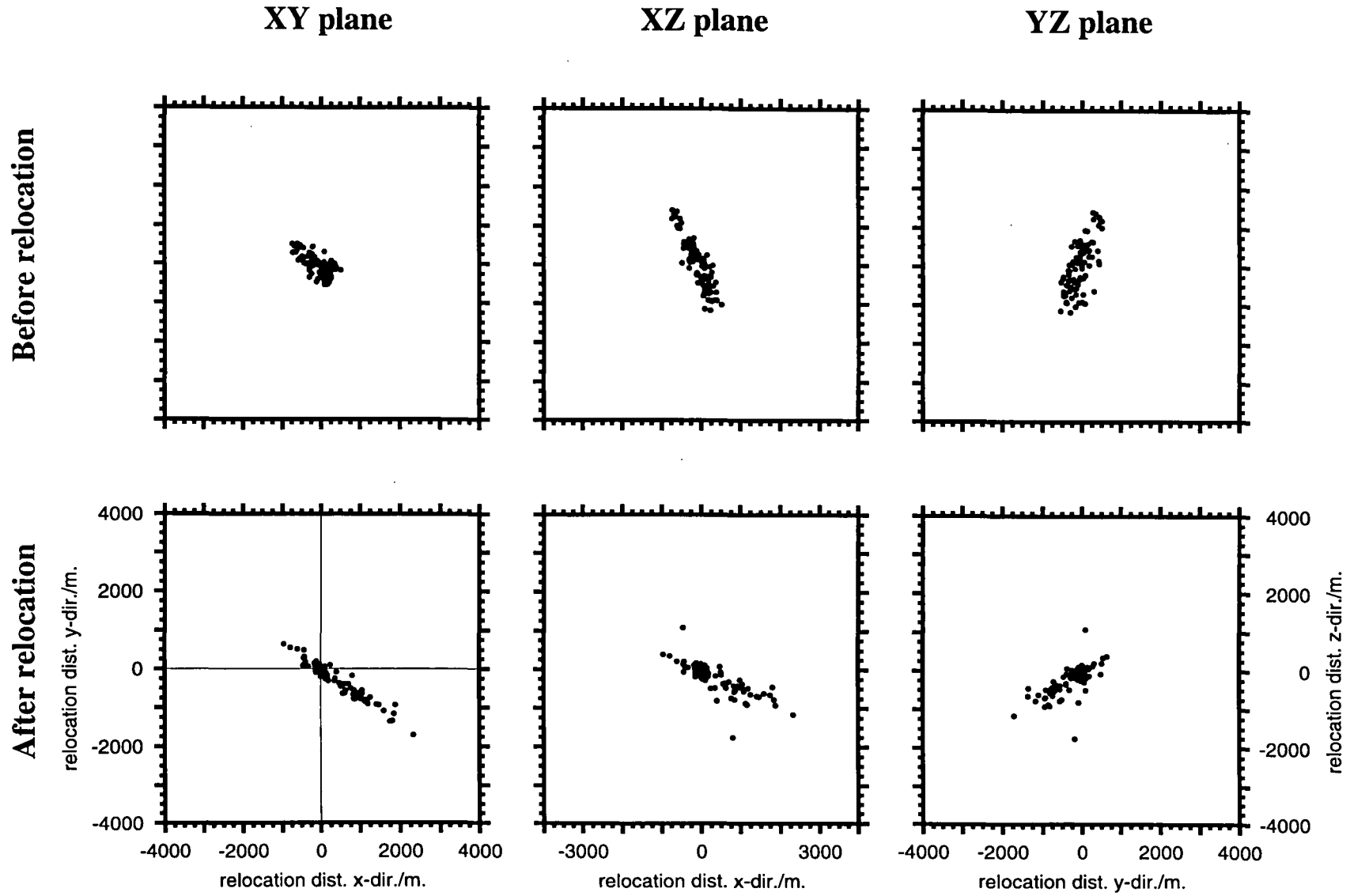

Figure 4.20: As for Figure 4.12 except for multiplet sr001_01_95_T2.

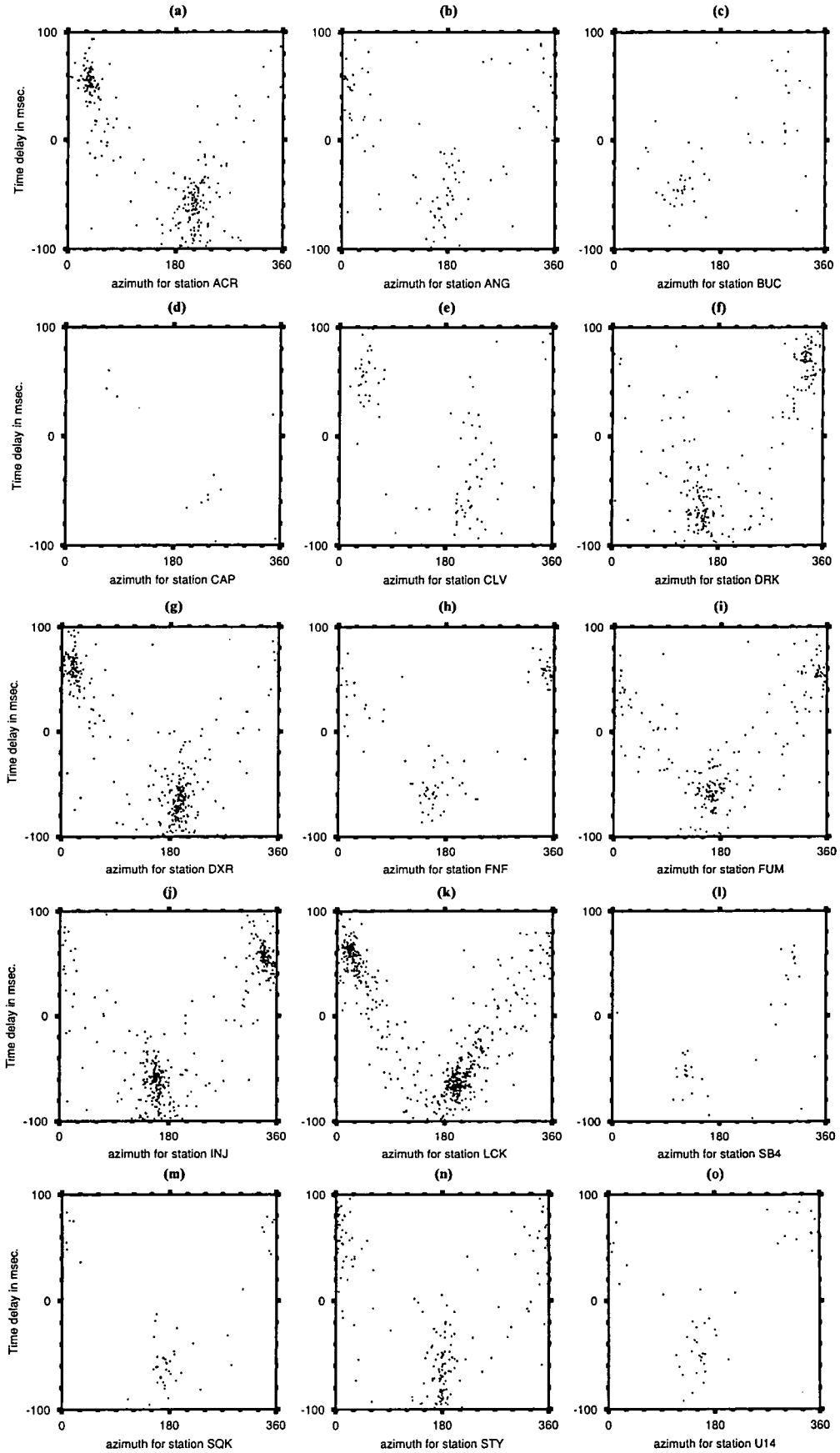

Figure 4.21: As for Figure 4.13 except for multiplet sr001_01_95_T2.

(a)

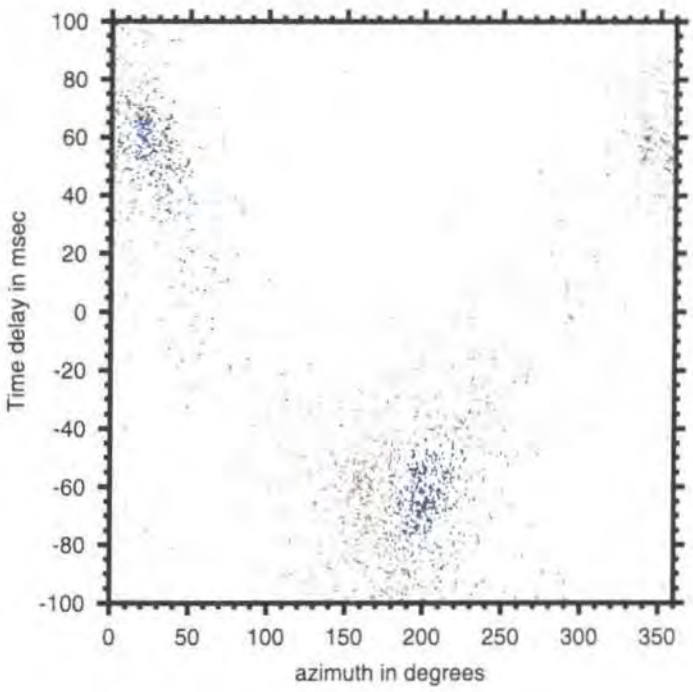

(b)

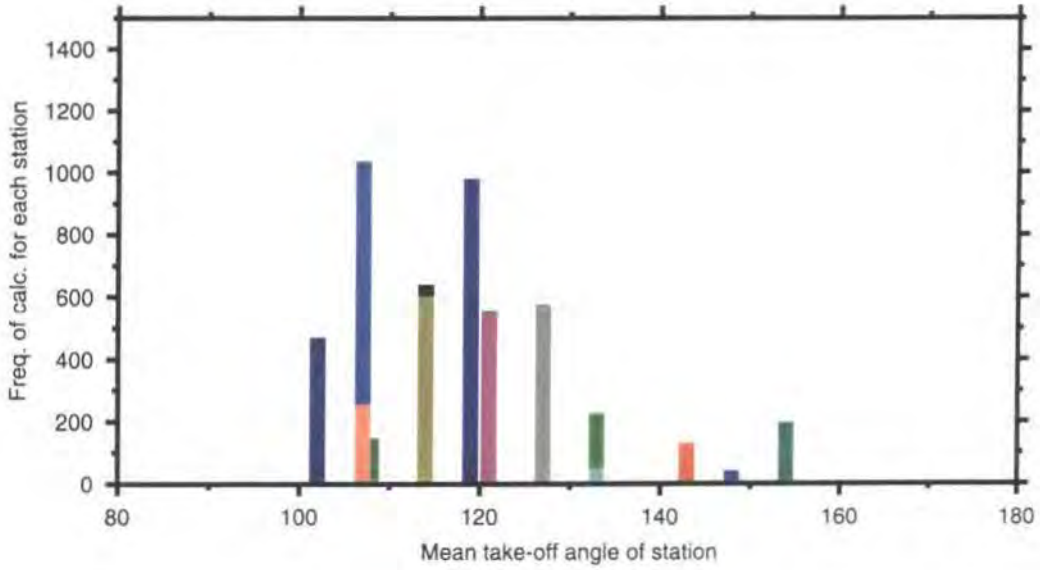

Stations with respect to colour coding for multiplet sr001_01_95_T2 :

ACR	ANG	BUC	CAP	CLV	DES	DRK
DVB	DXR	FNF	FUM	INJ	LCK	MNS
PER	SHAN	SQK	[illegible]	STY	TCH	[illegible]

Figure 4.22: As for Figure 4.14 except for multiplet sr001_01_95_T2.

Figure 4.23: As for Figure 4.12 except for multiplet sr001_01_95_T1.

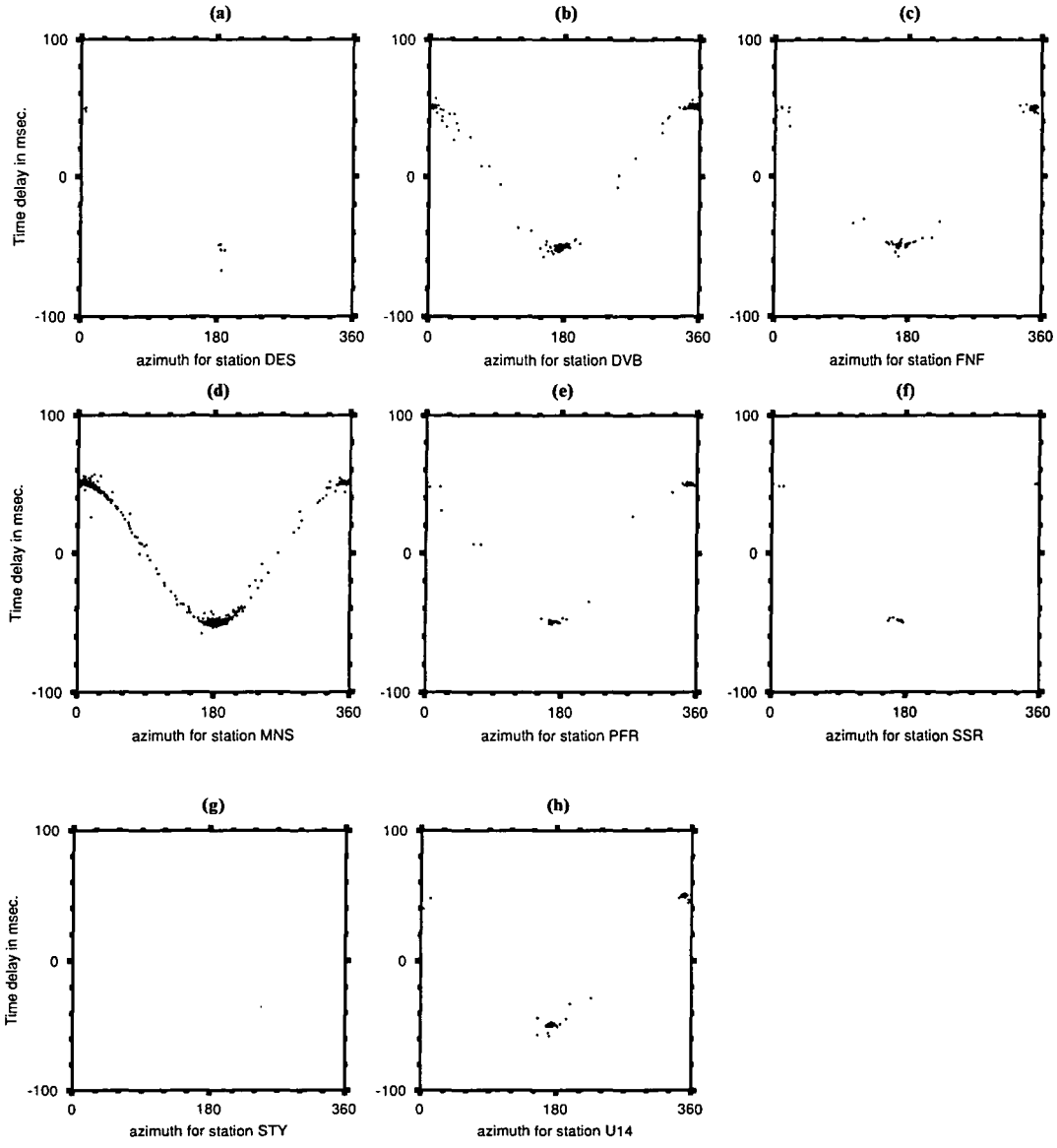

Figure 4.24: As for Figure 4.13 except for multiplet sr001_01_95_T1.

(a)

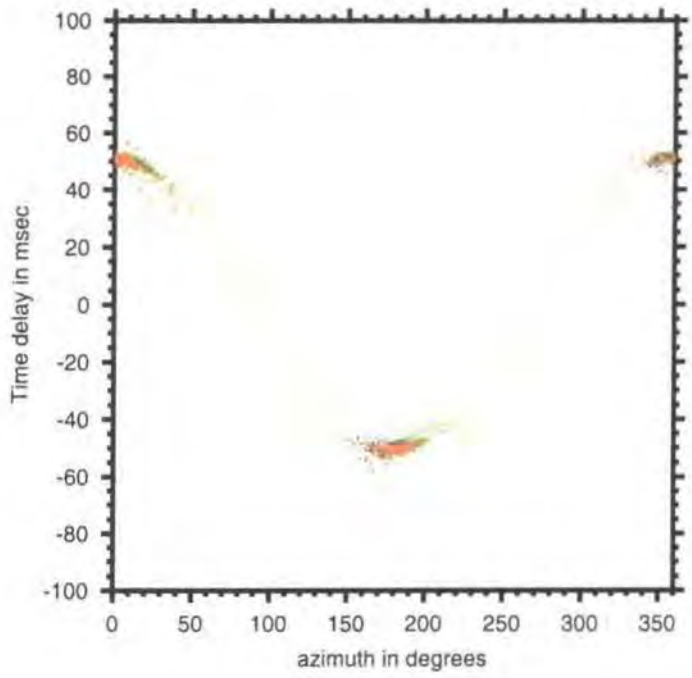

(b)

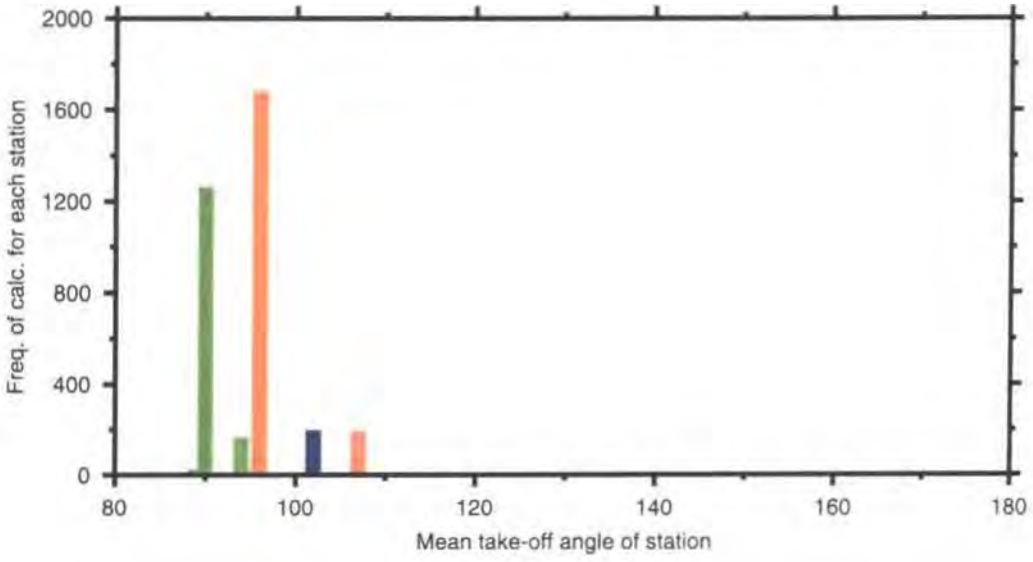

Stations with respect to colour coding for multiplet sr001_01_95_T1 :

ACR	ANG	BUC	CAP	CLV	DES	DRK
DVB	DXR	FNF	FUM	INJ	LCK	MNS
PFR	[illegible]	SQK	[illegible]	STY	TCH	[illegible]
WRK						

Figure 4.25: As for Figure 4.14 except for multiplet sr001_01_95_T1.

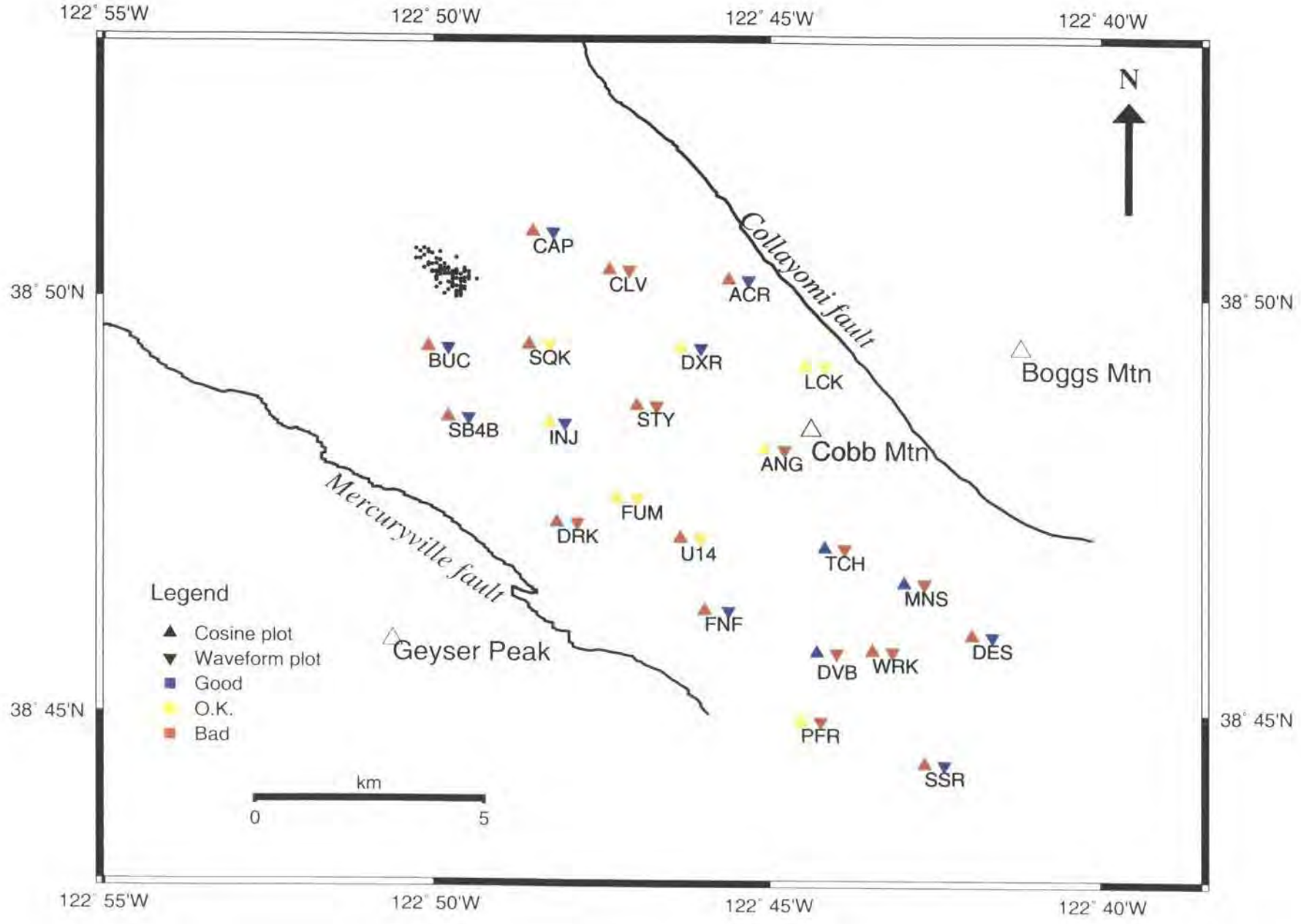

Figure 4.26: Map showing the quality of the cosine plots and waveforms for each UNOCAL station recording multiplet, sr001_01_95. The absolute locations of events of the multiplet are shown by black dots.

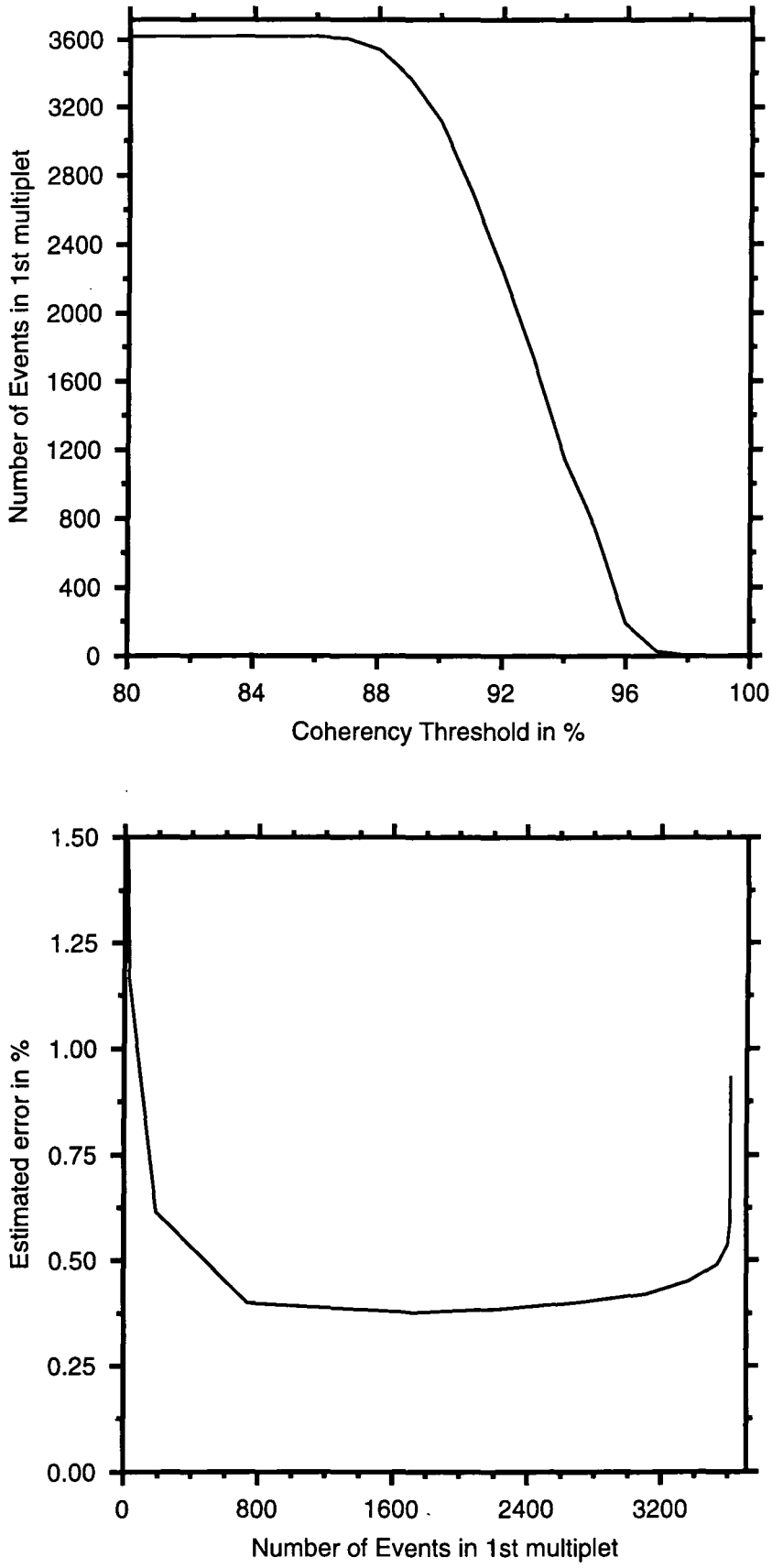

Figure 4.27: As for Figure 4.9 except for region sr002.

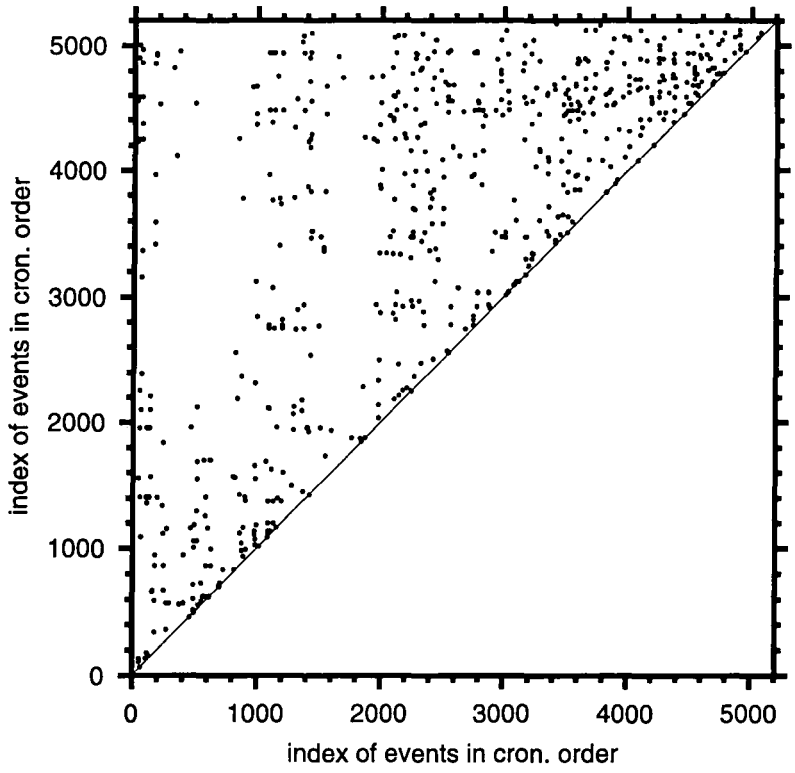

Figure 4.28: As for Figure 4.10 except for area sr002 for 96% coherency threshold.

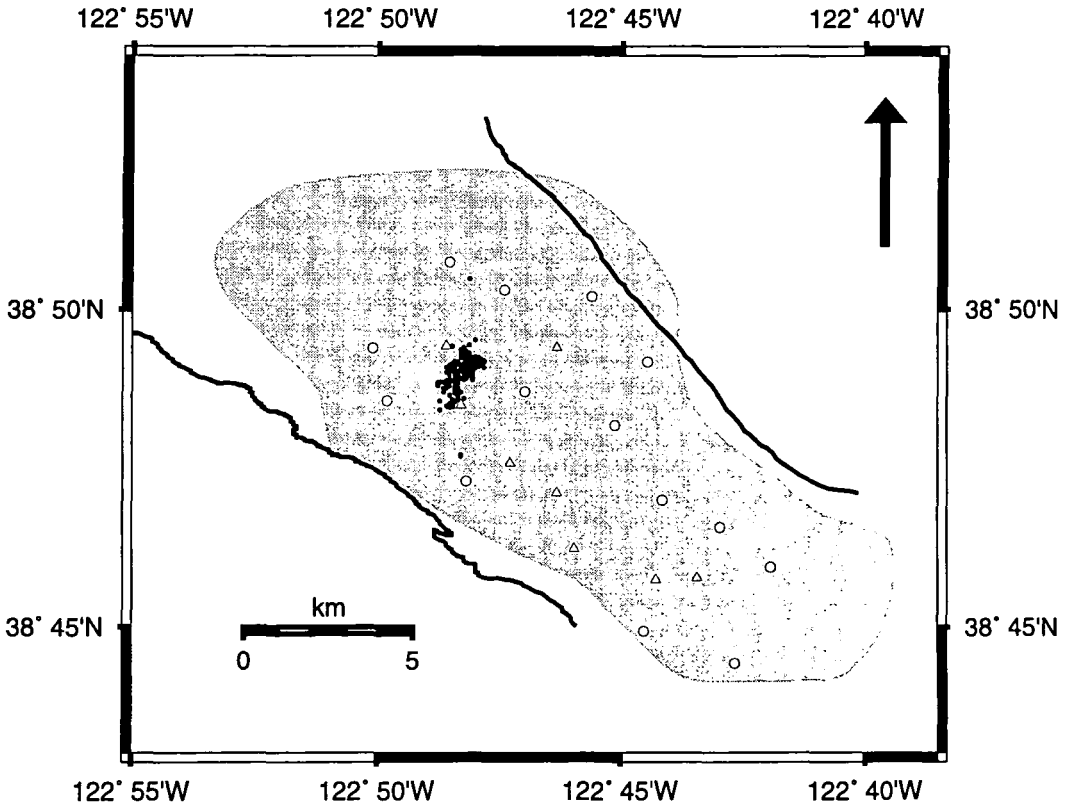

Figure 4.29: As for Figure 4.11 except for multiplet sr002_01_96.

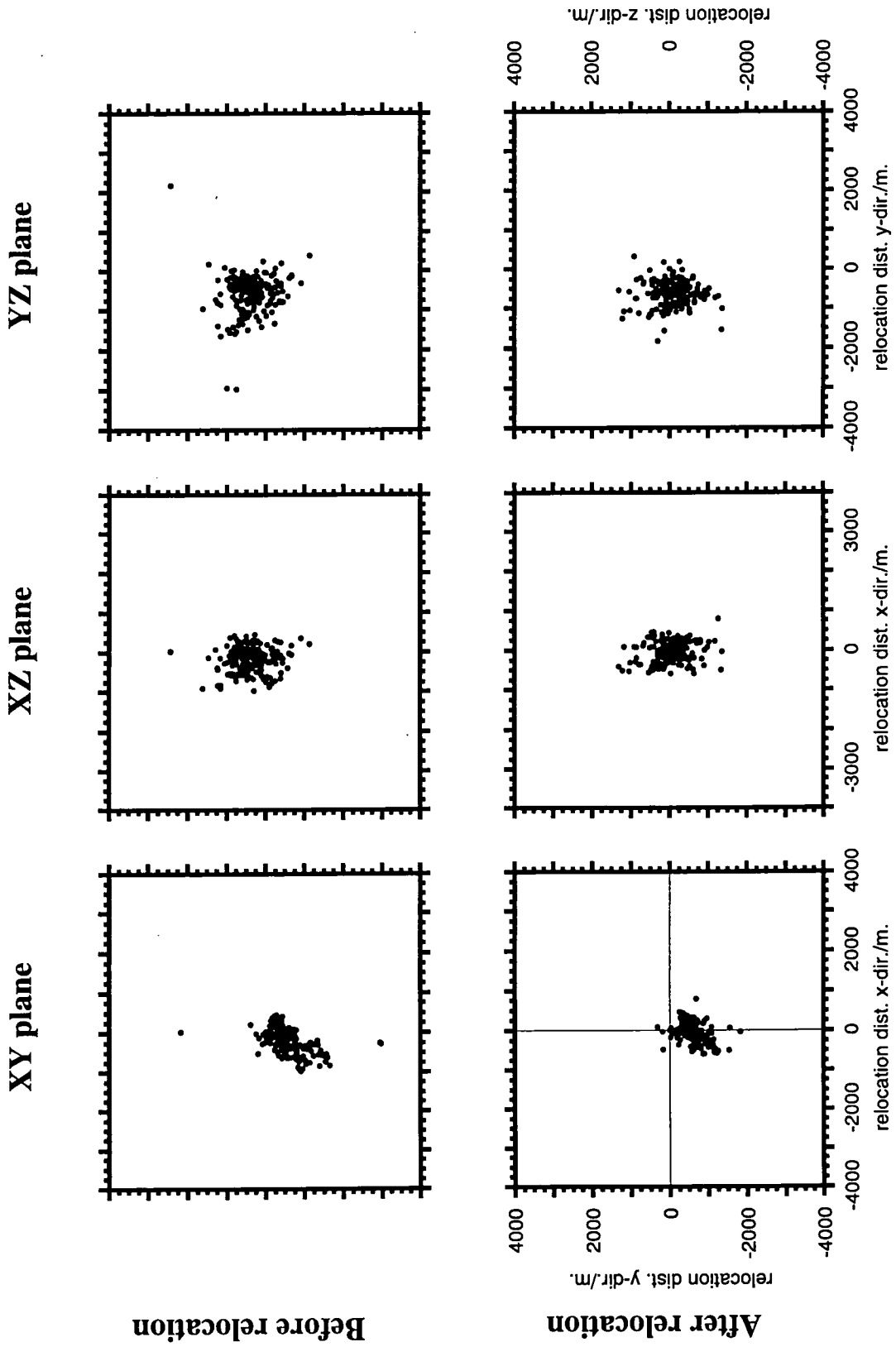

Figure 4.30: As for Figure 4.12 except for multiplet sr002_01_96.

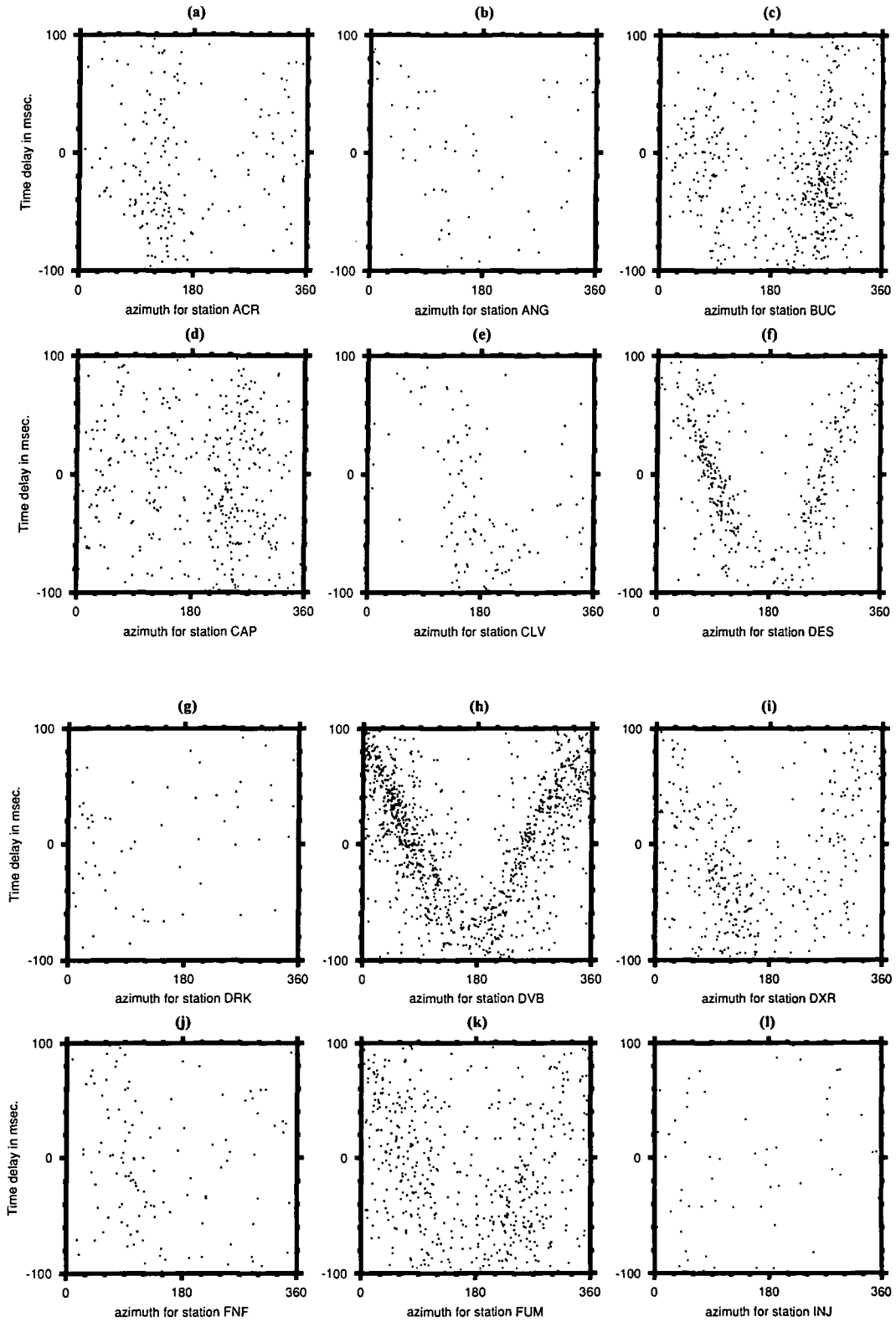

Figure 4.31: As for Figure 4.13 except for multiplet sr002_01_96.

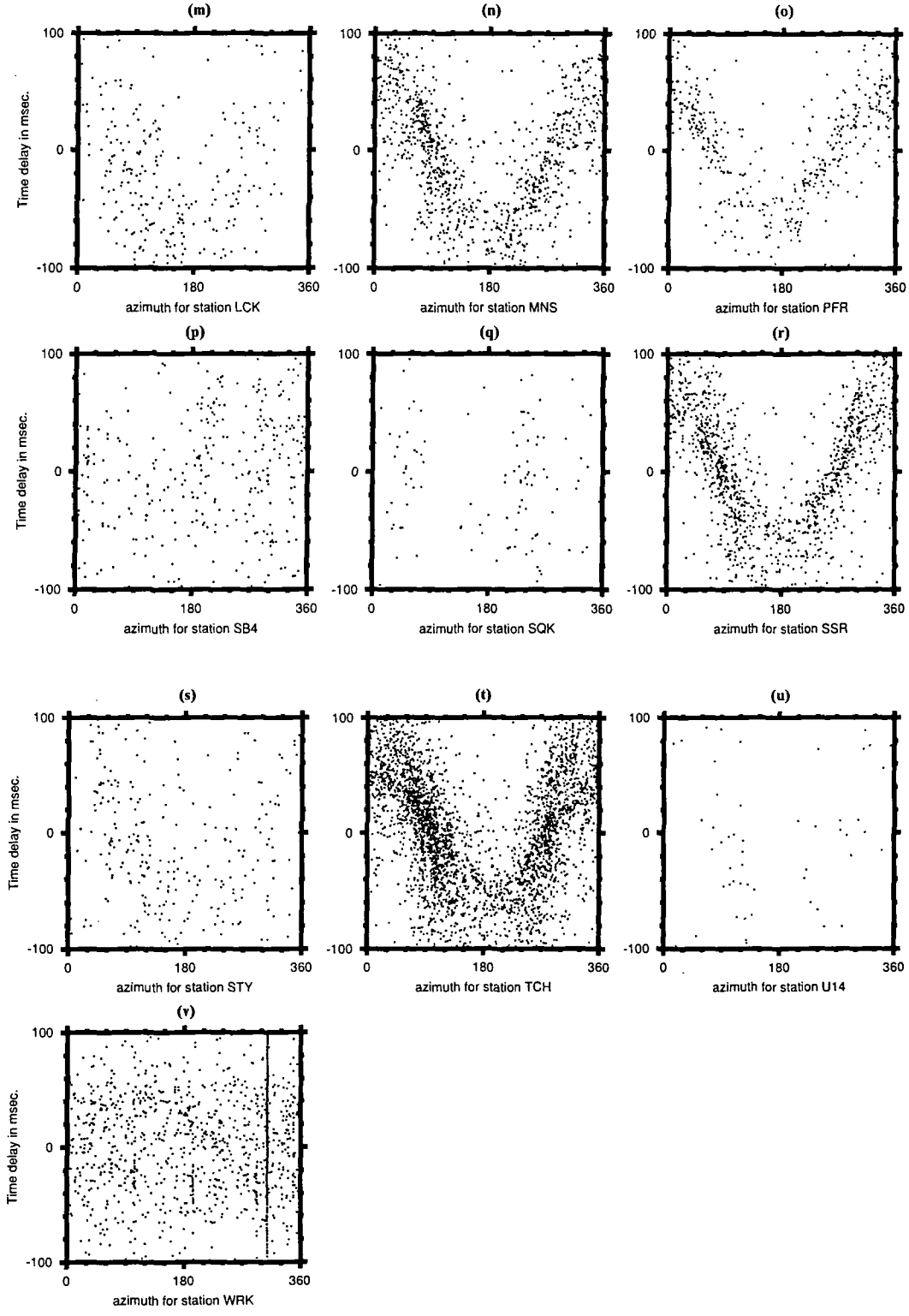

Figure 4.31 continued.

(a)

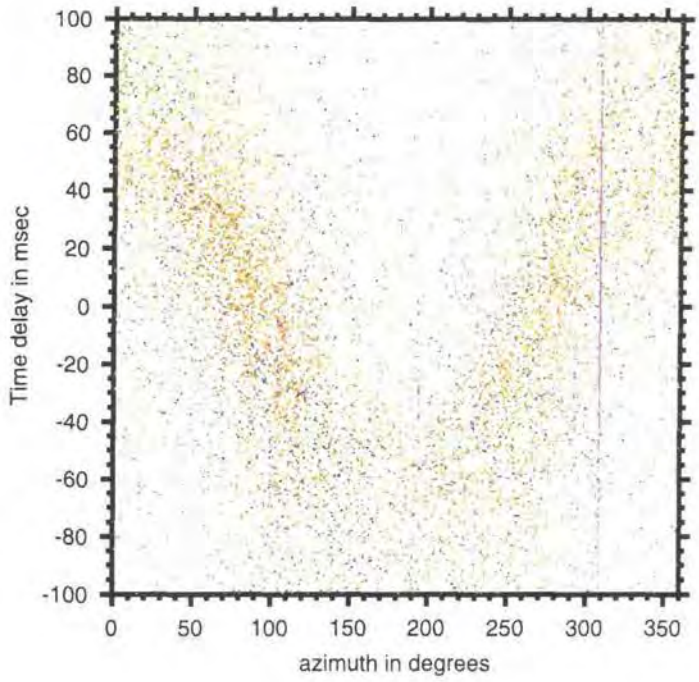

(b)

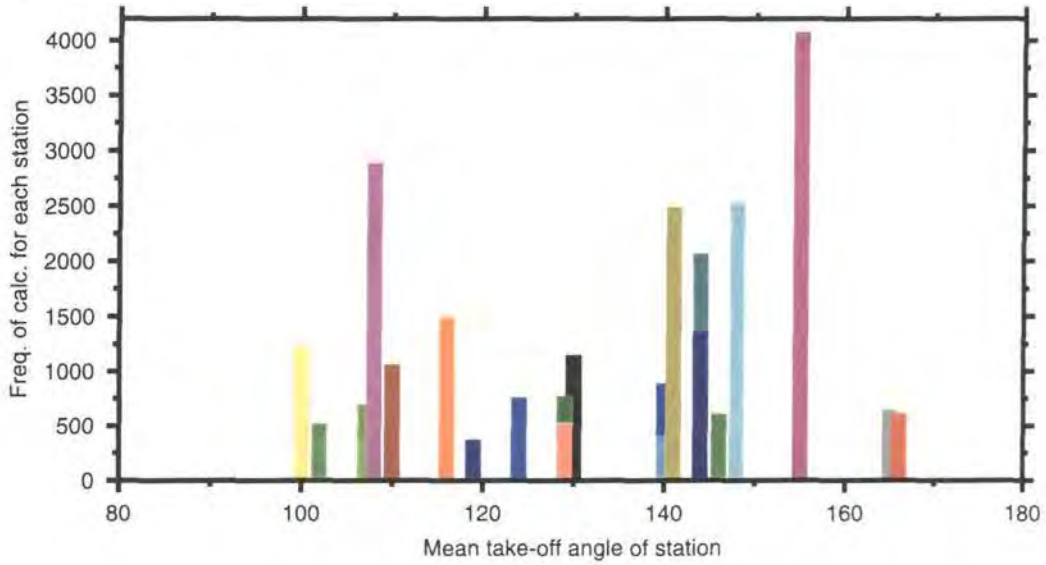

Stations with respect to colour coding for multiplet sr002_01_96 :

ACR	ANG	BUC	CAP	CLV	DES	DRK
DVB	DXR	FNF	FUM	[illegible]	LCK	MNS
PFR	[illegible]	SQK	[illegible]	STY	TUH	[illegible]
WRK						

Figure 4.32: As for Figure 4.14 except for multiplet sr002_01_96.

4.31v), the cosine plot for this station was a very poor miscalculation of the average inter event vector azimuth. Relocations were performed with and without station WRK, but the results did not improve significantly without station WRK.

The events were also processed using only the stations in the northern part of the network, multiplet sr002_01_96_T2. The relative relocation program exited after two iterations and achieved an RMS of 5.6 ms. The results showed tighter clusters than for multiplet sr002_01_96 (Figure 4.33). The cosine plots for this multiplet are very poor with no station showing a coherent pattern (Figures 4.34 and 4.35a). The most frequently used stations were FUM and STY (Figure 4.35b). In general, stations with good waveforms and good mean take-off angles were found to yield poor cosine plots (Figure 4.36).

4.4.3 Region sr003

Region sr003 contains 5467 events. 123 events displayed a coherency threshold of 95%, and the estimated error in relocation is approximately 1% (Figure 4.37). The coherency matrix revealed numerous very small multiplets that were sparsely distributed in time (Figure 4.38). The absolute locations show that multiplet sr003_01_95 is elongated in the direction of the dominant tectonic trend (Figure 4.39). The relative relocation program iterated twice and yielded an RMS of 5.7 ms. The resulting seismic volume is spherical in morphology and more tightly clustered than the original relocations (Figure 4.40). The seismic volume is about 1 km in diameter. The cosine plots exhibit a lot of scatter and the best results are for station SSR (Figure 4.41r) and to a lesser extent for stations CAP and LCK (Figure 4.41d, m). As illustrated in the composite cosine plot (Figure 4.42a) these stations were frequently used in the relocation process. The mean take-off angles from these stations are greater than 100° which is good for time-delay calculations (Figure 4.42b). In comparison to multiplet sr002_01_96, the good spatial coverage of stations for sr003_01_95 results in good relative relocation results. However, good waveforms but poor cosine plots were again seen to be the pattern (Figure 4.43).

Figure 4.33: As for Figure 4.12 except for multiplet sr002_01_96_T2.

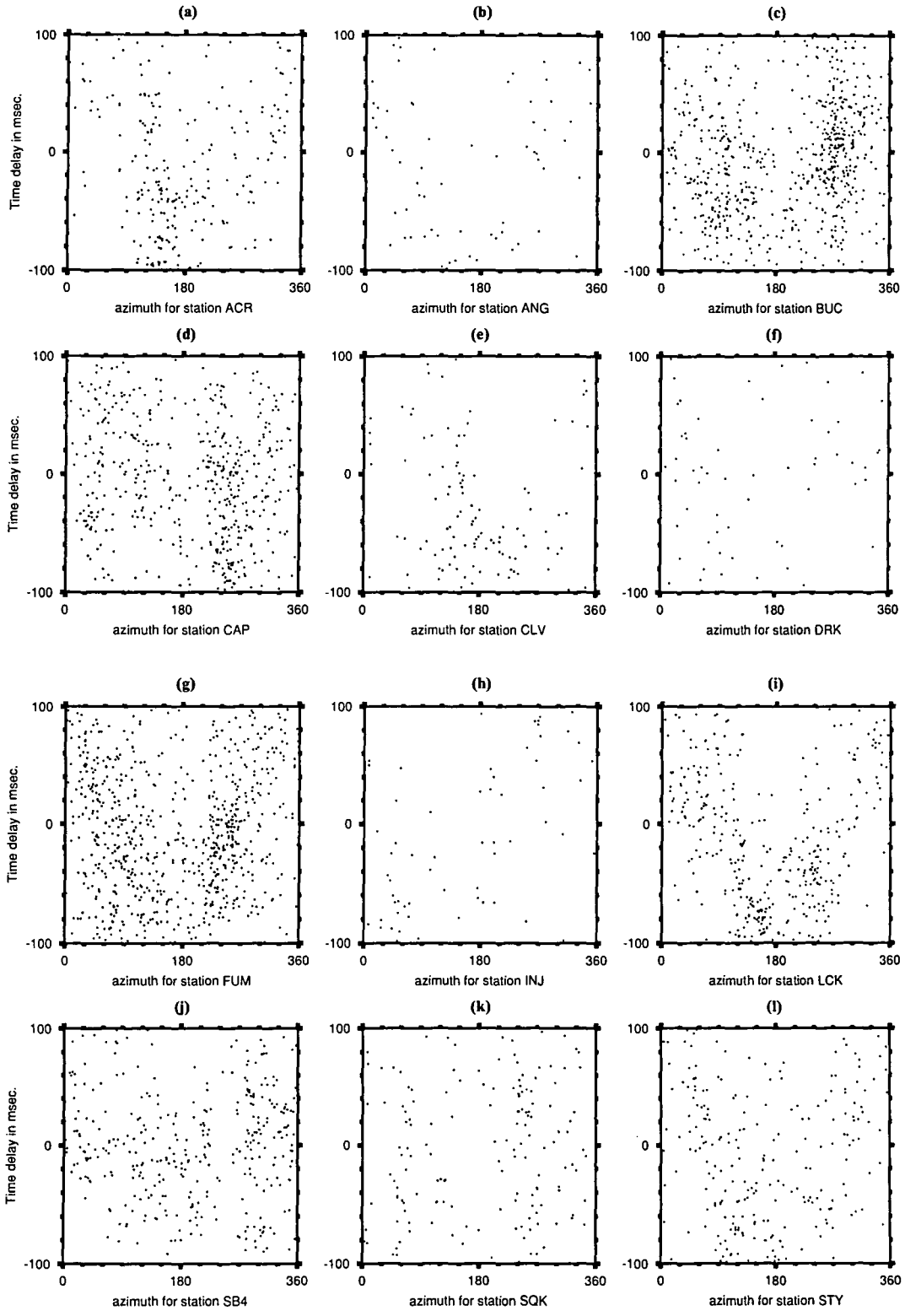

Figure 4.34: As for Figure 4.13 except for multiplet sr002_01_96_T2.

(a)

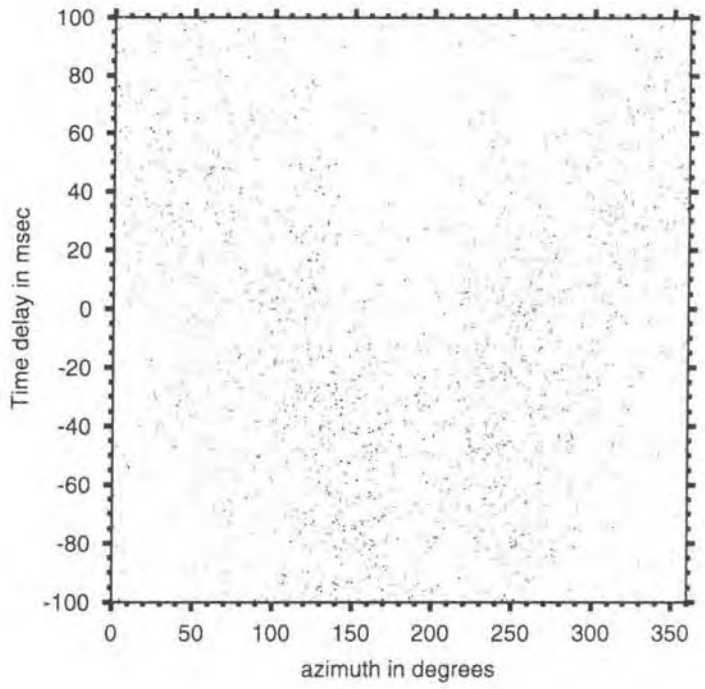

(b)

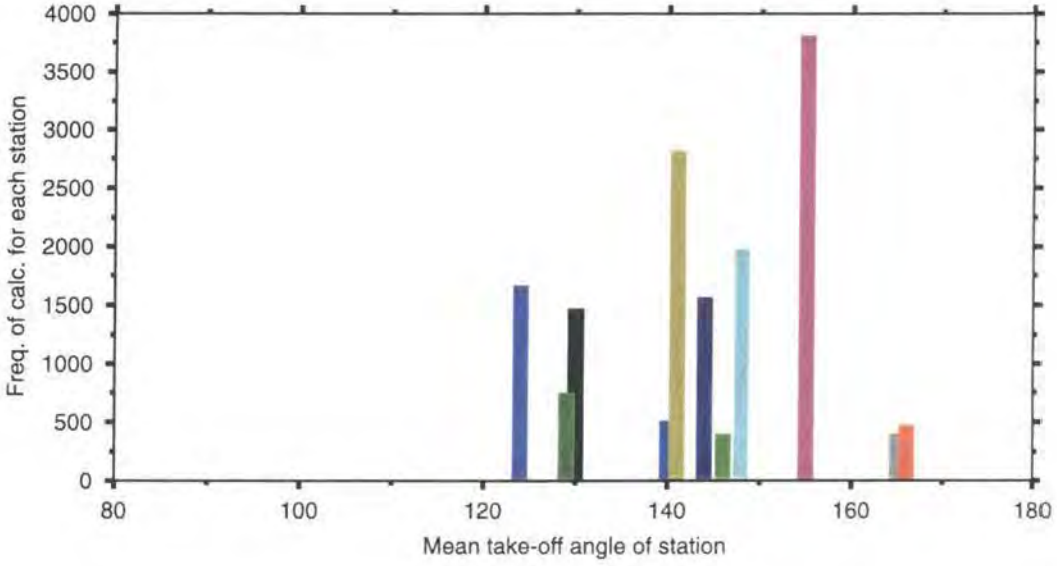

Stations with respect to colour coding for multiplet sr002_01_96_T2 :

ACR	ANG	BUC	CAP	CLV	DES	DRK
DVB	DXR	FNF	HOM	INV	LCK	MNS
PER	[illegible]	SQK	[illegible]	STY	TCH	[illegible]
WRK						

Figure 4.35: As for Figure 4.14 except for multiplet sr002_01_96_T2.

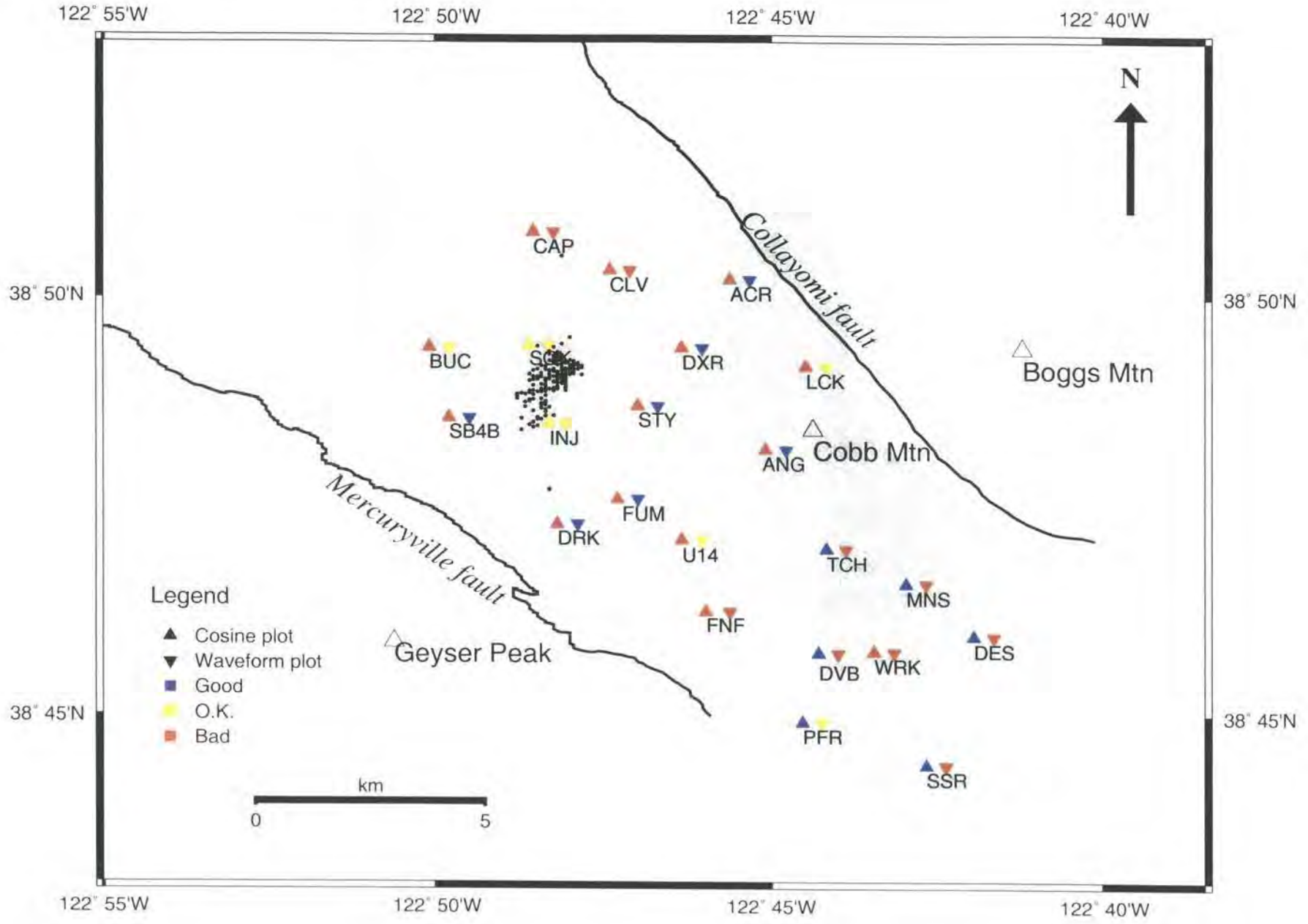

Figure 4.36: As for Figure 4.26 except for multiplet sr002_01_96.

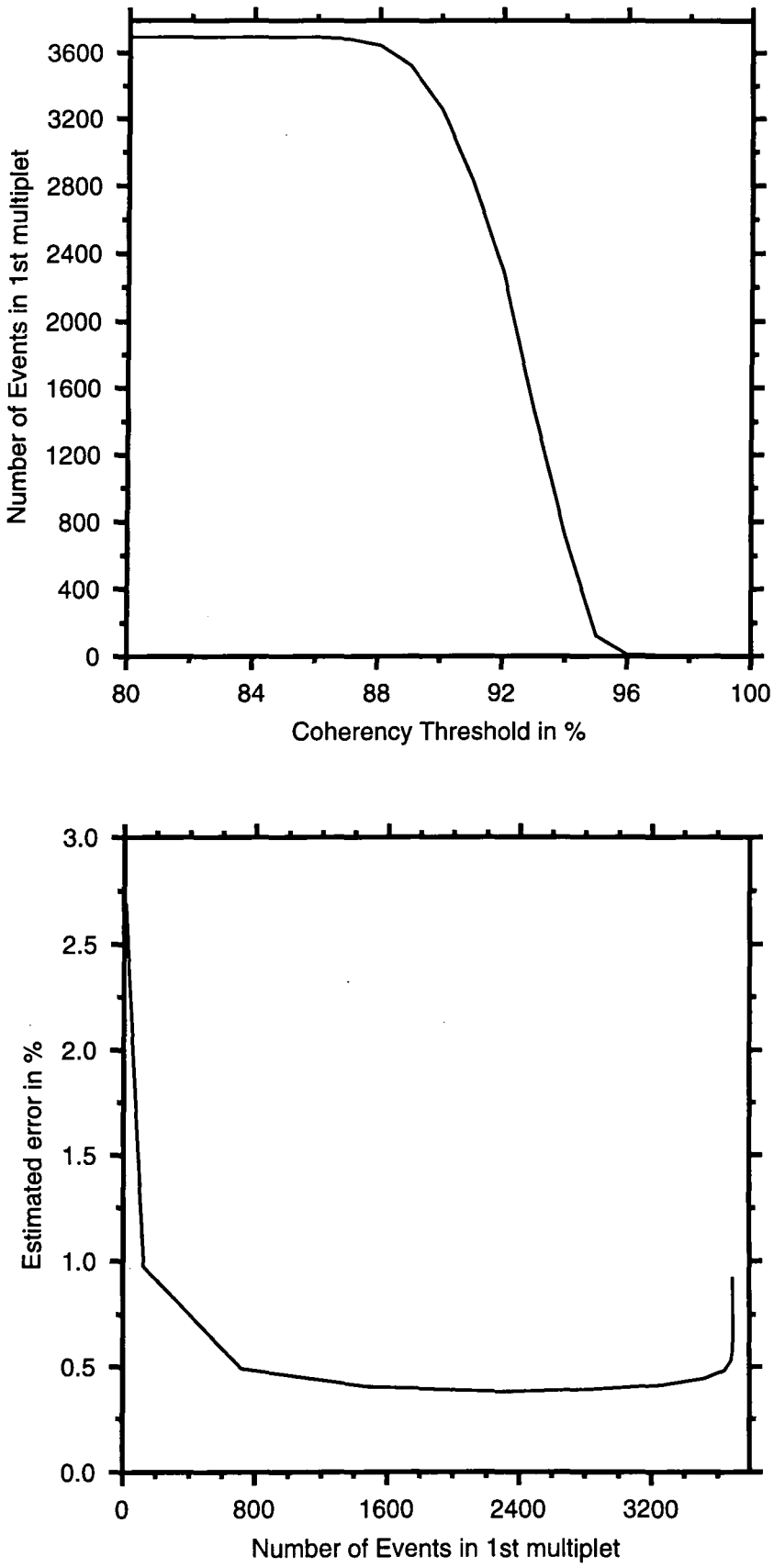

Figure 4.37: As for Figure 4.9 except for region sr003.

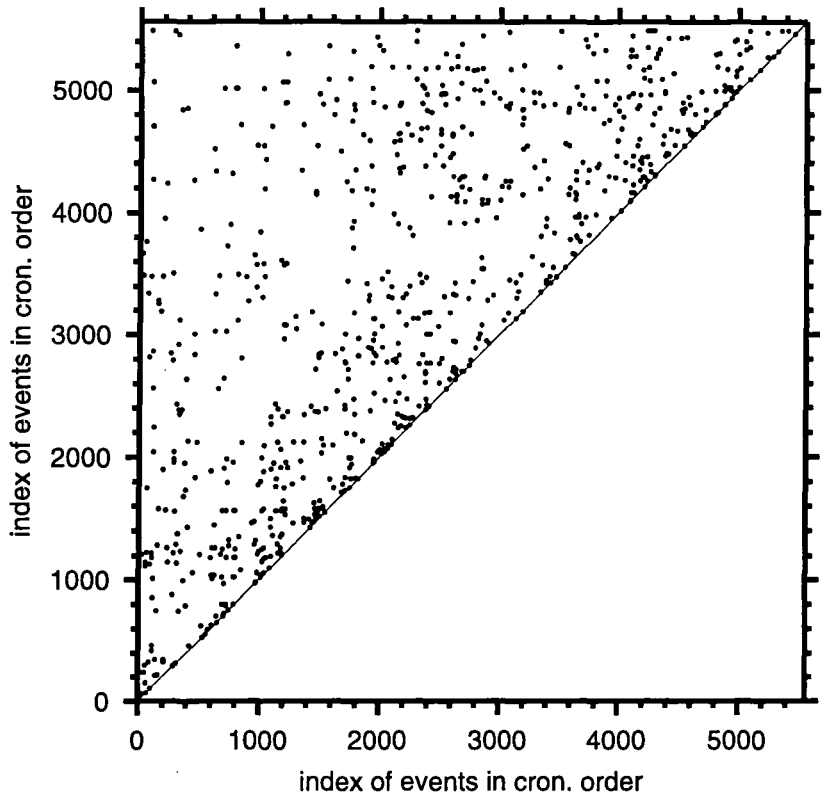

Figure 4.38: As for Figure 4.10 except for area sr003 for 95% coherency threshold.

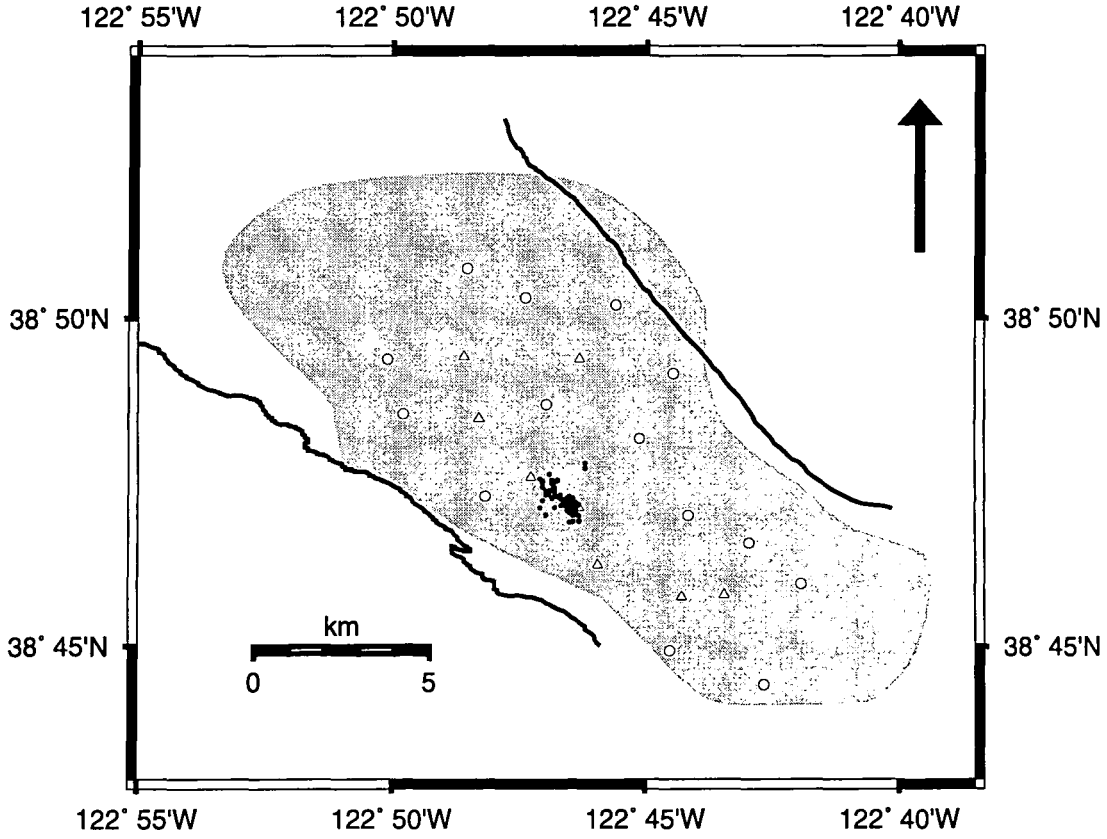

Figure 4.39: As for Figure 4.11 except for multiplet sr003_01_95.

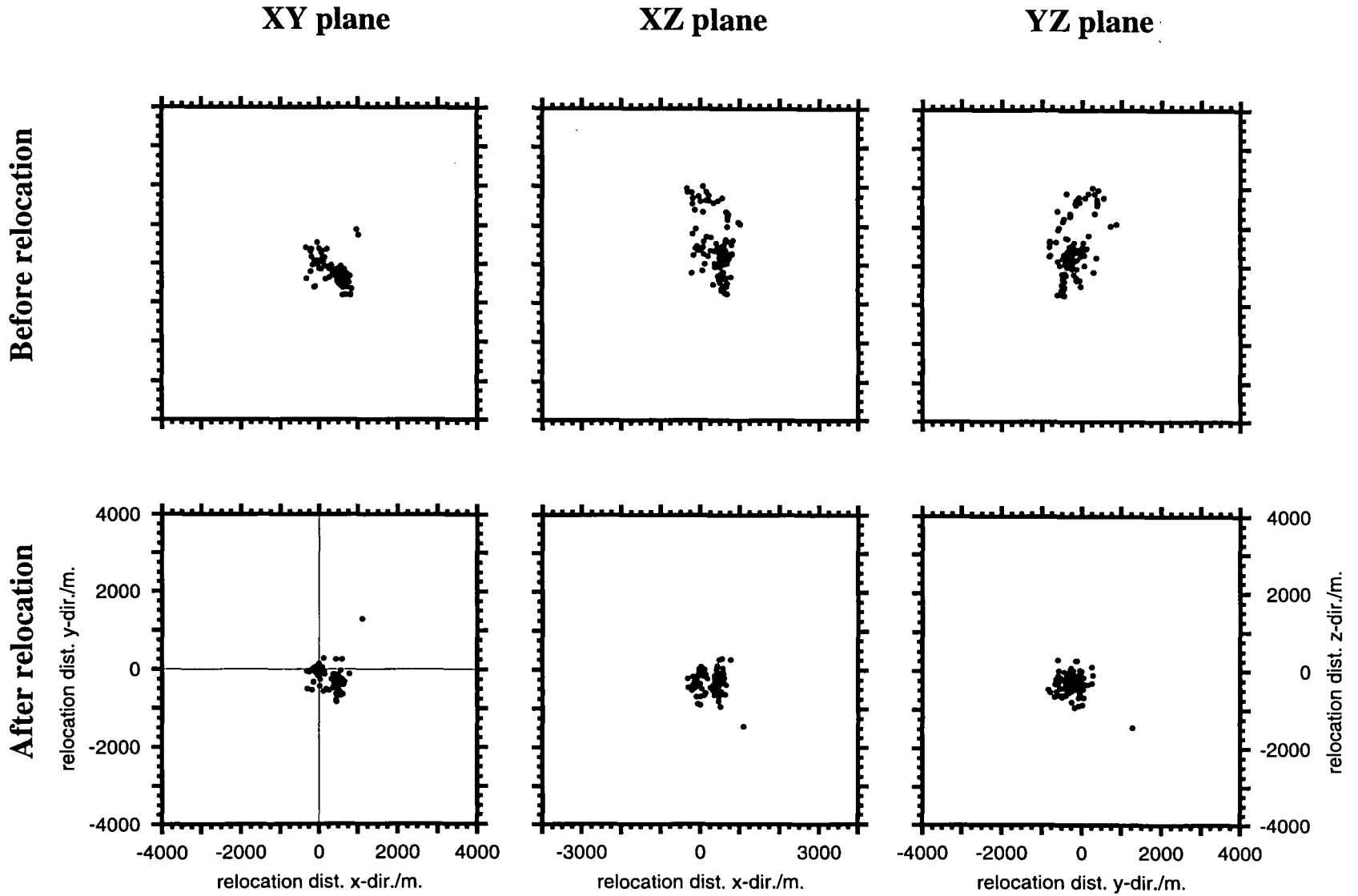

Figure 4.40: As for Figure 4.12 except for multiplet sr003_01_95.

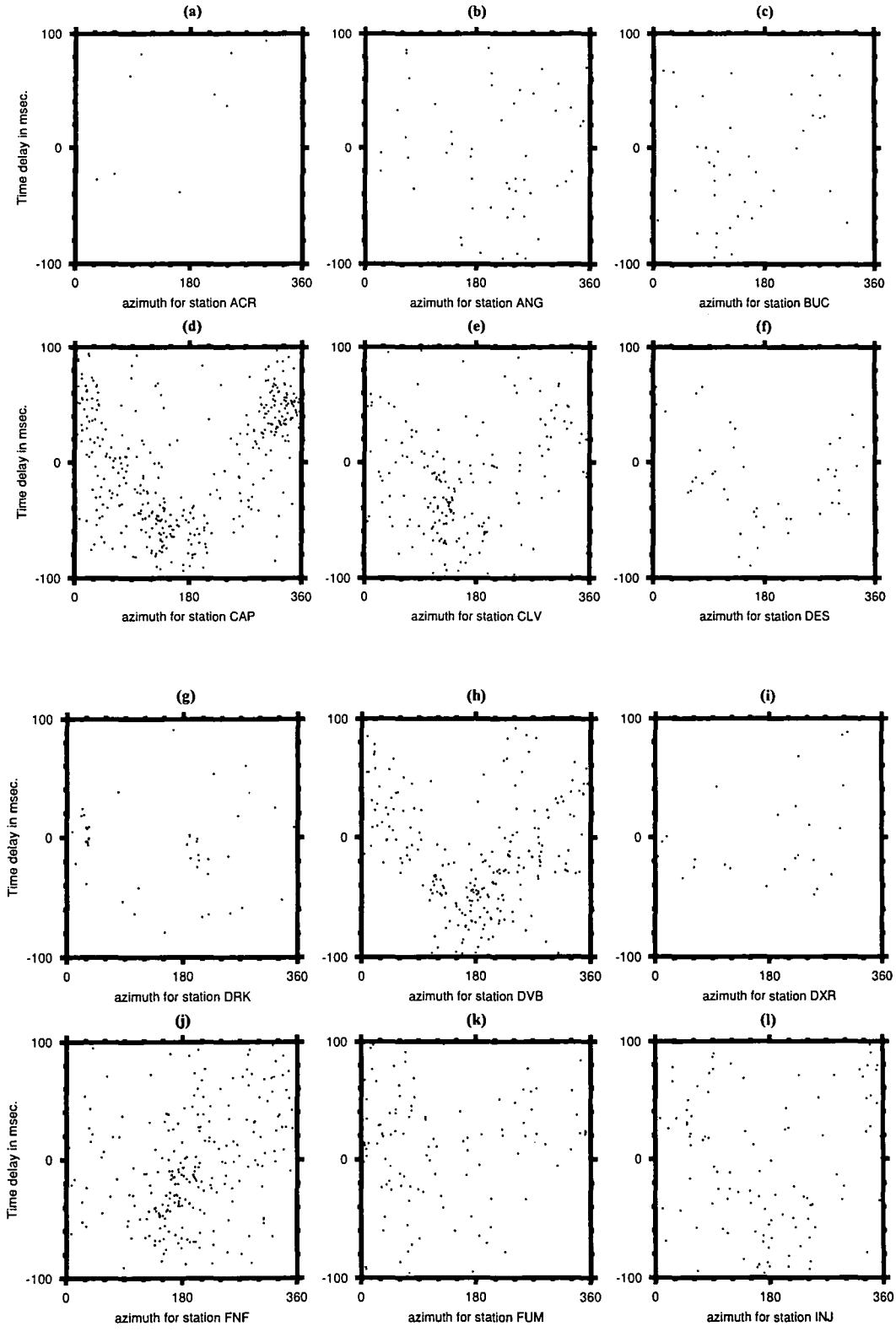

Figure 4.41: As for Figure 4.13 except for multiplet sr003_01_95.

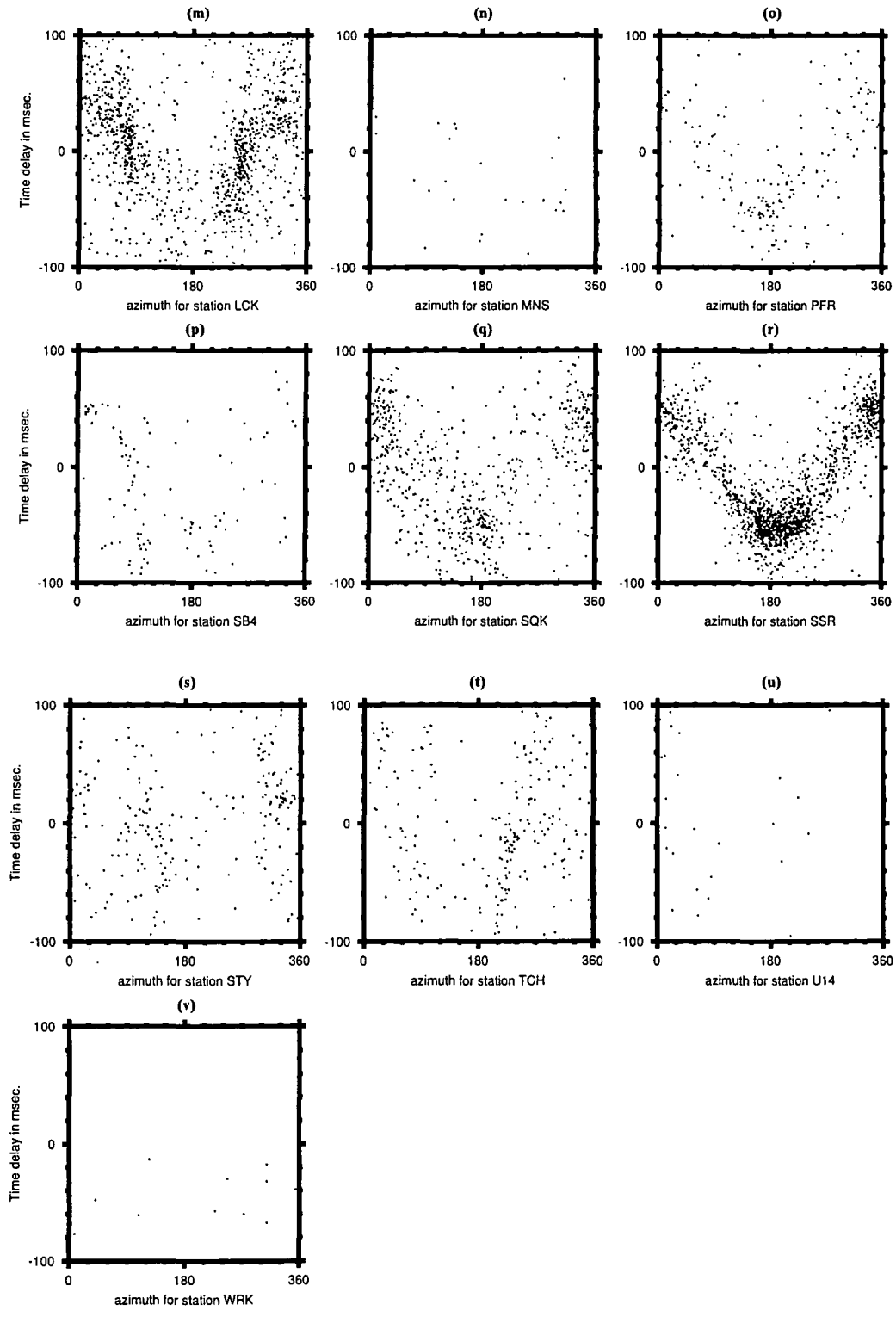

Figure 4.41 continued.

(a)

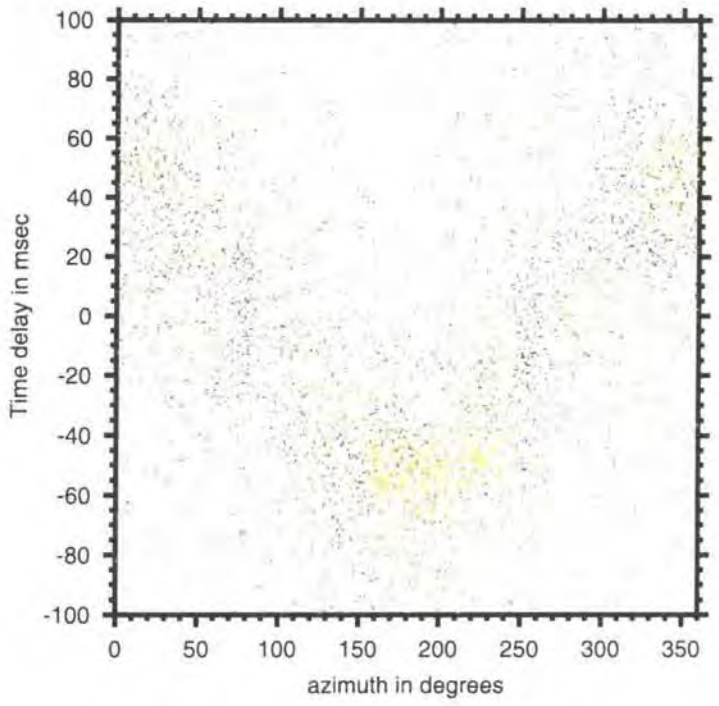

(b)

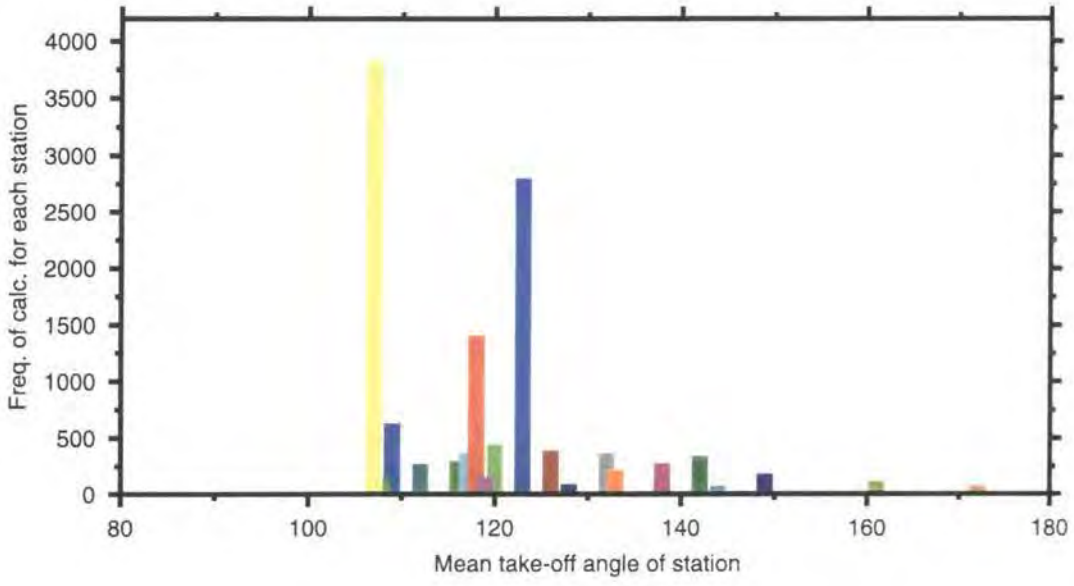

Stations with respect to colour coding for multiplet sr003_01_95 :

ACR	ANG	BUC	CAP	CLV	HES	HRK
DVB	DXR	FNF	HUM	ISA	LCK	MNS
PDR	RDSD	SQK	[illegible]	STY	TCH	ULA
WRK						

Figure 4.42: As for Figure 4.14 except for multilet sr003_01_95.

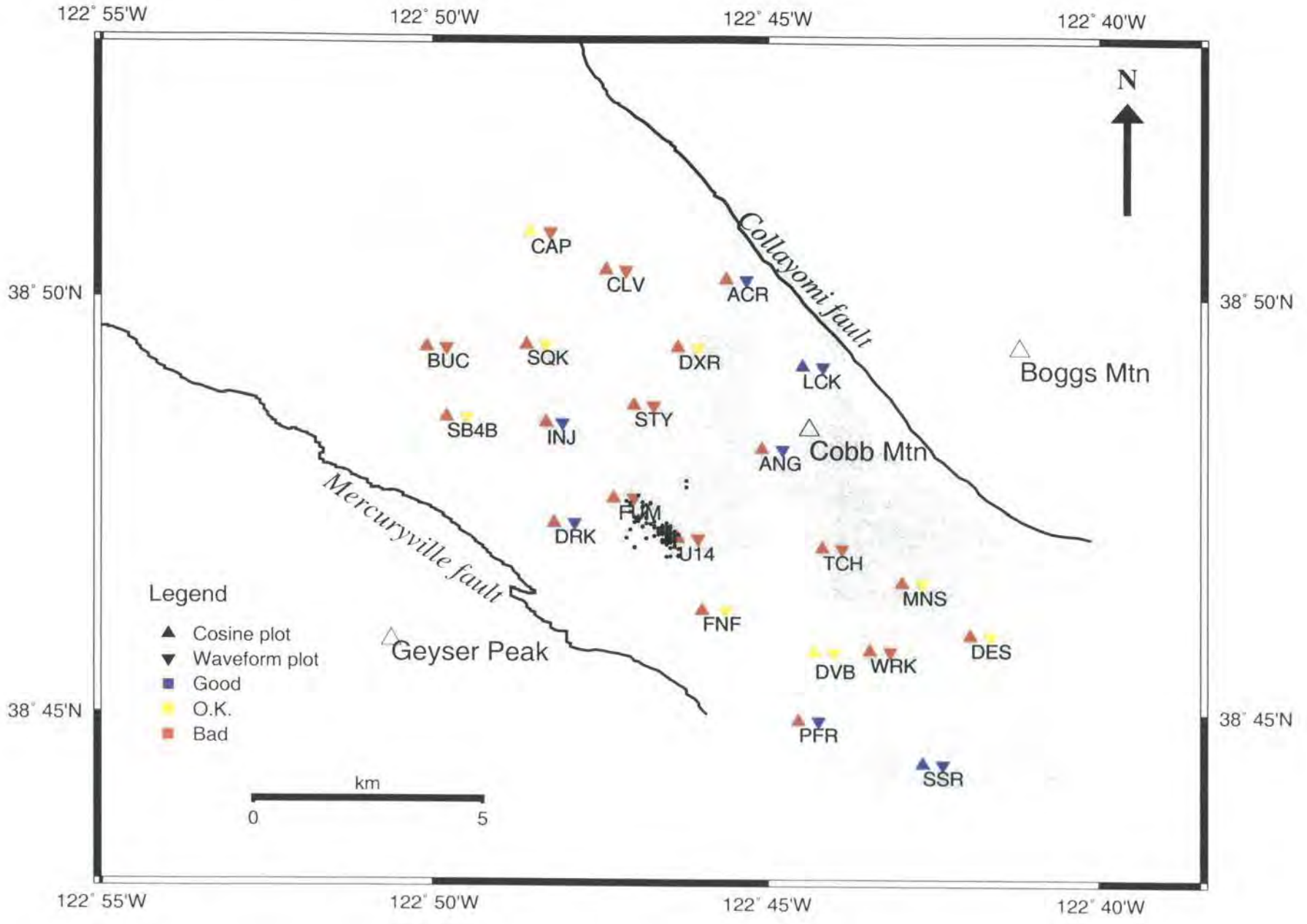

Figure 4.43: As for Figure 4.26 except for multiplet sr003_01_95.

4.4.4 Region sr004

A multiplet containing 134 events with a coherency threshold of 95% and an estimated statistical error of 0.9% was identified for region sr004 (Figure 4.44). There are smaller multiplets for a 95% coherency threshold (Figure 4.45). The absolute events locations show that sr004_01_95 contains three major sub-clusters (Figure 4.46). The relative relocation process required two iterations and resulted in an RMS of 5.0 ms, and gave a clustered event distribution with some elongation in the north-south direction (Figure 4.47). Although there is a lot of scatter in the cosine plots, stations BUC, CAP, SB4B and SSR show fairly good results (Figure 4.48c, d, p, r and Figure 4.49). Most stations with good waveforms yielded poor cosine plots (Figure 4.50).

Considering the spatial extent of the multiplet, its location and station geometry, multiplet sr004_01_95 gave the best results of the multiplets studied. A subset of stations that yielded high-frequency, strong signals was used to create a new muliplet called sr004_01_95_Tt. The stations selected were ACR, ANG, CLV, DES, DRK, FNF, LCK, MNS, PFR which have a wide spatial coverage and therefore varying take-off angles. Relative relocation of sr004_01_95_Tt was completed after two iterations with an RMS of 3.2 ms (Figure 4.51). Also, the cosine plots were very similar to those observed for these stations in multiplet sr004_01_95, except for station SSR, which improved and became very clear (Figure 4.52). Station SSR was also the most frequently used station (Figure 4.53). An average value of 4.5 km/s was selected as the optimum velocity, and was taken from the 3-D tomography structure near the hypocentre of the multiplet.

These results show that the use of only stations with visually-identified good waveforms does not necessarily improve the relative relocations significantly, although there is an improvement of 1.8 ms in the RMS of the multiplet. Also, poor cosine plots do not necessarily reflect insignificant improvements in the locations. However, noise in the data tends to be suppressed by the weighting scheme and averaged out in the inversion process.

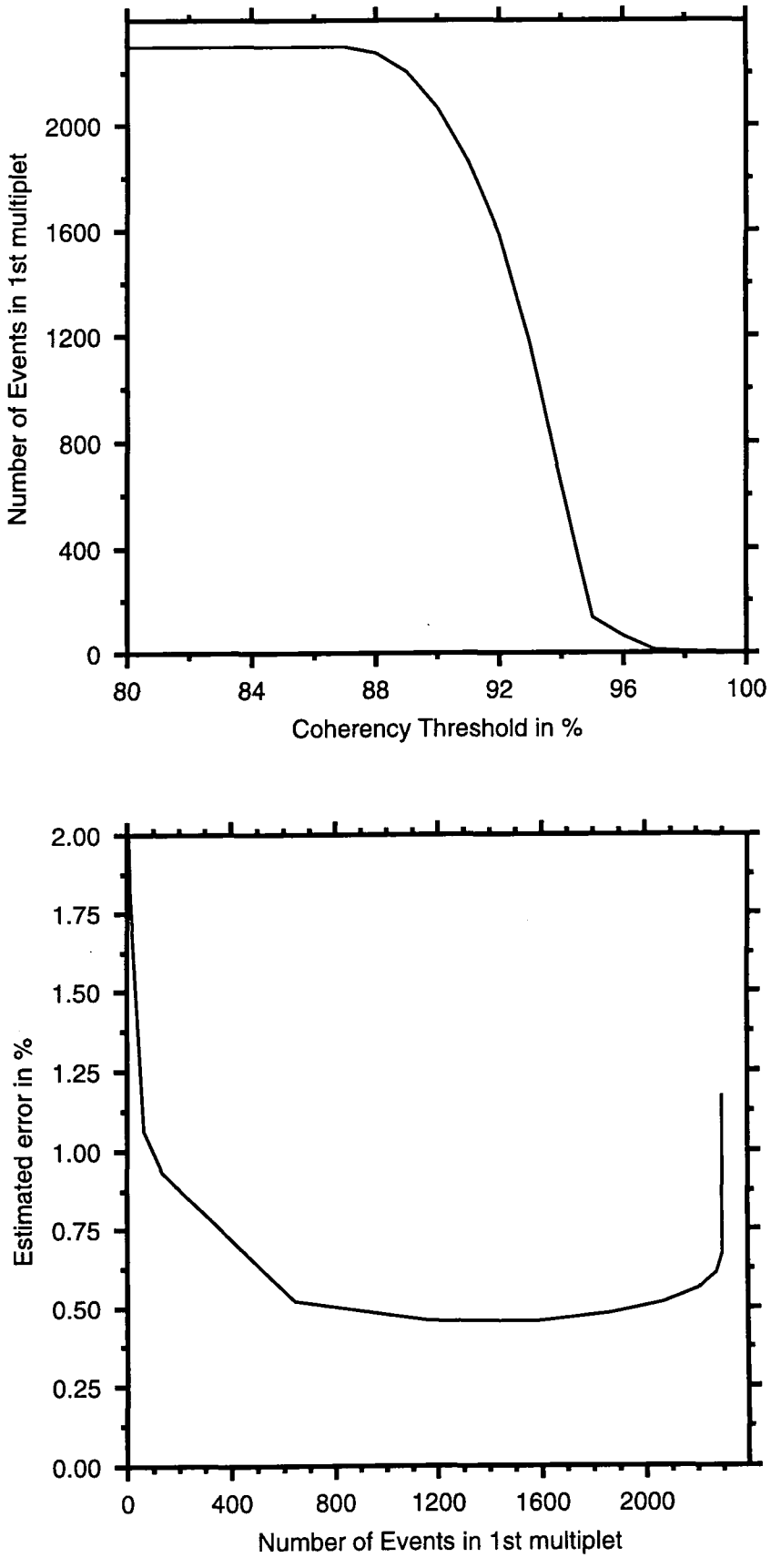

Figure 4.44: As for Figure 4.9 except for region sr004.

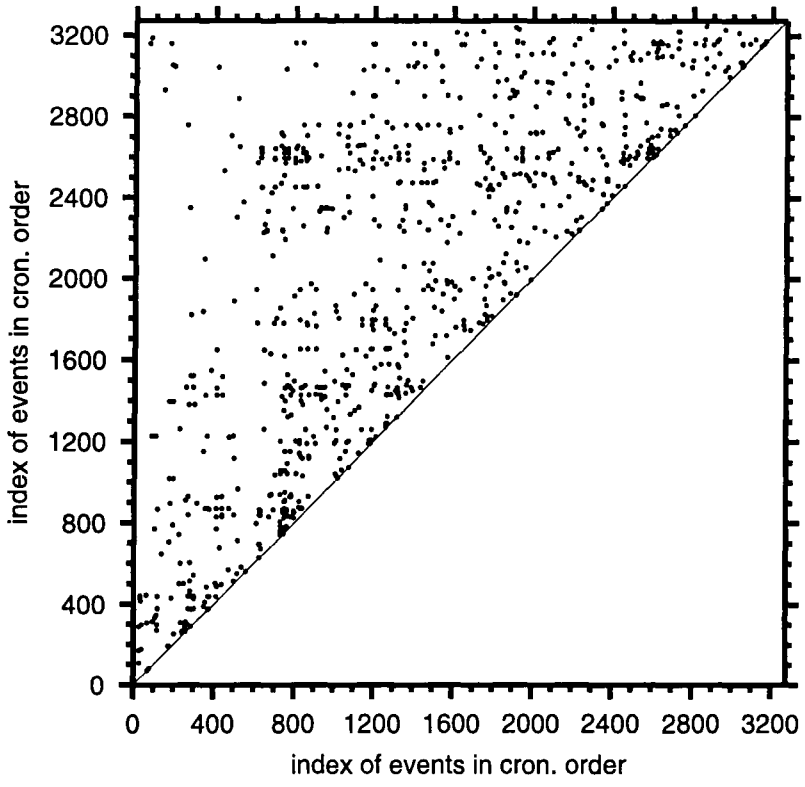

Figure 4.45: As for Figure 4.10 except for area sr004 for 95% coherency threshold.

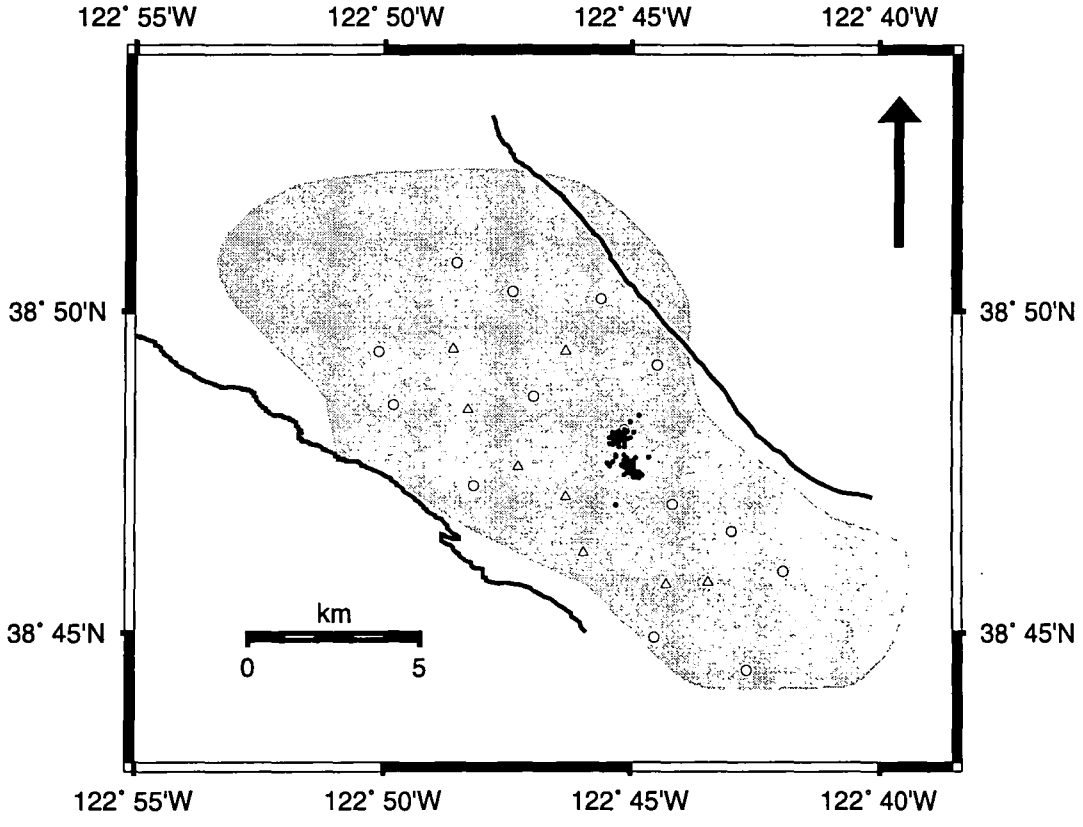

Figure 4.46: As for Figure 4.11 except for multiplet sr004_01_95.

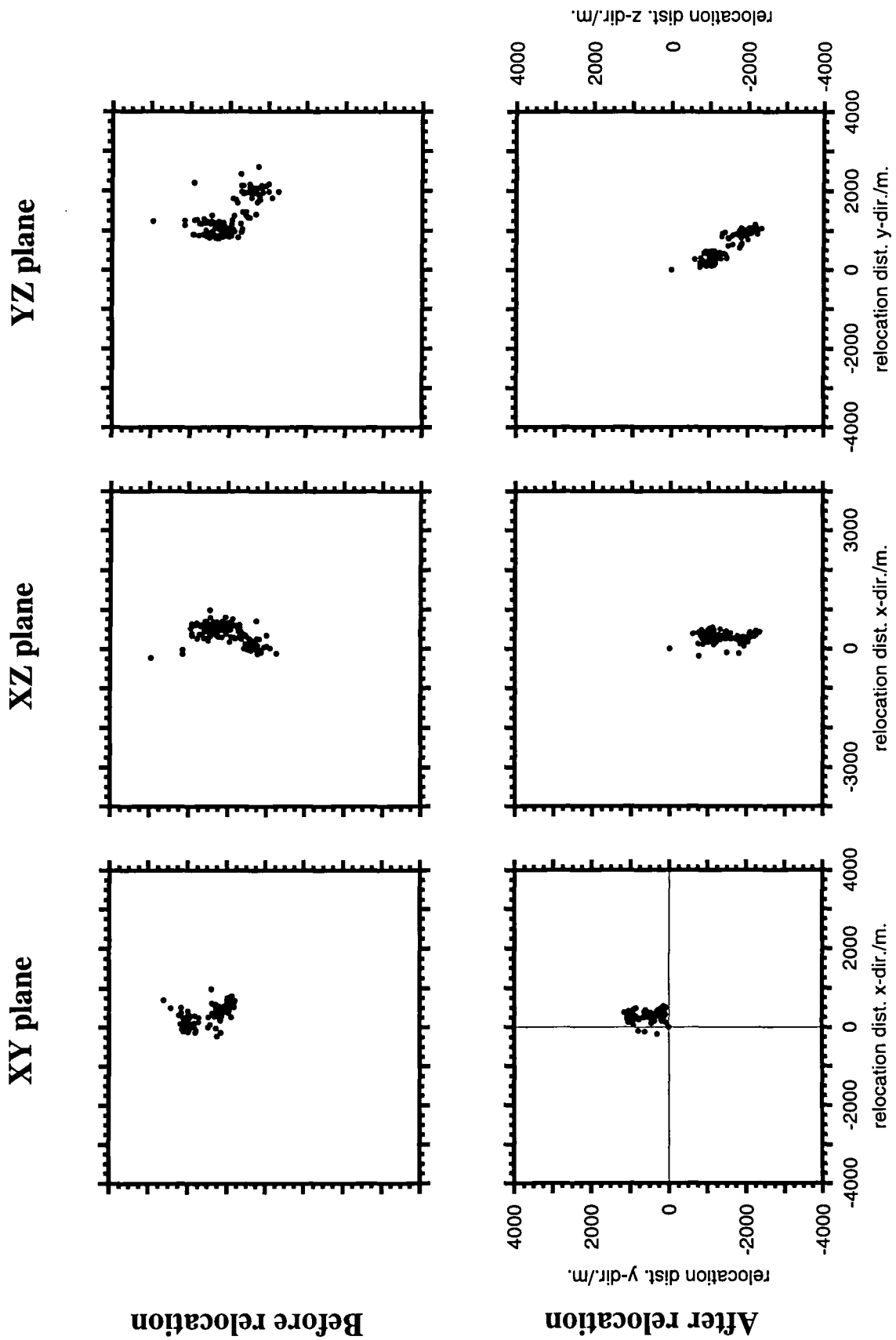

Figure 4.47: As for Figure 4.12 except for multiplet sr004_01_95.

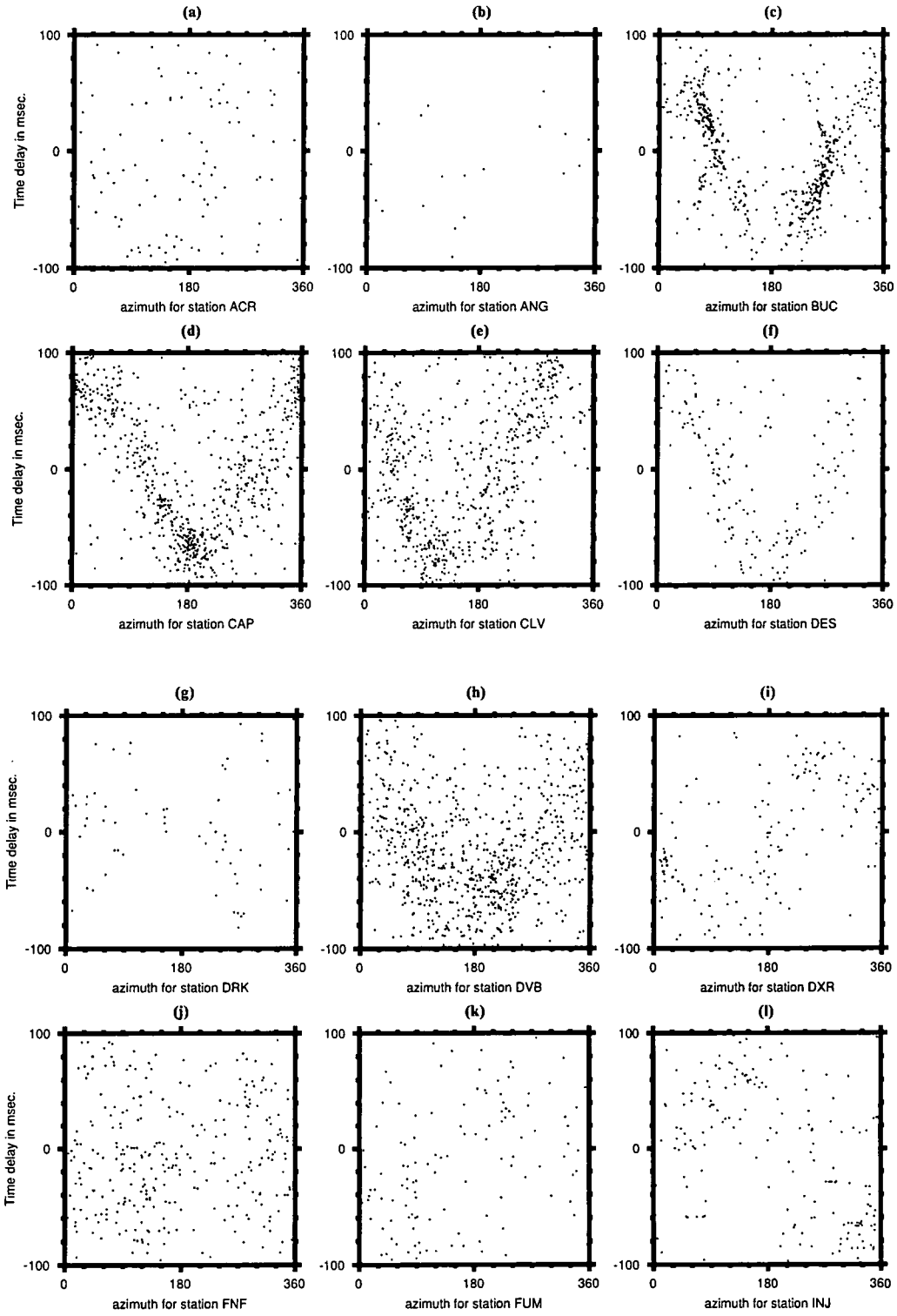

Figure 4.48: As for Figure 4.13 except for multiplet sr004_01_95.

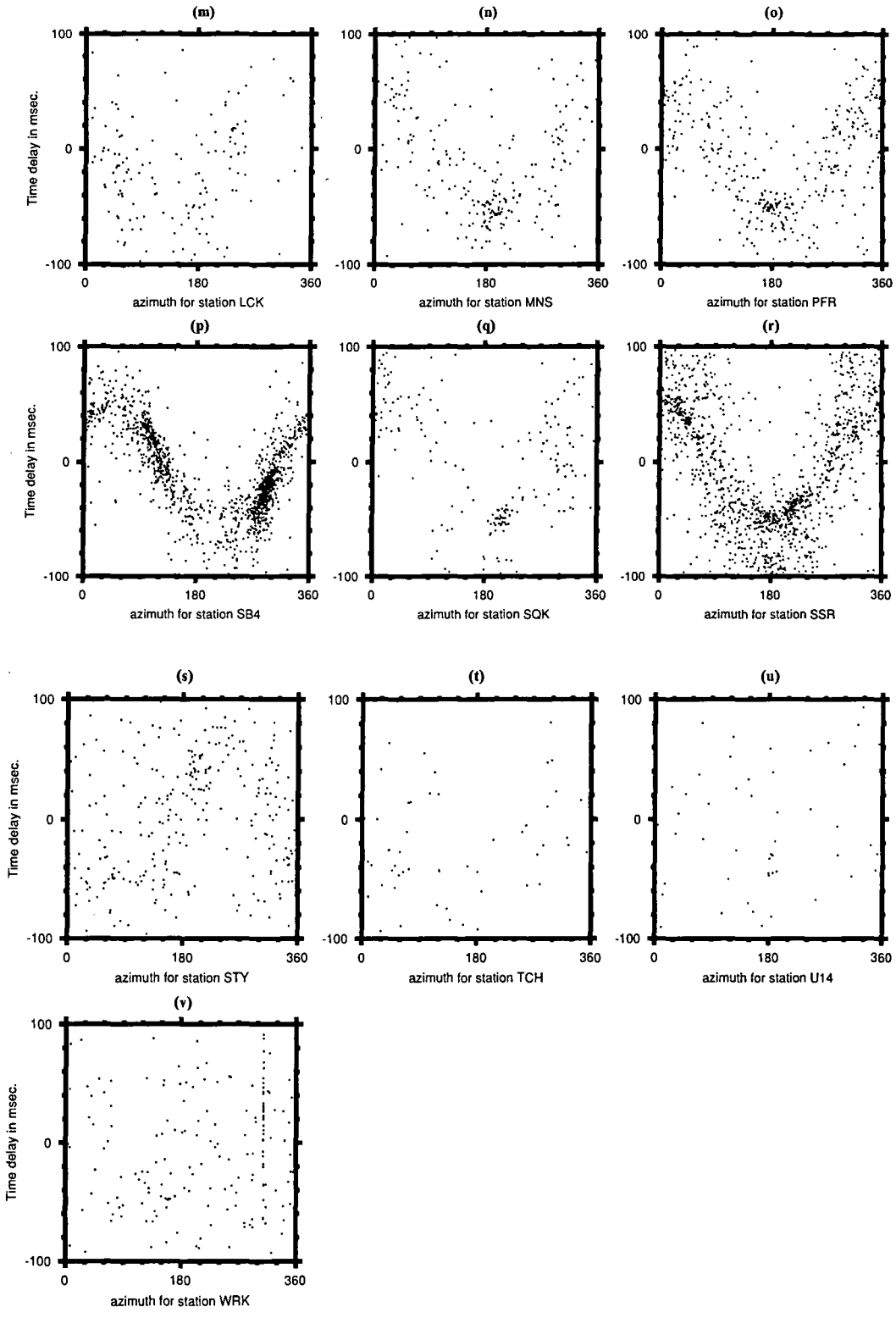

Figure 4.48 continued.

(a)

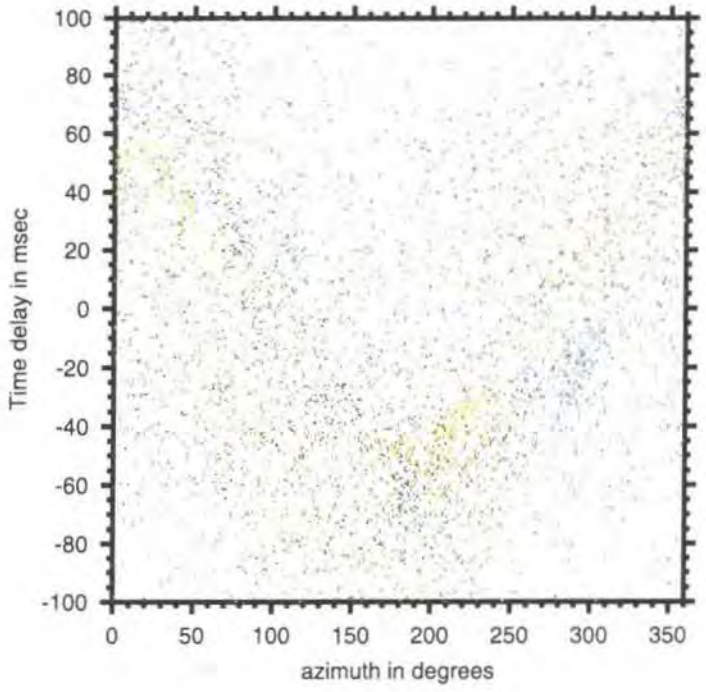

(b)

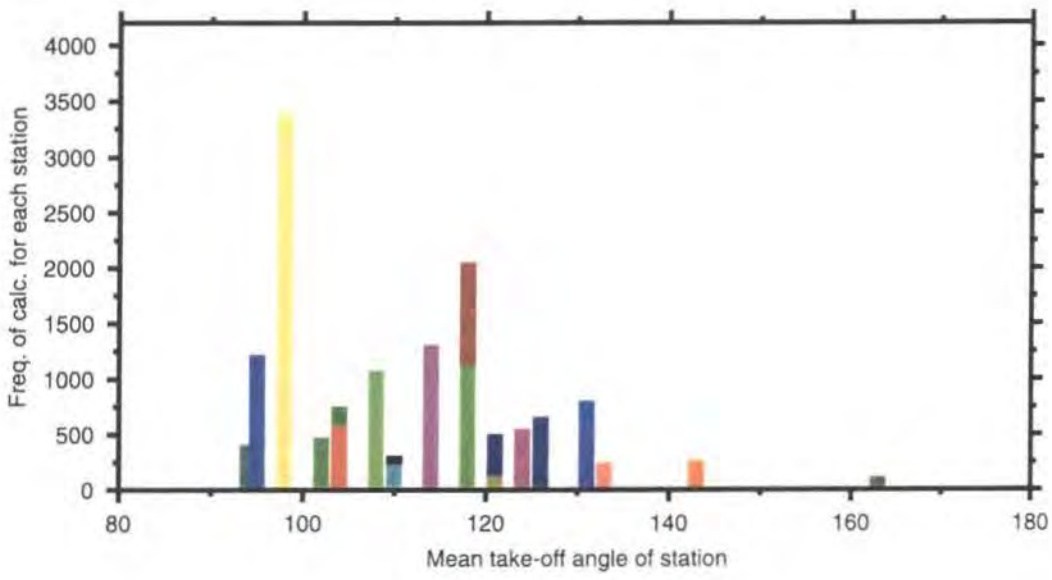

Stations with respect to colour coding for multiplet sr004_01_95 :

ACR	ANG	BUC	CAP	CLV	DBS	DRK
DVB	DXR	FNF	FUM	ISJ	LCK	MNS
PER	SHUB	SQK	[illegible]	STY	TCH	[illegible]
WRK						

Figure 4.49: As for Figure 4.14 except for multiplet sr004_01_95.

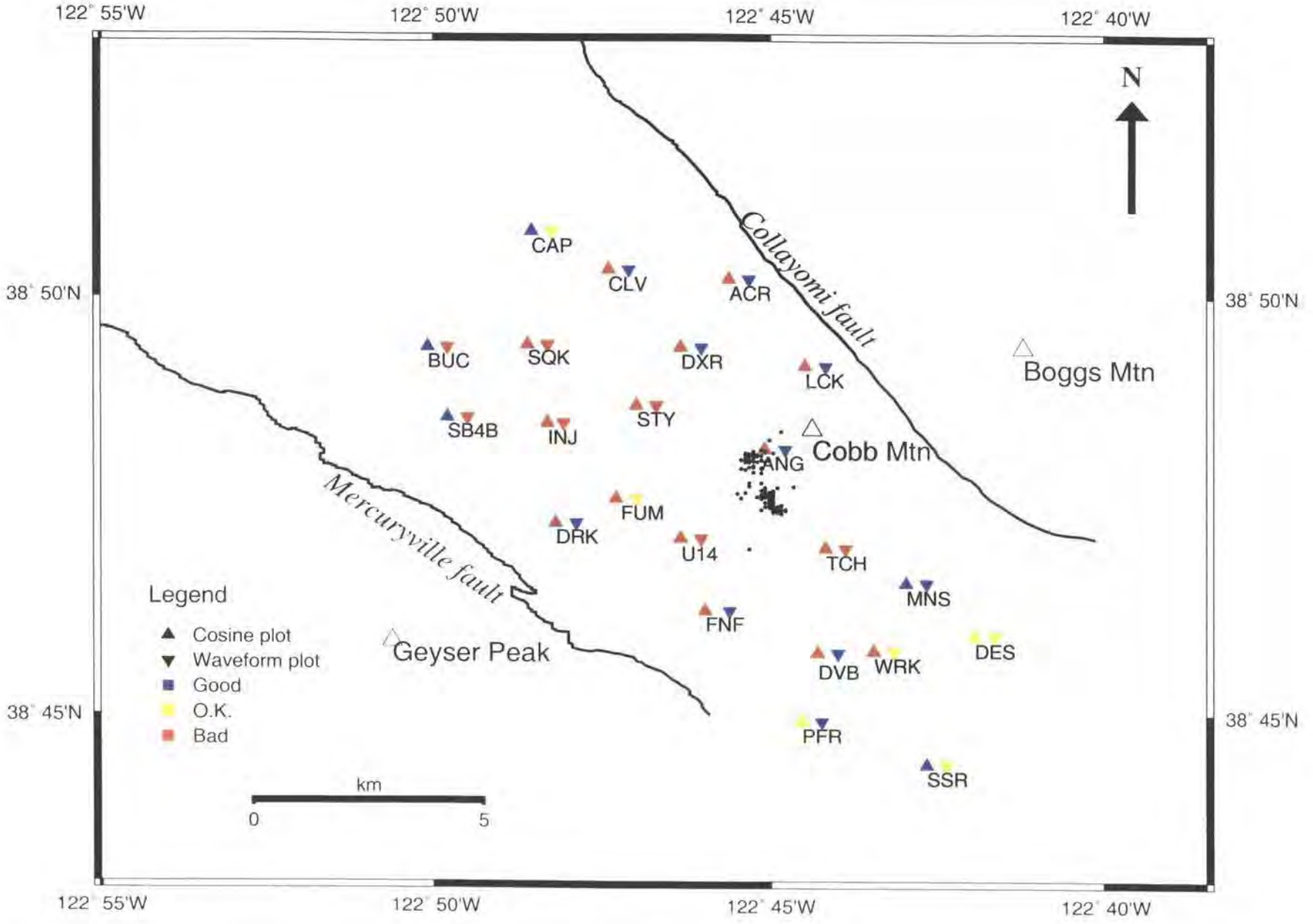

Figure 4.50: As for Figure 4.26 except for multiplet sr004_01_95.

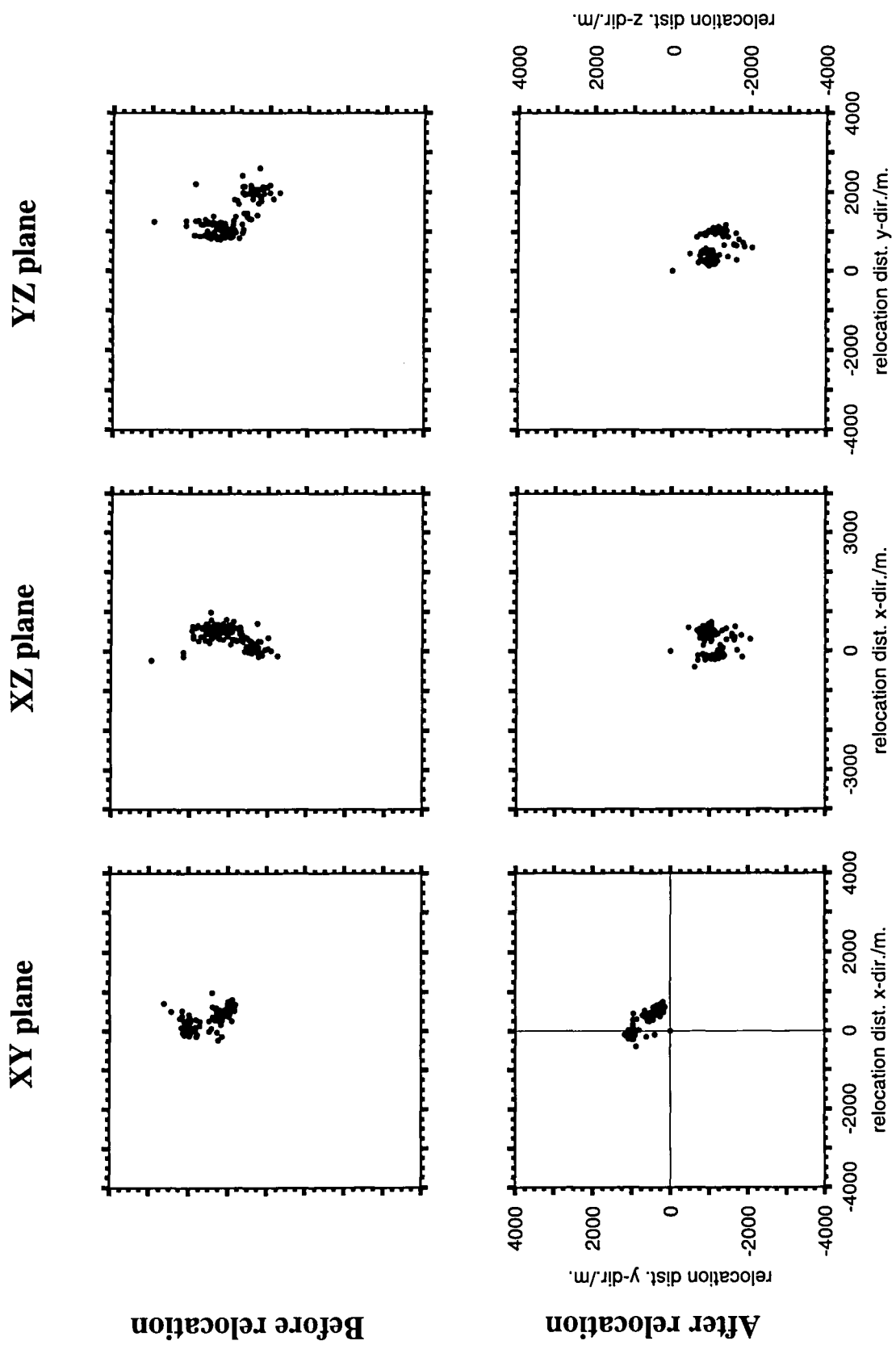

Figure 4.51: As for Figure 4.12 except for multiplet sr004_01_95Tt.

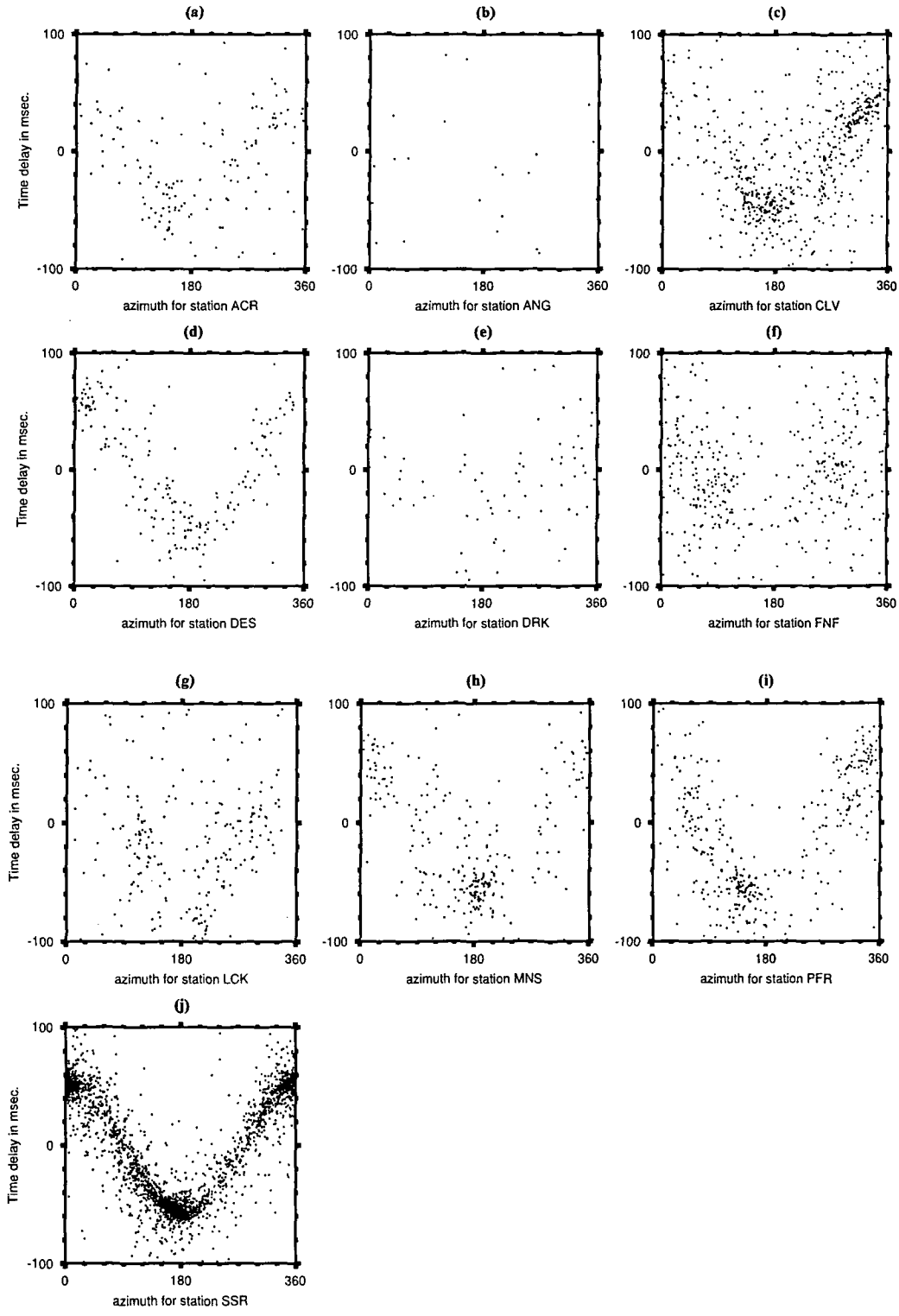

Figure 4.52: As for Figure 4.13 except for multiplet sr004_01_95_Tt.

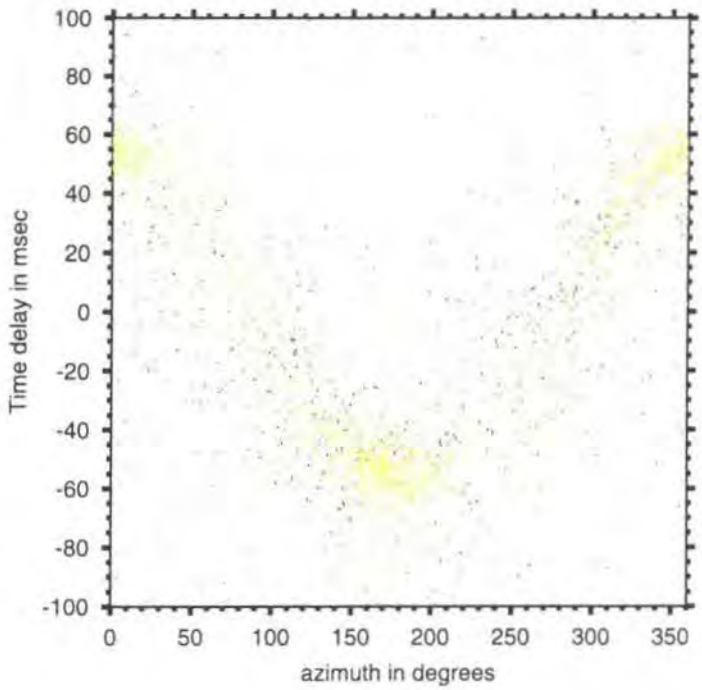

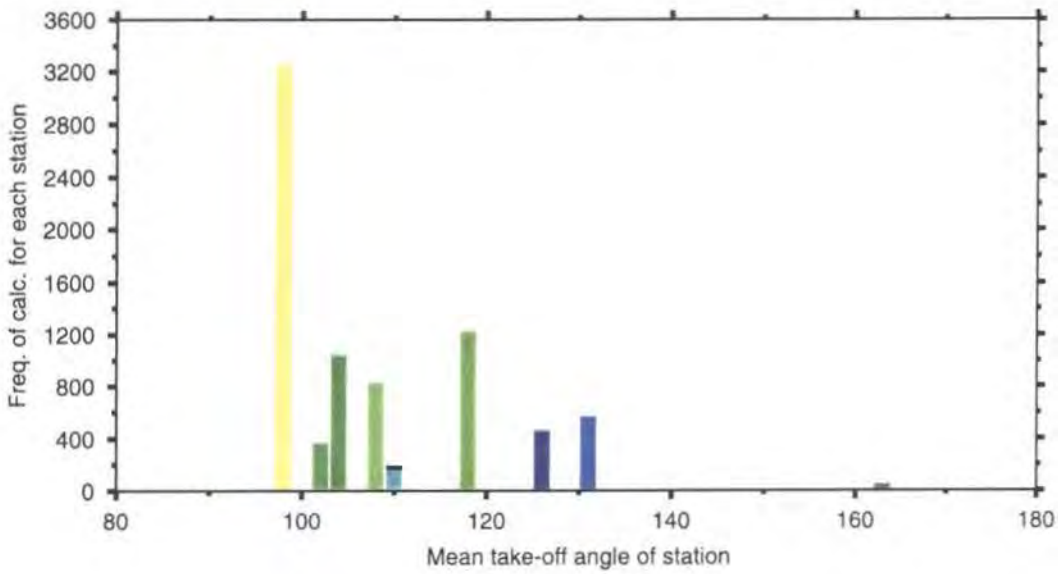

Stations with respect to colour coding for multiplet sr004_01_95_Tt :

ACR	ANG	BUC	CAP	CLV	DES	DRK
DVB	DXR	FNF	FUM	INJ	LCK	MNS
PFR	[illegible]	SQK	[illegible]	STY	TCH	[illegible]
WRK						

Figure 4.53: As for Figure 4.14 except for multiplet sr004_01_95_Tt.

4.4.5 Multiplet event distribution with time

Figure 4.54 shows the time distribution of events used in the four multiplets studied. It is possible that the time history of injection which is known to induce clustered earthquakes could affect relative relocations of events (Barton, 1999) (section 5.1.2). For 1990, there are few events in the multiplets since the 1990 dataset started in August. All the multiplets contain significant numbers of events from 1990 through 1994.

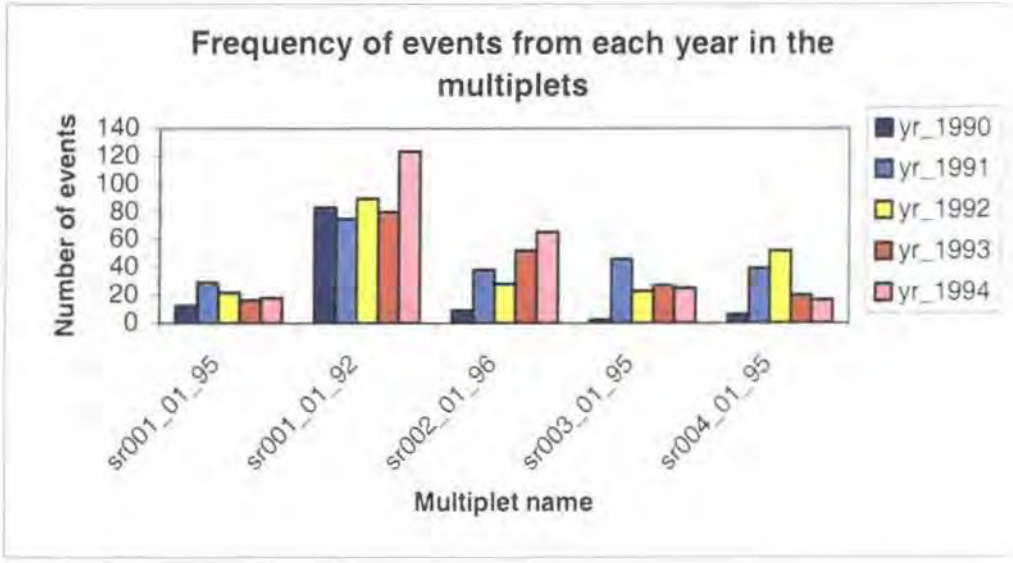

Figure 4.54: The frequency of events from each year used in each multiplet.

4.4.6 Locating multiplets with 3-D velocity model

All events used in the four multiplets studied from each of the seismic regions were located using a comprehensive 3-D velocity model of The Geysers by Julian et al. (1996) and Ross (1996). There are systematic differences in the location of the events between the 1-D and 3-D velocity models used in the study. All events are much more tightly clustered in the absolute locations using a 3-D velocity model (Figure 4.55). However, the overall shape of cluster of events does change between a 1-D and a 3-D velocity model. The absolute locations using a 3-D velocity model for multiplets sr001_01_95, sr002_01_96 and sr003_01_95 relate

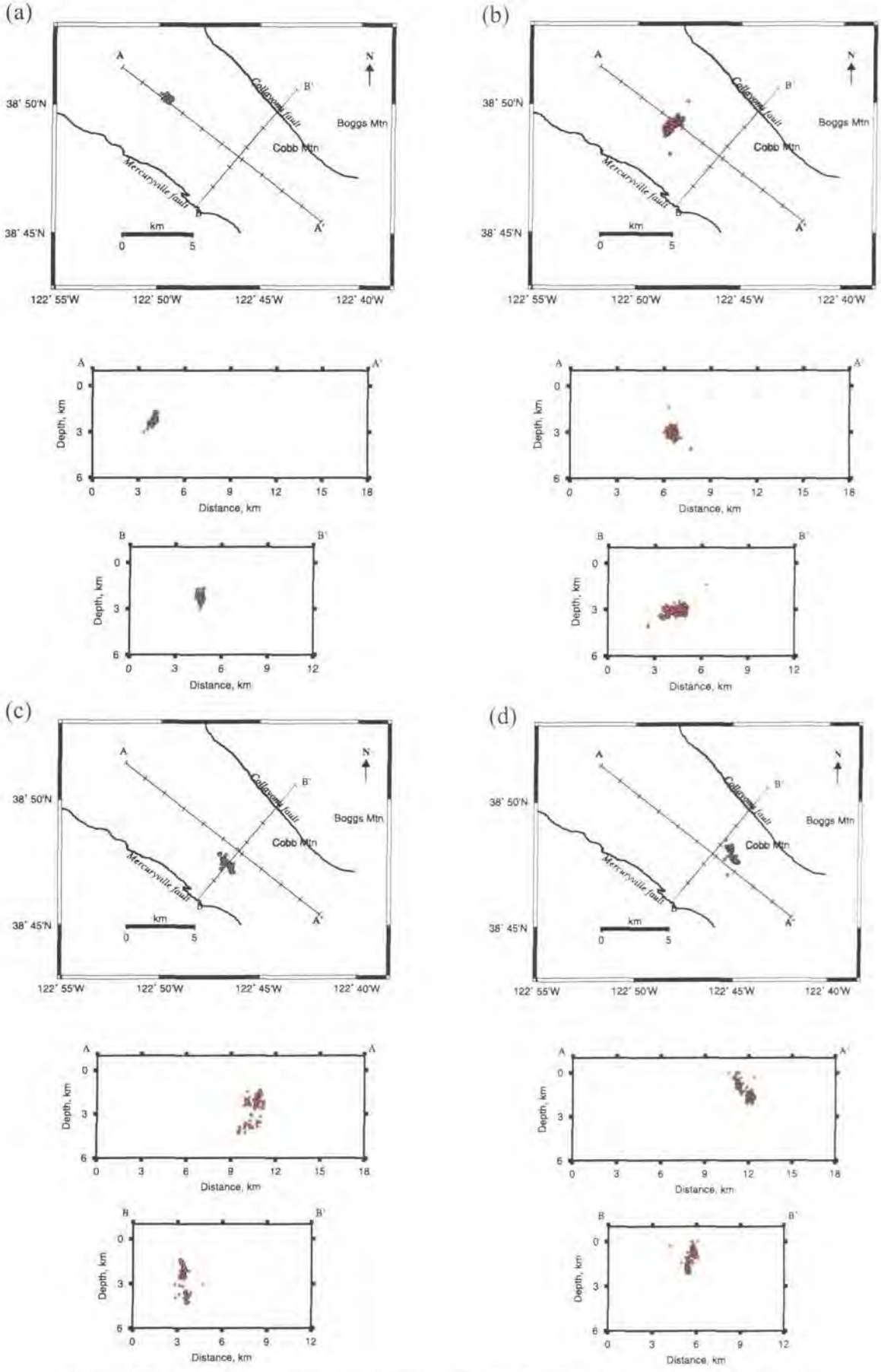

Figure 4.55: Maps and cross-sections of events used in the relative relocation study, located using a 3-D velocity model. All events used in the multiplets are shown as red dots. The multiplets are a) sr001_01_95, b) sr002_01_96, c) sr003_01_95 and d) sr004_01_95.

more closely to locations using a 1-D velocity model than post-relative relocations (Figure 4.55a-c). However, multiplet sr004_01_95 is more similar to post-relative relocations (Figure 4.55d). This could be a result of better ray path coverage for events in multiplet sr004_01_95.

4.4.7 Quality of cosine plots

There are several explanations for the poor quality cosine plots for some stations. The UNOCAL network was updated in October 1989 and included more seismic stations in the southeast Geysers. It is possible that these more recent seismic stations in the southeast are better than the rest of the network, in particular with better timing. There is less industrial noise in the southeast Geysers resulting in better S/N ratio. The poor cosine plots could also be due to small numbers of events in the multiplet. As the coherency threshold was relaxed for region sr001 from 95% to 92% and more events were introduced, the cosine curve improved for more stations (Figure 4.14 and 4.19). Good cosine plots correlate in general with poorer waveforms because they seem to characterise distant stations where the signals are weak. However, these factors probably do not entirely explain the observations and this effect at present is not fully understood (section 5.4.5).

4.5 Summary

Earthquake clusters can be potentially related to geological structures or tectonic activity by high-precision earthquake locations or by using relative event relocations. There are two classes of relative relocation methods that use either arrival times only or waveform cross-correlation. Waveform cross-correlation methods yield the best results.

The relative relocation approach used in this work, applied cross spectral methods (Got *et al.*, 1994). Similarity of the waveforms was measured using a coherency

matrix method to cross-correlate all events belonging to a particular multiplet. This generated all possible multiplet solutions that could be used in relative relocations. 1.28 s of the waveforms centred on the *P*-arrival, were used in the cross-correlation process. To relocate events the method of Frechet (1985) was used.

Four clusters in The Geysers were studied. Multiplet size was kept to a minimum of 100 events to reduce inaccuracies in time delay computations. Multiplet sr001, which was furthest northwest in the reservoir, suffered from poor distribution of stations. All multiplets relocated within 2 to 3 iterations. The RMS residuals of the relocated multiplets were extremely good and were approximately 5 ms for all multiplets. Most multiplets relocated into tighter clusters.

To study the quality and the accuracy of the relative relocations program *plotsin* was used. The program plots the normalised time delay between doublets against the difference in the azimuth of the wave vector and the inter-event vector. This should have a cosine-curve shape for accurate relocations. Paradoxically, good cosine curves were mostly associated with stations that had poor S/N ratios and stations with high S/N ratios had poor cosine plots. This correlation could result from non-uniform quality in the seismic instrumentation, but requires further study to completely ascertain its cause.

CHAPTER 5:

DISCUSSION AND CONCLUSIONS

5.1 Background

5.1.1 Commercial Development of The Geysers

With an approximate area of 75 km^2, The Geysers is the largest vapour-dominated geothermal area under commercial exploitation in the world. Since the early 1960s, steam has been extracted to generate electricity. The extraction rate of steam rapidly increased, fuelled by the UNOCAL and PG&E partnership. Although the resource is finite, and small decreases in reservoir pressure were noted in the 1960s, conservation measures were not taken until 1987 when production peaked and reservoir pressure rapidly decreased. Independent research programs could have predicted such a decline and proper resource management could have implemented contingency measures to pace production, and this would have resulted in greater overall return from the reservoir.

There is a well-documented and strong relationship between commercial activity at The Geysers and seismicity there. New installations of power plants have triggered seismic activity and when certain power plants were shut down for economic reasons seismic activity decreased again. The rate of steam extraction and more recently, fluid injection, have also a strong relationship to the number of earthquakes observed at The Geysers. Prior to completion of the SEGEP project in September 1997, 125 $M_D \geq 1.2$ earthquakes were recorded by the NCSN network. However, within a one year period, between August 1997 and August 1998 seismicity rate increased by an average of 50 – 80 earthquakes per month (Figure 5.1) (Barton, 1998).

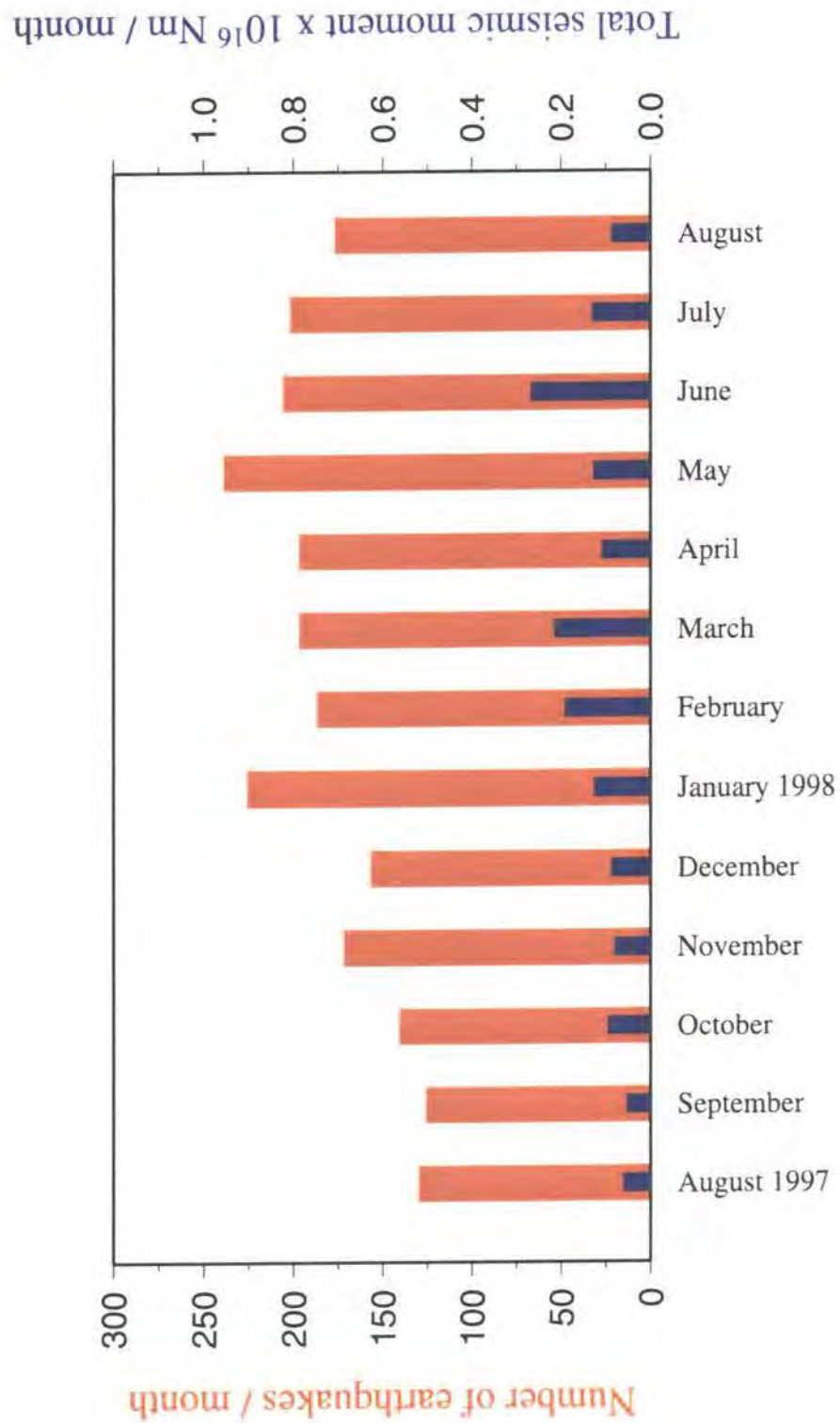

Figure 5.1 Number of events and total seismic moment per month for NCSN earthquakes with $M >= 1.2$ in The Geysers August 1997 - 1998.

5.1.2 Seismicity and well activity

There are 1571 wells drilled in the geothermal area. During the period 1989 to 1994, 337 of these wells were used for steam extraction, 24 for injection and 9 for both extraction and injection. Most wells are located in the central part of The Geysers reservoir in and around "the dead zone" (Barton, 1998). Lack of seismicity in the "dead zone" could be a result of less fracturing in the metagreywacke host rock. There are also some active wells (172 extraction, 14 injection) that have confidential histories making the establishment of a comprehensive well database for academic research impossible. Although, this hampers studying correlations between seismicity and injection, some patterns were reported by Barton (1998) (section 5.4.5):

- An injection pulse was followed closely by an increase in seismicity.
- Near wells with continuous injection punctuated by brief injection pulses, increase in seismicity closely follows each pulse.

5.1.3 Political implications for The Geysers area

As one of the oldest and largest commercially exploited reservoirs in the world, power generation sustenance at The Geysers has significant political and economical implications to the geothermal industry. Geothermal energy was once considered cheap, pollution free and limitless, and The Geysers geothermal area was viewed as an excellent model for alternative energy sources. However, lack of proper management, over-exploitation, and lack of proper understanding of the geothermal reservoir has caused great problems for power production at The Geysers.

There has also been growing opposition from the local community for the further development of The Geysers area due to the progressive increase in seismicity there in recent years, which has inflicted property damage. Increased injection at the southeast Geysers may produce even larger earthquakes and comprise a real

seismic hazard (Ross, 1996). The impact on The Geysers ecology of injecting "grey water" from nearby city of Santa Rosa is yet to be fully understood. There have been suggestions that education and research might benefit from the construction of nearby wetland at Leon Creek near Lakeport, which will contain four wetland cells that will collect excess water from Santa Rosa city that are not required at The Geysers. There is geochemical evidence that non-condensable gases such as H_2S are much lower in concentration in steam retrieved after injection. Furthermore, water is injected at temperatures of less than 10° C, which could have the effect of chilling the rock surface and causing well damage. However, injection of condensate has been successful in maintaining well productivity since steam temperature has not been greatly affected, even after prolonged injection (Enedy *et al.*, 1992). A high rate of injection might create deep channels in the metagreywacke, reducing the absorption rate into rock pores at shallow levels. Frequent rotation of the power plants has also made monitoring The Geysers reservoir increasingly difficult. Very recently due to the energy crisis in the state of California, The Geysers geothermal area has been under tremendous pressure to produce electricity from a depleting geothermal area.

5.2 Station polarity determination and calibration

The largest permanent seismic network deployed at The Geysers, the UNOCAL network, consists of 22 seismic stations, 8 of which have three components and the others only a vertical component. Although, the network records earthquakes well it was poorly calibrated and the orientations of the three-component stations and station polarities were not known. Using well-determined focal mechanism solutions from a temporary network deployed at The Geysers during April 1991, the UNOCAL station polarities and orientations were determined.

Most of the three-component seismometers are installed in 39-m-deep boreholes. When installing the seismometers the sensors were lowered into the boreholes using a torsion cable. As the instruments were lowered the cable might have rotated, resulting in the sensor being randomly orientated, an inference borne out

by the results which indicate orientations of 80° and 300° for the sensors. The only station orientated accurately north-south is the most recently installed three-component station FUM, which was converted to a three-component station from a single component station in 1992. I investigated whether independent confirmation could be obtained that this station was installed accurately orientated north-south, but the Calpine Corporation could not comment due to lack of the required information. Some three-component stations, such as U14, have the suffixes N and E for the horizontal components in the data files, suggesting that the stations are properly orientated. However, this is misleading and it is accepted that the stations are not so orientated (M. Stark, *pers. comm.*). An indication of the limitation of the method used to determine station orientations in this thesis (section 2.2.1) is the relatively large error inherent in the method, a factor that should be taken into account when using the results to re-orientate seismograms and calculate focal mechanism solutions. The best results from the study are for station WRK, where a standard deviation error of only 8.3° was obtained.

Seismic stations in the southern part of the reservoir tend to have normal polarities and stations in the northern half to tend to have their polarities reversed (Figure 2.9). No explanation for this result has been found and it is thus perhaps merely coincidence. The results are consistent except for stations DRK, DXR, SB4B and WRK. Although station FUM shows consistent and good results, it cannot be used for the current data as its polarity was determined when it was a single-component station and its sensor orientation determined when it was a three-component station. It is likely when installing the three-component station that a totally new sensor was installed and the polarity of the vertical sensor might have changed.

When considering deriving focal mechanism solutions using the UNOCAL network and the calibration results determined here, the best three-component station that could be made use of is station DVB. The station polarity of DVB is normal and orientated at an azimuth of 205.9° with an σ error of 12.9°.

5.3 4-D Local Earthquake Tomography

5.3.1 Local earthquake tomography at The Geysers

Local earthquake tomography at The Geysers by Ross (1996) and Julian *et al.* (1996) produced comprehensive three-dimensional *Vp* and *Vp/Vs* velocity models for The Geysers reservoir. Making use of the permanent, continuous seismic network at The Geysers and good quality microearthquakes, a four-dimensional image of the depleting reservoir was determined by Foulger *et al.* (1997) that showed evolution with time. The recent reduction in power generation, decreased production and increased injection has presented new interesting targets for four-dimensional LET at The Geysers. This study shows the areas of greatest concern are the central and southeast Geysers.

For the tomography inversions, the method of Thurber (1983) and Eberhart-Phillips (1986) was used. The first inversion, performed using data from 1991, was a "graded" inversion involving a sequential procedure of reducing nodal spacing and increasing resolution. All subsequent inversions used a direct inversion approach starting with the final model of the 1991 inversion (Foulger *et al.*, 1997). The objective was to monitor depletion since 1991. Because exploitation affects both *Vp* and *Vs*, the *Vp/Vs* model was found to provide the best monitor for depletion of the reservoir. The results help to establish the relationship between changes in *Vp*, *Vs*, and *Vp/Vs*. The results suggest which areas are drying most rapidly, which areas could be further exploited and which need further investigation. The results compliment other tomography studies such as that of Zucca *et al.* (1994). The modelled volume of Zucca *et al.* (1994) was only restricted to the central Geysers. However, this study had a very high resolution of 0.8 km (section 1.6.5). The model of Zucca *et al.* (1994) appears to have many more isolated anomalies than the model presented in this study. This could be attributed to different damping values and different nodal resolutions of the two studies. The results of this study also complement other geophysical studies e.g. gravity (Allis *et al.*, 2001) (Figure 5.2).

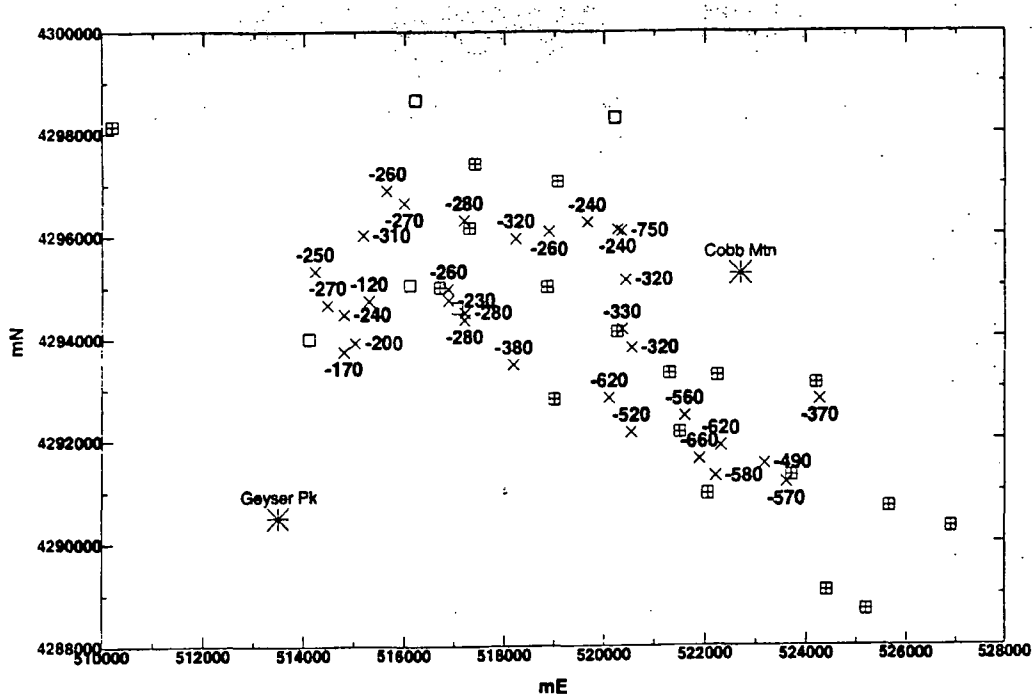

Figure 5.2: Changes in gravity between 1977 and 2000 at The Geysers reservoir, in μgal. The value of –750 μgal in the northeast is suspect. Boxes with cross indicate power plants. Geysers Peak and Cobb Mtn. on either side of the reservoir are shown by stars (*from* Allis *et al.*, 2001).

5.3.2 Development in integrated *Vp*, *Vs* and *Vp/Vs* anomalies

The variations in *Vp*, *Vs* and the *Vp/Vs* ratio with time at sea level and 1 km bsl are shown in Figure 5.3 as variations in the integrated anomalies. These are, for each parameter the arithmetic sum of the deviations from the average starting value for each depth. The total *Vp* anomalies at both sea level (Figure 5.3, top panel) and 1 km bsl (Figure 5.3, middle panel) are not significantly different in 1998 from their 1991 values. A large decrease occurs in December 1994 at both depths. This may be a result of that dataset having been picked by a different person (C. Grant), introducing analyst-dependent errors (section 5.3.5). The integrated *Vs* anomaly progressively increased between April 1991 and August 1998. The *Vp/Vs* ratio also increased progressively throughout this time period. As for *Vp*, the December 1994 epoch deviates somewhat from the trend of the other three post-1991 epochs.

The relationships between variations in the wave speeds *Vp* and *Vs* and the ratio *Vp/Vs* are shown in the Figure 5.4a along with regression lines. The numerical

(a)

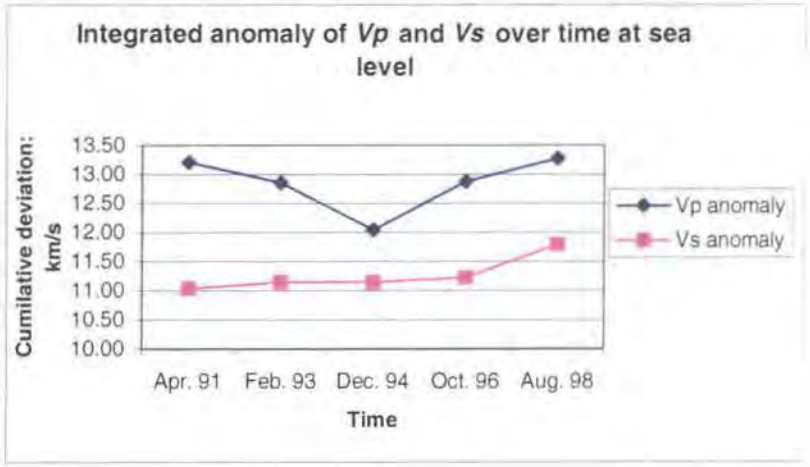

(b)

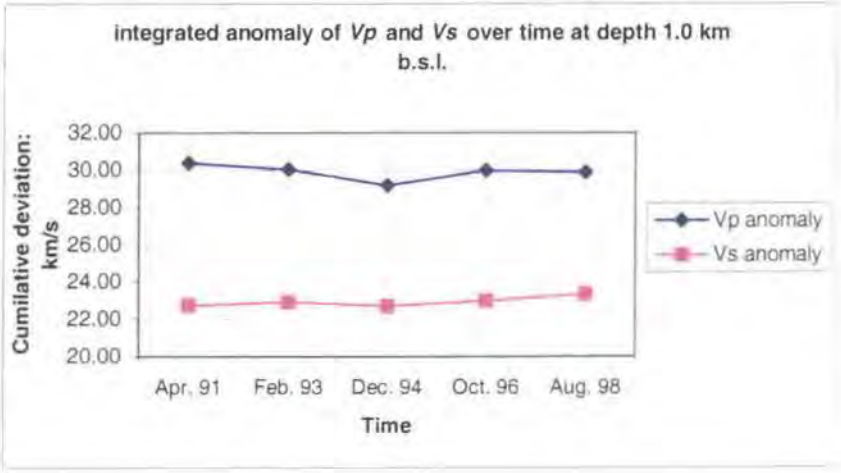

(c)

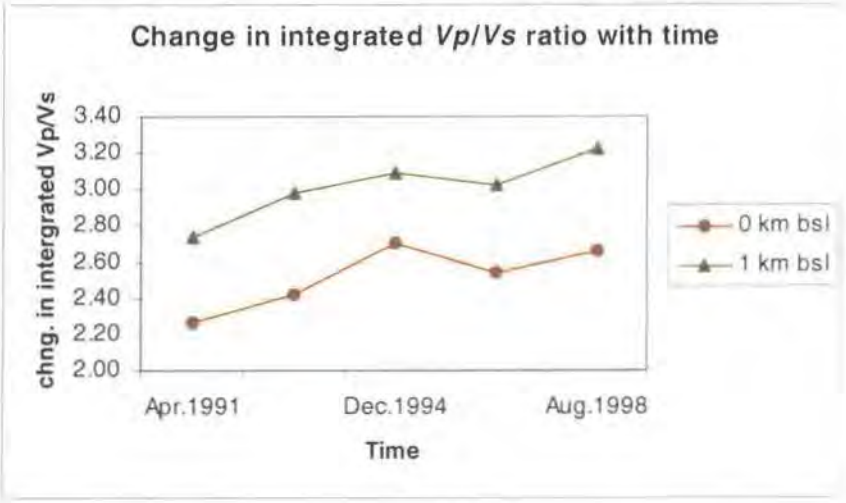

Figure 5.3: Plots of integrated anomalies in Vp, Vs, and Vp/Vs at sea level and 1 km bsl as a function of time. (a) Changes in integrated anomaly for Vp and Vs at sea level. (b) same as (a) except for 1 km bsl and (c) changes in integrated Vp/Vs anomaly with time at sea level and 1 km bsl.

results of regression are shown in Table 5.1, along with the 1σ errors. All wave-speed nodes that changed between April 1991 and August 1998 at sea level and 1 km bsl are plotted. The *Vp/Vs* ratio is weakly correlated with *Vp* at sea level and 1 km bsl. In the case of *Vs* however, strong negative correlations were found with *Vp/Vs* of –0.47 ±0.06 at sea level and –0.33 ±0.04 at 1 km bsl. The results of Romero *et al.* (1995) for the northwest Geysers (Figure 5.4b), Kirkpatrick *et al.* (1997) for the southeast Geysers (Figure 5.4c) and the results of a stochastic model simulation for the northwest Geysers (Boitnott, 1995) (Figure 5.4d) show a similar result, with variations in the *Vp/Vs* ratio apparently being caused in general by variations in *Vs*.

Table 5.1 Regression lines for *Vp/Vs* : *Vp* and *Vp/Vs* : *Vs* plots.

Depth, km bsl	*Vp, Vs*	Slope	1σ error
0	*Vp*	-0.99	0.46
0	*Vs*	-0.47	0.06
1	*Vp*	-0.44	0.11
1	*Vs*	-0.33	0.04

5.3.3 Variations in results of *Vp*, *Vs* : *Vp/Vs*.

Although, variations of *Vp/Vs* with *Vs* support an inverse correlation, the plot of *Vp/Vs* : *Vp* exhibits much scatter and errors are large (Figure 5.4a). Reasons for the discrepancies between different studies include lateral variations in *Vp* and *Vs*, field-scale of the tomographic inversions and differences in velocity models. Large lateral variations up to 1.4 km/s in *Vp* and 0.7 km/s in *Vs* at The Geysers exist, especially in the northwest Geysers where the HTR is located with low *Vp* and *Vs* anomalies to the southwest where high *Vp* and *Vs* anomalies correlate with the known geology. The study of Boitnott and Kirkpatrick (1997) incorporated two tomographic inversions, one confined to the northwest Geysers performed by Romero *et al.* (1995) and the other confined to the southeast Geysers

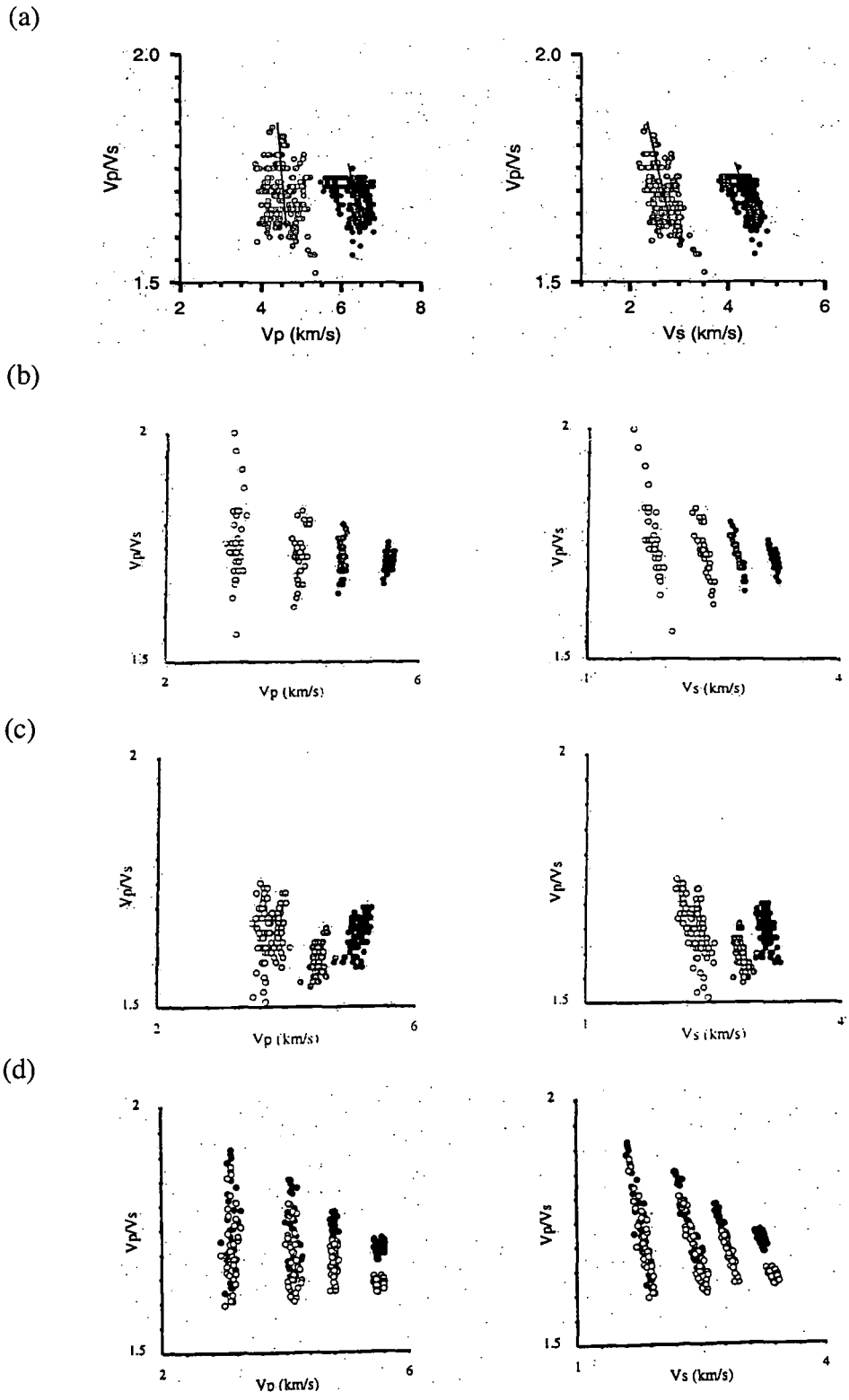

Figure 5.4: The relationship between Vp/Vs, Vp and Vs. Data points are wave-speed nodes taken from each of the models listed below. (a), Results from this study. Grey symbols are fro nodes at sea level, black symbols are for 1.0 km b.s.l. Regression lines are drawn to establish statistical significance. Velocity nodes at 1.0 km b.s.l. are DC shifted by 1.5 km/s in order to be distinguish from nodes at sea level. (b) Results from the work of Romero et al. (1995) for the northwest Geysers. Darker symbols indicate larger depths. (c) Results for the southeast Geysers, from the work of Kirkpatrick et al. (1997). (d) Results from a stochastic model simulation (Boitnott and Kirkpatrick, 1997). Open symbols represent a dry matrix and filled symbols a wet matrix.

and performed by Kirkpatrick *et al.* (1997). The area studied at the northwest Geysers was 5x5 km^2 in size. The study conducted as part of the present thesis involved an area of 20x20 km^2 encompassing both the northwest and southeast Geysers and involving greater lateral variation in velocity. Boitnott and Kirkpatrick (1997) make the assumption that matrix properties and field-scale features are isotropic. Anisotropy could also be introducing scatter into the results. The results are heavily dependent on the velocity model selected for the inversion. All three tomographic inversions used different 3-D velocity models, which differ significantly from one another.

Although the velocity nodes are well-resolved, they may not be accurate and velocity averaging occurs where nodes are widely separated. The number of seismic stations that provided *P*-waves is much greater than the number of 3-component stations that provided *S*-waves. On average, the numbers of *P*-waves used in the inversions were about 6 times higher than the numbers of *S*-waves used. This might have an impact on ray sampling and solution quality of the velocity nodes. Also, the *S*-wave structures were derived from an initial *Vp* structure. Thus, the *Vp*, *Vs* and *Vp/Vs* results are not entirely independent.

5.3.4 Causes of the *Vp/Vs* anomaly

Factors that affect *Vp*, *Vs* and the *Vp/Vs* ratio at The Geysers include lithology, temperature, pore pressure and pore fluid phase. Of these, the temperature of the reservoir has remained fairly constant in recent years (M. Stark, *pers. comm.*), despite exploitation. Thus changes in pore pressure, pore fluid phase and mechanical properties of the rock matrix caused by steam removal are probably responsible for the changes observed in the anomaly.

The effect of replacing liquid pore fluid (water/petroleum) with gas (CO_2) has been quantitatively studied in the McElroy oil field, West Texas (Wang *et al.*, 1998). The McElroy oil field is a good analogue of The Geysers. Porosity and permeability are variable, with an average porosity of 10% and permeabilities in the range 0.01 - 90 x 10^{-11} cm^2. The reservoir rock comprises dolostones and

evaporite cement, and was flooded with CO_2 at a depth of 900 m below surface in order to improve oil recovery. At the time of CO_2 flooding, the pore fluid was half water and half oil. The effect of flooding was monitored seismically. *Vp* was found to be reduced by 2-4 % on average by CO_2 flooding, and up to 9% in areas of high porosity, whilst *Vs* was little affected (Wang *et al.*, 1998). However, associated local increases in pore pressure accompanying the CO_2 flooding reduced *Vs* as a result of reduction in the shear modulus. In the case of the McElroy field, reduction in *Vp* and *Vs* went hand in hand and the net result was little change in the *Vp/Vs* anomaly (Wang *et al.*, 1989).

Similar behaviour has also been observed in laboratory experiments with reservoir rock samples, where increasing in pore pressure from 8.3 MPa to 15.9 MPa at a constant overburden pressure of 20 MPa caused *Vp* to decrease by 1.7% and *Vs* by 2.6% (Wang *et al.*, 1998). Increase in *Vs* with decreasing pore pressure was also observed in water-filled Berea sandstone at constant temperature of 145° C and other conditions representative of a steam reservoir. In that experiment, the *Vp/Vs* ratio was observed to decrease from 1.78 to 1.67 as pore pressure decreased by 0.3 MPa and liquid water converted to steam (Ito *et al.*, 1979) (Figure 5.5). At The Geysers, the removal of steam has the effect of causing pore water to be replaced by vapour, accompanied by pressure decrease (Table 5.2). Reservoir pressure data are proprietary, but pressure is known to have decreased from ~ 3.5 MPa to ~ 1.2 MPa in the last decade. These two processes have the effect of decreasing *Vp* and increasing *Vs*, both of which will lower the *Vp/Vs* ratio. This situation contrasts with that of the McElroy field where CO_2 flooding is accompanied by pressure increase and the effects on the *Vp/Vs* ratio tend to cancel out.

A third effect at The Geysers works to decrease the *Vp/Vs* ratio with exploitation. Water saturation has an unusually large chemo-mechanical weakening effect on argillaceous minerals such as illite, which are abundant at The Geysers. This has been explained using modified Biot-poro elastic theory that includes weakening of the shear modulus with saturation (Boitnott, 1995; Boitnott and Kirkpatrick, 1997). As pore fluid is removed, the minerals dry, the rock matrix stiffens, and the *Vp/Vs* ratio is lowered because *Vs* increases (the spaghetti effect).

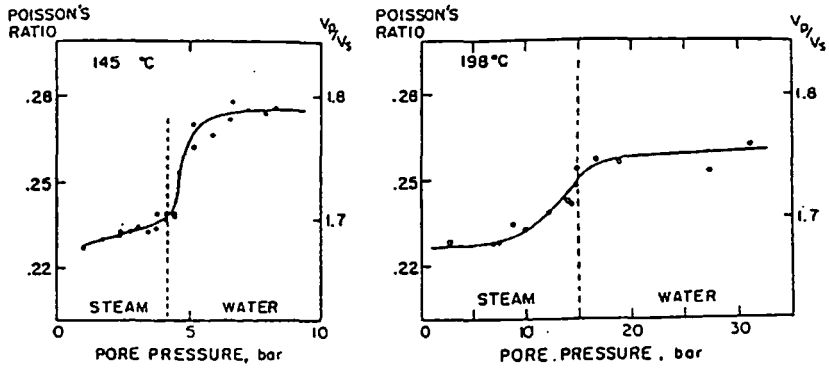

Figure 5.5: The effect on Poisson's ratio and the *Vp/Vs* ratio as pore-fluid pressure crosses the liquid-vapour boundary for a sample of Berea sandstone at temperature (a) 145° C and (b) 198° C (*from* Ito *et al.*, 1979).

Table 5.2: Effect on *Vp/Vs* ratio during liquid to vapour transition (*from* Julian *et al.*, 1996).

Cause	Porosity ϕ	
	0	0.02
Liquid → Vapour	0.00%	-14.00%
$\Delta T = +10^{\circ}$ C (Liquid)	-0.06%	-1.70%
$\Delta T = +10^{\circ}$ C (Vapour)	-0.06%	+0.10% to +0.68%
$\Delta P = -1$MPa (Liquid)	+0.004%	-0.20%
$\Delta P = -1$MPa (Liquid)	+0.004%	-6.6% to -10.0%

ΔT: Temperature change
ΔP: Pressure change

Thus, three different processes at The Geysers related to fluid saturation reinforce one another to cause lowering of the *Vp/Vs* ratio (Figure 5.6). The effect of saturation is depth dependant. At depths greater than ~ 1.3 km bsl the *Vp/Vs* ratio is largely controlled by the rock matrix properties, with a higher *Vp/Vs* ratio for a saturated matrix than a dry matrix. At shallower depths, the effect of saturation on the rock matrix is diminished by the effect of field-scale compliant features such as joints and faults (Boitnott and Kirkpatrick, 1997). The clear inverse relation between *Vs* and *Vp/Vs*, and smaller, weaker relation between *Vp* and *Vp/Vs* suggests that the effects of pressure decrease and mineral drying are predominant at The Geysers. Evidence from granular rocks also shows that the effect of packing is comparatively small as most of the *Vp/Vs* anomaly is affected by stiffness of the contact between grains (Manificat and Gueguen, 1998).

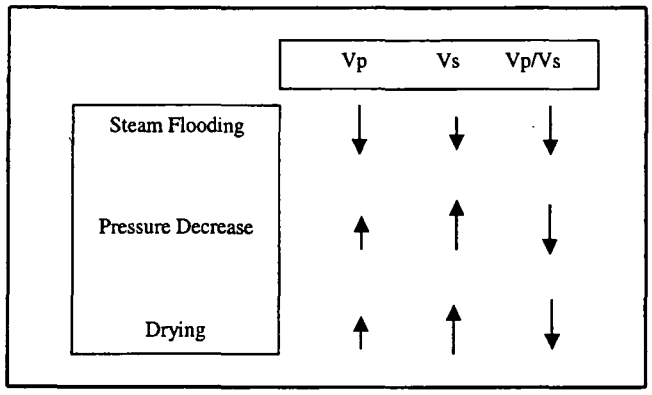

Figure 5.6: Summary diagram to show probable causes of *Vp/Vs* reduction at The Geysers.

5.3.5 The 1994 results

There is an apparently anomalous growth of the *Vp/Vs* anomaly in December 1994 (Figure 5.3). This is largely due to the apparently large decrease in the *Vp* anomaly that year. The 1994 inversion was not carried out by the author but by C. Grant (1995) and the results might thus reflect analyst-specific variations. For the December 1994 of inversion of Grant (1995) the ratio of *P*-waves to number of events used was 17.3:1, whereas for the other inversions it varied between 10.8:1 and 14.2:1. For *S*-waves in 1994 the ratio was 4.5:1 and for the other inversions it varied between 1.4:1 and 2.4:1 (Table 3.1). These figures suggest a very different picking strategy for the 1994 data.

Picking strategy can influence tomography results (Evans *et al.*, 1994). I re-picked and located a sample of events used in the 1994 inversion in order to study any systematic differences in earthquake locations that might have resulted from variations in picking strategy. From the studied sample, the numbers of *P*-waves and *S*-waves picked by C. Grant were much greater than those I made (Table 5.3).

Most striking is that the number of *S*-waves picked by C. Grant is nearly twice the number I picked. Earthquakes such as 19941217102638.34 were strong and their traces were clipped. It is often not possible to pick reliable *S*-waves on such traces

as the onsets are obscured by the strong P-wave coda. The number of *P*-waves picked by C. Grant was also much greater than the number I judged could be picked accurately. I could not judge the accuracy of the picks made by C. Grant as his original pick files were irretrievably lost in a disk crash several years ago, but this study suggests that the dataset of C. Grant may have been of lower quality than those used for the 1991, 1993, 1996 and 1998 inversions. The locations of the sampled events between the two studies are mostly, but not always, similar (Figure 5.7).

Table 5.3: Differences in locations and numbers of observations for 10 events located by C.Grant and the author.

Earthquake Id		Latitude	Longitude	Depth (km)	No. of picks	No. of *P* picks	No. of *S* picks
19941201045908.24	Grant	38:47.21	-122:46.49	1.13	27	20	7
	Gunasekera	38:47.19	-122:46.39	1.25	14	11	3
19941201053453.34	Grant	38:47.46	-122:48.22	4.30	20	15	5
	Gunasekera	38:47.33	-122:48.34	3.38	17	13	4
19941201110907.05	Grant	38:47.75	-122:45:03	0.83	19	12	7
	Gunasekera	38:47.79	-122:45:01	4.61	10	7	3
19941203224824.28	Grant	38:49.05	-122:48.71	3.12	19	15	4
	Gunasekera	38:49.17	-122:48.78	3.17	16	13	3
19941206003701.53	Grant	38:47.60	-122:46.39	1.29	28	20	8
	Gunasekera	38:47.61	-122:46.41	1.34	18	14	4
19941214184222.15	Grant	38:47.60	-122:44.72	0.40	27	21	6
	Gunasekera	38:47.63	-122:44.60	0.38	20	17	3
19941217102638.34	Grant	38:48.02	-122:48.41	1.85	25	23	2
	Gunasekera	38:48:00	-122:48:41	1.99	18	18	0
19941218122258.58	Grant	38:47.20	-122:46.49	1.39	26	23	3
	Gunasekera	38:47.20	-122:46.49	1.41	18	18	0
19941220015749.05	Grant	38:47.84	-122:45.40	0.92	28	22	6
	Gunasekera	38:47.86	-122:45.34	0.92	23	20	3
19941219061317.08	Grant	38:50.16	-122:49.34	1.94	13	12	1
	Gunasekera	38:50.17	-122:49.49	2.06	15	15	0

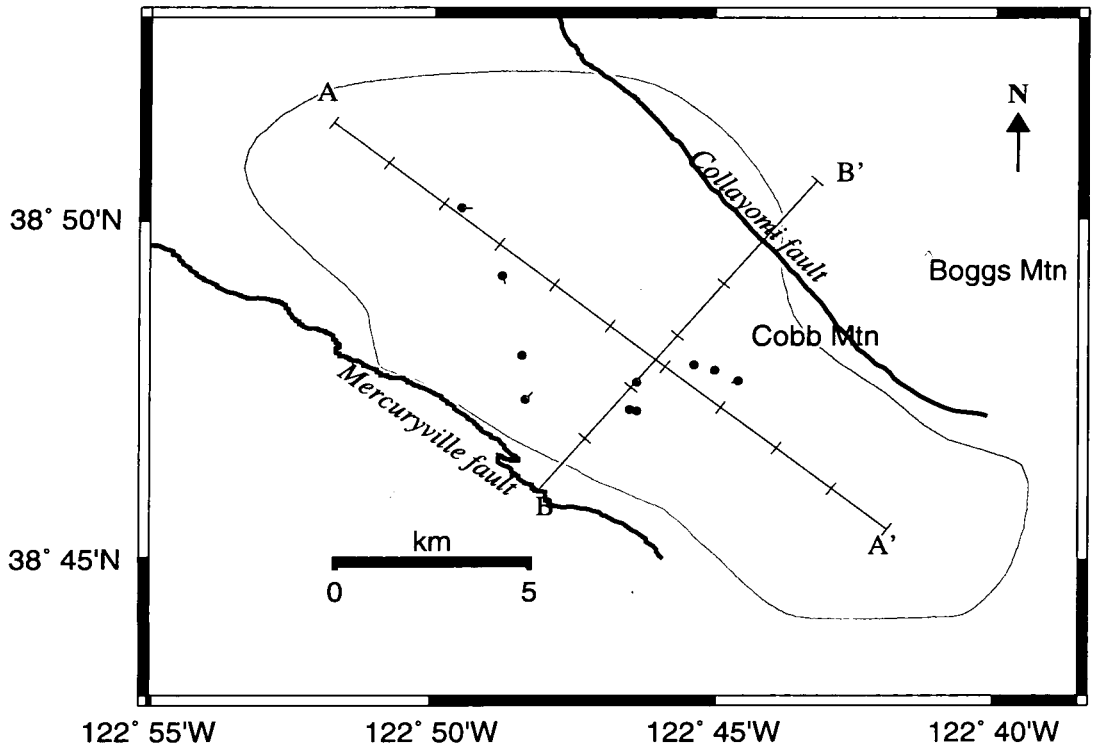

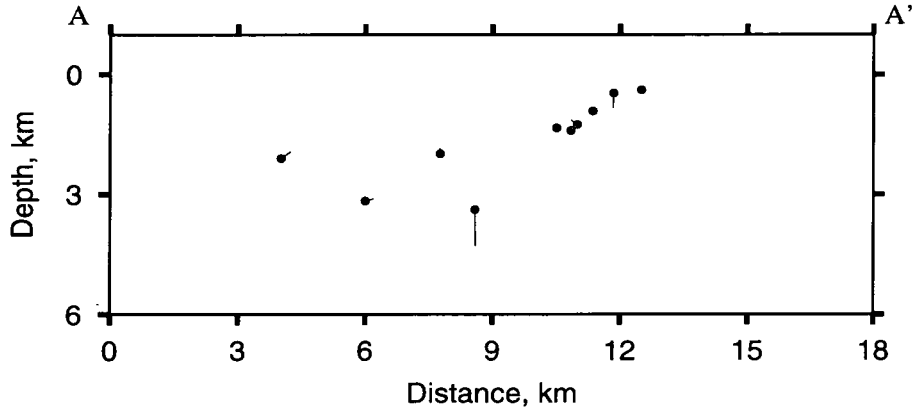

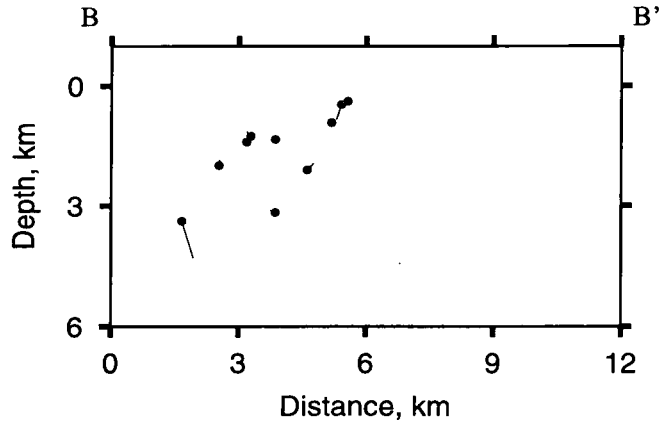

Figure 5.7: Maps showing the differences in locaton for a sample of events used in the 1994 tomography inversion. The red filled circle's are the author's picks while the tails of the vectors are the 1994 inversion picks. Pink triangles are mountains.

5.3.6 Interpretation of the growing anomaly at The Geysers

While the progressive growth in the *Vp/Vs* ratio ultimately results from depletion of liquid water in the reservoir, comparison of the separate *Vp* and *Vs* fields (Figures 3.12 and 3.13) indicates that different effects are dominant in different parts of the field. At sea level, the most southeasterly and the most northwesterly areas of *Vp/Vs* anomaly growth (Figure 3.14, upper rightmost panel) correlate with areas of progressive increase in *Vs* of up to 0.05 km/s from 1991-1998. A similar correlation is found from the deeper continuation of the southeasterly anomaly at 1 km bsl. This suggests that the strongest effects in this area are pressure decrease and mineral drying. In contrast, the middle anomaly at sea level and its continuation down to 1 km bsl is predominately caused by decrease in *Vp* of up to 0.27 km/s from 1991-1998, suggesting that increase in compressibility due to the replacement of pore water by vapour is the dominant effect.

Variation in the physical mechanism causing seismic wave-speed evolution at The Geysers may be partly related to the pattern of water reinjection, which is being progressively increased in an effort to slow reservoir pressure decline. Between 1994 and 1996, injection increased from 33% to 58% of the fluid extracted (Barker and Pinogol, 1997). Much water is injected in the extreme southeast of the reservoir but the amounts of reinjectate and the locations of the injector wells are proprietary. It is thus currently not possible to assess quantitatively the effect of reinjection.

The low-*Vp/Vs* anomaly observed at The Geysers correlates with the volume where the pore fluid is thought to be vapour-dominated, where pore-pressure is relatively low and argillaceous minerals relatively dry. Julian *et al.* (1996) concluded that The Geysers might have had an associated low-*Vp/Vs* anomaly prior to exploitation, since such conditions probably existed naturally then. Between April 1991 and August 1998 the anomaly grew in strength by up to ~ 0.5%/year at 1 km bsl. At this rate, the anomaly observed in 1991, which had a maximum strength of ~ 9%, would have taken ~ 18 years to develop. During the period 1991-1998, the rate of steam extraction was ~ 7-9 x 10^{10} kg/yr. Prior to this, it increased from low levels in the 1960s to peak at ~ 11 x 10^{10} kg/yr in 1987, and decreased

subsequently. Over the 32-year period 1960-1991, the average rate of steam production was ~ 5 x 10^{10} kg/yr, or equivalent to 22-17 years of production at 7-9 x 10^{10} kg/yr. This suggests that production over the entire period of exploitation at The Geysers could account for the whole of the *Vp/Vs* anomaly. Low-*Vp/Vs* anomalies have been reported for unexploited geothermal areas. Foulger *et al.* (1995) and Miller *et al.* (1998) reported *Vp/Vs* anomalies as strong as -4% in the area of most abundant hot springs and fumaroles in the unexploited Grensdalur geothermal field, Iceland. Thus, although exploitation at The Geysers could conceivably account for all of the observed *Vp/Vs* anomaly, it is possible that an anomaly existed there originally. The association of low-*Vp/Vs* anomalies and geothermal reservoirs might be important to the study of new prospects.

5.3.7 Comparison with LET at Mammoth Mtn.

Repeat LET has also been applied to investigate the migration of pore fluid at Mammoth Mtn., an active volcanic cone on the southwest corner of the Long Valley caldera (Foulger *et al.*, 2001). Mammoth Mtn. has been degassing up to 2 x 10^8 kg/yr of CO_2 since 1989. Similar seismic networks were deployed in 1989 and 1997 which recorded local earthquake datasets suitable for tomographic inversion. Comparison of the results revealed significant changes in the *Vp*, *Vs* and *Vp/Vs* fields that are consistent with the migration of CO_2 into the centre of the volcanic edifice, where pressure increased, migrating from the peripheral areas, where pressure has decreased. In contrast to the situation at The Geysers, the effects of CO_2 flooding and pressure changes at Mammoth Mtn. on the *Vp/Vs* ratio partially cancelled out, and as a result the evolving *Vp/Vs* field was less diagnostic of migration of subsurface fluids than at The Geysers. The reinforcement of changes in the *Vp/Vs* anomaly by the various reservoir effects at The Geysers, and perhaps other geothermal fields, renders the *Vp/Vs* ratio a serendipitously useful parameter for monitoring geothermal reservoir evolution.

5.4 Relative relocation of multiplets

5.4.1 Errors in relative relocation

Errors are introduced into relative relocations in several ways. The major sources of error are cross-correlating noisy traces or dissimilar traces, errors in the assumed event-station azimuth and take-off angles and inclusion of secondary arrivals in the cross-correlation window (Rubin *et al.*, 1999). The *relnew* program computes the mean take-off angle for the whole multiplet for each station. With large multiplets, the depth distribution of events may be large, so the take-off angles at the extremities of the cluster will differ considerably. This can lead to errors. If the stations are located close to the source (for example multiplet sr001_01_95; stations INJ and SQK) the take-off angles may be large and variable.

The heterogeneity of the geology at The Geysers may lead to error in the relative relocations. To reduce errors in event location the relocation method assumes the hypocentre distribution is much greater than the inter-event distance and that the velocity in the vicinity of the hypocentre is constant. However, The Geysers reservoir has a complex structure, with numerous fractures and large velocity variations at constant depth throughout the reservoir and this assumption might not hold true.

Timing inaccuracies of the data acquisition system could lead to error in relocation. A few of the stations used did not give accurate time-delay calculations. It is easy to detect this problem by looking at the residuals of the time delays from these stations. Unfortunately, this problem cannot be identified before relative relocation. It is also possible that the timing accuracy of these stations varied with time.

Table 5.4 shows the correlation between waveform, cosine plot and take-off angles for each station used in the multiplets. With a few exceptions, for most stations with take-off angles between 90 and 110° the cosine plots are of high quality do not correlate with high frequency of non-weighted residuals (Appendix 7).

Table 5.4: Correlation between waveform, cosine plot and take-off angles for each station used to relative relocate the main multiplets. Wave : waveform, Cos : cosine plot, TOA : take-off angle in degrees, G : good, B : bad and OK: average.

Station	Sr001	01	95	sr002	01	96	sr003	01	95	sr004	01	95
	Wave	Cos	TOA	Wave	Cos	TOA	Wave	Cos	TOA	Wave	Cos	TOA
ACR	G	B	114	G	B	130	G	B	116	G	B	110
ANG	B	OK	108	G	B	129	G	B	142	G	B	163
BUC	G	B	154	OK	B	144	B	B	112	B	G	94
CAP	G	B	148	B	B	140	B	OK	109	OK	G	95
CLV	B	B	133	B	B	146	B	B	116	G	B	104
DES	G	B	89	B	G	102	OK	B	108	OK	OK	102
DRK	B	B	114	G	B	140	G	B	144	G	B	110
DVB	B	G	96	B	G	110	OK	OK	126	G	B	118
DXR	G	OK	119	G	B	144	OK	B	128	G	B	121
FNF	B	G	102	B	B	119	OK	B	149	G	B	126
FUM	OK	OK	114	G	B	141	B	B	161	OK	B	121
INJ	G	OK	127	OK	B	165	G	B	132	B	B	108
LCK	OK	OK	107	OK	B	124	G	G	123	G	B	131
MNS	B	G	90	B	G	107	OK	B	117	G	G	118
PFR	B	OK	94	OK	B	107	G	B	120	G	OK	108
SB4B	G	B	133	G	B	148	OK	B	117	B	G	98
SQK	OK	OK	143	OK	B	166	OK	B	118	B	B	104
SSR	B	G	84	B	G	100	G	G	107	OK	G	98
STY	G	B	121	G	B	155	B	B	138	B	B	124
TCH	B	G	96	B	G	116	B	B	133	B	B	143
U14	OK	G	107	OK	B	129	B	B	172	B	B	133
WRK	B	B	-	B	B	108	B	B	119	OK	B	114

To solve the problems associated with distributed events in multiplets, a better approach is to perform progressive multiplet relative relocation. Progressive multiplet relative relocation involves relocating each event to its nearest, already-relocated neighbours. For example, a tightly clustered multiplet could be used as *a priori*. When the cluster has been relocated correctly, it could be used as a kernel for progressive multiplet relative relocation provided that its quality is maintained. The problems associated with locating The Geysers events could, however, be due to other problems associated with the relocation process and not be caused by elongated multiplets.

5.4.2 Different velocity models

The ablility to use a 3-D velocity model for The Geysers in relative relocations has not yet been programmed. However, the best possible 1-D model was used in this study. The minimum 1-D model used by Ross (1996) is significantly better than any other regional 1-D model for The Geysers area. The location errors in the regional 1-D model presented by Eberhart-Phillips and Oppenheimer (1984) are estimated to be ± 0.4 km horizontally and ± 0.7 km vertically. The 3-D model derived by Julian *et al.* (1996) and Ross (1996) using LET tomography reduced the vertical and horizontal errors of located earthquakes to an estimated ± 0.2 km. The horizontal median relocation vector for events located with the regional 1-D model of Eberhart-Phillips and Oppenheimer (1984) and relocated with the 3-D model was about twice the value than used with the minimum 1-D model and the 3-D model (Ross, 1996) (Table 5.5). In the vertical plane, the median relocation vector is similar for both pairs of models (Table 5.6).

Table 5.5: Median of horizontal and vertical relocation vectors for the 296 events from 1991 used to derive the 3-D velocity model (*from* Ross, 1996).

Models used	Median relocation vector, km	
	Horizontal	Vertical
Regional and 3-D model	0.570	0.170
Minimum 1-D and 3-D model	0.290	0.210

Although, the minimum 1-D velocity model for The Geysers does not account for 3-D heterogeneity, the tightly clustered nature of the relocated events suggests that this approximation does not prevent significant improvement of the original locations being achieved in many cases.

Table 5.6: Final RMS travel time residuals for earthquakes located with the 3-D model (*from* Ross, 1996).

Model	RMS travel time residual, *s*			% difference from regional model
	P-wave	*S*-wave	All waves	
Regional 1-D model	0.054			0.0
		0.130		0.0
			0.077	0.0
Minimum 1-D model	0.053			3.0
		0.113		16.0
			0.069	10.0
3-D model	0.041			24.0
		0.075		44.0
			0.058	25.0

5.4.3 Attenuation and micro tremor

A detailed study was conducted of multiplets sr001_01_95 and sr001_01_92. For stations in the southern part of The Geysers reservoir a very clear cosine curve was obtained showing that the time delays calculated from these stations are good. However, the waveforms show either noise or possible apparent monofrequential signal (Figure 5.8). As seen in Figure 5.8 the peak amplitude of first *P*-wave arrival in the case of the well-recorded event (left panel) is approximately 40 times greater than the peak amplitude observed for the poorly recorded event (right panel) at the distant station. The cross-correlation method used can detect very weakly recorded events, which are coherent even in noise-ridden stations (Got *et al.*, 1994).

Stations in the northern part of The Geysers reservoir recorded strong, coherent signals for the multiplets in regions sr001, sr002 and sr003. However, many of the cosine plots are poor, indicating poor time delays. It is unclear why the time-delays are scattered in these cases despite strong signals.

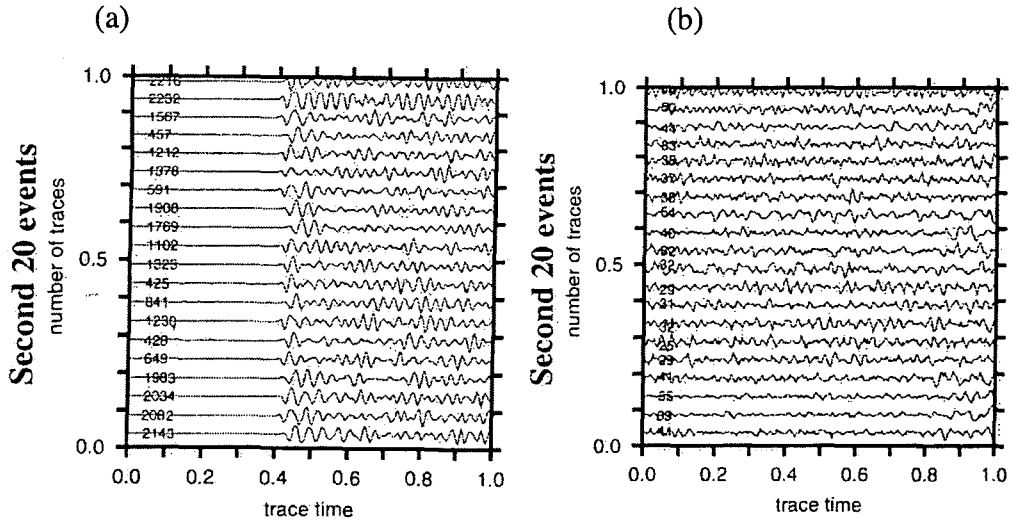

Figure 5.8: Waveforms with a 1.0 s trace time from events 20 to 40 in multiplet sr001_01_95, used in relative relocations from (a) station ACR and (b) station TCH. The peak amplitude of each trace is shown numerically at the left hand side. Clear, coherent traces such as recorded at (a) were deemed good traces while traces such as in (b) were deemed poor traces.

To investigate this further the northern stations alone were used for relocation (plots sr001_01_95_T2) (Figure 4.20). The difference between sr001__01_95_T2 and sr001_01_95 was minimal in the relative relocations and in the cosine plots. Relative relocations were also attempted using only the southern UNOCAL stations for the same multiplet. Although high-quality cosine curves were obtained, the relocations were poor especially in the depth domain. In horizontal section the relocated events were orientated in a northwest-southeast direction.

It is possible that these events are an effect of micro tremor, which are small-magnitude monofrequential waves involving only cylindrical waveforms and affecting only the horizontal plane (J. L. Got, *pers. comm.*), resulting in the poor depth relocations observed. As the distances to distant stations are approximately 12-14 km, with similar azimuths and take-off angles of ~ 90°, the accuracy of the results is poor. Several cosine plots were calculated using northern stations and southern stations separately. It is possible that there exists a signal within the embedded noise. However, as the epicentral distances are considerable and the ray paths pass through the inhomogeneous Geysers reservoir it is possible that high attenuation has removed higher frequencies from the waveforms. The time-delay

computations are required from at least 6 stations for a good result provided there is adequate station coverage.

Another possible alternative is that the events are not earthquakes but caused by commercial activity, such as heavy vehicles passing, or active power generators. Such signals might have the appearance of harmonic tremor. There is also evidence from tremor observed at Old Faithful geyser that suggests that harmonic tremor is a path effect (Kedar *et al.*, 1996).

5.4.4 Station effects

Poor waveforms could be a result of station site effects. A seismometer could be poorly coupled in the borehole, the local geology could be inhomogeneous or strong noise sources near the borehole such as power plants and production injection wells could exist. Also, stations that are close to focal mechanism node, such that the theoretical amplitudes would be zero and would show a weak first arrival. However, all these explanations may not be able to account for the possible noise or monofrequential signals at these stations. It is possible that the gains on the stations are different and this is not accounted for in cross correlation.

Relative relocations were also performed for all multiplets with and without station WRK as the waveforms at that station were poor. The inclusion or otherwise of this station in the relocation made little difference to any multiplet. The cosine plot revealed a miscalculation in the time-delays at an azimuth of about 300°, which was found to be caused by a single event with very low and unvarying time-delays (approx. 92 ms). However, the trace was of good quality and the station was included in relative relocations.

5.4.5 Interpretation of relative relocation results

All multiplets were relocated successfully after two to three iterations with average RMS of approximately 5.6 ms. With the exception of mutiplet sr001_01_95, all the

multiplets collapsed to tighter clusters than seen in the original locations. Although there are several northwest and northeast striking lineaments at The Geysers observed in shear-wave splitting studies (Evan *et al.*, 1995; Lou *et al.*, 1997), the studied multiplets with the exception of sr001_01_95 are not orientated in these directions. Multiplet sr001_01_95 is orientated in a northwest-southeast direction and has a tube-like morphology (Figures 4.12 and 4.20). However, this multiplet was located at the periphery of the network, the results are more diffuse than in the original locations, and so they are suspect. This may be because of the limited ray-path coverage. Multiplets sr002_01_96 and sr003_01_95 were clustered in small spherical volumes and cannot be attributed to any geological feature or lineament in the area. Multiplet sr004_01_95 is orientated in a north-south direction and steeply dipping in a southerly direction. Most high-angle faults that are observed at the surface at The Geysers are truncated above the reservoir and do not project to zones of high permeability within the reservoir (Thompson, 1992). The orientation of the multiplets do not correlate with the mostly-low-angle steam entries (Thomson and Gunderson, 1992) nor any known geological fault in the area.

The seismicity at The Geysers is largely non-tectonic in origin – it is industrially induced and thus it is expected that relative relocations (and other features of the seismicity) are not the same as for tectonic events. The results indicate that the induced seismicity does not occur on extensive fault planes as clusters of events are very tightly grouped and thus may result from very local changes in the stress field. Also, the seismicity may not be occurring on pre-existing fault planes aligned parallel to the tectonic trend but caused by fresh breaks in the reservoir. Further, if clusters are very compact and caused by industrial activity it suggests that the influence of production or reinjection at a well on seismicity is very localised.

5.4.6 Relation between commercial activity and multiplets

Seismic clusters at The Geysers were studied by Barton (1999) frequency-magnitude distribution and spatial fractal dimension of the seismicity. Certain seismic clusters incorporated in his study overlap the locations of the multiplets I studied using relative relocation (Table 5.7).

The study of seismic cluster 7 indicates multiple sr001_01_95 is adjacent to well 0970519 (Figure 5.9a). There is a possible link between increase in production and injection in 1991 and a burst in seismicity in 1991. There is also a possible correlation with an increase in seismicity and increase in injection in 1991. The typical production rate of this well was approximately 68 kg/s and the typical injection rate was 39 kg/s.

Table 5.7 Seismic clusters studied by Barton (1999) that are common to relocated multiplets.

Name of seismic cluster Studied by Barton (1999)	Multiplet name	Name of adjacent commercial Well
7	sr001_01_95	09790519
13	sr002_01_96	Prod. 1
10	sr003_01_95	09790565
14	sr004_01_95	Prod. 2

Multiplet sr002_01_96 lies in the vicinity of seismic cluster 13 studied by Barton (1999) (Figure 5.9b). This area has a low but continuous rate of production (extracting ~ 19 kg/s) with no known injection taking place. However, increases in seismicity and seismic moment in mid 1991, early 1992, mid 1993, and early 1994 were observed indicating the possible onset of injection in this area.

Seismic cluster 10 studied by Barton (1999) is located in the area of multiplet sr003_01_95 (Figure 5.9c). Although there are three injection wells in the vicinity of the cluster of events, the most prominent well is 0970565. Seismic clustering in the area of multiplet sr004_01_95 commenced in mid-1990 with the occurrence of ~ 20 events/month. Four major episodes of increased seismicity from 1991 to 1994 were observed with increased injection. Dense distribution of seismicity to the west of this cluster in 1992 migrating east and then north in 1993 to 1994 also broadly reflect the shape of the multiplet (Figure 5.9d). From mid 1990 approximately 20 events per month were recorded. However, during early 1993 this area was relatively quiescent.

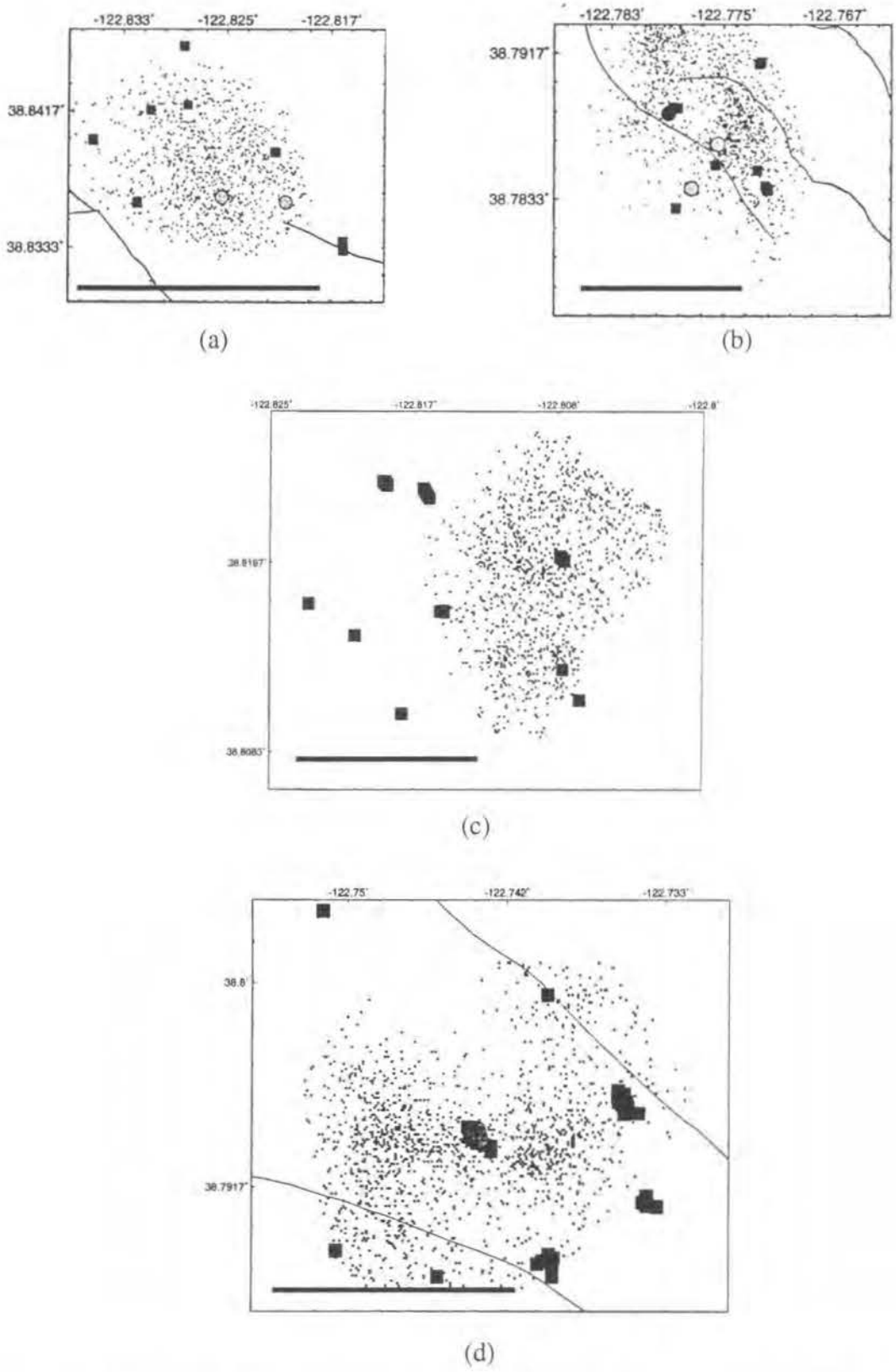

Figure 5.9: Seismic clusters that correspond to locations of multiplets (a) sr001_01_95 (b) sr002_01_96 (c) sr003_01_95 and (d) sr004_01_95. Thin black lines: local faults in the area, Circles: injection wells, squares: production wells and thick black horizontal lines: distance of 1 km (*from* Barton, 1998).

These studies show that the observed seismicity near these wells and production areas do not correlate with observed geological features such as surface faults (Figure 5.9). The effects of fluid flow paths and possible listric faults within the reservoir are yet to be studied in detail.

5.4.7 Comparison with other methods of relative relocation

Phillips *et al.* (1997) and Phillips *et al.* (2000) used a master-event technique and relocated events successfully at the Soultz Geothermal area in France. However, master-event techniques suffer from errors such as master-event mislocation and errors in the master-event arrival times propagate through the whole multiplet. The method of Got *et al.* (1994) does not require the selection of a master-event and in this respect is a superior relative relocation method. The key to the successful relative relocations at the Soultz geothermal area was the manual re-picking of all the arrival times.

Fehler *et al.* (2000) combined the joint hypocentre determination (JHD) technique of Block *et al.* (1994) and the "collapsing" technique of Jones and Stewart (1997) to relocate large number of events to the same accuracy of Phillips *et al.* (2000) where events were hand-picked. The hybrid "JHD-collapsing" method has been successful in geothermal areas such as Fenton Hills, New Mexico.

An efficient relocation technique which may combine the differential travel times derived from cross-spectral methods with travel-times differences formed from catalogue data is the "double difference technique" of Waldhauser and Ellsworth (2000). The double difference technique involves simultaneously determining inter-event and relocating other uncorrelated events to the accuracy of absolute travel time data without using station corrections (Waldhauser and Ellsworth, 2000). Such a method might be highly successful in an area such as The Geysers.

5.5 Future Work

- Obtain focal mechanism solutions using the new calibrations of the UNOCAL network.

- Perform more tomography inversions to continue monitoring the depletion of the reservoir.

- Develop quantitative interpretations of the changes in *Vp* and *Vs*.

- Apply 4-D LET to other geothermal and volcanic areas, as has already been done for Long Valley (Foulger *et al.*, 2001).

- Investigate why relative-relocation time delays are apparently inconsistent with the supposed ray parameters and computed relative relocations and quantitatively access the accuracy of the ray parameters.

- The *plotsin* program could be modified to incorporate relocation-related weights to improve the cosine plots.

- Events could be hand selected to improve the data quality.

- Comparison of the method of Got *et al.* (1994) with the relative relocation methods of Fehler *et al.* (2000) and Waldhauser and Ellsworth (2000) to determine the method best suited for The Geysers.

- Obtain focal mechanism solutions for the relocated events and attempt to establish if they are tectonic or industrially induced.

- Investigate whether the stations with monochromatic waveforms have true signals embedded in them or whether the signal is merely low-frequency noise. This could be achieved by analysing the cross-spectrum phase of the

signal or comparing the frequency bandwidth of the traces with those of strong clear events.

- Attempt progressive multiplet relative relocation to improve relocations.

- Make the relocation method more adaptable to an inhomogeneous structure by using a 3-D velocity model.

5.6 Conclusions

There is a direct correlation between seismicity and geothermal exploitation at The Geysers. In certain areas, seismicity increased rapidly with the onset of production and injection and subsided when production and injection were periodically curtailed as power plants ceased to be commercially viable due to decreases in reservoir pressure.

The orientations and polarities of previously uncalibrated stations of the UNOCAL network at The Geysers were studied. Uncalibrated seismic stations may be successfully calibrated using a simple method of identifying strong *P*-wave arrivals on the horizontal components and using good focal mechanisms solutions from known earthquakes. The best possible three-component station that could be used for focal mechanism solutions using the UNOCAL network is station DVB.

Commercial exploitation of The Geysers geothermal area is causing changes in local seismic structure that are detectable using repeat LET on a two-year time scale. The progressive depletion of pore fluid by the removal of steam causes the replacement of pore liquid with vapour. This increases compressibility, thereby reducing *Vp*, and also causes pore pressure decrease and the drying of argillaceous minerals e.g., illite, both of which increase the shear modulus and thus increase *Vs*. These three effects reinforce one another in reducing the *Vp/Vs* ratio.

In the period April 1991 to August 1998, three areas in the reservoir exhibited reductions in the *Vp/Vs* ratio of up to 4.8% consistent with a combination of these effects. Examination of the separate *Vp* and *Vs* fields indicates that water depletion was the most important process in the central part of the exploited reservoir, with pressure reduction and mineral drying being stronger effects more northwesterly and southeasterly.

The rate at which the *Vp/Vs* anomaly grew in strength between April 1991 and August 1998 suggests that the whole of the anomaly might have been caused by exploitation since the early 1960s. However, the observation that unexploited geothermal fields also exhibit low-*Vp/Vs* anomalies suggests that only part of the low-*Vp/Vs* anomaly may have been caused by exploitation.

Relative relocation of multiplets of earthquakes with coherent waveforms can improve locations and yield tightly clustered hypocentral distributions. This works best for events inside the seismic network, and poor for peripheral events. There is no evidence to suggest from relative relocation results that the earthquakes studied occur on planar fault surfaces, as they exhibited quasi-spherical hypocentral clusters. Further work is required to substantiate these results, which should be considered preliminary.

BIBLIOGRAPHY

Achauer, U., J. R. Evans and D. A. Stauber, High-resolution seismic tomography of compressional wave velocity structure at Newberry Volcano, Oregon Cascade Range, *J. Geophys. Res.*, **93**, 10135-10147, 1988

Aki, K. and W. H. K. Lee, Determination of three-dimensional velocity anomalies under a seismic array using first P arrival times from local earthquakes, I, A homogeneous initial model, *J. Geophys. Res.*, **81**, 4381-4399, 1976

Alessandrini, B., L. Filippi, A. Borgia, Upper-crust tomographic structure of the Central Apennines, Italy, from local earthquakes, *Tectonophysics*, **339**, 479-494, 2001

Allis, R. G., Mechanism of induced seismicity at The Geysers geothermal reservoir, California, *Geophys. Res. Lett.*, **9**, 629-632, 1982

Allis, R. G. and G. M. Shook, An alternative mechanism for the formation of The Geysers vapor-dominated reservoir, 24th *Workshop in Geotherm. Reservoir Engineering,* Stanford University, 53-63, 1999

Allis, R. G., P. Gettings, W. F. Isherwood and D. S. Chapman, Precision gravity changes at The Geysers geothermal reservoir 1975-2000, 26th *Workshop in Geotherm. Reservoir* Engineering Stanford University, 53-63, 2001

Amorose, D., J. L. Lagarde and E. Laville, Appoint pattern analysis of the distribution of earthquakes in Normandy (France), *Bull. Seismol. Soc. Am.*, **89**, 742-749, 1999

Atkinson, P., The continuing evolution of The Geysers project, draft manuscript, UNOCAL Exploration and Production Technology, Sugarland, Texas, 1998

Arnott, S. K. and G. R. Foulger, The Krafla spreading segment, Iceland 1 three-dimensional crustal structure and the spatial and temporal distribution of local earthquakes, *J. Geophys. Res.*, **99**, 23801-23825, 1994

Barker, B. J., M. S. Gulati, M. A. Byran, and K. L. Riedel, Geysers reservoir performance, *Geotherm. Res. Council Special Rep.*, **17**, 167-177, 1992

Barker, B. J and A. S. Pinogol, Geysers reservoir performance - an update, *Proceedings, 22nd Workshop on Reservoir Engineering*, Stanford University, 1997

Barton, D. J., Frequency-magnitude distribution and spatial fractual dimension of seismicity at The Geysers geothermal area and Long Valley Caldera California, *Ph.D.* Thesis University of Durham, UK, 1998.

Barton, D. J., G. R. Foulger, J. R. Henderson and B. R. Julian, Frequency-magnitude statistics and spatial correlation dimensions of earthquakes at Long Valley Caldera California, *Geophys. J. Int.*, **138**, 563-370, 1999

Benz, H. M., G. Zandt and D. H. Oppenheimer, Lithospheric structure of northern California from teleseismic images of the upper mantle, *J. Geophys. Res.*, **97**, 4791-4807, 1992

Blakely, R. J. and W. D. Stanley, The Geysers magma chamber, California: constraints from gravity data, density measurements and well information, *Geotherm. Res. Council Trans.*, **17**, 227-233, 1993

Block, L. V., C. H. Cheng, M. C. Fehler, and W. S. Phillips, Seismic imaging using microearthquakes induced by hydraulic fracturing, *Geophysics*, **59**, 102-112, 1994

Boitnott, G. N., Laboratory measurements on reservoir rocks from The Geysers geothermal field, *Proceedings, 20th Workshop on Reservoir Engineering*, Stanford University, 1995

Boitnott, G. N and P. J. Boyd, Permeability, electrical impedance and acoustic velocities on reservoir rocks from The Geysers geothermal field, *Proceedings, 21st Workshop on Reservoir Engineering*, Stanford University, 1996

Boitnott, G. N and A. Kirkpatrick, Interpretation of field seismic tomography at The Geysers geothermal field, California, *Proceedings, 22nd Workshop on Reservoir Engineering*, Stanford University, 1997

Bufe, C. G. and P. M. Shearer, Geothermal induced seismicity - Bane or blessing, *Proceedings Second DOE-ENEL Workshop for Cooperative Research in Geothermal Energy*, 86-97, National Technical Information Services, Springfield, VA, 1981

Bufe, C. G., S. M. Marks, F. W. Lester, R .S. Ludwin and M. C. Stickney, Seismicity of The Geysers-Clear Lake region, in *Research in The Geysers-Clear Lake Geothermal Area, Northern California, U. S. Geol. Surv. Prof. Pap.*, **1141**, 1128-138,1981

Bylee, J. D. and W. F. Brace, Modification of sliding characteristics by fluid injection and its significance for earthquake prevention (abstract), *EOS Trans. AGU*, **51**, 423, 1970

Castillo, D. A. and W. L. Ellsworth, Seismotectonics of the San Andreas fault system between Point Arena and Cape Mendocino in northern California; Implications for the development and evolution of a young transform, *J. Geophys. Res.*, **98**, 6543-6560, 1993

Dalrymple, G. B., M. Grove, O. M. Lovera, T. M. Harrison, J. B. Hulen and M. A. Lanphere, Age and thermal history of the Geysers plutonic complex (felsite unit), Geysers geothermal field, California: a 40 Ar/39 Ar and U-Pb study, *Earth Planet. Sci. Lett.*, **173**, 285-298, 1999

Deichmann, N. and M. Garcia-Fernandes, Rupture geometry from high-precision relative hypocentre locations of microearthquake clusters, *Geophys. J. Int.*, **110**, 510-517, 1992

Denlinger, R. P. *Geophysical constraints of The Geysers geothermal system, Northern California: Ph.D.* Thesis, Stanford University, 1979

Delenlinger, R. P. and R. L. Kovach, Seismic reflection investigations at Castle Rock Springs in The Geysers geothermal area, in *U.S. Geol. Surv. Prof. Pap.*, 1141, *Research in The Geysers-Clear Lake Geothermal Area, Northern California,* 83-96, 1981

Denlinger, R. P. and C. G. Bufe, Reservoir conditions related to induced seismicity at The Geysers steam reservoir, Northern California, *Bull. Seismol. Soc. Am.*, **72**, 1317-1327, 1982

Douglas, A., Joint epicentre determination, *Nature*, **215**, 47-48, 1967

Eberhart-Phillips D., Three-dimensional velocity structure in northern California Coast Ranges from inversion of local earthquake arrival times, *Bull. Seismol. Soc. Am.*, **76**, 1025-1062, 1986

Eberhart-Phillips D., Three-dimensional *P* and *S* velocity structure in the Coalinga region, California, *J. Geophys. Res.*, **95**,15343-15363, 1990

Eberhart-Phillips, D., Local earthquake tomography: earthquake source regions *in Seismic Tomography* eds. H.M.Iyer and K.Hirahara, 613-643, 1993

Eberhart-Phillips, D. and D. H. Oppenheimer, Induced seismicity in The Geysers geothermal area, California, *J. Geophys. Res.*, **89**, 1191-1207, 1984

Eberhart-Phillips, D. and A. J. Michael, Three-dimensional velocity structure, seismicity and fault structure in the Parkfield Region, Central California, *J. Geophys. Res.*, **98**, 15737-15758, 1993

Enedy, K. L. Downhole enthelpy and superheat evolution of Geysers Steam Wells *Geotherm. Res. Special Rep.*, **17**, 205-209, 1992

Evans, J. R. and J. J. Zucca, Active high-resolution seismic tomography of compressional wave velocity and attenuation structure at Medicine Lake volcano northern California Cascade Range, *J. Geophys. Res.*, **93**, 15016-15036, 1988

Evans, J. R. and J. J. Zucca, Active high-resolution (NeHT) tomography: velocity and *Q*, *in Seismic Tomography* eds. H.M.Iyer and K.Hirahara, 695-732, 1993

Evans J. R., D. Eberhart-Phillips and C. H. Thurber, User's manual for SIMULPS12 for imaging *Vp* and *Vp/Vs*: A derivative of the "Thurber" tomographic inversion SIMUL3 for local earthquakes and explosions, *U.S. Geol. Surv. Open-File Rept., 80-1060*, 1-50, 1994

Evans, J. R., B. R. Julian, G. R. Foulger and A. Ross, Shear-wave splitting from local earthquakes at The Geysers geothermal field, California, *Geophys. Res. Lett.* **22**, 501-504, 1995

Fehler, M., W. S. Phillips. L. House, R. H. Jones, R. Esther, and C. Rowe, Improved relative locations of clustered earthquakes using constrained multiple event location, *Bull. Seismol. Soc. Am.*, **90**, 775-780, 2000

Foulger, G. R. and D .R. Toomey, Structure and evolution of the Hengill-Grensdular central volcano complex, Iceland: Geology, Geophysics and seismic tomography, *J. Geophys. Res.*, **17**, 511-522, 1989

Foulger, G. R., C. C. Grant, A. Ross and B. R. Julian, Industrially induced changes in Earth structure at The Geysers geothermal area, California, *Geophys. Res. Lett.*, **24**, 135-137, 1997

Foulger, G. R., B. R. Julian, A. M. Pitt, D. P. Hill, P. E. Malin and E. Shalev, Tomographic crustal structure of Long Valley Caldera, California, and evidence for the migration of CO_2 between 1989 and 1997, *submitted.*

Foulger, G. R., A. D. Miller, B. R. Julian, and J. R. Evans, Three-dimensional *Vp* and *Vp/Vs* structure of the Hengill triple junction and geothermal area, Iceland and the repeatability of tomographic inversion, *Geophys. Res. Lett.*, **22**, 1309-1312, 1995

Frechet, J. *Sismogenese et doublets* sismiques, these d-Teat, pp207, Univ. Sci. Technolmedic., Grenoble, 1985

Furlong, K. P., Thermal-realogic evolution of the upper mantle and the development of the San Andreas fault system, *Tectonophysics*, **223**, 149-164,1993

Furlong, K. and S. M. Atkinson, Seismicity and thermal structure along the northern San Andreas fault system, California, USA, *Tectonophysics*, **217**, 23-30, 1993

Furlong, K. P., W. D. Hugo and G. Zandt, Geometry and evolution of the San Andreas fault zone in northern California, *J. Geophys. Res.*, **94**, 3100-3110, 1989

Grant, C. C., *Imaging the progressive depletion of The Geysers geothermal field, Northern California, using three-dimensional seismic tomography, M.Sc.* Thesis, University of Durham, 1995

Got, J-L. and O. Coutant, Anisotropic scattering and travel time delay analysis in Kilaeua volcano, Hawaii, earthquake coda waves, *J. Geophys. Res.*, **102**, 8397-8410, 1997

Got, J-L., J. Frechet and F. W. Kline, Deep fault plane geometry inferred from multiplet relative relocation beneath the south flank of Kilauea, *J. Geophys. Res.*, **99**, 15375-15386, 1994

Goyal, K. P., Injection experience in The Geysers California – A summary, *Geotherm. Res. Council Trans.*, **23**, 541-548, 1999

Gunderson, R. P., Distribution of Oxygen isotopes and non-condensible gas in steam at The Geysers, *Geotherm. Res. Council Trans.*, **17**, 133-138, 1991

Gunderson, R. P., Porosity of reservoir greywacke at The Geysers, in Stone C, *Geotherm. Res. Council Special Rep.*, **17**, 89-93, 1992

Hamilton, R. M. and L. J. P. Muffler, Earthquakes at The Geysers geothermal area, California, *J. Geophys. Res.*, **77**, 2081-2086, 1972

Hauksson, E. and Hasse, J. S., Three-dimensional *Vp* and *Vp/Vs* velocity models of the Los Angeles basin and central Traverse Ranges, California, *J. Geophys. Res.*, 102, 5423-5453, 1997

Hawley, B. W., G. Zandt and R. B. Smith, Simultaneous inversion for hypocentre and lateral velocity variations: an iterative solution with a layered model, *J. Geophys. Res.*, **86**, 7073-7076, 1981

Hearn, B. C., J. M. Donelly and F. E. Goff, Geology and chronology of the Clear Lake Volcanics, California, *United Nations Symposium on development and use of geothermal resources*, **1**, 423-428, 1976

Hearn, B. C., J. M. Donnely and F. E. Goff, Clear-Lake Volcanics:Tectonic setting and magma sources, *U. S. Geol. Surv. Prof. Pap.*, **1141**, 1981

Hill, D. P., J. P. Eaton and L. M. Jones, Seismicity, 1980-1986, *U.S. Geol. Surv. Prof. Pap.*, **1515**, in the San Andreas fault system California, (eds. R.E.Wallace)115-151, 1990

Hodgson, S. F., A Geysers album, *Geotherm. Res. Council Special Rep.*, **17**, 19-40, 1992

Hubbert, M. K. and W. W. Rubey, Role of fluid pressure in mechanics of over-thrust faulting, *Geol. Soc. Am. Bull.*, **70**, 115-166, 1959

Hulen, J. B., and D. L. Nielson, Interim report on geology of The Geysers felsite, northwest California, *Geothem. Res. Council Trans.*, **17**, 249-258, 1993

Isherwood, W. F., Gravity and magnetic studies of The Geysers-Clear Lake geothermal region, California, *United Nations Symposium on Development and Use of Geothermal Resources*, **2**, 1-65-1073, 1975b

Isherwood, W. F., Gravity and magnetic studies of The Geysers-Clear Lake geothermal region, California, *United Nations Symposium on Development and Use of Geothermal Resources, San Francisco, Proceedings*, **2**, 1065-1073, 1976

Isherwood, W. F., Geophysical overview of The Geysers, in *U.S. Geol. Surv. Prof. Pap.*, 1141, *Research in The Geysers-Clear Lake Geothermal Area, Northern California,* 83-96, 1981

Ito, A., High resolution relative hypocentre of similar earthquakes by cross-spectral analysis method, *J.Phys.Earth*, **33**, 279-294, 1985

Ito, H., J. De Vilbiss and A. Nur, Compressional and shear waves in saturated rocks during water-steam transition, *J. Geophys. Res.*, **84**, 4731-4735, 1979

Iyer, H. M., D. H. Oppenheimer, T. Hitchcock, J. N. Roloff and J. M. Coakley, Large teleseismic P-wave delays in The Geysers-Clear Lake geothermal area, in *Research in The Geysers-Clear Lake geothermal area, northern California*, R. J. Mclaughlin and J. M. Donnely-Nolan, Eds., *U. S. Geol. Surv. Prof. Pap.*, **1141**, 97-116, 1981

Jachens, R. C. and A. Grimson, Three-dimensional geometry of the Gorda plate beneath northern California, *J. Geophys. Res.*, **88**, 9375-9392, 1983

Jenkins, G. M. and D. G. Watts, *Spectral analysis and its applications*, Holden-Day, Oakland, Calif., 1968

Jones, R. and R. C. Stewart, A method for determining significant structures in a cloud of earthquakes, *J. Geophys. Res.*, **102**, 8245-8254, 1997

Julian, B. R. and G. R. Foulger, Earthquake mechanisms from linear-programming of seismic-wave amplitude ratios, *Bull. Seismol. Soc. Am.*, **86**, 972-980, 1996

Julian, B. R., A. D. Miller, and G. R. Foulger, Non-shear focal mechanism of earthquakes at The Geysers, California, and Hengill, Iceland, geothermal areas, *Geotherm. Res. Council Trans.*, **17**, 123-128, 1993

Julian, B. R., A. Ross, and G. R. Foulger, Three-dimensional seismic image of a geothermal reservoir: The Geysers, California, *Geophys. Res. Lett.*, **23**, 685-688, 1996

Julian, B. R., A. D. Miller, and G. R. Foulger, Non-double-couple earthquakes 1. theory, *Reviews of Geophysics*, **36**, 525-549, 1998

Julian, B. R., A. Ross, G. R. Foulger and J. R. Evans, Three-dimensional seismic image of a geothermal reservoir: the Geysers, California, *Geophys. Res. Lett.*, **23**, 685-688, 1996

Kedar, S., B. Sturtevamt and H. Kanamori, The origin of harmonic tremour at Old Faithful geyser, *Nature*, **379**, 708-711, 1996

Kennedy, B. M. and A. H. Truesdale, Active-degassing in NW Geysers High-temperature reservoir, *Geotherm. Res. Council Trans.*, **18**, 325-330, 1994

Kennedy, B. M. and A. H. Truesdell, The northwest Geysers high-temperature reservoir: evidence for active magmatic degassing and implications for the origin of the Geysers geothermal field, *Geothermics*, **25**, 365-387, 1996.

Kerr, R.A., Geothermal tragedy of the commons, *Science*, **235**, 134-135, 1991

Kirkpatrick, A., J. E. Peterson and E. L. Majer, Microearthquake monitoring at the south east geysers using a high resolution digital array, *Proceedings. 20th Workshop in Geotherm. Reservoir Engineering* Stanford University, 79-89, 1995

Kirkpatrick, A., J. E. Peterson. Jr., and E. L. Majer, Source mechanisms of microearthquakes at the southeast Geysers geothermal field, California, *Proceedings. 21st Workshop on Geothermal Reservoir Engineering,* Stanford University, 1996

Kirkpatrick, A., J. E. Peterson Jr., and E. L. Majer, Three-dimensional compressional and shear wave seismic velocity models for the southeast Geysers, *Proceedings, 22nd Workshop on Reservoir Engineering*, Stanford University, 1997

Kissling, E., W. L. Ellsworth, D. Eberhart-Phillips and U. Kradolfer, Initial reference models in local earthquake tomography, *J. Geophys. Res.,* **99**, 19635-19646, 1994

Lange, A. L. and W. H. Westphal, Microearthquakes near The Geysers, Sonoma Country, California, *J. Geophys. Res.,* **74**, 4377, 1969

Lawson, C. L. and R. J. Hanson, eds. Solving least square problems Prentice-Haul, Englewood Cliffs, New Jersey, 1974

Lees, J. M., Multiplet analysis at Coso Geothermal, *Bull. Seismol. Soc. Am.*, **88**, 1127-1143, 1998

Lin, X. D. and S. W. Roecker, Determination of earthquake hypocentres, focal mechanisms, and velocity structure in the Morgan Hill area through three-dimensional circular ray tracing, *EOS*, **71**, 1445, 1990

Lofgren, B. E., Monitoring crustal deformation in The Geysers - Clear Lake region, in *U.S. Geol. Surv. Prof. Pap.*, 1141, *Research in The Geysers-Clear Lake Geothermal Area, Nnorthern California,* 139-148, 1981

Lou, M., E. Shalev, and P. E. Malin, Shear-wave splitting and fracture alignments at the Northwest Geysers California, *Geophys. Res. Lett.*, **24**, 1895-1898, 1997

Ludwin, R.S. and C. G. Bufe, Continued seismic monitoring of The Geysers, California geothermal area, *U.S. Geol. Surv. Open-File Rept.,* 80-1060, 50, 1980

Ludwin, R. S., V. Cagnetti and C. G. Bufe, Comparison of seimcity in The Geysers geothermal area with the surrounding region, *Bull. Seismol. Soc. Am.*, **72**, 863-871, 1982

Majer E. L. and T. V. McEvilly, Seismological investigations at The Geysers geothermal field, *Geophysics*, **44**, 246-269, 1979

Manificat, G. and Y. Gueguen, What does control *Vp/Vs* in granular rocks, *Geophys. Res. Lett.,* **25**, 381-384, 1998

Marks, S. M., R. S. Ludwin, K. B. Louie, and C. G. Bufe, Seismic monitoring at The Geysers geothermal field, California, *U.S. Geol. Surv. Open-File Rept., 78-798*, 1978

Mavko, G. M., Velocity and attenuation in partially molten rocks, *J. Geophysics. Res.*, **85**, 5173-5189, 1980

Mavko, G. M. and A. Nur, Wave attenuation in partially saturated rocks, *Geophysics*, **44**, 161-178, 1979

McLaughlin, R. J., Tectonic setting of pre-tertiary rocks and its relation to geothermal resources in The Geysers-Clear Lake area, *U. S. Geol. Surv. Prof. Pap.*, **1141**, 1981

Menke, W., *Geophysical data analysis: discrete inverse theory*, Academic Press, San Diego, California, 1989

Michael, A. J., Effects of three dimensional velocity structure on the seismicity of the 1984 Morgan Hill, California aftershock sequence, *Bull. Seismol. Soc. Am.*, **78**, 1199-1221, 1988

Miller, A. D., Seismic structure and earthquake focal mechanism of the Hengill volcanic complex, SW Iceland *Ph.D.* Thesis pp208 University of Durham, England, 1996

Miller, A. D., G. R. Foulger, and Bruce R. Julian, Non-double-couple earthquakes 2. observations, *Reviews of Geophysics*, **36**, 551-568, 1998

Morelli, A., Teleseismic tomography: core-mantle boundary, in *Seismic Tomography* eds. H.M.Iyer and K.Hirahara, 163-189, 1993

Mossop A. and P. Segall, Subsidence at The Geysers geothermal field, N. California from a comparison of GPS and leveling, *Geophys. Res. Lett.*, **24**, 1839-1842, 1997

Mosteller, F. and J. W. Tukey, Data analysis and regression, Addision-Wesley, Redding Mass., 1979

Nicholson, C. and D. W. Simpson, Changes in *Vp/Vs* with depth: Implications for appropriate velocity models, improved earthquake locations, and material properties of the upper crust, *Bull. Seismol. Soc. Am.*, **75**, 1105-1123, 1985

O'Connell, D. R. H., Seismic velocity structure and microearthquake source properties at The Geysers, Califor nia, geothermal area, *Ph.D.* Thesis, University of California, Berkeley, California, 1986

O'Connell, D. R. H. and J. R. Johnson, Second-Order moment tensors of microearthquakes at The Geysers, geothermal field, California, *Bull. Seismol. Soc. Am.*, **78**, 1674 -1692, 1988

O'Connell, D. R. H. and J. R. Johnson, Progressive inversion for hypocentres and P wave and S wave velocity structure: Application to The Geysers, California, geothermal field, *J. Geophys. Res.*, **96**, 6223-6236, 1991

Oppenheimer, D. H., Extensional tectonics at The Geysers geothermal area, California, *J. Geophys. Res.*, **89**, 1191-1207, 1986

Oppenheimer, D. H. and J. P. Eaton, Moho orientation beneath central California from regional earthquake travel times, *J. Geophys. Res.*, **96**, 6223-6236, 1984

Oppenheimer, D. H. and K. E. Herkenhoff, Velocity-density properties of the lithosphere from three-dimensional modelling at The Geysers-Clear Lake Region, California, *J. Geophys. Res.*, **86**, 6057-6065, 1981

Oppenheimer, D. H., Extensional tectonics at The Geysers geothermal area, California, *J. Geophys. Res*, **91**, 11463-11476, 1986

Pavlis, G. L. and J. R. Booker, The mixed discrete-continuous inverse problem: application to the simultaneous determination of earthquake hypocentres and velocity structure *J. Geophys. Res.*, **85**, 4801-4810, 1980

Phillips, W. S., Precise microearthquake locations and fluid flow in the geothermal reservoir at Soults-Sous-Forets, France, *Bull. Seismol. Soc. Am.*, **90**, 212-228, 2000

Phillips, W. S., L. House, and M. Fehler, Detailed joint structure in a geothermal reservoir from studies of induced microearthquake clusters, *J. Geophys. Res.*, **102**, 11745-11763, 1997

Poupinet, G., W. L. Ellsworth and J. Frechet, Monitoring velocity variations in the crust using earthquake doublets: an application to the Calaveras fault, California, *J. Geophys. Res.*, **89**, 5719-5731, 1984

Romero Jr., A. E., A. Kirkpatrick, E. L. Majer and J. E. Peterson Jr., Seismic monitoring at The Geysers geothermal field, *Geotherm. Res. Council Trans*, **18**, 331-338, 1994

Romero Jr, A. E., T. V. McEvilly, E. L. Majer and D. Vasco, Characterization of the geothermal system beneath the Northwest Geysers steam field, California, from seismicity and velocity patterns, *Geothermics*, **24**, 471-487, 1995

Romero, A. E., T. V. McEvilly and E. L. Majer, 3-D microearthquake attenuation tomography at the NW Geysers geothermal region, California, *Geophysics*, **62**, 149-167, 1997

Ross, A., The Geysers geothermal area, California: Tomographic images of the depleted steam reservoir and non-double couple earthquakes, *Ph.D.* Thesis pp 240, University of Durham, England, 1996

Ross, A., G. R. Foulger, and Bruce R. Julian, Non-double-couple earthquake mechanism at The Geysers geothermal area, California, *Geophys. Res. Lett.*, **23**, 877-880, 1996

Ross, A., G. R. Foulger and B. R. Julian, Source processes of industry-induced earthquakes at The Geysers geothermal area, California, *Geophysics*, **64**, 1877-1889, 1999

Rubin, A. M., D. Gillard and J-L. Got, Streaks of microearthquakes along creeping faults, *Nature*, **400**, 635-641, 1999

Segall, P., Earthquakes triggered by fluid extraction, *Geology,* **17**, 942-946, 1989

Spencer, J. W. and A. M. Nur, The effects of pressure, temperature and pore water on velocities in westerly granite, *J. Geophys. Res.*, **81**, 889-904, 1976

Spenser, C. and D. Gubbins, Travel time inversion for simultaneous earthquake location and velocity structure determination in laterally varying media, *Geophys. J. R. Astron. Soc.*, **63**, 95-116, 1980

Stanley W. D. and R. J. Blakely The Geysers-Clear Lake geothermal area, California-an updated geophysical perspective of heat sources, *Geothermics*, **24**, 187-221, 1995

Stark, M. A., Imaging injected water in The Geysers reservoir using Microearthquake data, *Geotherm. Res. Council Trans.*, **14**, 1-8, 1990

Stark, M. A., Microearthquakes-A tool to track injected water in The Geysers reservoir, *Geotherm. Res. Council Special Rep.*, **17**, 111-117, 1992

Stark, M. A. and S. D. Davies, Remotely triggered microearthquakes at The Geysers geothermal field, California, *Geophys. Res. Lett.*, **23**, 945-948, 1996

Steeples, D. W. and H. M. Iyer., Teleseismic P-wave delays in geothermal exploration: *Proceedings United Nations Symposium on the development and use of Geothermal Resources, 2ed, San Francisco, 1975,* **2**, 1199-1206, 1976

Thompson, R. C., Structural stratiagraphy and intrusive rocks at The Geysers geothermal field, *Geotherm. Res. Council Special Rep.*, **17**, 59-63, 1992

Thompson, R. C. and R. P. Gunderson, The orientation of steam-bearing fractures at The Geysers geothermal field, *Geotherm. Res. Special Rep.*, **17**, 65-68, 1992

Toomey D. R. and G. R. Foulger, Tomographic inversion of local earthquake data from the Hengill-Grensdular central volcano complex, Iceland, *J. Geophys. Res.*, **17**, 497-510, 1989

Thurber, C. H., Earth structure and earthquake locations in the Coyote Lake Area, Central California, *Ph.D.* Thesis pp332, Massachusetts Institute of Technology Cambridge, Massachusetts, 1981

Thurber, C. H., Earthquake locations and three-dimensional crustal structure in the Coyote Lake area, central California, *J. Geophys. Res.*, **88**, 8226-8236, 1983.

Thurber, C. H., Local earthquake tomography: velocities and *Vp/Vs*-theory, *in Seismic Tomography* eds. H. M. Iyer and K. Hirahara, 563-583, 1993

Thurber, C. H. and W. L. Ellsworth, Rapid solution of rate tracing problems in heterogeneous media, *Bull. Seismol. Soc. Am.*, **70**, 1137-1148, 1980

Toksoz, M. N., C. H. Cheng and A. Timur, Velocities of seismic in porous rocks, *Geophysics*, **41**, 6211-645, 1976

Truesdell, A. H., J. R. Hairzlip, W. T. Box Jr. and F. D'Amore, A geochemical overview of The Geysers geothermal reservoir, *Geotherm. Res. Council Special Rep.*, **17**, 121-132, 1992

Truesdale, A. H., M. Walters, M. Kennedy and M. Lippermann, An intergrated model for the origin of The Geysers geothermal field, *Geotherm.l Res. Council Trans.*, **17**, 273-280, 1993

Um, J. and C. H. Thurber, A fast algorithm for two-point seismic ray tracing. *Bull. Seismol. Soc. Am.*, **77**, 786-792, 1987

Vidale, J. E., Finite-difference calculation of travel times in three dimensions, *Geophysics*, **55**, 521-526, 1990

Waldhauser, F. and W. L. Ellsworth, A double-difference earthquake location algorithm: method and application to the Northern Hayward fault, California, *Bull. Seismol. Soc. Am.*, **90**, 1353-1368, 2000

Walter, S. R., Intermediate-focus earthquakes associated with Gorda plate subduction in northern California, *Bull. Seismol. Soc. Am.*, **76**, 583-588, 1986

Walters, M. A., J. N. Sternfield, J. N. Haizlip, J. R. Drenick, A. F. Combs and J. Combs, A vapor-dominated reservoir at The Geysers, California, *Geotherm. Res. Council Special Rep.*, **17**, 121-132, 1992

Wang, Z., and A. M. Nur, Effects of CO_2 flooding on wave velocities in rocks with hydrocarbons, *Soc. Petr. Eng. Res. Eng.*, **3**, 429-436, 1989

Wang, Z., M. E. Cates and R. T. Langen, Seismic monitoring of a CO_2 flooding a carbonate reservoir: a rock physics study, *Geophysics*, **63**, 1604-1617, 1998

Ward, P. L., Microearthquakes: Prospecting tool and possible hazard in the development of geothermal resources, *Geothermics*, **1**, 1972

Young, C. Y. and R. W. Ward, Attenuation of teleseismic P-waves in The Geysers-Clear Lake region. *Research in The Geysers-Clear Lake Geothermal Area, Northern California, U.S. Geol. Surv. Prof. Pap.*, **1141**, 149-160, 1981

Zucca, J. J., L. J. Hutchings and P. W. Kasameyer, Seismic velocity and attenuation structure of the geysers geothermal field, California, *Geothermics*, **23**, 111-126, 1994

Appendix 1: Station co-ordinates for seismic stations at The Geysers

Co-ordinates of stations of the permanent CALNET, CCPA and LBL networks and the temporary IRIS network deployed for month of April 1991,in the WGS84 ellipsoid reference frame.

CALNET network

Station code	Latitude (°N)	Longitude (°W)	Height (m asl)	Sensor type
GACM	38:52.3642	-122:51.7969	969.01	Vertical-only
GAXM	38:42.6444	-122:45.3666	363.00	Vertical-only
GBGM	38: 48.8343	-122:40.8265	1108.86	Vertical-only
GBMM	39:08.5040	-122:29.7065	958.49	Vertical-only
GCMM	38:48.3443	-122:45.3766	1269.94	Vertical-only
GCRM	38:46.3843	-122:42.9866	702.93	Vertical-only
GCSM	39:01.3639	-123:31.3380	679.49	Vertical-only
GCVM	38:46.1742	-123:00.8970	134.21	Vertical-only
GCWM	39:07.8439	-123:04.6174	1073.04	Vertical-only
GDCM	38:46.0242	-123:14.3774	756.41	Vertical-only
GDXM	38:48.4543	-122:47.6967	914.98	Vertical-only
GGLM	38:53.7942	-122:46.6468	876.91	Vertical-only
GGPM	38:45.8743	-122:50.7168	1038.05	Vertical-only
GGUM	38:51.3840	-123:29.9378	645.57	Vertical-only
GHCM	38:36.3543	-123:11.8772	502.47	Vertical-only
GHGM	39:07.6939	-122:49.5370	886.81	Vertical-only
GHLM	39:02.4240	-123:01.1872	940.05	Vertical-only
GHOM	39:02.6638	-123:32.4780	671.49	Vertical-only
GHVM	39:05.0940	-122:44.1268	1019.75	Vertical-only
GMCM	38:47.5542	-123:07.8672	410.30	Vertical-only
GMKM	38:58.1641	-122:47.2868	889.88	Vertical-only
GMMM	38:50.2842	-122:47.9967	946.97	Vertical-only
GMOM	38:42.6043	-123:08.6572	786.36	Vertical-only
GPMM	38:50.8442	-122:56.8470	767.10	Vertical-only
GRTM	38:56.3142	-122:40.2466	602.78	Vertical-only
GSGM	38:51.9942	-122:42.6666	1063.86	Vertical-only
GSMM	38:46.1543	-122:46.9467	1000.99	Vertical-only
GSNM	38:56.4240	-123:11.5674	854.26	Vertical-only
GSSM	38:42.1143	-123:00.8770	266.25	Vertical-only
GTSM	39:18.6938	-122:36.2168	1086.49	Vertical-only
GWKM	39:03.1141	-122:29.5264	824.54	Vertical-only
GWRM	39:12.4237	-123:18.0578	642.19	Vertical-only
NFRM	38:31.3544	-123:09.7271	512.49	Vertical-only
NHBM	38:35.3544	-122:54.0667	149.22	Vertical-only
NMCM	38:35.4544	-122:54.8067	132.22	Vertical-only
NMHM	38:40.1644	-122:37.9963	1294.91	Vertical-only
NMTM	38:48.3343	-122:26.8261	405.65	Vertical-only
NMWM	38:33.0245	-122:43.4364	118.07	Vertical-only
NPVM	38:38.5445	-122:25.6160	196.72	Vertical-only
NSHM	38:31.1946	-122:36.4942	311.98	Vertical-only

IRIS network

Station code	Latitude (°N)	Longitude (°W)	Height (m asl)	Sensor type
G001	38:45:53.40336	-122:50:44.37724	1015.53	3-component
G002	38:47:15.05548	-122:48:59.53313	892.96	3-component
G003	38:47:55.96188	-122:51:29.70299	718.51	3-component
G004	38:45:31.63140	-122:45:09.96710	931.59	3-component
G005	38:47:13.69062	-122:45:57.86943	830.11	3-component
G006	38:47:49.55532	-122:42:50.31403	758.56	3-component
G007	38:50:34.25420	-122:42:40.84369	986.59	3-component
G008	38:49:27.90007	-122:48:37.51063	670.15	3-component
G009	38:50:16.31845	-122:47:31.71459	950.34	3-component
G010	38:51:48.98260	-122:48:0758314	734.90	3-component
G011	38:46:15.59994	-122:47:00.83818	1008.76	3-component
G012	38:43:56.88720	-122:47:41.33932	527.92	3-component
G013	38:50:40.33265	-122:53:58.03892	741.50	3-component
G014	38:49:4298632	-122:49:48.84715	586.40	3-component
G015	38:49:37.48337	-122:45:06.47180	911.08	3-component

CCPA network

Station code	Latitude (°N)	Longitude (°W)	Height (m asl)	Sensor type
01	38:50.0742	-122:48.9568	705.98	3-component
02	38:50.4742	-122:49.0968	860.98	3-component
03	38:50.5442	-122:49.4268	797.98	3-component
04	38:49.9642	-122:49.8168	485.99	3-component
05	38:49.7142	-122:49.8168	599.00	3-component
06	38:49.5142	-122:49.3086	688.99	3-component
07	38:49.6942	-122:48.7668	610.98	3-component
08	38:50.2342	-122:48.2768	885.97	3-component
09	38:50.7442	-122:48.6968	889.97	3-component
10	38:50.8142	-122:49.5968	799.98	3-component
11	38:50.4542	-122:50.2068	593.99	3-component
12	38:49.7842	-122:51.0868	668.02	3-component
13	38:50.6142	-122:51.3268	509.01	3-component
14	38:50.8842	-122:50.8968	633.00	3-component
15	38:51.5142	-122:50.3868	952.99	3-component
16	38:51.6442	-122:49.7068	968.97	3-component

LBL network

Station code	Latitude (°N)	Longitude (°W)	Height (m asl)	Sensor type
01	38 :46.0843	-122 :41.9565	616.91	3-component
02	38 :44.4043	-122 :42.6565	1055.90	3-component
03	38 :45.0443	-122 :41.4665	822.91	3-component
04	38 :46.5843	-122 :42.9066	678.92	3-component
05	38 :47.0043	-122 :44.1866	950.93	3-component
06	38 :46.2443	-122 :45.9466	839.97	3-component
07	38 :45.8143	-122 :45.2366	870.96	3-component
08	38 :45.7843	-122 :43.4266	978.94	3-component
09	38 :45.2443	-122 :43.1965	980.94	3-component
10	38 :45.3343	-122 :44.0666	913.95	3-component
11	38 :45.1643	-122 :44.6666	1002.90	3-component
12	38 :47.0343	-122 :45.1366	975.95	3-component
13	38 :46.3943	-122 :44.2766	977.94	3-component

Appendix 2: Script for finding sensor orientation and example of output of script *staor.sh*.

Script *Staor.sh*

```
#!/bin/sh

# script staor.sh

nawk '
# Compute seismic station orientation
# from P -wave amplitudes on horizontal components
# RCG August 1998

      #AZ = azimuth from station to earthquake;
      #RT = azimuth of P-wave particle motion;
      #DEV = sensor magnitude

      # convert string of form (+-)ddd.dd:mm.mm to angle
      function angle(s) {
            split (s,a,":")
            sign=1.0
            if (a[1] <0) {
                  sign= -1.0;
                  a[1]= -a[1];
            }
            return sign*(a[1] + (a[2] + a[3]/100)/60);
      }

      BEGIN {
                Deg = 57.2957795;
                Rearth = 6371.2;
                PI = 3.14159;
      }

       {
            #printf("earthquake %s\n",$1)

            # Earthquake locations
            stalat = angle($4)/Deg
            stalon = angle($5)/Deg

            #finding N - S Distance
            late= angle($2)/Deg

            #NDS= (late - stalat) * Rearth
            #printf("North-South Dist. from station to eq is %6.2f
km\n", NDS)

            #finding E - W Distance
            lone= angle($3)/Deg

            # Distance to Eq. axis
            r = Rearth * cos(late)
            EWD= (lone - stalon) * r
            #printf("East-West Dist. from station to eq is %.2f
km\n", EWD)
```

```
                    if (NDS==0 && EWD==0) {
                    printf(" Domain error, in line %d,check
coordinates\n",NR);
                    printf("\n")
                    next
                    }

              #calculating azimuth from station to earthquake
              AZ  = atan2(EWD,NDS)
              #printf("azimuth is %.2f degrees\n", AZ * Deg)

              if ($8==0 && $7==0) {
                          printf(" Domain error in line %d, check
amplitudes\n",NR);
                          printf("\n")
                    next
                    }

              # finding rotation angle of observed P wave amplitudes
              RT = atan2($8,$7)

              # finding sensor orientation for 1st motion polarity
              if ($6 == "u") {
                    DEV = AZ - RT
              }
              else if ($6 == "d") {
                    DEV = AZ - RT + PI
                    while (DEV > (2 * PI)) {
                          DEV -=  (2 * PI)
                    }
              }
              else
                    printf("error, check data file\n")
              while (DEV < 0) {
                    DEV += (2 * PI)
              }
              #printf(" final sensor orientation azimuth is %2.2f
degrees\n", DEV * Deg)
              AN= DEV * Deg
              print NR, $1, NDS, EWD, AN
      }' $*
```

Example of input file: for station FUM

```
033091e7 38:47:58 -122:45:00 38:47:35 -122:47:16 u   35   71
03315181 38:47:58 -122:44:88 38:47:35 -122:47:16 d  -40  -60
03602af1 38:47:51 -122:44:14 38:47:35 -122:47:16 d  -45  -98
04123169 38:50:51 -122:49:54 38:47:35 -122:47:16 d  -81   57
042147fa 38:46:36 -122:44:82 38:47:35 -122:47:16 d   93  -78
04218a29 38:47:77 -122:45:88 38:47:35 -122:47:16 d  -65 -136
043013bf 38:50:41 -122:49:16 38:47:35 -122:47:16 d  -95   41
04612c21 38:47:20 -122:45:43 38:47:35 -122:47:16 u  -32   64
05122abc 38:47:11 -122:45:47 38:47:35 -122:47:16 d   49  -65
052085a5 38:50:34 -122:49:22 38:47:35 -122:47:16 u  117  -24
0521802e 38:47:72 -122:44:54 38:47:35 -122:47:16 d  -65 -165
054223db 38:49:12 -122:48:16 38:47:35 -122:47:16 u  114  -41
```

```
05619897 38:48:67 -122:48:42 38:47:35 -122:47:16 u   92  -37
05620d95 38:48:98 -122:48:84 38:47:35 -122:47:16 d -440  293
057159fa 38:47:66 -122:46:00 38:47:35 -122:47:16 d -262 -422
05815b54 38:48:46 -122:46:33 38:47:35 -122:47:16 u   85   32
05818627 38:48:62 -122:48:30 38:47:35 -122:47:16 u   35   -8
0590235d 38:48:04 -122:48:26 38:47:35 -122:47:16 u   28  -36
059237c5 38:48:06 -122:46:20 38:47:35 -122:47:16 d -175 -139
0600811f 38:48:39 -122:48:75 38:47:35 -122:47:16 u   85  -81
```

Example of output:

results for station FUM:

NR#	Earthquake	N-S dist/km	E-W dist/km	azimuth/deg
1	033091e7	0.426261	3.12011	18.4619
2	03315181	0.426261	3.29345	26.3156
3	03602af1	0.296529	4.36244	20.7754
4	04123169	5.85645	-3.43554	4.73709
5	042147fa	-1.83477	3.38108	338.474
6	04218a29	0.778389	1.84887	2.71374
7	043013bf	5.67112	-2.88708	356.364
8	04612c21	-0.27800	2.4992	339.782
9	05122abc	-0.44479	2.44146	333.314
10	052085a5	5.54139	-2.97374	343.372
11	0521802e	0.685724	3.78445	11.2313
12	054223db	3.28035	-1.44397	356.022
13	05619897	2.44637	-1.8196	345.267
14	05620d95	3.02089	-2.42596	354.893
15	057159fa	0.574525	1.67558	12.9085
16	05815b54	2.05717	1.19868	9.59886
17	05818627	2.3537	-1.64632	337.903
18	0590235d	1.27878	-1.58877	0.955135
19	059237c5	1.31585	1.38656	8.03939
20	0600811f	1.92744	-2.29631	353.628

Example of seismic picks and program *epick*

(a)

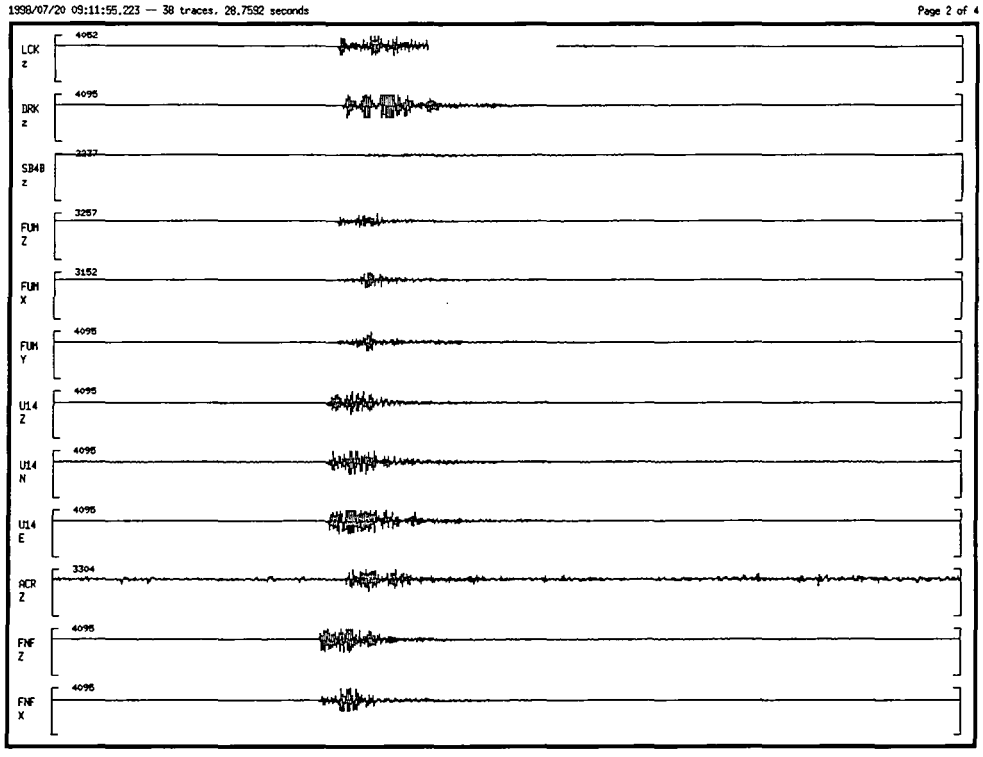

(b)

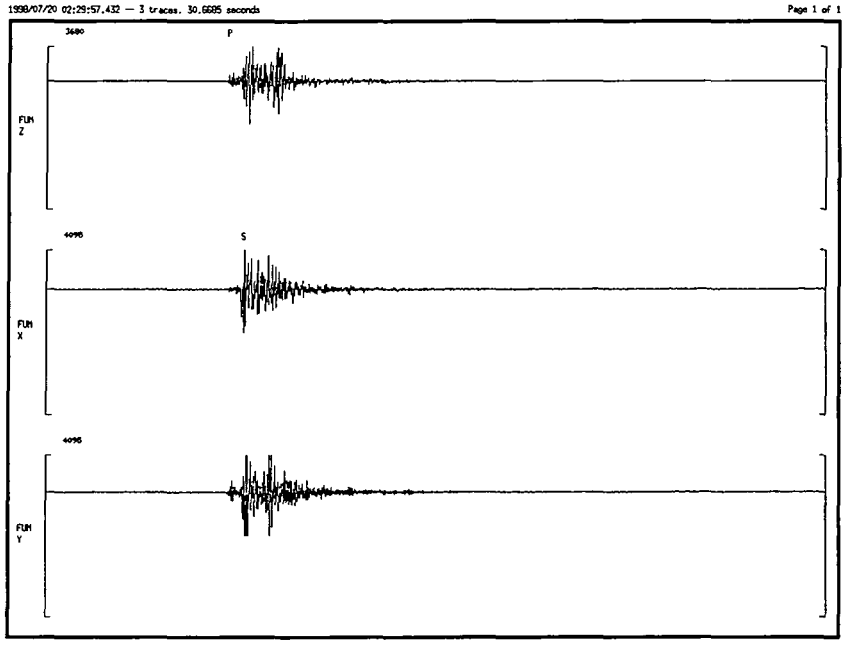

(a) Example of a squash window used by program *epick* to show earthqaukes. (b) Example of pick window where the selected trace is shown in detail and *P*- and *S*- picks were made.

Appendix 4: Parameters used in the *SIMULPS12* program and input files for Apr. 1991 to Aug. 1998.

Description of parameters

neqs	386	Number of earthquakes
Nshot	3	Number of shots
Nblast	0	Number of blasts
wtsht	1.0	Weight given to shots (relative to earthquakes)
kout	4	Output control parameter
kout2	1	Output control parameter
kout3	0	Output control parameter
Nitloc	10	Maximum number of iterations of event location routine
Wtsp	1.0	Weight given to *S-P* times (relative to *P* times)
Eigtol	0.020	SVD cut-off in hypocnetral adjustments
Rmscut	0.01	RMS residual cut-off to terminate location iterations
ZZmin	0.0	Minimum earthquake depth
Dxmax	0.50	Maximum horizontal hypocentre relocation per iteration
Rderr	0.01	Estimated reading uncertainty
Ercof	0.00	Used for hypocenter error calculations
Hitct	1	DWS cut-off to remove node from inversion
Dvpmax	0.10	Maximum *vp* adjustment
dvpvsmax	0.03	Maximum *vp/vs* adjustment
Idmp	1	Damping control parameter
Vpdmp	5.0	*vp* damping parameter
vpvsdmp	2.0	*vp/vs* damping parameter
Stadmp	99.0	Station delay damping parameter
Stepl	0.50	Raypath step length used in partial derivation calculations
Ires	1	Resolution output control parameter
i3d	2	Three-dimensional ray tracing control parameter
Nitmax	4	Maximum number of iterations of the hypocentral relocation model adjustment loop
Snrmct	0.005	Solution norm cut-off to terminate inversion
Ihomo	1	Number of iterations to use ray-tracing in vertical planes
Rmstop	0.01	RMS residual (for all events) to terminate inversion
Ifixl	0	Number of iterations to fix hypocenters for
delt1	20.0	Raylength cut-off used to weight residuals
delt2	35.0	Raylength cut-off used to weight residuals
res1	0.10	Residual cut-off used for weighting
res2	0.25	Residual cut-off used for weighting
res3	0.30	Residual cut-off used for weighting
Ndip	9	Number of planes searched during approximate ray-tracing (ART)
Iskip	2	Number of planes near horizontal to skip during ART
scale1	0.5	Ray segment length
scale2	0.5	Controls number of paths tried during ray-tracing
Xfax	1.2	Pseudo-bending control parameter
Tlim	0.001	Travel-time difference cut-off to terminate pseudo-bending iterations
nitpb1	15	Maximum number of iterations during pseudo-bending
nitpb2	15	Maximum number of iterations during pseudo-bending
Iusep	1	Flag to use *P* travel times (0=NO; 1=Y)
Iuses	1	Flag to use *S-P* times (0=NO; 1=Y)
Invdel	0	Flag to invert for station delays (0=NO; 1=Y)

Control files used for April 1991 to August 1998 final inversions.

April 1991 inversion

fort 1: control file

163 0 0 1.0 4 1 0 neqs, nshot, nblast, wtsht, kout, kout2, kout3
10 1.0 0.020 0.01 –1.0 0.50 0.01 0.00 nitloc wtsp, eigtol, rmscut, zmin, dxmax, rderr, ercof
5 0.10 0.03 1 5.0 2.0 99.00 0.50 hitct, dvpmax, dvpvsmax,idmp, vpdmp, vpvsdmp, stadmp, stepl
1 2 4 0.005 0 0,01 0 ires, i3d, nitmax, snrmct, ihomo, rmstop, ifixl
18.0 30.0 0.20 0.30 0.40 delt1, delt2, res1, res2, res3
9 2 0.5 0.5 ndip,iskip,scale1, scale2
1.2 0.001 15 15 xfax, tlim, nitpb1, nitpb2
1 1 0 iusep, iuses, invdel

February 1993 inversion

241 0 0 1.0 4 1 0 neqs, nshot, nblast, wtsht, kout, kout2, kout3
10 1.0 0.020 0.01 –1.0 0.50 0.01 0.00 nitloc wtsp, eigtol, rmscut, zmin, dxmax, rderr, ercof
5 0.10 0.03 1 20.0 20.0 99.00 0.50 hitct, dvpmax, dvpvsmax,idmp, vpdmp, vpvsdmp, stadmp, stepl
1 2 4 0.005 0 0,01 0 ires, i3d, nitmax, snrmct, ihomo, rmstop, ifixl
18.0 30.0 0.20 0.30 0.40 delt1, delt2, res1, res2, res3
9 2 0.5 0.5 ndip,iskip,scale1, scale2
1.2 0.001 15 15 xfax, tlim, nitpb1, nitpb2
1 1 0 iusep, iuses, invdel

December 1994 inversion

146 0 0 1.0 4 1 0 neqs, nshot, nblast, wtsht, kout, kout2, kout3
10 1.0 0.020 0.01 –1.0 0.50 0.01 0.00 nitloc wtsp, eigtol, rmscut, zmin, dxmax, rderr, ercof
5 0.10 0.03 1 5.0 2.0 99.00 0.50 hitct, dvpmax, dvpvsmax,idmp, vpdmp, vpvsdmp, stadmp, stepl
1 2 4 0.005 0 0,01 0 ires, i3d, nitmax, snrmct, ihomo, rmstop, ifixl
18.0 30.0 0.20 0.30 0.40 delt1, delt2, res1, res2, res3
9 2 0.5 0.5 ndip,iskip,scale1, scale2
1.2 0.001 15 15 xfax, tlim, nitpb1, nitpb2
1 1 0 iusep, iuses, invdel

October 1996 inversion

295 0 0 1.0 4 1 0 neqs, nshot, nblast, wtsht, kout, kout2, kout3
10 1.0 0.020 0.01 –1.0 0.50 0.01 0.00 nitloc wtsp, eigtol, rmscut, zmin, dxmax, rderr, ercof
5 0.10 0.03 1 5.0 5.0 99.00 0.50 hitct, dvpmax, dvpvsmax,idmp, vpdmp, vpvsdmp, stadmp, stepl
1 2 4 0.005 0 0,01 0 ires, i3d, nitmax, snrmct, ihomo, rmstop, ifixl
18.0 30.0 0.20 0.30 0.40 delt1, delt2, res1, res2, res3
9 2 0.5 0.5 ndip,iskip,scale1, scale2
1.2 0.001 15 15 xfax, tlim, nitpb1, nitpb2
1 1 0 iusep, iuses, invdel

August 1998 inversion

302 0 0 1.0 4 1 0 neqs, nshot, nblast, wtsht, kout, kout2, kout3
10 1.0 0.020 0.01 –1.0 0.50 0.01 0.00 nitloc wtsp, eigtol, rmscut, zmin, dxmax, rderr, ercof
5 0.10 0.03 1 5.0 2.0 99.00 0.50 hitct, dvpmax, dvpvsmax,idmp, vpdmp, vpvsdmp, stadmp, stepl
1 2 4 0.005 0 0,01 0 ires, i3d, nitmax, snrmct, ihomo, rmstop, ifixl
18.0 30.0 0.20 0.30 0.40 delt1, delt2, res1, res2, res3
9 2 0.5 0.5 ndip,iskip,scale1, scale2
1.2 0.001 15 15 xfax, tlim, nitpb1, nitpb2
1 1 0 iusep, iuses, invdel

Appendix 5: Location of events used in the tomographic inversions from Apr. 1991 to Aug. 1998

Events in April 1991 inversion

Earthquake	Lattitude (deg)	Longtide (deg)	Depth /km	Number of observations
910401230153.33	38:50.23	-122:46.37	1.66	11
910401232028.81	38:50.22	-122:46.38	1.72	10
910402172017.68	38:48.21	-122:45.29	1.33	18
910404004646.25	38:50.73	-122:47.39	1.76	9
910404020103.89	38:50.50	-122:48.36	1.61	8
910404075911.61	38:47.63	-122:47.55	1.15	14
910404080006.96	38:47.59	-122:47.63	1.24	15
910404223108.82	38:47.54	-122:44.81	1.43	13
910404224627.43	38:47.06	-122:45.59	0.61	13
910408132309.70	38:48.67	-122:47.79	1.42	16
910408142123.22	38:49.98	-122:47.26	0.84	9
910408172859.19	38:48.00	-122:44.63	2.15	13
910408194150.11	38:51.06	-122:47.67	2.23	9
910409051725.42	38:47.03	-122:43.21	1.61	17
910409082537.71	38:47.80	-122:43.54	4.49	9
910409085012.04	38:47.35	-122:44.89	1.00	7
910409103908.35	38:47.58	-122:46.93	1.90	17
910409193508.74	38:48.90	-122:49.56	0.58	14
910410040429.92	38:48.62	-122:49.80	0.82	9
910411073011.39	38:48.89	-122:48.72	2.69	13
910411131843.53	38:46.61	-122:43.31	1.91	14
910411154348.54	38:47.07	-122:45.10	0.85	15
910411184442.95	38:46.27	-122:44.67	1.82	16
910412000254.14	38:47.60	-122:44.83	1.82	19
910413031721.75	38:47.77	-122:44.11	1.60	13
910413105204.51	38:50.63	-122:44.26	2.42	11
910413200107.79	38:48.92	-122:50.14	0.25	10
910414002350.26	38:47.22	-122:47.02	3.25	20
910414050550.59	38:47.01	-122:46.43	1.68	19
910414073743.43	38:47.19	-122:46.49	1.92	20
910415011727.53	38:47.21	-122:45.07	4.19	20
910415172248.42	38:46.16	-122:42.99	0.69	13
910416005439.12	38:49.45	-122:50.11	1.32	17
910416033107.98	38:48.24	-122:46.08	1.06	14
910416061747.60	38:48.76	-122:48.26	2.00	12
910416170854.01	38:47.59	-122:44.90	2.03	10
910416184038.73	38:47.55	-122:44.97	0.79	23
910416213416.70	38:48.64	-122:48.21	1.54	10
910416220635.56	38:49.36	-122:47.15	0.50	19
910416222745.53	38:48.84	-122:49.65	0.97	17
910416222949.09	38:49.27	-122:47.23	0.43	9

910416233411.89	38:46.41	-122:44.93	1.37	14
910417015857.85	38:49.51	-122:49.62	0.86	10
910417043332.38	38:49.71	-122:48.19	1.03	9
910417051950.66	38:47.58	-122:46.93	2.34	14
910417094630.02	38:47.22	-122:44.74	0.87	11
910417102857.08	38:49.50	-122:47.64	1.51	13
910417114326.20	38:52.11	-122:49.17	2.32	8
910417131235.51	38:49.96	-122:47.99	1.40	17
910417133656.62	38:48.72	-122:48.24	2.00	19
910417162327.33	38:49.33	-122:46.98	2.19	14
910417163456.95	38:46.22	-122:44.78	2.38	22
910417164138.02	38:49.12	-122:47.13	2.43	22
910417180046.32	38:46.23	-122:44.76	2.10	23
910417183032.17	38:49.05	-122:46.11	1.56	16
910417185947.28	38:47.38	-122:45.24	1.45	13
910417225328.42	38:48.73	-122:48.14	2.78	16
910417234537.06	38:49.63	-122:49.69	1.60	18
910417234738.80	38:49.72	-122:49.66	1.54	10
910418010930.59	38:49.49	-122:49.51	0.67	10
910418021023.90	38:47.88	-122:48.72	3.38	16
910418042450.18	38:48.98	-122:47.12	0.62	20
910418042718.27	38:48.89	-122:47.36	0.47	12
910418044503.99	38:48.02	-122:48.19	1.74	8
910418061656.04	38:48.23	-122:46.36	1.44	20
910418092723.76	38:47.98	-122:48.73	3.73	12
910418121815.36	38:49.84	-122:47.99	1.25	21
910418142344.24	38:49.24	-122:46.16	0.89	15
910418142505.87	38:49.23	-122:46.15	0.81	16
910418160750.37	38:48.73	-122:47.95	3.03	19
910418162138.11	38:49.30	-122:47.81	0.54	14
910419120505.37	38:45.41	-122:43.50	3.06	18
910419132029.96	38:49.15	-122:50.31	0.91	8
910419142420.71	38:49.24	-122:48.37	3.28	22
910419143904.24	38:49.17	-122:47.57	2.25	11
910419144422.72	38:49.26	-122:48.33	2.90	18
910419183216.41	38:50.03	-122:49.69	2.05	10
910419190415.18	38:49.32	-122:49.28	1.57	14
910419232137.79	38:47.74	-122:45.16	1.60	13
910423044747.34	38:46.42	-122:46.27	2.78	16
910424015823.34	38:47.54	-122:45.15	2.41	20
910424094349.84	38:47.36	-122:46.65	2.17	22
910424115512.31	38:50.08	-122:49.54	1.84	11
910424124943.61	38:48.65	-122:46.87	1.94	22
910424141640.36	38:50.22	-122:49.41	1.94	10
910424141812.35	38:48.19	-122:48.75	0.76	20
910424212728.71	38:49.71	-122:49.31	1.15	13
910424214425.14	38:47.83	-122:46.18	2.39	24
910425022242.64	38:46.25	-122:44.72	2.14	23
910425022455.62	38:46.23	-122:44.73	2.30	19
910425045421.69	38:46.69	-122:43.52	1.15	16

910425062850.93	38:49.40	-122:47.59	1.53	12
910425085236.20	38:49.16	-122:48.39	3.26	21
910425100054.99	38:48.12	-122:46.39	1.26	10
910425125102.03	38:47.28	-122:45.20	1.26	12
910425134544.46	38:47.76	-122:45.05	1.68	20
910425142611.00	38:48.23	-122:48.13	1.61	22
910425142618.34	38:48.20	-122:48.18	1.87	20
910425143343.38	38:48.23	-122:48.06	1.98	24
910425150206.91	38:47.20	-122:46.15	0.11	19
910425155755.84	38:47.18	-122:46.48	2.14	19
910425160333.83	38:49.17	-122:48.37	3.26	15
910425161507.41	38:50.16	-122:49.58	2.08	9
910425180659.39	38:47.53	-122:46.55	0.21	17
910425192509.26	38:49.17	-122:48.40	3.40	11
910425214309.08	38:48.22	-122:48.53	0.45	17
910425225534.07	38:47.41	-122:46.89	3.93	20
910426031117.37	38:47.24	-122:46.48	1.89	23
910426040533.77	38:48.09	-122:48.24	3.77	22
910426050258.03	38:47.62	-122:44.93	1.60	21
910426052927.21	38:48.05	-122:48.34	3.68	20
910426063105.38	38:47.34	-122:46.54	2.28	20
910426114436.94	38:48.73	-122:46.54	2.04	12
910426120624.49	38:47.63	-122:46.94	2.15	19
910426153751.45	38:49.49	-122:47.13	1.51	13
910426171302.36	38:49.11	-122:48.74	3.20	10
910426201244.29	38:49.37	-122:46.74	0.95	20
910426220824.00	38:45.59	-122:43.74	1.23	17
910427011827.75	38:47.16	-122:45.22	1.94	14
910427062931.10	38:49.10	-122:48.27	3.24	16
910427102708.61	38:49.66	-122:48.57	0.91	12
910427111313.78	38:46.82	-122:44.57	0.17	12
910427132037.67	38:49.28	-122:47.65	1.58	14
910427144004.60	38:52.96	-122:49.15	2.53	7
910427150454.37	38:49.34	-122:46.95	1.65	8
910427153333.29	38:48.24	-122:48.65	1.58	20
910427154722.45	38:48.22	-122:48.64	1.30	9
910427154909.72	38:47.30	-122:46.53	1.01	19
910428020141.49	38:50.07	-122:49.77	2.39	11
910428020918.49	38:49.31	-122:46.82	2.18	18
910428033029.09	38:48.23	-122:48.64	0.78	16
910428033047.22	38:47.19	-122:46.47	2.58	24
910428051558.34	38:47.44	-122:46.62	2.14	17
910428062546.02	38:49.95	-122:48.58	1.73	12
910428161024.43	38:46.91	-122:56.37	6.57	21
910428171537.51	38:49.18	-122:48.50	3.29	15
910428183237.74	38:48.35	-122:46.91	3.54	20
910428213919.42	38:48.71	-122:48.29	1.97	21
910429021243.39	38:46.31	-122:44.72	1.89	20
910429023150.47	38:47.45	-122:46.81	2.48	16
910429061327.60	38:49.16	-122:47.47	2.13	13

910429063753.29	38:50.54	-122:46.45	1.47	10
910429115620.38	38:48.81	-122:49.89	1.05	9
910429124758.43	38:49.65	-122:47.79	1.86	15
910429152530.06	38:49.01	-122:48.99	0.11	13
910429221132.37	38:48.39	-122:47.05	1.30	16
910430013739.19	38:49.08	-122:48.72	3.30	13
910430021323.41	38:48.07	-122:48.33	2.15	20
910430023511.70	38:50.21	-122:49.29	1.46	14
910430075104.88	38:47.71	-122:46.92	2.12	11
910430095351.12	38:45.20	-122:43.05	1.21	13
910430151023.10	38:47.55	-122:45.23	2.14	16
910430194218.89	38:47.42	-122:46.65	2.37	18
910430225020.20	38:48.70	-122:49.18	0.33	14
910501002443.64	38:49.08	-122:48.58	2.88	11
910501013139.10	38:45.56	-122:43.58	0.73	14
910501022008.71	38:48.51	-122:46.36	2.66	20
910501054753.40	38:47.31	-122:46.99	3.51	20
910501065535.75	38:48.10	-122:48.32	-0.10	7
910501082413.77	38:48.88	-122:48.42	3.65	21
910501111441.68	38:48.90	-122:47.12	0.64	16
910501141659.54	38:47.77	-122:44.95	1.80	15
910501142750.81	38:47.44	-122:46.72	0.40	17

Events in February 1993 inversion

Earthquake	Lattitude (deg)	Longtide (deg)	Depth /km	Number of observations
930201165142.04	38:48.06	-122:46.34	1.93	23
930201200951.35	38:46.67	-122:43.34	1.98	12
930201223138.70	38:50.27	-122:48.89	1.26	11
930201230344.93	38:47.13	-122:46.57	1.31	12
930201234313.34	38:47.13	-122:46.42	2.89	23
930201235142.56	38:47.02	-122:45.29	0.66	15
930202034600.57	38:49.66	-122:48.09	1.06	17
930202034615.77	38:49.72	-122:48.07	0.80	9
930202041413.55	38:47.21	-122:46.65	0.87	15
930202070157.28	38:46.93	-122:46.11	0.63	17
930202071132.24	38:45.12	-122:44.51	1.28	15
930202075805.34	38:49.73	-122:49.26	1.16	10
930202090808.94	38:47.61	-122:44.90	1.05	18
930202150021.70	38:49.74	-122:50.41	1.91	8
930202150625.00	38:47.55	-122:45.02	0.93	19
930202164549.99	38:47.21	-122:46.53	1.67	20
930203001607.01	38:49.15	-122:48.70	2.71	17
930203020914.53	38:47.74	-122:46.52	0.48	18
930203060507.16	38:47.62	-122:46.81	1.77	21
930203072012.38	38:47.89	-122:48.16	1.70	23
930203101126.18	38:47.57	-122:44.39	1.62	17
930203111728.79	38:46.46	-122:45.09	1.39	17

930203142017.66	38:48.26	-122:48.09	2.08	21
930203185951.63	38:46.09	-122:43.70	1.35	15
930203230758.89	38:48.14	-122:48.49	3.60	24
930204025857.88	38:48.19	-122:46.25	2.40	22
930204035734.33	38:48.52	-122:46.84	1.74	20
930204081154.52	38:48.21	-122:48.16	1.53	19
930204091705.37	38:48.64	-122:46.38	2.93	24
930204112234.55	38:48.64	-122:48.34	0.48	15
930204181108.02	38:47.43	-122:44.78	0.79	18
930204194328.63	38:47.61	-122:46.69	1.86	22
930204200005.42	38:48.27	-122:48.28	0.96	21
930204205927.02	38:48.28	-122:48.62	0.67	17
930204234124.09	38:47.95	-122:46.53	0.70	15
930205000614.97	38:47.56	-122:46.72	1.63	16
930205024645.57	38:47.56	-122:44.81	1.22	20
930205063230.05	38:48.08	-122:48.20	1.94	20
930205104201.92	38:48.10	-122:48.79	0.89	15
930205104356.28	38:48.11	-122:48.70	0.85	19
930205131628.16	38:48.24	-122:48.05	1.56	14
930205180451.56	38:47.72	-122:47.26	0.61	10
930205221855.68	38:47.66	-122:44.92	1.27	14
930206081142.27	38:48.34	-122:48.38	2.45	19
930206082319.01	38:48.80	-122:49.87	0.71	7
930206082703.36	38:49.23	-122:47.78	0.21	13
930206085403.02	38:48.46	-122:46.47	1.56	9
930206094948.81	38:48.80	-122:48.46	2.73	10
930206102545.21	38:48.14	-122:48.81	0.60	19
930206103406.69	38:49.02	-122:46.45	0.88	24
930206112557.50	38:48.48	-122:46.44	1.59	18
930206210939.63	38:47.03	-122:44.99	0.72	18
930206215511.73	38:47.21	-122:44.84	0.74	19
930207071605.76	38:49.24	-122:48.30	3.32	24
930207092810.78	38:48.65	-122:47.08	0.64	18
930207103009.64	38:46.34	-122:44.64	1.87	18
930207113903.37	38:49.19	-122:47.88	3.14	14
930207153833.32	38:48.01	-122:46.34	0.77	22
930207153926.79	38:48.09	-122:46.33	0.75	17
930207154430.56	38:47.97	-122:46.37	0.74	24
930207154549.87	38:47.96	-122:46.40	1.08	20
930207205339.57	38:47.13	-122:45.38	1.08	16
930207222038.25	38:47.22	-122:46.54	1.41	24
930208024813.19	38:47.18	-122:45.44	1.59	20
930208072254.33	38:48.61	-122:47.13	1.07	21
930208073203.67	38:48.89	-122:46.72	1.04	24
930208083417.77	38:45.22	-122:43.32	1.85	14
930208134526.00	38:47.32	-122:46.48	2.23	20
930208153938.73	38:47.44	-122:44.55	1.64	18
930208181157.87	38:49.46	-122:46.70	0.90	21
930208214547.16	38:48.62	-122:46.31	1.72	19
930208215134.66	38:48.19	-122:48.72	1.89	20

930208215246.08	38:48.21	-122:48.55	1.82	23
930209002225.81	38:49.35	-122:50.40	1.46	10
930209003634.84	38:49.14	-122:48.75	3.65	24
930209065723.16	38:48.24	-122:48.45	0.74	20
930209101522.07	38:49.05	-122:49.96	0.73	17
930209102047.28	38:48.96	-122:49.83	0.37	11
930209172657.29	38:48.71	-122:48.14	0.88	13
930209175922.87	38:48.50	-122:46.41	1.86	20
930209192453.24	38:47.15	-122:46.49	0.80	23
930209193103.68	38:49.31	-122:48.09	3.13	23
930209202752.14	38:47.05	-122:46.11	1.05	19
930210000816.99	38:47.20	-122:46.44	2.37	25
930210001857.16	38:47.07	-122:45.43	0.71	19
930210012139.49	38:47.26	-122:46.40	2.49	21
930210072510.47	38:48.25	-122:47.04	-0.90	4 1
930210190350.90	38:47.56	-122:46.87	1.48	20
930210204839.59	38:48.58	-122:45.17	1.47	10
930210225656.30	38:49.66	-122:49.24	0.90	14
930210225917.14	38:49.78	-122:49.28	0.70	14
930210230046.41	38:49.88	-122:49.11	0.96	10
930210230606.79	38:49.32	-122:49.26	1.71	18
930211005552.89	38:48.67	-122:48.11	1.94	21
930211060543.49	38:47.57	-122:44.56	1.25	17
930211112501.37	38:49.34	-122:47.97	3.27	18
930211143402.24	38:46.18	-122:44.75	2.06	19
930211165903.38	38:49.64	-122:50.43	1.62	12
930211184333.91	38:47.77	-122:45.90	1.00	17
930211204528.35	38:48.25	-122:46.23	1.64	18
930211211625.52	38:51.20	-122:48.98	1.72	11
930211222216.36	38:49.33	-122:48.19	3.29	19
930211230914.89	38:47.47	-122:46.75	1.71	13
930212011606.45	38:50.36	-122:49.18	1.24	14
930212023414.76	38:45.68	-122:43.81	1.02	11
930212023547.44	38:48.08	-122:48.20	1.81	16
930212023835.20	38:48.47	-122:48.49	1.09	14
930212035216.29	38:50.29	-122:48.30	1.10	17
930212052014.75	38:48.05	-122:48.25	1.65	16
930212095806.57	38:48.21	-122:46.24	2.23	17
930212110027.68	38:48.26	-122:49.31	0.82	11
930212121616.99	38:46.70	-122:46.44	0.99	10
930212234558.65	38:49.35	-122:46.13	1.13	23
930213010020.90	38:48.40	-122:45.00	0.35	17
930213011030.48	38:48.16	-122:45.18	1.04	24
930213021841.09	38:48.75	-122:48.26	1.33	20
930213073332.62	38:47.22	-122:46.63	1.80	19
930213110736.78	38:48.22	-122:48.09	2.13	19
930213190344.59	38:47.58	-122:46.88	2.00	29
930213190447.60	38:47.57	-122:46.87	2.08	24
930213190544.91	38:47.54	-122:46.89	1.34	19
930214043401.76	38:47.72	-122:44.63	1.12	17

930214043526.41	38:47.69	-122:44.57	1.35	19
930214045334.94	38:48.10	-122:48.12	1.48	20
930214105807.21	38:50.06	-122:48.34	0.77	14
930214164607.68	38:47.60	-122:46.83	1.59	15
930214170127.84	38:45.32	-122:43.26	1.02	17
930214182540.99	38:47.70	-122:46.21	0.63	13
930214202017.18	38:47.17	-122:45.28	0.44	17
930214214821.70	38:48.31	-122:46.96	1.03	13
930215033646.98	38:46.00	-122:43.53	1.07	14
930215125144.78	38:47.17	-122:45.49	1.78	20
930215162158.08	38:48.53	-122:46.33	2.36	24
930215180423.48	38:47.28	-122:45.78	0.51	19
930215180604.33	38:46.99	-122:46.28	0.98	15
930215180859.05	38:48.37	-122:46.66	0.50	22
930215180939.85	38:47.93	-122:46.01	0.38	26
930215181005.82	38:47.29	-122:46.36	0.38	21
930215181114.84	38:47.93	-122:46.16	0.97	21
930216001745.99	38:48.02	-122:46.15	2.42	25
930216021808.91	38:47.35	-122:46.48	2.09	16
930216032524.67	38:50.39	-122:49.56	2.57	11
930216034859.02	38:46.98	-122:46.48	0.76	21
930216054333.34	38:48.92	-122:48.23	1.21	13
930216174608.30	38:47.51	-122:46.79	0.95	21
930216190413.26	38:48.08	-122:46.33	1.00	21
930216213735.28	38:48.58	-122:46.51	2.08	17
930216232912.48	38:47.39	-122:46.91	0.15	13
930217013332.87	38:46.99	-122:45.43	1.25	13
930217035123.71	38:48.01	-122:46.49	1.63	20
930217062128.26	38:47.12	-122:45.42	1.81	14
930217112222.39	38:48.06	-122:48.35	1.99	14
930217113218.88	38:47.12	-122:45.44	0.91	15
930217160930.57	38:48.87	-122:50.07	1.32	13
930217180554.39	38:47.70	-122:45.06	2.50	21
930217184231.71	38:47.72	-122:46.06	0.92	18
930217193419.08	38:51.61	-122:49.47	1.87	13
930217212306.87	38:46.99	-122:45.63	1.23	17
930218005238.17	38:46.25	-122:42.95	1.79	20
930218042305.20	38:45.59	-122:43.39	1.14	19
930218092953.14	38:48.27	-122:46.37	1.70	22
930218110248.26	38:48.00	-122:46.06	1.72	12
930218152211.01	38:49.33	-122:46.25	0.80	21
930218195641.78	38:49.39	-122:50.28	0.84	11
930218202859.52	38:49.93	-122:47.91	1.39	14
930218220324.82	38:47.86	-122:48.57	3.17	25
930219034937.30	38:47.83	-122:46.05	1.54	19
930219062707.75	38:48.55	-122:47.60	1.58	21
930219091748.74	38:49.28	-122:48.12	3.27	22
930219093427.50	38:49.34	-122:48.04	2.92	16
930219113646.04	38:48.23	-122:48.13	3.23	18
930219123722.56	38:47.99	-122:46.08	2.78	15

930219174007.00	38:48.85	-122:46.69	0.79	21
930219184940.24	38:47.59	-122:44.61	0.87	16
930219213754.61	38:48.72	-122:49.27	0.56	9
930220002527.73	38:47.57	-122:46.74	1.95	19
930220033246.92	38:49.82	-122:51.85	1.74	12
930220041221.41	38:48.42	-122:46.26	1.98	18
930220071912.35	38:48.24	-122:48.19	1.18	16
930220073959.95	38:45.22	-122:43.59	1.69	16
930220091624.79	38:50.28	-122:48.24	0.95	16
930220215808.63	38:49.69	-122:49.61	1.22	14
930220224554.47	38:47.12	-122:45.52	1.36	16
930220235839.82	38:48.60	-122:46.47	1.01	19
930221032022.44	38:49.48	-122:46.53	1.91	17
930221064714.80	38:47.00	-122:44.25	0.71	16
930221082411.08	38:50.52	-122:49.31	1.95	12
930221161114.41	38:47.63	-122:45.35	0.77	20
930221174306.57	38:46.63	-122:43.14	2.06	14
930221180046.00	38:47.61	-122:44.69	1.48	17
930221194939.18	38:50.00	-122:48.74	0.78	13
930221225817.87	38:47.01	-122:45.41	1.17	14
930221234917.26	38:48.56	-122:46.85	1.60	15
930223014843.37	38:49.82	-122:47.84	1.20	14
930223051741.56	38:48.88	-122:49.75	0.59	8
930223051805.69	38:48.81	-122:49.89	0.96	11
930223075640.61	38:49.84	-122:48.20	0.94	11
930223195403.77	38:49.19	-122:48.71	3.29	16
930223205334.33	38:49.10	-122:48.48	3.04	15
930223221626.95	38:49.22	-122:48.05	3.04	18
930224094812.41	38:47.56	-122:46.77	2.20	12
930224104022.35	38:48.21	-122:45.94	1.88	17
930224165008.73	38:47.99	-122:46.25	2.98	17
930224165343.96	38:49.17	-122:47.19	1.15	17
930224173050.40	38:45.34	-122:42.80	1.00	16
930225080757.14	38:47.54	-122:44.20	0.96	17
930225102216.11	38:49.37	-122:49.59	1.87	9
930225145652.55	38:47.97	-122:44.41	0.82	9
930225155533.45	38:48.99	-122:48.47	3.34	14
930225193638.12	38:48.99	-122:48.33	3.24	17
930225195214.37	38:49.22	-122:48.08	3.10	18
930225205756.21	38:49.17	-122:48.62	3.47	17
930225210135.41	38:46.23	-122:44.50	0.10	17
930225212305.23	38:49.36	-122:48.96	1.03	4
930226064310.24	38:48.67	-122:48.23	1.17	14
930226064657.41	38:48.97	-122:47.56	0.73	9
930226103028.99	38:48.10	-122:46.57	1.79	14
930226150134.21	38:49.07	-122:48.00	3.17	11
930226154232.96	38:47.73	-122:46.10	0.92	12
930226164739.19	38:48.87	-122:47.22	0.84	6
930226204705.92	38:47.57	-122:46.84	1.37	20
930226212851.38	38:47.59	-122:46.81	1.68	18

930227000538.09	38:47.52	-122:46.85	2.02	14
930227030114.29	38:49.19	-122:46.71	1.22	11
930227042541.36	38:48.06	-122:48.33	2.68	13
930227122715.62	38:49.42	-122:48.28	3.92	13
930227154825.69	38:48.63	-122:46.44	2.00	12
930227182617.32	38:48.65	-122:48.61	1.72	15
930227183103.67	38:47.62	-122:46.81	1.92	26
930227193854.16	38:48.16	-122:48.49	0.84	14
930227232701.47	38:47.72	-122:46.28	0.72	10
930228014555.43	38:47.90	-122:44.45	2.15	17
930228015028.70	38:49.27	-122:48.30	3.32	14
930228021428.26	38:48.09	-122:48.40	3.28	22
930228073428.53	38:49.69	-122:45.90	0.85	18
930228105141.98	38:46.37	-122:38.33	5.52	16
930228120836.02	38:45.85	-122:43.46	0.94	13
930228142905.90	38:49.87	-122:48.71	0.91	13
930228163825.83	38:49.24	-122:48.13	3.70	21
930228165223.59	38:49.27	-122:48.05	3.20	15
930228233308.93	38:48.16	-122:46.33	1.81	19

Events in December 1994 inversion

Earthquake	Lattitude (deg)	Longtide (deg)	Depth /km	Number of observations
941201045908.24	38:47.24	-122:46.47	1.11	27
941201051532.78	38:49.62	-122:49.87	1.33	13
941201053453.34	38:47.41	-122:48.30	4.04	20
941201071449.45	38:48.25	-122:48.40	1.66	23
941201110859.18	38:47.81	-122:44.89	0.97	12
941201110907.05	38:47.73	-122:45.08	0.67	19
941202052841.40	38:49.26	-122:48.06	3.23	26
941202112051.37	38:48.48	-122:46.60	0.79	22
941202152828.62	38:50.05	-122:49.48	1.98	20
941202171007.80	38:48.40	-122:46.38	1.86	24
941202171108.52	38:48.33	-122:46.25	1.63	19
941202171144.37	38:48.41	-122:46.24	1.64	22
941202173121.81	38:50.31	-122:49.25	1.76	17
941202173656.14	38:50.13	-122:47.52	0.83	22
941203001927.98	38:49.98	-122:47.96	1.44	19
941203074203.29	38:49.23	-122:46.06	0.92	23
941203142238.69	38:47.72	-122:47.25	0.31	19
941203181912.95	38:47.56	-122:46.47	1.10	18
941203182042.62	38:47.32	-122:45.31	1.36	21
941203214203.47	38:49.02	-122:48.73	2.93	24
941203224824.28	38:49.07	-122:48.73	2.99	19
941203225055.90	38:47.55	-122:44.60	1.09	25
941204022518.58	38:47.54	-122:44.61	1.07	20
941204065525.63	38:46.93	-122:44.72	0.14	18
941204071648.95	38:47.64	-122:44.51	1.17	20

941204072203.03	38:47.70	-122:46.09	0.63	20
941204072910.80	38:47.64	-122:44.49	1.16	19
941204072920.22	38:47.68	-122:46.06	1.00	26
941204072933.08	38:47.72	-122:46.04	0.70	25
941204181622.18	38:47.25	-122:46.24	0.45	22
941204192308.50	38:49.12	-122:48.71	2.91	20
941204205550.61	38:50.08	-122:49.93	2.54	17
941204220010.63	38:49.61	-122:47.81	0.69	20
941205031739.67	38:47.23	-122:45.50	1.54	24
941205032635.58	38:47.21	-122:45.45	1.44	23
941205092925.74	38:50.00	-122:49.88	0.65	16
941205125320.25	38:47.52	-122:44.69	1.32	25
941205173434.94	38:47.61	-122:44.49	1.05	25
941206003701.53	38:47.59	-122:46.43	1.28	28
941206112144.39	38:49.60	-122:47.06	2.82	23
941206123248.83	38:48.57	-122:46.79	0.67	24
941206134206.91	38:47.18	-122:45.53	1.71	24
941207001254.00	38:49.28	-122:47.82	3.25	25
941207083517.82	38:48.39	-122:46.32	1.79	23
941207101428.96	38:49.22	-122:48.19	2.95	25
941207104237.30	38:49.23	-122:47.90	3.52	22
941207140537.31	38:48.54	-122:46.78	0.55	19
941207201540.56	38:47.43	-122:44.37	1.84	25
941208064652.20	38:47.79	-122:44.45	1.66	21
941208080804.18	38:48.88	-122:49.40	1.31	20
941208135943.84	38:47.64	-122:46.10	1.67	28
941208151319.59	38:47.90	-122:45.36	0.98	22
941209145008.28	38:50.13	-122:47.94	1.20	21
941209201249.54	38:47.10	-122:46.57	1.23	26
941209234808.75	38:47.08	-122:45.43	1.73	23
941210030757.50	38:47.15	-122:45.63	0.42	24
941210064333.28	38:47.05	-122:45.57	1.97	25
941210065859.21	38:49.23	-122:48.27	1.12	19
941211000425.55	38:46.14	-122:43.86	1.54	23
941211001308.66	38:45.79	-122:44.36	1.11	27
941211074416.42	38:50.24	-122:48.26	0.90	22
941211074613.06	38:49.96	-122:47.51	0.88	23
941211204357.32	38:47.09	-122:46.34	2.52	26
941211221018.48	38:46.17	-122:43.50	1.14	23
941212052655.96	38:45.77	-122:44.38	2.02	24
941212062336.24	38:47.49	-122:48.37	3.77	24
941212065827.73	38:47.90	-122:46.62	1.18	26
941212071751.93	38:48.06	-122:46.07	0.70	23
941212071804.15	38:48.05	-122:46.10	0.74	21
941212201904.51	38:47.19	-122:45.54	1.34	24
941214002637.69	38:50.14	-122:49.85	2.33	17
941214075029.77	38:49.74	-122:46.75	1.05	21
941214142507.94	38:46.98	-122:46.38	0.31	20
941214142925.54	38:47.19	-122:45.71	0.31	18
941214183959.94	38:47.67	-122:44.82	0.36	18

941214184222.15	38:47.58	-122:44.82	0.68	27
941214214127.71	38:48.60	-122:48.27	0.70	20
941215015822.72	38:49.19	-122:47.76	0.52	18
941215021955.52	38:50.11	-122:48.45	1.48	21
941215141237.86	38:49.44	-122:47.60	0.72	16
941215141250.57	38:49.39	-122:47.53	0.86	24
941215181510.25	38:49.08	-122:46.88	2.27	22
941216041245.73	38:48.01	-122:46.84	0.54	23
941216041258.15	38:48.05	-122:46.96	0.42	24
941216060641.33	38:49.09	-122:47.19	0.69	19
941216105919.76	38:49.03	-122:46.90	1.82	21
941216113139.50	38:49.17	-122:46.85	1.78	26
941216192143.65	38:48.11	-122:46.89	0.70	18
941216202953.78	38:47.22	-122:46.58	1.57	26
941217001403.38	38:48.15	-122:46.28	2.65	23
941217064830.37	38:47.22	-122:45.53	1.43	22
941217074507.40	38:47.14	-122:43.30	1.87	21
941217081446.47	38:45.79	-122:44.32	0.88	19
941217095451.47	38:48.43	-122:46.98	1.73	21
941217095518.38	38:48.02	-122:46.71	1.04	16
941217100833.84	38:46.28	-122:44.84	1.71	18
941217102638.34	38:48.05	-122:48.37	1.90	25
941217102800.36	38:48.05	-122:48.41	1.89	24
941217175230.98	38:46.87	-122:45.68	1.36	22
941217183051.40	38:48.79	-122:50.37	0.60	12
941217184111.00	38:47.37	-122:45.35	1.88	18
941217185708.40	38:49.37	-122:47.61	0.53	13
941217203504.46	38:46.68	-122:46.01	1.68	23
941218015347.48	38:47.32	-122:46.63	1.80	24
941218072838.20	38:50.41	-122:47.06	1.43	23
941218082735.20	38:47.24	-122:45.62	0.65	26
941218085515.29	38:46.93	-122:43.47	1.98	26
941218102827.04	38:47.39	-122:45.03	0.88	24
941218103153.85	38:47.29	-122:44.92	0.60	28
941218120311.22	38:47.95	-122:45.35	0.82	26
941218122258.58	38:47.21	-122:46.55	1.44	26
941218130042.89	38:47.24	-122:46.56	1.03	26
941218152003.98	38:47.35	-122:45.04	0.76	16
941218201438.70	38:46.24	-122:42.75	1.70	24
941218201438.71	38:46.21	-122:42.75	1.72	25
941218213216.97	38:47.11	-122:45.42	1.90	26
941219020629.88	38:48.48	-122:48.68	2.29	24
941219000237.97	38:48.85	-122:48.60	3.34	21
941219061306.59	38:50.15	-122:49.47	1.18	6
941219061317.08	38:50.20	-122:49.52	2.23	13
941219061423.45	38:47.63	-122:44.48	1.33	14
941219071453.95	38:47.68	-122:46.13	0.30	17
941219083401.95	38:51.53	-122:49.09	1.91	6
941219083411.12	38:47.37	-122:45.11	0.91	20
941219134347.12	38:47.86	-122:45.47	0.88	21

941219134404.07	38:47.82	-122:45.41	0.95	20
941219134455.27	38:47.75	-122:45.50	0.92	18
941219183040.79	38:47.10	-122:45.51	1.74	23
941219202715.06	38:48.72	-122:46.44	1.70	21
941219203248.79	38:47.28	-122:46.79	0.60	26
941219225323.01	38:46.92	-122:45.60	1.56	26
941219225947.47	38:47.14	-122:45.37	1.83	22
941220001634.34	38:47.53	-122:45.06	0.92	27
941220002344.02	38:47.11	-122:45.46	2.01	24
941220015744.04	38:47.85	-122:45.45	0.96	28
941220021234.92	38:50.16	-122:48.96	0.90	22
941220021252.78	38:50.13	-122:48.93	0.78	22
941220023011.57	38:48.78	-122:47.61	0.91	22
941220065337.20	38:48.15	-122:46.00	0.82	25
941220132120.51	38:46.01	-122:43.69	1.56	25
941220165123.84	38:49.77	-122:47.64	1.14	22
941220173803.99	38:48.28	-122:46.57	0.26	24
941220185104.65	38:47.72	-122:44.50	1.49	22
941220194644.20	38:49.40	-122:47.65	1.06	24
941220201134.22	38:47.67	-122:46.14	0.68	25
941220234616.99	38:47.64	-122:48.21	0.89	25

Events in October 1996 inversion

Earthquake	Lattitude (deg)	Longtide (deg)	Depth /km	Number of observations
960930025134.28	38:48.85	-122:48.85	3.14	17
960930043548.97	38:46.36	-122:42.79	0.98	13
960930110305.04	38:49.08	-122:47.03	2.27	13
960930204137.33	38:47.77	-122:46.76	3.78	24
960930222750.70	38:45.34	-122:42.57	0.50	9
960930225123.08	38:50.14	-122:50.02	0.77	12
960930232644.20	38:49.05	-122:48.07	2.61	17
961001011917.60	38:49.96	-122:46.49	1.64	6
961001012517.54	38:49.31	-122:48.15	3.36	17
961001013900.57	38:52.90	-122:49.18	3.64	10
961001020806.94	38:49.03	-122:48.63	2.93	13
961001050314.56	38:47.75	-122:48.59	3.29	13
961001061705.48	38:48.08	-122:48.30	0.35	13
961001073200.13	38:45.38	-122:42.82	1.08	12
961001152947.48	38:48.26	-122:48.33	1.71	17
961001192410.11	38:48.82	-122:48.32	2.92	21
961001233040.90	38:48.82	-122:48.50	3.05	16
961002052322.77	38:46.42	-122:42.87	1.74	17
961002101338.84	38:49.19	-122:48.16	2.70	19
961002102331.25	38:47.83	-122:44.38	1.27	22
961002103216.09	38:50.36	-122:48.91	1.81	9
961002104457.96	38:46.81	-122:44.92	3.81	19
961002115143.64	38:50.28	-122:47.31	1.31	10

961002135230.88	38:44.71	-122:43.11	1.40	16
961002154837.82	38:47.46	-122:44.35	1.42	15
961002215828.78	38:46.11	-122:42.65	0.12	12
961002234936.99	38:48.21	-122:48.26	2.36	11
961003014019.95	38:47.09	-122:46.82	4.02	19
961003050906.54	38:49.39	-122:47.89	3.04	16
961003082023.90	38:48.18	-122:47.84	2.91	13
961003115635.76	38:49.27	-122:47.79	0.38	14
961003135920.39	38:47.28	-122:43.98	1.34	13
961003150922.02	38:48.46	-122:48.82	2.87	22
961003155545.09	38:45.36	-122:42.14	0.76	9
961003182656.42	38:49.40	-122:47.85	3.25	16
961003195330.37	38:47.83	-122:44.51	1.60	11
961003221243.86	38:47.58	-122:44.62	1.75	15
961004074002.43	38:46.31	-122:43.95	1.36	9
961004074032.54	38:46.05	-122:43.88	1.38	16
961004112412.63	38:48.13	-122:48.78	3.68	6
961004124606.43	38:48.17	-122:48.93	2.77	13
961004135211.39	38:47.75	-122:45.27	0.89	12
961004171251.40	38:49.32	-122:46.73	2.43	13
961004201805.79	38:47.61	-122:47.91	0.71	12
961004203842.41	38:47.73	-122:44.56	1.20	15
961004205047.75	38:48.74	-122:48.54	3.10	7
961004224906.27	38:49.25	-122:46.02	1.12	7
961005004845.50	38:47.77	-122:47.57	0.29	14
961005043032.45	38:49.38	-122:47.84	2.85	14
961005052853.04	38:49.12	-122:47.69	2.83	15
961005072124.69	38:49.31	-122:48.14	2.73	16
961005072440.51	38:48.86	-122:47.48	0.81	11
961005073925.44	38:47.70	-122:46.96	3.88	23
961005095641.21	38:47.09	-122:44.71	1.11	21
961005104133.00	38:47.91	-122:47.00	-0.90	1 6
961005192025.80	38:48.00	-122:45.19	1.09	12
961005230220.75	38:48.30	-122:46.63	1.73	17
961006100137.48	38:48.40	-122:45.36	1.42	17
961006115444.08	38:47.60	-122:44.97	0.74	12
961006124519.49	38:46.35	-122:44.81	1.79	16
961006162456.98	38:49.24	-122:48.40	2.79	16
961006180602.80	38:47.66	-122:45.07	0.77	17
961006183831.27	38:47.95	-122:45.39	1.09	12
961006192556.39	38:49.51	-122:48.31	2.80	16
961007014402.66	38:49.04	-122:48.46	3.03	19
961007045744.43	38:47.59	-122:46.97	0.25	10
961007050833.68	38:47.48	-122:43.42	0.98	13
961007121631.84	38:47.76	-122:45.13	0.98	13
961007135736.68	38:49.21	-122:47.88	2.98	13
961007135959.47	38:50.32	-122:47.95	1.71	15
961007162008.10	38:47.36	-122:44.00	0.96	15
961007174610.59	38:48.85	-122:48.24	3.06	13
961007224428.24	38:48.70	-122:48.17	1.60	7

961008003233.15	38:47.65	-122:44.43	1.10	14
961008003350.04	38:47.63	-122:44.53	1.30	15
961008052124.82	38:47.70	-122:47.97	1.00	12
961008055926.92	38:49.10	-122:48.73	3.21	15
961008064113.37	38:50.20	-122:53.86	2.88	9
961008090425.06	38:48.52	-122:48.74	3.39	18
961008090902.16	38:48.54	-122:48.74	3.33	15
961008212821.81	38:45.40	-122:42.37	0.37	8
961008213127.10	38:45.21	-122:41.93	0.88	8
961008220543.41	38:50.43	-122:46.41	1.26	9
961009023631.99	38:46.18	-122:43.82	1.11	15
961009024958.26	38:49.43	-122:47.99	3.45	18
961009072304.89	38:46.13	-122:43.66	0.66	9
961009081948.30	38:50.94	-122:47.67	1.91	14
961009092852.28	38:48.36	-122:46.38	1.97	14
961009103459.93	38:47.33	-122:46.51	3.62	14
961009111630.53	38:45.42	-122:43.97	0.64	8
961009151530.74	38:49.15	-122:48.13	2.88	15
961009232953.63	38:48.03	-122:48.79	3.07	16
961010005553.56	38:49.42	-122:48.32	2.65	16
961010053407.91	38:47.41	-122:46.60	2.41	17
961010122235.63	38:49.19	-122:46.69	1.27	14
961010130902.93	38:46.01	-122:43.36	1.10	9
961010140057.13	38:49.19	-122:47.48	0.78	13
961010144314.64	38:47.19	-122:47.01	3.46	24
961010175022.18	38:48.10	-122:46.18	1.53	9
961010225805.99	38:47.85	-122:48.56	3.34	13
961010234737.27	38:47.44	-122:44.10	0.95	12
961011043834.66	38:47.63	-122:44.65	0.69	13
961011052436.00	38:47.34	-122:48.69	2.52	10
961011053413.60	38:47.50	-122:47.90	1.15	14
961011131140.61	38:47.56	-122:46.94	2.69	15
961011163909.72	38:45.98	-122:42.81	1.32	11
961011190328.42	38:46.91	-122:43.34	1.70	12
961011215108.47	38:49.27	-122:48.29	3.02	15
961011234633.71	38:49.09	-122:46.64	2.13	19
961011235909.28	38:47.75	-122:44.48	1.00	9
961012042546.77	38:44.63	-122:42.88	1.36	9
961012043159.11	38:46.93	-122:43.41	1.94	15
961012110920.04	38:47.10	-122:43.42	1.95	14
961012115351.43	38:45.05	-122:42.51	1.61	7
961012124703.89	38:44.58	-122:42.62	1.61	8
961012160229.18	38:44.22	-122:42.53	1.79	10
961012174642.00	38:47.50	-122:48.13	3.30	20
961012185347.38	38:48.80	-122:48.64	2.58	12
961012210442.76	38:49.35	-122:47.20	0.28	10
961013025439.79	38:49.19	-122:48.59	3.03	16
961013031543.52	38:45.36	-122:42.81	0.78	13
961013065306.96	38:49.00	-122:48.57	3.19	17
961013074507.74	38:46.63	-122:45.34	0.68	16

961013082841.68	38:49.88	-122:51.08	1.46	8
961013082918.92	38:50.42	-122:54.66	2.07	14
961013111828.25	38:47.71	-122:43.75	1.48	15
961013173655.62	38:48.00	-122:48.21	0.58	12
961013193916.98	38:47.55	-122:44.73	0.79	16
961013201352.52	38:49.28	-122:46.79	2.26	15
961014010833.51	38:47.80	-122:44.51	1.08	16
961014013812.79	38:48.90	-122:48.67	3.24	6
961014112332.55	38:47.98	-122:48.88	1.05	14
961014112344.82	38:48.00	-122:49.00	0.99	13
961014124907.46	38:47.75	-122:48.67	3.30	18
961014124924.36	38:47.80	-122:48.76	3.28	22
961014130811.21	38:47.81	-122:46.75	3.84	23
961014153434.01	38:47.92	-122:44.51	2.15	17
961014162539.48	38:49.12	-122:46.79	1.98	12
961014233244.81	38:49.01	-122:48.47	3.08	16
961015073307.57	38:49.31	-122:47.97	2.97	13
961015085229.46	38:47.56	-122:44.57	1.67	15
961015093219.02	38:47.10	-122:47.00	3.75	5
961015093517.62	38:49.99	-122:45.67	1.64	10
961015121401.59	38:49.24	-122:48.34	2.86	15
961015123749.82	38:46.47	-122:44.70	2.73	10
961015152331.14	38:47.47	-122:46.90	2.52	16
961015164056.23	38:49.12	-122:49.58	0.45	9
961015193136.51	38:48.08	-122:44.98	2.32	7
961015221534.22	38:48.29	-122:48.74	3.42	19
961016000044.80	38:47.40	-122:45.47	1.68	14
961016003108.01	38:48.72	-122:48.83	2.94	13
961016015412.96	38:47.87	-122:46.85	3.45	17
961016094645.03	38:47.46	-122:46.94	2.62	16
961016110353.72	38:47.82	-122:47.30	0.12	13
961016135527.93	38:46.54	-122:44.62	2.46	16
961016141436.66	38:47.49	-122:48.23	3.54	17
961016223827.25	38:48.85	-122:49.86	1.11	7
961016235707.83	38:49.01	-122:48.60	2.96	16
961017001547.46	38:48.26	-122:46.52	1.79	20
961017001815.11	38:49.49	-122:46.81	0.71	13
961017024834.55	38:47.03	-122:47.13	3.98	22
961017040445.26	38:46.50	-122:42.85	1.75	10
961017070801.16	38:46.33	-122:45.06	0.67	12
961017082055.96	38:48.81	-122:48.83	0.67	9
961017132647.48	38:49.14	-122:48.15	3.06	15
961017202110.33	38:49.41	-122:48.41	2.99	13
961017205019.69	38:49.27	-122:48.13	3.19	13
961017224332.77	38:47.58	-122:46.22	3.90	18
961018013552.79	38:48.15	-122:47.35	0.22	8
961018061059.37	38:46.11	-122:43.86	1.22	11
961018073417.29	38:48.31	-122:48.80	3.00	17
961018084839.69	38:47.32	-122:45.57	1.30	10
961018122758.51	38:48.64	-122:48.27	1.05	12

961018135415.32	38:49.00	-122:46.32	1.18	12
961018140152.37	38:47.86	-122:47.61	0.19	13
961018200907.97	38:48.13	-122:48.87	1.56	14
961018200939.20	38:47.69	-122:47.50	4.08	5
961018214053.68	38:48.71	-122:48.37	2.75	14
961019071816.05	38:47.29	-122:45.48	1.28	13
961019120843.96	38:47.74	-122:48.51	3.18	16
961019121714.91	38:49.23	-122:48.94	1.31	13
961019121846.76	38:48.92	-122:49.53	-0.90	4 6
961019121906.82	38:48.85	-122:49.44	0.49	10
961019121927.97	38:48.98	-122:49.20	0.94	9
961019122524.96	38:49.48	-122:48.82	0.83	10
961019155259.90	38:48.25	-122:44.47	2.15	10
961019231636.45	38:48.61	-122:48.95	1.09	7
961020000225.34	38:48.26	-122:48.74	3.39	22
961020102431.74	38:47.72	-122:44.46	0.40	8
961020113256.63	38:48.08	-122:48.71	3.12	16
961020132022.12	38:47.82	-122:48.47	1.05	10
961020135807.61	38:49.24	-122:48.10	3.11	12
961020141051.34	38:49.25	-122:48.04	2.72	13
961020143726.71	38:49.28	-122:47.74	2.84	15
961020144657.60	38:48.01	-122:48.15	1.38	7
961020154208.66	38:48.09	-122:48.89	3.95	10
961020190908.29	38:49.33	-122:48.19	2.90	9
961021023647.83	38:46.08	-122:43.71	1.07	8
961021100759.17	38:49.25	-122:48.47	3.22	14
961021111404.28	38:46.98	-122:46.54	1.47	15
961021151929.16	38:49.00	-122:48.32	3.00	15
961021171952.71	38:48.29	-122:48.72	3.31	19
961021191157.41	38:47.66	-122:45.10	1.89	12
961021193029.78	38:48.51	-122:46.42	2.30	8
961021222736.78	38:48.37	-122:48.55	0.63	6
961022023600.34	38:49.43	-122:46.98	2.18	14
961022101556.51	38:47.07	-122:45.79	0.12	11
961022113215.62	38:48.13	-122:46.33	1.16	14
961022120804.45	38:48.59	-122:47.95	3.10	15
961022124642.73	38:48.63	-122:48.01	2.90	11
961022163116.82	38:47.18	-122:45.45	1.37	15
961022191238.84	38:46.52	-122:44.74	2.61	13
961022205919.80	38:46.53	-122:42.99	1.79	9
961022222438.70	38:47.78	-122:48.55	3.32	13
961022222949.80	38:47.77	-122:48.54	3.27	17
961023022537.27	38:46.40	-122:42.92	1.61	8
961023031153.86	38:48.50	-122:48.84	2.76	11
961023041838.48	38:48.53	-122:48.91	1.11	14
961023062947.12	38:50.89	-122:50.62	1.68	7
961023094420.76	38:46.29	-122:43.85	1.35	13
961023113608.28	38:48.16	-122:44.32	0.96	7
961023132223.50	38:47.64	-122:48.54	4.28	17
961023151820.61	38:49.39	-122:47.96	3.03	12

961023183631.30	38:48.82	-122:48.61	2.61	10
961023194244.60	38:46.39	-122:43.21	1.61	9
961024005513.74	38:47.99	-122:44.54	1.95	11
961024054525.67	38:48.84	-122:47.83	3.49	21
961024082439.03	38:48.52	-122:48.84	3.01	8
961024104803.49	38:49.52	-122:48.38	3.37	7
961024111455.21	38:47.73	-122:45.17	1.24	13
961024192331.09	38:47.62	-122:44.33	1.37	9
961024233604.12	38:46.97	-122:45.49	0.83	5
961025001319.82	38:46.36	-122:42.96	1.70	10
961025001508.01	38:46.39	-122:42.97	1.73	8
961025004851.63	38:46.76	-122:44.71	4.67	12
961025012631.06	38:47.69	-122:45.08	1.44	12
961025012806.18	38:48.10	-122:45.26	0.46	6
961025012851.85	38:47.80	-122:45.06	0.22	10
961025012915.21	38:47.58	-122:44.96	1.58	8
961025053113.63	38:49.02	-122:48.64	2.66	14
961026021840.37	38:49.16	-122:46.82	1.89	10
961026064551.63	38:50.89	-122:47.88	1.12	6
961026084732.37	38:46.34	-122:45.06	0.51	14
961026134109.78	38:48.87	-122:48.65	2.56	9
961026162531.13	38:48.87	-122:48.75	2.93	12
961026163404.08	38:49.12	-122:48.14	2.92	14
961026202221.85	38:49.02	-122:47.11	0.80	12
961026202416.38	38:49.06	-122:47.19	0.65	9
961026202655.92	38:49.06	-122:47.13	1.02	11
961026203420.14	38:47.65	-122:48.48	4.08	15
961027031443.88	38:49.16	-122:47.84	2.89	11
961027042722.44	38:47.70	-122:47.23	0.45	13
961027103530.28	38:49.25	-122:48.35	3.14	12
961027162417.07	38:50.74	-122:47.65	1.70	10
961027162442.58	38:50.97	-122:47.46	1.62	6
961027192943.25	38:49.09	-122:46.58	1.49	10
961027192956.19	38:49.14	-122:46.56	1.25	7
961027202508.12	38:47.61	-122:46.23	3.87	19
961027203643.07	38:47.63	-122:46.23	3.59	16
961027212020.52	38:47.62	-122:46.24	3.96	20
961028001317.13	38:46.97	-122:45.37	1.63	11
961028001922.93	38:48.63	-122:46.67	0.52	11
961028171522.01	38:48.69	-122:46.37	2.04	8
961028173122.62	38:47.16	-122:44.41	0.95	13
961028192626.40	38:49.52	-122:48.25	2.94	10
961028192825.48	38:48.16	-122:46.49	1.50	11
961028215406.72	38:50.38	-122:49.27	1.21	6
961029023418.64	38:49.00	-122:48.29	3.50	16
961029033236.54	38:48.73	-122:47.88	3.01	15
961029035455.32	38:49.40	-122:48.20	2.86	13
961029052448.39	38:50.70	-122:47.92	1.52	8
961029105139.06	38:46.97	-122:45.43	1.03	11
961029125740.65	38:46.33	-122:43.01	1.64	6

961029142928.21	38:47.59	-122:44.61	0.80	11
961029163304.78	38:49.72	-122:46.15	1.25	14
961029201949.02	38:48.25	-122:46.98	1.42	11
961029225831.19	38:47.11	-122:46.50	3.16	15
961030030725.45	38:49.65	-122:46.44	0.80	8
961030034812.40	38:45.22	-122:42.41	1.68	13
961030104021.18	38:47.60	-122:44.48	1.05	11
961030104224.86	38:47.59	-122:44.58	1.04	16
961030142913.20	38:46.17	-122:43.94	1.99	15
961030172052.42	38:49.37	-122:48.26	2.84	9
961030194241.40	38:48.82	-122:48.28	2.69	16
961030231200.02	38:47.91	-122:44.51	1.61	12
961030231315.81	38:47.79	-122:44.49	1.40	10
961030234737.17	38:48.03	-122:46.60	-1.00	6
961031005119.64	38:47.40	-122:45.31	0.77	9
961031012817.01	38:46.47	-122:44.69	2.30	14
961031031305.20	38:44.95	-122:41.72	0.63	6
961031032337.27	38:44.88	-122:41.71	1.18	7
961031072213.10	38:49.05	-122:48.65	2.79	14
961031072746.90	38:48.87	-122:48.91	3.28	8
961031082454.06	38:47.54	-122:46.47	4.29	17
961031163604.20	38:45.54	-122:42.81	1.24	10

Events in August 1998 inversion

Earthquake	Lattitude (deg)	Longtide (deg)	Depth /km	Number of observations
980719065205.07	38:44.82	-122:42.91	1.60	14
980719112952.30	38:48.08	-122:46.71	3.64	23
980719120304.21	38:48.49	-122:48.92	2.85	19
980719132851.68	38:49.17	-122:48.08	2.84	18
980719161239.50	38:48.01	-122:44.21	2.29	17
980719195843.37	38:45.30	-122:43.36	1.84	13
980719203100.46	38:48.06	-122:48.85	2.97	16
980719234203.19	38:47.89	-122:48.84	2.61	16
980719235138.55	38:49.20	-122:47.80	3.07	14
980720010639.86	38:49.16	-122:47.92	3.16	16
980720023003.63	38:47.99	-122:48.75	3.13	24
980720045901.96	38:47.86	-122:48.07	0.55	15
980720085053.61	38:45.98	-122:41.76	2.30	14
980720091202.73	38:46.47	-122:43.20	1.62	15
980720095058.69	38:46.31	-122:43.02	1.62	15
980720132829.49	38:47.87	-122:44.12	3.00	15
980720165705.34	38:46.84	-122:45.81	1.12	11
980721060502.00	38:48.58	-122:48.80	2.61	13
980721062843.72	38:47.93	-122:46.79	3.70	21
980721063448.96	38:49.18	-122:48.32	3.27	16
980721091241.11	38:48.83	-122:48.22	3.02	17
980721154133.93	38:48.88	-122:48.13	2.95	19

980721192513.71	38:47.36	-122:46.78	2.50	14
980721203304.28	38:47.97	-122:46.77	3.45	17
980722043832.58	38:49.44	-122:47.82	3.16	20
980722113037.48	38:49.38	-122:48.02	3.27	17
980722114043.37	38:47.82	-122:47.12	4.05	18
980722120338.10	38:47.68	-122:46.96	3.89	22
980722165802.68	38:49.33	-122:48.27	3.23	16
980722201942.93	38:49.99	-122:51.82	2.55	9
980723020130.52	38:45.99	-122:41.86	2.09	13
980723134325.75	38:48.15	-122:47.93	3.29	23
980723162610.25	38:49.45	-122:48.39	2.89	18
980723172631.55	38:48.06	-122:44.27	2.63	12
980724083643.01	38:48.63	-122:46.48	1.86	21
980724101524.22	38:43.67	-122:41.76	3.34	8
980724112258.72	38:48.27	-122:48.80	3.21	23
980724145045.39	38:49.30	-122:48.55	2.65	14
980724173033.63	38:49.18	-122:46.77	0.76	15
980724180309.64	38:49.39	-122:48.06	3.60	17
980724184019.65	38:49.39	-122:48.04	3.49	16
980724214258.94	38:47.31	-122:46.76	3.64	19
980724215131.98	38:48.44	-122:48.92	2.94	18
980724220707.03	38:48.55	-122:48.41	2.56	19
980725022930.04	38:49.19	-122:48.18	2.76	19
980725055147.53	38:45.99	-122:42.48	1.50	13
980725150142.11	38:49.10	-122:47.85	3.19	18
980725164508.38	38:47.69	-122:48.75	3.22	24
980725170153.15	38:49.12	-122:48.03	3.43	20
980725202947.75	38:47.68	-122:48.70	3.28	23
980725211612.01	38:49.21	-122:47.81	3.05	12
980726000734.09	38:48.33	-122:49.03	2.79	17
980726004748.27	38:49.27	-122:48.48	3.02	17
980726071614.62	38:49.00	-122:48.44	3.17	15
980726091612.01	38:49.16	-122:48.34	2.81	19
980726144037.25	38:47.94	-122:43.95	2.04	14
980726175147.32	38:49.19	-122:47.80	3.19	18
980726180713.12	38:49.64	-122:48.48	1.03	13
980726181304.07	38:48.32	-122:48.96	3.06	18
980726221259.03	38:48.05	-122:48.77	2.91	19
980727055805.53	38:49.16	-122:47.72	3.25	13
980727072333.91	38:47.65	-122:46.90	1.19	21
980727091219.78	38:48.74	-122:48.53	2.59	11
980727103902.26	38:49.43	-122:48.25	2.91	12
980727135834.37	38:47.78	-122:46.54	3.67	24
980727151128.54	38:48.15	-122:44.21	2.12	13
980727160812.99	38:47.60	-122:46.24	3.90	22
980727194622.77	38:50.30	-122:49.99	1.62	10
980728072747.36	38:49.55	-122:48.12	2.56	19
980728111014.13	38:46.08	-122:42.76	1.45	15
980728130112.16	38:48.16	-122:48.45	1.97	18
980728130230.45	38:48.16	-122:48.44	1.86	19

980728163317.02	38:48.27	-122:48.24	1.08	18
980728175840.16	38:48.00	-122:44.09	2.76	16
980728181037.35	38:48.76	-122:48.58	2.86	17
980729000535.06	38:49.44	-122:47.94	2.94	19
980729010440.32	38:48.72	-122:48.77	2.92	16
980729010535.77	38:48.58	-122:48.85	3.06	15
980729013229.65	38:47.75	-122:48.65	3.33	22
980729082842.05	38:49.78	-122:49.69	0.98	14
980729143716.72	38:49.32	-122:48.53	2.89	17
980729153754.81	38:47.53	-122:46.80	2.60	23
980729205252.37	38:49.53	-122:48.09	3.00	20
980729231531.28	38:48.51	-122:48.84	3.23	15
980730035314.51	38:48.11	-122:46.72	3.64	23
980730043302.11	38:49.52	-122:47.97	3.34	20
980730054641.86	38:49.02	-122:47.84	3.14	19
980730073802.20	38:47.67	-122:48.85	3.29	16
980730100200.25	38:47.95	-122:48.94	3.13	23
980730132132.00	38:46.45	-122:42.91	1.68	16
980730132250.27	38:46.41	-122:42.93	1.41	17
980730135805.24	38:49.28	-122:48.08	3.33	16
980730152445.47	38:49.43	-122:48.45	3.10	10
980730173249.68	38:48.93	-122:48.04	2.28	16
980731043511.05	38:46.92	-122:47.12	4.13	21
980731072614.35	38:48.77	-122:48.72	2.85	16
980731073007.39	38:48.64	-122:48.58	2.65	14
980731084833.28	38:49.37	-122:47.88	3.06	17
980731111940.95	38:47.90	-122:44.09	1.96	19
980731114645.64	38:48.12	-122:46.82	3.76	17
980731125442.75	38:49.88	-122:51.97	2.28	13
980731145711.16	38:49.68	-122:52.00	2.13	15
980731163835.49	38:47.62	-122:48.76	3.14	14
980731201541.46	38:49.92	-122:51.52	1.59	13
980801044121.60	38:49.65	-122:48.45	0.63	15
980801064643.46	38:49.18	-122:48.24	2.90	20
980801091814.46	38:47.71	-122:48.06	3.48	19
980801105557.41	38:46.97	-122:45.59	-0.20	7 1
980801142348.90	38:49.37	-122:47.89	3.18	16
980801164616.18	38:49.44	-122:48.34	2.63	18
980801184023.90	38:47.84	-122:48.39	3.36	23
980801191850.85	38:47.92	-122:45.81	0.63	14
980801204923.72	38:48.77	-122:48.81	3.29	15
980801230345.99	38:48.76	-122:48.44	2.65	12
980802025129.81	38:48.84	-122:48.62	2.76	13
980802041419.57	38:48.57	-122:48.45	2.82	15
980802045144.24	38:47.75	-122:47.25	3.68	22
980802064017.02	38:48.97	-122:48.08	2.86	15
980802083849.66	38:47.65	-122:47.11	0.15	14
980802094903.34	38:49.27	-122:47.66	2.75	11
980802200032.32	38:48.91	-122:48.71	2.42	17
980802201525.34	38:48.01	-122:48.83	3.03	16

980802212630.72	38:49.84	-122:45.76	3.61	16
980802230923.62	38:48.30	-122:48.74	3.26	10
980803053008.51	38:47.09	-122:45.46	1.60	18
980803055011.34	38:46.23	-122:43.86	1.62	17
980803062840.35	38:46.19	-122:44.86	1.32	17
980803092645.74	38:47.30	-122:46.71	2.67	19
980803092800.41	38:47.49	-122:46.47	3.70	23
980803092848.04	38:47.30	-122:46.67	2.70	22
980803141209.35	38:48.76	-122:48.56	2.90	17
980803182214.35	38:48.63	-122:48.64	2.98	14
980803183105.69	38:45.78	-122:44.32	2.03	19
980803203500.44	38:48.04	-122:45.55	1.41	6
980804055249.63	38:47.99	-122:46.91	3.56	24
980804063244.06	38:48.56	-122:46.18	1.83	19
980804090835.81	38:48.04	-122:48.13	1.39	16
980804120555.45	38:48.91	-122:47.85	3.44	13
980804123716.53	38:47.70	-122:48.20	3.03	12
980804133227.14	38:48.17	-122:48.24	2.23	15
980804152735.95	38:44.93	-122:42.34	0.69	6
980804162955.44	38:46.07	-122:43.87	2.07	8
980804214609.70	38:47.35	-122:46.55	1.01	17
980805024547.15	38:47.46	-122:46.95	3.98	22
980805025325.29	38:49.26	-122:47.86	2.50	5
980805031148.23	38:48.13	-122:44.25	2.56	18
980805034037.52	38:47.59	-122:46.82	2.19	18
980805034620.26	38:47.35	-122:46.75	2.61	19
980805053018.68	38:49.82	-122:45.81	3.95	17
980805060451.64	38:47.32	-122:46.73	2.64	14
980805065725.12	38:47.39	-122:46.78	2.55	21
980805080714.60	38:49.23	-122:47.85	2.87	20
980805144036.95	38:49.28	-122:48.07	3.09	16
980806035823.74	38:46.45	-122:43.34	1.20	14
980806062008.29	38:46.19	-122:43.70	1.81	13
980806111600.50	38:49.37	-122:47.98	3.22	16
980806123111.74	38:47.11	-122:45.48	2.22	8
980806161048.07	38:48.92	-122:48.72	2.66	13
980806172559.99	38:49.47	-122:48.30	3.03	13
980806191227.10	38:49.22	-122:48.33	3.10	15
980806191327.06	38:50.68	-122:48.68	1.74	13
980806212317.43	38:48.17	-122:48.99	3.34	18
980806232409.20	38:49.35	-122:47.87	2.90	15
980807040858.23	38:49.55	-122:47.60	0.22	12
980807074455.86	38:49.22	-122:48.75	3.35	16
980807091822.93	38:48.25	-122:48.76	2.39	11
980807100434.97	38:49.18	-122:47.88	3.16	16
980807140802.30	38:48.72	-122:48.77	2.60	15
980807161740.14	38:47.98	-122:44.19	2.32	15
980807170518.56	38:47.96	-122:44.23	2.35	10
980807220108.39	38:49.53	-122:48.26	2.83	15
980807230608.65	38:45.60	-122:44.31	1.98	17

980807233452.72	38:49.36	-122:47.86	3.28	18
980808015246.93	38:49.26	-122:46.58	1.73	16
980808022320.62	38:49.26	-122:48.40	3.16	16
980808024609.52	38:48.41	-122:47.71	3.42	18
980808031518.86	38:48.09	-122:48.15	0.95	17
980808105813.09	38:48.05	-122:44.12	2.55	13
980808195325.93	38:49.38	-122:47.97	3.03	16
980808202939.12	38:48.17	-122:48.78	2.33	20
980808232609.71	38:47.65	-122:48.74	3.43	10
980809002534.66	38:48.65	-122:48.81	2.77	19
980809020400.12	38:48.03	-122:44.15	2.62	20
980809034347.89	38:49.30	-122:47.79	2.88	17
980809051952.28	38:49.33	-122:47.81	3.21	18
980809054041.32	38:47.87	-122:47.40	0.12	15
980809171122.29	38:49.23	-122:48.08	2.86	17
980809173352.75	38:49.25	-122:48.55	2.34	11
980809183826.35	38:48.50	-122:48.85	3.44	21
980809192355.98	38:49.73	-122:47.18	0.32	15
980809214331.92	38:48.92	-122:47.79	3.08	19
980810061024.96	38:48.84	-122:47.81	3.18	13
980810075721.37	38:48.19	-122:48.75	2.58	21
980810085131.60	38:47.65	-122:46.65	3.41	26
980810100340.74	38:49.51	-122:45.95	0.93	18
980810111356.97	38:47.64	-122:46.80	3.63	19
980810122412.72	38:49.22	-122:47.77	2.97	16
980810185736.08	38:48.37	-122:47.85	3.33	14
980810192109.95	38:48.04	-122:44.30	2.22	16
980810194613.42	38:48.09	-122:48.72	3.03	11
980810235833.16	38:47.53	-122:48.72	3.48	13
980811025853.34	38:47.97	-122:48.73	2.86	17
980811070049.39	38:47.68	-122:48.73	3.33	23
980811103249.48	38:49.20	-122:48.37	2.67	14
980811103552.55	38:48.36	-122:48.05	3.02	18
980811154945.90	38:48.14	-122:44.12	2.46	14
980811182929.67	38:47.73	-122:46.25	3.91	18
980811183626.06	38:47.71	-122:46.29	4.02	21
980811205840.76	38:49.20	-122:48.08	3.03	15
980811221212.42	38:48.89	-122:48.02	2.62	14
980811224755.67	38:47.49	-122:47.72	0.93	15
980812033108.09	38:48.91	-122:48.64	2.48	12
980812055130.24	38:49.42	-122:48.42	3.27	14
980812090051.03	38:47.95	-122:44.17	2.21	14
980812132135.00	38:48.19	-122:48.76	2.71	18
980812145520.08	38:47.70	-122:46.93	1.86	15
980812175525.50	38:47.69	-122:48.30	3.27	18
980812214956.51	38:49.35	-122:48.34	2.92	15
980812215220.52	38:47.36	-122:43.64	0.84	11
980813024148.70	38:48.77	-122:48.67	2.68	17
980813024524.41	38:48.30	-122:49.03	3.14	17
980813065946.72	38:49.33	-122:47.94	2.95	19

980813134357.65	38:46.56	-122:43.00	1.48	14
980813172420.80	38:47.68	-122:43.68	1.17	15
980813174706.95	38:47.87	-122:47.99	0.98	18
980813183928.07	38:49.21	-122:47.84	3.17	15
980813214754.36	38:47.55	-122:46.43	3.66	23
980813220536.59	38:46.48	-122:44.73	2.16	18
980814094052.19	38:45.12	-122:42.60	0.87	7
980814095657.63	38:47.40	-122:46.62	1.36	20
980814101043.20	38:47.74	-122:44.19	2.20	11
980814102650.68	38:48.11	-122:44.21	2.20	15
980814102803.77	38:48.10	-122:44.07	2.13	14
980814103813.88	38:48.11	-122:44.08	2.60	15
980814113844.36	38:49.23	-122:47.81	3.00	16
980814202244.82	38:47.66	-122:43.76	1.29	15
980814203526.95	38:48.83	-122:47.86	3.32	13
980814233916.70	38:49.17	-122:48.58	2.50	15
980815020525.84	38:49.27	-122:47.87	3.03	17
980815025140.22	38:49.09	-122:48.02	2.79	16
980815042625.63	38:47.53	-122:47.75	1.08	17
980815042953.86	38:49.16	-122:47.84	3.09	17
980815054633.01	38:48.50	-122:48.02	2.94	16
980815101908.93	38:48.95	-122:48.55	2.82	13
980815124614.07	38:48.40	-122:47.93	3.00	15
980815153856.34	38:49.12	-122:48.19	3.18	15
980815170239.16	38:49.35	-122:48.50	2.95	14
980815175241.22	38:49.17	-122:48.04	3.00	14
980816001059.65	38:49.30	-122:47.99	2.87	16
980816010846.23	38:49.12	-122:48.69	2.93	14
980816013832.35	38:49.15	-122:48.14	2.60	16
980816015819.47	38:48.90	-122:48.67	3.03	12
980816054448.92	38:49.30	-122:48.36	2.80	14
980816065305.17	38:48.37	-122:47.95	3.11	16
980816120106.03	38:49.21	-122:47.84	3.20	18
980816135013.70	38:48.02	-122:48.87	3.00	20
980816135812.50	38:50.23	-122:46.20	1.70	15
980817053535.27	38:47.35	-122:44.64	1.83	15
980817054311.55	38:47.81	-122:48.41	3.24	11
980817061738.86	38:49.04	-122:47.90	3.05	18
980817113300.33	38:49.16	-122:48.61	2.43	16
980817161847.57	38:47.63	-122:46.89	4.10	22
980817202529.20	38:49.24	-122:47.94	3.02	16
980817205556.90	38:48.27	-122:48.91	2.93	19
980817205854.56	38:48.63	-122:48.89	3.00	16
980817223519.22	38:51.03	-122:48.07	1.70	12
980818033029.28	38:49.31	-122:52.12	2.06	10
980818050426.17	38:49.27	-122:48.11	3.05	15
980818065333.81	38:46.15	-122:43.63	0.56	11
980818075209.57	38:45.29	-122:41.01	4.79	8
980818093535.63	38:47.35	-122:44.63	1.35	17
980818104504.81	38:49.07	-122:48.01	2.83	14

980818190204.83	38:46.12	-122:43.82	1.38	11
980818203003.65	38:49.03	-122:48.39	3.64	15
980818220812.89	38:48.10	-122:44.28	2.17	15
980819005249.69	38:46.23	-122:43.85	1.58	15
980819005409.75	38:47.97	-122:44.23	2.11	12
980819073322.40	38:48.25	-122:47.92	3.19	17
980819122943.40	38:48.46	-122:48.81	3.51	17
980819154427.32	38:49.33	-122:47.95	3.08	17
980819213434.80	38:50.09	-122:47.54	0.90	12
980819220824.49	38:50.87	-122:48.10	1.57	16
980819223243.77	38:48.96	-122:46.36	1.09	13
980819225746.85	38:48.49	-122:48.92	3.67	16
980819232010.61	38:48.18	-122:46.58	3.87	15
980820013253.35	38:49.13	-122:48.08	2.83	16
980820055132.90	38:49.22	-122:47.91	2.92	14
980820071952.52	38:45.68	-122:43.45	1.55	11
980820102245.53	38:47.86	-122:44.12	2.47	19
980820114934.98	38:48.35	-122:46.30	2.18	23
980820171608.94	38:48.14	-122:46.70	3.95	23
980820182029.93	38:49.11	-122:48.32	3.18	16
980820185455.63	38:47.58	-122:43.70	1.15	11
980820190658.36	38:48.17	-122:44.09	2.65	17
980820191558.74	38:48.86	-122:48.43	2.57	18
980821004316.55	38:48.00	-122:43.94	2.28	12
980821005703.48	38:49.18	-122:47.86	2.81	21
980821010212.98	38:47.93	-122:44.11	1.94	14
980821014516.85	38:47.12	-122:45.54	0.45	15
980821020513.50	38:48.14	-122:48.73	2.97	15
980821042312.03	38:50.45	-122:47.84	1.39	14
980821043917.30	38:45.75	-122:44.33	1.90	21

Depth = 0 km

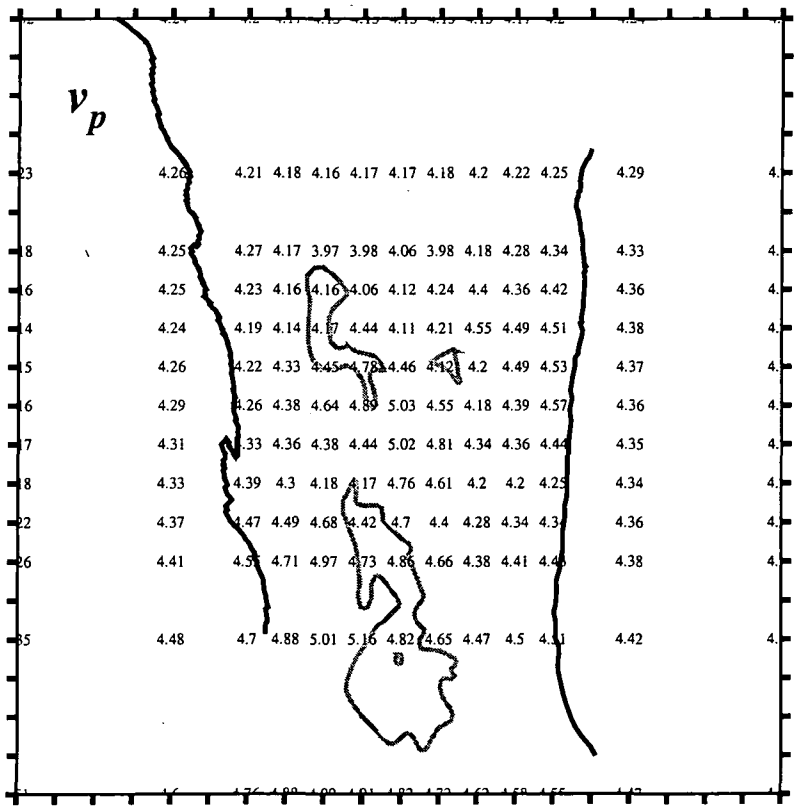
v_p
4.21 4.18 4.16 4.17 4.17 4.18 4.2 4.22 4.25
4.27 4.17 3.97 3.98 4.06 3.98 4.18 4.28 4.34
4.23 4.16 4.16 4.06 4.12 4.24 4.4 4.36 4.42
4.19 4.14 4.17 4.44 4.11 4.21 4.55 4.49 4.51
4.22 4.33 4.45 4.78 4.46 4.12 4.2 4.49 4.53
4.26 4.38 4.64 4.89 5.03 4.55 4.18 4.39 4.57
4.33 4.36 4.38 4.44 5.02 4.81 4.34 4.36 4.44
4.39 4.3 4.18 4.17 4.76 4.61 4.2 4.2 4.25
4.47 4.49 4.68 4.42 4.7 4.4 4.28 4.34
4.71 4.97 4.73 4.66 4.38 4.41
4.7 4.88 5.01 5.16 4.82 4.65 4.47 4.5

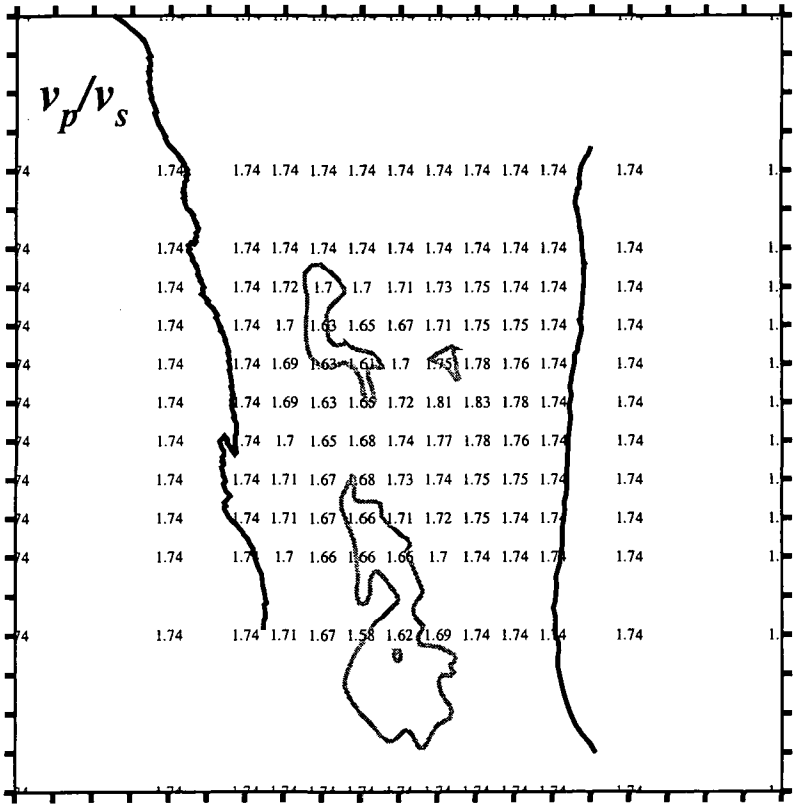
v_p/v_s
1.74 1.74 1.74 1.74 1.74 1.74 1.74 1.74 1.74
1.74 1.72 1.7 1.7 1.71 1.73 1.75 1.74 1.74
1.74 1.7 1.65 1.67 1.71 1.75 1.75 1.74
1.74 1.69 1.63 1.7 1.78 1.76 1.74
1.74 1.69 1.63 1.72 1.81 1.83 1.78 1.74
1.74 1.7 1.65 1.68 1.74 1.77 1.78 1.76 1.74
1.74 1.71 1.67 1.68 1.73 1.74 1.75 1.75 1.74
1.74 1.71 1.67 1.66 1.71 1.72 1.75 1.74
1.7 1.66 1.66 1.7 1.74 1.74
1.74 1.71 1.67 1.62 1.69 1.74 1.74

Depth = 1 km

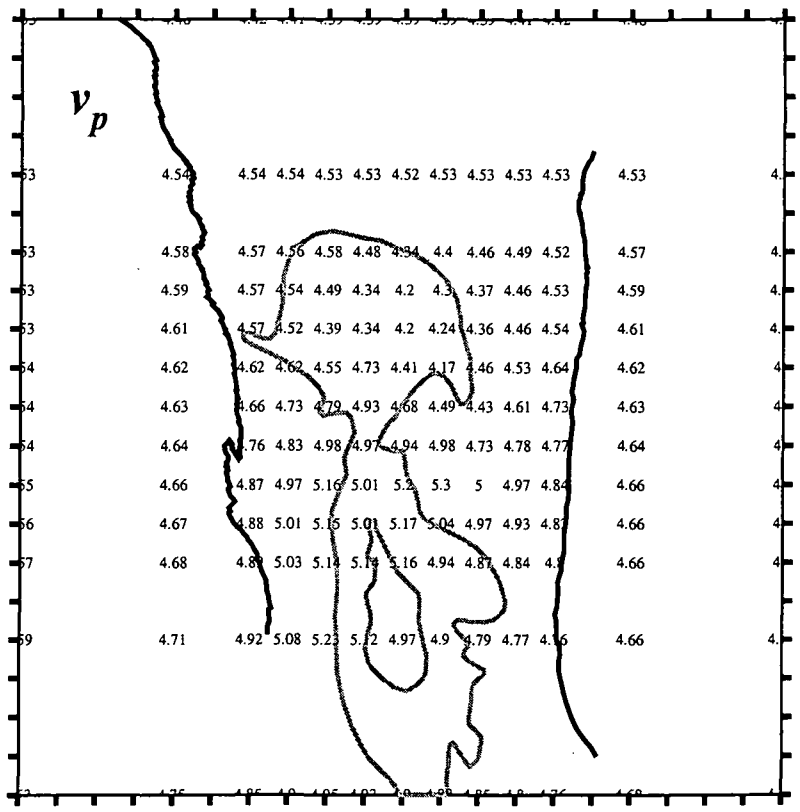

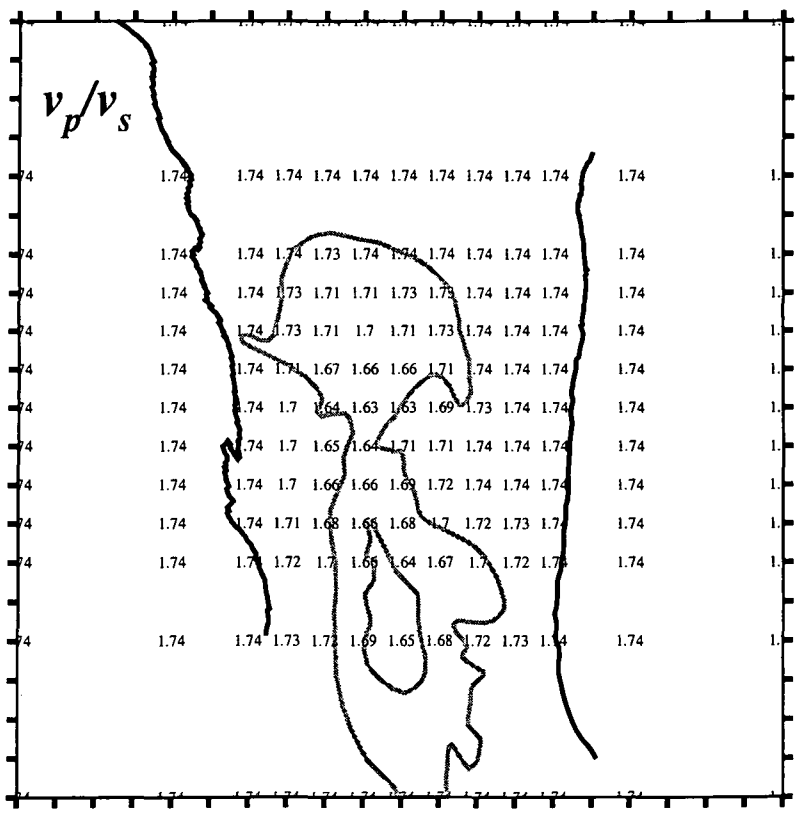

Depth = 0 km

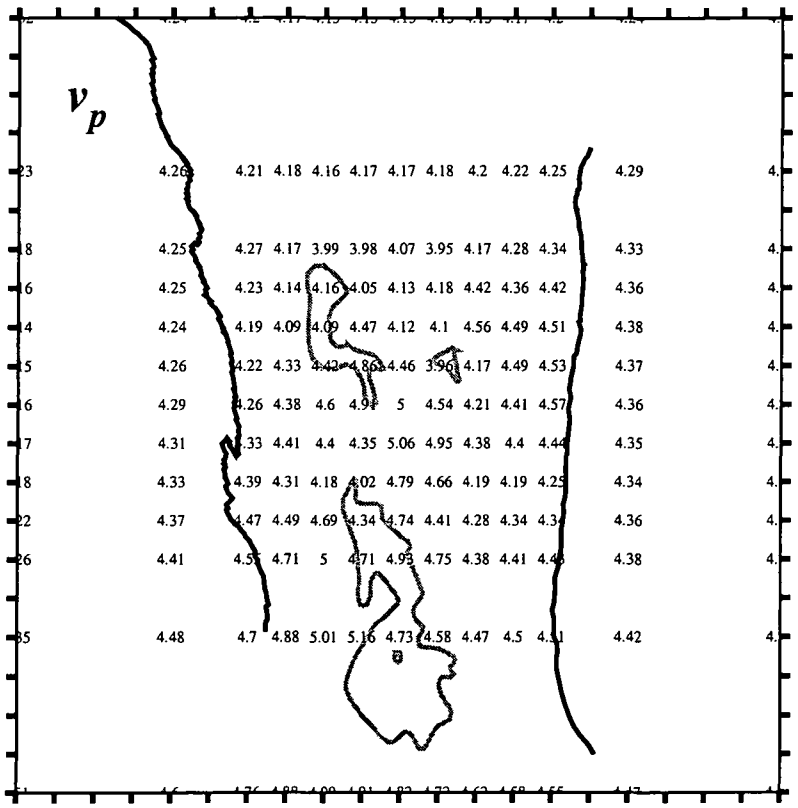
v_p
4.26 4.21 4.18 4.16 4.17 4.17 4.18 4.2 4.22 4.25 4.29
4.25 4.27 4.17 3.99 3.98 4.07 3.95 4.17 4.28 4.34 4.33
4.25 4.23 4.14 4.16 4.05 4.13 4.18 4.42 4.36 4.42 4.36
4.24 4.19 4.09 4.09 4.47 4.12 4.1 4.56 4.49 4.51 4.38
4.26 4.22 4.33 4.42 4.86 4.46 3.96 4.17 4.49 4.53 4.37
4.29 4.26 4.38 4.6 4.94 5 4.54 4.21 4.41 4.57 4.36
4.31 4.33 4.41 4.4 4.35 5.06 4.95 4.38 4.4 4.44 4.35
4.33 4.39 4.31 4.18 4.02 4.79 4.66 4.19 4.19 4.25 4.34
4.37 4.47 4.49 4.69 4.34 4.74 4.41 4.28 4.34 4.34 4.36
4.41 4.5 4.71 5 4.71 4.93 4.75 4.38 4.41 4.46 4.38
4.48 4.7 4.88 5.01 5.16 4.73 4.58 4.47 4.5 4.51 4.42

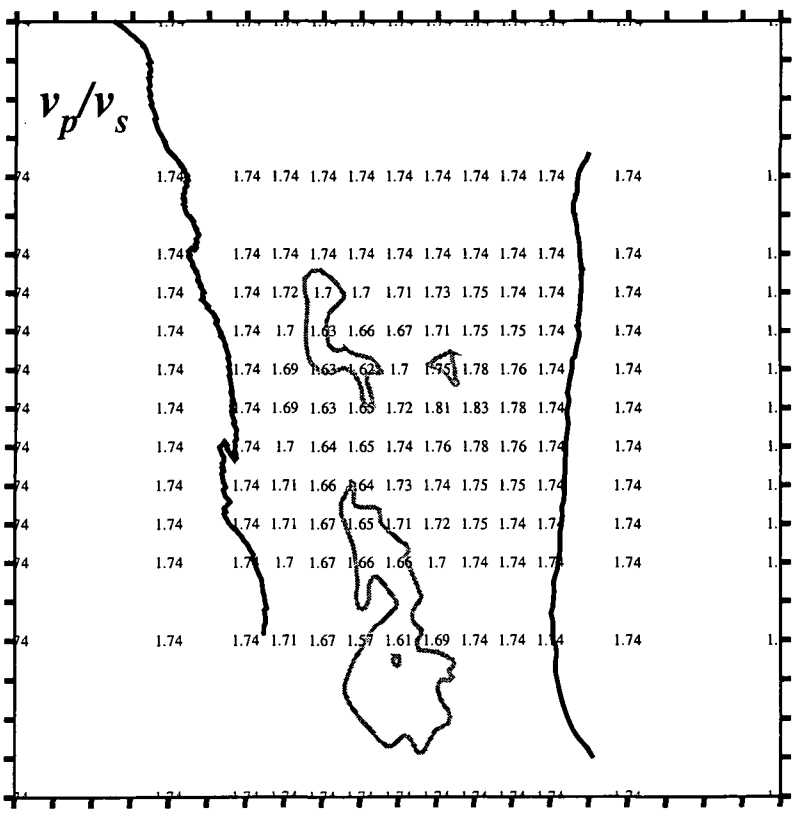
v_p/v_s
1.74 1.74 1.74 1.74 1.74 1.74 1.74 1.74 1.74 1.74 1.74
1.74 1.74 1.74 1.74 1.74 1.74 1.74 1.74 1.74 1.74 1.74
1.74 1.74 1.72 1.7 1.7 1.71 1.73 1.75 1.74 1.74 1.74
1.74 1.74 1.7 1.63 1.66 1.67 1.71 1.75 1.75 1.74 1.74
1.74 1.74 1.69 1.63 1.62 1.7 1.75 1.78 1.76 1.74 1.74
1.74 1.74 1.69 1.63 1.65 1.72 1.81 1.83 1.78 1.74 1.74
1.74 1.74 1.7 1.64 1.65 1.74 1.76 1.78 1.76 1.74 1.74
1.74 1.74 1.71 1.66 1.64 1.73 1.74 1.75 1.75 1.74 1.74
1.74 1.74 1.71 1.67 1.65 1.71 1.72 1.75 1.74 1.74 1.74
1.74 1.74 1.7 1.67 1.66 1.66 1.7 1.74 1.74 1.74 1.74
1.74 1.74 1.71 1.67 1.57 1.61 1.69 1.74 1.74 1.74 1.74

Depth = 1 km

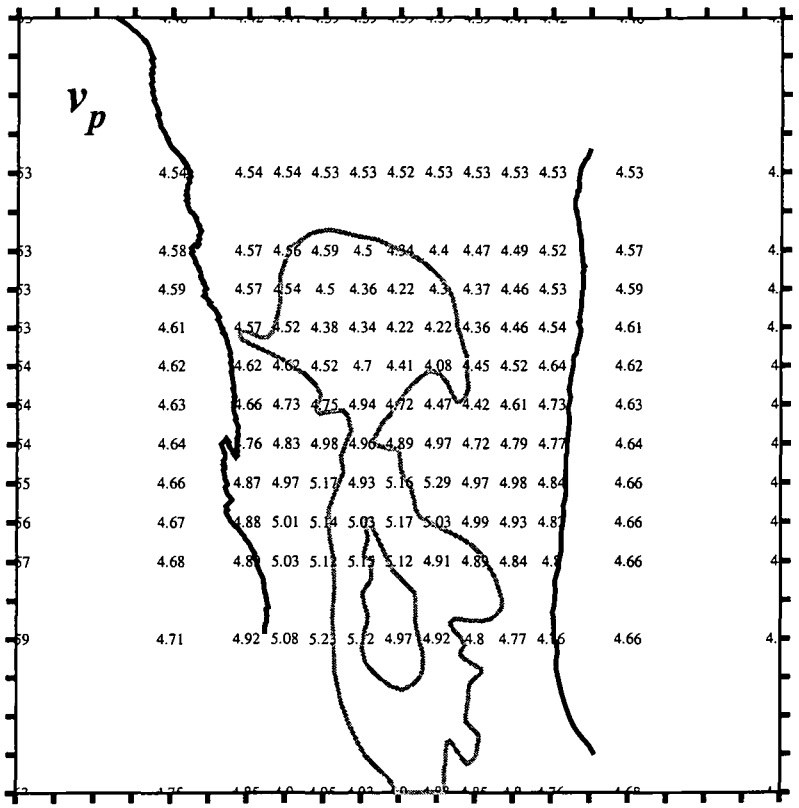
v_p
4.54 4.54 4.53 4.53 4.52 4.53 4.53 4.53 4.53 4.53
4.58 4.57 4.56 4.59 4.5 4.34 4.4 4.47 4.49 4.52 4.57
4.59 4.57 4.54 4.5 4.36 4.22 4.3 4.37 4.46 4.53 4.59
4.61 4.57 4.52 4.38 4.34 4.22 4.22 4.36 4.46 4.54 4.61
4.62 4.62 4.62 4.52 4.7 4.41 4.08 4.45 4.52 4.64 4.62
4.63 4.66 4.73 4.75 4.94 4.72 4.47 4.42 4.61 4.73 4.63
4.64 4.76 4.83 4.98 4.96 4.89 4.97 4.72 4.79 4.77 4.64
4.66 4.87 4.97 5.17 4.93 5.16 5.29 4.97 4.98 4.84 4.66
4.67 4.88 5.01 5.14 5.03 5.17 5.03 4.99 4.93 4.87 4.66
4.68 4.89 5.03 5.12 5.15 5.12 4.91 4.89 4.84 4.8 4.66
4.71 4.92 5.08 5.23 5.22 4.97 4.92 4.8 4.77 4.66

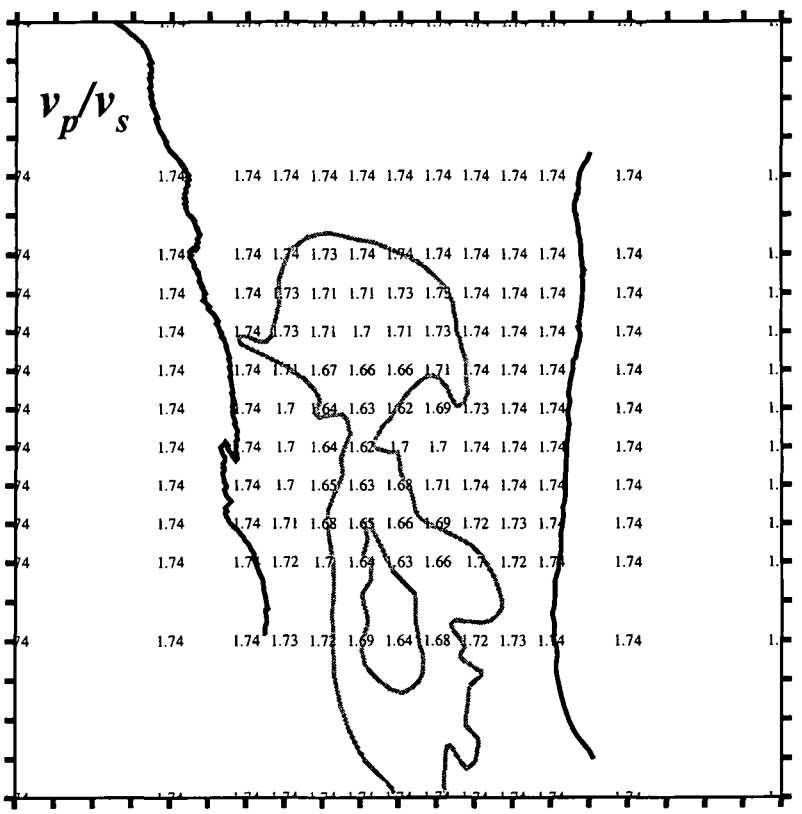
v_p/v_s
1.74 1.74 1.74 1.74 1.74 1.74 1.74 1.74 1.74 1.74 1.74
1.74 1.74 1.74 1.73 1.74 1.74 1.74 1.74 1.74 1.74 1.74
1.74 1.74 1.73 1.71 1.71 1.73 1.73 1.74 1.74 1.74 1.74
1.74 1.74 1.73 1.71 1.7 1.71 1.73 1.74 1.74 1.74 1.74
1.74 1.74 1.71 1.67 1.66 1.66 1.71 1.74 1.74 1.74 1.74
1.74 1.74 1.7 1.64 1.63 1.62 1.69 1.73 1.74 1.74 1.74
1.74 1.74 1.7 1.64 1.62 1.7 1.7 1.74 1.74 1.74 1.74
1.74 1.74 1.7 1.65 1.63 1.68 1.71 1.74 1.74 1.74 1.74
1.74 1.74 1.71 1.68 1.65 1.66 1.69 1.72 1.73 1.74 1.74
1.74 1.74 1.72 1.7 1.64 1.63 1.66 1.7 1.72 1.74 1.74
1.74 1.74 1.73 1.72 1.69 1.64 1.68 1.72 1.73 1.74 1.74

Depth = 0 km

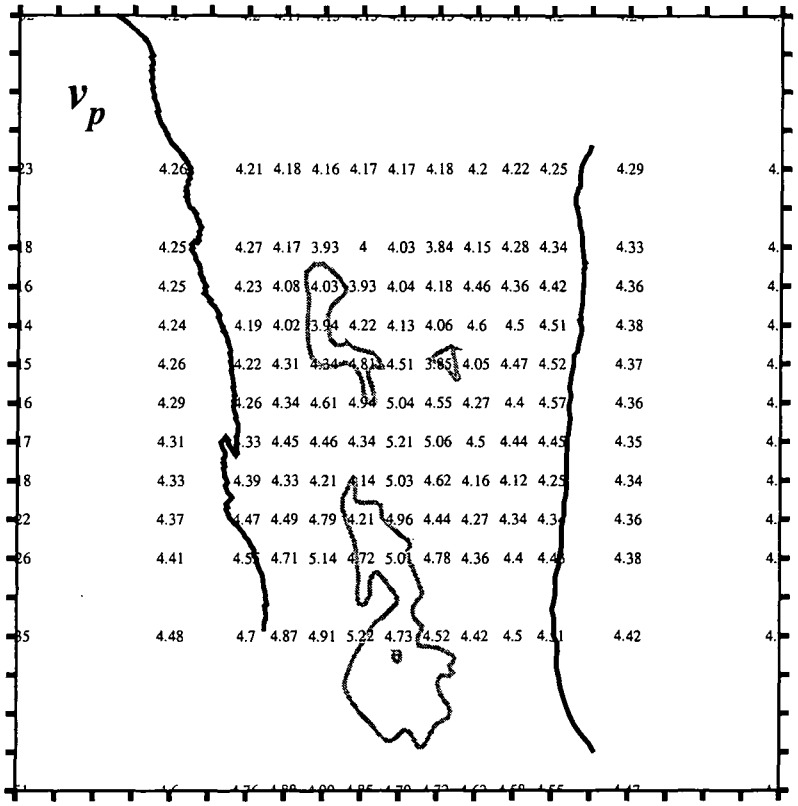
v_p
4.26 4.21 4.18 4.16 4.17 4.17 4.18 4.2 4.22 4.25 4.29
4.25 4.27 4.17 3.93 4 4.03 3.84 4.15 4.28 4.34 4.33
4.25 4.23 4.08 4.03 3.93 4.04 4.18 4.46 4.36 4.42 4.36
4.24 4.19 4.02 3.94 4.22 4.13 4.06 4.6 4.5 4.51 4.38
4.26 4.22 4.31 4.34 4.13 4.51 3.85 4.05 4.47 4.52 4.37
4.29 4.26 4.34 4.61 4.94 5.04 4.55 4.27 4.4 4.57 4.36
4.31 4.33 4.45 4.46 4.34 5.21 5.06 4.5 4.44 4.45 4.35
4.33 4.39 4.33 4.21 4.14 5.03 4.62 4.16 4.12 4.25 4.34
4.37 4.47 4.49 4.79 4.21 4.96 4.44 4.27 4.34 4.3 4.36
4.41 4.5 4.71 5.14 4.72 5.01 4.78 4.36 4.4 4.43 4.38
4.48 4.7 4.87 4.91 5.22 4.73 4.52 4.42 4.5 4.51 4.42

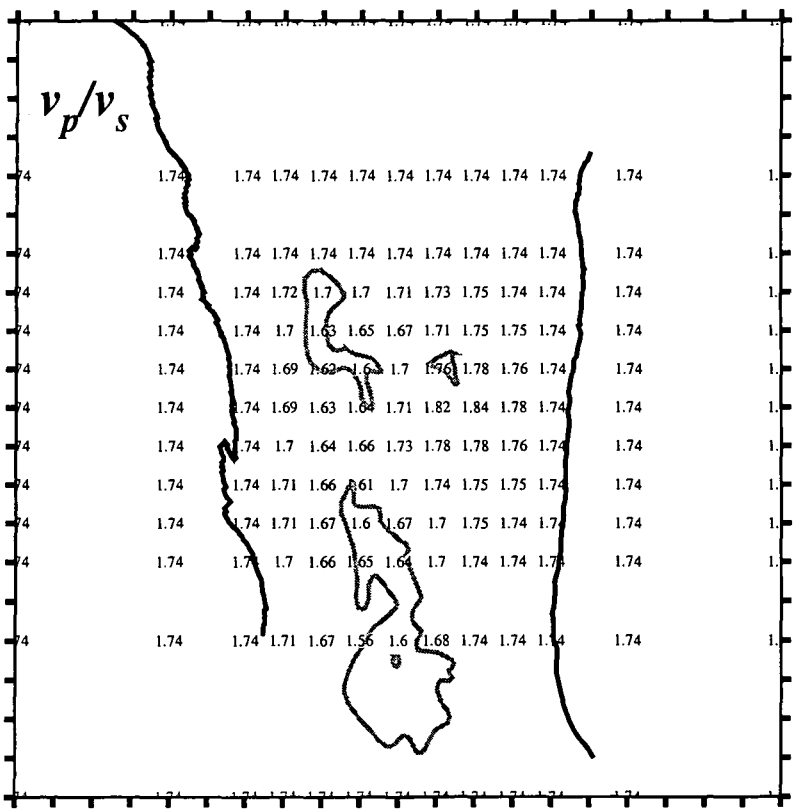
v_p/v_s
1.74 1.74 1.74 1.74 1.74 1.74 1.74 1.74 1.74 1.74 1.74
1.74 1.74 1.74 1.74 1.74 1.74 1.74 1.74 1.74 1.74 1.74
1.74 1.74 1.72 1.7 1.7 1.71 1.73 1.75 1.74 1.74 1.74
1.74 1.74 1.7 1.63 1.65 1.67 1.71 1.75 1.75 1.74 1.74
1.74 1.74 1.69 1.62 1.64 1.7 1.76 1.78 1.76 1.74 1.74
1.74 1.74 1.69 1.63 1.64 1.71 1.82 1.84 1.78 1.74 1.74
1.74 1.74 1.7 1.64 1.66 1.73 1.78 1.78 1.76 1.74 1.74
1.74 1.74 1.71 1.66 1.61 1.7 1.74 1.75 1.75 1.74 1.74
1.74 1.74 1.71 1.67 1.6 1.67 1.7 1.75 1.74 1.74 1.74
1.74 1.74 1.7 1.66 1.65 1.64 1.7 1.74 1.74 1.74 1.74
1.74 1.74 1.71 1.67 1.56 1.6 1.68 1.74 1.74 1.74 1.74

Depth = 1 km

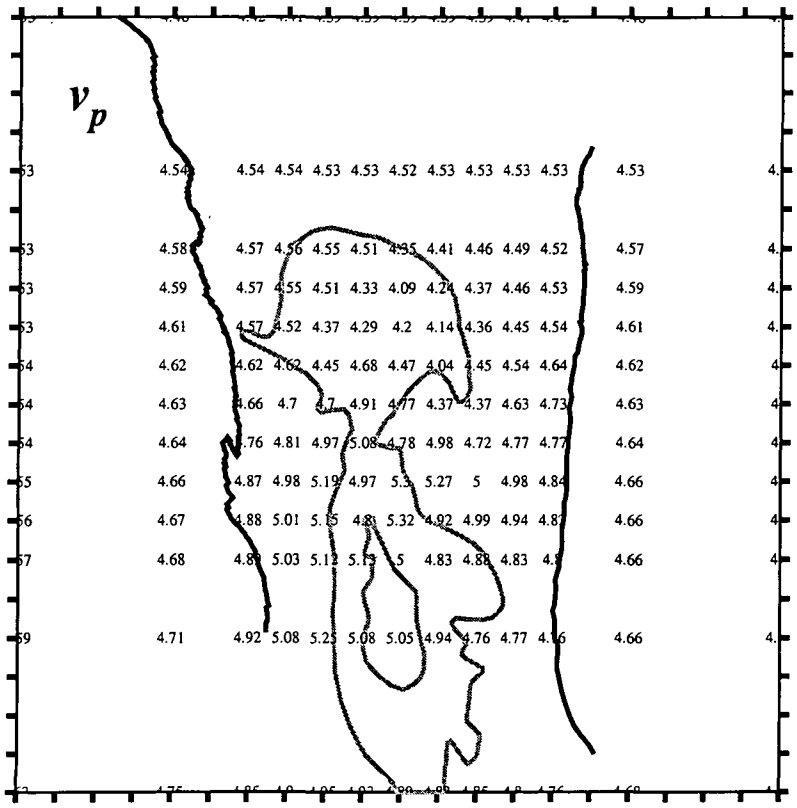
v_p
4.54 4.54 4.54 4.53 4.53 4.52 4.53 4.53 4.53 4.53 4.53
4.58 4.57 4.56 4.55 4.51 4.35 4.41 4.46 4.49 4.52 4.57
4.59 4.57 4.55 4.51 4.33 4.09 4.24 4.37 4.46 4.53 4.59
4.61 4.57 4.52 4.37 4.29 4.2 4.14 4.36 4.45 4.54 4.61
4.62 4.62 4.62 4.45 4.68 4.47 4.04 4.45 4.54 4.64 4.62
4.63 4.66 4.7 4.7 4.91 4.77 4.37 4.37 4.63 4.73 4.63
4.64 4.76 4.81 4.97 5.08 4.78 4.98 4.72 4.77 4.77 4.64
4.66 4.87 4.98 5.19 4.97 5.3 5.27 5 4.98 4.84 4.66
4.67 4.88 5.01 5.15 4.8 5.32 4.92 4.99 4.94 4.8 4.66
4.68 4.89 5.03 5.12 5.15 5 4.83 4.88 4.83 4.8 4.66
4.71 4.92 5.08 5.25 5.08 5.05 4.94 4.76 4.77 4.66 4.66

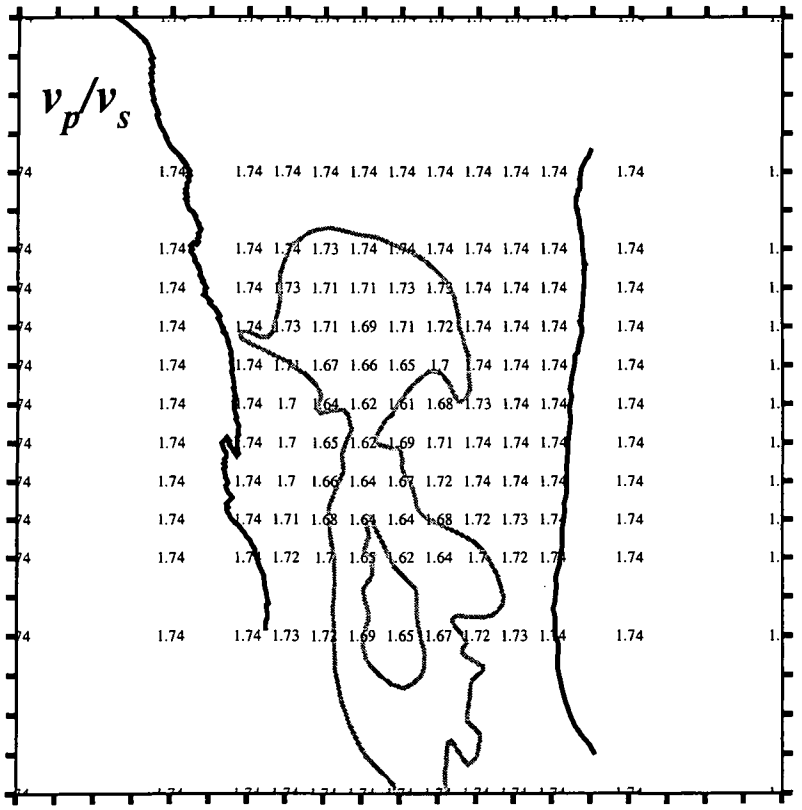
v_p/v_s
1.74 1.74 1.74 1.74 1.74 1.74 1.74 1.74 1.74 1.74 1.74
1.74 1.74 1.74 1.73 1.74 1.74 1.74 1.74 1.74 1.74 1.74
1.74 1.74 1.73 1.71 1.71 1.73 1.73 1.74 1.74 1.74 1.74
1.74 1.74 1.73 1.71 1.69 1.71 1.72 1.74 1.74 1.74 1.74
1.74 1.74 1.71 1.67 1.66 1.65 1.7 1.74 1.74 1.74 1.74
1.74 1.74 1.7 1.64 1.62 1.61 1.68 1.73 1.74 1.74 1.74
1.74 1.74 1.7 1.65 1.62 1.69 1.71 1.74 1.74 1.74 1.74
1.74 1.74 1.7 1.66 1.64 1.67 1.72 1.74 1.74 1.74 1.74
1.74 1.74 1.71 1.68 1.64 1.64 1.68 1.72 1.73 1.74 1.74
1.74 1.74 1.72 1.7 1.65 1.62 1.64 1.7 1.72 1.74 1.74
1.74 1.74 1.73 1.72 1.69 1.65 1.67 1.72 1.73 1.74 1.74

Depth = 0 km

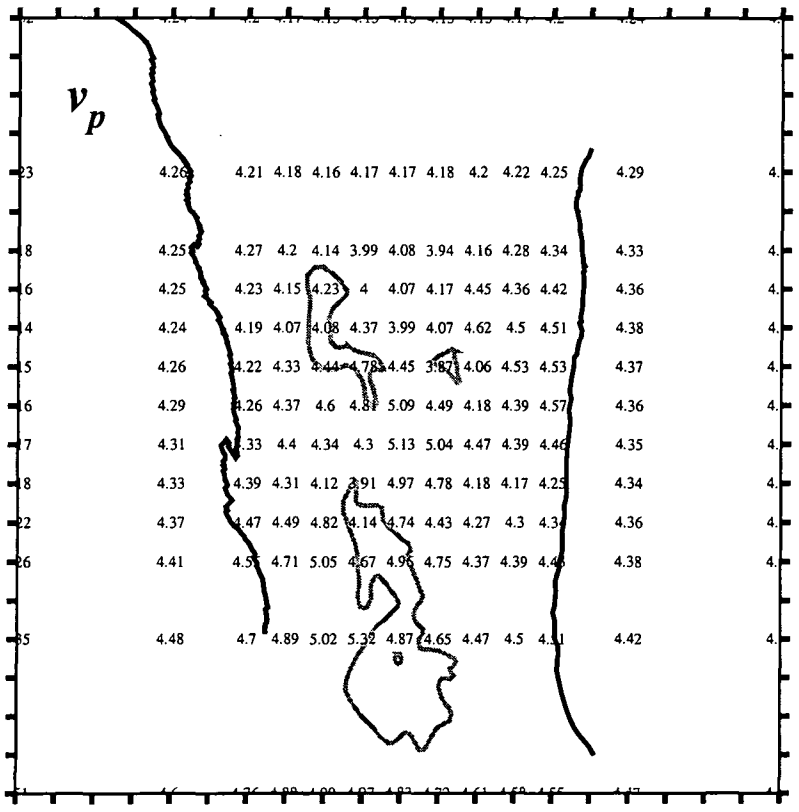
v_p
4.26 4.21 4.18 4.16 4.17 4.17 4.18 4.2 4.22 4.25 4.29
4.25 4.27 4.2 4.14 3.99 4.08 3.94 4.16 4.28 4.34 4.33
4.25 4.23 4.15 4.23 4 4.07 4.17 4.45 4.36 4.42 4.36
4.24 4.19 4.07 4.08 4.37 3.99 4.07 4.62 4.5 4.51 4.38
4.26 4.22 4.33 4.44 4.78 4.45 3.87 4.06 4.53 4.53 4.37
4.29 4.26 4.37 4.6 4.81 5.09 4.49 4.18 4.39 4.57 4.36
4.31 4.33 4.4 4.34 4.3 5.13 5.04 4.47 4.39 4.46 4.35
4.33 4.39 4.31 4.12 3.91 4.97 4.78 4.18 4.17 4.25 4.34
4.37 4.47 4.49 4.82 4.14 4.74 4.43 4.27 4.3 4.36
4.41 4.71 5.05 4.67 4.96 4.75 4.37 4.39 4.38
4.48 4.7 4.89 5.02 5.32 4.87 4.65 4.47 4.5 4.42

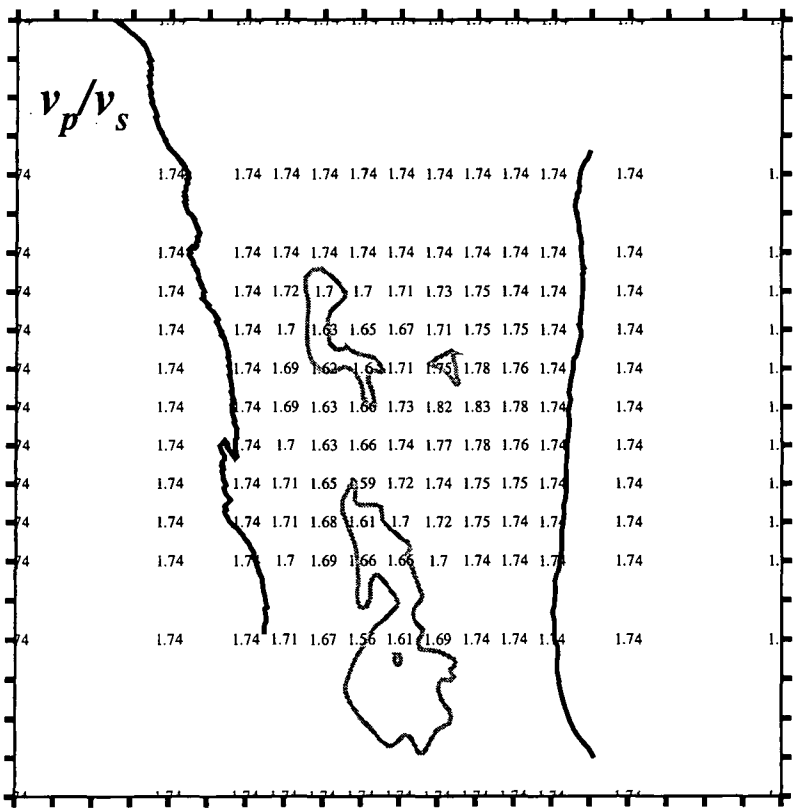
v_p/v_s
1.74 1.74 1.74 1.74 1.74 1.74 1.74 1.74 1.74 1.74 1.74
1.74 1.74 1.74 1.74 1.74 1.74 1.74 1.74 1.74 1.74 1.74
1.74 1.74 1.72 1.7 1.7 1.71 1.73 1.75 1.74 1.74 1.74
1.74 1.74 1.7 1.63 1.65 1.67 1.71 1.75 1.75 1.74 1.74
1.74 1.74 1.69 1.62 1.64 1.71 1.75 1.78 1.76 1.74 1.74
1.74 1.74 1.69 1.63 1.66 1.73 1.82 1.83 1.78 1.74 1.74
1.74 1.74 1.7 1.63 1.66 1.74 1.77 1.78 1.76 1.74 1.74
1.74 1.74 1.71 1.65 1.69 1.72 1.74 1.75 1.75 1.74 1.74
1.74 1.74 1.71 1.68 1.61 1.7 1.72 1.75 1.74 1.74 1.74
1.74 1.74 1.7 1.69 1.66 1.66 1.7 1.74 1.74 1.74 1.74
1.74 1.74 1.74 1.71 1.67 1.56 1.61 1.69 1.74 1.74 1.74 1.74

Depth = 1 km

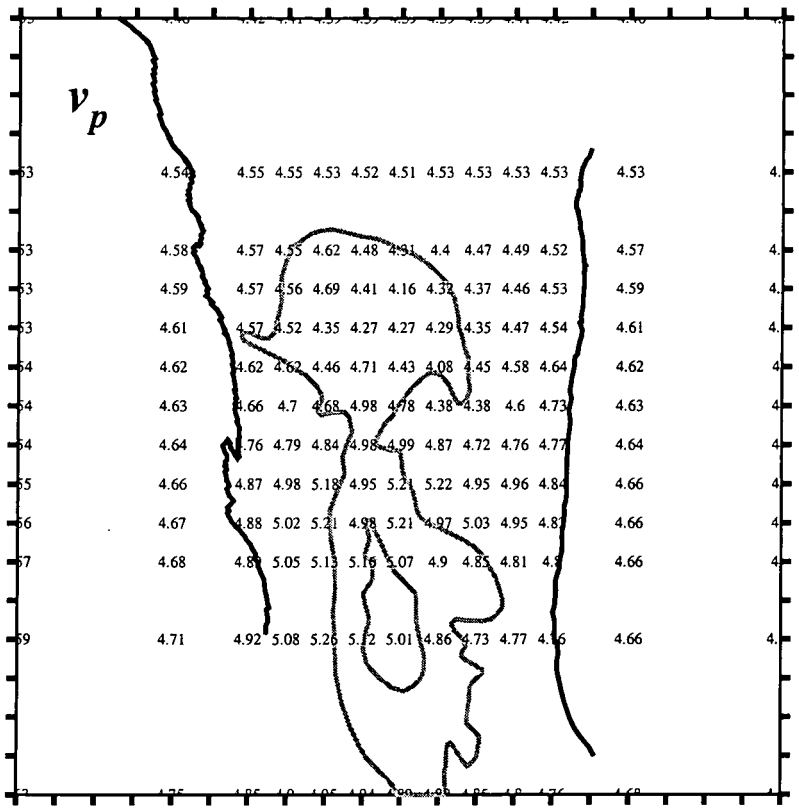

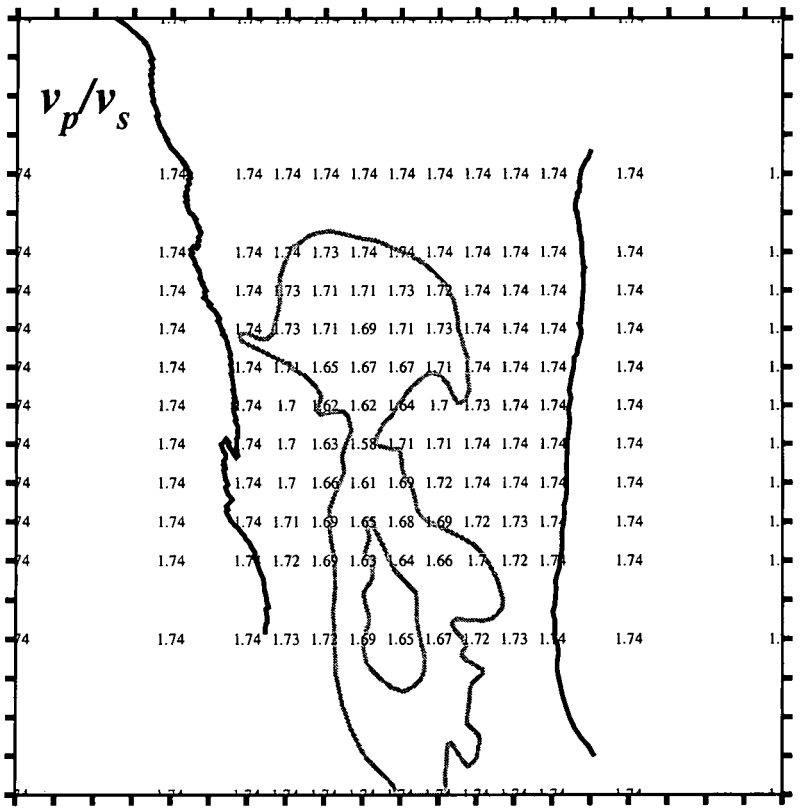

Depth = 0 km

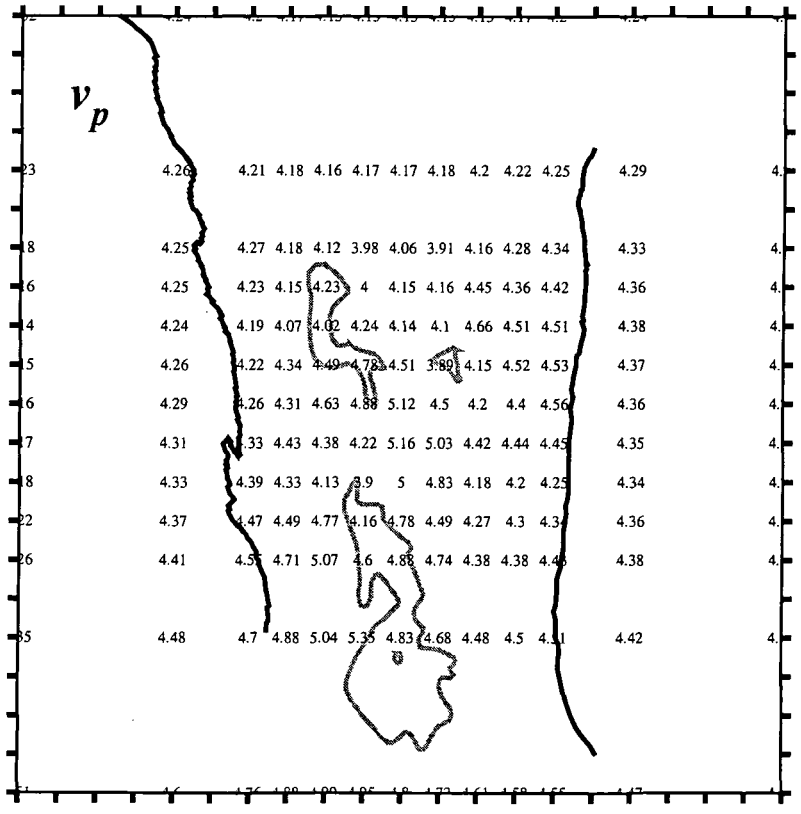
v_p
4.26 4.21 4.18 4.16 4.17 4.17 4.18 4.2 4.22 4.25 4.29
4.25 4.27 4.18 4.12 3.98 4.06 3.91 4.16 4.28 4.34 4.33
4.25 4.23 4.15 4.23 4 4.15 4.16 4.45 4.36 4.42 4.36
4.24 4.19 4.07 4.02 4.24 4.14 4.1 4.66 4.51 4.51 4.38
4.26 4.22 4.34 4.49 4.78 4.51 3.89 4.15 4.52 4.53 4.37
4.29 4.26 4.31 4.63 4.88 5.12 4.5 4.2 4.4 4.56 4.36
4.31 4.33 4.43 4.38 4.22 5.16 5.03 4.42 4.44 4.45 4.35
4.33 4.39 4.33 4.13 3.9 5 4.83 4.18 4.2 4.25 4.34
4.37 4.47 4.49 4.77 4.16 4.78 4.49 4.27 4.3 4.36
4.41 4.71 5.07 4.6 4.74 4.38 4.38 4.38
4.48 4.7 4.88 5.04 5.35 4.83 4.68 4.48 4.5 4.42

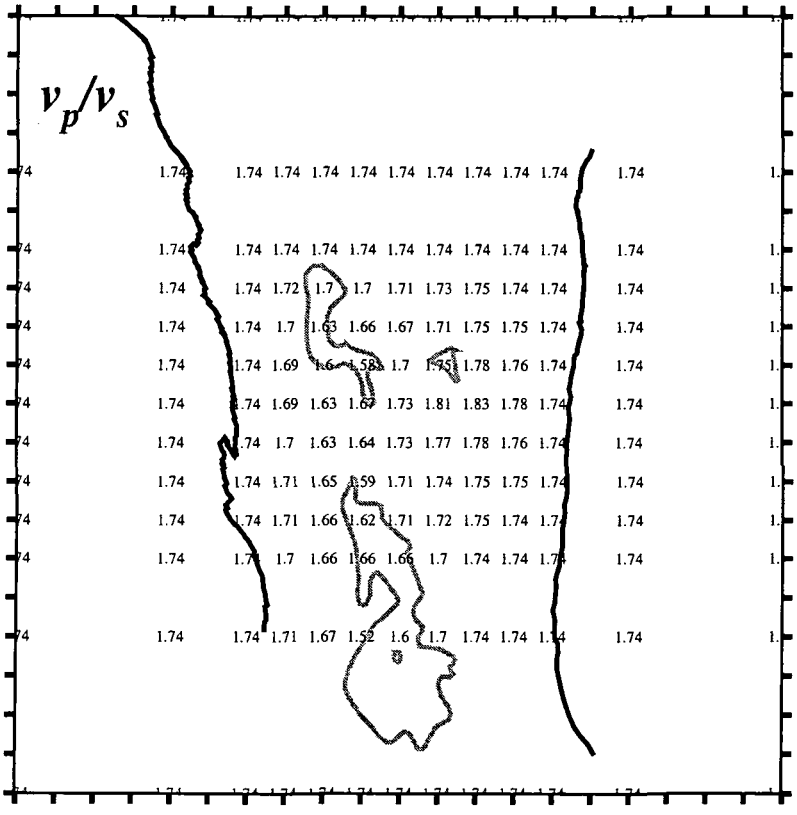
v_p/v_s
1.74 1.74 1.74 1.74 1.74 1.74 1.74 1.74 1.74 1.74 1.74
1.74 1.74 1.74 1.74 1.74 1.74 1.74 1.74 1.74 1.74 1.74
1.74 1.74 1.72 1.7 1.7 1.71 1.73 1.75 1.74 1.74 1.74
1.74 1.74 1.7 1.63 1.66 1.67 1.71 1.75 1.75 1.74 1.74
1.74 1.74 1.69 1.6 1.58 1.7 1.75 1.78 1.76 1.74 1.74
1.74 1.74 1.69 1.63 1.67 1.73 1.81 1.83 1.78 1.74 1.74
1.74 1.74 1.7 1.63 1.64 1.73 1.77 1.78 1.76 1.74 1.74
1.74 1.74 1.71 1.65 1.59 1.71 1.74 1.75 1.75 1.74 1.74
1.74 1.74 1.71 1.66 1.62 1.71 1.72 1.75 1.74 1.74 1.74
1.74 1.74 1.7 1.66 1.66 1.66 1.7 1.74 1.74 1.74 1.74
1.74 1.74 1.71 1.67 1.52 1.6 1.7 1.74 1.74 1.74 1.74

Depth = 1 km

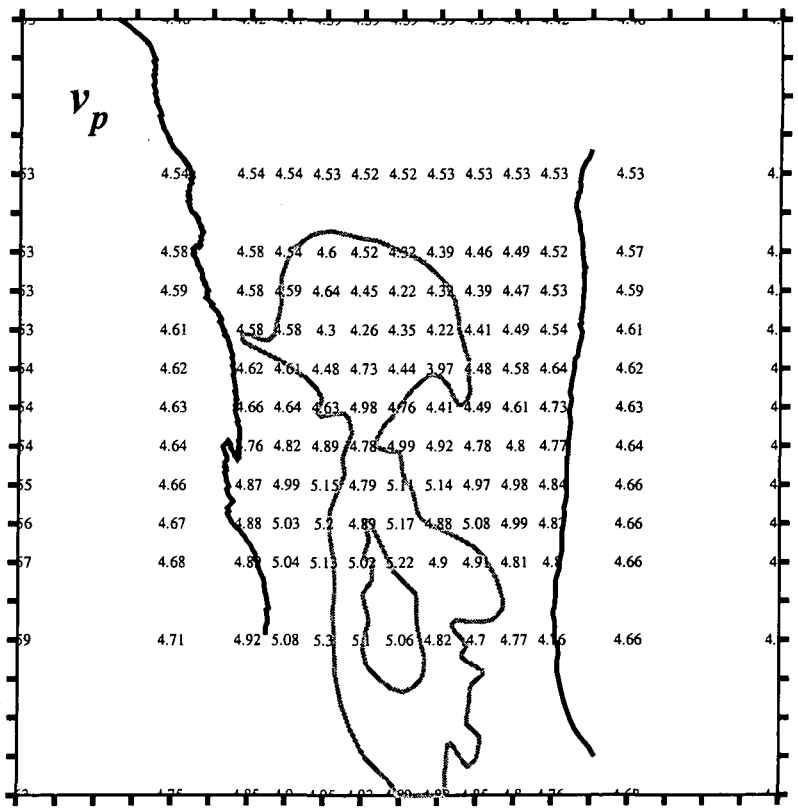
v_p
4.54 4.54 4.54 4.53 4.52 4.52 4.53 4.53 4.53 4.53 4.53
4.58 4.58 4.54 4.6 4.52 4.52 4.39 4.46 4.49 4.52 4.57
4.59 4.58 4.59 4.64 4.45 4.22 4.32 4.39 4.47 4.53 4.59
4.61 4.58 4.58 4.3 4.26 4.35 4.22 4.41 4.49 4.54 4.61
4.62 4.62 4.61 4.48 4.73 4.44 3.97 4.48 4.58 4.64 4.62
4.63 4.66 4.64 4.63 4.98 4.76 4.41 4.49 4.61 4.73 4.63
4.64 4.76 4.82 4.89 4.78 4.99 4.92 4.78 4.8 4.77 4.64
4.66 4.87 4.99 5.15 4.79 5.11 5.14 4.97 4.98 4.84 4.66
4.67 4.88 5.03 5.2 4.89 5.17 4.88 5.08 4.99 4.87 4.66
4.68 4.89 5.04 5.13 5.02 5.22 4.9 4.91 4.81 4.8 4.66
4.71 4.92 5.08 5.3 5.1 5.06 4.82 4.7 4.77 4.76 4.66

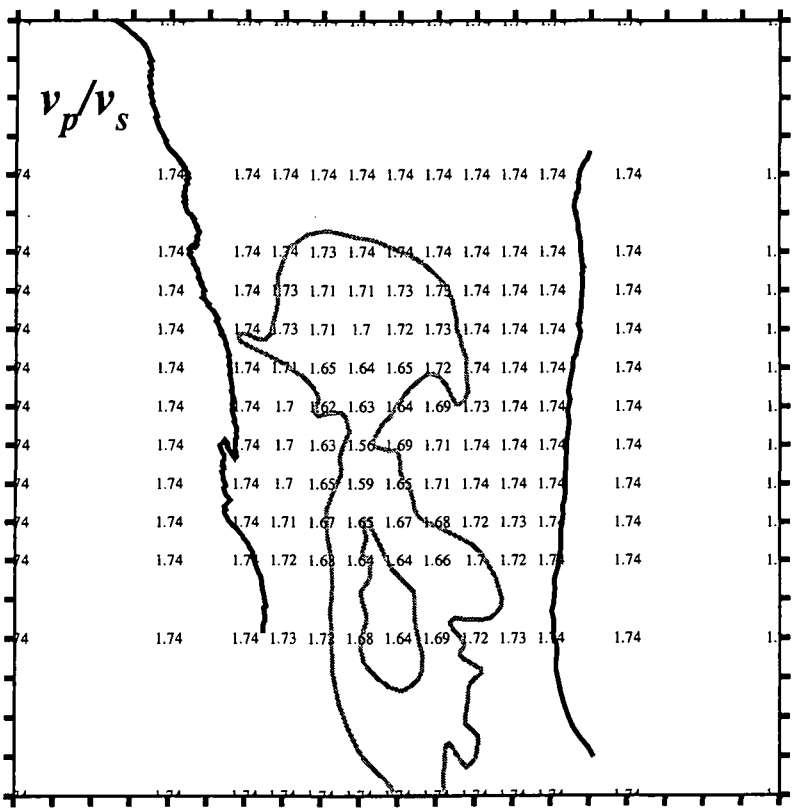
v_p/v_s
1.74 1.74 1.74 1.74 1.74 1.74 1.74 1.74 1.74 1.74 1.74
1.74 1.74 1.74 1.73 1.74 1.74 1.74 1.74 1.74 1.74 1.74
1.74 1.74 1.73 1.71 1.71 1.73 1.73 1.74 1.74 1.74 1.74
1.74 1.74 1.73 1.71 1.7 1.72 1.73 1.74 1.74 1.74 1.74
1.74 1.74 1.71 1.65 1.64 1.65 1.72 1.74 1.74 1.74 1.74
1.74 1.74 1.7 1.62 1.63 1.64 1.69 1.73 1.74 1.74 1.74
1.74 1.74 1.7 1.63 1.56 1.69 1.71 1.74 1.74 1.74 1.74
1.74 1.74 1.7 1.65 1.59 1.65 1.71 1.74 1.74 1.74 1.74
1.74 1.74 1.71 1.67 1.65 1.67 1.68 1.72 1.73 1.74 1.74
1.74 1.74 1.72 1.68 1.64 1.64 1.66 1.7 1.72 1.73 1.74
1.74 1.74 1.73 1.72 1.68 1.64 1.69 1.72 1.73 1.74 1.74

Appendix 7: Output of program *rms* and sample of waveforms from each of the multiplets

Output of program *rms* for the main multiplets studied at The Geysers

Multiplet sr001_01_95

Station	Common Az.	Common TOA	Freq. non-weighted res.	Freq. weighted res.
ACR	91	114	694	353
ANG	119	108	105	925
BUC	195	154	331	1257
CAP	63	148	42	1296
CLV	88	133	231	1305
DES	125	89	24	1050
DRK	157	114	143	757
DVB	136	96	572	503
DXR	108	119	1401	413
FNF	143	102	108	802
FUM	143	114	214	510
INJ	146	127	708	573
LCK	104	107	395	491
MNS	124	90	949	328
PFR	142	94	138	801
SB4B	180	133	48	1176
SQK	131	143	107	796
SSR	136	84	6	952
STY	125	121	600	790
TCH	126	96	762	442
U14	139	107	102	726

Multiplet sr001_01_92

Station	Common Az.	Common TOA	Freq. non-weighted res.	Freq. weighted res.
ACR	90	108	884	766
ANG	119	103	645	892
BUC	201	151	363	1523
CAP	61	143	1078	1229
CLV	87	128	929	1081
DES	125	86	217	885
DRK	157	109	844	878
DVB	136	89	11487	592
DXR	107	114	896	743
FNF	143	97	912	874
FUM	144	108	770	805
INJ	146	122	1296	852
LCK	104	101	1249	797

MNS	124	87	20028	368
PFR	142	89	4562	879
SB4B	181	128	293	1327
SQK	128	139	292	1228
SSR	136	83	265	956
STY	125	116	1294	743
TCH	126	95	19847	326
U14	139	102	1455	778
WRK	132	87	186	585

Multiplet sr002_01_96

Station	Common Az.	Common TOA	Freq. non-weighted res.	Freq. weighted res.
ACR	60	130	1152	632
ANG	108	129	777	500
BUC	285	144	2063	423
CAP	314	140	890	939
CLV	27	146	608	980
DES	122	102	522	901
DRK	178	140	411	948
DVB	136	110	1063	670
DXR	76	144	1370	481
FNF	146	119	373	766
FUM	152	141	2497	352
INJ	174	165	644	1087
LCK	87	124	759	700
MNS	120	107	701	685
PFR	144	107	377	909
SB4B	251	148	2531	501
SQK	301	166	617	1070
SSR	136	100	1223	823
STY	107	155	4082	320
TCH	121	116	1494	546
U14	141	129	527	559
WRK	130	108	2895	648

Multiplet sr003_01_95

Station	Common Az.	Common TOA	Freq. non-weighted res.	Freq. weighted res.
ACR	14	116	163	571
ANG	50	142	341	597
BUC	309	112	276	803
CAP	337	109	632	760
CLV	348	116	300	632
DES	109	108	151	811
DRK	274	144	76	1190
DVB	129	126	393	690
DXR	15	128	88	1056

FNF	151	149	186	1320
FUM	304	161	115	886
INJ	315	132	374	601
LCK	40	123	2799	231
MNS	102	117	131	1280
PFR	144	120	444	430
SB4B	299	117	368	385
SQK	325	118	1410	332
SSR	132	107	3837	209
STY	343	138	280	975
TCH	96	133	220	1121
U14	105	172	73	1360
WRK	120	119	154	912

Multiplet sr004_01_95

Station	Common Az.	Common TOA	Freq. non-weighted res.	Freq. weighted res.
ACR	350	110	311	682
ANG	227	163	109	1135
BUC	293	94	411	559
CAP	318	95	1222	728
CLV	324	104	755	661
DES	125	102	473	435
DRK	261	110	232	755
DVB	163	118	2057	431
DXR	329	121	505	689
FNF	205	126	658	646
FUM	264	121	125	680
INJ	287	108	359	565
LCK	18	131	806	954
MNS	124	118	1130	390
PFR	171	108	1081	380
SB4B	285	98	656	458
SQK	302	104	573	645
SSR	150	98	3394	383
STY	303	124	555	523
TCH	135	143	264	875
U14	238	133	250	626
WRK	146	114	1308	321

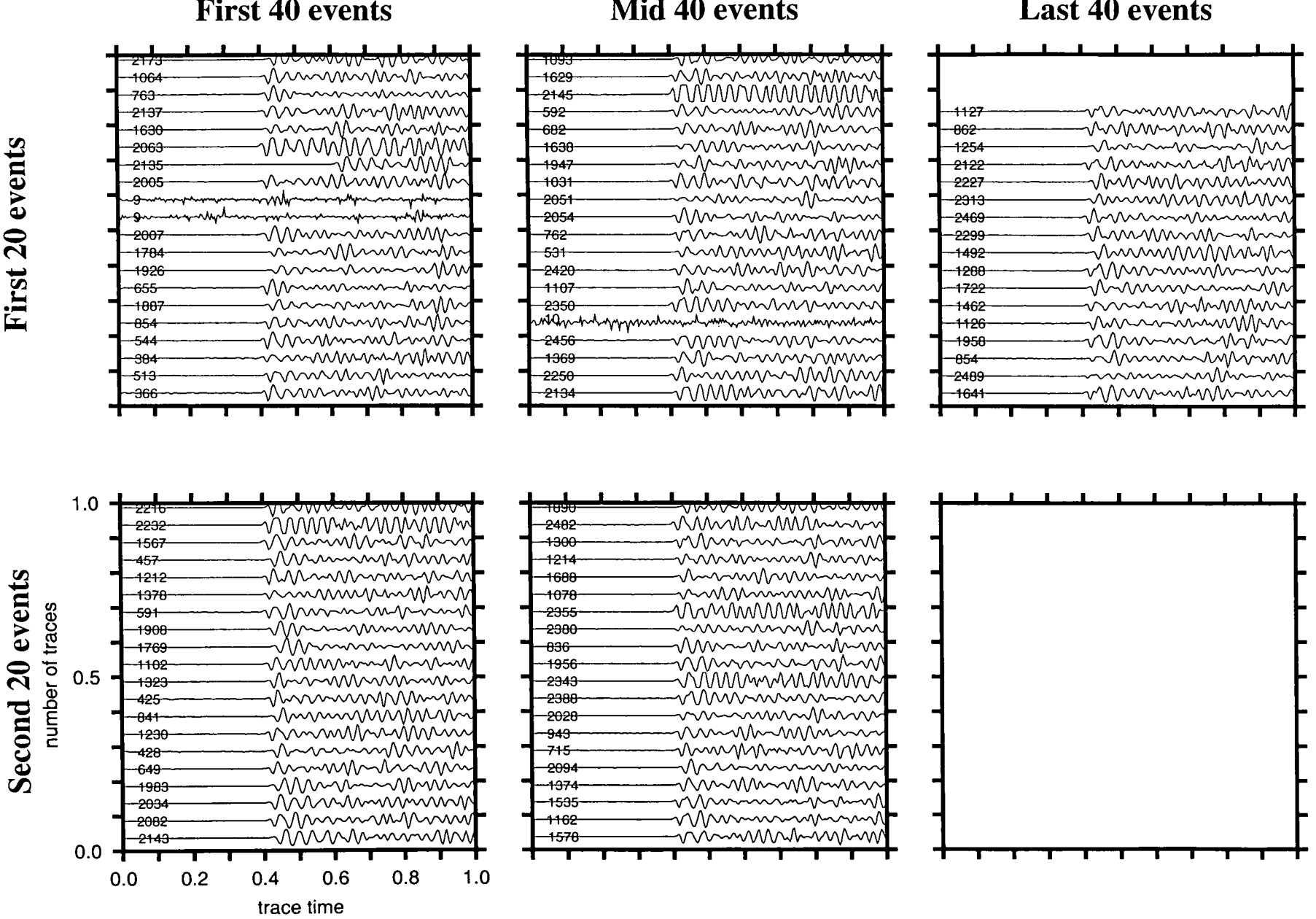

Waveform for events in multiplet sr001_01_95, for station ACR.

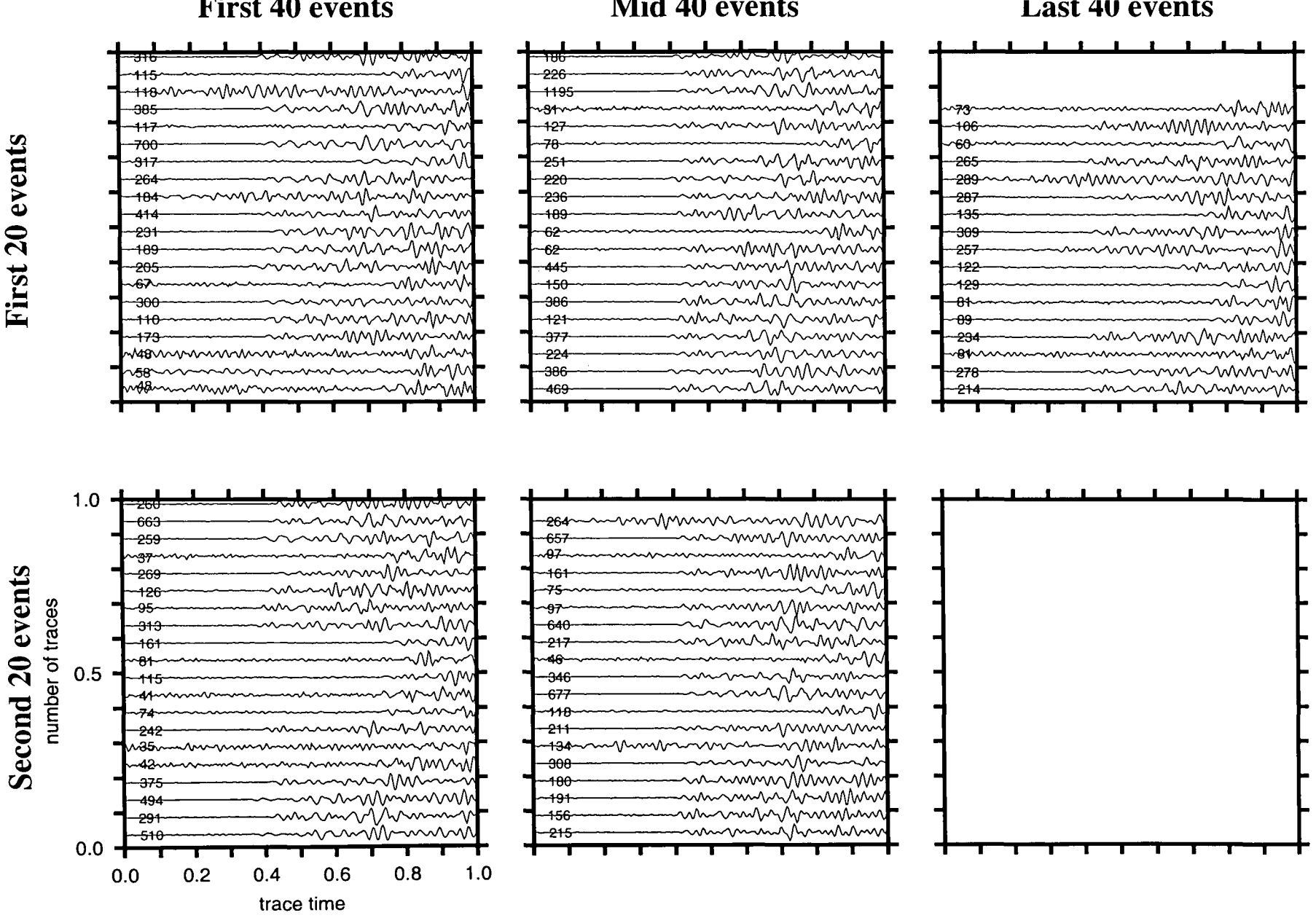

Waveform for events in multiplet sr001_01_95, for station ANG.

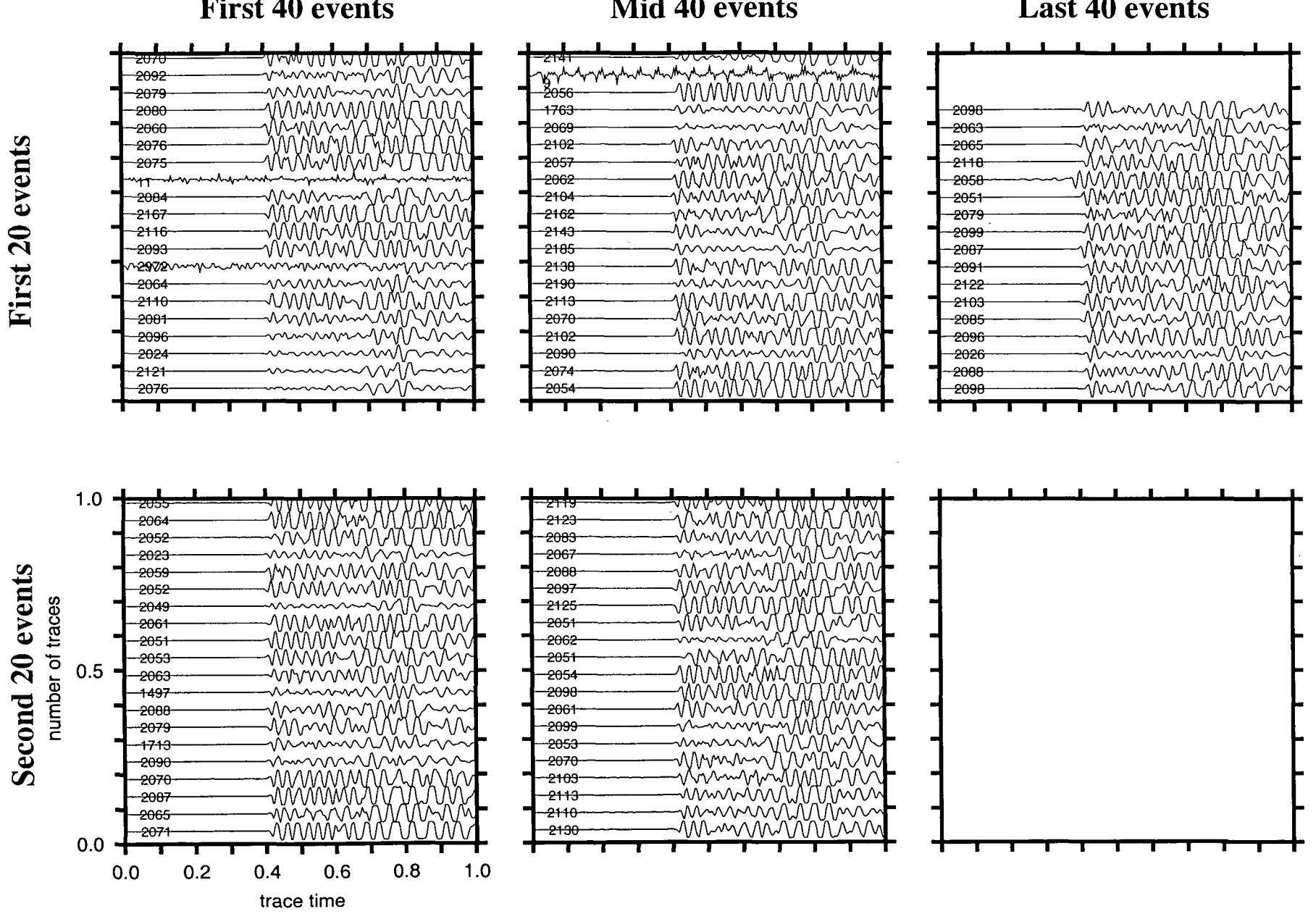

Waveform for events in multiplet sr001_01_95, for station CAP.

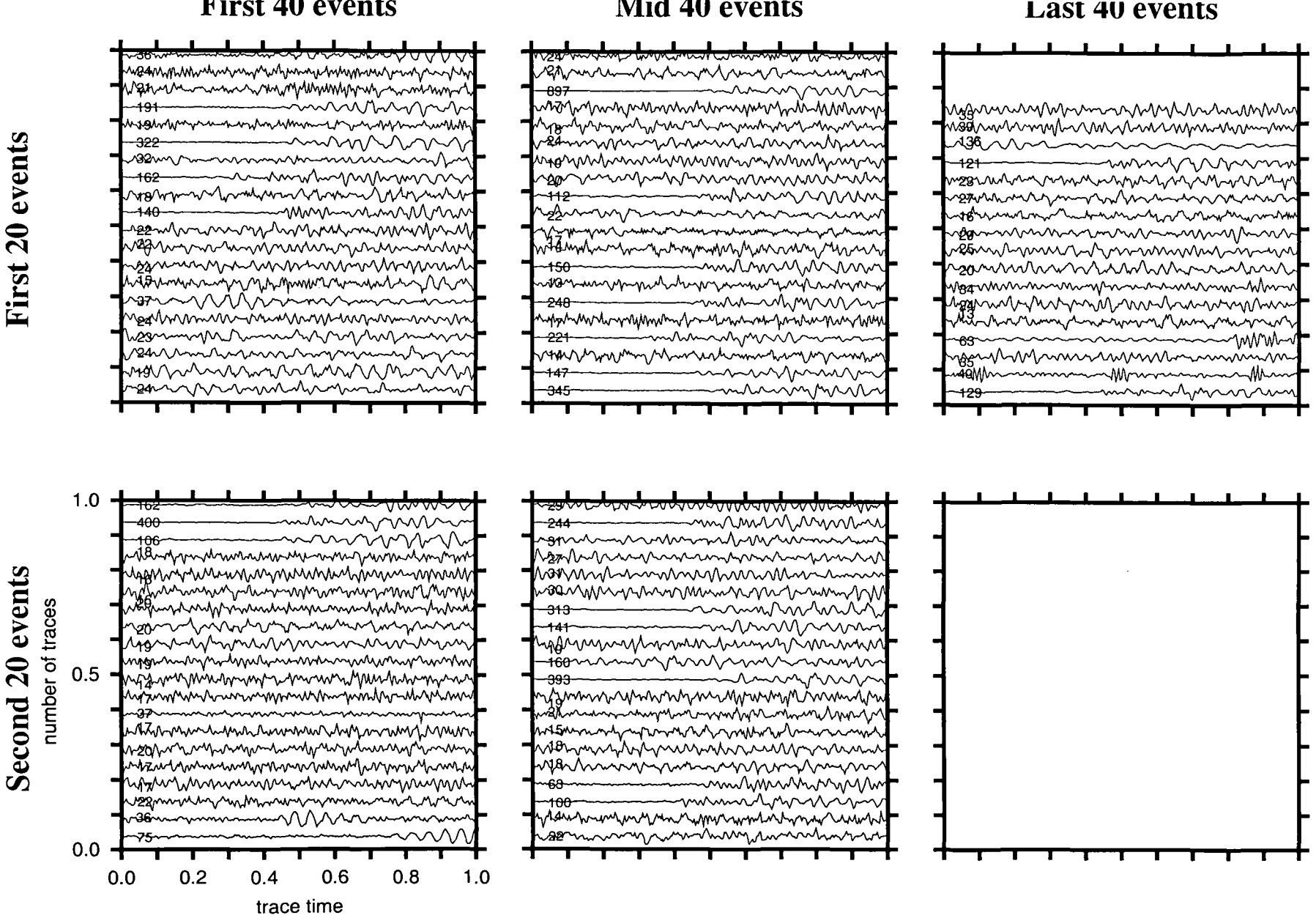

Waveform for events in multiplet sr001_01_95, for station SSR.

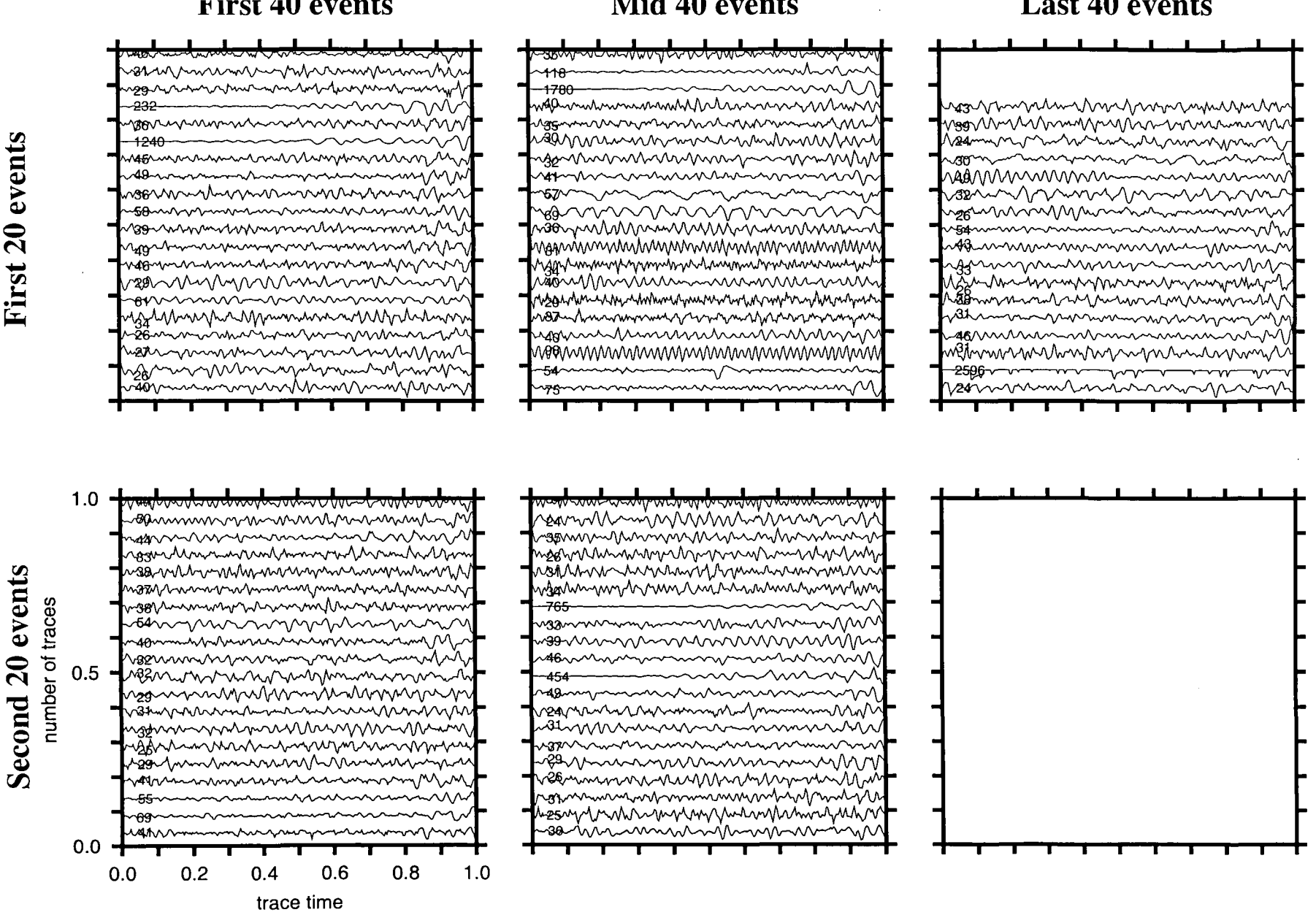

Waveform for events in multiplet sr001_01_95, for station TCH.

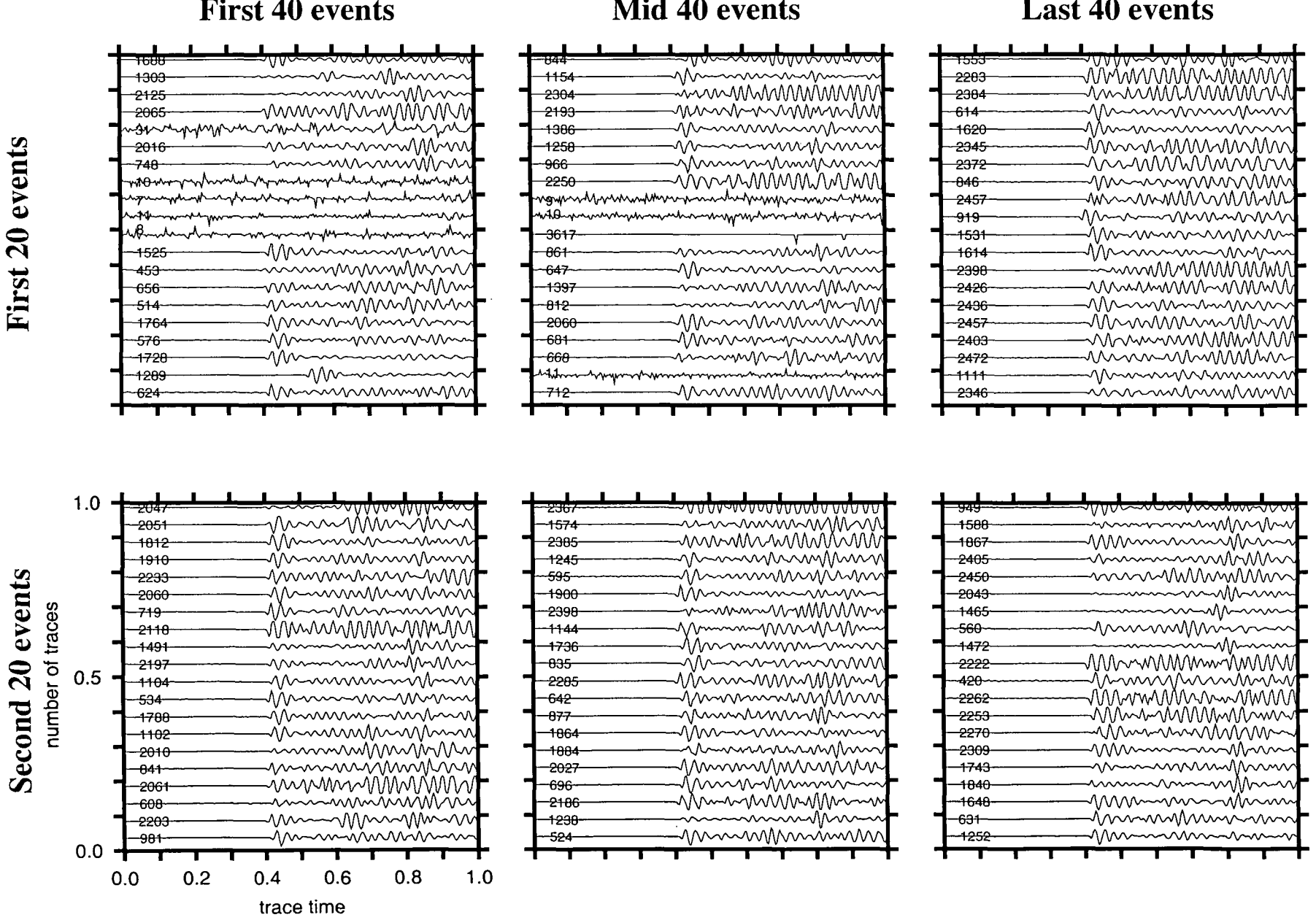

Waveform for events in multiplet sr002_01_96, for station ACR.

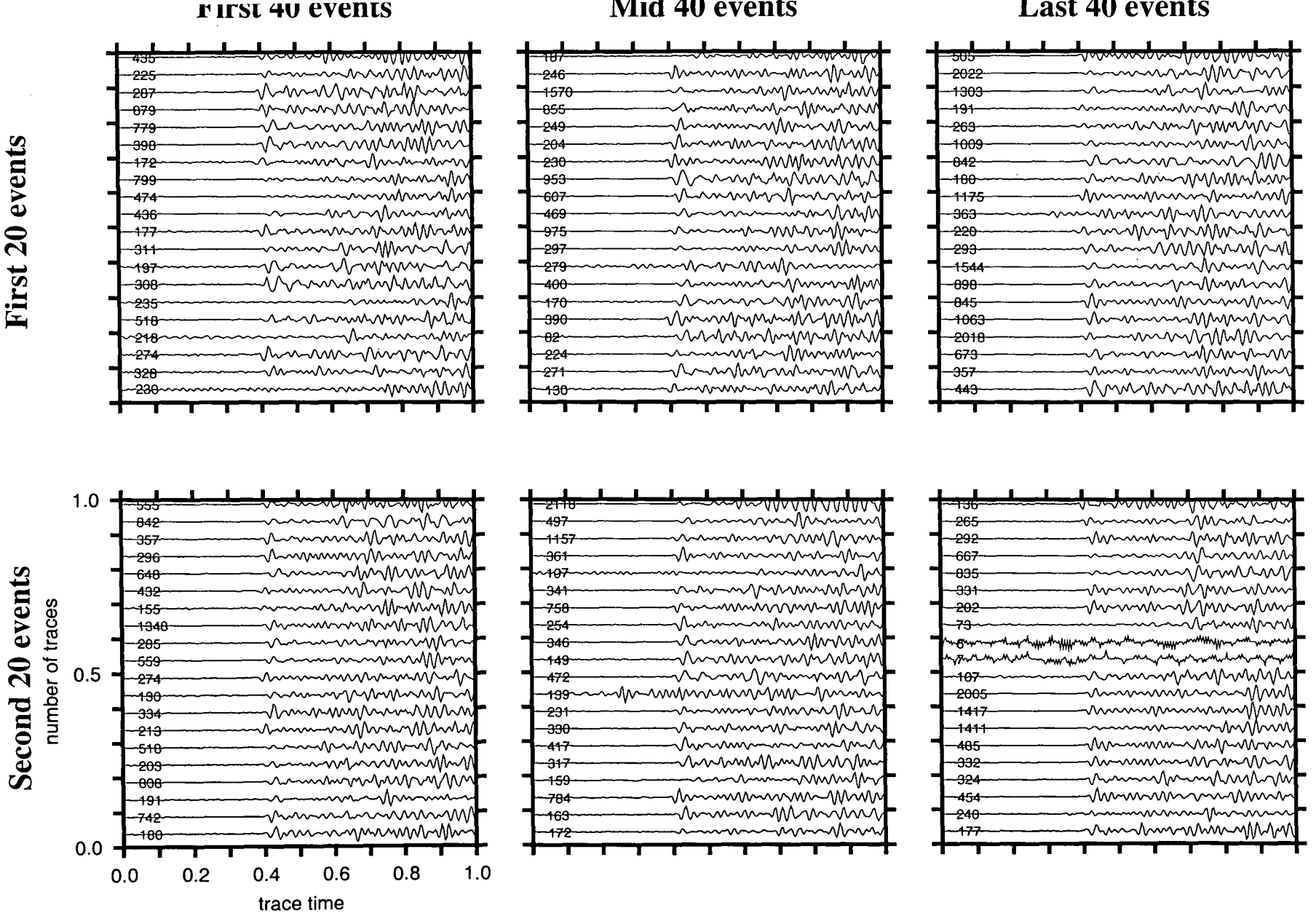

Waveform for events in multiplet sr002_01_96, for station ANG.

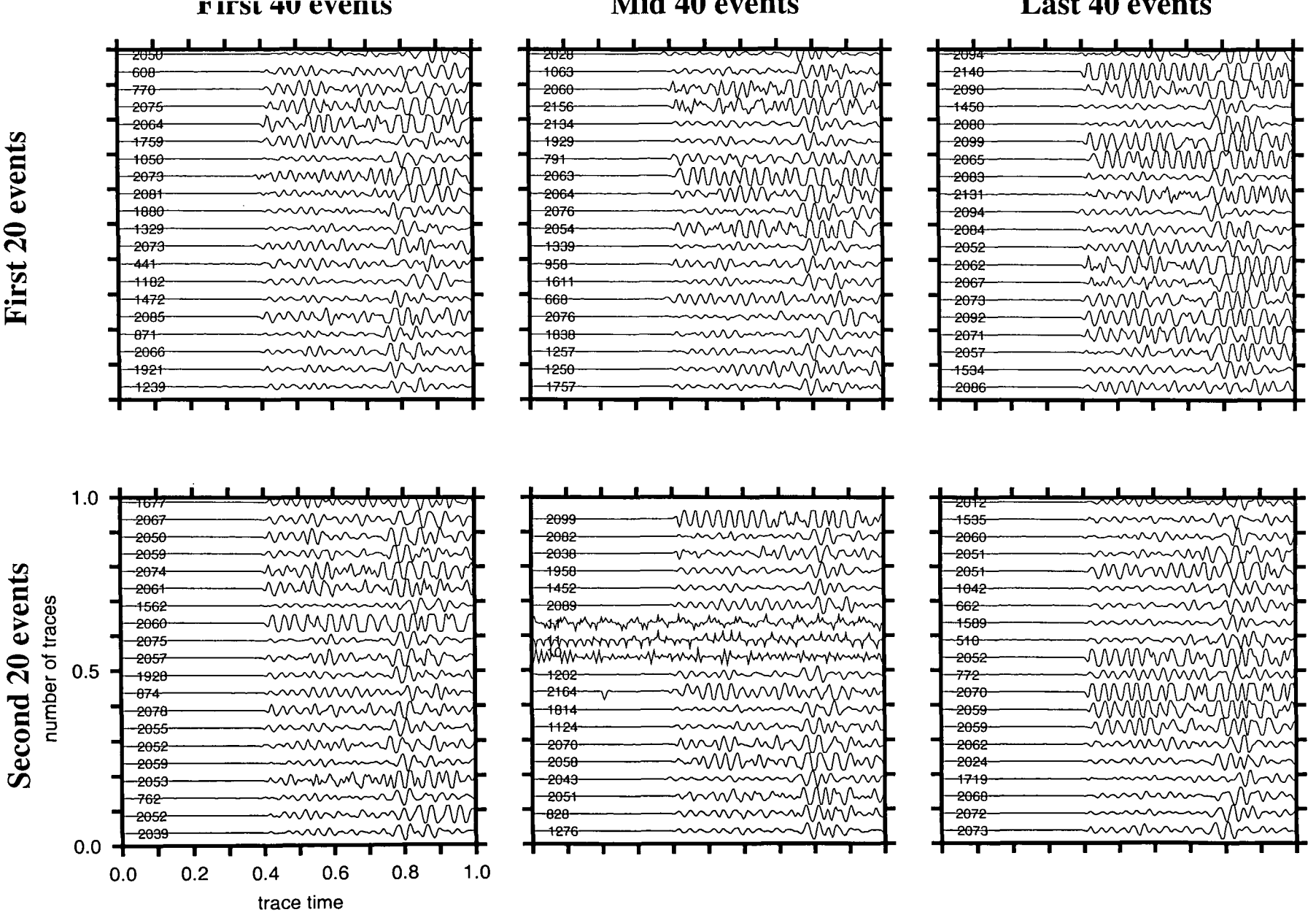

Waveform for events in multiplet sr002_01_96, for station CAP.

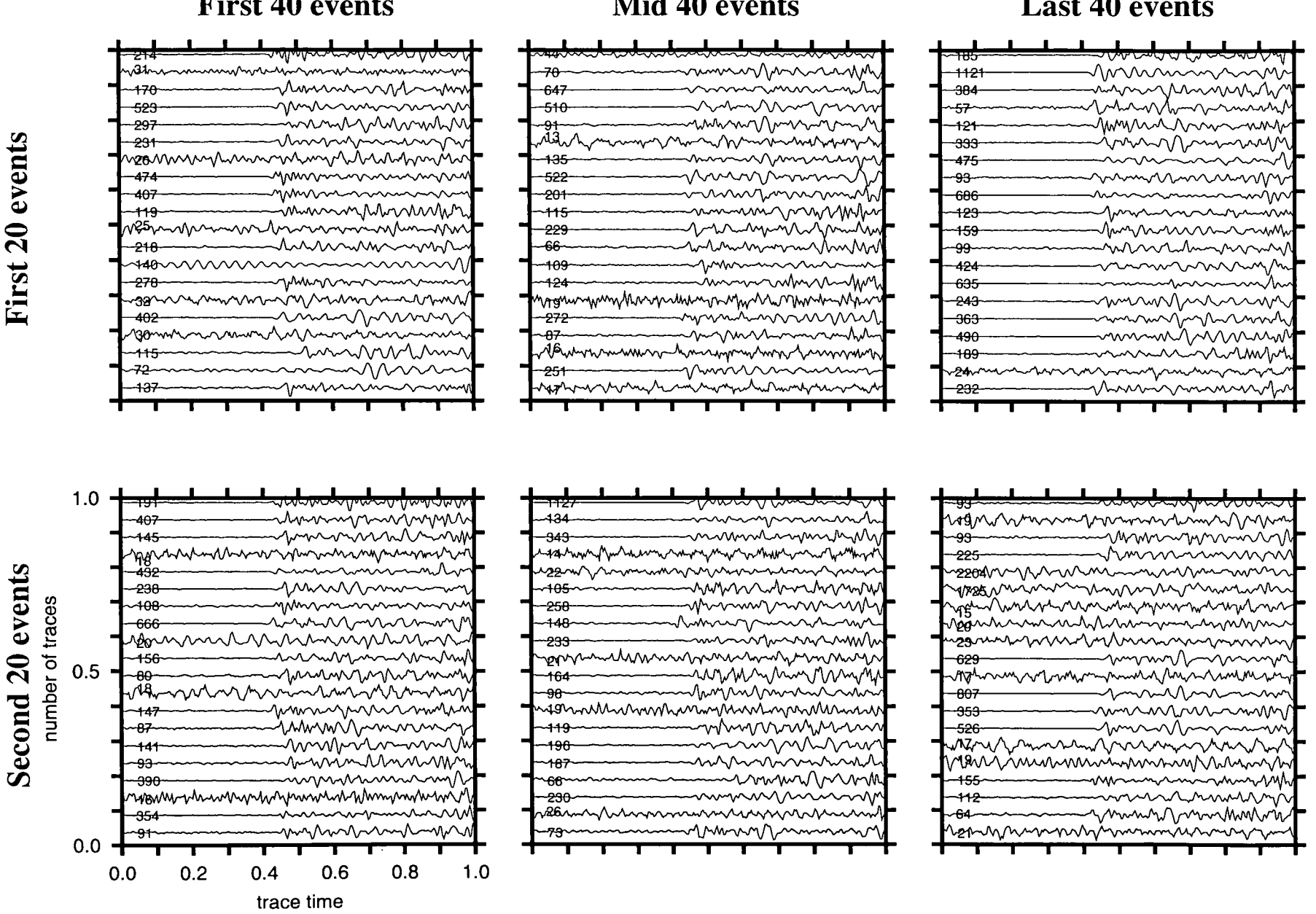

Waveform for events in multiplet sr002_01_96, for station SSR.

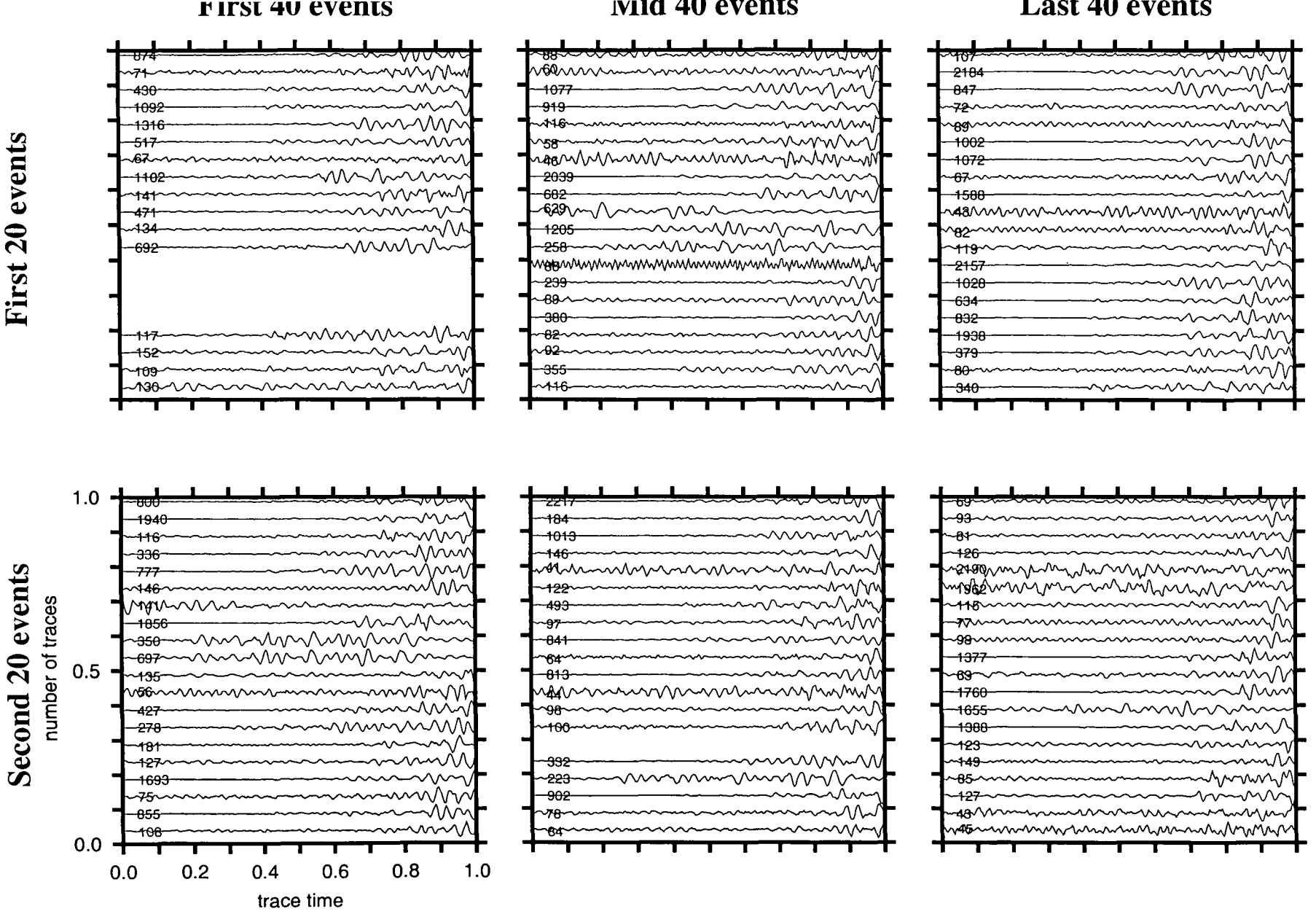

Waveform for events in multiplet sr002_01_96, for station TCH.

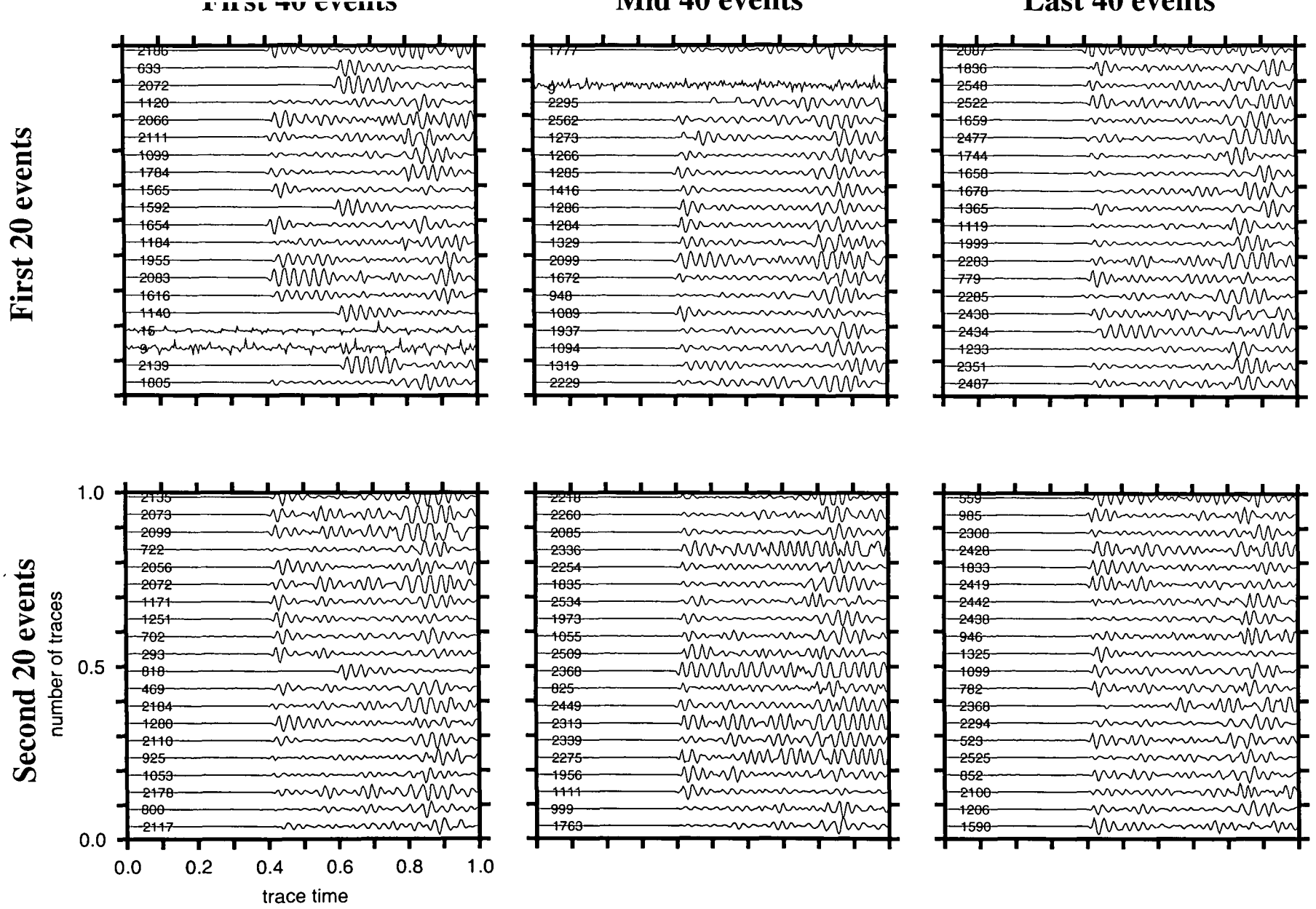

Waveform for events in multiplet sr003_01_95, for station ACR.

Waveform for events in multiplet sr003_01_95, for station ANG.

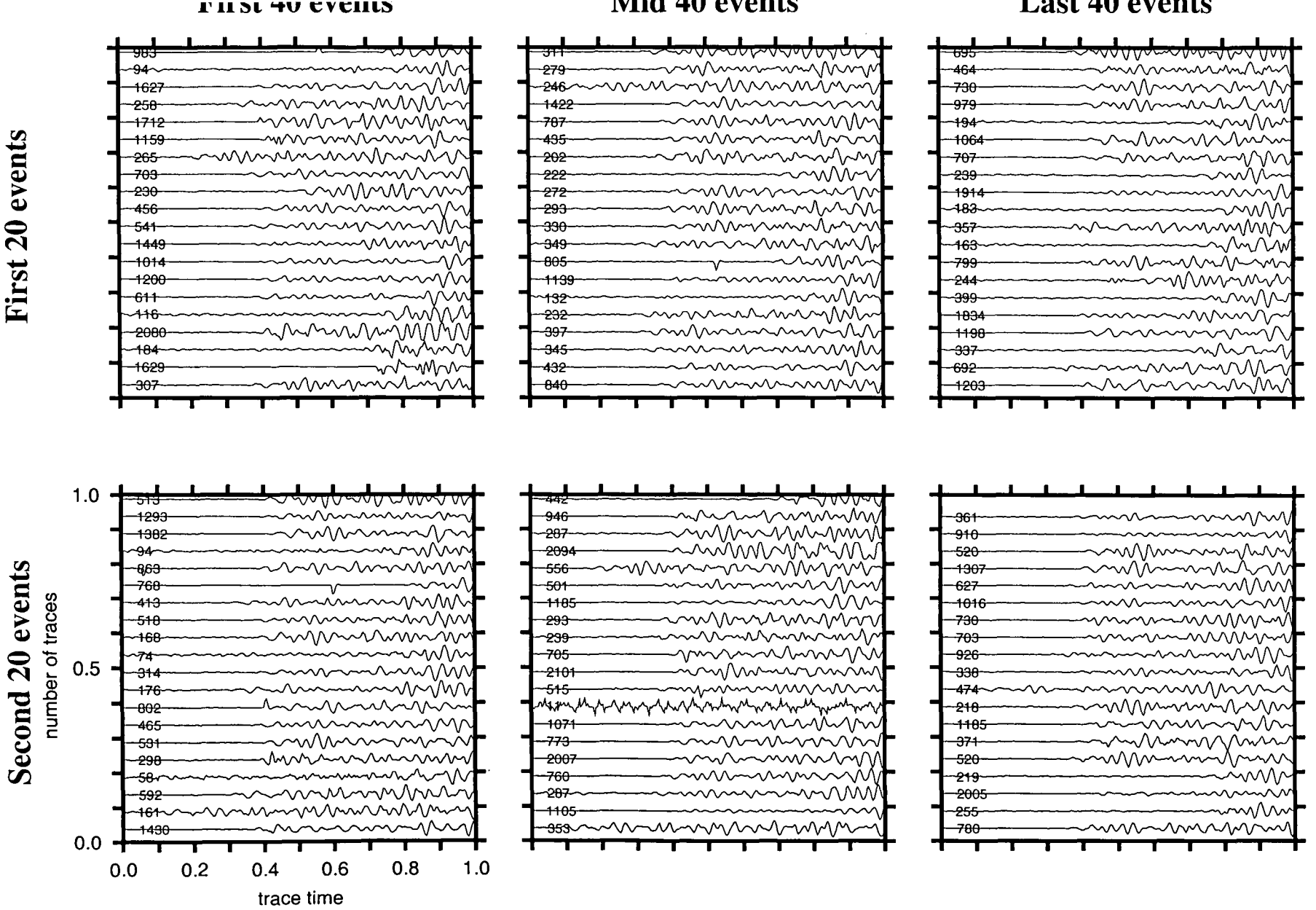

Waveform for events in multiplet sr003_01_95, for station CAP.

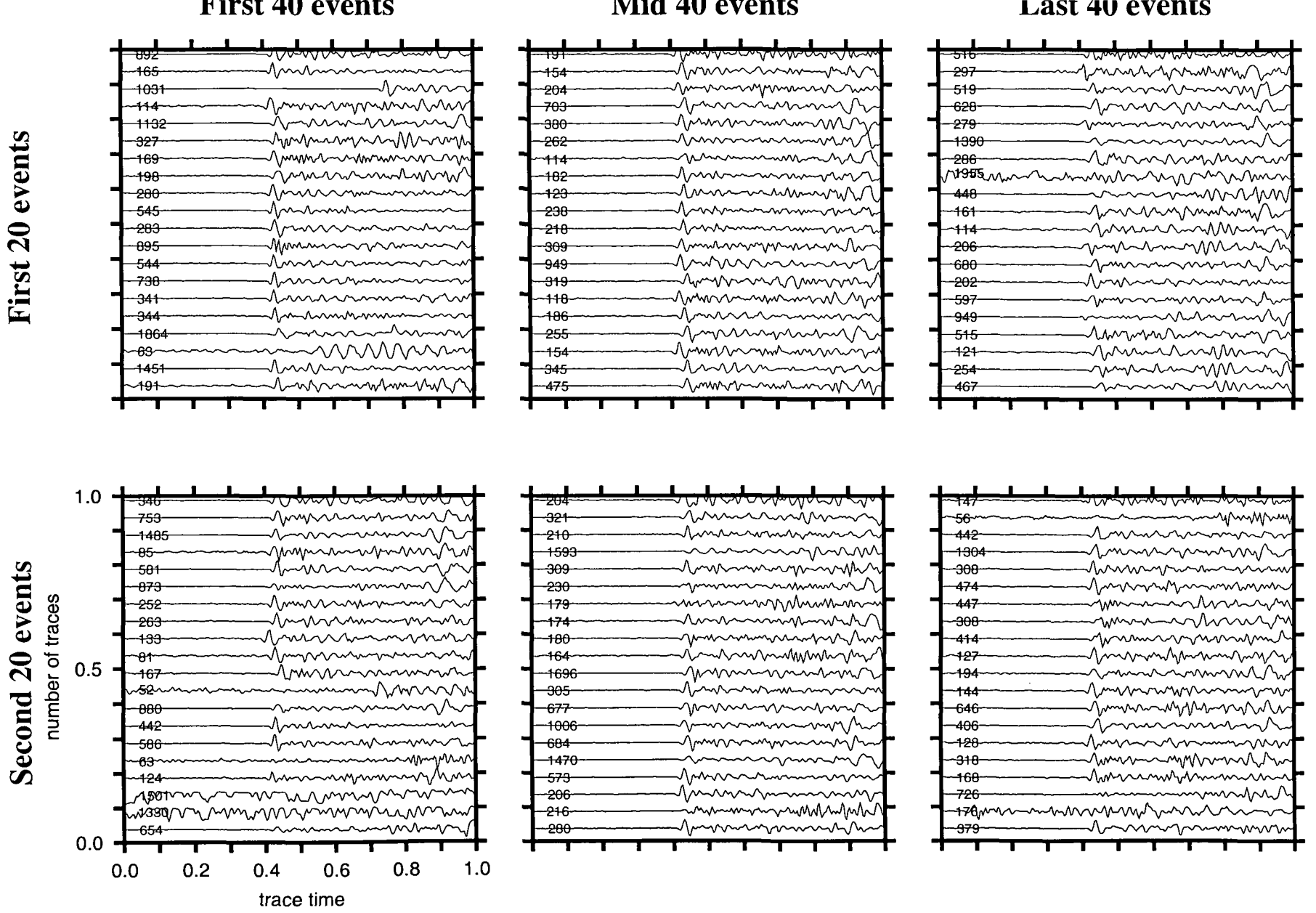

Waveform for events in multiplet sr003_01_95, for station SSR.

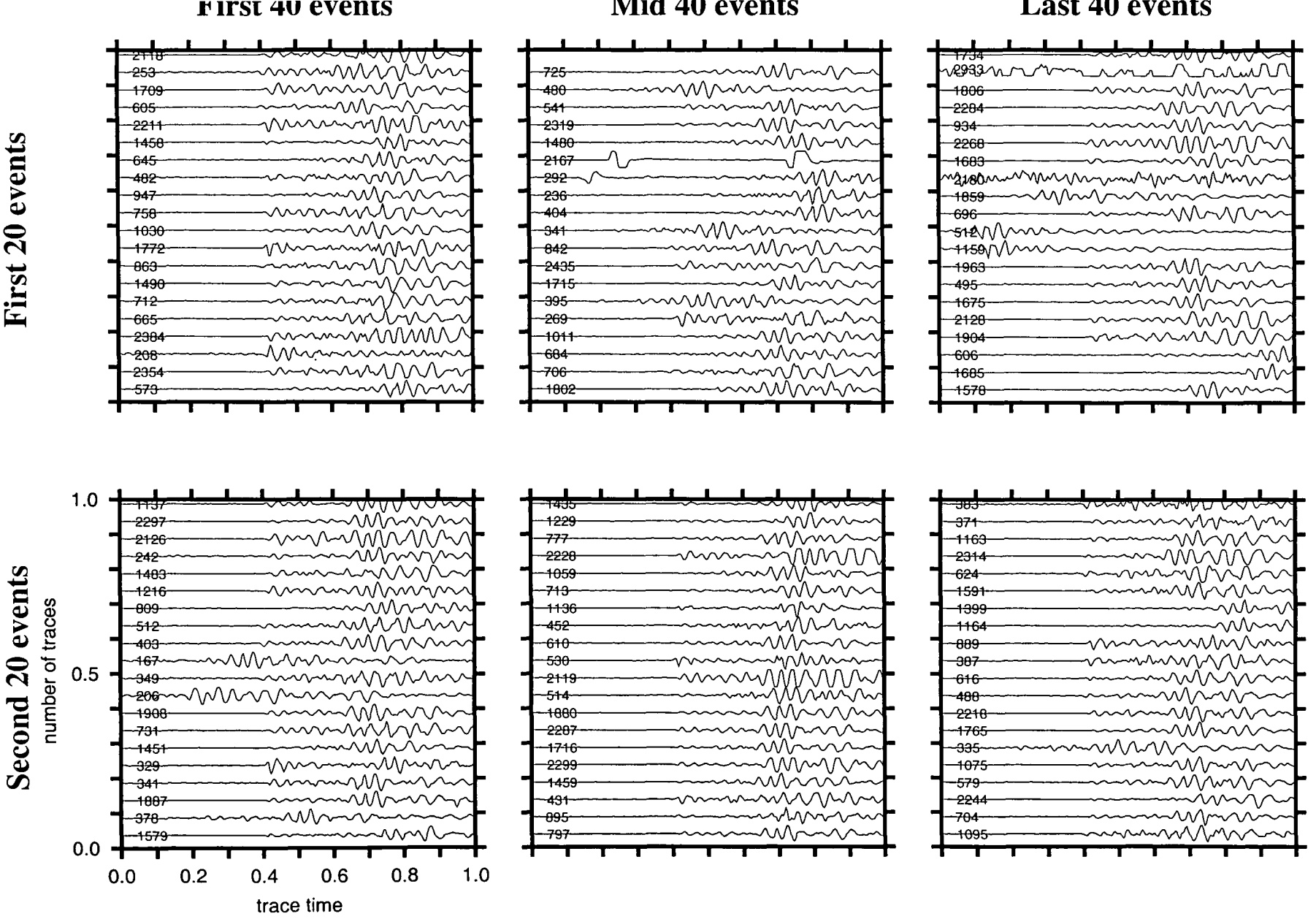

Waveform for events in multiplet sr003_01_95, for station TCH.

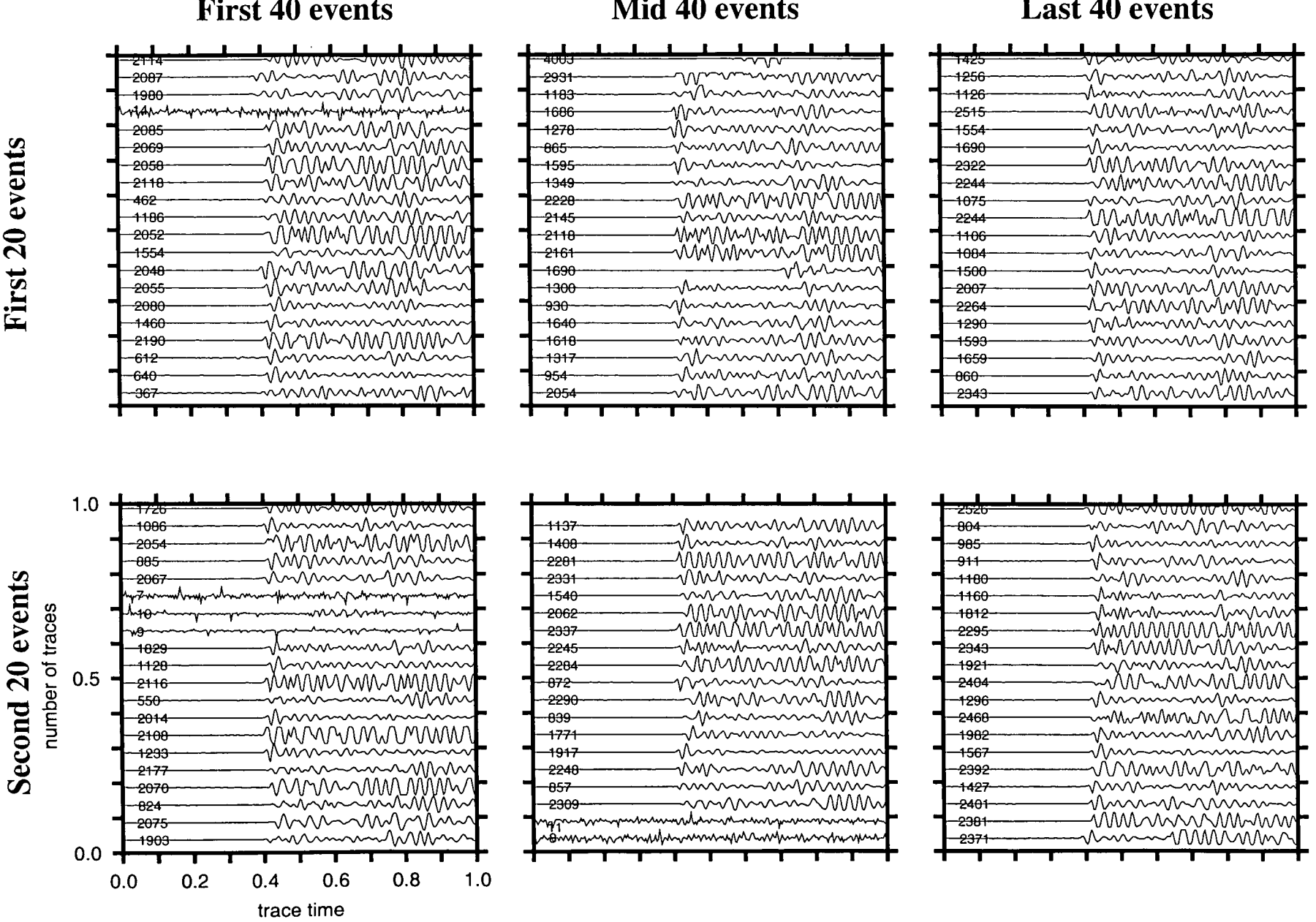

Waveform for events in multiplet sr004_01_95, for station ACR.

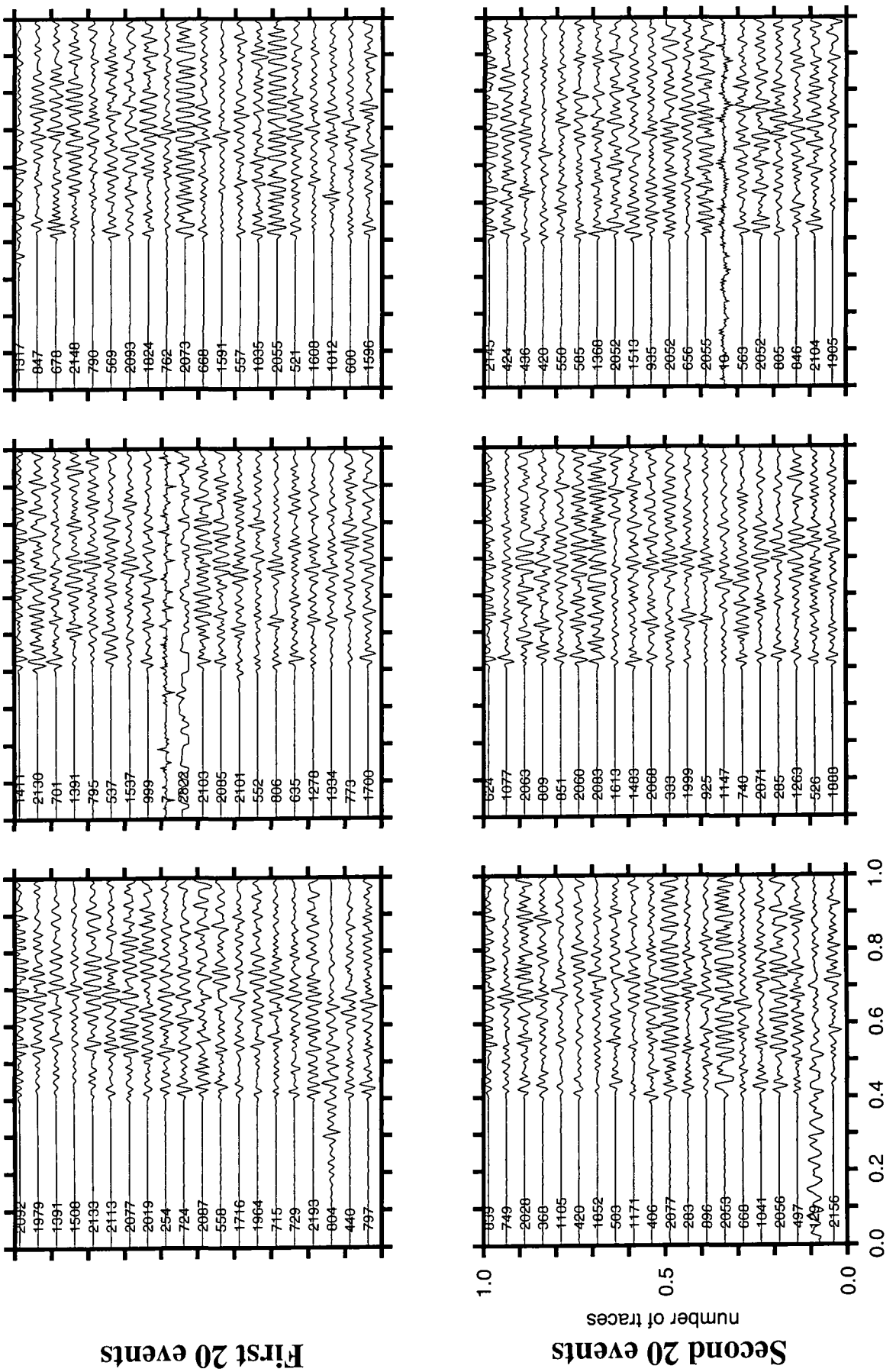

Waveform for events in multiplet sr004_01_95, for station ANG.

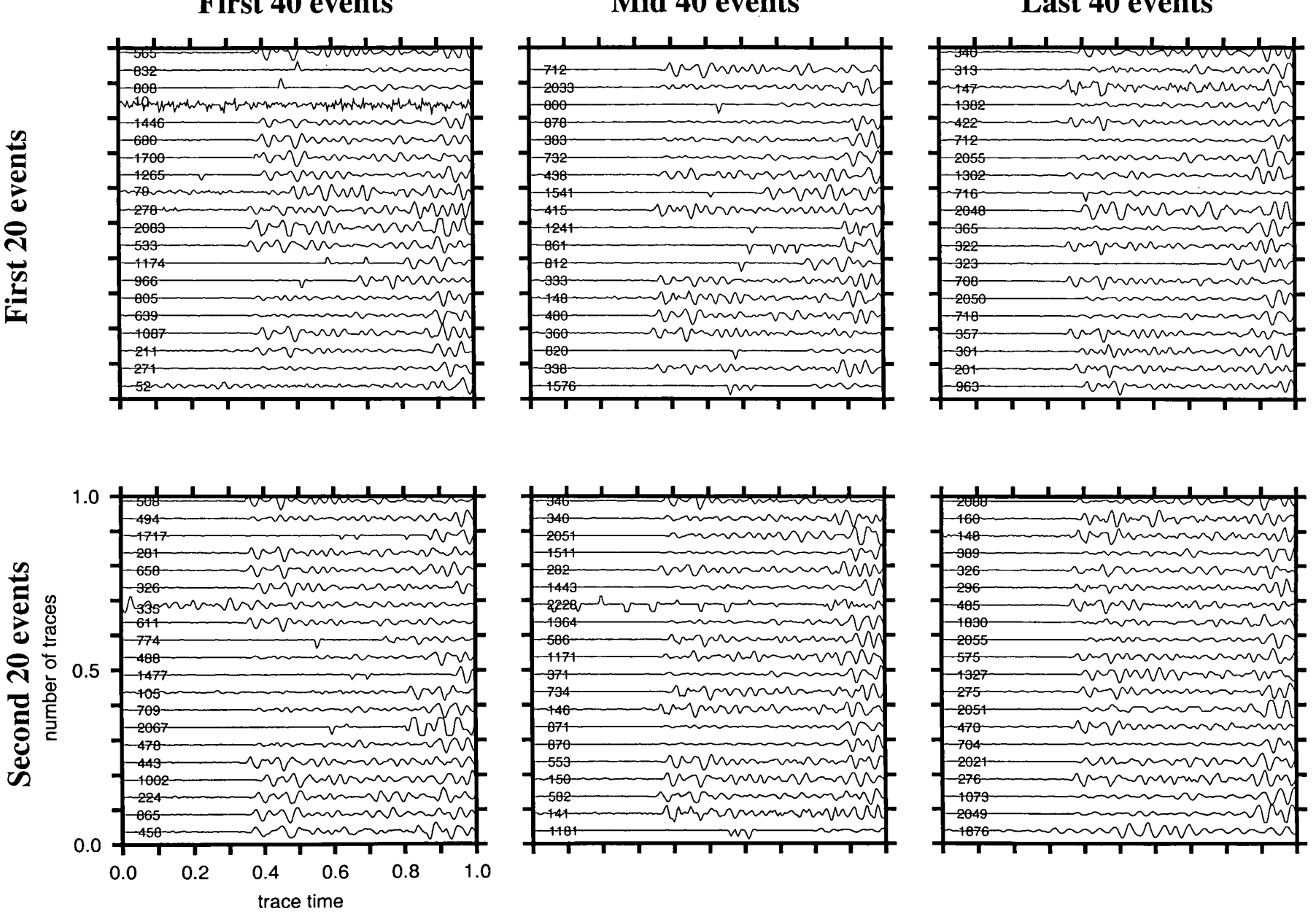

Waveform for events in multiplet sr004_01_95, for station CAP.

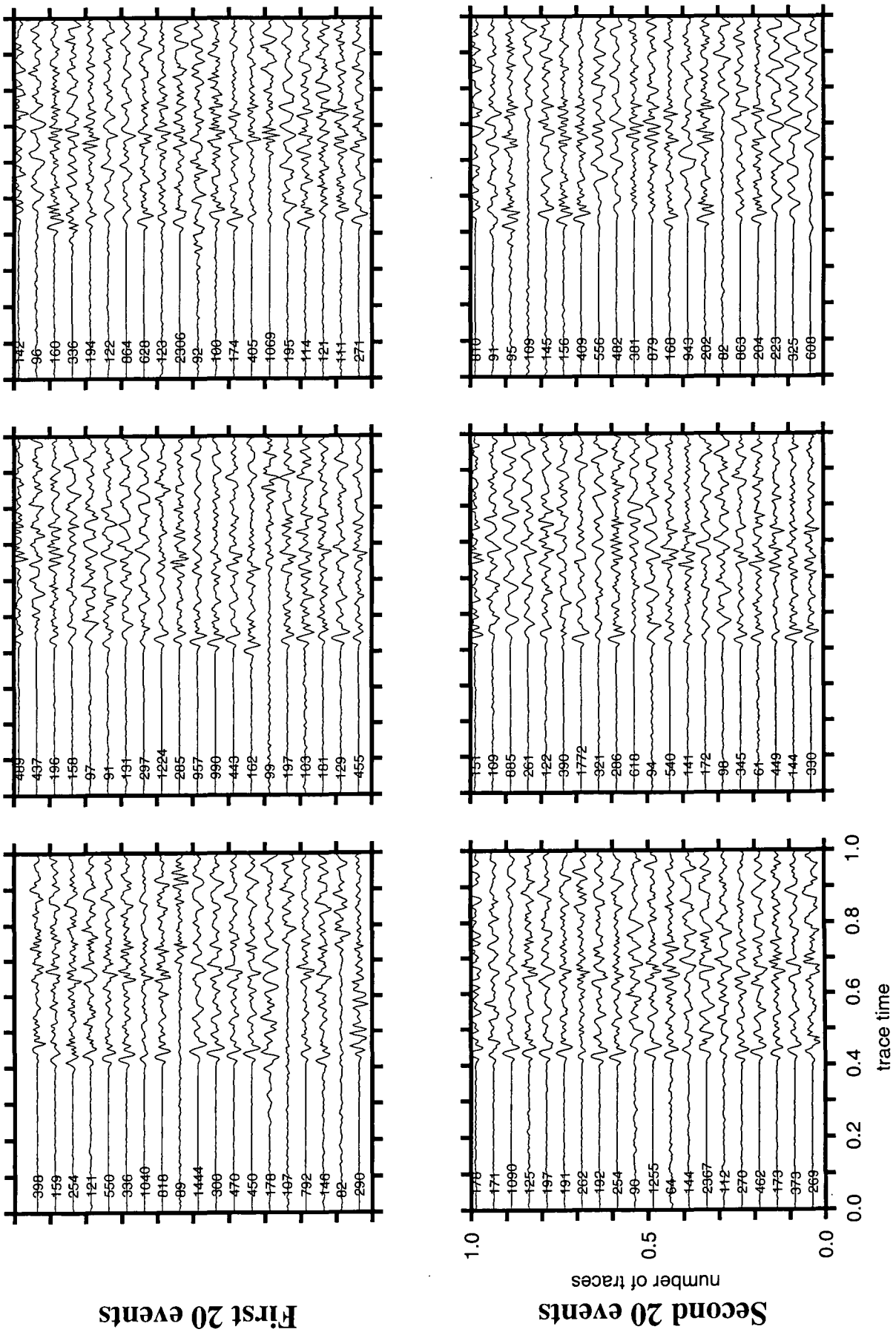

Waveform for events in multiplet sr004_01_95, for station SSR.

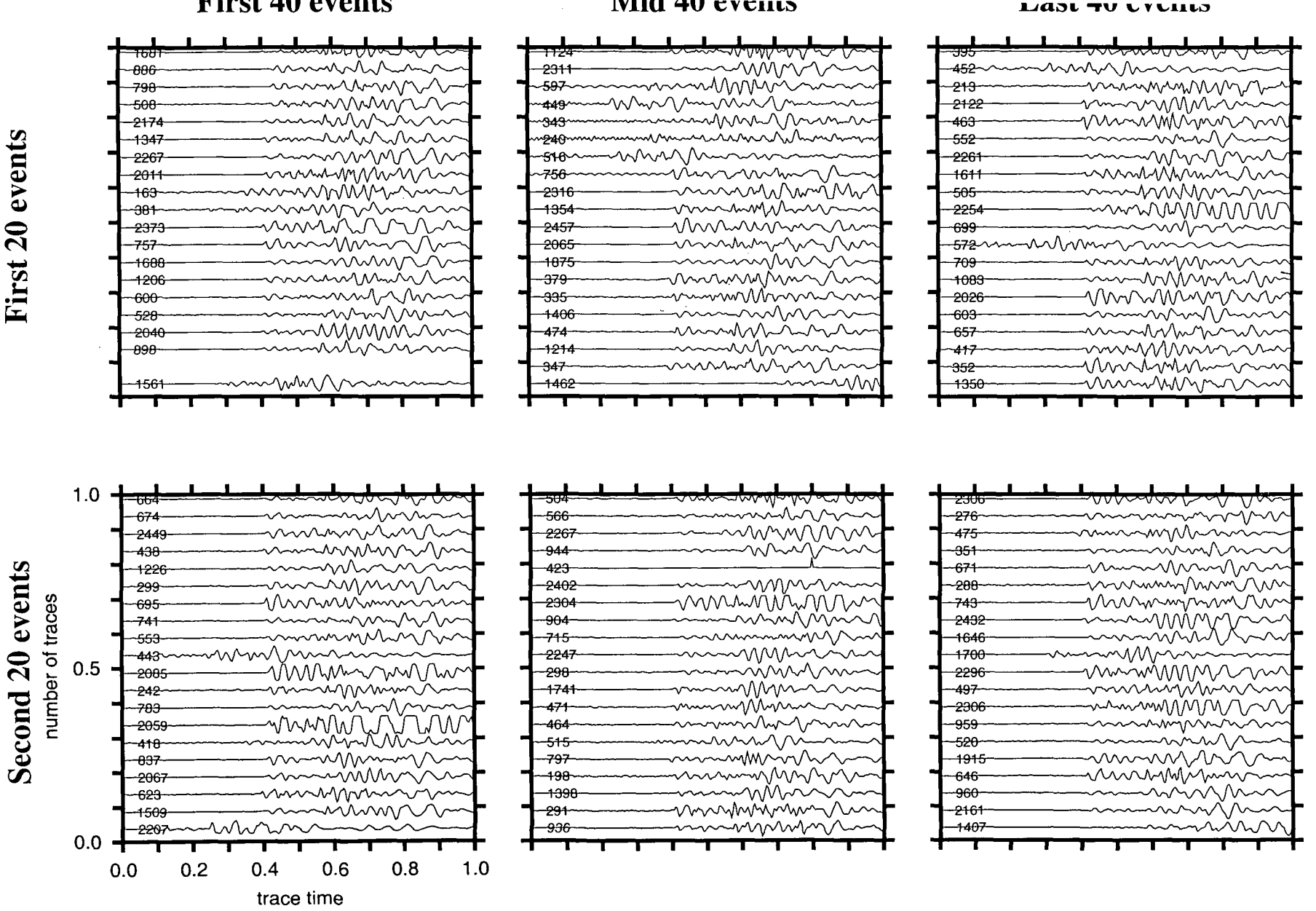

Waveform for events in multiplet sr004_01_95, for station TCH.